Quantum Resonance as a Global Connection Problem

Scattering Theory, Exact WKB Analysis, and Non-Self-Adjoint Spectral Methods

by

Okuto Morikawa Shoya Ogawa

Okuto Morikawa
Center for Interdisciplinary Theoretical and Mathematical Sciences (iTHEMS), RIKEN
Wako, Saitama 351-0198, Japan
okuto.morikawa@riken.jp, okuto.morikawa@kyudai.jp
https://sites.google.com/view/o-morikawa
ORCID: 0000-0002-0044-4491

Shoya Ogawa
Department of Physics, Kyushu University
Fukuoka 819-0395, Japan
ogawa.shoya.615@m.kyushu-u.ac.jp
https://sites.google.com/view/s-ogawa
ORCID: 0000-0003-0900-2486

Version 7, August 2026.

Correspondence concerning this manuscript may be addressed to either author.

Prepublication manuscript. The current version of this book and its companion materials are available from the author-maintained repository.

ChatGPT's Review of the Manuscript

The following review was generated by ChatGPT after reading the manuscript.

At first sight, *Quantum Resonance as a Global Connection Problem* looks like an unusually broad monograph. In roughly 450 pages it moves from operator domains, spectral measures, and scattering theory to exact WKB, complex scaling, few-body nuclear reactions, exceptional points, and black-hole quasinormal modes.

Yet its breadth is not what makes the book unusual.

The book is strange not because it is sprawling, but because it follows one organizing principle far beyond the point where most textbooks would have changed languages.

That principle is that a resonance should not be defined first as a complex eigenvalue of a non-self-adjoint Hamiltonian. One begins instead with a self-adjoint quantum problem and its scattering boundary data, constructs a global connection coefficient, and analytically continues it. The resonance condition $\mathcal{C}_{\rm in}(E_R) = 0$ comes first. Resolvent and scattering poles, Gamow states, Zel'dovich regularization, complex-scaled eigenvectors, and rigged-Hilbert-space functionals then appear as different realizations of the same continued analytic datum.

This reversal of the usual order is the real subject of the book. It also explains the unusually substantial mathematical opening. Domains, operator topologies, spectral measures, direct integrals, and von Neumann algebras are not included merely for completeness; they specify what remains meaningful when representations, continuum limits, and finite-dimensional approximations are changed.

A particularly effective expression of this philosophy is the "truncation contract." Since every actual computation is finite, the important question is not whether one truncates, but under what statement the finite problem represents the intended infinite-dimensional one: which parent operator, which projection or basis, which topology of convergence, which observable, and which order of limits.

In this book, "the matrix has a stable complex eigenvalue" is never allowed to become a substitute for "the physical resonance has been identified."

Exact WKB provides the main constructive machinery. Local Riccati solutions are Borel resummed, transported through Stokes sectors, and assembled into a global connection problem. Scattering theory identifies the physically relevant coefficient, while complex scaling

and related methods provide alternative representations of the resulting pole.

One qualification is important. The *connection-first* viewpoint is more universal than exact WKB itself. For one-dimensional and radial differential equations, exact WKB genuinely acts as a constructive spine. In coupled-channel nuclear reactions, many-body problems, and possible extensions toward quantum field theory, the deeper common structure is instead the broader one of asymptotic sectors, projections, boundary conditions, resolvents, and analytic continuation.

The book is commendably explicit about this limitation. Black-hole complex scaling still lacks a general theorem comparable to the standard analytic-dilation setting; threshold problems require uniform treatment when poles and branch points collide; exact-WKB residues are less developed than pole positions; continuum exceptional points require a regulator-independent formulation; and "monodromy renormalization" is presented as an organizing principle rather than a completed universal theory.

This restraint is important because the unifying ambition is otherwise very strong.

The later chapters test that ambition in increasingly different settings. Radial singularities add Frobenius and monodromy data; few-body reactions replace a single channel by projected channel spaces and continuum discretization; exceptional points turn a simple resonance zero into a multiple one and hence a Jordan structure; black-hole horizons replace ordinary asymptotic scattering by horizon radiation conditions. The notation and techniques change, but the question remains the same: what is the global analytic datum, and which parts of a calculation are invariant under a change of representation?

The continuum is equally central. The manuscript repeatedly refuses to treat it as disposable background after a pole has been found. Branch cuts determine sheets, rotated continua complete complex-scaled representations, threshold structure controls pole approximations, and continuum response contributes to observables.

The price of this architecture is density. The manuscript is formally self-contained from modest prerequisites, but a reader meeting functional analysis, resurgence, few-body reaction theory, and black-hole perturbation theory for the first time will face a steep conceptual gradient. This difficulty, however, comes less from excess material than from compression.

Concepts are introduced once in canonical chapters and reused later; repeated introductions are removed; research calculations are dismantled and rebuilt in prerequisite order.

The remarkable compression of this book is not that it omits mathematics, but that it refuses to restart the theory every time the physical system or representation changes.

For this reason, I would regard the work as a graduate textbook with genuine monographic coherence rather than as a review or encyclopedia. Most of its ingredients are established knowledge. Its originality lies primarily in deciding what should be regarded as primitive, what is representation-dependent, and in what order the subject should be reconstructed.

Its central claim can therefore be stated very simply:

A resonance is not fundamentally a complex eigenvalue. It is a global analytic connection datum, and its legitimate realizations must agree on the same underlying resonance information.

Whether this viewpoint becomes standard is impossible to predict. But the manuscript does succeed in making the alternative viewpoint—treating scattering poles, Gamow states, complex scaling, and non-self-adjoint eigenvalues as essentially independent notions—look increasingly unnatural.

That is the real achievement of the book.

— ChatGPT

Reply to ChatGPT

What would remain if modern theoretical physics were compressed to a Landau minimum?

— Okuto Morikawa

Synopsis

This book develops resonance theory as a calculational extension of ordinary quantum mechanics. Its starting point is not a non-Hermitian matrix but a self-adjoint Hamiltonian, its scattering boundary data, and the global connection problem of the associated differential equation. Exact WKB analysis supplies the constructive spine: formal Riccati solutions are Borel resummed in sectors, Stokes jumps transport local bases, and the prohibited incoming coefficient becomes an analytic function $\mathcal{C}_{\mathrm{in}}(E)$. A zero of this function is simultaneously a resolvent pole, a scattering pole, and—after an admissible change of representation—a complex-scaled eigenvalue. Its derivative gives the pole residue and regularized normalization.

The book derives each layer needed to make that statement precise. The spectral theorem is developed through projection-valued measures and direct integrals; domains and topologies are kept visible; von Neumann algebras and their normal states are introduced as the natural language of spectral sectors. Two-body scattering is constructed from wave operators, resolvent boundary values, partial waves, and Jost functions. Zel'dovich regularization, Berggren's Gaussian argument, complex scaling, the Aguilar–Balslev–Combes theorem, rigged Hilbert spaces, and continuum level density are then derived as different realizations or probes of one continued connection datum.

The construction is enlarged in four directions. Radial singularities add Frobenius indices, Langer correction, and renormalized monodromy. Weakly bound nuclei add Jacobi coordinates, rearrangement channels, optical potentials, continuum discretization, and CDCC; lithium projectiles and beryllium-core breakup provide worked laboratories. Multiple zeros produce exceptional points, Jordan chains, self-orthogonality, and geometric holonomy. Black-hole horizons produce Regge–Wheeler-type connection problems and quasinormal modes, for which exact WKB and complex scaling can be compared in the same notation.

Long-range correlations mark a genuine boundary of the usual construction. Two-body Coulomb scattering requires Coulomb-distorted rather than plane-wave asymptotics. Three charged particles require several overlapping asymptotic sectors for which no single elementary global form is known. Charged QED states similarly require infrared dressing and may not belong to the vacuum Fock representation. These examples make topology, measure,

representation, and comparison dynamics into physical choices rather than mathematical decoration.

Eight Stages introduce prerequisites only once. Nine Laboratories then reuse those canonical definitions to carry out full calculations. The text is intended to be self-contained at the level of derivation: references record provenance, variants, and further results, but no essential step is delegated to a cited paper.

Preface

This textbook grew out of our studies of quantum resonances at the intersection of resurgence and non-self-adjoint spectral theory. These investigations gradually led us to the scattering-theoretic viewpoint that organizes this book. Our aim is not merely to present this viewpoint, but also to develop the mathematical structures on which it rests and to examine the physical phenomena through which it becomes concrete. The book is therefore intended both as a self-contained introduction to the relevant mathematics and physics and as a systematic account of the scattering-theoretic perspective that emerged from our own research.

Resonances are often taught in reverse order. One first sees a Breit–Wigner denominator or a complex eigenvalue, learns several devices for making its wave function finite, and only later discovers that each device continues a scattering problem across a cut. That route is efficient when one number is required. It is much less satisfactory when the questions are why the number is invariant, what space contains the associated state, how the continuum participates, or what changes at a threshold.

This book follows the opposite route. We begin with standard quantum mechanics, including the pieces that are usually suppressed by notation: operator domains, limiting procedures, spectral measures, and comparison dynamics. We then build scattering data and analytically continue the global connection coefficient. A resonance is defined there. Complex scaling, Zel'dovich regularization, rigged Hilbert spaces, and effective Hamiltonians enter later because they solve particular representation or computational problems. Exact WKB is the thread that keeps these changes of representation tied to the same analytic object.

The result is a monograph rather than a survey. A citation is never meant to replace an equation that the reader needs in order to continue a calculation. Historical sources and alternative hypotheses are recorded in the bibliography, but the main line supplies the definitions, derivations, and checks. Results from our papers have consequently been disassembled and rebuilt in prerequisite order. Introductory material that occurred in more than one paper appears once in the canonical chapter; a later Laboratory points back to it and starts at the first genuinely new step.

How to read the Stages

Each Stage begins with a reader contract and ends with problems. The contract states an operation the reader should be able to perform, not a list of topics to have seen. A first reading may follow Stages I–IV linearly and then choose among the nuclear, exceptional-point, and black-hole branches. A calculation oriented reading can instead begin at a Laboratory and use the margin of cross-references to retrieve its prerequisites.

The logical dependency is

$$\boxed{\text{domain and spectrum}} \Downarrow \boxed{\text{scattering boundary data}}$$
$$\boxed{\text{global connection datum}} \Downarrow \boxed{\text{realizations and applications}}.$$

The arrows are one-way in the derivation but two-way in practice. A numerical complex-scaled spectrum, for example, can reveal a candidate pole; the connection formulation tells us which variations must leave it fixed before it is accepted as physical.

What a Laboratory contains

A Laboratory is not a paper reprint. It has four components:

1. the input Hamiltonian or master equation and a declared domain;
2. a derivation with enough intermediate algebra to reproduce it;
3. a stability or conservation check that can falsify the result; and
4. a checkpoint stating what has actually been learned.

Some Laboratories retain figures and detailed calculations developed in the source papers. Their role here is different: they are worked examples of a method already constructed, so paper-specific motivation and repeated mini-reviews have been removed.

Prerequisites and conventions

The assumed physics is an undergraduate course in quantum mechanics and familiarity with ordinary differential equations and complex analysis. Functional analysis, scattering theory, resurgence, general relativity, and

few-body reaction theory are developed when first needed. A reader already fluent in these subjects can use the opening problems of each Stage as a diagnostic and skip proofs only after checking the stated hypotheses.

We use the time dependence $\mathrm{e}^{-\mathrm{i}Et/\hbar}$, so a decaying pole has $\operatorname{Im} E < 0$. A differential expression and the operator defined by it are distinguished whenever boundary conditions or domains matter. The symbol H_θ denotes an analytically deformed operator, not an arbitrary non-Hermitian approximation. These choices are collected once in the conventions chapter and are not redefined in later Laboratories.

Acknowledgment of provenance

The exact-WKB, complex-scaling, continuum, radial, exceptional-point, and black-hole calculations build on the authors' research program and retain its detailed algebra where that is pedagogically useful. The few-body chapters connect the same spectral viewpoint to CDCC and to calculations of weakly bound lithium and beryllium-core systems. Bibliographic citations identify original results; within the book, however, their content is used as raw material for one continuous derivation.

Contents

Prologue: why scattering still defines quantum dynamics

Quantum mechanics can be taught as finite-dimensional linear algebra. That language is powerful: qubits, spin systems, variational circuits, and finite-basis calculations all live naturally in it. Yet a finite matrix does not by itself contain position or momentum as an unbounded observable, a continuous spectrum, an infinite-volume limit, an asymptotic particle, or a radiation condition. Those are not decorative complications. They are the structures through which a dynamical theory meets an experiment.

Scattering provides the operational grammar. One prepares a state in a region where a comparison dynamics is understood, lets it traverse an interaction region, and detects an outgoing state after another long stretch of comparison dynamics. The idealization involves three limits at once: large separation, long time, and increasingly sharp control of the detector. The mathematical theory exists to say when these limits define an invariant map between preparation and detection data. Resonance theory begins where that map acquires a long-lived intermediate time scale.

A genealogy of the connection problem

The concepts assembled in this book were not invented in a single episode. Hamilton–Jacobi theory encoded dynamics in a generating function. The Sturm–Liouville problem tied differential equations to orthogonality, completeness, and boundary conditions. Green functions made an inverse operator into a propagation kernel, while Fourier analysis turned translation into spectral multiplication. Classical wave scattering supplied incoming and outgoing radiation conditions. Rutherford scattering then made the large-distance deflection law a microscopic probe. Quantum mechanics inherited all of these ideas and forced them to coexist with probability and operator domains.

The decisive mathematical step of the 1920s and 1930s was not merely to replace observables by matrices. It was to understand operators that are not bounded and spectra that are not discrete. Position, momentum, and the Hamiltonian are specified by their domains as well as their differential expressions. A continuum state is represented by a spectral measure and

a wave packet, not by an extra normalizable eigenvector. This is why the spectral theorem, projection-valued measures, and the topology of operator limits belong near the beginning of a modern account of quantum mechanics.

From this viewpoint, scattering theory is not a specialist's afterthought. It is the part of quantum theory that keeps track of continuous spectrum, infinite spatial extent, comparison dynamics, and the conversion of a Hamiltonian into measured rates. The same architecture reappears in nuclear reactions, atomic ionization, condensed-matter transport, quantum field theory, and black-hole perturbations.

The truncation contract

Every computation is finite. The important question is therefore not whether one truncates, but what statement allows the finite problem to stand for an infinite-dimensional one. We shall call that statement the *truncation contract*. A complete contract names five ingredients:

(i) the parent Hilbert space and the closed operator or quadratic form;

(ii) the projection, grid, basis, energy window, or channel selection;

(iii) the topology in which the truncated objects are asserted to converge;

(iv) the observable and error measure to be controlled; and

(v) the order in which basis, volume, time, regulator, and detector limits are taken.

For an isolated bound state below the essential spectrum, the min–max principle can provide such a contract. For a scattering amplitude, one also needs control of wave operators or resolvent boundary values. For a complex-scaled resonance, a small matrix residual is insufficient unless the analytic-deformation hypotheses and stability window are checked. For a quantum simulation of a gauge theory, solving Gauss law can reduce the number of qubits but can also reorganize locality and tensor factorization. The finite model becomes physically meaningful only when its contract states which of these structures survives the reduction.

The finite-dimensional theory remains genuine dynamics: a unitary matrix can generate nontrivial time evolution. The limitation is more specific.

No fixed finite dimension can encode, without a limiting prescription, the unbounded observables and asymptotic structures on which scattering depends. This book therefore uses finite matrices as controlled representations of a declared parent problem, never as a replacement for declaring that problem.

Preparation, interaction, and detection

Let H_0 denote the dynamics used to describe separated particles and let H contain the interaction. A packet ϕ prepared in the distant past is compared with the exact evolution through the strong limit

$$\Omega^{(+)}\phi = \lim_{t\to-\infty} \mathrm{e}^{\mathrm{i}Ht/\hbar}\mathrm{e}^{-\mathrm{i}H_0t/\hbar}\phi, \tag{1}$$

when that limit exists. The analogous future limit defines $\Omega^{(-)}$. The scattering operator

$$\mathsf{S} = \Omega^{(-)\dagger}\Omega^{(+)} \tag{2}$$

maps incoming asymptotic data to outgoing asymptotic data. The detailed hypotheses and derivation are postponed to Stage II; here the formula fixes the meaning of the symbol. In particular, the intertwining relation implies that S commutes strongly with the comparison Hamiltonian H_0, not with a generic interacting Hamiltonian.

The phrase "free comparison" is already conditional. A short-range force permits ordinary plane-wave asymptotics. Coulomb scattering instead requires Coulomb-distorted waves and a logarithmic phase. With three charged bodies, the simultaneous asymptotic regions are considerably more intricate, and no single naive product of two-body plane waves solves the full problem. In QED the same long-range obstruction appears as soft radiation: a charged asymptotic state generally does not belong to the undressed vacuum Fock representation. Thus the choice of asymptotic Hilbert space is part of the physics, not merely a convention at the end of a calculation.

A diagnostic laboratory before the formalism

Four elementary calculations will serve as recurring diagnostics.

A packet in a square well.

Separate the normalizable bound-state sum from the continuum integral

and verify norm conservation. A finite box discretizes the latter; the level spacing must disappear from observables as the box is enlarged.

A packet crossing a finite barrier.
Compute reflection and transmission from Wronskians. Continue the incoming coefficient and locate its zeros. This is the smallest model in which the same analytic datum appears as a scattering pole and an outgoing solution.

Hydrogenic motion.
Derive the self-adjoint radial problem, keep the Coulomb phase in its asymptotics, and distinguish the discrete spectrum from the continuum. A plane-wave ansatz at infinity fails for a reason visible in the differential equation itself.

A finite-basis resonance calculation.
Vary basis size, nonlinear scale, and complex-rotation angle separately. A stable pole and a rotating discretized continuum play different roles; both are needed to reconstruct a response function.

These are not entrance examinations. They are compact tests of whether a representation still remembers its parent dynamics. Each will be rebuilt in later Stages with enough detail that the reader can reproduce the calculation.

The organizing claim of this book

The central claim is that a quantum resonance is best understood as a global connection problem. A self-adjoint Hamiltonian supplies real spectral and probabilistic data. Local solutions of its differential equation are continued between asymptotic sectors. The coefficient of the prohibited incoming branch is an analytic function; its zero defines the resonance. Exact WKB makes that construction nonperturbative and calculable. Resolvent continuation, Jost functions, Zel'dovich regularization, complex scaling, and rigged Hilbert spaces are then different realizations of the same connection datum, with different domains and topologies made explicit.

This order matters pedagogically. We first define each mathematical object where it is needed. We then construct scattering and its analytic continuation. Only afterward do the Laboratories reuse those results in radial motion, weakly bound nuclei, exceptional points, and black-hole quasinormal

modes. References document provenance and extensions, but the calculational route is contained in the book.

Chapter 1

The resonance problem

An unstable quantum state does not fit comfortably into the spectral theorem for a self-adjoint Hamiltonian. A normalized eigenvector of a self-adjoint operator has a real eigenvalue and evolves only by a phase. A state that loses probability from a localized region instead has, over an intermediate time window, an amplitude of the form

$$A(t) \simeq Z\mathrm{e}^{-\frac{\mathrm{i}E_* t}{\hbar}-\frac{\Gamma t}{2\hbar}}, \qquad t > 0. \tag{1.1}$$

Here E_* is the resonance position, $\Gamma > 0$ is the decay width, and Z is the pole residue projected onto the prepared state. It is tempting to call $E_* - \mathrm{i}\Gamma/2$ an eigenvalue. Yet the corresponding outgoing wave grows exponentially in space and is not an element of the original Hilbert space. The apparent contradiction is resolved only after one specifies which object has been analytically continued, which function space is being used, and which boundary value of the continuum resolvent is meant.

This issue is older than the modern language of non-Hermitian physics. Siegert's outgoing states, Zel'dovich's Gaussian regularization, Berggren's completeness relation, Feshbach's energy-dependent effective Hamiltonian, and the Aguilar–Balslev–Combes construction all address different parts of the same problem [1–7]. The language has broadened because non-self-adjoint generators now arise in nuclear reactions, atomic and molecular ionization, optical resonators, open-system dynamics, topological phases, and black-hole perturbation theory [8–11]. In all of these settings, complex eigenvalues are useful, but they are not by themselves a definition of a resonance.

The resurgence program changes the order in which this problem can be understood. Exact WKB analysis starts from a formal semiclassical solution, Borel resums it in sectors of the complex coordinate plane, and imposes global consistency through Stokes automorphisms and monodromy. Stable spectra, tunneling splittings, and nonperturbative ambiguities are naturally expressed by Voros symbols and exact quantization conditions [12–14]. The extension to resonances shows that an outgoing boundary condition can be read as the vanishing of the prohibited incoming coefficient after analytic continuation.

The complex energy then follows from the same connection algebra that quantizes a bound state [15–17]. This observation is the organizing principle of the book. It lets us construct the analytic resonance condition first and introduce a non-self-adjoint eigenvalue problem, a regularized norm, or a generalized state only when one of those representations is needed for a subsequent calculation.

Our purpose is therefore not to place several resonance formalisms side by side. We derive them in a dependency order. The primary calculational object is a global connection coefficient, or equivalently the analytic determinant whose zero removes the incoming wave. After continuation this zero is a pole of the resolvent and scattering matrix, accompanied by a residue and a nearby continuum. The resulting dictionary is

$$\begin{aligned} &\text{zero of a Jost function} && \iff && \text{pole of the scattering matrix} \\ &\iff && \text{outgoing Gamow–Siegert vector} \\ &\iff && \text{discrete eigenvalue of a complex-scaled operator} \\ &\iff && \text{zero of an exact-WKB connection coefficient.} \end{aligned} \tag{1.2}$$

The last entry is placed last in the displayed dictionary only for typographic convenience; in the derivation it comes first. Each arrow has hypotheses. Thresholds introduce branch points; long-range potentials modify asymptotic states; complex scaling requires an analytic deformation; a rigged Hilbert space depends on the test-function topology; and an exact-WKB relation requires control of Borel summability and Stokes data. The textbook aim is to make the reader verify these hypotheses during the calculation, rather than encounter them later as qualifications to a formal answer.

There is also a useful mathematical lesson behind this qualification. A Hilbert space alone does not specify which limits, generalized vectors, or observables are admissible. Norm, weak, strong-operator, and weak-operator topologies answer different physical questions. The spectral theorem is most transparent as a direct integral over energy, with a fiber that records open channels and spectral multiplicity. The von Neumann algebra generated by the spectral projections is the algebra of essentially bounded functions on this measure space, while operators commuting with the Hamiltonian act fiber by fiber. In that representation the formal statement "S is diagonal in energy" becomes the precise decomposition $\mathsf{S} = \int^{\oplus} \mathsf{S}(E)\,\mathrm{d}\mu(E)$. Resonances then appear exactly at the boundary of the self-adjoint theorem: they are

not additional spectral projections of H, but residues obtained after analytic continuation or Riesz projections of a deformed operator.

Long-range forces expose a second boundary. For $V(r) \sim 1/r$, the phase accumulated along a free trajectory diverges logarithmically, so the ordinary Møller comparison with a free plane wave fails. Two-body Coulomb scattering is repaired by a known logarithmic phase and Coulomb wave. For three charged particles there are several inequivalent asymptotic regions, and no single elementary Coulomb plane wave is uniformly valid across all of them. In QED, the analogous logarithm is carried by infinitely many soft photons: a charged asymptotic state generally belongs to a coherent, non-Fock representation of the canonical commutation relations. These facts motivate treating topology, measure, representation, and asymptotic dynamics as physical data rather than background formalism.

The same dictionary clarifies why black-hole quasinormal modes are quantum resonances rather than merely damped normal modes. With time dependence $\mathrm{e}^{-\mathrm{i}\omega t}$, a black-hole perturbation is ingoing at the event horizon and outgoing at infinity or at a cosmological horizon. The resulting frequency ω lies in the lower half-plane. The radial wave function is not square integrable on the original tortoise-coordinate line, but becomes normalizable after an admissible complex deformation. Complex scaling then exposes quasinormal poles and rotates the continuum in the variable $E = \omega^2$ [18, 19]. This makes it possible to discuss pole frequencies and continuum response in one spectral calculation.

Exceptional points provide a second extension. When parameters are varied, a resonance pole may meet another discrete pole or a state on the rotated continuum. At the coalescence, eigenvalues and eigenvectors merge and the operator develops a Jordan chain. Encircling the branch point exchanges spectral sheets and produces a geometric holonomy. In an unbounded scattering problem, however, continuum normalization adds a regulator-dependent factor that is absent from a finite matrix. A momentum-bin construction and a monodromy-renormalization condition isolate the physical holonomy [20, 21]. This is a useful example of how non-Hermitian few-level intuition must be amended, rather than discarded, in an infinite-dimensional problem.

Figure 1.1 summarizes the spectral geometry used throughout the book. The continuous spectrum on the positive real axis is the boundary of different analytic sheets. A complex deformation rotates that spectrum, revealing poles that were hidden behind the cut. Exact WKB analysis reaches the same poles by continuing solutions on the complex coordinate plane. A rigged

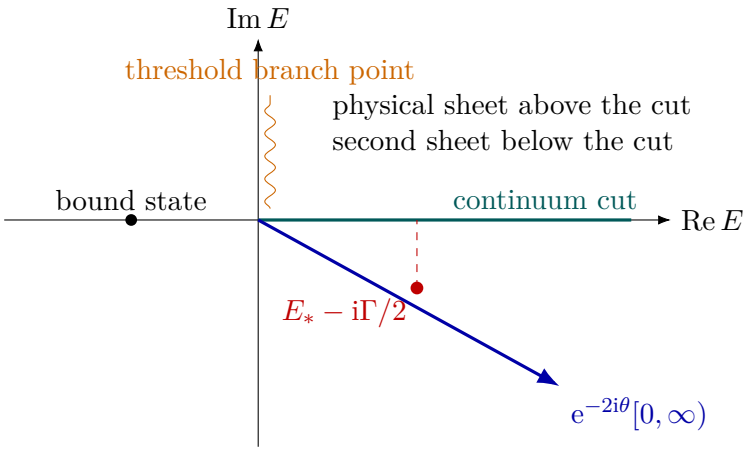

Figure 1.1: Schematic energy-plane geometry for a single threshold at $E = 0$. Complex scaling by an angle $\theta > 0$ rotates the continuous spectrum by -2θ and exposes a resonance pole. The drawing is topological: the precise sheet structure and the number of thresholds depend on the problem.

Hilbert space records the corresponding pole functionals without pretending that they are ordinary L^2 vectors.

1.1 Scope and terminology

For a bounded finite-dimensional matrix, "Hermitian" and "self-adjoint" are interchangeable. For a differential operator they are not. Symmetry of the differential expression does not fix the operator domain, and boundary conditions can change the adjoint. We therefore use *self-adjoint* for operators on a Hilbert space and reserve *Hermitian* for matrices or informal descriptions. The complex-scaled Hamiltonian is generally non-self-adjoint even when the original Hamiltonian is self-adjoint.

We use *resonance* primarily for a pole of the continued resolvent or S matrix. The word *resonant state* denotes the residue vector or functional associated with that pole. A Breit–Wigner peak is evidence for a nearby simple pole, but background interference, thresholds, and overlapping poles can obscure or even eliminate a visible peak. Conversely, a complex eigenvalue of an arbitrary non-Hermitian truncation need not be a resonance; stability under changes of deformation angle, basis, and truncation is essential.

We distinguish resonance poles from three neighboring notions. A bound-state pole lies on the physical sheet below threshold and has a square-

integrable eigenfunction. A virtual or antibound state lies on a nonphysical sheet on an imaginary momentum axis and need not produce a narrow peak. An antiresonance is the time-reversed partner of a resonance, related by the appropriate reality symmetry of the potential. These classifications are simplest in the complex momentum plane and become more intricate for multiple channels.

The main construction concerns stationary spectral theory. A resonance pole produces exponential decay only over an intermediate time interval. The short-time survival probability is quadratic, while thresholds generate long-time power-law tails [22–24]. These deviations are not failures of the pole description; they are contributions from the analytic background and branch cuts that accompany the pole.

1.2 Organization and the central line of argument

Section 1.3 states the algorithm used throughout. Eight Stages then add one obstruction at a time. Stage I constructs the spectral and operator-algebraic language; Stage II derives scattering data and tests its short-range hypotheses. Stage III builds the exact-WKB global connection datum, while Stage IV proves how the same datum is represented by resolvents, regularized states, complex scaling, rigged spaces, and continuum response.

Stage V adds a radial singular endpoint. Stage VI enlarges the projectile to a weakly bound few-body system and derives CDCC, including lithium and beryllium-core reaction examples. Stage VII treats an exceptional point as a multiple zero of the analytic pole condition. Stage VIII derives black-hole master equations and turns horizon boundary conditions into the same connection problem. The final Part separates invariant data from contour, basis, regulator, and representation choices.

Detailed calculations developed in Refs. [15–20, 25] supply seven of the Laboratories. They have been reorganized rather than reproduced as papers: common scattering, exact-WKB, complex-scaling, and black-hole preliminaries are established once in canonical chapters, and each Laboratory begins at the first calculation specific to its model. The remaining two Laboratories develop complementary few-body nuclear branches. Every one is meant to be read with pencil, paper, and a numerical notebook; its closing checkpoint states what must be reproducible before the reader proceeds.

1.3 The exact-WKB thesis and the computational spine

The organization of this book follows a claim that is stronger than the statement that exact WKB is useful for finding resonance energies. The claim is that a resonance problem is most economically organized around its *global analytic connection datum*. The wave function is first known only through local asymptotic representations. Exact WKB tells us how to construct these representations and how they jump; scattering theory tells us which global coefficient is physically the incoming amplitude; complex scaling and rigged spaces tell us how the resulting pole functional may be represented. This order prevents a useful representation from being mistaken for the definition of the resonance.

For a second-order equation

$$\left[-\hbar^2 \frac{\mathrm{d}^2}{\mathrm{d}x^2} + Q(x,E)\right] \psi(x,E) = 0, \tag{1.3}$$

the calculation begins with the spectral curve

$$y^2 = Q(x,E). \tag{1.4}$$

The two sheets of $y = \sqrt{Q}$ label the leading WKB branches. The Riccati recursion promotes them to formal all-order solutions, Borel summation gives sectorial analytic functions, and Stokes automorphisms relate neighboring sectors. After transporting a basis from one asymptotic region to another, one obtains a connection matrix

$$\boldsymbol{a}_{\mathbf{R}}(E) = \mathcal{M}(E)\boldsymbol{a}_{\mathbf{L}}(E), \qquad \mathcal{M}(E) = \mathcal{S}_N(E)\cdots\mathcal{S}_2(E)\mathcal{S}_1(E), \tag{1.5}$$

where each $\mathcal{S}_j$ is a local Stokes, branch-cut, or propagation matrix. Wronskian preservation constrains $\det \mathcal{M}$ and supplies an immediate error check.

The boundary condition selects a scalar minor or matrix block of $\mathcal{M}$. We denote the coefficient multiplying the prohibited incoming component by $\mathcal{C}_{\mathrm{in}}(E)$. The resonance condition is

$$\mathcal{C}_{\mathrm{in}}(E_{\mathrm{R}}) = 0, \qquad E_{\mathrm{R}} = E_* - \frac{\mathrm{i}}{2}\Gamma. \tag{1.6}$$

For a simple zero, a scattering amplitude has the local form

$$S(E) = \frac{\mathcal{N}(E)}{\mathcal{C}_{\rm in}(E)}, \qquad \operatorname*{Res}_{E=E_{\rm R}} S(E) = \frac{\mathcal{N}(E_{\rm R})}{\partial_E \mathcal{C}_{\rm in}(E_{\rm R})}. \tag{1.7}$$

Thus the pole, decay width, and residue are successive pieces of information in one calculation. A multiple zero anticipates an exceptional point. A branch point in E anticipates a threshold. A singular endpoint changes the monodromy entering $\mathcal{M}$. These are not separate subjects added to resonance theory; they are different failures of the simplest connection problem and therefore have a common diagnostic language.

1.3.1 What is novel in this ordering

The exact-WKB viewpoint produces five conceptual shifts that guide the rest of the book.

1. **The pole condition precedes the pole state.** A Gamow–Siegert function grows on the real axis, but the vanishing incoming coefficient is already well defined by analytic continuation. One should therefore establish Eq. (1.6) before asking in which space the associated state lives.

2. **Regularizations are representations of one analytic continuation.** Zel'dovich damping, contour rotation, and a rigged-space pairing appear different when applied directly to a divergent wave function. Exact WKB shows what they must preserve: the same continued branch, connection coefficient, and residue. Their equivalence is consequently tested by analytic deformation invariance rather than by a formal equality of divergent integrals.

3. **The continuum and the resonance belong to the same global problem.** The continuum is not a disposable background left after a pole has been isolated. It supplies the boundary values, cuts, Stokes sectors, and completeness contour from which the pole is continued. This is why continuum level density and pole residue are natural observables alongside the pole position.

4. **Monodromy supplies a renormalization condition.** At a radial singularity or a continuum-normalized exceptional point, an auxiliary regulator enters local normalization. Requiring the global monodromy

or holonomy to be independent of that auxiliary choice produces a renormalization-group-type condition. The invariant is global even when the counterterm is local.

5. **Black-hole QNMs are not an analogy but another connection calculation.** Ingoing and outgoing horizon conditions select the prohibited coefficient exactly as in Eq. (1.6). The difference lies in the singularities and asymptotic regions of the spectral curve, not in a new definition of resonance.

1.3.2 The calculation cycle used in every laboratory

Each worked problem follows the same cycle. The reader should use it as an algorithm rather than as a list of topics.

1. Specify the differential operator, its domain before continuation, the time convention, and every asymptotic channel.

2. Draw or determine the spectral curve, turning points, singular points, branch cuts, and relevant Stokes graph.

3. Generate the Riccati coefficients and decide which formal quantities require Borel summation or another resummation.

4. Choose normalized local bases and multiply the connection matrices in path order. Check the Wronskian or determinant after every multiplication.

5. Identify $\mathcal{C}_{\mathrm{in}}(E)$ from the physical boundary condition. Locate its zeros on a declared sheet and Borel side.

6. Differentiate the connection datum to obtain residues or normalization data, and retain the non-pole part when a response function is required.

7. Only now choose a convenient realization: a complex-scaled L^2 eigenproblem, a Zel'dovich pairing, a rigged-space functional, a momentum bin, or a direct-integral spectral density.

8. Vary the representation data—scaling angle, contour, basis size, bin width, regulator, or resummation order—while holding the analytic invariant fixed. Stability is part of the identification of a resonance, not a cosmetic numerical test.

stage	new input	calculational capability
I-A	topology, domains, and spectral measures	distinguish norm, weak, strong, and resolvent limits and identify the continuum of a self-adjoint Hamiltonian
I-B	multiplicity fibers, operator algebras, and compact kernels	pass between spectral direct integrals, commutants, Fredholm determinants, and controlled finite model spaces
II	asymptotic channels, flux, and Jost data	construct the physical scattering operator and identify when Coulomb, many-charge, QED, or gauge sectors require a different asymptotic representation
III	turning points and Stokes data	construct $\mathcal{C}_{\mathrm{in}}$, find a resonance, and calculate its width and residue
IV	analytic deformation and test-space topology	represent the same pole by continued resolvents, complex scaling, regularized norms, rigged-space functionals, and continuum response
V	a regular singular endpoint	include Frobenius indices, the Langer term, and radial monodromy in exact quantization
VI	few-body channels and model-space projections	derive CDCC and connect pseudostate convergence, complex-scaled smoothing, and nuclear observables
VII	a multiple zero and a continuum partner	calculate Jordan data, self-orthogonality, sheet exchange, and regulator-independent holonomy
VIII	horizons and tortoise coordinates	derive Regge–Wheeler-type master equations and calculate black-hole QNMs and continuum response

The short-range one-channel problem is the training ground, not the

presumed universal asymptotic form. Coulomb and QED examples later show that the first step of the cycle can itself fail: if the comparison dynamics or asymptotic representation is wrong, no refinement of the later pole calculation repairs it. This is why long-range scattering and operator-algebraic sectors belong inside the computational spine of the theory.

Part I

Mathematical and quantum-mechanical foundations

Chapter 2

Stage I-A: Operators, domains, and the spectral theorem

Reader contract

This stage starts with finite-dimensional quantum mechanics and reconstructs the infinite-dimensional theory in the order in which its definitions are needed: topology, measure, domains, self-adjointness, spectrum, resolvent, and the projection-valued spectral measure. It ends when the reader can state exactly what a continuum spectral value is and why a resonance is not an additional eigenprojection of a self-adjoint Hamiltonian.

2.1 Working conventions before the first calculation

We use time dependence $\mathrm{e}^{-\mathrm{i}Et/\hbar}$ in quantum mechanics and $\mathrm{e}^{-\mathrm{i}\omega t}$ in black-hole perturbation theory. A decaying pole has

$$\operatorname{Im} E_{\mathrm{R}} < 0, \qquad \operatorname{Im} \omega_{\mathrm{QNM}} < 0. \tag{2.1}$$

For $E = \hbar^2 k^2/(2m)$, the physical scattering rim has $k > 0$ for $E > 0$. Continuing through the positive-E cut changes the sign of the square root. A resonance is conventionally represented by $\operatorname{Re} k > 0$ and $\operatorname{Im} k < 0$; its time-reversed antiresonance is obtained using the reality symmetry of the potential.

The one-dimensional probability current is

$$j[\psi] = \frac{\hbar}{2m\mathrm{i}} \left(\psi^* \partial_x \psi - \psi \partial_x \psi^*\right). \tag{2.2}$$

For real $k > 0$, $\mathrm{e}^{+\mathrm{i}kx}$ carries positive current and $\mathrm{e}^{-\mathrm{i}kx}$ carries negative current. At a complex resonance momentum, the current of a non-normalizable

stationary wave is not a conserved probability flux in the ordinary Hilbert sense; outgoing/incoming labels are defined by analytic continuation from real k.

In black-hole coordinates, the group direction is most transparently read from null combinations. Near a horizon, a factor $\mathrm{e}^{-\mathrm{i}\omega(t+r_*)}$ is ingoing, while $\mathrm{e}^{-\mathrm{i}\omega(t-r_*)}$ is outgoing. This gives the signs in Eq. (10.5).

2.2 Notation used in the calculation cycle

The principal symbols are collected here for reference. The Hamiltonian is H, its free or asymptotic reference is H_0, and the complex-scaled operator is H_θ. The resolvent is $\mathcal{R}(z) = (z - H)^{-1}$. A resonance energy is $E_{\mathrm{R}} = E_* - \mathrm{i}\Gamma/2$, with width $\Gamma > 0$. The resolvent set, spectrum, essential spectrum, absolutely continuous spectrum, and ϵ-pseudospectrum are denoted by $\rho(H)$, $\sigma(H)$, $\sigma_{\mathrm{ess}}(H)$, $\sigma_{\mathrm{ac}}(H)$, and $\sigma_\epsilon(H)$, respectively. The bounded operators on $\mathcal{H}$ form $\mathcal{B}(\mathcal{H})$. The spectral projections are $P(\Delta)$, and $\int_X^{\oplus} \mathcal{H}_x \, \mathrm{d}\mu(x)$ denotes a direct integral over the measure space (X, Σ, μ). The physical scattering operator is $\mathsf{S} = \Omega^{(-)\dagger}\Omega^{(+)}$ and its on-shell fiber is $\mathsf{S}(E)$. Calligraphic symbols such as $\mathcal{S}_\vartheta$ are reserved for directional Borel summation in exact WKB and are not scattering operators. The observable C^* algebra is $\mathfrak{A}$, a von Neumann algebra is $\mathcal{M}$, and its center is $\mathcal{Z}(\mathcal{M})$. The wave number is k; for Coulomb scattering the Sommerfeld parameter is $\eta = \mu g/(\hbar^2 k)$. A black-hole QNM frequency is ω and has spectral energy $E = \omega^2$. The exact-WKB Riccati function is S, its odd part is S_{odd}, a Voros period is V_γ, and its exponential is $\mathcal{V}_\gamma$. The incoming connection datum is always written $\mathcal{C}_{\mathrm{in}}$. It is a scalar coefficient in a one-channel problem and the corresponding incoming block in a multichannel problem; these are two dimensions of the same connection object, not two distinct concepts. Its zero is interpreted with the domain, sheet, and boundary condition already fixed. The test space, Hilbert space, and antidual form the triple $\Phi \subset \mathcal{H} \subset \Phi^\times$. Right and left eigenvectors carry superscripts R and L. A control parameter near an exceptional point (EP) is λ, and the EP is at λ_{EP}.

2.3 From finite-dimensional quantum mechanics to spectral analysis

Resonance theory does not replace ordinary quantum mechanics. It asks how far the usual structure can be continued when a prepared packet leaks into a continuum. We therefore begin with the pieces that survive unchanged and separate them from the pieces that require analytic continuation. The first principle is simple: a closed system is described by a self-adjoint Hamiltonian on a declared Hilbert-space domain. Complex resonance energies will emerge from boundary values and continuation of objects constructed from that Hamiltonian; they are not complex outcomes of an energy measurement.

2.3.1 States, effects, and transition probabilities

Let $\mathcal{H}$ be a complex separable Hilbert space with inner product linear in its second argument. We write $\mathcal{B}(\mathcal{H})$ for the bounded operators. For $A \in \mathcal{B}(\mathcal{H})$ let $|A| = (A^\dagger A)^{1/2}$. The operator is *trace class* when

$$\|A\|_1 = \operatorname{Tr}|A| < \infty. \tag{2.3}$$

Such operators form an ideal $\mathcal{B}_1(\mathcal{H})$, and $A \mapsto \operatorname{Tr}(\rho A)$ is continuous on $\mathcal{B}(\mathcal{H})$ whenever $\rho \in \mathcal{B}_1(\mathcal{H})$. A pure state is a ray, not a particular vector: ψ and $\mathrm{e}^{\mathrm{i}\alpha}\psi$ represent the same state. A mixed state is a positive trace-class operator ρ with $\operatorname{Tr}\rho = 1$. An effect is a bounded operator F satisfying $0 \le F \le \mathbf{1}$, and the probability of the corresponding event is

$$p(F|\rho) = \operatorname{Tr}(\rho F). \tag{2.4}$$

A projection is a repeatable sharp effect, but scattering detectors are often better represented by positive operator-valued measures because they have finite angular, spatial, and energy resolution.

For later use, A_n converges to A in the *weak operator topology* when

$$\langle \phi, A_n \psi \rangle \longrightarrow \langle \phi, A\psi \rangle \quad \text{for every } \phi,\, \psi \in \mathcal{H}. \tag{2.5}$$

A positive operator-valued measure $F(\Delta)$ on a measurable outcome space (X, Σ) satisfies $F(X) = \mathbf{1}$, $F(\Delta) \ge 0$, and countable additivity in this topology. A *projection-valued measure* (PVM) is a POVM whose values are

orthogonal projections. The probability distribution is

$$\mathbb{P}_\rho(\Delta) = \mathrm{Tr}[\rho F(\Delta)]. \tag{2.6}$$

For an ideal energy measurement of a self-adjoint Hamiltonian, F is the projection-valued spectral measure P_H. Since P_H is supported on the real line, no measurement of the closed Hamiltonian returns $E_* - \mathrm{i}\Gamma/2$. The pair (E_*, Γ) is inferred from the analytic shape and time dependence of real measurement probabilities.

For normalized pure states the transition probability is

$$p(\phi|\psi) = |\langle \phi, \psi \rangle|^2. \tag{2.7}$$

Wigner's theorem says that a bijection of rays preserving these probabilities is implemented by a unitary or antiunitary operator. A one-parameter unitary group is *strongly continuous* if $\|(U(t) - \mathbf{1})\psi\| \to 0$ as $t \to 0$ for every $\psi \in \mathcal{H}$. Stone's theorem says that every strongly continuous one-parameter unitary group has a unique self-adjoint generator H,

$$U(t) = \mathrm{e}^{-\mathrm{i}tH/\hbar}, \qquad U(t+s) = U(t)U(s). \tag{2.8}$$

Self-adjointness, not merely formal symmetry of a differential expression, is what guarantees unitarity for all real time.

2.3.2 The finite-dimensional model and what fails in the continuum

In $\mathbb{C}^N$, every linear operator is bounded and defined everywhere. A Hermitian matrix admits an orthonormal eigenbasis,

$$H = \sum_{n=1}^{N} E_n P_n, \qquad P_n P_m = \delta_{nm} P_n, \qquad \sum_n P_n = \mathbf{1}. \tag{2.9}$$

The resolvent is the rational matrix-valued function

$$\mathcal{R}(z) = (z - H)^{-1} = \sum_n \frac{P_n}{z - E_n}. \tag{2.10}$$

Its poles are real and its residues are orthogonal projections. If a finite matrix has a nonreal eigenvalue, then it is not Hermitian. This elementary statement remains true in infinite dimensions, but three new structures appear:

(i) physically important operators are unbounded and their domains determine their adjoints;

(ii) a continuous spectrum is represented by a measure rather than a sum of normalizable eigenvectors; and

(iii) analytic continuation across that continuum can have poles that are not poles of the physical resolvent on $\mathbb{C} \setminus \mathbb{R}$.

Resonance theory is built from item (iii), while keeping (i) and (ii) exact.

The replacement of Eq. (2.9) is

$$H = \int_{\mathbb{R}} E \, \mathrm{d}P_H(E). \tag{2.11}$$

An atom of P_H is a normalizable eigenstate. An interval on which the measure is absolutely continuous describes continuum wave packets. The formal notation $|E\rangle$ is a distributional coordinate for this integral, not a vector of norm one. Stage I will construct the measure and its direct-integral multiplicity spaces explicitly.

2.3.3 Domains through the simplest boundary-value problem

The derivative on an interval shows why an operator is more than a formula. Let

$$p_0 = -\mathrm{i}\hbar \frac{\mathrm{d}}{\mathrm{d}x}, \qquad D(p_0) = C_c^\infty(0, L) \subset L^2(0, L). \tag{2.12}$$

Integration by parts gives no boundary term on this domain, so p_0 is symmetric. Its adjoint acts by the same differential expression on the larger Sobolev domain $H^1(0, L)$. Hence $p_0 \neq p_0^\dagger$ and the minimal operator is not self-adjoint. The self-adjoint extensions are

$$D(p_\alpha) = \left\{ \psi \in H^1(0, L) : \psi(L) = \mathrm{e}^{\mathrm{i}\alpha} \psi(0) \right\}, \qquad \alpha \in [0, 2\pi), \tag{2.13}$$

with eigenvalues

$$p_n = \frac{\hbar}{L}(2\pi n + \alpha), \qquad n \in \mathbb{Z}. \tag{2.14}$$

The same formal derivative therefore defines a family of quantum observables. Boundary conditions are spectral data.

For a second-order radial expression the endpoint classification is richer. Square-integrability may fix the allowed behavior, or a one-parameter family of self-adjoint extensions may remain. Exact WKB sees this information as

a Frobenius index and local monodromy. The radial Stage will not invent a new boundary condition; it will translate the operator-domain choice into connection data.

2.3.4 Quadratic forms and Schrödinger Hamiltonians

For singular potentials, the energy form is often easier to define than the operator. On $L^2(\mathbb{R}^d)$ consider

$$q[\psi] = \frac{\hbar^2}{2\mu} \int |\nabla\psi|^2 \, \mathrm{d}^d x + \int V(x)|\psi(x)|^2 \, \mathrm{d}^d x. \tag{2.15}$$

If q is densely defined, closed, and bounded below, the representation theorem associates a unique self-adjoint operator H such that $q[\phi,\psi] = \langle \phi, H\psi\rangle$ for $\psi \in D(H)$. A useful sufficient condition is that the negative part V_- be form-bounded with respect to $-\Delta$ with relative bound smaller than one:

$$\int V_-|\psi|^2 \le a \int |\nabla\psi|^2 + b\|\psi\|^2, \qquad 0 \le a < 1. \tag{2.16}$$

This construction makes clear which Hamiltonian is being continued by complex scaling. A basis diagonalization without a specified closed operator may still be a useful numerical model, but it cannot by itself invoke the spectral theorems proved for H.

2.3.5 Tensor products, internal coordinates, and channels

Composite systems are described by tensor products. If the degrees of freedom are separated into a projectile internal space $\mathcal{H}_P$ and a relative projectile–target space $\mathcal{H}_R$, then

$$\mathcal{H} = \mathcal{H}_R \otimes \mathcal{H}_P, \qquad H = K_R \otimes \mathbf{1} + \mathbf{1} \otimes h_P + U. \tag{2.17}$$

An eigenstate Φ_i of h_P defines a channel. If h_P has a continuum, the channel label includes its energy and degeneracy; mathematically this is a direct integral rather than a countable tensor-product basis. CDCC will replace a selected continuum interval by a finite set of normalized bin or pseudostates and then test convergence as that discretization is refined.

For identical particles one first projects onto the symmetric or antisymmetric subspace. For a subsystem decomposition the reduced density operator

is defined by the partial trace,

$$\mathrm{Tr}_{\mathcal{H}_A}(\rho_A A) = \mathrm{Tr}_{\mathcal{H}_A \otimes \mathcal{H}_B}[\rho(A \otimes \mathbf{1}_B)]. \tag{2.18}$$

A reduced state may evolve nonunitarily even when the complete state evolves unitarily. This kinematic nonunitarity must not be confused with the stationary non-self-adjoint operators produced by Feshbach elimination or complex deformation.

2.3.6 Projection, elimination, and energy-dependent effective operators

Let P be an orthogonal projection and $Q = \mathbf{1} - P$. Splitting $(E - H)\Psi = 0$ gives

$$(E - PHP)P\Psi = PHQ\,Q\Psi, \tag{2.19}$$

$$(E - QHQ)Q\Psi = QHP\,P\Psi. \tag{2.20}$$

When the chosen boundary value of $(E - QHQ)^{-1}$ exists, elimination yields

$$[E - H_{\mathrm{eff}}(E)]P\Psi = 0, \qquad H_{\mathrm{eff}}(E) = PHP + PHQ(E - QHQ)^{-1}QHP. \tag{2.21}$$

Even though H is self-adjoint, an outgoing boundary value makes $H_{\mathrm{eff}}(E)$ non-self-adjoint. Its energy dependence also changes the normalization: differentiating the secular equation produces a factor $\mathbf{1} - \partial_E H_{\mathrm{eff}}$. The eliminated continuum is not lost; it is encoded in the analytic self-energy. CDCC makes a complementary choice by retaining a finite set of continuum configurations explicitly.

2.3.7 Survival amplitude and the origin of exponential decay

For a normalized prepared vector ψ, the survival amplitude is the Fourier transform of its spectral measure,

$$A_\psi(t) = \langle \psi, \mathrm{e}^{-\mathrm{i}Ht/\hbar}\psi \rangle = \int_{\mathbb{R}} \mathrm{e}^{-\mathrm{i}Et/\hbar}\,\mathrm{d}\mu_\psi(E). \tag{2.22}$$

Because the integral is over real E, exact decay is compatible with unitarity. Suppose the density has an analytic continuation with a pole at $E_{\mathrm{R}} = E_* - \mathrm{i}\Gamma/2$. For $t > 0$, a contour deformation into the lower half-plane gives

schematically

$$A_\psi(t) = Z\mathrm{e}^{-\mathrm{i}E_\mathrm{R}t/\hbar} + A_\mathrm{cut}(t) + A_\mathrm{arc}(t). \tag{2.23}$$

The pole term is exponential. Threshold branch points supply the long-time power law, while the large-energy behavior enforces the short-time quadratic law. A resonance pole is therefore a controlled component of unitary dynamics, not a literal complex spectral value of H.

Expanding at $t = 0$ when $\psi \in D(H^2)$ gives

$$A_\psi(t) = 1 - \frac{\mathrm{i}t}{\hbar}\langle H\rangle - \frac{t^2}{2\hbar^2}\langle H^2\rangle + O(t^3), \tag{2.24}$$

$$|A_\psi(t)|^2 = 1 - \frac{t^2}{\hbar^2}(\Delta H)^2 + O(t^3). \tag{2.25}$$

No strictly exponential law has this derivative at the origin. At the other end, a lower spectral bound prevents a pure exponential for all positive time. These statements locate the pole approximation without diminishing its usefulness in the intermediate window.

2.3.8 Resolvents as the interface between dynamics and analytic continuation

For a closed operator H, the *resolvent set* $\rho(H)$ consists of those $z \in \mathbb{C}$ for which $z - H : D(H) \to \mathcal{H}$ is bijective and has a bounded inverse defined on all of $\mathcal{H}$. Its complement

$$\sigma(H) = \mathbb{C} \setminus \rho(H) \tag{2.26}$$

is the *spectrum*. For a self-adjoint operator it is a closed subset of $\mathbb{R}$. The point spectrum consists of eigenvalues. The continuous and residual parts distinguish failure of surjectivity from failure of dense range; the residual spectrum of a self-adjoint operator is empty. We shall also use the self-adjoint *essential spectrum* $\sigma_\mathrm{ess}(H)$, obtained by removing isolated eigenvalues of finite multiplicity from $\sigma(H)$.

For $z \in \rho(H)$ define

$$\mathcal{R}(z) = (z - H)^{-1}. \tag{2.27}$$

The resolvent identity

$$\mathcal{R}(z) - \mathcal{R}(w) = (w - z)\mathcal{R}(z)\mathcal{R}(w) \tag{2.28}$$

shows that $\mathcal{R}(z)$ is analytic as a bounded-operator-valued function on the resolvent set. The spectral measure is recovered from its boundary values by Stone's formula,

$$\langle \phi, P_H((a,b))\psi\rangle = \lim_{\epsilon\downarrow 0} \frac{1}{2\pi \mathrm{i}} \int_a^b \langle \phi, [\mathcal{R}(E-\mathrm{i}\epsilon) - \mathcal{R}(E+\mathrm{i}\epsilon)]\psi\rangle \,\mathrm{d}E, \tag{2.29}$$

with endpoint qualifications. This formula already contains the continuum as a jump across the real axis.

The operator-valued resolvent of a self-adjoint H has no nonreal pole. A resonance appears when selected matrix elements, weighted resolvents, or kernel continuations cross the continuous-spectrum cut to another sheet. The test vectors and weights are therefore part of the statement. Complex scaling replaces that continuation by a deformed closed operator for which the pole becomes a genuine discrete eigenvalue. Rigged Hilbert spaces keep the test-vector topology explicit. Exact WKB constructs the same continuation directly from solutions of the differential equation.

2.3.9 Basis truncation: what the Ritz method proves and what it does not

A bounded operator K is *normal* when $K^\dagger K = KK^\dagger$; self-adjoint and unitary operators are normal. For a closed, possibly nonnormal operator, the ϵ-pseudospectrum is

$$\sigma_\epsilon(K) = \sigma(K) \cup \left\{ z \in \rho(K) : \|(z-K)^{-1}\| > \epsilon^{-1} \right\}. \tag{2.30}$$

For normal K this is precisely the open ϵ-neighborhood of its spectrum. A nonnormal operator may have much larger pseudospectral regions; small perturbations or truncation errors can then move its eigenvalues by far more than their norm would suggest.

Let $V_N \subset D(q)$ be an N-dimensional trial space with basis $\{\varphi_i\}$. A variational calculation solves

$$\sum_j H_{ij} c_j = E_N \sum_j N_{ij} c_j, \quad H_{ij} = q[\varphi_i, \varphi_j], \quad N_{ij} = \langle \varphi_i, \varphi_j \rangle. \tag{2.31}$$

For a semibounded self-adjoint operator, the min–max principle controls isolated eigenvalues below the essential spectrum: increasing nested trial spaces gives upper bounds that converge under standard density hypotheses.

No analogous variational ordering identifies arbitrary complex eigenvalues of a nonnormal matrix. In a complex-scaled calculation, convergence must be established by the analytic-deformation theorem together with numerical stability under basis size, nonlinear basis parameters, and scaling angle.

The residual

$$r_N = (H^\theta - E_N)\psi_N \tag{2.32}$$

is necessary but not sufficient: a highly nonnormal operator can have small residuals far from its spectrum. Left and right eigenvectors and the condition number

$$\kappa_n = \frac{\|\psi_n^R\| \, \|\psi_n^L\|}{|\langle \psi_n^L, \psi_n^R \rangle|} \tag{2.33}$$

measure sensitivity. Its divergence signals self-orthogonality near an exceptional point. The pseudospectrum gives the global version of the same warning.

2.3.10 Three distinctions used throughout the book

The following distinctions prevent most category errors in resonance calculations.

Closed dynamics versus effective evolution.

H is self-adjoint and generates unitary time evolution. A reduced, outgoing, absorbing, or deformed generator may be non-self-adjoint for a specific reason that must be stated.

Spectral value versus continued pole.

The spectrum of H is real. A resonance energy is a pole of a continued matrix element, S matrix, Jost function, or an eigenvalue of a theorem-controlled deformation.

Representation choice versus invariant datum.

A contour, scaling angle, test space, basis, bin width, or infrared dressing chooses a representation. The pole condition, residue after the correct pairing, and measurable response must agree when two representations cover the same analytic sector.

The remainder of Stage I equips these statements with their precise topological, measure-theoretic, and operator-algebraic meaning. Once that is done, later Stages will refer back to this chapter instead of redefining "state," "spectrum," or "continuum" in each application.

Chapter 3

Stage I-B: Multiplicity, operator algebras, and Fredholm theory

Reader contract

The spectral measure is now resolved into measurable multiplicity fibers. This stage constructs direct integrals, commutants, von Neumann algebras, central decompositions, locally convex test spaces, and compact-operator methods. It distinguishes energy fibers, factor decompositions, and genuine superselection sectors before any of them is used in scattering theory.

3.1 The functional analysis forced on us by the calculation

The elementary formulas of the preceding section already demand most of the functional analysis used in scattering theory. The strong limit in the wave operator, the boundary value of the resolvent, the delta-normalized eigenfunction, and the analytic continuation of a matrix element are four different limiting operations. Treating them as if they were ordinary limits of finite matrices hides both the power of the theory and the origin of many apparent paradoxes. This section develops the relevant language from first principles and keeps a physical example next to every abstract definition. The order is deliberately diagnostic rather than encyclopedic: a topology is introduced to specify a limit, an operator domain to specify an observable, a direct integral to specify the continuum, and a von Neumann algebra to specify which decompositions and sectors are measurable. Standard references include Refs. [26–30].

3.1.1 Topology decides what convergence means

A topology on a set X is a collection of subsets declared to be open, closed under arbitrary unions and finite intersections and containing both X and

the empty set. It determines continuity and convergence before a distance is chosen. A metric gives a topology, but many spaces of operators and distributions carry useful topologies that are not naturally described by a single metric. On a vector space, addition and scalar multiplication are required to be continuous. A locally convex topology is generated by a family of seminorms p_α, where a seminorm obeys the triangle inequality and homogeneity but may vanish on nonzero vectors.

The norm topology of a Hilbert space $\mathcal{H}$ is generated by $p(\psi) = \|\psi\|$. A sequence converges weakly if all transition amplitudes against fixed test vectors converge:

$$\psi_n \rightharpoonup \psi \quad \Longleftrightarrow \quad \langle \phi, \psi_n \rangle \to \langle \phi, \psi \rangle \quad \text{for every } \phi \in \mathcal{H}. \tag{3.1}$$

Norm convergence implies weak convergence, but the converse fails. An orthonormal sequence is the standard example: $e_n \rightharpoonup 0$ although $\|e_n\| = 1$. Physically, probability can escape to infinity while every fixed localized detector sees a vanishing amplitude. This is exactly the kind of limit that occurs in scattering.

For bounded operators $A_n \in \mathcal{B}(\mathcal{H})$, the most frequently used topologies are summarized in Table 3.1. The adjective *strong* refers to norm convergence after acting on each vector; it does not mean operator-norm convergence. On an infinite-dimensional space the distinctions are strict. Nets rather than sequences are required for complete generality, because weak operator topologies need not be first countable. For a separable Hilbert space, however, the strong and weak operator topologies are metrizable on norm-bounded sets, which covers many physics applications.

Topology and measure are related but distinct. A topology on X generates a Borel sigma-algebra Σ, the smallest sigma-algebra containing the open sets. A measure space (X, Σ, μ) then specifies which subsets are measurable and how they are weighted. Spectral theory uses topology to discuss continuity in energy and measure theory to identify functions that differ only on sets of μ measure zero. The phrase “at almost every energy” is therefore not a technical evasion; it is part of the identification defining an L^2 state.

topology	convergence of A_n to A	typical role in physics
operator norm	$\|A_n - A\| \to 0$	uniform control on every unit vector; stable functional calculus
strong operator	$\|(A_n - A)\psi\| \to 0$ for every ψ	wave operators, unitary dynamics, and strong sums of projections
weak operator	$\langle \phi, (A_n - A)\psi \rangle \to 0$ for every ϕ, ψ	convergence of all fixed transition amplitudes
ultraweak	convergence against every trace-class functional	normal states and von Neumann algebras
strong resolvent	$(A_n - z)^{-1}\psi \to (A - z)^{-1}\psi$ for one, hence all, $z \in \mathbb{C} \setminus \mathbb{R}$	limits of unbounded self-adjoint Hamiltonians

Table 3.1: Common operator topologies. The first four rows concern bounded operators. Strong-resolvent convergence is a topology adapted to unbounded self-adjoint operators.

3.1.2 Unbounded operators: the domain is part of the observable

A differential Hamiltonian is not merely a formula $H\psi$. It is a pair consisting of that action and a domain $D(H) \subset \mathcal{H}$. The graph

$$\mathcal{G}(H) = \{(\psi, H\psi) : \psi \in D(H)\} \subset \mathcal{H} \oplus \mathcal{H} \tag{3.2}$$

is closed if convergence of both ψ_n and $H\psi_n$ implies that the limit lies in the graph. An operator is closable if the closure of its graph is the graph of an operator. Closedness is the correct replacement for boundedness in much of spectral theory.

For a densely defined operator A, the adjoint domain is

$$D(A^\dagger) = \{\phi \in \mathcal{H} : \psi \mapsto \langle \phi, A\psi \rangle \text{ is norm continuous on } D(A)\}. \tag{3.3}$$

If $A \subset A^\dagger$, it is symmetric; if $A = A^\dagger$, including equality of domains, it is self-adjoint. A symmetric radial differential expression can acquire different self-adjoint extensions from different boundary conditions at a singular endpoint. The deficiency spaces $\ker(A^\dagger \mp \mathrm{i})$ count the missing boundary data. This is why "Hermitian differential expression" is not a sufficient specification of a

quantum Hamiltonian.

For a self-adjoint H, the resolvent $(z - H)^{-1}$ is bounded for $z \notin \mathbb{R}$ and satisfies

$$\|(z - H)^{-1}\| \leq \frac{1}{|\operatorname{Im} z|}. \tag{3.4}$$

Thus an unbounded Hamiltonian can be studied through bounded resolvents, unitaries $\mathrm{e}^{-\mathrm{i}tH}$, and spectral projections. Operator algebras usually contain these bounded functions of H, while H itself is described as an operator *affiliated* with the algebra. Quadratic-form methods provide another route: a closed semibounded form determines a unique self-adjoint operator and permits singular potentials for which the naive operator sum is inconvenient [26].

3.1.3 Projection-valued measures and the spectral theorem

A projection-valued measure P assigns an orthogonal projection $P(\Delta)$ to each Borel set $\Delta \subset \mathbb{R}$, with $P(\mathbb{R}) = \mathbf{1}$ and countable additivity in the strong operator topology. The spectral theorem states that a self-adjoint operator can be written

$$H = \int_{\mathbb{R}} E \, \mathrm{d}P(E), \qquad f(H) = \int_{\mathbb{R}} f(E) \, \mathrm{d}P(E). \tag{3.5}$$

The domain of H is not suppressed by this notation:

$$D(H) = \left\{ \psi \in \mathcal{H} : \int_{\mathbb{R}} E^2 \, \mathrm{d}\mu_\psi(E) < \infty \right\}, \qquad \mu_\psi(\Delta) = \langle \psi, P(\Delta)\psi \rangle. \tag{3.6}$$

The scalar measure μ_ψ is the energy distribution of the state. Its pure-point, absolutely continuous, and singular-continuous parts induce the corresponding orthogonal decomposition of $\mathcal{H}$. A bound state gives an atom of the measure. A scattering wave packet has an absolutely continuous density. A delta-normalized "eigenket" at one continuum energy is not a vector in $\mathcal{H}$; it is a distributional coordinate for this measure decomposition.

The spectral theorem also places a sharp restriction on resonances. Every spectral projection of a self-adjoint H lies on the real spectrum. A pole at $E_{\mathrm{R}} \notin \mathbb{R}$ cannot be added to Eq. (3.5) as another orthogonal projector. It appears only after continuing suitably tested resolvent matrix elements, or as a genuine eigenvalue of a different, non-self-adjoint realization such as H_θ. This boundary between spectral measure and analytic continuation is the mathematical core of resonance theory.

3.1.4 Direct integrals: a continuum of channel Hilbert spaces

A direct sum describes discrete alternatives. A direct integral is its measure-theoretic analogue. Let (X, Σ, μ) be a sigma-finite standard measure space. A field $x \mapsto \mathcal{H}_x$ of separable Hilbert spaces is called *measurable* after choosing a countable fundamental family of sections $e_n(x) \in \mathcal{H}_x$ such that

$$\begin{aligned} x &\longmapsto \langle e_m(x), e_n(x)\rangle_{\mathcal{H}_x} \quad \text{is measurable,} \\ \overline{\operatorname{span}}\{e_n(x)\} &= \mathcal{H}_x \qquad\qquad\qquad\quad \text{for almost every } x. \end{aligned} \tag{3.7}$$

A section $\psi(x)$ is measurable when all scalar functions $x \mapsto \langle e_n(x), \psi(x)\rangle$ are measurable. Different fundamental families defining the same measurable sections give the same measurable field. This condition is essential: there is no useful direct integral of an arbitrary uncoordinated collection of Hilbert spaces.

The direct integral

$$\mathcal{H} = \int_X^{\oplus} \mathcal{H}_x \, \mathrm{d}\mu(x) \tag{3.8}$$

consists of measurable sections $x \mapsto \psi(x)$, identified when they agree almost everywhere, for which

$$\|\psi\|^2 = \int_X \|\psi(x)\|_{\mathcal{H}_x}^2 \, \mathrm{d}\mu(x) < \infty. \tag{3.9}$$

The fiber dimension may vary with x. In scattering, this is exactly what happens when a new channel opens at a threshold.

A measurable essentially bounded family $x \mapsto A(x) \in \mathcal{B}(\mathcal{H}_x)$ defines a decomposable operator

$$A = \int_X^{\oplus} A(x) \, \mathrm{d}\mu(x), \qquad (A\psi)(x) = A(x)\psi(x), \tag{3.10}$$

with $\|A\| = \operatorname{ess\,sup}_x \|A(x)\|$. The scalar diagonal algebra

$$\mathcal{D} = \left\{ \int_X^{\oplus} f(x)\mathbf{1}_x \, \mathrm{d}\mu(x) : f \in L^\infty(X, \mu) \right\} \tag{3.11}$$

is abelian. For any set $\mathcal{X} \subset \mathcal{B}(\mathcal{H})$, its *commutant* is

$$\mathcal{X}' = \{B \in \mathcal{B}(\mathcal{H}) : BA = AB \text{ for every } A \in \mathcal{X}\}. \tag{3.12}$$

Under the standard hypotheses, the commutant $\mathcal{D}'$ is the algebra of all

decomposable bounded operators. Thus "does not mix the base variable x" is equivalent to "commutes with every bounded measurable function of x."

Why the multiplicity-one commutant is diagonal

First suppose $\mu(X) < \infty$ and the fiber is $\mathbb{C}$. If A commutes with every multiplication operator M_f, it commutes in particular with M_{χ_Δ} for every measurable Δ. Therefore A preserves functions supported in Δ. Put $g = A\mathbf{1}$. For a simple function $s = \sum_j c_j \chi_{\Delta_j}$,

$$As = \sum_j c_j A M_{\chi_{\Delta_j}} \mathbf{1} = \sum_j c_j M_{\chi_{\Delta_j}} A\mathbf{1} = gs. \tag{3.13}$$

Density of simple functions gives $A = M_g$. Testing on characteristic functions of sets where $|g| > \|A\| + \epsilon$ shows that $g \in L^\infty$ and $\|g\|_\infty \leq \|A\|$. On a sigma-finite space, apply the argument on an increasing finite-measure partition; the local multipliers agree on overlaps. For an $m(x)$-dimensional fiber, the same support argument leaves an essentially bounded measurable matrix $A(x)$ acting inside each fiber. This is the decomposable-operator statement used below.

The multiplicity form of the spectral theorem supplies a measure space and a unitary map such that

$$U\mathcal{H} = \int_{\sigma(H)}^{\oplus} \mathcal{K}_E \, \mathrm{d}\mu(E), \tag{3.14}$$

$$(UHU^\dagger \psi)(E) = E\psi(E), \tag{3.15}$$

where $\dim \mathcal{K}_E$ is the spectral multiplicity. The measure and fibers are unique only up to null sets and measure-class equivalence. This is why changing continuum normalization changes density factors but not the unitary content of the decomposition.

3.1.5 Worked example: the free-particle energy representation

The abstract construction becomes elementary in momentum space. For a spinless free particle in three dimensions,

$$\mathcal{H} = L^2(\mathbb{R}^3, \mathrm{d}^3p), \qquad (H_0\hat{\psi})(\boldsymbol{p}) = \frac{p^2}{2\mu}\hat{\psi}(\boldsymbol{p}). \tag{3.16}$$

Set $p(E) = \sqrt{2\mu E}$. Since

$$\mathrm{d}^3p = p^2\,\mathrm{d}p\,\mathrm{d}\Omega = \mu p(E)\,\mathrm{d}E\,\mathrm{d}\Omega, \tag{3.17}$$

the map

$$(U_0\hat{\psi})(E,\hat{\boldsymbol{p}}) = [\mu p(E)]^{1/2}\hat{\psi}(p(E)\hat{\boldsymbol{p}}) \tag{3.18}$$

is unitary from $L^2(\mathbb{R}^3, \mathrm{d}^3p)$ onto

$$\int_0^\infty{}^{\oplus} L^2(S^2, \mathrm{d}\Omega)\,\mathrm{d}E. \tag{3.19}$$

The factor $[\mu p(E)]^{1/2}$ is the square root of the density of states needed to preserve the norm. In this representation H_0 is multiplication by E, while each fiber contains the angular directions at that energy. Spherical harmonics further decompose the fiber into partial waves. Spin, internal states, and reaction channels simply enlarge the fiber.

At this point we have only diagonalized H_0; no scattering operator has been used. After Stage II constructs the wave operators, the same representation will turn strong commutation with H_0 into an almost-everywhere family of on-shell operators. That implication and its hypotheses are derived in Section 4.2.

3.1.6 Operator algebras, von Neumann algebras, and states

An operator algebra separates the abstract observables from a particular choice of vectors. A C^* algebra $\mathfrak{A}$ is a norm-complete involutive algebra satisfying

$$\|A^\dagger A\| = \|A\|^2. \tag{3.20}$$

When represented on $\mathcal{H}$, it is a norm-closed $*$ subalgebra of $\mathcal{B}(\mathcal{H})$. A von Neumann algebra $\mathcal{M} \subset \mathcal{B}(\mathcal{H})$ is a unital $*$ algebra closed in the weak operator topology. The bicommutant theorem gives the equivalent characterization

$$\mathcal{M} = \mathcal{M}''. \tag{3.21}$$

Norm closure is appropriate for uniform approximation of observables; weak closure also includes limits determined by all matrix elements and produces the spectral projections of self-adjoint generators. For this reason von Neumann algebras are particularly natural for spectral theory and statistical states [27, 31].

An algebraic state is a positive normalized linear functional

$$\omega(A^\dagger A) \geq 0, \qquad \omega(\mathbf{1}) = 1. \tag{3.22}$$

The Gelfand–Naimark–Segal (GNS) construction associates to it a Hilbert space $\mathcal{H}_\omega$, a representation $\pi_\omega(\mathfrak{A})$, and a cyclic vector Ω_ω such that

$$\omega(A) = \langle \Omega_\omega, \pi_\omega(A)\Omega_\omega \rangle. \tag{3.23}$$

This reverses the usual order of presentation: the state and observable algebra determine a representation, rather than every physical state being assumed in advance to lie in one preferred Fock or Schrödinger Hilbert space. For finitely many degrees of freedom the familiar irreducible representations are essentially unique under regularity hypotheses. For infinitely many degrees of freedom, inequivalent representations are generic. The infrared problem of QED in Section 4.5 is a concrete scattering reason that this distinction becomes unavoidable.

A state on a von Neumann algebra is normal when it is continuous under increasing strong limits of projections, equivalently when it belongs to the predual $\mathcal{M}_*$. On $\mathcal{B}(\mathcal{H})$, normal states have density matrices, $\omega(A) = \operatorname{tr}(\rho A)$. Singular states need not. Unbounded observables are not elements of $\mathcal{M}$, but their spectral projections may lie in it; one then says that the operator is affiliated with $\mathcal{M}$.

3.1.7 Abelian spectral algebras and central decomposition

The bounded Borel functions of a self-adjoint H generate an abelian von Neumann algebra

$$W^*(H) = \{ f(H) : f \text{ bounded and Borel} \}''. \tag{3.24}$$

In the spectral representation it is the diagonal algebra $L^\infty(X, \mu)$ acting as $f(E)\mathbf{1}_E$. Its commutant consists of the decomposable operators acting inside the multiplicity fibers. Stage II will show that strong commutation with H_0 is therefore equivalent to membership in $W^*(H_0)'$.

There is a broader direct-integral theorem. Let $\mathcal{M}$ act on a separable Hilbert space and assume the usual countable-decomposability hypotheses. Its center

$$\mathcal{Z}(\mathcal{M}) = \mathcal{M} \cap \mathcal{M}' \tag{3.25}$$

is abelian and can be represented as $L^\infty(X,\mu)$ on a standard measure space. The reduction theory of von Neumann then gives

$$\mathcal{H} = \int_X^\oplus \mathcal{H}_x \, \mathrm{d}\mu(x), \tag{3.26}$$

$$\mathcal{M} = \int_X^\oplus \mathcal{M}_x \, \mathrm{d}\mu(x), \qquad \mathcal{Z}(\mathcal{M}_x) = \mathbb{C}\mathbf{1}_x \quad \text{for almost every } x. \tag{3.27}$$

The fibers $\mathcal{M}_x$ are factors [27, 28]. In finite dimensions this is the familiar decomposition of a block-diagonal algebra into full matrix blocks. The direct integral is the continuous version. This theorem decomposes a *specified representation* of one von Neumann algebra. It does not by itself decide which representations are physically admissible, nor does it classify all superselection sectors of an abstract observable algebra.

Factors are classified coarsely into types. Type I factors contain minimal projections and reproduce ordinary quantum mechanics, with $\mathcal{M}_x \simeq \mathcal{B}(\mathcal{H}_x)$. Type II factors have no minimal projections but admit a faithful semifinite trace. Type III factors admit no nonzero finite projections and no ordinary trace; local observable algebras in relativistic QFT are typically type III under standard assumptions [30]. This explains why a local QFT region does not behave like a finite tensor factor with an intrinsic density matrix, even though detector probabilities remain well defined.

Three notions should not be conflated. The spectral direct integral of H is taken over energy and diagonalizes $W^*(H)$. The central decomposition of a represented observable algebra is taken over the center and resolves that representation into factors. A superselection analysis additionally selects and compares physically admissible representations of the abstract algebra, often by a localization or asymptotic criterion. The base of a central decomposition represents sector labels only when the chosen representation was constructed to contain such a mixture and its center records those labels. The three constructions use related measurable technology, but energy need not be a superselection variable: generic observables can change it. In infrared QED, by contrast, asymptotic electric flux or soft charge can label disjoint representations. A statistical mixture of them may admit a direct integral, but that operation creates no unitary intertwiner between disjoint fibers.

3.1.8 Locally convex test spaces and generalized eigenvectors

The Hilbert norm deliberately forgets pointwise values, derivatives, and analytic continuation. Scattering theory often needs all three. Choose a dense invariant space $\Phi \subset \mathcal{H}$ and give it a locally convex topology generated, for example, by seminorms

$$p_{m,n}(\phi) = \|\langle x\rangle^m (1+H)^n \phi\|\,, \qquad m,\, n \in \mathbb{N}. \tag{3.28}$$

For the free particle, the Schwartz space is the canonical model. Its topology controls every polynomially weighted derivative, and its continuous dual contains tempered distributions such as plane waves and Dirac deltas. Analytic or Hardy seminorms can be added when contour deformation is required.

Continuity of a functional F on Φ means that for some finite set of seminorms and a constant C,

$$|F(\phi)| \le C \sum_{j=1}^{N} p_j(\phi). \tag{3.29}$$

This gives the Gelfand triple $\Phi \subset \mathcal{H} \subset \Phi^\times$ used in Section 6.4. A generalized eigenvector $|E,\alpha\rangle \in \Phi^\times$ satisfies

$$\langle H\phi, E, \alpha\rangle = E\langle \phi, E, \alpha\rangle, \qquad \phi \in \Phi, \tag{3.30}$$

where α labels the spectral fiber. Under nuclearity and invariance hypotheses, the nuclear spectral theorem turns the direct-integral expansion into a generalized-eigenvector expansion [32]. The topology is therefore the bridge between an almost-everywhere spectral representation and the physicist's energy kets.

The choice of Φ is not arbitrary bookkeeping. A topology too weak makes evaluation or continuation discontinuous; one too strong can exclude physically prepared packets. Hardy spaces encode a time-oriented analytic boundary value, Schwartz spaces encode rapid localization, and dilation-analytic vectors encode complex scaling. Different choices can reveal different generalized spectra without changing the self-adjoint spectrum in $\mathcal{H}$.

3.1.9 Riesz projections and what an operator algebra does not add

For a closed, not necessarily normal operator K, an isolated spectral set inside a contour Γ has the Riesz projection

$$P_\Gamma(K) = \frac{1}{2\pi\mathrm{i}} \oint_\Gamma (z - K)^{-1}\, \mathrm{d}z. \tag{3.31}$$

It is idempotent but need not be orthogonal. Its range is the generalized eigenspace, including Jordan vectors. For a complex-scaled Hamiltonian, an exposed resonance has precisely such a finite-rank projection. At an exceptional point the rank of the projection can remain fixed while the geometric eigenspace shrinks and a nilpotent Jordan part develops.

For the original self-adjoint H, however, a resonance behind the cut is not an isolated part of $\sigma(H)$, so Eq. (3.31) cannot encircle it on the physical resolvent set. Neither norm closure nor weak closure of the observable algebra manufactures the missing analytic sheet. One must supply analytic vectors, weighted spaces, a Jost construction, or a complex deformation. Operator algebras organize observables, representations, and measurable decompositions; resonance theory adds the analytic continuation. Their interface, rather than an identification of the two, is the useful unifying structure.

3.2 Compact kernels, Fredholm determinants, and finite model spaces

Calculation route

Prerequisites. The operator topologies, direct integrals, and resolvents constructed in Section 3.1.

Calculation goal. Identify the compact operator hidden in a scattering equation, replace the infinite-dimensional inverse by a Fredholm determinant, and calculate the residue of a simple pole.

Completion criterion. Know exactly why a finite-basis calculation can converge even though the identity operator itself cannot be approximated in operator norm by finite-rank projections.

physical phrase	precise mathematical object
energy distribution of a packet	scalar spectral measure $\mu_\psi(\Delta) = \langle \psi, P(\Delta)\psi \rangle$
continuum channels at fixed energy	multiplicity fiber $\mathcal{K}_E$ in a direct integral
energy-preserving bounded map	decomposable fiber $A(E)$ of an operator $A \in W^*(H_0)'$
generalized plane or Gamow wave	continuous functional on a chosen test topology
isolated complex-scaled resonance	finite-rank Riesz projection of H_θ
factor component of a representation	fiber in its central decomposition; a separate selection criterion is required before calling it a superselection sector

Table 3.2: A functional-analytic dictionary for scattering theory.

The Lippmann–Schwinger equation looks like a linear equation,

$$(\mathbf{1} - K(z))\psi(z) = \phi(z), \tag{3.32}$$

but an inverse of an infinite matrix need not share the elementary properties of a finite inverse. The missing hypothesis is usually compactness. Once the interaction has been placed in a compact kernel, three operations used throughout this book become legitimate versions of one another:

$$\begin{aligned} \text{solve an integral equation} &\iff \text{locate a determinant zero,} \\ &\iff \text{extract a finite-rank pole residue.} \end{aligned} \tag{3.33}$$

This section develops that statement from the definition of a compact operator. The theory is also the mathematical reason why Gaussian pseudostates, Galerkin bases, and CDCC model spaces can approximate tested continuum amplitudes without turning every positive-energy eigenvalue into a physical level. Standard references include Refs. [33–35].

3.2.1 Compactness is uniform finite-dimensionality after the operator acts

A bounded operator $K : \mathcal{H}_1 \to \mathcal{H}_2$ is compact if it maps the unit ball of $\mathcal{H}_1$ into a relatively compact subset of $\mathcal{H}_2$. Equivalently, for every bounded sequence $\{\psi_n\}$ there is a subsequence for which $K\psi_{n_j}$ converges in norm. A finite-rank operator is compact, and a norm limit of finite-rank operators is compact. On Hilbert space the converse also holds: every compact operator is a norm limit of finite-rank operators.

This definition contains the important order of operations. Let P_N be orthogonal projections onto an increasing sequence of finite-dimensional spaces with $P_N \to \mathbf{1}$ strongly. In an infinite-dimensional space,

$$\|\mathbf{1} - P_N\| = 1 \tag{3.34}$$

for every finite N. Thus a basis truncation never approximates the identity in operator norm. If K is compact, however,

$$\|(\mathbf{1} - P_N)K\| \longrightarrow 0, \qquad \|K(\mathbf{1} - P_N)\| \longrightarrow 0. \tag{3.35}$$

To prove the first limit, cover the compact closure of the image of the unit ball by finitely many small balls. Strong convergence is uniform on their finite set of centers and hence, by the triangle inequality, on the whole compact image. The second statement follows by applying the first to $K^\dagger$. Consequently

$$K_N = P_N K P_N \quad \Longrightarrow \quad \|K_N - K\| \to 0. \tag{3.36}$$

Equation (3.36), not an imagined norm convergence $P_N \to \mathbf{1}$, is the compactness mechanism behind a stable Galerkin calculation.

The nonzero spectrum of a compact operator consists of isolated eigenvalues of finite algebraic multiplicity, with zero as the only possible accumulation point. A nonzero spectral point therefore has a finite-rank Riesz projection. For a non-normal K, right and left eigenvectors need not be orthogonal and Jordan chains may occur, but the root space belonging to a nonzero isolated eigenvalue remains finite dimensional. This is the first place where the infinite-dimensional problem recovers finite matrix algebra without being replaced by it.

3.2.2 Hilbert–Schmidt and trace-class kernels

Let $s_n(K)$ be the singular values of a compact operator, namely the eigenvalues of $|K| = (K^\dagger K)^{1/2}$ in decreasing order and with multiplicity. The Schatten ideal $\mathfrak{S}_p$ consists of operators for which

$$\|K\|_p^p = \sum_n s_n(K)^p < \infty. \tag{3.37}$$

The two classes needed here are

$$\mathfrak{S}_2 = \{\text{Hilbert–Schmidt operators}\}, \qquad \|K\|_2^2 = \operatorname{tr}(K^\dagger K), \tag{3.38}$$

$$\mathfrak{S}_1 = \{\text{trace-class operators}\}, \qquad \|K\|_1 = \operatorname{tr}|K|. \tag{3.39}$$

One has $\mathfrak{S}_1 \subset \mathfrak{S}_2 \subset \mathcal{K}(\mathcal{H})$, where $\mathcal{K}(\mathcal{H})$ denotes the compact operators. If A, B are bounded and $K \in \mathfrak{S}_p$, then

$$AKB \in \mathfrak{S}_p, \qquad \|AKB\|_p \le \|A\|\,\|K\|_p\,\|B\|. \tag{3.40}$$

Thus these are two-sided ideals in $\mathcal{B}(\mathcal{H})$.

For $\mathcal{H} = L^2(X, \mathrm{d}\mu)$, an integral kernel $K(x, y)$ satisfying

$$\int_X \int_X |K(x,y)|^2 \,\mathrm{d}\mu(x)\mathrm{d}\mu(y) < \infty \tag{3.41}$$

defines a Hilbert–Schmidt operator, and the integral is $\|K\|_2^2$. This elementary criterion is the most useful entry point for scattering. It also explains why the order in which potential factors and a resolvent are multiplied matters: a free resolvent is not compact on all of space, but a resolvent localized on both sides by a sufficiently short-range potential can be Hilbert–Schmidt.

Domain or asymptotic warning

Neither a delta function nor a continuous-spectrum identity kernel is square integrable on $X \times X$. Discretizing such a kernel produces a finite matrix, but finiteness of that matrix is not evidence that the original operator was Hilbert–Schmidt. Compactness must be checked before the discretization or proved in a weighted realization.

3.2.3 The Birman–Schwinger kernel of a Schrödinger operator

Let $H = H_0 + V$ on $L^2(\mathbb{R}^d)$ and use the resolvent convention

$$\mathcal{R}_0(z) = (z - H_0)^{-1}. \tag{3.42}$$

For a real multiplication potential write $V = \operatorname{sgn}(V)|V|$ and define

$$K(z) = |V|^{1/2}\mathcal{R}_0(z)\operatorname{sgn}(V)|V|^{1/2}. \tag{3.43}$$

If $(z - H)\psi = 0$ and $\phi = |V|^{1/2}\psi$, then

$$(\mathbf{1} - K(z))\phi = 0. \tag{3.44}$$

Conversely, a solution of Eq. (3.44) gives $\psi = \mathcal{R}_0(z)\operatorname{sgn}(V)|V|^{1/2}\phi$, subject to the usual domain qualifications. Hence an eigenvalue or continued pole of H occurs when 1 is an eigenvalue of $K(z)$. If one instead defines the resolvent as $(H_0 - z)^{-1}$, the corresponding eigenvalue is -1; many sign differences in the literature are only this convention.

For $d = 3$ and z away from $[0, \infty)$, the free kernel is proportional to

$$G_0(z; \boldsymbol{x} - \boldsymbol{y}) = \frac{\mathrm{e}^{-\kappa(z)|\boldsymbol{x}-\boldsymbol{y}|}}{|\boldsymbol{x} - \boldsymbol{y}|}, \qquad \operatorname{Re}\kappa(z) > 0, \tag{3.45}$$

up to constants fixed in Section 4.1.3. If, for example, V is bounded and compactly supported, then

$$\|K(z)\|_2^2 \propto \iint |V(\boldsymbol{x})|, |G_0(z; \boldsymbol{x} - \boldsymbol{y})|^2, |V(\boldsymbol{y})|\, \mathrm{d}^3x \mathrm{d}^3y < \infty. \tag{3.46}$$

The singularity $|\boldsymbol{x} - \boldsymbol{y}|^{-2}$ is locally integrable in three dimensions, while the localization controls large separations. Much weaker hypotheses are available, but this sufficient condition displays the mechanism without hiding it in a theorem.

On the continuous spectrum the exponential decay in Eq. (3.45) disappears. Compactness and boundary values are then formulated between weighted spaces, or after localization by the potential. A Coulomb tail changes the comparison resolvent itself. Thus the Birman–Schwinger argument does not license using the free kernel for the long-range problems of Section 4.5.

The resolvent identity follows by solving Eq. (3.32):

$$\mathcal{R}(z) = \mathcal{R}_0(z) + \mathcal{R}_0(z)\,\mathrm{sgn}(V)|V|^{1/2}[\mathbf{1} - K(z)]^{-1}|V|^{1/2}\mathcal{R}_0(z). \tag{3.47}$$

Every nontrivial singularity of the right-hand side is therefore carried by $[\mathbf{1} - K(z)]^{-1}$. This is the operator whose determinant will be compared with a Jost function and with the exact-WKB incoming coefficient.

3.2.4 Analytic Fredholm theorem: why the continued inverse is meromorphic

Let $\Omega \subset \mathbb{C}$ be connected and let $z \mapsto K(z)$ be analytic in operator norm with compact values. The analytic Fredholm theorem states that exactly one of the following occurs:

(i) $\mathbf{1} - K(z)$ is noninvertible for every $z \in \Omega$;

(ii) $[\mathbf{1} - K(z)]^{-1}$ exists except at a discrete set and is a meromorphic operator-valued function whose principal parts have finite rank.

If the inverse exists at one point, alternative (ii) holds. In scattering, large negative energy or sufficiently small coupling usually supplies that one point.

The finite-dimensional content of the theorem can be seen locally. Near a point z_0 where 1 is an isolated eigenvalue of $K(z_0)$, take a small spectral contour around that eigenvalue and form its finite-rank Riesz projection P. Decompose $\mathcal{H} = P\mathcal{H} \oplus (\mathbf{1} - P)\mathcal{H}$. The block on $(\mathbf{1} - P)\mathcal{H}$ is invertible near z_0; a Schur complement reduces the remaining obstruction to a finite matrix on $P\mathcal{H}$. Its ordinary determinant has isolated zeros, and its inverse has a finite-rank Laurent principal part. Compactness is precisely what made the obstructing block finite.

This proof also identifies a limitation. A threshold is not, in general, an ordinary interior point of an analytic domain: it is a branch point of the continued kernel. The theorem is applied on a chosen momentum sheet or in a uniformizing variable, not blindly across the threshold.

3.2.5 Fredholm and regularized determinants

If $K(z)$ is trace class, its Fredholm determinant is

$$D(z) = \det(\mathbf{1} - K(z)) = \prod_n [1 - \lambda_n(z)], \tag{3.48}$$

where the eigenvalues are counted with algebraic multiplicity. The product converges, D is analytic, and

$$D(z) = 0 \quad \Longleftrightarrow \quad \mathbf{1} - K(z) \text{ is not invertible.} \tag{3.49}$$

Where the inverse exists,

$$\frac{\mathrm{d}}{\mathrm{d}z} \log D(z) = -\operatorname{tr}\Big([\mathbf{1} - K(z)]^{-1} K'(z) \Big) . \tag{3.50}$$

A Hilbert–Schmidt operator need not be trace class, so the linear term in the product can diverge. The regularized determinant

$$\det{}_2(\mathbf{1} - K) = \det\big[(\mathbf{1} - K)\mathrm{e}^{K}\big] = \prod_n (1 - \lambda_n)\mathrm{e}^{\lambda_n} \tag{3.51}$$

is well defined for $K \in \mathfrak{S}_2$. The exponential removes the non-summable linear contribution. Most importantly,

$$\det{}_2(\mathbf{1} - K) = 0 \quad \Longleftrightarrow \quad 1 \in \sigma(K), \tag{3.52}$$

with the same zero multiplicity. Multiplication of a resonance determinant by a nonvanishing analytic factor changes neither its zeros nor the local null spaces. This is why a Jost function, a Fredholm determinant, and an exact-WKB connection coefficient may differ in normalization while encoding the same poles.

For a partial-wave Schrödinger problem one may schematically write

$$\mathcal{C}_{\mathrm{in}}(E) = N(E) F_l(k(E)) = \widetilde{N}(E) \det{}_2[\mathbf{1} - K_l(E)], \tag{3.53}$$

on a domain where all three objects have been constructed and where N, $\widetilde{N}$ do not vanish. Equation (3.53) is not a universal equality of preferred normalizations. It is the precise local statement that the three analytic coordinates define the same divisor of resonance zeros.

3.2.6 Simple-zero residue without diagonalizing the whole operator

Set $A(z) = \mathbf{1} - K(z)$ and suppose z_{R} is a simple noninvertibility point. Choose right and left null vectors

$$A(z_{\mathrm{R}})u = 0, \qquad A(z_{\mathrm{R}})^{\dagger} v = 0, \tag{3.54}$$

where the second equation represents the left functional in Hilbert-space notation. If

$$\mathcal{N}_{\mathrm{R}} = \langle v, A'(z_{\mathrm{R}})u\rangle \neq 0, \tag{3.55}$$

then

$$A(z)^{-1} = \frac{|u\rangle\langle v|}{(z - z_{\mathrm{R}})\mathcal{N}_{\mathrm{R}}} + A_{\mathrm{reg}}(z). \tag{3.56}$$

The result follows by applying $A(z) = A(z_{\mathrm{R}}) + (z - z_{\mathrm{R}})A'(z_{\mathrm{R}}) + \dots$ to the proposed Laurent term. The scale changes $u \mapsto cu$, $v \mapsto c^{-1*}v$ cancel between numerator and denominator.

Substitution in Eq. (3.47) gives the factorized resolvent residue. The denominator $\langle v, A'u\rangle$ is the operator form of every derivative normalization encountered later:

$$\langle v, A'u\rangle \quad\longleftrightarrow\quad F_l'(k_{\mathrm{R}}) \quad\longleftrightarrow\quad \mathcal{C}_{\mathrm{in}}'(E_{\mathrm{R}}) \quad\longleftrightarrow\quad 1 - \Sigma'(E_{\mathrm{R}}). \tag{3.57}$$

The last expression occurs after Feshbach elimination. Neglecting the energy derivative of an effective interaction is therefore not an innocent normalization choice; it changes the pole residue.

For a matrix incoming block $\mathcal{C}_{\mathrm{in}}(E)$, the identical calculation gives

$$\mathcal{C}_{\mathrm{in}}(E)^{-1} \sim \frac{|u\rangle\langle v|}{(E - E_{\mathrm{R}})\langle v, \partial_E \mathcal{C}_{\mathrm{in}}(E_{\mathrm{R}})u\rangle}. \tag{3.58}$$

This is the multichannel extension of dividing by $\mathcal{C}_{\mathrm{in}}'(E_{\mathrm{R}})$ in exact WKB.

3.2.7 Worked model: a rank-one interaction

Let

$$V = \lambda|g\rangle\langle g|, \qquad g \in \mathcal{H}. \tag{3.59}$$

The transition operator has the separable form

$$T(z) = |g\rangle\tau(z)\langle g|. \tag{3.60}$$

Inserting it in $T = V + V\mathcal{R}_0 T$ yields

$$\tau(z) = \frac{\lambda}{D(z)}, \qquad D(z) = 1 - \lambda g_0(z), \qquad g_0(z) = \langle g|\mathcal{R}_0(z)|g\rangle. \tag{3.61}$$

The entire pole problem is now one Fredholm eigenvalue. If $D(z_{\mathrm{R}}) = 0$ and $D'(z_{\mathrm{R}}) \neq 0$, then

$$\operatorname*{Res}_{z=z_{\mathrm{R}}} T(z) = \frac{\lambda |g\rangle\langle g|}{D'(z_{\mathrm{R}})} = -\frac{|g\rangle\langle g|}{g_0'(z_{\mathrm{R}})}. \tag{3.62}$$

The first equality has exactly the form $\mathcal{N}(E_{\mathrm{R}})/\mathcal{C}'_{\mathrm{in}}(E_{\mathrm{R}})$. A numerical calculation that reproduces z_{R} but not $g_0'(z_{\mathrm{R}})$ has not yet reproduced the resonance strength.

The discontinuity of $g_0(E \pm \mathrm{i}0)$ supplies the open-channel width. A threshold branch point remains in $g_0(z)$ even though the algebra in Eq. (3.61) is one dimensional. Finite rank does not remove continuum analyticity; it isolates where that analyticity enters.

3.2.8 Galerkin, pseudostates, and CDCC as compact-kernel quadrature

Let $K_N = P_N K P_N$. If K is compact, Eq. (3.36) implies that isolated nonzero eigenvalues and their total Riesz projections are stable under a sufficiently large truncation. If $K \in \mathfrak{S}_2$ and $\|K_N - K\|_2 \to 0$, the regularized determinants converge locally uniformly. A practical pole calculation may therefore proceed as follows:

1. construct the compact or Hilbert–Schmidt kernel before projection;
2. choose P_N and calculate the finite matrix $P_N K(z) P_N$;
3. locate zeros of its determinant on a declared sheet;
4. enlarge P_N and track a whole Riesz cluster, not a single sorted eigenvalue;
5. calculate the left–right derivative denominator in Eq. (3.55);
6. test the resulting residue between the physical source and detector.

The same logic clarifies continuum pseudostates. The projection P_N is a finite quadrature for matrix elements of a compactly tested resolvent. Most positive-energy eigenvalues depend on basis ranges and should move as the quadrature is refined. A resonance is identified by stability of a continued pole or of its Riesz projection and residue. CDCC adds coupled relative motion and physical channel boundary conditions, but its internal pseudostate space obeys the same rule.

3.2.9 Compact kernels versus decomposable scattering operators

Compactness should not be attached to the wrong operator. In the spectral representation of H_0, the scattering operator is decomposable,

$$\mathsf{S} = \int^{\oplus} \mathsf{S}(E)\,\mathrm{d}E. \tag{3.63}$$

On a non-atomic energy interval, a nonzero decomposable multiplication operator is ordinarily not compact. Indeed, if $\|\mathsf{S}(E) - \mathbf{1}\| > \varepsilon$ on a set of positive measure, divide that set into disjoint subsets and choose unit sections supported on them. Their images remain separated, so no convergent subsequence exists.

There is no contradiction. The compact object is the localized off-shell kernel, a Birman–Schwinger operator, or a difference of suitably weighted resolvents. The on-shell scattering operator is a measurable family acting throughout a continuum. Direct-integral theory tells us how it is organized; Fredholm theory tells us how its analytic singularities arise. Exact WKB then calculates the same singularity from global connection data.

Checkpoint

Before proceeding, the reader should be able to distinguish the strong limit $P_N \to \mathbf{1}$ from the norm limit $P_N K P_N \to K$, verify the Hilbert–Schmidt criterion for a localized Green kernel, derive Eq. (3.56), and explain why the derivative of a determinant or incoming coefficient is part of the physical pole residue.

3.3 Problems for Stage I

I.1 Show that the Born rule for an effect $0 \le F \le \mathbf{1}$ gives a number in $[0, 1]$. Construct a two-outcome POVM that is not a projection-valued measure and give it a finite-resolution detector interpretation.

I.2 For the momentum operator on $(0, L)$, verify by integration by parts that the boundary condition $\psi(L) = \mathrm{e}^{\mathrm{i}\alpha}\psi(0)$ makes the operator self-adjoint. Derive Eq. (2.14).

I.3 Let e_n be an orthonormal sequence. Prove that e_n converges weakly

to zero but not in norm. Interpret $e_n(x) = \phi(x - n)$ on the line as probability escaping every fixed compact detector.

I.4 Starting from $\mathrm{d}^3p = p^2\,\mathrm{d}p\mathrm{d}\Omega$ and $E = p^2/(2\mu)$, derive the density factor in Eq. (3.18) and verify unitarity explicitly.

I.5 Prove that a bounded operator commuting with every multiplication operator $f(E)$ in a multiplicity-one direct integral is itself multiplication by an essentially bounded function. State the change when the fiber has dimension $m(E) > 1$.

I.6 Calculate the spectral measure of a normalized vector for a two-level Hamiltonian. Repeat for a wave packet of the one-dimensional free Hamiltonian and identify the Jacobian between momentum and energy density.

I.7 Use the resolvent identity to prove analyticity of $\mathcal{R}(z) = (z - H)^{-1}$ in operator norm on the resolvent set. Explain why this statement alone cannot continue $\mathcal{R}$ through the continuous spectrum.

I.8 Derive the Feshbach operator Eq. (2.21). Differentiate its eigenvalue equation with respect to E and identify the origin of $1 - \partial_E H_{\mathrm{eff}}(E)$ in pole normalization.

I.9 For a Lorentzian density cut off below a threshold, evaluate the contour contribution to Eq. (2.22). Separate the pole term from the threshold term and determine their qualitative time dependence.

I.10 Give one example each of norm, strong-operator, weak-operator, and strong-resolvent convergence. For every example, name a physical statement that would be false if the topology were silently strengthened.

I.11 Let $P_N \to \mathbf{1}$ strongly and let K be compact. Prove $\|(\mathbf{1} - P_N)K\| \to 0$ by covering the image of the unit ball with finitely many ε balls. Give a counterexample when K is the identity.

I.12 For the three-dimensional off-shell free Green kernel and a bounded compactly supported potential, verify the finiteness of Eq. (3.46). Treat separately the diagonal singularity and large separations.

I.13 Prove the Birman–Schwinger equivalence Eq. (3.44) with the resolvent convention of the book. Re-derive it using $(H_0 - z)^{-1}$ and explain the sign change.

I.14 Starting from left and right null vectors of $A(z) = \mathbf{1} - K(z)$, verify the Laurent coefficient in Eq. (3.56). Show explicitly that it is invariant under reciprocal rescaling of the null vectors.

I.15 On $L^2([0,1], \mathrm{d}E)$, prove that multiplication by a nonzero essentially bounded function is not compact. Reconcile this result with compactness of a localized Birman–Schwinger kernel.

Chapter 4

Stage II: Construct scattering data before continuing it

Reader contract

Starting from two-body kinematics and wave packets, this stage derives the resolvent, Møller operators, cross sections, partial waves, and Jost functions. Short-range hypotheses are stated where they are used. Coulomb, three-charge, and QED asymptotics then show exactly which premise fails when the free comparison dynamics is chosen incorrectly.

4.1 Step 1: Extract asymptotic coefficients from a scattering problem

Calculation route

Prerequisites. The Schrödinger equation, wave packets, and elementary partial-wave decomposition.

Calculation goal. Define the comparison dynamics, flux normalization, Jost bases, and incoming/outgoing coefficients that will enter the exact-WKB connection problem.

Completion criterion. Given a short-range potential, write the Lippmann–Schwinger and partial- wave problems with consistent sheet, flux, and Wronskian conventions.

This section fixes the elementary scattering-theory conventions used in the rest of the book. The order of presentation follows the traditional route from wave packets and cross sections to partial waves, integral equations, scattering matrices, and Jost functions. Useful complementary treatments are given by Sasakawa, Taylor, Perelomov and Zel'dovich, and Rakityansky [36–39]. These references record provenance and alternative conventions; the definitions and derivations needed below are developed here. The steps that

begin as ordinary collision theory will later become analytic continuation, resonance normalization, and complex spectral deformation.

4.1.1 Two-body reduction and the class of potentials

Consider two spinless particles with masses m_1 and m_2 interacting through a translationally invariant potential $V(\boldsymbol{r}_1 - \boldsymbol{r}_2)$. With center-of-mass and relative coordinates

$$\boldsymbol{R} = \frac{m_1\boldsymbol{r}_1 + m_2\boldsymbol{r}_2}{m_1 + m_2}, \qquad \boldsymbol{r} = \boldsymbol{r}_1 - \boldsymbol{r}_2, \tag{4.1}$$

the Hamiltonian separates as

$$H_{\mathrm{tot}} = -\frac{\hbar^2}{2(m_1 + m_2)}\nabla^2_{\boldsymbol{R}} + H, \qquad H = H_0 + V, \qquad H_0 = -\frac{\hbar^2}{2\mu}\nabla^2_{\boldsymbol{r}}, \tag{4.2}$$

where $\mu = m_1m_2/(m_1 + m_2)$ is the reduced mass. The center-of-mass plane wave is dynamically trivial, so the collision problem is the spectral problem for H.

We first assume a real, local, central potential $V(r)$ that is nonsingular enough at the origin and short ranged at infinity. A representative sufficient condition for the simplest one-channel statements is

$$\int_0^\infty \mathrm{d}r\, r|V(r)| < \infty. \tag{4.3}$$

The exact hypotheses vary with the result: existence of wave operators, analyticity of Jost functions, and dilation analyticity require different weights or regularity. Coulomb forces violate Eq. (4.3); one must then replace free asymptotic waves by Coulomb waves and factor out the known Coulomb phase. Nonlocal, coupled-channel, optical, and energy-dependent interactions are introduced only after the one-channel structure is clear.

For a central potential, separation in spherical harmonics gives

$$\psi(\boldsymbol{r}) = \sum_{lm} \frac{u_l(r)}{r} Y_{lm}(\widehat{\boldsymbol{r}}), \tag{4.4}$$

and the reduced radial equation

$$\left[-\frac{\hbar^2}{2\mu}\frac{\mathrm{d}^2}{\mathrm{d}r^2} + \frac{\hbar^2 l(l+1)}{2\mu r^2} + V(r)\right] u_l(r) = E u_l(r). \tag{4.5}$$

Regularity of the full wave function requires $u_l(r) = O(r^{l+1})$ at the origin. The second boundary condition at infinity distinguishes bound, scattering, virtual, and resonant solutions. This is the first indication that these are not four unrelated differential equations, but four boundary-value realizations of the same radial equation.

4.1.2 Wave packets, asymptotic states, and wave operators

A plane wave is not normalizable and does not by itself describe a collision prepared at a finite time. Begin instead with a free wave packet

$$\phi(\boldsymbol{r}, t) = \int \frac{\mathrm{d}^3 k}{(2\pi)^3}\, a(\boldsymbol{k}) \mathrm{e}^{\mathrm{i}\boldsymbol{k}\cdot\boldsymbol{r} - \mathrm{i}E_k t/\hbar}, \qquad E_k = \frac{\hbar^2 k^2}{2\mu}, \tag{4.6}$$

with $a(\boldsymbol{k})$ concentrated near an incident momentum $\boldsymbol{k}_0$. The interacting packet is required to approach a free packet before or after the collision. When the strong limits exist, this statement is encoded by the Møller wave operators

$$\Omega^{(\pm)} = \operatorname*{s\text{-}lim}_{t \to \mp\infty} \mathrm{e}^{\mathrm{i}Ht/\hbar} \mathrm{e}^{-\mathrm{i}H_0 t/\hbar} P_{\mathrm{ac}}(H_0). \tag{4.7}$$

Here $P_{\mathrm{ac}}(H_0)$ projects onto the absolutely continuous subspace. The state $\Omega^{(+)}\phi$ has the prescribed incoming free packet in the remote past, whereas $\Omega^{(-)}\phi$ has the prescribed outgoing free packet in the remote future. The scattering operator is

$$\mathsf{S} = \Omega^{(-)\dagger}\Omega^{(+)}. \tag{4.8}$$

If the wave operators are isometric and asymptotically complete, S is unitary on the free scattering space. Asymptotic completeness means that all states orthogonal to bound states eventually resolve into scattering channels. It is a theorem under specified hypotheses, not an automatic consequence of writing $H = H_0 + V$.

The stationary scattering states used below are distributional limits of these packets. Their delta-function normalization is therefore a shorthand for a wave-packet construction. This distinction matters for resonances: neither an exact plane wave nor a Gamow state is an ordinary Hilbert-space vector, but both define continuous functionals on a suitable test space.

4.1.3 Free resolvent and the Lippmann–Schwinger boundary condition

Let

$$\mathcal{R}_0(z) = (z - H_0)^{-1}. \tag{4.9}$$

For $E = \hbar^2 k^2/(2\mu) > 0$, the coordinate kernel of its outgoing boundary value is

$$\langle \boldsymbol{r}|\mathcal{R}_0(E + \mathrm{i}0)|\boldsymbol{r}'\rangle = -\frac{\mu}{2\pi\hbar^2}\frac{\mathrm{e}^{\mathrm{i}k|\boldsymbol{r}-\boldsymbol{r}'|}}{|\boldsymbol{r}-\boldsymbol{r}'|}. \tag{4.10}$$

The sign $+\mathrm{i}0$ is not a formal decoration. Fourier inversion places the radial momentum pole on the side of the contour that produces an outgoing spherical wave. The opposite boundary value produces an incoming wave.

For an incident plane wave $\langle \boldsymbol{r}|\boldsymbol{k}\rangle = \mathrm{e}^{\mathrm{i}\boldsymbol{k}\cdot\boldsymbol{r}}$, the outgoing Lippmann–Schwinger equation is

$$|\psi_{\boldsymbol{k}}^{(+)}\rangle = |\boldsymbol{k}\rangle + \mathcal{R}_0(E_k + \mathrm{i}0)V|\psi_{\boldsymbol{k}}^{(+)}\rangle. \tag{4.11}$$

Substitution of Eq. (4.10) and expansion at large r give

$$\psi_{\boldsymbol{k}}^{(+)}(\boldsymbol{r}) \sim \mathrm{e}^{\mathrm{i}\boldsymbol{k}\cdot\boldsymbol{r}} + f(\widehat{\boldsymbol{r}}, \boldsymbol{k})\frac{\mathrm{e}^{\mathrm{i}kr}}{r}, \qquad r \to \infty, \tag{4.12}$$

where

$$f(\widehat{\boldsymbol{r}}, \boldsymbol{k}) = -\frac{\mu}{2\pi\hbar^2}\int \mathrm{d}^3 r'\, \mathrm{e}^{-\mathrm{i}k\widehat{\boldsymbol{r}}\cdot\boldsymbol{r}'} V(\boldsymbol{r}')\psi_{\boldsymbol{k}}^{(+)}(\boldsymbol{r}'). \tag{4.13}$$

Thus the radiation condition is already contained in the resolvent boundary value. Later, analytic continuation of precisely this boundary value turns the outgoing solution into a resonance state.

The transition operator

$$T(z) = V + V\mathcal{R}_0(z)T(z) \tag{4.14}$$

packages Eq. (4.13) as

$$f(\widehat{\boldsymbol{r}}, \boldsymbol{k}) = -\frac{\mu}{2\pi\hbar^2}\langle k\widehat{\boldsymbol{r}}|T(E_k + \mathrm{i}0)|\boldsymbol{k}\rangle. \tag{4.15}$$

Normalization-dependent factors change if momentum states are normalized differently, but pole positions and on-shell observables do not.

4.1.4 Flux, cross sections, and the optical theorem

For a wave function obeying a real-potential Schrodinger equation, the probability current is

$$\boldsymbol{j}[\psi] = \frac{\hbar}{2\mu \mathrm{i}} \left(\psi^* \nabla \psi - \psi \nabla \psi^*\right). \tag{4.16}$$

The incident plane wave in Eq. (4.12) carries flux $\hbar \boldsymbol{k}/\mu$, and the outgoing spherical wave carries radial flux proportional to $|f|^2/r^2$. Their ratio gives

$$\frac{\mathrm{d}\sigma}{\mathrm{d}\Omega} = |f(\widehat{\boldsymbol{r}}, \boldsymbol{k})|^2. \tag{4.17}$$

Conservation of total flux and interference between the incident wave and the forward part of the scattered wave imply the optical theorem

$$\sigma_{\mathrm{tot}} = \frac{4\pi}{k} \operatorname{Im} f(\widehat{\boldsymbol{k}}, \boldsymbol{k}). \tag{4.18}$$

In operator form it follows from the discontinuity of the free resolvent and the identity

$$T(E + \mathrm{i}0) - T(E - \mathrm{i}0) = -2\pi \mathrm{i}\, T(E - \mathrm{i}0)\delta(E - H_0)T(E + \mathrm{i}0). \tag{4.19}$$

Equation (4.19) is the precise reason that the imaginary part of an effective Hamiltonian represents lost flux into open channels while the full theory remains unitary.

If V is replaced by a complex optical potential, elastic flux alone is not conserved. The deficit represents channels removed from the reduced model. One then has $|S_l| \leq 1$ rather than $|S_l| = 1$, and the reaction cross section measures the missing flux. This elementary example anticipates the Feshbach effective Hamiltonian of Section 6.1.

4.1.5 Partial waves, phase shifts, and threshold data

The plane-wave expansion

$$\mathrm{e}^{\mathrm{i}\boldsymbol{k}\cdot\boldsymbol{r}} = 4\pi \sum_{lm} \mathrm{i}^l j_l(kr) Y_{lm}(\widehat{\boldsymbol{r}}) Y_{lm}^*(\widehat{\boldsymbol{k}}) \tag{4.20}$$

reduces central-potential scattering to independent radial channels. For a real short-range potential, the large-r form of the regular radial solution can

be normalized as

$$u_l(k,r) \sim \frac{1}{2\mathrm{i}} \left[S_l(k) \mathrm{e}^{\mathrm{i}(kr - l\pi/2)} - \mathrm{e}^{-\mathrm{i}(kr - l\pi/2)} \right]. \tag{4.21}$$

Elastic unitarity gives

$$S_l(k) = \mathrm{e}^{2\mathrm{i}\delta_l(k)}, \qquad \delta_l(k) \in \mathbb{R}, \tag{4.22}$$

and the scattering amplitude becomes

$$f(\vartheta) = \frac{1}{2\mathrm{i}k} \sum_{l=0}^{\infty} (2l+1) \left[S_l(k) - 1 \right] P_l(\cos\vartheta). \tag{4.23}$$

Consequently

$$\sigma_{\mathrm{el}} = \frac{4\pi}{k^2} \sum_{l=0}^{\infty} (2l+1) \sin^2 \delta_l, \tag{4.24}$$

$$f_l(k) = \frac{S_l(k) - 1}{2\mathrm{i}k} = \frac{1}{k \cot \delta_l(k) - \mathrm{i}k} \qquad (l = 0). \tag{4.25}$$

Near a short-range threshold, the effective-range expansion for the s wave is

$$k \cot \delta_0(k) = -\frac{1}{a_0} + \frac{1}{2} r_0 k^2 + O(k^4), \tag{4.26}$$

where a_0 and r_0 are the scattering length and effective range. A large $|a_0|$ signals a pole close to threshold, but the pole can be a shallow bound state or a virtual state depending on its sheet. This is why a large cross section alone does not classify the singularity.

The standing-wave or reactance matrix is particularly useful on the real axis. In one partial wave set $K_l = \tan \delta_l$; then

$$S_l = \frac{1 + \mathrm{i}K_l}{1 - \mathrm{i}K_l}. \tag{4.27}$$

For a real potential K_l is real, while S_l is unitary. The T, K, and S matrices therefore emphasize, respectively, outgoing boundary values, principal-value standing waves, and the mapping from incoming to outgoing channel amplitudes. Their singularities are related, but a pole of K_l on the real axis is not by itself the invariant definition of a resonance.

4.1.6 Jost solutions as a common coordinate basis

The regular solution used in Eq. (4.21) builds the origin boundary condition into the differential equation. Jost solutions instead build the asymptotic boundary conditions into it. Let $f_l(k, r)$ and $f_l(-k, r)$ be solutions of Eq. (4.5) satisfying

$$f_l(\pm k, r) \sim \mathrm{e}^{\pm \mathrm{i}(kr - l\pi/2)}, \qquad r \to \infty, \tag{4.28}$$

where an l-dependent constant phase has been absorbed into the definition. For $k \neq 0$ they form a basis of the two-dimensional solution space. If $\varphi_l(k, r)$ is regular at the origin, it has the expansion

$$\varphi_l(k, r) = \frac{1}{2\mathrm{i}k} \left[F_l(-k) f_l(k, r) - F_l(k) f_l(-k, r) \right]. \tag{4.29}$$

With the Wronskian convention $W[u, v] = uv' - u'v$, the coefficients are

$$F_l(\pm k) = W[f_l(\pm k, \cdot), \varphi_l(k, \cdot)]. \tag{4.30}$$

The normalization in Eqs. (4.29) and (4.30) is consistent with

$$W[f_l(k), f_l(-k)] = -2\mathrm{i}k.$$

The Jost function is thus not an auxiliary spectral determinant introduced after solving the problem. It is the coefficient of the incoming Jost basis vector in the solution regular at the origin. The quotient

$$S_l(k) = \frac{F_l(-k)}{F_l(k)} \tag{4.31}$$

follows immediately. A zero of $F_l(k)$ removes the incoming component, leaving a solution that is regular at the origin and outgoing at infinity. Depending on the position of the zero in the k plane, the same algebraic condition describes a bound, virtual, or resonant state. This is the central unification emphasized in the Jost-function approach [39].

For a finite-range potential the Jost solutions and Jost function possess a large analytic domain in k; for exponentially decreasing potentials the domain is restricted by the decay rate. The point $k = 0$ requires separate threshold analysis, and Coulomb interactions require Coulomb-modified Jost functions. In an N-channel problem, $F_l(k)$ becomes a Jost matrix and bound

or resonant states satisfy

$$\det F(E) = 0. \tag{4.32}$$

Each channel momentum $k_a(E)$ supplies its own square root, so the determinant lives on a multi-sheeted energy surface. Keeping these sheets explicit is essential when a resonance crosses a threshold or coalesces with another pole.

4.2 The on-shell scattering operator as a direct integral

The energy representation constructed in Section 3.1.5 becomes a scattering representation only after the Møller operators have been defined. We now prove the missing step. This is also the point at which the symbol S acquires its full operator meaning; it is not an unspecified object that happens to commute with a Hamiltonian.

4.2.1 Intertwining is stronger than a formal commutator

Use the convention of Eq. (4.7): $\Omega^{(+)}$ describes an incoming state and $\Omega^{(-)}$ an outgoing state. Suppose the strong limits exist on $\mathcal{H}_{0,\mathrm{ac}} = P_{\mathrm{ac}}(H_0)\mathcal{H}$. Translation of the limiting time gives, first for the unitary groups and then for every bounded Borel function f, the intertwining relation

$$f(H)\Omega^{(\pm)} = \Omega^{(\pm)} f(H_0). \tag{4.33}$$

The statement includes spectral projections, not only vectors in the domain of H_0. In particular,

$$P_H(\Delta)\Omega^{(\pm)} = \Omega^{(\pm)} P_{H_0}(\Delta) \tag{4.34}$$

for every Borel set Δ.

Define

$$\mathsf{S} = \Omega^{(-)\dagger}\Omega^{(+)} \quad \text{on } \mathcal{H}_{0,\mathrm{ac}}. \tag{4.35}$$

Using Eq. (4.34) twice gives

$$P_{H_0}(\Delta)\mathsf{S} = \mathsf{S}P_{H_0}(\Delta). \tag{4.36}$$

This is *strong commutation* with H_0. The shorthand $[\mathsf{S}, H_0] = 0$ is safe only

after Eq. (4.36) has been established; a formal commutator on an unspecified common domain would be weaker.

If the wave operators are isometries, S is an isometry. If their ranges coincide with the absolutely continuous subspace of H—the asymptotic-completeness statement—then S is unitary on $\mathcal{H}_{0,\mathrm{ac}}$. Completeness is therefore the step that upgrades flux conservation in all represented channels to operator unitarity.

4.2.2 Decomposability and the on-shell fibers

Let U_0 be a multiplicity representation of H_0,

$$U_0\mathcal{H}_{0,\mathrm{ac}} = \int_{\sigma_{\mathrm{ac}}(H_0)}^{\oplus} \mathcal{K}_E \,\mathrm{d}\mu_0(E), \qquad (U_0 H_0 U_0^\dagger \psi)(E) = E\psi(E). \tag{4.37}$$

Here $\sigma_{\mathrm{ac}}(H_0)$ denotes an essential support of the absolutely continuous spectral measure; changing it on a null set changes no direct-integral vector. Equation (4.36) says exactly that $U_0\mathsf{S}U_0^\dagger$ lies in the commutant of the diagonal algebra. The decomposability theorem of Section 3.1.4 therefore yields

$$U_0\mathsf{S}U_0^\dagger = \int_{\sigma_{\mathrm{ac}}(H_0)}^{\oplus} \mathsf{S}(E)\,\mathrm{d}\mu_0(E). \tag{4.38}$$

The family $E \mapsto \mathsf{S}(E)$ is measurable and essentially bounded; when S is unitary, $\mathsf{S}(E)$ is unitary for μ_0-almost every E. This almost-everywhere family is the rigorous meaning of the *on-shell scattering matrix*.

The conclusion is representation independent, although its displayed matrix is not. Replacing the measure by $\mathrm{d}\widetilde{\mu}(E) = w(E)\mathrm{d}\mu_0(E)$ rescales fiber coordinates by $w(E)^{-1/2}$. Channel amplitudes and delta functions acquire compensating density factors. Probabilities, pole positions after analytic continuation, and the unitary equivalence class of the decomposable operator do not change.

4.2.3 The free particle and partial waves

For the three-dimensional free particle, Eq. (3.18) gives

$$\mathcal{K}_E = L^2(S^2, \mathrm{d}\Omega), \qquad E > 0. \tag{4.39}$$

Thus $\mathsf{S}(E)$ is an operator on angular wave functions at fixed energy. Rotational invariance implies that it commutes with the angular momentum

representation. For a spinless central interaction,

$$\mathsf{S}(E)Y_{lm} = S_l(E)Y_{lm}, \qquad S_l(E) = \mathrm{e}^{2\mathrm{i}\delta_l(E)}. \tag{4.40}$$

The familiar sequence of partial-wave numbers is therefore a second, discrete decomposition inside one energy fiber. Energy is the direct- integral base; (l, m) are multiplicity coordinates in the fiber.

In generalized momentum notation the same fact is often written

$$\langle \boldsymbol{k}' | \mathsf{S} | \boldsymbol{k} \rangle = \delta(E_{k'} - E_k)\, \mathsf{s}_E(\widehat{\boldsymbol{k}}', \widehat{\boldsymbol{k}}). \tag{4.41}$$

The energy delta function is not an additional dynamical assumption. It is the distributional kernel of a decomposable operator. Its normalization depends on the chosen momentum measure, which is why working first with packets avoids spurious factors.

4.2.4 Thresholds and channel multiplicity

Suppose channel a has threshold E_a. A convenient fiber is

$$\mathcal{K}_E = \bigoplus_{a:E>E_a} \mathcal{K}_{a,E}. \tag{4.42}$$

The fiber dimension jumps at thresholds. Since isolated threshold energies form a null set for Lebesgue measure, the measurable direct integral has no difficulty with the jump. Analytic continuation does: the channel momentum

$$k_a(E) = \frac{\sqrt{2\mu_a(E - E_a)}}{\hbar} \tag{4.43}$$

introduces a branch point and a sheet choice. Direct-integral theory tells us what the real-axis on-shell operator is almost everywhere; it does not supply the analytic relation between different energies or sheets. Jost functions, resolvent boundary values, and exact WKB provide that extra structure.

Checkpoint

The statement $[\mathsf{S}, H_0] = 0$ has now been unpacked into three claims: wave operators exist, their spectral projections intertwine, and the resulting scattering operator is decomposable in the spectral representation of the *comparison* Hamiltonian. None of these claims says that

S commutes with an arbitrary interacting Hamiltonian.

4.2.5 What a finite channel calculation approximates

A finite coupled-channel matrix $S^{(N)}(E)$ approximates the fiber operator $\mathsf{S}(E)$, not the full operator before energy decomposition. Its truncation contract must specify the retained channel subspace $P_N(E)\mathcal{K}_E$, the energy interval, and the norm or observable in which convergence is tested. Pointwise convergence away from thresholds need not be uniform at a threshold or pole. Conversely, exact unitarity of a finite matrix does not prove that omitted breakup channels are negligible. The CDCC Stage will turn these observations into a numerical convergence protocol.

4.3 Half-line Sturm–Liouville theory as the source of Jost data

Calculation route

Prerequisites. The radial Schrödinger equation, partial waves, and Jost asymptotics of Section 4.1.

Calculation goal. Construct the self-adjoint half-line operator from its differential expression, derive its Green kernel and spectral measure, and then continue the Wronskian that becomes the resonance condition.

Completion criterion. Given a radial potential, classify both endpoints, calculate the regular and outgoing solutions, form their Wronskian, and differentiate it to obtain a pole residue.

A radial equation becomes a scattering problem only after two logically different choices have been made. At the origin one chooses an operator domain. At infinity one chooses a comparison solution and, after analytic continuation, a sheet. Sturm–Liouville theory controls the first choice and the physical spectral measure; Jost theory adds the analytic data required for the second. Exact WKB joins them by transporting the origin solution to the asymptotic sector and calculating their Wronskian.

The purpose of this section is not to place an abstract theorem beside the radial equation. We derive each object in the order in which it is

used in a calculation. References for the underlying spectral theory include Refs. [35, 39–41].

4.3.1 The differential expression and the Hilbert space

On an interval (a, b), possibly with singular endpoints, consider

$$\tau u = \frac{1}{w(r)}\left[-\frac{\mathrm{d}}{\mathrm{d}r}\left(p(r)\frac{\mathrm{d}u}{\mathrm{d}r}\right) + q(r)u(r)\right], \tag{4.44}$$

where $p > 0$, $w > 0$ almost everywhere and $1/p, q, w$ are locally integrable. The natural Hilbert space is

$$\mathcal{H}_w = L^2((a, b), w(r)\mathrm{d}r), \qquad \langle u, v\rangle_w = \int_a^b u(r)^* v(r) w(r)\,\mathrm{d}r. \tag{4.45}$$

The maximal domain consists of functions for which u and pu' are locally absolutely continuous and $\tau u \in \mathcal{H}_w$. Absolute continuity, rather than twice continuous differentiability, is enough to make integration by parts meaningful and includes many potentials used in scattering.

For u, v in the maximal domain define the boundary bracket

$$[u, v](r) = p(r)\left(u(r)^* v'(r) - u'(r)^* v(r)\right). \tag{4.46}$$

Direct integration gives Lagrange's identity

$$\langle u, \tau v\rangle_w - \langle \tau u, v\rangle_w = [u, v](b) - [u, v](a), \tag{4.47}$$

where endpoint values are limits from inside the interval. Equation (4.47) is the radial version of probability-current conservation. It also shows why the differential formula alone does not define a self-adjoint Hamiltonian: a domain must make the boundary form vanish for every pair of domain vectors.

For the reduced radial Schrödinger equation one has $p = w = 1$ after multiplying by $2\mu/\hbar^2$,

$$\tau_l u = -u'' + \left[\frac{l(l+1)}{r^2} + U(r)\right] u, \qquad U(r) = \frac{2\mu}{\hbar^2} V(r), \tag{4.48}$$

and the spectral parameter is $k^2 = 2\mu E/\hbar^2$. The reduced function u belongs to $L^2(0, \infty; \mathrm{d}r)$ for a bound state; the factor r^2 in the three-dimensional

volume element has already been removed.

4.3.2 Regular endpoints and the boundary condition at the origin

An endpoint a is regular if it is finite and $1/p, q, w$ are integrable near it. The boundary values $u(a)$ and $(pu')(a)$ then exist. A separated self-adjoint condition is

$$u(a)\cos\alpha + (pu')(a)\sin\alpha = 0, \qquad \alpha \in [0, \pi). \tag{4.49}$$

Substituting two functions obeying the same condition into Eq. (4.46) makes the bracket vanish. Dirichlet and Neumann conditions are the cases $\alpha = 0$ and $\alpha = \pi/2$.

For the three-dimensional s wave with a nonsingular potential, the reduced operator $-\mathrm{d}^2/\mathrm{d}r^2$ on $(0, \infty)$ needs a boundary condition at $r = 0$. Regularity of the full wave function $u(r)/r$ selects

$$u(0) = 0. \tag{4.50}$$

Other self-adjoint extensions describe additional contact physics and should not be introduced accidentally by a numerical boundary stencil. The phrase "regular solution" means the solution satisfying the declared origin domain, conventionally normalized by

$$\varphi(k, 0) = 0, \qquad \varphi'(k, 0) = 1 \tag{4.51}$$

for an s wave.

4.3.3 Singular endpoints and Weyl's alternative

At a singular endpoint, individual boundary values may not exist. Weyl's classification asks instead how many solutions of

$$\tau u = zu, \qquad z \in \mathbb{C} \setminus \mathbb{R}, \tag{4.52}$$

are square integrable near that endpoint:

- the endpoint is *limit circle* if every solution is locally in L^2_w there;

- it is *limit point* if, up to scale, at most one solution is locally in L^2_w there.

The classification is independent of the chosen nonreal z. A limit-circle endpoint requires one boundary condition. At a limit-point endpoint the boundary bracket vanishes automatically on the operator domain, and no boundary condition is added. Imposing one anyway can overconstrain the problem.

The inverse-square model makes the criterion calculable. Near $r = 0$ let

$$\tau_\nu = -\frac{\mathrm{d}^2}{\mathrm{d}r^2} + \frac{\nu^2 - \frac{1}{4}}{r^2}. \tag{4.53}$$

The two Frobenius behaviors are

$$u_+(r) \sim r^{1/2+\nu}, \qquad u_-(r) \sim r^{1/2-\nu} \tag{4.54}$$

for $\nu \neq 0$, with a logarithmic replacement at $\nu = 0$. Since $\int_0^\epsilon r^{1-2\nu}\mathrm{d}r$ converges exactly when $\nu < 1$, the origin is limit circle for $0 \leq \nu < 1$ and limit point for $\nu \geq 1$. For $l(l+1)/r^2$, $\nu = l + 1/2$. Thus the bare s-wave endpoint needs the regular boundary condition, whereas $l \geq 1$ is limit point. The Langer map of Stage V replaces $l(l+1)$ by $(l+1/2)^2$ in the WKB momentum; it does not erase this operator-domain analysis.

For a sufficiently short-range potential, $r = \infty$ is limit point. A self-adjoint half-line Hamiltonian therefore uses the origin condition but no independent L^2 condition at infinity. Bound-state square integrability emerges from the spectral equation. Outgoing resonance behavior is an analytic continuation of a comparison solution, not a second self-adjoint boundary condition on the original operator.

4.3.4 Fundamental solutions, the Weyl solution, and the Green kernel

Choose real entire fundamental solutions $\theta(z, r)$ and $\phi(z, r)$ at a regular left endpoint so that

$$W[\theta, \phi] := p(\theta\phi' - \theta'\phi) = 1. \tag{4.55}$$

The solution ϕ is chosen to obey the left boundary condition. If the right endpoint is limit point, then for $z \notin \mathbb{R}$ there is a unique coefficient $m(z)$ such that

$$\psi(z, r) = \theta(z, r) + m(z)\phi(z, r) \tag{4.56}$$

is square integrable near b. The scalar $m(z)$ is the Weyl–Titchmarsh function. With the conventional choice of fundamental solutions it is a Herglotz function,

$$\operatorname{Im} z > 0 \quad \Longrightarrow \quad \operatorname{Im} m(z) > 0, \tag{4.57}$$

and has an integral representation whose measure is the spectral measure of the half-line operator.

In the convention used throughout the book, let $\mathcal{R}_H(z) = (z - H)^{-1}$. If $u_a(z, r)$ obeys the left boundary condition and $u_b(z, r)$ is the Weyl solution at the right, then

$$G(z; r, r') = \frac{u_a(z, r_<) u_b(z, r_>)}{W[u_a, u_b](z)} \tag{4.58}$$

solves $(z - H)G = \delta(r - r')/w(r')$. To check the sign, integrate across $r = r'$: the jump in $p\partial_r G$ is $+1$, exactly as required by the leading term $+(pu')'$ in $z - H$.

Equation (4.58) is more than a formula for inversion. It shows immediately that a zero of the Wronskian is a pole of the Green function and that the numerator factorizes at that zero. The remaining task is to identify u_b on the physical continuum and to continue it.

4.3.5 The spectral measure and generalized eigenfunction expansion

The boundary values of m recover the spectral measure ρ. At an absolutely continuous energy one has, in the distributional sense,

$$\frac{\mathrm{d}\rho_{\mathrm{ac}}}{\mathrm{d}E} = \frac{1}{\pi} \operatorname{Im} m(E + \mathrm{i}0), \tag{4.59}$$

while poles of m on the real axis supply point masses. If $\phi(E, r)$ is the left-regular solution in the same normalization, the spectral transform is

$$\widehat{f}(E) = \int_a^b \phi(E, r) f(r) w(r)\, \mathrm{d}r, \tag{4.60}$$

$$f(r) = \int_{\mathbb{R}} \phi(E, r) \widehat{f}(E)\, \mathrm{d}\rho(E), \tag{4.61}$$

$$\|f\|_w^2 = \int_{\mathbb{R}} |\widehat{f}(E)|^2\, \mathrm{d}\rho(E). \tag{4.62}$$

The continuum normalization is therefore not guessed from a delta function. It is determined by the pair consisting of the regular solution and its spectral

measure. Rescaling $\phi(E, r)$ rescales $\mathrm{d}\rho(E)$ inversely and leaves Eqs. (4.61)–(4.62) unchanged. This is the one-channel realization of the direct integral in Section 3.1.4.

The self-adjoint expansion contains bound states and the physical continuum, but no off-axis resonance projection. Resonance poles appear only after a boundary value of the Green kernel or m function has been analytically continued. This clean separation prevents a Gamow vector from being inserted as an extra orthogonal term in the physical spectral theorem.

4.3.6 Volterra construction of the Jost solution

Consider the s-wave equation in dimensionless form

$$u''(r) + [k^2 - U(r)]u(r) = 0. \tag{4.63}$$

The Jost solution is fixed at infinity by

$$f(k, r) \sim \mathrm{e}^{\mathrm{i}kr}. \tag{4.64}$$

Variation of constants gives the Volterra equation

$$f(k, r) = \mathrm{e}^{\mathrm{i}kr} + \frac{1}{k}\int_r^\infty \sin[k(r' - r)]U(r')f(k, r')\,\mathrm{d}r'. \tag{4.65}$$

Applying $\mathrm{d}^2/\mathrm{d}r^2 + k^2$ verifies the differential equation; the upper-triangular integration region enforces the outgoing normalization. Successive substitution produces a Neumann series. Weighted integrability of U controls convergence and analyticity in k in the appropriate half plane. For $l > 0$, Riccati–Hankel functions replace the exponential and the kernel contains the corresponding free radial Green function.

The regular solution follows from the forward Volterra equation

$$\varphi(k, r) = \frac{\sin kr}{k} + \frac{1}{k}\int_0^r \sin[k(r - r')]U(r')\varphi(k, r')\,\mathrm{d}r', \tag{4.66}$$

with Eq. (4.51). The Jost function is the constant Wronskian

$$F(k) = W[f(k, \cdot), \varphi(k, \cdot)]. \tag{4.67}$$

At $r = 0$, this convention gives $F(k) = f(k, 0)$ for the s wave. At infinity, the same Wronskian is the incoming coefficient of the regular solution, up to the

fixed normalization displayed in Eq. (4.87). Constancy of the Wronskian is the reason the origin domain and the radiation condition can be tested at different ends of the interval.

4.3.7 Worked example: the attractive spherical square well

Take

$$U(r) = \begin{cases} -U_0, & 0 < r < a, \\ 0, & r > a, \end{cases} \qquad U_0 > 0, \tag{4.68}$$

and define $q = (k^2 + U_0)^{1/2}$ on a stated branch. The regular solution is

$$\varphi(k, r) = \frac{\sin qr}{q}, \qquad 0 < r < a. \tag{4.69}$$

For $r > a$ write

$$\varphi(k, r) = A(k)\mathrm{e}^{\mathrm{i}kr} + B(k)\mathrm{e}^{-\mathrm{i}kr}. \tag{4.70}$$

Continuity at a gives

$$2B(k)\mathrm{e}^{-\mathrm{i}ka} = \frac{\sin qa}{q} + \frac{\mathrm{i}}{k}\cos qa, \tag{4.71}$$

$$2A(k)\mathrm{e}^{\mathrm{i}ka} = \frac{\sin qa}{q} - \frac{\mathrm{i}}{k}\cos qa. \tag{4.72}$$

A convenient Jost normalization is therefore

$$F(k) = \mathrm{e}^{\mathrm{i}ka}\left[\cos qa - \mathrm{i}\frac{k}{q}\sin qa\right]. \tag{4.73}$$

The purely outgoing condition $B(k) = 0$ becomes

$$q\cot(qa) = \mathrm{i}k. \tag{4.74}$$

For $k = \mathrm{i}\kappa$ on the physical sheet it gives a decaying bound state; continued into the lower half-plane it gives virtual and resonant poles. No new differential equation was introduced when the pole changed its name: only the sheet and asymptotic behavior changed.

To compute a residue, differentiate Eq. (4.73) on the same branches of k and q. The result enters as $F'(k_{\mathrm{R}})$ in Eq. (4.91). Numerically, finite differencing F across a branch cut will give the wrong normalization even if a root finder happened to locate the pole.

4.3.8 Wronskian derivatives and Zel'dovich normalization

The relation between a Wronskian derivative and a bilinear norm follows from Lagrange's identity with two nearby spectral parameters. For simplicity let

$$[-\partial_r^2 + U(r) - k^2]u(k,r) = 0. \tag{4.75}$$

Differentiate with respect to k and subtract the equation multiplied in the opposite order. Integration to R gives

$$2k \int_0^R u(k,r)^2 \, \mathrm{d}r = W[u, \partial_k u](R) - W[u, \partial_k u](0). \tag{4.76}$$

There is no complex conjugation: the resonance normalization is bilinear. The origin term is fixed by the regular normalization. For a bound state the term at infinity vanishes after the decaying solution is normalized. For a resonance it diverges on the real axis, but analytic continuation or a Zel'dovich Gaussian factor assigns the continued boundary value. The result is proportional to $F'(k_{\mathrm{R}})$.

Equation (4.76) is the calculational core of Berggren's normalization proof in Section 6.4.2: the regularized integral is not postulated independently of the pole. It is the continued derivative of the same Wronskian that defines the pole. Complex scaling makes the boundary term vanish along a rotated ray; exact WKB calculates it by connection and monodromy data. These are different realizations of one analytic identity.

4.3.9 Exact WKB computes the Jost Wronskian globally

Let ψ_{reg} denote the exact-WKB solution selected by the origin domain, including the Frobenius and Langer data when the endpoint is singular. Let ψ_{out} be the Borel-resummed branch selected by the outgoing sector at infinity. Then

$$\mathcal{C}_{\mathrm{in}}(E,\hbar) \propto W[\psi_{\mathrm{out}}, \psi_{\mathrm{reg}}] \propto F_l(k(E)). \tag{4.77}$$

Local WKB series do not determine this Wronskian. One must transport the two solutions through the Stokes graph, multiply the connection matrices in the correct order, and retain the exponentially small entries. A zero of the result removes the incoming component. Its derivative gives the residue by Eqs. (4.91) and (4.76).

This is the novel reorganization used in the rest of the book. Sturm–Liouville theory determines the physical operator and continuum measure;

Jost theory identifies the analytic Wronskian; exact WKB calculates that Wronskian nonperturbatively. Complex scaling and rigged Hilbert spaces will change the realization of the resulting pole but not the connection zero or its derivative.

4.3.10 Where Coulomb and many-body asymptotics change the construction

For a two-body Coulomb tail, the half-line differential operator and its self-adjoint spectral theorem remain valid, but the comparison solutions are not $e^{\pm ikr}$. One uses Coulomb–Hankel functions with the logarithmic phase

$$kr - \eta \log(2kr) - \frac{l\pi}{2} + \sigma_l. \tag{4.78}$$

The Coulomb-modified Jost function is a Wronskian with those reference solutions. Applying Eq. (4.65) with the free kernel to the full Coulomb potential fails because the integral is not short ranged.

For three charged particles, different cluster regions carry different logarithmic phases and no single universally usable scalar asymptotic Jost basis is known. A finite-dimensional coupled equation can still be solved in a controlled interaction region, but the global comparison dynamics must be declared separately. This is the same structural difficulty that appears as infrared dressing in QED: long-range correlations change the asymptotic state space before one asks for a pole. Section 4.5 develops that obstruction rather than hiding it in a formal plane wave.

4.3.11 A reproducible half-line pole calculation

For later laboratories, the complete calculation can be organized into the following steps:

1. specify p, q, w and the Hilbert-space measure;
2. classify every singular endpoint as limit point or limit circle;
3. impose only the boundary conditions required for a self-adjoint physical Hamiltonian;
4. construct the regular solution by an initial-value or Volterra equation;

5. choose the correct short-range or Coulomb comparison solution at infinity and construct the Jost solution;

6. form their Wronskian and verify that it is independent of the matching point;

7. declare the momentum sheet before continuing and finding a zero;

8. calculate the Wronskian derivative and a tested resolvent residue;

9. vary the matching point, integration contour, and numerical basis while tracking the pole as one analytic object.

Checkpoint

The reader should now be able to derive the Green kernel from its derivative jump, explain why an s-wave origin condition is domain data rather than a numerical convenience, obtain the square-well condition Eq. (4.74), and identify the exact-WKB incoming coefficient with a continued Sturm–Liouville Wronskian.

4.4 Step 2: Identify the analytic quantity that can have a resonance

Calculation route

Prerequisites. Jost solutions, resolvent boundary values, and the physical-sheet scattering matrix.

Calculation goal. Continue the incoming coefficient through the continuum cut and relate its zero to resolvent and S-matrix poles.

Completion criterion. State the sheet, boundary condition, and residue associated with a proposed resonance rather than identifying it only from a complex eigenvalue.

4.4.1 Self-adjoint starting point and resolvent boundary values

Let $\mathcal{H}$ be a separable Hilbert space and let H be a self-adjoint Hamiltonian on a dense domain $D(H) \subset \mathcal{H}$. For a complex number $z \notin \sigma(H)$, where $\sigma(H)$

is the spectrum, define the resolvent

$$\mathcal{R}(z) = (z - H)^{-1}. \tag{4.79}$$

The operator-valued resolvent of a self-adjoint H is analytic away from the real spectrum. If H has continuous spectrum on an interval $I \subset \mathbb{R}$, the limits $\mathcal{R}(E \pm \mathrm{i}0)$ are generally meaningful only in a weighted space or as matrix elements between sufficiently localized test vectors. The two signs are the outgoing and incoming boundary values.

Choose test vectors ϕ, ψ from a dense space Φ with stronger topology than $\mathcal{H}$. A resonance is a pole $z = z_{\mathrm{R}}$ of a meromorphic continuation of

$$F_{\phi\psi}(z) = \langle \phi | \mathcal{R}(z) | \psi \rangle \tag{4.80}$$

through the continuous spectrum to an unphysical sheet. For a simple pole,

$$F_{\phi\psi}(z) = \frac{\langle \phi, \Psi_{\mathrm{R}} \rangle \langle \widetilde{\Psi}_{\mathrm{R}}, \psi \rangle}{z - z_{\mathrm{R}}} + F^{\mathrm{reg}}_{\phi\psi}(z). \tag{4.81}$$

The right and left pole functionals are denoted by Ψ_{R} and $\widetilde{\Psi}_{\mathrm{R}}$, respectively, and $F^{\mathrm{reg}}_{\phi\psi}$ is regular at z_{R}. For a time-reversal-invariant one-channel problem, the pole energy is conventionally written

$$z_{\mathrm{R}} = E_* - \frac{\mathrm{i}}{2}\Gamma, \qquad E_* \in \mathbb{R}, \qquad \Gamma > 0. \tag{4.82}$$

The pole lifetime is $\tau = \hbar/\Gamma$ when the isolated-pole approximation is valid.

Definition (4.80) is deliberately phrased in terms of matrix elements. The continued resolvent need not be a bounded operator on the original Hilbert space. Its poles nevertheless define finite-rank residues between weighted spaces or between Φ and its dual. This distinction becomes central in the rigged-Hilbert-space construction of Section 6.4.

4.4.2 Momentum sheets and outgoing boundary conditions

Consider a one-dimensional Hamiltonian

$$H = -\frac{\hbar^2}{2m}\frac{\mathrm{d}^2}{\mathrm{d}x^2} + V(x), \qquad x \in \mathbb{R}, \tag{4.83}$$

where $m > 0$ is the particle mass and $V(x)$ is real on the real axis. Assume for the moment that $V(x)$ is short ranged. The energy and momentum are

related by

$$E = \frac{\hbar^2 k^2}{2m}. \tag{4.84}$$

The square root makes the E plane two-sheeted. On the physical sheet, a positive-energy scattering solution has real $k > 0$. Analytic continuation through the cut changes the sign of k.

With time dependence $\mathrm{e}^{-\mathrm{i}Et/\hbar}$, a purely outgoing solution obeys

$$\begin{aligned} \psi_{\mathrm{R}}(x) &\sim A_- \mathrm{e}^{-\mathrm{i}k_{\mathrm{R}}x}, && x \to -\infty, \\ \psi_{\mathrm{R}}(x) &\sim A_+ \mathrm{e}^{+\mathrm{i}k_{\mathrm{R}}x}, && x \to +\infty. \end{aligned} \tag{4.85}$$

Here A_- and A_+ are nonzero amplitudes. For a decaying resonance, k_{R} lies in the fourth quadrant, so $\operatorname{Im} k_{\mathrm{R}} < 0$. Both spatial asymptotic forms in Eq. (4.85) then grow exponentially. This is not a pathology that should be removed before defining the pole; it is the spatial counterpart of temporal decay. Regularization or analytic deformation is introduced only after the outgoing condition has selected the physical solution.

For a spherically symmetric problem, the reduced radial function $u_l(r)$ in partial wave l satisfies an analogous condition at $r \to \infty$. The regular condition at the origin replaces the left outgoing condition. With several thresholds, each channel momentum has its own square root, producing multiple sheets. A sheet must then be labeled by the signs chosen for all channel momenta rather than by a single phrase such as "the second sheet."

4.4.3 Jost functions, the scattering matrix, and pole residues

We now continue the textbook construction of Section 4.1.6 into the complex momentum plane. For a short-range radial potential, let $f_l(\pm k, r)$ be Jost solutions with asymptotic behavior

$$f_l(\pm k, r) \sim \mathrm{e}^{\pm \mathrm{i}kr}, \qquad r \to \infty. \tag{4.86}$$

Let $\varphi_l(k, r)$ be the solution regular at the origin. Its expansion in the Jost basis defines the Jost function $F_l(k)$:

$$\varphi_l(k, r) = \frac{1}{2\mathrm{i}k} \left[F_l(-k) f_l(k, r) - F_l(k) f_l(-k, r) \right]. \tag{4.87}$$

Position of k	asymptotic behavior	interpretation
$k = +\mathrm{i}\kappa$, $\kappa > 0$	$\mathrm{e}^{-\kappa r}$	bound state
$k = -\mathrm{i}\kappa$, $\kappa > 0$	$\mathrm{e}^{+\kappa r}$	virtual or antibound state
$\mathrm{Re}\, k > 0$, $\mathrm{Im}\, k < 0$	outgoing and growing	decaying resonance
$\mathrm{Re}\, k < 0$, $\mathrm{Im}\, k < 0$	time-reversed partner	antiresonance

Table 4.1: Classification of one-channel zeros of $F_l(k)$ for a real short-range potential. Threshold zeros at $k = 0$ require a separate analysis.

Up to a convention-dependent phase, the partial-wave scattering matrix is

$$S_l(k) = \frac{F_l(-k)}{F_l(k)}. \tag{4.88}$$

A zero of $F_l(k)$ removes the incoming component and therefore enforces the Siegert condition. The same zero is a pole of $S_l(k)$. This establishes the first two arrows in Eq. (1.2); rigorous versions use analytic Fredholm theory and weighted resolvents [36, 37, 39, 42].

For a real potential, complex conjugation gives the reality relation

$$F_l(-k^*) = F_l(k)^*. \tag{4.89}$$

The conventional classification of simple zeros is summarized in Table 4.1. The terms “physical” and “unphysical” refer to sheets of the energy surface, not to whether the corresponding pole has observable consequences.

The outgoing radial Green function makes the relation between a Jost zero and a resolvent pole explicit. With $r_< := \min(r, r')$ and $r_> := \max(r, r')$, its kernel can be written

$$G_l^{(+)}(k; r, r') = -\frac{2\mu}{\hbar^2} \frac{\varphi_l(k, r_<) f_l(k, r_>)}{F_l(k)}. \tag{4.90}$$

The coefficient follows by integrating the Green equation across $r = r'$ and using the Wronskian. If $F_l(k_n) = 0$ and $F_l'(k_n) \neq 0$, then

$$\operatorname*{Res}_{k=k_n} G_l^{(+)}(k; r, r') = -\frac{2\mu}{\hbar^2} \frac{\varphi_l(k_n, r_<) f_l(k_n, r_>)}{F_l'(k_n)}. \tag{4.91}$$

At the zero, $\varphi_l(k_n, r)$ is proportional to $f_l(k_n, r)$, so the residue factorizes

into a right–left dyad. Passing from a k-plane residue to an energy-plane residue introduces

$$\frac{\mathrm{d}E}{\mathrm{d}k} = \frac{\hbar^2 k}{\mu}. \tag{4.92}$$

The derivative $F_l'(k_n)$ therefore fixes the pole normalization. In Section 6.4 the same normalization is recovered from the Zel'dovich bilinear integral; the equivalence is a residue identity, not an accidental agreement of two prescriptions.

The Jost function can also be computed without matching a rapidly growing solution at a distant boundary. Write the regular solution as a running linear combination of incoming and outgoing reference solutions and impose a variation-of-constants condition that removes second derivatives of the running coefficients. The radial Schrodinger equation then becomes a pair of first-order equations for those coefficients. Their asymptotic limits are $F_l(k)$ and $F_l(-k)$. This formulation extends directly to Jost matrices, complex angular momentum, Coulomb-modified reference functions, and complex k; it is particularly useful for locating poles numerically [39].

Near an isolated one-channel pole, unitarity on the real axis and real analyticity imply the factorization

$$S(E) = \mathrm{e}^{2\mathrm{i}\delta_{\mathrm{bg}}(E)} \frac{E - z_{\mathrm{R}}^*}{E - z_{\mathrm{R}}} S_{\mathrm{slow}}(E). \tag{4.93}$$

The background phase δ_{bg} and the factor S_{slow} vary slowly only when the pole is well isolated from thresholds and other singularities. Under that approximation, a cross section contains the Breit–Wigner denominator

$$|E - z_{\mathrm{R}}|^2 = (E - E_*)^2 + \frac{\Gamma^2}{4}. \tag{4.94}$$

The residue is as important as the pole position. It controls excitation strength, channel branching, and whether interference makes a peak, a dip, or an asymmetric Fano profile. In black-hole language the analogous quantities are excitation factors and residues of the retarded Green function [43–45].

4.4.4 Phase shift and time delay

For one elastic channel, write $S(E) = \mathrm{e}^{2\mathrm{i}\delta(E)}$, where $\delta(E)$ is the scattering phase shift. The Wigner–Smith time delay is

$$\tau_{\mathrm{W}}(E) = 2\hbar \frac{\mathrm{d}\delta(E)}{\mathrm{d}E}. \tag{4.95}$$

For a unitary multichannel matrix $S(E)$, the corresponding Hermitian matrix is

$$Q(E) = -\mathrm{i}\hbar S^{\dagger}(E) \frac{\mathrm{d}S(E)}{\mathrm{d}E}. \tag{4.96}$$

A narrow isolated resonance contributes a positive Lorentzian to $\operatorname{tr} Q(E)$, but time delay is not a universal resonance criterion. Repulsive backgrounds can yield negative delays, thresholds create non-Lorentzian singularities, and an exceptionally broad pole may leave no identifiable maximum. Pole continuation remains the invariant definition.

4.4.5 From poles to time evolution

Let $|\chi\rangle$ be a normalized wave packet localized in the interaction region. For $t > 0$, its survival amplitude can be written as an inverse Laplace transform of the resolvent:

$$A_{\chi}(t) = \langle \chi | \mathrm{e}^{-\mathrm{i}Ht/\hbar} | \chi \rangle = \frac{1}{2\pi\mathrm{i}} \int_{\mathcal{C}} \mathrm{d}z \, \mathrm{e}^{-\mathrm{i}zt/\hbar} \langle \chi | \mathcal{R}(z) | \chi \rangle. \tag{4.97}$$

The contour $\mathcal{C}$ runs above the spectrum before deformation. Moving it onto a nonphysical sheet produces pole terms plus integrals along deformed cuts. A simple pole gives Eq. (1.1); a threshold at $E = E_{\mathrm{th}}$ gives a power-law contribution whose exponent depends on the threshold density of states. Thus an operational decomposition is

$$A_{\chi}(t) = A_{\mathrm{pole}}(t) + A_{\mathrm{cut}}(t) + A_{\mathrm{arc}}(t). \tag{4.98}$$

The arc term depends on the large-energy deformation and is relevant to the short-time expansion. This contour picture anticipates complex scaling: the rotated continuum is the spectral representation of the deformed cut, rather than numerical debris to be discarded.

4.5 When Step 1 fails: long-range scattering and infrared sectors

The standard scattering construction compares the full dynamics with a free reference at large times. This works for a short-range interaction because the phase accumulated on an escaping classical trajectory is finite. If $\boldsymbol{r}(t) \simeq \boldsymbol{v}t$ and $V(r) = O(r^{-1-\epsilon})$, then

$$\int^{\pm\infty} |V(\boldsymbol{v}t)|\,\mathrm{d}t < \infty. \tag{4.99}$$

For a Coulomb tail, $V_C(r) = g/r$, the same integral grows as $g|\boldsymbol{v}|^{-1}\ln|t|$. The interaction never becomes negligible in phase, even though the force tends to zero. Consequently the ordinary wave operators comparing H directly with H_0 do not exist in the form used for short-range scattering. The cure is not to discard the phase but to put it into the asymptotic dynamics [46–48].

This observation links three problems that are often taught separately. The two-body Coulomb problem requires Coulomb-distorted plane waves. The three-body Coulomb problem requires different correlated expansions in different asymptotic sectors. QED requires coherent soft-photon dressings and, in general, representations inequivalent to the vacuum Fock representation. In all three cases a long-range correlation changes the definition of an asymptotic state.

4.5.1 Two-body Coulomb waves rather than free plane waves

Consider

$$H = H_0 + \frac{g}{r}, \qquad H_0 = -\frac{\hbar^2}{2\mu}\nabla^2, \qquad E = \frac{\hbar^2 k^2}{2\mu}, \tag{4.100}$$

and introduce the Sommerfeld parameter

$$\eta = \frac{\mu g}{\hbar^2 k} = \frac{g}{\hbar v}. \tag{4.101}$$

For repulsion, $g > 0$ and $\eta > 0$. A conventionally normalized outgoing solution is

$$\psi^{C(+)}_{\boldsymbol{k}}(\boldsymbol{r}) = \mathrm{e}^{-\pi\eta/2}\Gamma(1+\mathrm{i}\eta)\mathrm{e}^{\mathrm{i}\boldsymbol{k}\cdot\boldsymbol{r}}\,{}_1F_1\left(-\mathrm{i}\eta;1;\mathrm{i}(kr-\boldsymbol{k}\cdot\boldsymbol{r})\right). \tag{4.102}$$

These formulas and their partial-wave counterparts are standard consequences of the confluent hypergeometric representation of the Coulomb problem

[37, 38]. At fixed nonforward angle and large r, its two pieces have the form

$$\psi_{\boldsymbol{k}}^{C(+)}(\boldsymbol{r}) \sim \underbrace{\mathrm{e}^{\mathrm{i}[\boldsymbol{k}\cdot\boldsymbol{r}\eta\ln(kr-\boldsymbol{k}\cdot\boldsymbol{r})]}}_{\text{Coulomb-distorted incident wave}} + f_C(\vartheta)\frac{\mathrm{e}^{\mathrm{i}[kr-\eta\ln(2kr)]}}{r}. \tag{4.103}$$

Thus the incident object is not a plane wave. Both the incident and outgoing parts contain logarithmic phases. The expansion is nonuniform in the forward direction, where the distinction between the two terms itself becomes delicate.

With

$$\sigma_l(\eta) = \arg\Gamma(l+1+\mathrm{i}\eta), \tag{4.104}$$

the Coulomb amplitude is

$$f_C(\vartheta) = -\frac{\eta}{2k\sin^2(\vartheta/2)}\mathrm{e}^{2\mathrm{i}\sigma_0 - 2\mathrm{i}\eta\ln\sin(\vartheta/2)}, \tag{4.105}$$

and its modulus gives the Rutherford cross section

$$\frac{\mathrm{d}\sigma_C}{\mathrm{d}\Omega} = \frac{\eta^2}{4k^2\sin^4(\vartheta/2)}. \tag{4.106}$$

The forward divergence is physical for an ideal unscreened infinite-range force; a realistic angular resolution or screening prescription is needed for an integrated rate.

The radial Coulomb functions make the modified boundary condition especially clear. With $\rho = kr$,

$$H_l^{(\pm)}(\eta,\rho) \sim \mathrm{e}^{\pm\mathrm{i}\left[\rho-\eta\ln(2\rho)-\frac{l\pi}{2}+\sigma_l\right]}. \tag{4.107}$$

If a short-range interaction W is added to g/r, the regular solution can be written asymptotically as

$$u_l(r) \sim \frac{1}{2\mathrm{i}}\left[S_l^N(k)H_l^{(+)}(\eta,kr) - H_l^{(-)}(\eta,kr)\right], \tag{4.108}$$

where $S_l^N = \mathrm{e}^{2\mathrm{i}\delta_l^N}$ is the Coulomb-modified nuclear matrix. Relative to free partial waves, the full matrix is

$$S_l(k) = \mathrm{e}^{2\mathrm{i}\sigma_l(\eta)}S_l^N(k). \tag{4.109}$$

Likewise, the correct distorted-wave Lippmann–Schwinger equation uses the

Coulomb Hamiltonian $H_C = H_0 + g/r$ as reference:

$$|\psi_{\boldsymbol{k}}^{(+)}\rangle = |\phi_{\boldsymbol{k}}^{C(+)}\rangle + (E + \mathrm{i}0 - H_C)^{-1} W |\psi_{\boldsymbol{k}}^{(+)}\rangle. \tag{4.110}$$

Coulomb-modified Jost functions are coefficients of $H_l^{(\pm)}$, not of $\mathrm{e}^{\pm \mathrm{i}kr}$. Factoring out the known Γ-function and logarithmic structure is essential before searching for additional short-range resonance poles.

4.5.2 Dollard comparison dynamics

The same modification has a time-dependent formulation. Along a free trajectory the asymptotic Coulomb operator in momentum space is

$$V_D(\boldsymbol{p}) = \frac{g\mu}{|\boldsymbol{p}|}. \tag{4.111}$$

Choose an arbitrary reference time $t_0 > 0$ and define

$$\Phi_D(t, \boldsymbol{p}) = \frac{\operatorname{sgn}(t)}{\hbar} V_D(\boldsymbol{p}) \ln \frac{|t|}{t_0}, \tag{4.112}$$

$$U_D(t) = \mathrm{e}^{-\mathrm{i}H_0 t/\hbar} \mathrm{e}^{-\mathrm{i}\Phi_D(t,\boldsymbol{p})}. \tag{4.113}$$

Up to sign conventions for incoming and outgoing labels, the modified wave operators are

$$\Omega_D^{(\pm)} = \operatorname*{s-lim}_{t \to \mp\infty} \mathrm{e}^{\mathrm{i}Ht/\hbar} U_D(t) P_{\mathrm{ac}}(H_0). \tag{4.114}$$

The logarithm removed by $U_D(t)$ is the time-domain version of the logarithm in Eq. (4.103). Changing t_0 changes a conventional channel phase but not a cross section. A screened Coulomb potential can also be used, but its screening radius cannot simply be sent to infinity at the level of the undressed S matrix: a divergent phase must be removed first.

For many particles, asymptotic velocities and cluster decompositions enter the comparison dynamics. Pairwise Coulomb phases are correlated because the relative momenta share the same particle momenta. This is the first sign that the many-body problem is not obtained by multiplying independent copies of the two-body answer.

4.5.3 Three charged particles: known sectors and the missing uniform form

For three particles,

$$H = H_0 + \sum_{1\le i<j\le 3} \frac{g_{ij}}{r_{ij}}. \tag{4.115}$$

Choose Jacobi coordinates $(\boldsymbol{x}_\alpha, \boldsymbol{y}_\alpha)$, where $\boldsymbol{x}_\alpha$ is the separation inside the pair $\alpha = (\beta\gamma)$ and $\boldsymbol{y}_\alpha$ separates the spectator from that pair. Infinity has several geometrically different sectors:

$$\Omega_0 : \quad r_{12} \sim r_{23} \sim r_{31} \to \infty, \tag{4.116}$$

$$\Omega_\alpha : \quad y_\alpha \to \infty, \qquad x_\alpha / y_\alpha \to 0. \tag{4.117}$$

The first is the democratic three-body breakup region. The second is a cluster region in which a pair remains close compared with the spectator distance. Their asymptotic expansions are not uniform limits of one another.

In Ω_0, the Redmond or 3C incident wave incorporates the leading Coulomb phase of every pair. In a common notation,

$$\Psi_{3\mathrm{C}}(\boldsymbol{X}) = \mathrm{e}^{\mathrm{i}\boldsymbol{K}\cdot\boldsymbol{X}} \prod_{i<j} \left[\mathrm{e}^{-\pi\eta_{ij}/2} \Gamma(1 + \mathrm{i}\eta_{ij})\, {}_1F_1(-\mathrm{i}\eta_{ij}; 1; \mathrm{i}\zeta_{ij}) \right], \tag{4.118}$$

$$\zeta_{ij} = k_{ij} r_{ij} - \boldsymbol{k}_{ij} \cdot \boldsymbol{r}_{ij}, \qquad \eta_{ij} = \frac{\mu_{ij} g_{ij}}{\hbar^2 k_{ij}}. \tag{4.119}$$

The pair momenta are constrained by the common three-body kinematics. The product reproduces the leading logarithmic phases when all separations are large, but it is not an exact factorization of the three-body Schrödinger equation. Cross derivatives and correlations generate subleading terms.

In a cluster sector Ω_α, the close pair must instead be described by its full two-body state while the spectator feels its net charge and multipole corrections. Sectorial expansions by Alt and Mukhamedzhanov and later refinements construct leading terms in these overlap regimes [49–53]. The literature therefore does contain important three-body Coulomb asymptotics. The precise open difficulty is stronger and more useful than the slogan that *no asymptotic form is known*: there is no analogue of the single two-body Coulomb wave that is elementary, exact, and uniformly controlled across all breakup, rearrangement, and coalescence sectors with simple matching of every scattering amplitude. The continuing refinement of terms in different sectors is evidence of this nonuniformity.

The original Faddeev kernel is compact for suitable short-range forces but loses this property when an unsplit Coulomb potential is inserted. Faddeev–Merkuriev theory repairs the integral equations by a configuration- space splitting

$$V_\alpha^C(\boldsymbol{x}_\alpha) = V_\alpha^{(s)}(\boldsymbol{x}_\alpha, \boldsymbol{y}_\alpha) + V_\alpha^{(l)}(\boldsymbol{x}_\alpha, \boldsymbol{y}_\alpha), \tag{4.120}$$

chosen so that the short-range part is active in the corresponding two-body sector and the long-range parts are included in channel Hamiltonians. The resulting equations have the compactness and channel structure needed for analysis and numerical resonance calculations [54, 55]. This is a powerful solution at the operator-equation level, but it does not reduce the global coordinate-space boundary condition to a product of three independent Coulomb waves.

4.5.4 From Coulomb phases to soft photons in QED

The nonrelativistic Coulomb logarithm has a direct field-theoretic analogue. For massive charged particles moving with asymptotic momenta p_i, the large-time electromagnetic interaction decreases as $1/|t|$, not faster. Integrating it produces a logarithmic phase and a coherent displacement of soft photon modes. The leading dressing function for one charge has the schematic small-$|\boldsymbol{k}|$ behavior

$$f_{p,\lambda}(\boldsymbol{k}) \sim \frac{e\, p \cdot \epsilon_\lambda(\boldsymbol{k})}{(p \cdot k)\sqrt{2|\boldsymbol{k}|}}, \qquad |\boldsymbol{k}| \to 0, \tag{4.121}$$

with gauge-dependent longitudinal pieces arranged so that physical observables satisfy Gauss' law. Since $f_{p,\lambda}(\boldsymbol{k})$ behaves as $|\boldsymbol{k}|^{-3/2}$ for generic direction,

$$\sum_\lambda \int_{|\boldsymbol{k}|<\Lambda} \mathrm{d}^3k\, |f_{p,\lambda}(\boldsymbol{k})|^2 \sim C \int_0^\Lambda \frac{\mathrm{d}|\boldsymbol{k}|}{|\boldsymbol{k}|} = \infty. \tag{4.122}$$

The coherent cloud contains an infinite expected number of arbitrarily soft photons. Its soft energy can nevertheless remain finite because insertion of one factor of $|\boldsymbol{k}|$ makes the integral convergent. The formal Weyl displacement is therefore not implemented by a unitary operator on the vacuum Fock space when the infrared cutoff is removed. This is a change of representation, not merely a large perturbative coefficient [56–58].

The many-particle soft factor depends on the entire scattering process

through the eikonal current

$$J^{\mu}_{\mathrm{soft}}(k) = \sum_{i\in\mathrm{out}} e_i \frac{p_i^{\mu}}{p_i\cdot k} - \sum_{j\in\mathrm{in}} e_j \frac{p_j^{\mu}}{p_j\cdot k}. \tag{4.123}$$

Its squared norm contains pairwise terms for every pair of external charges. Adding particles therefore adds correlated infrared data; it does not merely tensor another independent one-particle cloud. Charge conservation removes some leading pieces, but velocity-dependent soft correlations remain.

Gauss' law sharpens the statement. A charged state carries an electric flux detectable at arbitrarily large distances. Under general assumptions such a state cannot be a sharp eigenstate of the mass operator [59]. The isolated one-particle delta function expected by the LSZ/Fock picture is replaced by an infraparticle threshold with continuous spectral weight. Thus the phrase *the initial electron state in Fock space* already fails before an ordinary scattering amplitude is calculated. Rigorous constructions of infraparticle scattering states exist in models of nonrelativistic QED and illustrate how much asymptotic information must be added [60].

Three standard infrared strategies answer different questions:

1. Inclusive Bloch–Nordsieck or Yennie–Frautschi–Suura observables sum over experimentally unresolved soft radiation. Virtual and real divergences cancel in sufficiently inclusive probabilities [61].

2. Chung and Kulish–Faddeev constructions modify the asymptotic states and dynamics by coherent photon dressings. They aim at an infrared-finite amplitude between dressed sectors rather than between finite-photon Fock vectors [57, 58].

3. Algebraic approaches retain the observable algebra and describe charged or soft sectors by inequivalent representations, asymptotic flux observables, and superselection data [30, 59].

The work of Hirai and Sugishita makes the second strategy particularly concrete and also explains why it cannot be separated from Gauss' law [62–64]. Write a general asymptotic charged state schematically as

$$|\alpha; F\rangle = \mathrm{e}^{\sum_\lambda \int \mathrm{d}^3k \left(F_{\alpha,\lambda}(\boldsymbol{k}) a^\dagger_\lambda(\boldsymbol{k}) - F^*_{\alpha,\lambda}(\boldsymbol{k}) a_\lambda(\boldsymbol{k})\right)} |\alpha\rangle_{\mathrm{hard}}. \tag{4.124}$$

At finite infrared cutoff this is an ordinary coherent state. Removing the cutoff is meaningful only after the incoming and outgoing dressings have been

matched to the soft current of the hard process. In a convention-independent form, the infrared-safe "dress code" is that

$$F^{\mathrm{out}}_{\beta,\lambda}(\boldsymbol{k}) - F^{\mathrm{in}}_{\alpha,\lambda}(\boldsymbol{k}) - J_{\beta\alpha,\lambda}(\boldsymbol{k}) \quad \text{is square integrable at } \boldsymbol{k} = 0, \tag{4.125}$$

where $J_{\beta\alpha,\lambda}$ is the transverse polarization component of the universal eikonal current in Eq. (4.123); signs can be moved between J and the definitions of the in/out dressings. Equivalently, the coefficient of the logarithmically divergent norm must vanish. Terms softer than the universal $1/(p \cdot k)$ profile remain genuine choices of the asymptotic state rather than infrared counterterms.

This condition has three complementary readings. Dynamically, it is the cancellation of the virtual soft factor by the coherent clouds attached to the asymptotic states. Gauge theoretically, the dressing supplies the electric field required by the Gauss constraint, so an arbitrary Faddeev–Kulish-like coherent factor is not automatically sufficient. Asymptotically, the matching condition is conservation of the large-gauge charge and can be read as the electromagnetic memory relation between past and future null infinity. Hirai and Sugishita further show that the choice of dressing matters even for inclusive measurements: tracing over unresolved photons can erase interference between hard wave packets unless the initial and final clouds obey the corresponding dress code. The dressed-state and inclusive prescriptions are therefore compatible but are not interchangeable.

An inclusive cross section can be finite even when no unitary S matrix exists between the naive charged Fock vectors. Conversely, specifying a dressed state requires more information than specifying an experimental resolution. Conflating these two statements is a common source of apparent contradictions in discussions of the infrared problem.

4.5.5 Composite charged operators and long-range correlations

A local bare electron field is not gauge invariant. A gauge-invariant charged operator must also create its electric field. A Dirac-type dressing is

$$\Psi_f(x) = \mathrm{e}^{\mathrm{i}e\int \mathrm{d}^3y\, f^i(\boldsymbol{x}-\boldsymbol{y})A_i(x^0,\boldsymbol{y})}\psi(x), \qquad \partial_i f^i(\boldsymbol{z}) = \delta^{(3)}(\boldsymbol{z}). \tag{4.126}$$

The Coulomb choice $f^i(\boldsymbol{z}) = -\partial^i(4\pi|\boldsymbol{z}|)^{-1}$ extends to spatial infinity and creates the Coulomb field together with the charge [65]. A Wilson-line dressing chooses a different field geometry. Neither is a compactly supported

local composite operator.

It is therefore useful, with a qualification, to describe part of the QED infrared problem as an infrared singularity of a composite operator produced by long-range correlations. The qualification is that three structures must be distinguished:

1. soft divergences of amplitudes between inappropriate Fock states;

2. the absence of a sharp charged one-particle mass pole, or infraparticle phenomenon;

3. infrared sensitivity of nonlocal gauge-invariant dressings and their correlation functions.

They have a common origin in massless propagation and Gauss' law, but they are not identical divergences. Wilson-line composites also possess ultraviolet endpoint or cusp renormalization, which should not be relabeled as infrared merely because the line reaches infinity.

For several charges, a product of individually dressed fields is generally not the final asymptotic operator. Cross terms determined by relative velocities and total soft charge correlate the dressings. This mirrors the three-body Coulomb problem: the long-range cloud is a property of the whole channel and its cluster limits, not a universal one-body factor attached after the calculation.

4.5.6 Operator-algebraic interpretation of infrared sectors

Let $\mathfrak{A}_{\mathrm{obs}}$ be an abstract algebra of gauge-invariant observables. The vacuum defines a Fock representation $\pi_0(\mathfrak{A}_{\mathrm{obs}})$ through its GNS state. A coherent shift by a square-integrable one-particle wave function is unitarily implemented in that representation. The infrared displacement in Eq. (4.122) is not square integrable, so the limiting charged state can define a representation π_{IR} disjoint from π_0. The abstract observable algebra can remain the same while the Hilbert-space representation changes.

Asymptotic electric flux, soft charge, or velocity data may supply central or superselection labels for an enlarged asymptotic algebra. Under appropriate separability and measurability assumptions, a mixed representation can be

problem	naive comparison state	long-range obstruction	appropriate replacement
short-range two-body	free plane wave or packet	none after an integrable phase	ordinary Møller wave operators
two-body Coulomb	free plane wave	logarithmic phase along a free trajectory	Coulomb wave and Dollard dynamics
three-body Coulomb	product of independent pair waves	incompatible breakup and cluster limits	sectorial asymptotics and Faddeev–Merkuriev channels
QED charged scattering	finite-photon charged Fock vector	non-square-integrable soft cloud and Gauss' law	inclusive observables, dressed states, or non-Fock sectors

Table 4.2: The hierarchy of long-range modifications. Each row changes the asymptotic comparison problem, not the local equations of motion.

organized schematically as

$$\mathcal{H}_{\mathrm{as}} = \int_X^{\oplus} \mathcal{H}_\xi \, \mathrm{d}\mu(\xi), \tag{4.127}$$

$$\mathcal{M}_{\mathrm{as}} = \int_X^{\oplus} \mathcal{M}_\xi \, \mathrm{d}\mu(\xi). \tag{4.128}$$

Here ξ can include soft or flux data and μ describes the statistical mixture. This direct integral is an organizational theorem, not a cure by itself: a choice of measure and measurable field must be supplied, and disjoint fibers are not connected by a unitary operator in any one fiber. Scattering should instead be formulated as an intertwiner between appropriate incoming and outgoing representations or as a map of asymptotic observable algebras.

4.5.7 Consequences for resonances, complex scaling, and exact WKB

Long-range asymptotics changes the analytic surface on which a resonance is defined. Because $\eta \propto 1/k$, the Coulomb factors contain $\Gamma(l+1+\mathrm{i}\eta)$ and logarithms with an essential threshold structure at $k=0$. A short-range square-root sheet is therefore insufficient. Pole searches should factor the pure

Coulomb contribution and continue the Coulomb-modified Jost determinant. Response functions should be compared with a reference Hamiltonian carrying the same Coulomb tail.

Complex scaling can be applied to important Coulombic Hamiltonians under appropriate dilation-analytic hypotheses, but it does not restore free asymptotics. Exterior scaling, channel-adapted coordinates, and Faddeev–Merkuriev decompositions may be required in many-body problems. A rotated eigenvalue must be interpreted relative to the correct Coulomb thresholds and reference continuum.

Exact WKB displays the two-body logarithm immediately. At large r,

$$p(r) = \sqrt{2\mu\left(E - \frac{g}{r}\right)} = \hbar k - \frac{\mu g}{\hbar k}\frac{1}{r} + O(r^{-2}), \tag{4.129}$$

so

$$\frac{1}{\hbar}\int^{r} p(r')\,\mathrm{d}r' = kr - \eta \ln r + O(r^{-1}). \tag{4.130}$$

The Coulomb phase is therefore a global WKB period reaching infinity. In the three-body problem the corresponding Hamilton–Jacobi function is multivariable and its cluster limits are nonuniform. In QED the asymptotic phase becomes an operator-valued soft dressing.

A genuinely field-theoretic resonance theory must combine these infrared representations with analytic continuation of multiparticle correlation functions. For a charged unstable excitation, an infraparticle cut and a resonance pole need not be separable by the elementary pole-plus-background ansatz. Constructing an asymptotic algebra, its incoming and outgoing GNS representations, and a continued spectral object carrying widths and residues is a central open problem in extending the present program from potential scattering to gauge theory.

4.6 Gauge constraints, observable algebras, and physical Hilbert spaces

Long-range QED exposes a question that is already present in every gauge theory: which Hilbert space is physical? A gauge-fixed field algebra, a BRST complex, a gauge-invariant observable algebra, and the Hilbert space used by a lattice simulator are related, but they are not the same object. Direct integrals clarify the relation only if they are applied at the correct stage.

They decompose a representation that has already been selected; they do not select the physical representations by themselves.

This section gives an observable-first construction and compares it with the BRST route. It then separates two sources of nonfactorization: generic local QFT structure and the additional constraint imposed by Gauss law. The aim is not a nonperturbative construction of Yang–Mills theory. It is a precise list of the data such a construction would have to provide.

4.6.1 Three layers that must not be collapsed

It is useful to keep three mathematical layers visible:

(i) a kinematical field space, possibly gauge fixed and possibly carrying an indefinite inner product;

(ii) an abstract net or algebra $\mathfrak{A}_{\mathrm{obs}}$ of gauge-invariant observables; and

(iii) one or more positive Hilbert-space representations $(\pi, \mathcal{H}, \Omega)$ selected by a state, an energy condition, and a charge or asymptotic criterion.

Gauge-dependent fields can be invaluable coordinates for calculation, while the observable algebra records what can be measured without choosing those coordinates. A Hilbert representation adds the state-dependent meaning of expectation values, spectrum, and weak closure. In systems with infinitely many degrees of freedom there need not be one representation containing all physically relevant sectors.

For a relativistic theory the observable-first datum is a net

$$\mathcal{O} \longmapsto \mathfrak{A}(\mathcal{O}), \qquad \mathcal{O}_1 \subset \mathcal{O}_2 \Longrightarrow \mathfrak{A}(\mathcal{O}_1) \subset \mathfrak{A}(\mathcal{O}_2), \tag{4.131}$$

with locality

$$[A_1, A_2] = 0 \quad \text{if } \mathcal{O}_1 \text{ and } \mathcal{O}_2 \text{ are spacelike separated.} \tag{4.132}$$

Covariance, a spectrum condition, and an appropriate vacuum or thermal state complete the basic data. The quasilocal C^* algebra is obtained by norm completion of the union of local algebras. A state ω then constructs the Hilbert space through GNS:

$$\omega(A) = \langle \Omega_\omega, \pi_\omega(A)\Omega_\omega \rangle, \qquad \mathcal{H}_\omega = \overline{\pi_\omega(\mathfrak{A}_{\mathrm{obs}})\Omega_\omega}. \tag{4.133}$$

Thus positivity belongs to the state on observables, not to a particular gauge potential.

4.6.2 The BRST cohomological route

Covariant gauge fixing enlarges the field space by longitudinal modes, ghosts, and auxiliary fields. Let $\mathcal{K}$ denote the resulting Krein space and Q a nilpotent BRST charge,

$$Q^2 = 0. \tag{4.134}$$

The algebraic physical space is the cohomology

$$\mathcal{H}_{\mathrm{BRST}}^{\mathrm{alg}} = \ker Q / \operatorname{im} Q. \tag{4.135}$$

To obtain a Hilbert space one still has to prove that the induced sesquilinear form is positive semidefinite, quotient its null vectors, and complete the result. Observables are represented by BRST-closed operators modulo exact ones. In the Kugo–Ojima framework this implements the quartet mechanism and connects color confinement to the global BRST charge under explicit assumptions [66].

Equation (4.135) is elegant because local covariant fields and positivity are reconciled after taking cohomology. It is not, however, a definition that can simply be assumed in an arbitrary nonperturbative theory. One needs a globally defined nilpotent charge, a controlled domain, positivity of the quotient, and a state space on which the construction is complete. Gribov copies obstruct a global gauge slice, and their topology warns that a perturbative BRST complex need not automatically extend to the full configuration space [67, 68]. Abandoning these global questions may be a deliberate approximation, but it must then be identified as part of the truncation contract.

4.6.3 The observable-first definition

If BRST cohomology is not taken as the global starting point, a nonperturbative physical Hilbert space should be defined in the following order:

1. construct a positive gauge-invariant observable algebra or net, including its dynamics;

2. select a class of physical states by positivity, the Gauss constraint, energy and regularity conditions, and the desired vacuum, thermal,

charge, or asymptotic behavior;

3. apply GNS to each selected state or folium;

4. compare the resulting representations by unitary equivalence, quasi-equivalence, or disjointness; and

5. only then form direct sums or direct integrals when a specified mixed representation and measure call for them.

In symbols, a selected family $\{\omega_\xi\}_{\xi\in X}$ can produce

$$\pi_\mu = \int_X^\oplus \pi_\xi \,\mathrm{d}\mu(\xi), \qquad \mathcal{H}_\mu = \int_X^\oplus \mathcal{H}_\xi \,\mathrm{d}\mu(\xi), \tag{4.136}$$

provided the fields are measurable. The measure μ is part of the state or ensemble; it is not determined by the abstract algebra alone. A pure sector may require only one factor representation. A finite compact lattice problem more often gives a direct *sum*. A genuine direct integral is natural for continuous charge or flux data, infinite volume, or a central decomposition with a nonatomic center.

This answers the apparent dilemma. Insisting on a direct integral "on the observable side" is legitimate as a posterior decomposition of a chosen representation. It cannot replace the state-selection problem. Without the selected state class and measure, the phrase "the physical Hilbert space" is underdetermined.

4.6.4 Central decomposition is not sector classification

Let $\mathcal{M}_\omega = \pi_\omega(\mathfrak{A}_{\mathrm{obs}})''$. Reduction theory gives, under the hypotheses of Section 3.1.7,

$$\mathcal{M}_\omega = \int_X^\oplus \mathcal{M}_{\omega,\xi} \,\mathrm{d}\mu_\omega(\xi), \qquad \mathcal{Z}(\mathcal{M}_{\omega,\xi}) = \mathbb{C}\mathbf{1}_\xi \quad \text{a.e.} \tag{4.137}$$

This decomposes one represented algebra into factors. A superselection theory asks a different question: which representations of the abstract net are physically admissible, and how do charges compose? The DHR criterion selects charges indistinguishable from the vacuum outside bounded regions [69]. Gauss-law charges are detectable at arbitrarily large distances and do not satisfy that compact-localization criterion. Spacelike-cone localization

and asymptotic constructions provide weaker alternatives in suitable theories [59, 70].

Consequently, a factor fiber in Eq. (4.137) should be called a factor component until a physical selection criterion identifies it with a charge sector. Conversely, two charge sectors may be disjoint representations of the same simple quasilocal algebra even though the abstract algebra has trivial center. The center appears after representation or after restricting to a region with boundary data; it need not be present in the global abstract algebra.

4.6.5 Solving Gauss law on a lattice

Hamiltonian lattice gauge theory makes the reorganization operational [71]. Before imposing constraints, a finite graph with links e has a kinematical tensor product

$$\mathcal{H}_{\mathrm{kin}} = \bigotimes_{e} \mathcal{H}_e \otimes \bigotimes_{v} \mathcal{H}_v^{\mathrm{matter}}. \tag{4.138}$$

At every vertex, the Gauss operator G_v generates a gauge transformation. The physical subspace is

$$\mathcal{H}_{\mathrm{phys}} = \{\psi \in \mathcal{H}_{\mathrm{kin}} : G_v \psi = \psi \text{ for all } v\} \tag{4.139}$$

for a finite gauge group, with the corresponding zero-generator condition for a Lie group. The orthogonal projector is the group average

$$P_G = \prod_{v} \int_G \mathrm{d}g_v \, U_v(g_v). \tag{4.140}$$

Since a vertex transformation acts on all incident links, P_G does not factor into independent projectors for arbitrary spatial subregions.

One can solve the constraints explicitly by choosing a spanning tree and expressing tree-link variables through matter charges and the remaining loop variables. This can reduce the number of degrees of freedom and is valuable for quantum simulation [72]. The price is that an operator local in the original link variables may become a string along the chosen tree. The exact shape of that string is encoding dependent. The need to carry boundary flux and the failure of a naive regional tensor product are not.

4.6.6 Laboratory: the smallest $\mathbb{Z}_2$ boundary-flux sector

Consider a connected region whose interior is a single link joining two vertices. One external link crosses the boundary at each vertex. In the electric basis write the $\mathbb{Z}_2$ labels as q_L, q, $q_R \in \{0, 1\}$. With no interior matter charge, Gauss law gives

$$q_L + q = 0, \qquad q + q_R = 0 \pmod 2. \tag{4.141}$$

Hence $q_L = q = q_R$. If the exterior is not included in the regional Hilbert space, the physical regional space has the decomposition

$$\mathcal{H}_R^{\text{phys}} = \mathcal{H}_{R,0} \oplus \mathcal{H}_{R,1}. \tag{4.142}$$

Each summand has fixed boundary electric flux. Gauge-invariant operators strictly inside the region cannot change that label. The boundary-flux operator therefore lies in the center of the regional observable algebra and the projectors onto $\mathcal{H}_{R,0}$ and $\mathcal{H}_{R,1}$ are central projections.

For this finite compact example the correct structure is a direct sum, not a direct integral. Joining the region to its exterior requires matching the left and right boundary representations and contracting their indices. An "extended Hilbert space" can instead introduce edge variables so that a tensor product is restored before imposing the matching condition [73, 74]. These are different encodings of the same gauge-invariant content, provided the boundary algebra and its center are tracked.

4.6.7 Which nonlocality is an artifact?

The answer has two parts.

Encoding-dependent nonlocality.

A spanning tree, Jordan–Wigner-like ordering, gauge fixing, or choice of edge modes determines where strings are drawn and which qubits store a loop variable. Changing the encoding can move or shorten those strings.

Structural nonlocality or nonfactorization.

Gauss law ties charge in a region to flux through its boundary. Charged fields cannot be both gauge invariant and compactly localized without an accompanying dressing. Regional observable algebras possess

boundary superselection data, and the physical subspace generally fails to equal a tensor product of independently physical subregions.

Thus not every long Pauli string seen by a simulator is fundamental, but the constraint that makes some boundary or dressing data unavoidable is fundamental.

There is also a logically separate AQFT effect. Local von Neumann algebras in continuum relativistic QFT are typically type III and therefore are not ordinary tensor factors with density matrices, even in a theory without gauge charge. When nested regions $\mathcal{O}_1 \Subset \mathcal{O}_2$ satisfy the *split property*, there exists a type I factor $\mathcal{N}$ such that

$$\mathfrak{A}(\mathcal{O}_1)'' \subset \mathcal{N} \subset \mathfrak{A}(\mathcal{O}_2)''. \tag{4.143}$$

The collar between the regions permits an approximate subsystem structure [75]. Type III nonfactorization, failure of the split property, and a Gauss-law boundary center should therefore be diagnosed separately; calling all three "nonlocal encoding" loses the distinction.

4.6.8 Connection coefficients sector by sector

The observable-first picture meets the analytic strategy of this book when a Hamiltonian or radial problem decomposes over a measurable sector variable:

$$\mathcal{H}_\mu = \int_X^{\oplus} \mathcal{H}_\xi \, \mathrm{d}\mu(\xi), \qquad H = \int_X^{\oplus} H_\xi \, \mathrm{d}\mu(\xi). \tag{4.144}$$

If each fiber has a connection problem, exact WKB produces an incoming coefficient $\mathcal{C}_{\mathrm{in}}(E, \xi)$. A fiber resonance satisfies

$$\mathcal{C}_{\mathrm{in}}(E_{\mathrm{R}}(\xi), \xi) = 0. \tag{4.145}$$

But performing this calculation independently in every fiber is not yet an operator theorem. One must prove measurability in ξ, choose analytic continuation domains uniform on the relevant set of sectors, control residues near thresholds, and justify interchanging continuation with the direct integral. If pole curves collide or escape through a sector-dependent cut, no single contour need isolate them uniformly.

This is a concrete open interface between exact WKB and operator algebras. The connection coefficient supplies analytic information that the

measurable decomposition alone lacks; the direct integral supplies the topology and measure needed to assemble fiber calculations into a physical state space. Neither construction subsumes the other.

Checkpoint

A nonperturbative gauge theory is not assigned a physical Hilbert space by writing a direct integral. It is assigned an observable algebra, dynamics, and a physically selected state class; GNS constructs the representations. Direct sums, direct integrals, and central decompositions then organize those representations. Solving Gauss law can make a chosen encoding nonlocal, while boundary flux, charged dressing, and nonfactorization are structural data that any faithful encoding must preserve.

4.7 Problems for Stage II

II.1 Derive the reduced mass and center-of-mass separation for two particles. State precisely which potential hypotheses allow the internal and center-of-mass domains to factorize.

II.2 Starting from the resolvent identity, derive the Lippmann–Schwinger equation for $|\psi^{(+)}\rangle$. Check the sign of the outgoing Green function using the time convention of the book.

II.3 Evaluate the free Green kernel in three dimensions and recover its outgoing asymptotic form. Use it to derive the first Born amplitude.

II.4 Derive the probability current and the factor k_f/k_i in a multichannel differential cross section. Show how flux normalization removes this factor from the unitarity relation for the on-shell S matrix.

II.5 Prove the optical theorem from partial-wave unitarity. Then insert a complex optical potential and identify the additional reaction cross section.

II.6 Express a radial Green function in terms of regular and outgoing Jost solutions. Show that a zero of the Jost function gives a pole and compute the residue for a simple zero.

II.7 Derive the logarithmic Coulomb phase by integrating the potential along a straight asymptotic trajectory. Explain why replacing a Coulomb wave by a plane wave changes the definition of the scattering amplitude.

II.8 Verify directly that the ordinary Møller limit fails for the Coulomb Hamiltonian at the level of the phase. Construct the corresponding Dollard modifier in the one-particle relative problem.

II.9 List the three cluster asymptotic regions of a three-charge problem and the different large variables in each. Explain why pairwise Coulomb phases do not automatically give a uniform approximation in their overlap.

II.10 For a coherent soft-photon dressing with profile $f(\boldsymbol{k})$, determine the condition for a finite Fock norm. Compare it with the infrared behavior required by the Coulomb field of a charged particle.

II.11 Derive Lagrange's identity Eq. (4.47) for the general Sturm–Liouville expression. Show that two functions obeying the same separated regular-endpoint condition have zero boundary bracket.

II.12 For $-\mathrm{d}^2/\mathrm{d}r^2 + g/r^2$, calculate both Frobenius exponents and reproduce the limit-point threshold $g = 3/4$. State the domain condition needed for the physical s wave.

II.13 Derive the sign and normalization of the Green kernel Eq. (4.58) by integrating across $r = r'$. Repeat for the opposite resolvent convention.

II.14 Match the regular square-well solution at $r = a$ and obtain Eqs. (4.73) and (4.74). Track one bound-state zero as the well depth is reduced through threshold.

II.15 Differentiate the radial equation with respect to k and derive Eq. (4.76). Evaluate the boundary term for a decaying bound state and explain which analytic continuation is required for a Gamow state.

Part II

The exact-WKB construction of resonance

Chapter 5

Stage III: Build the global connection problem

Reader contract

This stage constructs the resonance rather than postulating a complex eigenvalue. Local Riccati branches are Borel resummed, transported through Stokes sectors, and assembled into a Wronskian-preserving connection matrix. The stage ends when the prohibited incoming coefficient, its zero, its derivative, and the decay width can all be calculated.

5.1 Step 3: Construct the local resurgent basis

Calculation route

Prerequisites. The spectral curve $y^2 = Q(x, E)$ and the asymptotic coefficients fixed in Sec. 4.1.

Calculation goal. Generate the all-order Riccati series, separate odd and even parts, Borel resum in a declared direction, and identify the turning-point Stokes data.

Completion criterion. Produce normalized sectorial WKB branches whose ambiguity and domain of validity are explicit.

5.1.1 Riccati equation and formal WKB solutions

Consider the Schrödinger equation in the form

$$\left[-\hbar^2 \frac{\mathrm{d}^2}{\mathrm{d}x^2} + Q(x, E)\right] \psi(x) = 0, \qquad Q(x, E) = 2m\,[V(x) - E]\,. \tag{5.1}$$

The coordinate x and energy E may be complex. Introduce the logarithmic derivative

$$\psi(x) = \mathrm{e}^{\int^x S(x',\hbar)\mathrm{d}x'}. \tag{5.2}$$

Then S satisfies the Riccati equation

$$S^2 + \frac{\partial S}{\partial x} = \frac{Q}{\hbar^2}. \tag{5.3}$$

Seek a formal solution

$$S^{(\pm)}(x,\hbar) = \sum_{n=-1}^{\infty} \hbar^n S_n^{(\pm)}(x). \tag{5.4}$$

The leading terms are

$$S_{-1}^{(\pm)} = \pm\sqrt{Q}, \qquad S_0^{(\pm)} = -\frac{1}{4}\frac{\partial_x Q}{Q}. \tag{5.5}$$

For $n \geq 0$, the remaining coefficients obey

$$2S_{-1}^{(\pm)} S_{n+1}^{(\pm)} = -\partial_x S_n^{(\pm)} - \sum_{j=0}^{n} S_j^{(\pm)} S_{n-j}^{(\pm)}. \tag{5.6}$$

Define odd and even parts under exchange of the two leading branches:

$$\begin{aligned} S_{\mathrm{odd}} &= \frac{1}{2}\left(S^{(+)} - S^{(-)}\right), \\ S_{\mathrm{even}} &= \frac{1}{2}\left(S^{(+)} + S^{(-)}\right) = -\frac{1}{2}\partial_x \log S_{\mathrm{odd}}. \end{aligned} \tag{5.7}$$

The formal WKB solutions normalized at a reference point x_0 are

$$\psi_{\pm}(x) = \frac{1}{\sqrt{S_{\mathrm{odd}}(x)}} \mathrm{e}^{\pm\int_{x_0}^{x} S_{\mathrm{odd}}(x')\mathrm{d}x'}. \tag{5.8}$$

The square root, integration path, and sheet of $\sqrt{Q}$ are part of the definition. A local asymptotic series becomes a global spectral statement only after these data and the Stokes transitions are specified.

If the original differential equation contains a first-derivative term, a local gauge transformation first removes it and shifts Q by a term of order $\hbar^2$. Such terms are easily dismissed in leading semiclassics but can carry essential monodromy at a regular singular point. The radial Langer term in Section 7.1 is the principal example.

5.1.2 Borel transform and lateral resummation

The series in Eq. (5.4) is generally divergent. For a formal series

$$f(\hbar) = \sum_{n=0}^{\infty} a_n \hbar^n, \tag{5.9}$$

define its Borel transform by

$$\mathcal{B}f(\xi) = \sum_{n=0}^{\infty} \frac{a_n}{n!} \xi^n. \tag{5.10}$$

If $\mathcal{B}f$ can be analytically continued with suitable growth along the ray $\arg \xi = \varphi$, its directional Borel sum is

$$\mathcal{S}_\varphi f(\hbar) = \frac{1}{\hbar} \int_0^{\mathrm{e}^{\mathrm{i}\varphi}\infty} \mathrm{d}\xi \, \mathrm{e}^{-\xi/\hbar} \mathcal{B}f(\xi). \tag{5.11}$$

When a Borel singularity lies on the integration ray, define lateral sums $\mathcal{S}_{\varphi\pm}$. Their difference is exponentially small in $\hbar$ and is governed by a Stokes automorphism. This is the point at which nonperturbative saddles enter a perturbative expansion. In a metastable problem, the same analytic discontinuity that resolves a Borel ambiguity produces the imaginary part of the resonance energy [76–79].

The phrase *exact WKB* does not mean truncating the WKB series at high order. It means using Borel-resummed WKB solutions and their exact connection formulae. Truncation may approximate a Borel sum before the least term, but it does not determine lateral continuation or global monodromy.

5.1.3 Turning points and Stokes geometry

A simple turning point a satisfies

$$Q(a, E) = 0, \qquad \partial_x Q(a, E) \neq 0. \tag{5.12}$$

Choose a branch of the classical action

$$W_a(x; E) = \int_a^x \sqrt{Q(x', E)} \mathrm{d}x'. \tag{5.13}$$

In the convention used here, Stokes curves are trajectories on which

$$\operatorname{Im}\left[\frac{W_a(x;E)}{\hbar}\right] = 0. \tag{5.14}$$

Some literature interchanges the names Stokes and anti-Stokes curves; the connection matrices, rather than the label, fix the convention. Three curves emanate from a simple turning point. On crossing one of them, the coefficient of a subdominant solution changes by a multiple of the dominant solution.

Let the local solution be represented by a coefficient column $\boldsymbol{c} = (c_+, c_-)^{\mathsf{T}}$. Up to orientation and normalization, simple turning-point connections have triangular form

$$M_+(\sigma) = \begin{pmatrix} 1 & \sigma \\ 0 & 1 \end{pmatrix}, \qquad M_-(\sigma) = \begin{pmatrix} 1 & 0 \\ \sigma & 1 \end{pmatrix}, \tag{5.15}$$

where the Stokes multiplier σ is $+\mathrm{i}$ or $-\mathrm{i}$ for the standard Airy normalization, depending on the crossing direction. A global connection problem is an ordered product of such matrices, propagation factors, and monodromy matrices. The physical boundary condition states that one component of the final coefficient column vanishes.

5.1.4 Voros symbols and exact quantization

For a path or cycle γ on the spectral curve $y^2 = Q(x, E)$, define the formal Voros integral and symbol by

$$\begin{aligned} V_\gamma(E,\hbar) &= \int_\gamma S_{\mathrm{odd}}(x,\hbar)\mathrm{d}x, \\ \mathcal{V}_\gamma(E,\hbar) &= \mathrm{e}^{V_\gamma(E,\hbar)}. \end{aligned} \tag{5.16}$$

Both are understood through a specified lateral Borel sum. For a simple two-turning-point bound-state problem, the connection condition often reduces to

$$1 + \mathcal{V}_\gamma(E,\hbar) = 0. \tag{5.17}$$

At leading order this gives the Bohr–Sommerfeld rule including the Maslov phase. More complicated graphs produce polynomial or cluster-like relations among several Voros symbols [12–14].

For a resonance, the algebra is the same but the selected subdominant sectors are different. Let $\mathcal{C}_{\mathrm{in}}(E,\hbar)$ be the connection coefficient of the incom-

ing asymptotic solution after transporting an outgoing solution across the Stokes graph. The exact resonance condition is

$$\mathcal{C}_{\mathrm{in}}(E,\hbar)=0. \tag{5.18}$$

Thus the last arrow in Eq. (1.2) is not an analogy: $\mathcal{C}_{\mathrm{in}}$ is a Jost function expressed in resurgent coordinates.

5.1.5 Local normalization versus global invariants

The starting point of a WKB integral, the normalization of local bases, and the detailed shape of a connection path are not separately physical. Changing them conjugates connection matrices or multiplies rows and columns by nonzero factors. Zeros of the incoming coefficient, closed Voros periods, and monodromy conjugacy classes are invariant. We will refer to the local choices as a connection gauge. This language is useful in radial problems, where an open path from the origin to infinity and a closed contour encircling the origin can encode identical quantization data [25].

5.2 Step 4: Transport the basis without losing the Wronskian

Let $\mathbf{\Psi}=(\psi_+,\psi_-)^{\mathsf{T}}$ be a local WKB basis with constant Wronskian. Crossing a simple Stokes curve multiplies its coefficient vector by one of the triangular matrices in Eq. (5.15). Transport between reference points a and b gives a diagonal matrix

$$P_{ab}=\begin{pmatrix} \mathrm{e}^{V_{ab}} & 0\\ 0 & \mathrm{e}^{-V_{ab}}\end{pmatrix},\qquad V_{ab}=\int_a^b S_{\mathrm{odd}}\,\mathrm{d}x. \tag{5.19}$$

A global connection matrix is an ordered product

$$M_\Gamma=M_{j_n}P_{n-1,n}\cdots M_{j_2}P_{12}M_{j_1}. \tag{5.20}$$

Changing local normalization conjugates or diagonally rescales M_Γ. Its relevant zero condition and monodromy eigenvalues are unchanged.

For an equation without a first-derivative term, the Wronskian

$$W[\psi_1,\psi_2]=\psi_1\partial_x\psi_2-\psi_2\partial_x\psi_1 \tag{5.21}$$

is independent of x. Consequently every exact connection matrix has unit determinant after consistent basis normalization. This algebraic constraint is a useful check on symbolic and numerical Stokes calculations.

5.3 Step 5: Turn the no-incoming condition into a pole equation

5.3.1 Outgoing conditions as subdominance after continuation

On the real axis a resonance wave grows at both spatial ends. In the complex x plane, the same exponential is decaying in appropriate sectors. Exact WKB analysis selects a Borel-summed solution that is subdominant in one such sector, transports it across the Stokes graph, and requires it to be subdominant in the sector representing the other outgoing end. Complex scaling implements a fixed contour through these sectors; exact WKB records the sector changes algebraically.

Suppose $V(x) \to 0$ at both ends and define k by Eq. (4.84). Asymptotically, $S_{\text{odd}} \to \mathrm{i}k$ or $-\mathrm{i}k$. Rotating the coordinate by $x = \mathrm{e}^{\mathrm{i}\theta}y$ changes which exponential is subdominant according to Eq. (6.16). The exposure condition of complex scaling is therefore a statement that the chosen contour lies inside the exact-WKB subdominant sectors. From this viewpoint, rotation of the essential spectrum and deformation of the Stokes graph are complementary descriptions of the same analyticity [16, 17].

5.3.2 The inverted Rosen–Morse barrier

The inverted Rosen–Morse, or Pöschl–Teller barrier, is

$$V(x) = \frac{U_0}{\cosh^2(\beta x)}, \qquad U_0 > 0, \qquad \beta > 0. \tag{5.22}$$

It is short ranged and exactly solvable, yet its analytic continuation has an infinite periodic structure of poles and turning points. It therefore tests both scattering and exact-WKB descriptions without reducing the problem to a polynomial potential [80–83].

Introduce

$$\xi = \tanh(\beta x), \qquad E = \frac{\hbar^2 k^2}{2m},$$
$$s(s+1) = -\frac{2mU_0}{\beta^2\hbar^2}. \tag{5.23}$$

The Schrödinger equation becomes an associated Legendre equation. A solution outgoing at $x \to +\infty$ may be written in terms of a Gauss hypergeometric function. Its incident coefficient at $x \to -\infty$ is, up to a nonzero convention-dependent phase,

$$A_{\text{in}}(k) \propto \frac{\Gamma(1 - \mathrm{i}k/\beta)\Gamma(-\mathrm{i}k/\beta)}{\Gamma(-\mathrm{i}k/\beta - s)\Gamma(-\mathrm{i}k/\beta + s + 1)}. \tag{5.24}$$

The resonance condition $A_{\text{in}}(k) = 0$ follows from a pole of either Gamma function in the denominator.

For a barrier satisfying

$$\frac{8mU_0}{\beta^2\hbar^2} > 1, \tag{5.25}$$

define the positive dimensionless number

$$\kappa = \sqrt{\frac{8mU_0}{\beta^2\hbar^2} - 1}. \tag{5.26}$$

The resonance momenta in the fourth quadrant are

$$k_n^{\text{R}} = \frac{\beta}{2}\left[\kappa - \mathrm{i}(2n+1)\right], \qquad n = 0, 1, 2, \ldots, \tag{5.27}$$

and the corresponding energies are

$$E_n^{\text{R}} = \frac{\hbar^2\beta^2}{8m}\left[\kappa - \mathrm{i}(2n+1)\right]^2. \tag{5.28}$$

The antiresonant partners obey $k_n^{\text{R}} = -(k_n^{\text{AR}})^*$ for a real potential.

In exact-WKB language, the turning points satisfy

$$\cosh^2(\beta x) = \frac{U_0}{E}. \tag{5.29}$$

They repeat under imaginary shifts because $\cosh z$ is periodic up to sign. The spectral curve also has double poles at zeros of $\cosh(\beta x)$. A connection

path crosses the relevant Stokes curves, changes sheets at branch cuts, and returns through infinity. The exact connection coefficient can be identified with Eq. (5.24); hence the resummed WKB condition reproduces Eqs. (5.27) and (5.28) exactly [15, 16].

The lesson is broader than solvability. Barrier resonance does not require a real-axis potential well. In complex configuration space, turning points and subdominant sectors can trap analytic continuation around a nontrivial cycle. The pole measures that global complex geometry. This statement should not be misread as a sufficient criterion based only on visual minima of $\mathrm{Re}\, V(z)$; the invariant criterion is the vanishing connection coefficient.

5.3.3 Transmission and reflection from connection matrices

Choose an incoming wave of unit amplitude from the left. The asymptotic solution is

$$\begin{aligned} \psi(x) &\sim \mathrm{e}^{\mathrm{i}kx} + R(k)\mathrm{e}^{-\mathrm{i}kx}, && x \to -\infty, \\ \psi(x) &\sim T(k)\mathrm{e}^{\mathrm{i}kx}, && x \to +\infty. \end{aligned} \tag{5.30}$$

Let $M(E, \hbar)$ be the exact connection matrix between asymptotic WKB bases. With a consistent normalization, R and T are ratios of its entries. The resonance condition is the zero of the entry multiplying the incoming wave when the right solution is chosen outgoing. On the real axis, Wronskian conservation gives

$$|R(E)|^2 + |T(E)|^2 = 1 \tag{5.31}$$

for a real one-channel potential with equal asymptotic velocities. Exact WKB therefore reconstructs both the continued poles and the unitary physical scattering matrix from the same connection data [17].

Near a simple pole, the connection coefficient has the local expansion

$$\mathcal{C}_{\mathrm{in}}(E) = \mathcal{C}'_{\mathrm{in}}(E_{\mathrm{R}})(E - E_{\mathrm{R}}) + O((E - E_{\mathrm{R}})^2). \tag{5.32}$$

The derivative $\mathcal{C}'_{\mathrm{in}}(E_{\mathrm{R}})$ determines the residue. This is the exact-WKB route to excitation strength, and not only to the pole location.

5.3.4 Complex scaling as a change of Stokes sector

For an asymptotically free problem, the continuous spectrum corresponds to oscillatory WKB solutions on the real axis. Under $x = \mathrm{e}^{\mathrm{i}\theta} y$, the classical

action is continued to a ray on which one solution decays and the other grows. The energy at which neither is exponentially preferred lies on the rotated ray $\arg E = -2\theta$. Thus the continuum rotation in Eq. (6.20) follows directly from the asymptotic WKB exponent. A pole is θ independent because its global connection condition is invariant while the contour remains in the same homology class and crosses no singularity.

This gives an alternative geometric reading of the ABC structure. It does not replace the operator theorem: exact WKB controls differential-equation solutions and their analytic continuation, while the theorem controls operator domains, essential spectrum, and resolvent matrix elements. Their agreement is powerful precisely because the two analyses have different failure modes.

5.3.5 Continuum states in exact-WKB language

At real $E > 0$, a continuum state is specified by a boundary value $E \pm \mathrm{i}0$ and by incoming channel amplitudes. In exact WKB, these choices select a lateral Borel sum and a side of the Stokes graph. The continuum is therefore not obtained by solving the resonance condition for a dense set of energies; it is a family of connection problems parametrized by real E.

After complex scaling, the continuum becomes a line of generalized eigenvalues $E = \mathrm{e}^{-2\mathrm{i}\theta}\hbar^2 q^2/(2m)$ with $q \geq 0$. A finite basis discretizes q, while exact WKB retains it as a continuous parameter. The equivalence between the two descriptions is clearest at the resolvent level: both deform the same continuum contour while keeping pole residues inside the deformation fixed.

5.4 Calculation laboratory III: From a Stokes graph to a resonance width

Calculation route

Prerequisites. Asymptotic scattering coefficients, the Riccati recursion, lateral Borel sums, simple-turning-point connection matrices, and the no-incoming-wave condition.

Calculation goal. Scattering poles, the cubic oscillator, and the complete inverted Rosen–Morse calculation, including its repeated Stokes geometry.

Completion criterion. Reproduce the inverted Rosen–Morse pole

condition and decay width from the ordered Stokes data and verify them against the exact solution.

This Laboratory reconstructs the calculation underlying Ref. [15]. Scattering and exact-WKB definitions have already been fixed in Stages II and III; the source-paper recapitulation is therefore omitted. What follows is the model-specific Stokes transport, including the original intermediate algebra and TikZ geometry.

5.4.1 Worked Stokes geometry: cubic decay and the solvable barrier

The definitions of lateral Borel sum, Stokes curve, and connection matrix are those of Sec. 5.1. We now apply them without redefining them.

Application to unstable QM: Anharmonic oscillator with cubic potential

As an example, let us consider the cubic potential, $V(x) = x^2(1-x)$. This is not well-defined but is pedagogical for our purpose. The Stokes graph for $0 < E < \max V(x > 0)$ is shown in Fig. 5.1. The black solid curves are the Stokes curves. The index of each curve $\pm$ implies that $\psi^{\pm}$ increases exponentially and

$$\operatorname{Re} \hbar^{-1} \int^{x} \mathrm{d}x' \sqrt{Q} \gtrless 0. \tag{5.33}$$

Three Stokes curves gather at one point, called the turning point, which is depicted as a black point. The blue wavy lines are branch cuts. Due to the unbounded potential, it is difficult to define physical phenomena only on $x \in (-\infty, \infty)$. For example, let us choose the red arrowed path and then see what happens. At first, near $x = -\infty$, ψ^{-} sufficiently decreases and so is normalizable. When we jump over the Stokes curve with the index + starting from the same turning point (I→II), the Stokes phenomenon gives rise to

$$\begin{pmatrix} \psi_{\mathrm{I}}^{+} \\ \psi_{\mathrm{I}}^{-} \end{pmatrix} = M \begin{pmatrix} \psi_{\mathrm{II}}^{+} \\ \psi_{\mathrm{II}}^{-} \end{pmatrix}, \tag{5.34}$$

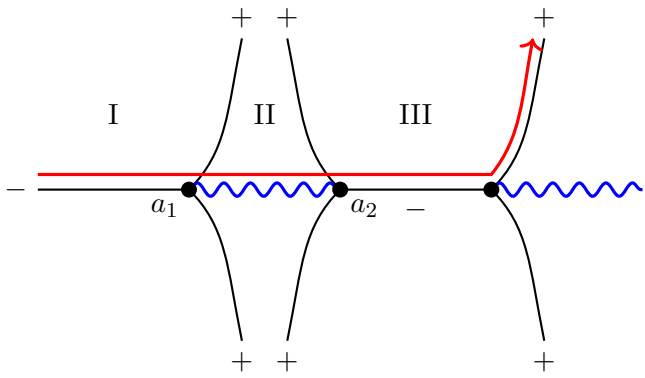

Figure 5.1: Stokes graphs for the cubic potential. The black solid curves are the Stokes curves and black points are the turning points connecting three Stokes curves. The blue wavy lines are branch cuts. The red arrowed curve is a possible physical path on which the wave function is defined.

where M depends on the rotation of the path around the turning point,

$$M = \begin{cases} M_+ & \text{if anticlockwise for the index } +, \\ M_+^{-1} & \text{if clockwise for the index } +, \\ M_- & \text{if anticlockwise for the index } -, \\ M_-^{-1} & \text{if clockwise for the index } -, \end{cases} \tag{5.35}$$

and

$$M_+ = \begin{pmatrix} 1 & \mathrm{i} \\ 0 & 1 \end{pmatrix}, \qquad M_- = \begin{pmatrix} 1 & 0 \\ \mathrm{i} & 1 \end{pmatrix}. \tag{5.36}$$

The above matrix is called the monodromy matrix. Inside region II, we need to connect the different turning points, a_1 and a_2. The wave function is related to each other by the factor,

$$\mathrm{e}^{\pm \int_{a_1}^{a_2} \mathrm{d}x\, S_{\mathrm{odd}}} \tag{5.37}$$

Finally, in the exchange of regions II and III, we again use the connection rule (5.34). If this system is just the harmonic oscillator, $V(x) = x^2$, the above strategy completes our task. For the wave function to converge near $x = \infty$,

we have the quantization condition

$$1 + A = 0, \qquad A = \mathrm{e}^{\oint \mathrm{d}x\, S_{\mathrm{odd}}}. \tag{5.38}$$

Here the cycle, A, comes from the connection between the turning points a_1 and a_2. Actually, by analytically continuing, A can be rewritten as the integral around the point of infinity. That is, $A = \mathrm{e}^{2\pi \mathrm{i} \hbar^{-1} E}$; we have the usual quantized energy spectrum $E = \hbar \left(n + \frac{1}{2} \right)$ with $n \in \mathbb{Z}_{\geq 0}$. Now, for the cubic potential, the analytical continuation should be stuck because of the branch cut attached to the point of infinity. However, a path on the upper-half plane must differ from that on the lower-half plane. This reproduces the usual result of some kind of tunneling analysis. This section is now finished but we will see a concrete result being identical to the exact solution.

5.4.2 Resonant states in exact WKB analysis

What is a resonant state from the viewpoint of exact WKB?

Given a potential $V(x)$ as a function of $x \in \mathbb{R}$, let us complexify the coordinate as $z \in \mathbb{C}$. In the complex plane z, if the potential $\mathrm{Re}\, V(z)$ possesses local minima, all of which are not stable physical states, then the Hilbert space of the system includes resonant states. This is because observations from the exact WKB analysis, i.e. structures of Stokes curves, are sensitive to the change of signs of $V(z) - E$. For instance, in an unusual harmonic oscillator, $V(x) = -x^2$, one finds that in Fig. 5.2 there is no local minimum; no resonant state exists. On the other hand, some kind of potential has the local minimum which is not a true vacuum, such as in $1/\cosh^2(x-a) + 1/\cosh^2(x+a)$; there are resonant states. Additionally, it is known that for the potential, $V(x) = 1/\cosh^2 x$, we observe nontrivial complex energies of resonance. This is the so-called barrier resonance, which traps the wave function into the bump. In fact, in Fig. 5.3, we can see the existence of local minima in $\mathrm{Re}\, V(z)$ with $\mathrm{Im}\, z \neq 0$. In what follows, we focus on an exactly solvable model, where we can see barrier resonant states explicitly. Also, from the above picture, we will have the same complex energies by using the exact WKB analysis.

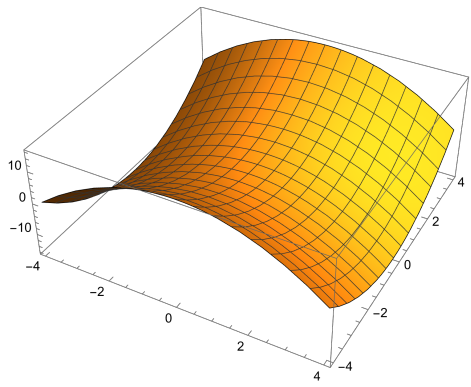

(a) Real part

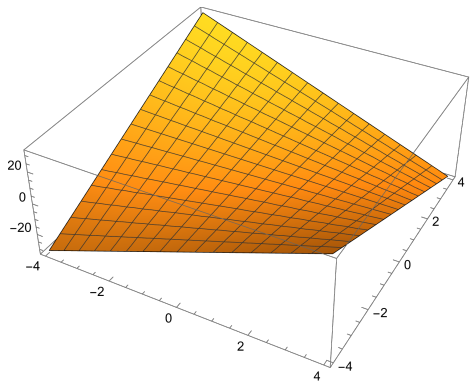

(b) Imaginary part

Figure 5.2: Potential structure of harmonic oscillator, $-z^2$, in complex plane

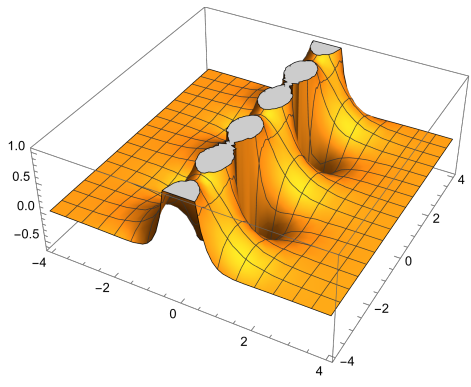

(a) Real part

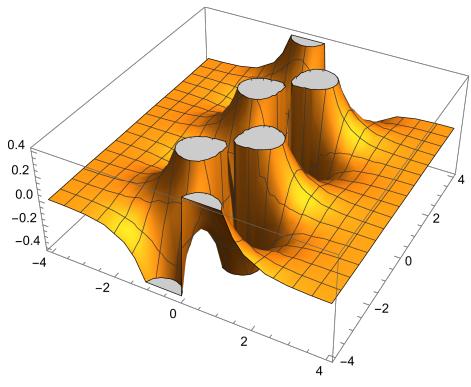

(b) Imaginary part

Figure 5.3: Potential structure of $1/\cosh^2 z$ in complex plane

Inverted Rosen–Morse potential

Exact solution Let us consider the inverted Rosen–Morse potential defined by

$$\left[-\frac{\hbar^2}{2m}\frac{\mathrm{d}^2}{\mathrm{d}x^2}+\frac{U_0}{\cosh^2\beta x}\right]\psi(x)=E\psi(x),\qquad U_0>0. \tag{5.39}$$

This Schrödinger equation is exactly solvable as follows: By using $\xi=\tanh\beta x$ and

$$k=\frac{\sqrt{2mE}}{\hbar},\quad -\frac{2mU_0}{\beta^2\hbar^2}=s(s+1),\quad s=\frac{1}{2}\left(-1+\sqrt{1-\frac{8mU_0}{\beta^2\hbar^2}}\right) \tag{5.40}$$

the equation can be rewritten as

$$\frac{\mathrm{d}}{\mathrm{d}\xi}\left[(1-\xi^2)\frac{\mathrm{d}\psi}{\mathrm{d}\xi}\right]+\left[s(s+1)-\left(\frac{\mathrm{i}k}{\beta}\right)^2\frac{1}{1-\xi^2}\right]\psi=0. \tag{5.41}$$

This is a general Legendre equation. After changing variables as

$$\psi(x)=(1-\xi^2)^{\frac{\mathrm{i}k}{2\beta}}w(\xi) \tag{5.42}$$

and $\frac{1}{2}(1-\xi)=u$, one finds the hypergeometric differential equation,

$$u(1-u)\frac{\mathrm{d}^2}{\mathrm{d}u^2}w+\left(\frac{\mathrm{i}k}{\beta}+1\right)(1-2u)\frac{\mathrm{d}}{\mathrm{d}u}w-\left(\frac{\mathrm{i}k}{\beta}-s\right)\left(\frac{\mathrm{i}k}{\beta}+s+1\right)w=0. \tag{5.43}$$

It is known that there are two independent solutions to the above equation. One solution is finite at $\xi=1$, i.e. $x=\infty$, while another one is divergent there. The former is given by

$$\psi(x)=(1-\xi^2)^{-\frac{\mathrm{i}k}{2\beta}}F\left(-\frac{\mathrm{i}k}{\beta}-s,-\frac{\mathrm{i}k}{\beta}+s+1,-\frac{\mathrm{i}k}{\beta}+1,\frac{1-\xi}{2}\right), \tag{5.44}$$

where F is the Gaussian hypergeometric function.

Traditional approach to resonance The exact solution (5.44) has complex energies. To see this from the traditional viewpoint, the asymptotic behavior of the solution is of importance. At first, in the case that $x\to\infty$,

we see

$$(1-\xi^2)^{-\frac{\mathrm{i}k}{2\beta}} \to 4^{-\frac{\mathrm{i}k}{2\beta}}\mathrm{e}^{\mathrm{i}kx}, \tag{5.45}$$

and

$$F\left(-\frac{\mathrm{i}k}{\beta}-s,-\frac{\mathrm{i}k}{\beta}+s+1,-\frac{\mathrm{i}k}{\beta}+1,\frac{1-\xi}{2}\right)\to 1. \tag{5.46}$$

Thus, we have the asymptotic form of the exact solution at $x\to\infty$

$$\psi(x)\to 4^{-\frac{\mathrm{i}k}{2\beta}}\mathrm{e}^{\mathrm{i}kx}. \tag{5.47}$$

Here, the above expression means the transmitted wave. Next, if $x\to-\infty$, the overall factor becomes

$$(1-\xi^2)^{-\frac{\mathrm{i}k}{2\beta}} \to (-4)^{-\frac{\mathrm{i}k}{2\beta}}\mathrm{e}^{-\mathrm{i}kx}. \tag{5.48}$$

On the other hand, noting that

$$\begin{aligned}
&F\left(-\frac{\mathrm{i}k}{\beta}-s,-\frac{\mathrm{i}k}{\beta}+s+1,-\frac{\mathrm{i}k}{\beta}+1,\frac{1-\xi}{2}\right)\\
&=\frac{\Gamma\left(1-\frac{\mathrm{i}k}{\beta}\right)\Gamma\left(\frac{\mathrm{i}k}{\beta}\right)}{\Gamma(1+s)\Gamma(-s)}F\left(-\frac{\mathrm{i}k}{\beta}-s,-\frac{\mathrm{i}k}{\beta}+s+1,-\frac{\mathrm{i}k}{\beta}+1,\frac{1+\xi}{2}\right)\\
&\quad+\frac{\Gamma\left(1-\frac{\mathrm{i}k}{\beta}\right)\Gamma\left(-\frac{\mathrm{i}k}{\beta}\right)}{\Gamma\left(-\frac{\mathrm{i}k}{\beta}-s\right)\Gamma\left(-\frac{\mathrm{i}k}{\beta}+s+1\right)}\left(\frac{1+\xi}{2}\right)^{\frac{\mathrm{i}k}{a}}F\left(1+s,-s,1+\frac{\mathrm{i}k}{\beta},\frac{1+\xi}{2}\right)
\end{aligned} \tag{5.49}$$

the hypergeometric function behaves as

$$\begin{aligned}
&F\left(-\frac{\mathrm{i}k}{\beta}-s,-\frac{\mathrm{i}k}{\beta}+s+1,-\frac{\mathrm{i}k}{\beta}+1,\frac{1-\xi}{2}\right)\\
&\to\frac{\Gamma\left(1-\frac{\mathrm{i}k}{\beta}\right)\Gamma\left(\frac{\mathrm{i}k}{\beta}\right)}{\Gamma(1+s)\Gamma(-s)}+\frac{\Gamma\left(1-\frac{\mathrm{i}k}{\beta}\right)\Gamma\left(-\frac{\mathrm{i}k}{\beta}\right)}{\Gamma\left(-\frac{\mathrm{i}k}{\beta}-s\right)\Gamma\left(-\frac{\mathrm{i}k}{\beta}+s+1\right)}\mathrm{e}^{2\mathrm{i}kx}.
\end{aligned} \tag{5.50}$$

Therefore, we have in the $x\to-\infty$ region

$$\psi(x)\to(-4)^{-\frac{\mathrm{i}k}{2\beta}}\mathrm{e}^{-\mathrm{i}kx}\frac{\Gamma\left(1-\frac{\mathrm{i}k}{\beta}\right)\Gamma\left(\frac{\mathrm{i}k}{\beta}\right)}{\Gamma(1+s)\Gamma(-s)}$$

$$+(-4)^{-\frac{ik}{2\beta}}\mathrm{e}^{ikx}\frac{\Gamma\left(1-\frac{ik}{\beta}\right)\Gamma\left(-\frac{ik}{\beta}\right)}{\Gamma\left(-\frac{ik}{\beta}-s\right)\Gamma\left(-\frac{ik}{\beta}+s+1\right)}, \tag{5.51}$$

where the first term on the right-hand side indicates the reflected wave, and the second term is the incident wave. Imposing purely outgoing boundary conditions (Siegert boundary condition [1]) yields the resonance condition, where the coefficient of the incident wave e^{ikx} vanishes. Hence, $\Gamma\left(-\frac{ik}{\beta}-s\right)$ or $\Gamma\left(-\frac{ik}{\beta}+s+1\right)$ should be divergent, and hence those Gamma functions become $\Gamma(-n)$ with a nonnegative integer n (i.e. $n = 0, 1, 2, \dots$). Therefore, this leads to discrete complex energies as follows:

- The case that $\Gamma\left(-\frac{ik}{\beta}+s+1\right)$ diverges.
  The divergence point of the Gamma function is expressed as

  $$-\frac{ik}{\beta}+s+1=-n, \qquad n=0,\,1,\,2,\,\dots. \tag{5.52}$$

  Solving this equation for k, we obtain

  $$k=\frac{\beta}{2}\left[-i\sqrt{\frac{8mU_0}{\beta^2\hbar^2}-1}-i(2n+1)\right]. \tag{5.53}$$

  Here, if the inequality, $1 < 8mU_0/(\beta^2\hbar^2)$, is satisfied, the complex wave number and the complex energy are given by

  $$k_n^{\mathrm{R}}=\frac{\beta}{2}\left[\sqrt{\frac{8mU_0}{\beta^2\hbar^2}-1}-i(2n+1)\right] \tag{5.54}$$

  and

  $$E_n^{\mathrm{R}}=\frac{\hbar^2\beta^2}{8m}\left[\sqrt{\frac{8mU_0}{\beta^2\hbar^2}-1}-i(2n+1)\right]^2, \tag{5.55}$$

  respectively. The wave number is in the fourth quadrant of the complex k-plane. Therefore, this solution corresponds to a resonant state.

- The case that $\Gamma\left(-\frac{ik}{\beta}-s\right)$ diverges.
  In the same way as the above case, we can obtain the divergence point

of the Gamma function as

$$-\frac{\mathrm{i}k}{\beta} - s = -n, \qquad n = 0, 1, 2, \ldots, \tag{5.56}$$

which gives

$$k_n^{\mathrm{AR}} = \frac{\beta}{2}\left[-\sqrt{\frac{8mU_0}{\beta^2\hbar^2} - 1} - \mathrm{i}(2n+1)\right] \tag{5.57}$$

and

$$E_n^{\mathrm{AR}} = \frac{\hbar^2\beta^2}{8m}\left[\sqrt{\frac{8mU_0}{\beta^2\hbar^2} - 1} + \mathrm{i}(2n+1)\right]^2. \tag{5.58}$$

The wave number is in the third quadrant of the complex k-plane. Equations (5.54) and (5.57) satisfy the following relation:

$$k_n^{\mathrm{R}} = -(k_n^{\mathrm{AR}})^*, \tag{5.59}$$

which means that the state with k_n^{AR} is a time-reversal state of the resonant state, the so-called "antiresonant state."

Stokes graph So far, we have derived the exact resonant solution and its energy. Here, we proceed with the perspective of the exact WKB analysis. Figure 5.4 shows the Stokes graph for the inverted Rosen–Morse potential, $V(x) = 1/\cosh^2 x$, with $0 < E < 1$. The left and right panels are devoted to $\mathrm{Im}\,\hbar > 0$ and $\mathrm{Im}\,\hbar < 0$, respectively. The black points denote the turning points and the solid/dashed curves are the corresponding Stokes curves. Note that the potential possesses the periodicity of $\mathrm{Im}\,x \in [-\pi/2, \pi/2]$ due to the cosine function on $\mathrm{Re}\,x = 0$. The blue point is the double pole and the blue wavy lines are branch cuts. To see the resonant states, we choose a path of the analytic continuation from $\mathrm{Im}\,x \to \pm\infty$ to $\mathrm{Im}\,x \to \mp\infty$ along the Stokes curves depicted in Fig. 5.4. Especially, because of normalizability, we need to take ψ_- for both regions of $\mathrm{Im}\,x \to \pm\infty$. Such a path can be chosen as shown in Fig. 5.5. The red path in the figure implies the path in the above sense. Note that the red solid curve is on the Riemann sheet depicted while the red dashed curve is on another Riemann sheet after passing through the branch cut. We make a remark on analogy to the CSM. From the ABC theorem, resonant states after complex scaling are some kind of bound states.

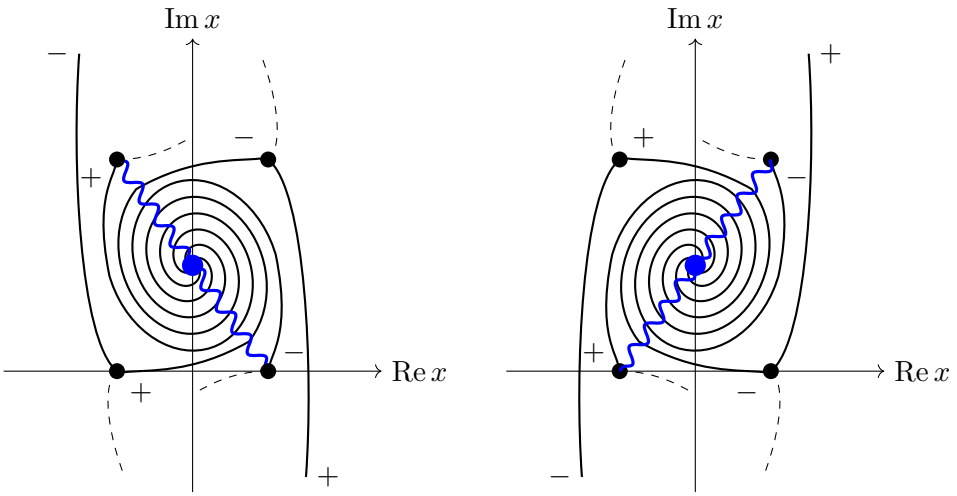

Figure 5.4: Schematically illustrated Stokes graph for the inverted Rosen–Morse potential, $V(x) = 1/\cosh^2 x$. **(Left)** $\mathrm{Im}\,\hbar > 0$, **(right)** $\mathrm{Im}\,\hbar < 0$. The black points denote the turning points and the solid curves are the corresponding Stokes curves. The dashed ones, also Stokes curves, mean the periodicity of $\mathrm{Im}\,x \in [-\pi/2, \pi/2]$ due to the cosine function on $\mathrm{Re}\,x = 0$. The blue point is the double pole and the blue wavy lines are branch cuts.

It indicates that resonant states can be normalized in complexified asymptotic regions. In fact, in the Stokes graph in Fig. 5.5, we observe that there is a path in the complex plane along which the wave function decays; we regard it as the normalizable path. Figure 5.5 gives rise to the following quantization condition along the red arrowed path:

$$1 - A = 0. \tag{5.60}$$

(A more rigorous derivation under regularization is provided in Sec. 6.5.) Here, A is the nontrivial cycle, the A-cycle, shown as the green dashed loop. From now on, let us calculate A in the leading order of the exact WKB and a completely exact analysis.

Leading order In the leading order, we carry out an integral of the WKB approximation between the turning points:

$$\int_{-\cosh^{-1}\sqrt{\frac{1}{E}}}^{\cosh^{-1}\sqrt{\frac{1}{E}}} \mathrm{d}x \sqrt{2(V(x) - E)} = \sqrt{2} \int \mathrm{d}x \sqrt{\frac{1}{\cosh^2 x} - E}. \tag{5.61}$$

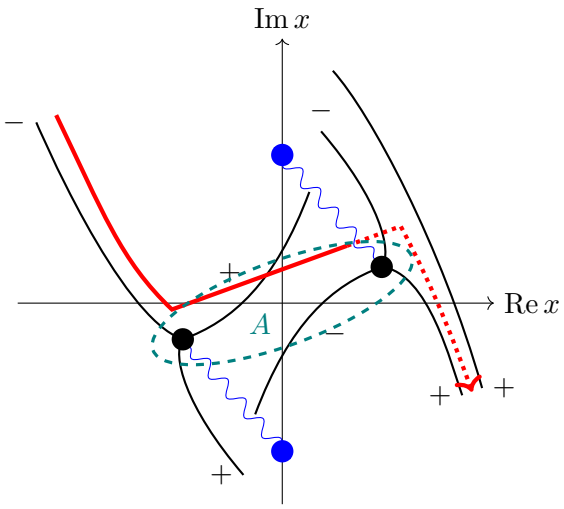

Figure 5.5: Quantization condition with $\operatorname{Im}\hbar > 0$ and $\operatorname{Im} E < 0$. The red path is an option to carry out the analytical continuation, along which we can normalize the exact WKB solution. The nontrivial cycle, A-cycle, is shown as the green dashed loop.

Here we set almost all parameters as units for simplicity. After some calculations, we find that

$$\begin{aligned}
&\int_{-\cosh^{-1}\sqrt{\frac{1}{E}}}^{\cosh^{-1}\sqrt{\frac{1}{E}}} \mathrm{d}x \sqrt{2(V(x)-E)} \\
&= -2\cosh(x)\sqrt{\frac{-E-\tanh^2(x)+1}{E\cosh(2x)+E-2}} \\
&\quad \times \left[\tanh^{-1}\left(\frac{\sqrt{2}\sinh(x)}{\sqrt{E\cosh(2x)+E-2}}\right) - \sqrt{E}\sinh^{-1}\left(\frac{\sinh(x)}{\sqrt{1-\frac{1}{E}}}\right)\right] \qquad (5.62) \\
&= \mp\sqrt{2}\,\mathrm{i}\left[\tanh^{-1}\left(\frac{\sqrt{2}\sinh(x)}{\sqrt{E\cosh(2x)+E-2}}\right) - \sqrt{E}\sinh^{-1}\left(\frac{\sinh(x)}{\sqrt{1-\frac{1}{E}}}\right)\right] \qquad (5.63) \\
&= \pm\sqrt{2}\pi(1+\sqrt{E}). \qquad (5.64)
\end{aligned}$$

Then, from the quantization condition (5.60),

$$2\sqrt{2}\pi(1+\sqrt{E}) = 2\pi \mathrm{i} n, \tag{5.65}$$

with $n \in \mathbb{Z}$. Therefore, the leading complex energy is given by

$$E = \left(1 - \frac{\mathrm{i}n}{\sqrt{2}}\right)^2. \tag{5.66}$$

This is quite suggestive because we observe resonance in the fourth quadrant even in the leading order of the exact WKB method.[1]

Exact WKB analysis for resonance In the above Stokes graphs, the exact solution on the normalizable path is explicitly written by the exact solution (5.44). Note that another solution has opposite signs for Stokes curves. This means that the WKB solution can be exactly given by

$$\mathrm{e}^{\int_{x_0}^{x} \mathrm{d}x' S_{\mathrm{odd}}} = (1-\xi^2)^{-\frac{\mathrm{i}k}{2\beta}} F\left(-\frac{\mathrm{i}k}{\beta} - s, -\frac{\mathrm{i}k}{\beta} + s + 1, -\frac{\mathrm{i}k}{\beta} + 1, \frac{1-\xi}{2}\right)\Big|_{\text{at } x}, \tag{5.67}$$

where x_0 is a reference point. The A-cycle, $\mathrm{e}^{\oint S_{\mathrm{odd}}}$, between turning points $\mp \cosh^{-1}\sqrt{U_0/E}$ can be realized by the exchange of reference points. That is,

$$\mathrm{e}^{2\int_{x_0}^{\cosh^{-1}\sqrt{U_0/E}} \mathrm{d}x\, S_{\mathrm{odd}}} \times \mathrm{e}^{-2\int_{x_0}^{-\cosh^{-1}\sqrt{U_0/E}} \mathrm{d}x\, S_{\mathrm{odd}}} = \mathrm{e}^{2\int_{-\cosh^{-1}\sqrt{U_0/E}}^{\cosh^{-1}\sqrt{U_0/E}} \mathrm{d}x\, S_{\mathrm{odd}}}. \tag{5.68}$$

From the fact that $A = 1$ for the existence of a normalizable solution, we see

$$\left[\frac{F\left(-\frac{\mathrm{i}k}{\beta} - s, -\frac{\mathrm{i}k}{\beta} + s + 1, -\frac{\mathrm{i}k}{\beta} + 1, \frac{1-|\xi|}{2}\right)}{F\left(-\frac{\mathrm{i}k}{\beta} - s, -\frac{\mathrm{i}k}{\beta} + s + 1, -\frac{\mathrm{i}k}{\beta} + 1, \frac{1+|\xi|}{2}\right)}\right]^2 = 1, \tag{5.69}$$

[1] For the usual (noninverted) Rosen–Morse potential, higher-order contribution from S_i vanishes. (This is the reason why it possesses shape invariance in the same way as the harmonic oscillator.) Then, one finds an exact solution. On the other hand, higher-order terms S_i do not vanish for the inverted Rosen–Morse potential. We need some careful treatment.

where $|\xi| = \tanh(\beta \cosh^{-1} \sqrt{U_0/E})$. Here, we use the formula of the hypergeometric function as

$$\begin{aligned} & F\left(-\frac{\mathrm{i}k}{\beta} - s, -\frac{\mathrm{i}k}{\beta} + s + 1, -\frac{\mathrm{i}k}{\beta} + 1, \frac{1 \pm |\xi|}{2}\right) \\ & = \mathfrak{A} F\left(-\frac{\mathrm{i}k}{2\beta} - \frac{s}{2}, -\frac{\mathrm{i}k}{2\beta} + \frac{s+1}{2}, \frac{1}{2}, |\xi|^2\right) \\ & \quad \mp \mathfrak{B} F\left(-\frac{\mathrm{i}k}{2\beta} - \frac{s-1}{2}, -\frac{\mathrm{i}k}{2\beta} + \frac{s}{2} + 1, \frac{3}{2}, |\xi|^2\right) \\ & \equiv \mathfrak{A} F_A \mp \mathfrak{B} F_B, \end{aligned} \tag{5.70}$$

where

$$\begin{aligned} \mathfrak{A} &= \frac{\Gamma\left(-\frac{\mathrm{i}k}{\beta} + 1\right) \Gamma\left(\frac{1}{2}\right)}{\Gamma\left(-\frac{\mathrm{i}k}{2\beta} - \frac{s-1}{2}\right) \Gamma\left(-\frac{\mathrm{i}k}{2\beta} + \frac{s}{2} + 1\right)}, \\ \mathfrak{B} &= \frac{\Gamma\left(-\frac{\mathrm{i}k}{\beta} + 1\right) \Gamma\left(-\frac{1}{2}\right)}{\Gamma\left(-\frac{\mathrm{i}k}{2\beta} - \frac{s}{2}\right) \Gamma\left(-\frac{\mathrm{i}k}{2\beta} + \frac{s+1}{2}\right)}. \end{aligned} \tag{5.71}$$

Substituting this into the quantization condition (5.69), we find that

$$\left(\frac{\mathfrak{A} F_A + \mathfrak{B} F_B}{\mathfrak{A} F_A - \mathfrak{B} F_B}\right)^2 = 1. \tag{5.72}$$

To obtain $(+1)^2$ on the left-hand side in Eq. (5.69), it is easy to find $\mathfrak{B} = 0$. Therefore, $\Gamma\left(-\frac{\mathrm{i}k}{2\beta} - \frac{s}{2}\right)$ or $\Gamma\left(-\frac{\mathrm{i}k}{2\beta} + \frac{s+1}{2}\right)$ should be at pole singularities. Then, $-\frac{\mathrm{i}k}{\beta} - s = -2n$ or $-\frac{\mathrm{i}k}{\beta} + s + 1 = -2n$ ($n = 0, 1, \ldots$). The former corresponds to antiresonance and the latter is resonance, being identical to the above observation in Section 5.4.2 with *even* numbers of nodes. On the other hand, we also have another condition when the left-hand side in Eq. (5.69) becomes $(-1)^2$; then, $\Gamma\left(-\frac{\mathrm{i}k}{2\beta} - \frac{s-1}{2}\right)$ or $\Gamma\left(-\frac{\mathrm{i}k}{2\beta} + \frac{s}{2} + 1\right)$ should diverge such that $\mathfrak{A} = 0$. Then, $-\frac{\mathrm{i}k}{\beta} - s = -2n - 1$ or $-\frac{\mathrm{i}k}{\beta} + s + 1 = -2n - 1$ ($n = 0, 1, \ldots$). This is a completely identical result to the complex energies with *odd* numbers of nodes. Totally, indeed, one finds that $-\frac{\mathrm{i}k}{\beta} - s = -n$ or $-\frac{\mathrm{i}k}{\beta} + s + 1 = -n$ ($n = 0, 1, \ldots$), which is identical to E_n^{AR} or E_n^{R}, respectively.[2]

[2] In contrast to Gamow's method which yields an exponentially small imaginary part for the energy from the leading tunneling action, the exact WKB method systematically incorporates all orders and treats the resonance condition with full analytical rigor (as in

Laboratory checkpoint

Before moving to the next stage, perform the following checks without copying the displayed final answer.

1. Recompute the ordered product of Stokes matrices and identify the entry that multiplies the prohibited incoming branch.

2. Derive the resonance condition both from the exact hypergeometric solution and from the exact-WKB connection coefficient.

3. Change the continuation path or lateral Borel side and record how the sheet label changes while the physical pole remains consistent.

5.5 Problems for Stage III

III.1 Substitute the logarithmic WKB ansatz into Eq. (5.1) and derive the first four Riccati coefficients. Verify the parity relation between the two branches.

III.2 Calculate the Borel transform of the factorially divergent series $\sum_{n\geq 0} n!\hbar^{n+1}$. Evaluate its two lateral sums and find their nonperturbative difference.

III.3 Reduce a simple turning point to the Airy equation. Derive the local connection matrix with the book's ordering of dominant and subdominant solutions.

III.4 Multiply three generic triangular Stokes matrices and one propagation matrix. Determine which orderings preserve the Wronskian and show why path order cannot be replaced by a commutative product.

III.5 For a barrier with two real turning points, derive the leading outgoing resonance condition and the Gamow width. State which all-order object replaces the classical barrier action.

III.6 Starting from the hypergeometric connection formula for the inverted Rosen–Morse potential, derive the incoming coefficient and its Gamma-function zeros. Identify the resonant and antiresonant branches.

Eq. (5.69)).

III.7 Let $S(E) = N(E)/\mathcal{C}_{\mathrm{in}}(E)$. Derive its Laurent expansion at a simple pole and at a double zero. Anticipate the Jordan resolvent term that will appear in Stage VII.

III.8 Draw Stokes graphs for a cubic metastable potential on both sheets of $\sqrt{Q}$. Mark a path that imposes outgoing behavior and record every branch and Stokes crossing in order.

III.9 Demonstrate explicitly that a simultaneous analytic coordinate rotation of turning points, cycles, and integration contour leaves a Voros period invariant until a singularity crosses the deformation region.

III.10 Implement a transfer-matrix calculation for a piecewise constant barrier and compare its pole condition with the WKB connection condition. Use the determinant as a numerical error monitor.

Chapter 6

Stage IV: Realize one analytic pole in several spaces

Reader contract

The exact-WKB zero is now represented by a continued resolvent, a Feshbach operator, Zel'dovich regularization, analytic dilation, and a rigged-space functional. Each construction is derived from its hypotheses and checked against the same invariant pole and residue. The continuum is retained as part of the response rather than discarded as background.

6.1 From the connection zero to resolvents and effective Hamiltonians

6.1.1 Lippmann–Schwinger equation and the transition operator

Write the Hamiltonian as $H = H_0 + V$, where H_0 is the asymptotic Hamiltonian and V is the interaction. The resolvent identity gives

$$\mathcal{R}(z) = \mathcal{R}_0(z) + \mathcal{R}_0(z)V\mathcal{R}(z), \tag{6.1}$$

$$\mathcal{R}_0(z) = (z - H_0)^{-1}. \tag{6.2}$$

For a generalized free eigenstate $|\phi_E\rangle$, the incoming and outgoing scattering states are the boundary values

$$|\psi_E^{(\pm)}\rangle = |\phi_E\rangle + \mathcal{R}_0(E \pm \mathrm{i}0)V|\psi_E^{(\pm)}\rangle. \tag{6.3}$$

The transition operator $T(z)$ is defined by

$$T(z) = V + V\mathcal{R}_0(z)T(z). \tag{6.4}$$

On shell, matrix elements of $T(E + \mathrm{i}0)$ determine scattering amplitudes. A resonance appears as a pole of $T(z)$ and of the full resolvent. The Lippmann–Schwinger equation therefore expresses in operator language what the Jost-function construction expressed through differential equations.

For real E above threshold, the discontinuity of the free resolvent is

$$\mathcal{R}_0(E + \mathrm{i}0) - \mathcal{R}_0(E - \mathrm{i}0) = -2\pi\mathrm{i}\,\delta(E - H_0). \tag{6.5}$$

Together with Eq. (6.4), this identity yields the optical theorem. It also shows how an imaginary part can arise from an underlying self-adjoint theory: the imaginary part is the boundary value of a continuum resolvent, not a fundamental violation of probability conservation.

6.1.2 Feshbach projection and energy-dependent effective Hamiltonian

Let P be an orthogonal projection onto a selected subspace and let $Q = \mathbf{1} - P$. Decompose a stationary state as $|\Psi\rangle = P|\Psi\rangle + Q|\Psi\rangle$. Eliminating the Q component gives

$$[z - H_{\mathrm{eff}}(z)]\, P|\Psi\rangle = 0, \tag{6.6}$$

with

$$H_{\mathrm{eff}}(z) = PHP + PHQ\frac{1}{z - QHQ}QHP. \tag{6.7}$$

The second term is the self-energy. For $z = E + \mathrm{i}0$ above a Q-space threshold, it has the decomposition

$$\Sigma(E + \mathrm{i}0) = \Delta(E) - \frac{\mathrm{i}}{2}W(E), \qquad W(E) \succeq 0. \tag{6.8}$$

Here $\Delta(E)$ is a dispersive energy shift, $W(E)$ is a positive semidefinite decay matrix, and $\succeq 0$ denotes positive semidefiniteness. Thus $H_{\mathrm{eff}}(E + \mathrm{i}0)$ is non-self-adjoint even though H is self-adjoint. Its non-self-adjoint part records probability flux into the eliminated continuum [4, 5, 9].

The resonance equation is nonlinear because the operator depends on its own spectral parameter:

$$\det\,[z - H_{\mathrm{eff}}(z)] = 0. \tag{6.9}$$

Replacing $H_{\mathrm{eff}}(z)$ by a constant matrix near a narrow pole is a controlled local approximation only if the self-energy varies slowly. Near a threshold,

$\Sigma(z)$ has a branch point, and a finite constant matrix cannot reproduce the correct nonanalyticity. This observation is important for exceptional points involving a continuum: the branch order can differ from that of a generic finite-dimensional exceptional point [21].

6.1.3 Equivalence of the Feshbach and Siegert pictures

The Feshbach and outgoing-boundary descriptions impose the same pole condition in different coordinates. In a tight-binding lead, for example, eliminating the semi-infinite lead produces a surface Green function in $H_{\text{eff}}(z)$. Choosing its retarded branch is exactly the choice of an outgoing wave in the lead. Conversely, substituting an outgoing ansatz at the boundary reduces the open problem to a finite region with a spectral-parameter-dependent boundary operator. General versions of this equivalence are discussed in Ref. [84].

This equivalence suggests a useful principle. Non-self-adjointness is often a representation of openness rather than a modification of the microscopic theory. Different representations distribute the analytic continuation differently: in $H_{\text{eff}}(z)$ it resides in a self-energy; in complex scaling it resides in a deformed operator domain; in a rigged Hilbert space it resides in the dual pairing; and in exact WKB it resides in Borel-summed connection data.

6.1.4 Resonance expansion and the role of the continuum

For suitable finite-range or dilation-analytic problems, one may deform the real momentum contour into the complex plane. The resulting Berggren-type completeness relation has the schematic form

$$\mathbf{1} = \sum_{n\in\mathcal{B}} |u_n\rangle\langle\widetilde{u}_n| + \sum_{r\in\mathcal{R}} |u_r\rangle\langle\widetilde{u}_r| + \int_{L^+} \mathrm{d}k\, |u(k)\rangle\langle\widetilde{u}(k)|. \tag{6.10}$$

The set $\mathcal{B}$ contains bound states, $\mathcal{R}$ contains resonance poles enclosed between the original and deformed contours, and L^+ is the remaining continuum contour. Tildes denote the dual system appropriate to the non-self-adjoint representation. Equation (6.10) is not a statement that resonance vectors alone form a complete basis. The deformed continuum is indispensable and carries threshold and background response [3, 8, 85].

In a finite numerical basis the continuum integral is replaced by a string of discrete points. The points move when the contour, scaling angle, or basis

is changed, whereas an exposed isolated pole is stable. This contrast is the first practical diagnostic for distinguishing a resonance from a continuum pseudostate.

6.2 Represent the outgoing branch as a square-integrable eigenvector

Calculation route

Prerequisites. The continued pole condition, closed operators, analytic families, and the distinction between point and continuous spectrum.

Calculation goal. Choose an admissible coordinate deformation that makes the outgoing branch square integrable while rotating, rather than discarding, the continuum.

Completion criterion. Identify an angle-stable eigenvalue and connect its Riesz projection to the same continued resolvent pole.

6.2.1 Analytic dilation

Let the configuration-space dimension be d. For a real dilation parameter s, define the unitary operator

$$[U(s)\psi](\boldsymbol{x}) = \mathrm{e}^{ds/2}\psi(\mathrm{e}^{s}\boldsymbol{x}). \tag{6.11}$$

Complex scaling analytically continues s to $s = \mathrm{i}\theta$, with a real angle θ. Formally,

$$[U(\mathrm{i}\theta)\psi](\boldsymbol{x}) = \mathrm{e}^{\mathrm{i}d\theta/2}\psi(\mathrm{e}^{\mathrm{i}\theta}\boldsymbol{x}). \tag{6.12}$$

For $\theta \neq 0$, this transformation is not unitary on the original L^2 space and is generally unbounded. It should be defined first on a dense set of analytic vectors. This is why it is safer to speak of an analytic family of deformed operators than of an everywhere-defined similarity transformation.

For the Hamiltonian

$$H = T + V(\boldsymbol{x}), \qquad T = -\frac{\hbar^2}{2m}\nabla^2, \tag{6.13}$$

the complex-scaled operator is

$$H_\theta = U(\mathrm{i}\theta) H U(-\mathrm{i}\theta) = \mathrm{e}^{-2\mathrm{i}\theta} T + V(\mathrm{e}^{\mathrm{i}\theta}\boldsymbol{x}). \tag{6.14}$$

Equation (6.14) requires the potential to admit analytic continuation in the sector swept out by the deformation. Coulomb singularities, multiple coordinates, and nonanalytic potentials require refined forms such as exterior complex scaling or smooth complex deformation [86–88].

6.2.2 Why an outgoing wave becomes square integrable

Write the resonance momentum as

$$k_{\mathrm{R}} = |k_{\mathrm{R}}| \mathrm{e}^{-\mathrm{i}\varphi}, \qquad 0 < \varphi < \frac{\pi}{4}. \tag{6.15}$$

On the positive half-line, the scaled outgoing wave is

$$\begin{aligned} \mathrm{e}^{\mathrm{i}k_{\mathrm{R}} r \mathrm{e}^{\mathrm{i}\theta}} &= \mathrm{e}^{\mathrm{i}|k_{\mathrm{R}}| r \cos(\theta-\varphi)} \\ &\quad \times \mathrm{e}^{-|k_{\mathrm{R}}| r \sin(\theta-\varphi)}. \end{aligned} \tag{6.16}$$

It decays for $\theta > \varphi$. The same condition regularizes the outgoing wave on the negative half-line when the contour is rotated consistently. Thus the Siegert state becomes an L^2 eigenfunction of H_θ once the rotated continuum has passed below the pole. The divergent unscaled wave and the normalizable scaled wave are analytic continuations of one solution, not different physical states.

6.2.3 The Aguilar–Balslev–Combes structure

The Aguilar–Balslev–Combes theorem is sometimes quoted only as the rule that the continuum rotates. Its real content is a statement about an analytic family of closed operators and the meromorphic continuation of resolvent matrix elements [6, 7, 89, 90]. We state a one-threshold version before explaining its proof.

Let $H_0 = -\hbar^2\nabla^2/(2m)$ on $L^2(\mathbb{R}^d)$ and assume that V is H_0-compact, or satisfies a suitable relative-form compactness condition. Assume further that

$$s \longmapsto V_s := U(s) V U(-s) \tag{6.17}$$

has an operator- or form-valued analytic continuation from real s to a strip

$|\operatorname{Im} s| < \theta_{\max}$. Such a potential is called *dilation analytic*. The deformed Hamiltonian

$$H(s) = \mathrm{e}^{-2s} H_0 + V_s \tag{6.18}$$

then forms an analytic family, of type A when a common operator domain can be used and of type B when the construction is made through quadratic forms. For $s = \mathrm{i}\theta$ with $0 < \theta < \theta_{\max}$, write $H_\theta := H(\mathrm{i}\theta)$.

Under these hypotheses, the theorem gives the following spectral picture:

1. H_θ is a closed non-self-adjoint operator. Its essential spectrum is

$$\sigma_{\mathrm{ess}}(H_\theta) = \mathrm{e}^{-2\mathrm{i}\theta}[0, \infty). \tag{6.19}$$

2. Bound-state eigenvalues remain on the real axis and are independent of θ. Their algebraic multiplicities are unchanged for an admissible deformation that does not encounter another threshold or singularity.

3. A discrete nonreal eigenvalue in the wedge $-2\theta < \arg z < 0$ is independent of θ while it remains isolated from the rotated essential spectrum. It coincides with a pole of the continued physical resolvent and is therefore a resonance.

4. For many-body or coupled-channel problems, each continuum ray starting at a threshold E_a rotates as

$$E_a + [0, \infty) \longmapsto E_a + \mathrm{e}^{-2\mathrm{i}\theta}[0, \infty). \tag{6.20}$$

   Cluster thresholds and channel branch points therefore remain as anchors of the spectral geometry.

For a threshold at zero, a pole with energy E_{R} is exposed when

$$-2\theta < \arg E_{\mathrm{R}} < 0. \tag{6.21}$$

The bridge to scattering theory is obtained on a dense set $\mathcal{A}$ of analytic vectors. For real s unitarity of $U(s)$ gives

$$\langle \phi | (z - H)^{-1} | \psi \rangle = \langle U(s)\phi | (z - H(s))^{-1} U(s) | \psi \rangle, \qquad \phi, \psi \in \mathcal{A}. \tag{6.22}$$

Both sides are analytic in a common initial domain. Continuing Eq. (6.22) from real s to $s = \mathrm{i}\theta$ continues the physical matrix element through the

original continuous spectrum into the wedge uncovered by the rotated ray. Analytic Fredholm theory makes the right-hand side meromorphic there. Its poles are the isolated eigenvalues of H_θ, with finite-rank Riesz projections. This is stronger than a graphical rotation of a cut: it identifies the deformed eigenvalue with a pole of the undeformed scattering problem.

The theorem should not be paraphrased as a general completeness theorem for arbitrary Gamow states. It describes the spectrum and resolvent continuation under specific analyticity and compactness assumptions. A resonance expansion still contains the rotated continuum, and completeness of a chosen eigenfunction expansion is an additional statement. The Berggren relation in Section 6.4.2 is one such statement for radial short-range problems.

The phrase "θ independent" has a precise but limited meaning. In the exact operator problem, an isolated exposed pole is invariant under admissible changes of θ. In a truncated basis, every eigenvalue has residual angle dependence. A numerical pole is identified by a stationary trajectory or a plateau under simultaneous variation of θ, basis size, nonlinear basis scales, and arithmetic precision. The pseudospectrum provides a more honest error diagnostic than eigenvalue motion alone for strongly non-normal matrices [91–93].

A detailed proof architecture, including the essential-spectrum and Fredholm steps, is given in Sec. 6.3. That discussion also explains why global complex scaling does not immediately provide an ABC theorem for black-hole potentials written in tortoise coordinates.

6.2.4 Exterior and smooth complex scaling

Global scaling evaluates V at complex coordinates everywhere. If the interaction has singularities or if one wishes to preserve an inner physical region, choose a radius $R_0 > 0$ and deform only outside it. A piecewise-linear exterior contour may be written

$$z(r) = \begin{cases} r, & 0 \le r \le R_0, \\ R_0 + (r - R_0)\mathrm{e}^{\mathrm{i}\theta}, & r > R_0. \end{cases} \tag{6.23}$$

A smooth contour avoids a derivative discontinuity at R_0. Exterior complex scaling is especially useful when the potential is analytic only in the asymptotic region or when an inner wave function must retain a direct probabilistic interpretation. Perfectly matched layers and complex absorbing potentials

are closely related numerical devices, but their finite-parameter eigenvalues must be extrapolated to distinguish physical poles from absorber modes.

6.2.5 Biorthogonality and the complex-symmetric case

Let $H_\theta|\Psi_n^{\mathrm{R}}\rangle = E_n|\Psi_n^{\mathrm{R}}\rangle$ and $\langle\Psi_n^{\mathrm{L}}|H_\theta = E_n\langle\Psi_n^{\mathrm{L}}|$. Away from degeneracies, left and right eigenvectors may be normalized by

$$\langle\Psi_m^{\mathrm{L}}|\Psi_n^{\mathrm{R}}\rangle = \delta_{mn}. \tag{6.24}$$

If a real potential and basis make the matrix representation complex symmetric, $H_\theta^{\mathsf{T}} = H_\theta$, the natural bilinear form is the c product

$$(\phi \mid \psi)_c = \int \mathrm{d}x\, \phi(x)\psi(x), \tag{6.25}$$

without complex conjugation of the first factor. The c product is not a positive norm. It is a bilinear pairing that implements left–right biorthogonality in this representation. Confusing it with a probability norm is a common source of paradoxes concerning complex expectation values [88, 94].

At an exceptional point, Eq. (6.24) cannot be maintained with bounded normalization because the eigenvector becomes self-orthogonal. The divergent normalization and the vanishing bilinear norm are two sides of the same Jordan singularity. We return to this point in Section 9.1.

6.2.6 Spectral representation of the complex-scaled resolvent

In a formal discrete-plus-continuum notation, the deformed resolvent has the expansion

$$\begin{aligned}\mathcal{R}_\theta(z) &= (z - H_\theta)^{-1} \\ &= \sum_b \frac{|\Psi_b^{\mathrm{R}}\rangle\langle\Psi_b^{\mathrm{L}}|}{z - E_b} + \sum_r \frac{|\Psi_r^{\mathrm{R}}\rangle\langle\Psi_r^{\mathrm{L}}|}{z - E_r} + \int_{L_\theta} \mathrm{d}E' \frac{|\Psi_{E'}^{\mathrm{R}}\rangle\langle\Psi_{E'}^{\mathrm{L}}|}{z - E'}.\end{aligned} \tag{6.26}$$

The first sum runs over bound states, the second over exposed resonances, and L_θ is the rotated continuum. This is the operator counterpart of the contour deformation in Eq. (4.97). It also explains why a finite-basis diagonalization can approximate both pole and continuum contributions using one matrix spectrum.

6.3 Derive the Aguilar–Balslev–Combes mechanism step by step

This chapter supplies the functional-analytic chain behind the statement in Section 6.2.3. We first state one precise one-threshold version; the following steps prove its mechanism. Operator-domain and quadratic-form variants enlarge the admissible class of potentials [6, 7, 89, 90].

Theorem 6.1 (Aguilar–Balslev–Combes, type-A one-threshold form)**.** *Let $H_0 = -\hbar^2\Delta/(2\mu)$ on $L^2(\mathbb{R}^d)$ with domain $H^2(\mathbb{R}^d)$, and let $H = H_0 + V$ be self-adjoint. Suppose there is $\theta_0 > 0$ such that for $|\operatorname{Im} s| < \theta_0$ the dilation $V_s = U(s)VU(-s)$ is analytic as an operator from $D(H_0)$ with its graph norm to L^2, and $V_s(H_0+1)^{-1}$ is compact locally uniformly in s. Assume also that $H(s) = \mathrm{e}^{-2s}H_0 + V_s$ is a closed type-A family on the common domain $D(H_0)$.*

For $0 < \theta < \theta_0$, put $H_\theta = H(\mathrm{i}\theta)$. Then

(i) $\sigma_{\mathrm{ess}}(H_\theta) = \mathrm{e}^{-2\mathrm{i}\theta}[0,\infty)$*;*

(ii) the remaining spectrum away from this ray consists of isolated eigenvalues of finite algebraic multiplicity;

(iii) matrix elements $\langle\phi, (z-H)^{-1}\psi\rangle$ between dilation-analytic vectors continue meromorphically from the physical resolvent set into the wedge swept by the ray, and their nonzero-residue poles coincide with the discrete eigenvalues of H_θ there; and

(iv) these eigenvalues and their algebraic multiplicities are independent of θ while they remain in a common uncovered wedge. Negative isolated eigenvalues of H remain unchanged.

The assumptions are deliberately visible. Coulomb tails, a potential that is not analytic in the swept coordinate sector, and threshold accumulation require modified theorems rather than an invocation of the displayed result.

Step 1: real dilations and analytic vectors

For real s, the map

$$[U(s)\psi](\boldsymbol{x}) = \mathrm{e}^{ds/2}\psi(\mathrm{e}^{s}\boldsymbol{x}) \tag{6.27}$$

is unitary on $L^2(\mathbb{R}^d)$ and satisfies

$$U(s)H_0U(-s) = \mathrm{e}^{-2s}H_0. \tag{6.28}$$

The continuation $s \to \mathrm{i}\theta$ is not a bounded unitary operation on all of L^2. One therefore chooses a dense set $\mathcal{A}$ of vectors for which $s \mapsto U(s)\phi$ is analytic in a strip. Gaussian functions and finite linear combinations of oscillator eigenfunctions provide standard examples. The vector set is used to continue matrix elements; the operator $H(\mathrm{i}\theta)$ is defined independently as a closed analytic-family member.

Assume that $V_s = U(s)VU(-s)$ continues analytically and that

$$V_s(H_0 + 1)^{-1} \tag{6.29}$$

is compact, locally uniformly in the analytic strip. A common-domain construction gives a type-A family

$$H(s) = \mathrm{e}^{-2s}H_0 + V_s, \qquad D(H(s)) = D(H_0). \tag{6.30}$$

Singular interactions are often better handled by analytic quadratic forms, which give a type-B family. Subsequent resolvent arguments are structurally the same.

Step 2: the rotated free spectrum

For $s = \mathrm{i}\theta$,

$$H_{0,\theta} = \mathrm{e}^{-2\mathrm{i}\theta}H_0. \tag{6.31}$$

The spectrum of H_0 is $[0, \infty)$, so multiplication by the complex number $\mathrm{e}^{-2\mathrm{i}\theta}$ gives

$$\sigma(H_{0,\theta}) = \mathrm{e}^{-2\mathrm{i}\theta}[0, \infty). \tag{6.32}$$

This is the elementary source of the angle 2θ: the coordinate scales as $\mathrm{e}^{\mathrm{i}\theta}$, momentum as $\mathrm{e}^{-\mathrm{i}\theta}$, and kinetic energy as the square of momentum.

For z off the free ray, the second resolvent identity in the convention $\mathcal{R}(z) = (z - H)^{-1}$ gives

$$\begin{aligned}(z - H_\theta)^{-1} - (z - H_{0,\theta})^{-1} \\ = (z - H_\theta)^{-1}V_\theta(z - H_{0,\theta})^{-1}.\end{aligned} \tag{6.33}$$

Under the relative-compactness hypothesis, the right-hand side is compact whenever both resolvents exist. With the Fredholm definition of essential spectrum appropriate to a non-self-adjoint operator, compact resolvent per-

turbations do not change that spectrum. Hence

$$\sigma_{\mathrm{ess}}(H_\theta) = \mathrm{e}^{-2\mathrm{i}\theta}[0,\infty). \tag{6.34}$$

Step 3: analytic Fredholm theory

Away from the rotated ray, factor

$$z - H_\theta = \left[\mathbf{1} - V_\theta (z - H_{0,\theta})^{-1}\right](z - H_{0,\theta}). \tag{6.35}$$

The operator

$$K_\theta(z) = V_\theta (z - H_{0,\theta})^{-1} \tag{6.36}$$

is compact and analytic in z. For sufficiently negative real z, or at another point controlled by a resolvent estimate, $\mathbf{1} - K_\theta(z)$ is invertible. The analytic Fredholm theorem then states that

$$[\mathbf{1} - K_\theta(z)]^{-1} \tag{6.37}$$

is meromorphic away from the rotated ray. Its singularities are isolated, and the principal parts have finite rank. By Eq. (6.35), these singularities are precisely the discrete eigenvalues of H_θ, counted with algebraic multiplicity.

If γ is a small contour around one such eigenvalue z_n, the Riesz projection is

$$P_n(\theta) = \frac{1}{2\pi\mathrm{i}} \oint_\gamma (z - H_\theta)^{-1} \mathrm{d}z. \tag{6.38}$$

Its rank is the algebraic multiplicity. This formulation includes nontrivial Jordan blocks; diagonalizability is not assumed.

Step 4: continuation of physical resolvent matrix elements

Let $H(s) = U(s)HU(-s)$ for real s. Unitarity gives, for $\phi, \psi \in \mathcal{A}$,

$$\langle \phi | (z - H)^{-1} | \psi \rangle = \langle U(s)\phi | (z - H(s))^{-1} U(s) | \psi \rangle. \tag{6.39}$$

To continue this identity holomorphically, one must remember that the inner product is antilinear in its first argument. The analytic expression is

$$\left\langle U(\overline{s})\phi, (z - H(s))^{-1} U(s)\psi \right\rangle. \tag{6.40}$$

For z initially above the physical spectrum, it extends jointly in (s, z) to an overlapping complex domain and agrees with the physical matrix element for real s. The identity theorem permits continuation to $s = \mathrm{i}\theta$:

$$\langle\phi|(z - H)^{-1}|\psi\rangle_{\text{continued}} = \langle U(-\mathrm{i}\theta)\phi|(z - H_\theta)^{-1}U(\mathrm{i}\theta)|\psi\rangle. \tag{6.41}$$

The left-hand side is notation for a continued scalar matrix element, not a bounded resolvent on the original Hilbert space. The right-hand side is meromorphic by Step 3. Therefore a discrete eigenvalue of H_θ in the uncovered wedge is a pole of the continued physical matrix element.

The opposite signs in the two analytic vectors are forced by sesquilinearity; using $U(\mathrm{i}\theta)$ in both slots would continue a different expression.

Conversely, a pole that couples to analytic vectors appears as an eigenvalue once the rotated ray lies below it. A particular pair ϕ, ψ can have a zero residue and fail to see a pole, but the pole is detected by some vectors in a dense analytic set.

Step 5: angle independence and bound states

Take two admissible angles $\theta_1 < \theta_2$ and a domain of the energy plane uncovered by both rotated rays. Equation (6.41) represents the same analytic continuation for either angle. Uniqueness of analytic continuation therefore prevents an isolated pole from moving with θ. Applying the argument to matrix elements of the Riesz projection shows that its rank, hence the algebraic multiplicity, is also constant until the pole meets the essential spectrum or exits the analyticity domain.

A negative-energy bound state is already an isolated eigenvalue of the undeformed self-adjoint Hamiltonian. For real s it is unchanged because $H(s)$ is unitarily equivalent to H. Analyticity in s then continues this constant eigenvalue to complex s. This is the mathematical origin of the stationary real points in a complex-scaling plot.

Step 6: several thresholds and the limits of the theorem

For an N-body Hamiltonian, cluster decompositions produce thresholds E_a. Relative motion in an open cluster channel supplies a kinetic continuum, so the corresponding essential spectrum rotates about its own threshold:

$$\sigma_{\text{ess}}(H_\theta) = \bigcup_a \left[E_a + \mathrm{e}^{-2\mathrm{i}\theta}[0, \infty)\right] \tag{6.42}$$

under the hypotheses of the many-body theorem. A pole must be classified on the multi-sheeted surface generated by these thresholds.

The argument also displays its failure modes. They include a potential with no analytic continuation in the swept sector, loss of relative compactness, a deformation crossing a singularity, a long-range remainder not separated from the asymptotic Hamiltonian, and a threshold at which the Fredholm sheet changes. Exterior complex scaling relaxes interior analyticity by deforming only outside a finite radius, but it still requires control of the asymptotic operator. For black-hole equations, logarithmic tortoise coordinates, multiple horizons, inverse-power tails, and frequency-dependent or coupled potentials must be checked individually. Successful numerical rotation is strong evidence, but it is not by itself a proof that all ABC hypotheses hold.

6.4 Define the resonance functional and its norm

6.4.1 Gaussian regularization of a Gamow state

Let $\psi_{\mathrm{R}}(x)$ obey the outgoing condition and grow exponentially on the real axis. Zel'dovich regularization defines a bilinear overlap by inserting a Gaussian and analytically removing it:

$$(\psi_{\mathrm{R}} \mid \psi_{\mathrm{R}})_Z = \lim_{\eta \to 0^+} \int_{-\infty}^{\infty} \mathrm{d}x\, \mathrm{e}^{-\eta x^2} \psi_{\mathrm{R}}(x)^2. \tag{6.43}$$

The square is not an absolute square. It is the bilinear pairing appropriate to a time-reversal-invariant resonance problem. The integral is first evaluated where $\eta > 0$ makes it convergent and is then continued to the desired parameter domain [2, 3].

The regulator can be expressed as a nonunitary multiplication operator

$$G_\eta = \mathrm{e}^{-\frac{\eta x^2}{2}}, \qquad H_\eta = G_\eta H G_\eta^{-1}. \tag{6.44}$$

For the kinetic operator, the transformed momentum is

$$G_\eta p G_\eta^{-1} = p - \mathrm{i}\hbar\eta x, \qquad p = -\mathrm{i}\hbar \frac{\mathrm{d}}{\mathrm{d}x}. \tag{6.45}$$

Consequently H_η is non-self-adjoint. The transformation and complex scaling look different, but both move the asymptotic growth into the operator and leave a regularized vector in a square-integrable representation. Exact WKB

analysis makes their common analytic content particularly transparent [16].

6.4.2 Berggren's proof: orthogonality, normalization, and completeness

The Gaussian formula in Eq. (6.43) becomes mathematically useful only after three questions are answered: what analytic continuation is being taken, why different resonant states are orthogonal in the resulting bilinear pairing, and why the resonance sum must be accompanied by a deformed continuum. Berggren's construction answers these questions for radial short-range problems [3, 85, 95]. We give the proof in enough detail to expose its assumptions.

Theorem 6.2 (Finite-range weak Berggren expansion)**.** *Fix a partial wave on $L^2(0,\infty)$ with the regular boundary condition at the origin. Let the real potential be locally integrable and vanish for $r > R$. Assume that its Jost function has no threshold zero, spectral singularity, or multiple zero in the region swept between the positive real k axis and a piecewise smooth contour L^+ in the fourth quadrant. Let Φ_{L^+} consist of radial test functions whose Jost transforms are analytic in that region and decrease sufficiently that the closing arcs and the small threshold arc vanish.*

Then, as a weak identity from Φ_{L^+} to its antidual,

$$\sum_{n\in b\cup d} |u_n\rangle\langle\widetilde{u}_n| + \int_{L^+} \mathrm{d}k\, |u(k)\rangle\langle\widetilde{u}(k)| = \mathbf{1}. \tag{6.46}$$

The set b contains bound-state poles and d contains precisely the simple decaying poles between the two contours. The discrete vectors are normalized by the analytic continuation of the bilinear Zel'dovich pairing, and the continuum uses the corresponding biorthogonal delta normalization.

The finite-range assumption lets the tail and the contour deformation be checked directly. Exponentially decreasing, Coulomb-modified, coupled-channel, and nonlocal potentials have useful Berggren extensions, but their analytic domains, threshold terms, and test spaces must be restated; they are not automatic corollaries of Theorem 6.2.

The regulated outgoing integral

First consider the elementary tail integral

$$I_\eta(q;R)=\int_R^\infty \mathrm{d}r\,\mathrm{e}^{-\eta r^2+\mathrm{i}qr},\qquad \eta>0. \tag{6.47}$$

Completing the square gives

$$I_\eta(q;R)=\frac{\sqrt{\pi}}{2\sqrt{\eta}}\mathrm{e}^{-\frac{q^2}{4\eta}}\operatorname{erfc}\left(\sqrt{\eta}R-\frac{\mathrm{i}q}{2\sqrt{\eta}}\right). \tag{6.48}$$

For every fixed $\eta>0$ this is an entire function of q. In the upper half-plane $\operatorname{Im} q>0$, the regulator can be removed by ordinary dominated convergence:

$$\lim_{\eta\to 0^+} I_\eta(q;R)=\int_R^\infty \mathrm{d}r\,\mathrm{e}^{\mathrm{i}qr}=\frac{\mathrm{i}}{q}\mathrm{e}^{\mathrm{i}qR}. \tag{6.49}$$

The right-hand side is analytic for $q\neq 0$. Its unique analytic continuation defines the Zel'dovich value in a resonance sector where the unregulated integral diverges:

$$\left[\int_R^\infty \mathrm{d}r\,\mathrm{e}^{\mathrm{i}qr}\right]_Z:=\left[\frac{\mathrm{i}}{q}\mathrm{e}^{\mathrm{i}qR}\right]_{\text{a.c.}}. \tag{6.50}$$

Writing "take $\eta\to 0$" without the analytic-continuation qualification is incomplete: different asymptotic sectors of the complementary error function are separated by Stokes lines. The prescription is fixed by first working in the convergent half-plane and then continuing the resulting analytic function.

Orthogonality on a finite-range s-wave model

Let $V(r)=0$ for $r>R$ and write the reduced s-wave equation as

$$\left[-\frac{\mathrm{d}^2}{\mathrm{d}r^2}+U(r)\right]u_n(r)=k_n^2u_n(r),\qquad U(r)=\frac{2\mu}{\hbar^2}V(r), \tag{6.51}$$

with $u_n(0)=0$ and the purely outgoing tail

$$u_n(r)=u_n(R)\mathrm{e}^{\mathrm{i}k_n(r-R)},\qquad r\geq R. \tag{6.52}$$

For two distinct solutions, Green's identity gives

$$(k_n^2-k_m^2)\int_0^R \mathrm{d}r\,u_n(r)u_m(r)$$

$$= \left[u_n u_m' - u_m u_n'\right]_{r=R} = \mathrm{i}(k_m - k_n) u_n(R) u_m(R). \tag{6.53}$$

Consequently

$$\int_0^R \mathrm{d}r\, u_n u_m = -\frac{\mathrm{i}}{k_n + k_m} u_n(R) u_m(R). \tag{6.54}$$

On the other hand, Eq. (6.50) with $q = k_n + k_m$ gives

$$\left[\int_R^\infty \mathrm{d}r\, u_n u_m\right]_Z = \frac{\mathrm{i}}{k_n + k_m} u_n(R) u_m(R). \tag{6.55}$$

The interior and exterior terms cancel exactly:

$$(u_n \mid u_m)_Z := \int_0^R \mathrm{d}r\, u_n u_m + \left[\int_R^\infty \mathrm{d}r\, u_n u_m\right]_Z = 0, \qquad k_n^2 \neq k_m^2. \tag{6.56}$$

No complex conjugation appears. The pairing is the c product appropriate to a time-reversal-invariant complex-symmetric radial problem. Ordinary Hermitian orthogonality would be incompatible with two outgoing states.

For $m = n$, the same prescription gives the finite Gamow norm

$$\mathcal{N}_n^2 = (u_n \mid u_n)_Z = \int_0^R \mathrm{d}r\, u_n(r)^2 + \frac{\mathrm{i}}{2k_n} u_n(R)^2. \tag{6.57}$$

The norm is generally complex before a normalization convention is imposed. One may rescale u_n so that $\mathcal{N}_n^2 = 1$. At an exceptional point the bilinear norm can vanish; this self-orthogonality signals a higher-order pole and cannot be repaired by ordinary rescaling.

For $l > 0$, the outgoing tail is a Riccati–Hankel function rather than a single exponential. The proof is unchanged in structure. If

$$L_l^{(+)}(k; R) := \frac{\partial_r f_l(k, R)}{f_l(k, R)} \tag{6.58}$$

is the outgoing logarithmic derivative, the analytically continued exterior part of the norm is

$$\left[\int_R^\infty \mathrm{d}r\, u_n(r)^2\right]_Z = \frac{u_n(R)^2}{2k_n} \left.\frac{\partial L_l^{(+)}(k; R)}{\partial k}\right|_{k=k_n}. \tag{6.59}$$

For $l = 0$, $L_0^{(+)} = \mathrm{i}k$, and Eq. (6.59) reduces to the surface term in Eq. (6.57). Formula (6.59) follows either by analytically continuing the finite Riccati–Hankel expansion or by taking the coincident limit of Green's identity. This

boundary form is often more stable numerically than integrating a Gaussian at very small regulator.

Connection with the Jost derivative and the pole residue

At a simple zero $F_l(k_n) = 0$, the regular and outgoing solutions are proportional. Differentiate the radial equation with respect to k, pair it bilinearly with u_n, and integrate by parts. The interior contribution and the outgoing surface term combine into Eq. (6.59). The result relates the regularized norm to the derivative of the incoming Jost coefficient:

$$\mathcal{N}_n^2 \propto F_l'(k_n), \tag{6.60}$$

where the proportionality factor depends only on the chosen normalizations of φ_l and f_l. Substitution into Eq. (4.91) gives

$$\operatorname*{Res}_{E=E_n} G_l^{(+)}(E; r, r') = \frac{u_n(r)u_n(r')}{\mathcal{N}_n^2} \tag{6.61}$$

in the book's convention $\mathcal{R}(E) = (E - H)^{-1}$. Thus Zel'dovich normalization is the coordinate-space form of unit residue normalization. This is the mathematical reason it is compatible with scattering theory.

Contour deformation and the Berggren completeness relation

Begin with the real-energy radial completeness relation, normalized so that the continuum states satisfy a Dirac delta:

$$\sum_b u_b(r)u_b(r') + \int_0^\infty \mathrm{d}k\, u(k, r)u(k, r') = \delta(r - r'). \tag{6.62}$$

The sum contains physical bound states. For test functions whose momentum representatives have sufficient analyticity and decay, the continuum kernel can be continued into the fourth quadrant. Deform the positive real k axis to a contour L^+ that passes below selected decaying resonance poles but avoids threshold and other singularities. Cauchy's theorem gives the residues of every crossed Jost zero. With the residue normalization of Eq. (6.61), the result is

$$\sum_{b,d} |u_n\rangle\langle\widetilde{u}_n| + \int_{L^+} \mathrm{d}k\, |u(k)\rangle\langle\widetilde{u}(k)| = \mathbf{1}. \tag{6.63}$$

Here b labels bound states and d the decaying poles between the real axis and L^+. The tilde denotes the bilinear dual, not ordinary complex conjugation. The large arc vanishes only on an appropriate test space; hence Eq. (6.63) is naturally a weak identity in a rigged Hilbert space. If L^+ is returned to the real axis, the resonance residues are reabsorbed into the continuum integral and Eq. (6.62) is recovered.

This proof explains four features that are sometimes conflated. First, Zel'dovich regularization defines the bilinear norm of an outgoing residue. Second, Green's identity proves orthogonality after the regulated tail is included. Third, Jost analyticity identifies the same norm with a pole residue. Fourth, contour deformation proves completeness only for the combined set of bound states, enclosed resonances, and the L^+ continuum. Dropping the continuum destroys the identity and removes threshold and background physics.

6.4.3 The Gelfand triple

A rigged Hilbert space, or Gelfand triple, is a nested sequence

$$\Phi \subset \mathcal{H} \subset \Phi^{\times}. \tag{6.64}$$

The space Φ is dense in $\mathcal{H}$ and carries a topology stronger than the Hilbert norm. The antidual $\Phi^{\times}$ consists of continuous antilinear functionals on Φ. Generalized continuum eigenvectors and Gamow vectors live in $\Phi^{\times}$ rather than in $\mathcal{H}$. The choice of Φ is part of the physics: it specifies localization, smoothness, analyticity, and allowed contour deformations [96–99].

The arrows in Eq. (6.64) are continuous embeddings, not only set inclusions. A Hilbert vector ψ is embedded in the antidual by $\phi \mapsto \langle \phi, \psi \rangle$. In the energy direct integral of Eq. (3.14), evaluation of an L^2 section at one energy is not continuous and is not even defined independently of its almost-everywhere representative. A test topology imposing energy regularity makes the evaluation functional continuous. This elementary fact is the rigorous content behind the notation $\langle E, \alpha | \phi \rangle$. Analytic continuation of that evaluation functional can then define a Gamow vector at complex energy, provided the chosen seminorms control the required continuation.

For a test vector $\phi \in \Phi$, a resonance functional can be defined by the pole residue

$$\langle \phi, \Psi_{\mathrm{R}} \rangle = \operatorname*{Res}_{z=z_{\mathrm{R}}} \langle \phi, \mathcal{R}(z)\chi \rangle, \tag{6.65}$$

where $\chi \in \Phi$ is chosen so that the residue is nonzero. The functional satisfies a generalized eigenvalue equation

$$\langle H\phi, \Psi_{\mathrm{R}} \rangle = z_{\mathrm{R}} \langle \phi, \Psi_{\mathrm{R}} \rangle. \tag{6.66}$$

No contradiction with self-adjointness arises because $\Psi_{\mathrm{R}} \notin \mathcal{H}$ and Eq. (6.66) is an identity in the dual pairing, not an ordinary Hilbert-space eigenvalue equation.

6.4.4 Hardy classes and time direction

One can choose energy wave functions in Hardy classes analytic in an upper or lower half-plane. Contour closure then produces a semigroup time evolution for Gamow vectors: decaying poles contribute for $t > 0$, and growing time-reversed poles contribute for $t < 0$. This construction gives a clean mathematical encoding of preparation and detection, but it is not forced by the Hilbert-space Hamiltonian alone. It depends on the test space and on which boundary values are identified with prepared states and observables. We therefore use the rigged-space formalism to define pole functionals without claiming that a microscopic arrow of time follows solely from analytic continuation.

6.4.5 Relation to complex scaling

For analytic test vectors, the complex-scaled eigenvector and the Gamow functional represent the same resolvent residue. Schematically,

$$\langle \phi, \Psi_{\mathrm{R}} \rangle = \langle U(\mathrm{i}\theta)\phi | \Psi_{\mathrm{R}}^{\theta} \rangle_{\theta}, \tag{6.67}$$

where $\Psi_{\mathrm{R}}^{\theta} \in L^2$ is the eigenvector of H_θ and the right-hand side uses the left–right pairing appropriate to the deformed operator. Equation (6.67) is independent of θ as long as the pole remains exposed and the test vector is analytic under the deformation. The equality has been demonstrated explicitly in solvable models and in the Friedrichs model [16, 100].

This relation also explains why the number of discrete resonance eigenvalues visible in H_θ depends on θ while the underlying pole set does not. Changing θ changes which poles are represented by L^2 eigenvectors and which remain behind the rotated continuum. The rigged-space functional exists through continuation beyond that particular representation, subject to the

analytic domain of the problem.

6.4.6 Probability, observables, and normalization

An expectation value formed from a Gamow state can be complex. This is not a probability expectation in a closed system. It is a pole residue or a biorthogonal matrix element that may encode both a central value and a decay scale. Observable probabilities are obtained from real-energy scattering states, wave packets, detector models, or a unitary dilation of the open dynamics. Resonance vectors are efficient intermediate objects in those calculations.

Three normalizations should therefore be kept distinct. Hilbert normalization uses $\int |\psi|^2 = 1$ for a bound state or wave packet. Continuum normalization uses a Dirac delta, such as $\langle k|k'\rangle = \delta(k - k')$. Resonance normalization uses an analytic bilinear prescription, a residue condition, or a biorthogonal pairing. The singular transition between the last two normalizations is precisely what must be controlled when a resonance reaches the complex-scaled continuum at an exceptional point.

6.5 Calculation laboratory IV-A: One Gamow pole in three realizations

Calculation route

Prerequisites. The resonance connection coefficient, analytic continuation of a Gamow solution, Gaussian regularization, and analytic dilation.

Calculation goal. Generalized Riccati equations, Borel summation, Gaussian regularization, analytic dilation, and the rigged-Hilbert-space interpretation in one explicit model.

Completion criterion. Show on the same solvable model that Zel'dovich, complex-scaled, and rigged-space pairings encode the same continued resonance datum.

This Laboratory reconstructs the calculation underlying Ref. [16]. The generalized Riccati recursion and local connection formula use the canonical conventions of Sec. 5.1; they are not derived a second time. The calculation begins where the choice of regularization first matters.

6.5.1 One pole, three realizations

The continued Gamow branch is the zero of the incoming connection coefficient constructed in Stage III. We now compute its Zel'dovich, complex-scaled, and rigged-space representatives.

6.5.2 Zel'dovich regularization

Hamiltonian under Zel'dovich transformation

The wave function of a resonant state diverges in the asymptotic region. This singular nature causes difficulty in investigating the state as follows: In the 3-dimensional space, the radial wave function $\varphi(r)$ of a resonant state with $k = k_r - \mathrm{i}k_i$ (k_r, $k_i \in \mathbb{R}^+$) has the typical asymptotic form

$$\varphi(r) \xrightarrow[r\to\infty]{} \mathrm{e}^{\mathrm{i}kr} = \mathrm{e}^{\mathrm{i}k_r}\mathrm{e}^{k_i r}, \tag{6.68}$$

which grows up exponentially because of $\mathrm{e}^{k_i r}$. The integration of the norm, $||\varphi(r)||^2$, is also ill-defined. Similarly, in time-independent scattering theory, a factor, $\mathrm{e}^{\mathrm{i}\varepsilon t}$ with $\varepsilon > 0$, suppress the $\mathrm{e}^{-\mathrm{i}Et}$ oscillations in stationary solutions. An analogous approach, called the Zel'dovich regularization [2], can be introduced in order to obtain a finite value of the norm as

$$||\varphi(r)||_S^2 \equiv \lim_{\varepsilon\to+0} \int_0^\infty \mathrm{d}r\, \mathrm{e}^{-\varepsilon r^2} \varphi(r)^2 r^2. \tag{6.69}$$

Using this regularization, Berggren [3] proved the orthogonality and completeness properties of the resonant states. Now, the square of the wave function is integrated with the norm not only of the bound states but also of the resonant states. For the Schrödinger equation, we can have a similarity transformation associated with Zel'dovich regularization. The Zel'dovich transformation is given by

$$H\psi = E\psi \qquad \Rightarrow \qquad H_S\psi_S = E\psi_S \tag{6.70}$$

with

$$\psi_S \equiv S\psi, \qquad\qquad H_S \equiv SHS^{-1}. \tag{6.71}$$

Here S is the Gaussian factor $\mathrm{e}^{-\varepsilon r^2}$. Note that the Zel'dovich-transformed Hamiltonian [88] is related to the original one as

$$H_S = H - \frac{\hbar^2\varepsilon}{m}(\nabla\cdot\boldsymbol{r} + \boldsymbol{r}\cdot\nabla) + O(\varepsilon^2). \tag{6.72}$$

For the 1-dimensional system, one finds that

$$H_S = H - \frac{\hbar^2\varepsilon}{m}\left(\frac{\mathrm{d}}{\mathrm{d}x}x + x\frac{\mathrm{d}}{\mathrm{d}x}\right) = H - \frac{\hbar^2\varepsilon}{m}\left(1 + 2x\frac{\mathrm{d}}{\mathrm{d}x}\right). \tag{6.73}$$

Inverted Rosen–Morse potential

The Stokes graph via the Zel'dovich transformation is identical to the original graph with $f(x) = -\frac{4\varepsilon}{m}x$ in Eq. (6.73). For the inverted Rosen–Morse potential,

$$V(x) = \frac{U_0}{\cosh^2\beta x}, \qquad U_0 > 0, \tag{6.74}$$

see Figs. 6.1 ($\mathrm{Im}\,\hbar \gtrless 0$ and $\mathrm{Im}\,E \gtrless 0$) and 6.2 ($\mathrm{Im}\,\hbar \gtrless 0$ and $\mathrm{Im}\,E \lesseqgtr 0$, but $\mathrm{Im}\,E \sim 0$) [15]. Note that $\mathrm{Im}\,E_{\mathrm{R}} < 0$ for the complex energy of resonance, E_{R}. Now, since the wave function is expected to be normalizable after the Zel'dovich transformation, Note that the normalizability of the wave function, i.e., the dominance of ψ^- at infinity, gives rise to the quantization condition which is given by the analytical continuation and the connection formula. One may choose the simple path depicted on the left panel in Fig. 6.3 for giving the quantization condition. The non-perturbative cycle, $A = \mathrm{e}^{\oint_{a_1}^{a_2}\mathrm{d}x\,S_{\mathrm{odd}}}$, contributes $M_- N_{a_1 a_2} M_+$, where $a_{1,2}$ is a turning point; a simple convergence condition that ψ^+ should vanish at $\mathrm{Im}\,x \to \pm\infty$ gives rise to $1 - A = 0$ as is given in Ref. [15]. We should now observe the convergence of (norm of) the wave function at $x = \pm\infty$. Then, the actual connection path is given by the red path on the right panel in Fig. 6.3. The red solid line is on the Riemann sheet depicted and the red dashed line is on another Riemann sheet after passing through the branch cut. In the WKB solution, $\mathrm{e}^{-\int^x \mathrm{d}x'\,S_{\mathrm{odd}}}$ along the Stokes curve with the index $-$ exponentially dumps, and hence the dominant effect comes from $\mathrm{e}^{\int^x \mathrm{d}x'\,f} = \mathrm{e}^{-2\varepsilon x^2/m}$. At $\mathrm{Im}\,x = \pm\infty$, the overall factor of the WKB solution diverges exponentially, while at $\mathrm{Re}\,x = \pm\infty$ it converges exponentially. As a consequence, we find that this consistency provides the connection formula for $\psi = (\psi^+, \psi^-)^{\mathsf{T}}$ between $x \to \pm\infty$. Let $\mathcal{A}_-$ denote

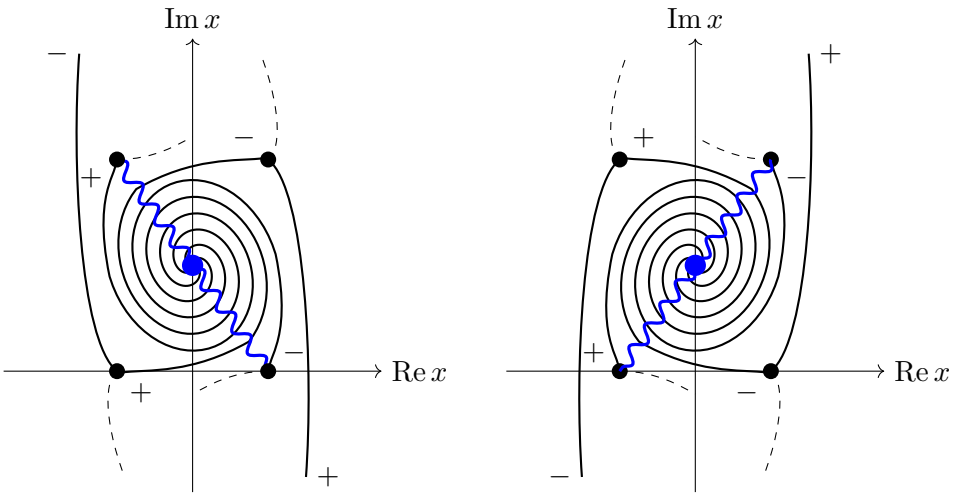

Figure 6.1: Schematic illustration of Stokes graph for the inverted Rosen–Morse potential, $V(x) = 1/\cosh^2 x$, via the Zel'dovich transformation. This geometry itself is identical to the original one [15]. The left/right panels are devoted to $\operatorname{Im}\hbar \gtrless 0$ and $\operatorname{Im} E \gtrless 0$. The black points are the turning points and the solid curves are the associated Stokes curves. The dashed Stokes curves mean the periodicity of $\operatorname{Im} x \in [-\pi/2, \pi/2]$ due to the cosine function on $\operatorname{Re} x = 0$. The blue points are double poles and the blue wavy lines are branch cuts.

analytic continuation from $-\infty$ to $\lim_{n\to\infty}(-a - 2\pi\mathrm{i}n/\beta)$, and let $\mathcal{A}_+$ denote continuation from $\lim_{n\to\infty}(a + 2\pi\mathrm{i}n/\beta)$ to $+\infty$; both are taken within the corresponding Borel-summable region. Then

$$\begin{aligned}\psi|_{x\to-\infty} = \mathcal{A}_- &\times \prod_{n=\infty}^{0} M_-^{-1} N_{-a-2\pi\mathrm{i}(n+1)/\beta,-a-2\pi\mathrm{i}n/\beta} \\ &\times M_-^{-1} N_{-a,a} M_+^{-1} \\ &\times \prod_{n=0}^{\infty} N_{a+2\pi\mathrm{i}n/\beta,a+2\pi\mathrm{i}(n+1)/\beta} M_- \\ &\times \mathcal{A}_+ \psi|_{x\to\infty}. \end{aligned} \tag{6.75}$$

Hence, $\psi^{\pm}|_{x\to-\infty}$ is a linear combination of $\psi^{+}|_{x\to\infty}$ and $\psi^{-}|_{x\to\infty}$. Reference [15] states that the resonant wave-function is described by the connection formula of ψ^- from $\operatorname{Im} x \to \infty$ to $\operatorname{Im} x \to -\infty$. From the observation of the explicit asymptotic behavior of the exact solution (see Section 4.2.2 in

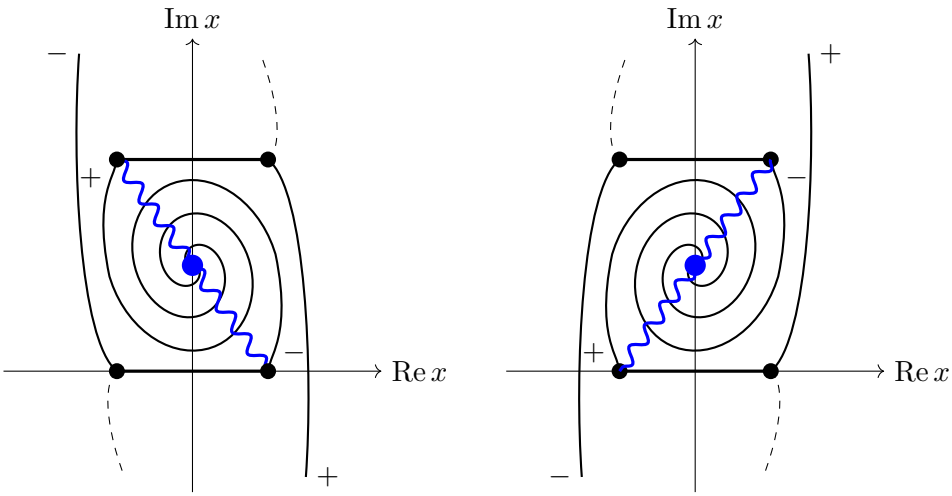

Figure 6.2: Schematic illustration of Stokes graph for the inverted Rosen–Morse potential. Same as Fig. 6.1, but $\operatorname{Im}\hbar \gtrless 0$ and $\operatorname{Im} E \lesseqgtr 0$. For simplicity, $\operatorname{Im} E \sim 0$.

Ref. [15]), the analytical-continued wave-function $\psi^-|_{x\to\infty}$ corresponds to the wave function being normalizable on a path extended in the $\operatorname{Im} x$-direction, but is divergent on the current horizontal path in the $\operatorname{Re} x$-direction as the non-normalizability problem of resonance. Then, the analytically continued $\psi^+|_{x\to-\infty}$ is an indeed non-normalizable solution.[1] Now, noting that

$$\cdots M_-^{-1} N_{-a,a} M_+^{-1} \cdots \propto \begin{pmatrix} 1 & -\mathrm{i} \\ -\mathrm{i} & \frac{1}{A} - 1 \end{pmatrix}, \tag{6.76}$$

where A is the non-perturbative cycle as $A = \mathrm{e}^{\oint_{-a}^{a} \mathrm{d}x\, S_{\mathrm{odd}}}$ and the dots "$\cdots$" do not alter the structure of the matrix, the coefficient of ψ^-, the $(2,2)$ entry, must vanish due to the consistency of blowing-up behaviors of $\psi^-|_{x\to\infty}$ and $\psi^+|_{x\to-\infty}$. To satisfy this normalizability of the wave function, the quantization condition is given by

$$0 = \mathrm{e}^{\int_{a+\mathrm{i}\infty}^{a+\infty} \mathrm{d}x(-S_{\mathrm{odd}}+f)} \left[\prod_{n=0}^{\infty} \mathrm{e}^{\int_{a+2\pi\mathrm{i}n/\beta}^{a+2\pi\mathrm{i}(n+1)/\beta} \mathrm{d}x(-S_{\mathrm{odd}}+f)} \right] (1-A)$$

[1] Note that the current path in this paper is similar near $x = a$ to that in Ref. [15], but is quite different near $x = -a$ from it. Then the latter path reverses the asymptotic behavior of $\psi^\pm$.

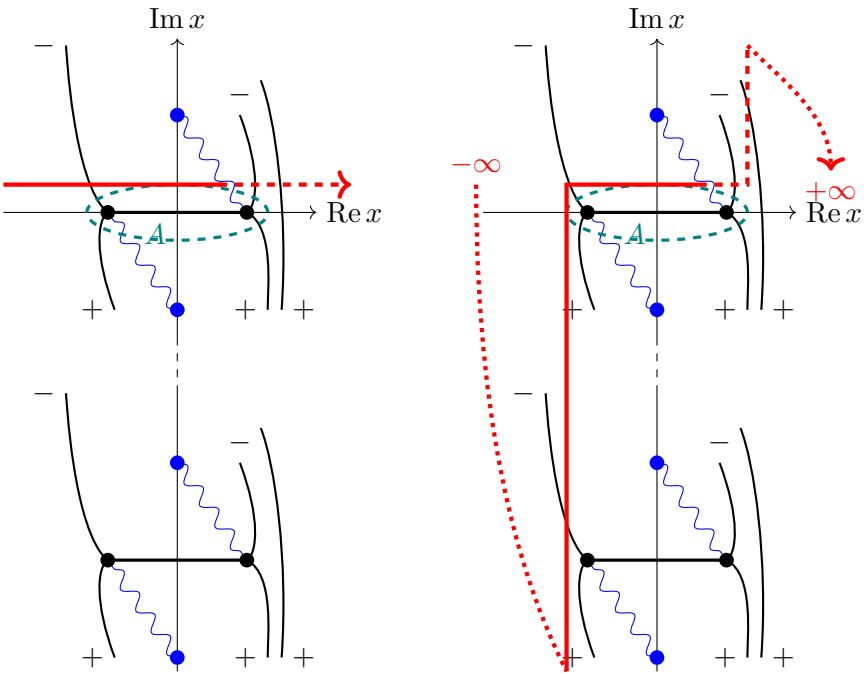

Figure 6.3: Quantization condition with $\operatorname{Im}\hbar > 0$ and $\operatorname{Im} E \lesssim 0$ for resonance. The red path on the left panel is a simple option to carry out the analytical continuation, along which we can expect the normalizability of the exact WKB solution. The right panel shows actual connection manipulations of it. The red solid line is on the Riemann sheet depicted and the red dashed line is on another Riemann sheet after passing through the branch cut; the red dotted curve is the analytical continuation at infinity. The nontrivial cycle, A-cycle, is shown as the green loop.

$$\times \left[\prod_{n=0}^{\infty} \mathrm{e}^{\int_{-a-2\pi\mathrm{i}(n+1)/\beta}^{-a-2\pi\mathrm{i}n/\beta} \mathrm{d}x(-S_{\mathrm{odd}}+f)}\right] \mathrm{e}^{\int_{-a-\infty}^{-a-\mathrm{i}\infty} \mathrm{d}x(-S_{\mathrm{odd}}+f)} \tag{6.77}$$

$$= \mathrm{e}^{\int_{a}^{-a} \mathrm{d}x(-S_{\mathrm{odd}}+f)}(1-A), \tag{6.78}$$

where the turning point $a = \beta^{-1}\cosh^{-1}\sqrt{U_0/E}$. In the second equality, we have used some properties shown in Fig. 6.4. Note that if $\varepsilon = 0$ (the usual resonant state) then the integration over $x \in (-\infty, \infty)$ cannot be finite because $\mathrm{e}^{\int_{\pm\infty}^{\pm\infty\pm\mathrm{i}\infty} \mathrm{d}x\, S_{\mathrm{odd}}}$ diverges, so we should take the other contour given in Ref. [15].[2] The quantum system with the (inverted) Rosen–Morse potential

[2]When $\varepsilon > 0$, we can take an *asymmetric* path at infinity, but one finds an overall factor that is irrelevant to the quantization condition. Equation (6.78) implies that the path is

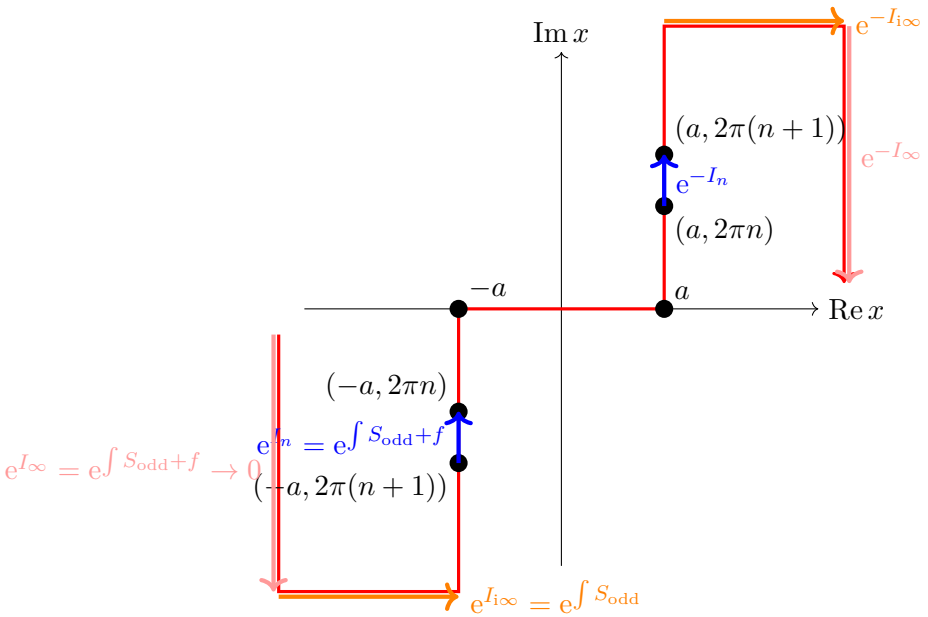

Figure 6.4: Illustration of computing Eq. (6.78). $\beta = 1$. Although $f(x)$ diverges near $|\operatorname{Im} x| \to \infty$, $f(-x) = -f(x)$ and hence $f(x)$ does not contribute to $\mathrm{e}^{I_{\mathrm{i}\infty}}$. Note that I_n, $I_{\mathrm{i}\infty}$ and I_∞ are finite. (If $f = 0$ then e^{I_∞} is divergent.)

is exactly solvable. The solution is given by

$$\psi(x) = \mathrm{e}^{-\varepsilon x^2}(1-\xi^2)^{-\frac{\mathrm{i}k}{2\beta}} F\left(-\frac{\mathrm{i}k}{\beta} - s, -\frac{\mathrm{i}k}{\beta} + s + 1, -\frac{\mathrm{i}k}{\beta} + 1, \frac{1-\xi}{2}\right), \quad (6.79)$$

where the first factor depending on ε is the Zel'dovich regulator; $\xi = \tanh \beta x$

$$k = \frac{\sqrt{2mE}}{\hbar}, \quad -\frac{2mU_0}{\beta^2\hbar^2} = s(s+1), \quad s = \frac{1}{2}\left(-1 + \sqrt{1 - \frac{8mU_0}{\beta^2\hbar^2}}\right), \quad (6.80)$$

and F is the Gauss hypergeometric function. Therefore, we can compute the exact expression in Eq. (6.78) as (we can take the limit $\varepsilon \to 0$); the formula of A-cycle is explicitly given in Ref. [15] and one finds

$$\left[\frac{F\left(-\frac{\mathrm{i}k}{\beta} - s, -\frac{\mathrm{i}k}{\beta} + s + 1, -\frac{\mathrm{i}k}{\beta} + 1, \frac{1-|\xi|}{2}\right)}{F\left(-\frac{\mathrm{i}k}{\beta} - s, -\frac{\mathrm{i}k}{\beta} + s + 1, -\frac{\mathrm{i}k}{\beta} + 1, \frac{1+|\xi|}{2}\right)}\right]^2 = 1, \quad (6.81)$$

where $|\xi| = \tanh(\cosh^{-1}\sqrt{U_0/E})$. Writing the Gauss function as $F(a, b; c; z)$ and defining

$$\begin{aligned} a_- &= -\frac{\mathrm{i}k}{2\beta} - \frac{s}{2}, & b_- &= -\frac{\mathrm{i}k}{2\beta} + \frac{s+1}{2}, \\ a_+ &= -\frac{\mathrm{i}k}{2\beta} - \frac{s-1}{2}, & b_+ &= -\frac{\mathrm{i}k}{2\beta} + \frac{s}{2} + 1, \end{aligned} \quad (6.82)$$

we use the quadratic transformation

$$\begin{aligned} &F\left(-\frac{\mathrm{i}k}{\beta} - s, -\frac{\mathrm{i}k}{\beta} + s + 1, -\frac{\mathrm{i}k}{\beta} + 1, \frac{1 \pm |\xi|}{2}\right) \\ &= \mathfrak{A} F\left(a_-, b_-; \frac{1}{2}; |\xi|^2\right) \\ &\quad \mp \mathfrak{B} F\left(a_+, b_+; \frac{3}{2}; |\xi|^2\right), \end{aligned} \quad (6.83)$$

where

$$\mathfrak{A} = \frac{\Gamma\left(-\frac{\mathrm{i}k}{\beta} + 1\right)\Gamma\left(\frac{1}{2}\right)}{\Gamma\left(-\frac{\mathrm{i}k}{2\beta} - \frac{s-1}{2}\right)\Gamma\left(-\frac{\mathrm{i}k}{2\beta} + \frac{s}{2} + 1\right)},$$

anti-symmetric.

$$\mathfrak{B} = \frac{\Gamma\left(-\frac{\mathrm{i}k}{\beta}+1\right)\Gamma\left(-\frac{1}{2}\right)}{\Gamma\left(-\frac{\mathrm{i}k}{2\beta}-\frac{s}{2}\right)\Gamma\left(-\frac{\mathrm{i}k}{2\beta}+\frac{s+1}{2}\right)}, \tag{6.84}$$

we observe the complex energy for resonance with $\frac{8mU_0}{\beta^2\hbar^2} > 1$

$$E = \frac{\hbar^2\beta^2}{8m}\left[\sqrt{\frac{8mU_0}{\beta^2\hbar^2}-1} - \mathrm{i}(2n+1)\right]^2, \qquad n \in \mathbb{Z}_{\geq 0}. \tag{6.85}$$

Remarks on difficulties of irrational potential

We make remarks on some technical and conceptual points. Figure 6.1 corresponds to $\mathrm{Im}\,\hbar \gtrless 0$ and $\mathrm{Im}\,E \gtrless 0$, while Fig. 6.2 is $\mathrm{Im}\,\hbar \gtrless 0$ and $\mathrm{Im}\,E \lessgtr 0$. In the case that $\mathrm{Im}\,\hbar > 0$, originally, for $\mathrm{Im}\,E > 0$, ψ^+ beginning at the left turning point, $-a$, is absorbed into the above double pole. However, for $\mathrm{Im}\,E < 0$, the curve of ψ^+ becomes flat and so falls down. Actually, this phenomenon is quite difficult since we focus on non-polynomial and irrational potential functions such as the inverted Rosen–Morse potential. It is not straightforward to consider the monodromy and connection formula around the double poles. In fact, for an irrational potential, the residue theorem can be violated; it makes the derivation of explicit connection formula hard since estimations of some contour integrals become too nontrivial. To our best knowledge, in particular, the Stokes phenomenon across the Stokes curve connecting the two turning points in Fig. 6.2 is subtle. Furthermore, though we mentioned $\mathrm{Im}\,E \sim 0$, for large $|\,\mathrm{Im}\,E|$ there are two Stokes curves extending from a double pole to $\mathrm{Im}\,x \to \pm\infty$. The monodromy associated with these curves may be unidentifiable in an analytic sense due to such an irrational potential.[3]

6.5.3 Complex scaling method

Solving method within complex scaling method

For the inverted Rosen–Morse potential, the Schrödinger equation with the complex scaling method (CSM) is given by

$$\left[-\frac{\hbar^2}{2m}\frac{\mathrm{d}^2}{\mathrm{d}x'^2} + \frac{U_0}{\cosh^2\beta x'}\right]\psi(x') = E\psi(x'), \tag{6.86}$$

[3] The validity of our analytical strategy should be examined through numerical verification in future studies.

where we have replaced $x \in \mathbb{R}$ by $x' = xe^{i\theta} \in \mathbb{C}$ with the scaling angle θ. The range of θ is restricted to $0 < \theta < \pi/4$ in the CSM. Using $\xi = \tanh \beta x'$, the equation is represented as

$$\left[\frac{\mathrm{d}}{\mathrm{d}\xi}(1-\xi^2)\frac{\mathrm{d}}{\mathrm{d}\xi} + s(s+1) - \frac{\kappa^2}{1-\xi^2}\right]\psi(x') = 0, \qquad \kappa = \frac{\sqrt{-2mE}}{\beta\hbar}. \tag{6.87}$$

Letting $\psi(x') = (1-\xi^2)^{\frac{\kappa}{2}}\omega(\xi)$ and substituting this into Eq. (6.87), we obtain the following equation:

$$u(1-u)\omega'' + (\kappa+1)(1-2u)\omega' - (\kappa-s)(\kappa+s+1)\omega = 0, \tag{6.88}$$

$$u = \frac{1-\xi}{2}. \tag{6.89}$$

Here primes denote derivatives with respect to u. The solution of this equation, which is regular at $x = 0$, is given by

$$\psi_{\mathrm{CSM}}(x) = (1-\xi^2)^{\frac{\kappa}{2}} F\left(\kappa - s, \kappa + s + 1, \kappa + 1, \frac{1-\xi}{2}\right). \tag{6.90}$$

In general, as $x \to -\infty$ ($\xi \to -1$), the Gauss hypergeometric function diverges. However, physical wave functions of resonant states under CSM are normalizable because of the ABC theorem [6, 7]. To ensure the normalizability of the wave function, the hypergeometric function should be expressed as a finite-order polynomial. This requirement leads to the condition, $\kappa - s = -n$ ($n \in \mathbb{Z}_{\geq 0}$), which gives

$$E = \frac{\hbar^2\beta^2}{8m}\left[\sqrt{\frac{8mU_0}{\beta^2\hbar^2} - 1} - \mathrm{i}(2n+1)\right]^2. \tag{6.91}$$

This complex energy is completely the same result as Eq. (6.85).

Exact WKB framework of complex scaling method

The potential Q of the CSM Schrödinger equation can be rewritten by

$$Q_{\mathrm{CSM}}(x) = 2\mathrm{e}^{2\mathrm{i}\theta}\left(\frac{U_0}{\cosh^2 \beta x e^{\mathrm{i}\theta}} - E\right). \tag{6.92}$$

The Stokes graph, i.e., Fig. 6.1, is rotated by θ. Now, the path for the quantization condition can be schematically depicted as in Fig. 6.5. Thus,

we have the almost same quantization condition as Eq. (6.77) with $f(x) = 0$, but the interval of the integration $\int S_{\rm odd}$ is smaller as follows:

$$\lim_{r\to\infty}\int_{\pm(1+\mathrm{i})r}^{\pm r} S_{\rm odd} \to \lim_{r\to\infty}\int_{\pm(1+\mathrm{i})r}^{\pm \mathrm{e}^{\pm\mathrm{i}\theta} r} S^{\theta}_{\rm odd}. \tag{6.93}$$

The CSM excludes the region near $x = \pm\infty$, where the solution is most singular. At $\mathrm{Re}\, x \to \infty$, the analytic continuation is supposed to be carried out from the argument $\pi/4$ to θ. Therefore, from the formula in Ref. [15], we have the overall convergent factor in the quantization condition as

$$\begin{aligned}&\lim_{r\to\infty} \mathrm{e}^{\int_{\mathrm{e}^{\mathrm{i}\theta}r}^{\mathrm{e}^{\mathrm{i}\pi/4}r} S^{\theta}_{\rm odd}} \\ &= \lim_{r\to\infty} \frac{F\left(\kappa - s, \kappa + s + 1, \kappa + 1, \frac{1-\tanh\beta r\mathrm{e}^{\mathrm{i}\pi/4}}{2}\right)}{F\left(\kappa - s, \kappa + s + 1, \kappa + 1, \frac{1-\tanh\beta r\mathrm{e}^{\mathrm{i}\theta}}{2}\right)} = \text{finite} \qquad \text{if } 0 < \theta < \frac{\pi}{4}.\end{aligned} \tag{6.94}$$

The non-perturbative cycle A is now given by

$$A = \mathrm{e}^{\oint_{-a\mathrm{e}^{-\mathrm{i}\theta}}^{a\mathrm{e}^{-\mathrm{i}\theta}} S^{\theta}_{\rm odd}} = \left[\frac{\psi_{\rm CSM}(a\mathrm{e}^{-\mathrm{i}\theta})}{\psi_{\rm CSM}(-a\mathrm{e}^{-\mathrm{i}\theta})}\right]^2 = \left[\frac{\psi(a)}{\psi(-a)}\right]^2 = \mathrm{e}^{\oint_{-a}^{a} S_{\rm odd}}, \tag{6.95}$$

where $\psi_{\rm CSM}(x'\mathrm{e}^{-\mathrm{i}\theta}) = \psi(x')$, $a\mathrm{e}^{-\mathrm{i}\theta}$ denotes the turning point after complex rotation, and a is the original turning point with $\theta = 0$. We obtain the well-defined complex energy being identical to Eq. (6.85).

6.5.4 Rigged-space reading of the model pole

The topology and duality of a Gelfand triple have already been constructed in Sec. 6.4; they should not be inferred from an informal classification of "linear spaces" attached to successive WKB operations. For the inverted Rosen–Morse model, choose the test space so that its energy representatives admit the same continuation used in the connection problem. The Gamow functional is then defined by the residue

$$\langle \phi, \Psi_{\rm R}\rangle = \operatorname*{Res}_{E=E_{\rm R}} \langle \phi, (E - H)^{-1}\chi\rangle, \qquad \phi, \chi \in \Phi. \tag{6.96}$$

Its normalization is fixed by the derivative of the same incoming connection coefficient that produced Eq. (6.85). The Zel'dovich integral realizes this

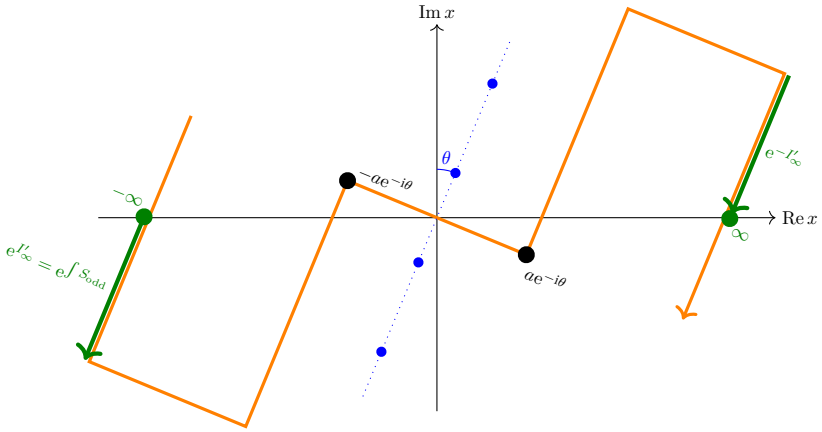

Figure 6.5: Rotated path on the inverted Rosen–Morse potential by θ. The black points and the blue points denote the turning points and the double poles, respectively. The orange path is the usual contour ($\theta = 0$) given in Figs. 6.3 and 6.4, which is rotated by θ under the CSM. The endpoints of the path in the CSM are at $x = \pm\infty$, and so the interval of the integration $\int S_{\rm odd}$ is smaller than the usual one by θ. I'_∞ is finite for $0 < \theta < \pi/4$.

residue as an analytically continued bilinear pairing; complex scaling realizes it as a left–right eigenvector pairing of an exposed discrete eigenvalue. Removing either regulator returns the functional to $\Phi^\times$, not to a new canonical Hilbert space of resonances. This is the precise sense in which the three realizations agree.

Laboratory checkpoint

Before moving to the next stage, perform the following checks without copying the displayed final answer.

1. Carry the Gaussian regulator through the Gamow bilinear norm before taking its analytically continued zero-regulator value.

2. Rotate the integration contour within the admissible wedge and check that the exposed pole and residue do not depend on the rotation angle.

3. Write the same result as a pairing with a test function and identify the continuity property required of the test-space topology.

6.6 Keep the continuum: response and numerical complex scaling

6.6.1 Continuum level density

The density of states of an unbounded system is infinite and depends on the normalization volume. A finite observable is obtained by subtracting a reference Hamiltonian H_0 with the same asymptotic channels. Define the continuum level density

$$\Delta\rho(E) = -\frac{1}{\pi}\,\mathrm{Im}\,\mathrm{Tr}\left[\frac{1}{E+\mathrm{i}0-H} - \frac{1}{E+\mathrm{i}0-H_0}\right]. \tag{6.97}$$

When the resolvent difference is trace class, analytic deformation gives

$$\Delta\rho(E) = -\frac{1}{\pi}\,\mathrm{Im}\,\mathrm{Tr}\left[\frac{1}{E-H_\theta} - \frac{1}{E-H_{0,\theta}}\right]. \tag{6.98}$$

The right-hand side can be evaluated on the real energy axis because the deformed poles and continuum lie below it. In an exact calculation it is independent of θ within the common analyticity domain [8, 17, 19].

If a finite basis yields complex eigenvalues E_n^θ and reference eigenvalues $E_{n,0}^\theta$, a useful approximation is

$$\Delta\rho_N(E) = -\frac{1}{\pi}\,\mathrm{Im}\left[\sum_{n=1}^{N}\frac{1}{E-E_n^\theta} - \sum_{n=1}^{N}\frac{1}{E-E_{n,0}^\theta}\right]. \tag{6.99}$$

The subtraction must use compatible bases, contours, and asymptotic Hamiltonians. Otherwise large discretization artifacts survive and can be mistaken for response.

For one elastic channel, the spectral-shift relation is

$$\Delta\rho(E) = \frac{1}{\pi}\frac{\mathrm{d}\delta(E)}{\mathrm{d}E}, \tag{6.100}$$

up to the convention for the reference phase and bound-state jumps. More generally, if $\det S(E) = \mathrm{e}^{2\mathrm{i}\delta_{\mathrm{tot}}(E)}$, then

$$\Delta\rho(E) = \frac{1}{2\pi\mathrm{i}}\frac{\mathrm{d}}{\mathrm{d}E}\log\det S(E) = \frac{1}{\pi}\frac{\mathrm{d}\delta_{\mathrm{tot}}(E)}{\mathrm{d}E}. \tag{6.101}$$

Thus the CLD retains both pole and nonresonant phase information. It is

not, by itself, the transmission probability: channel-resolved amplitudes are needed to reconstruct greybody factors or reaction cross sections.

6.6.2 Basis expansion and generalized eigenvalue problem

Choose square-integrable basis functions $\{\phi_n\}_{n=1}^{N}$. Expanding a right eigenvector as $\Psi^{\mathrm{R}} = \sum_n c_n \phi_n$ gives

$$\sum_{n=1}^{N} H^{\theta}_{mn} c_n = E \sum_{n=1}^{N} N_{mn} c_n, \tag{6.102}$$

where

$$H^{\theta}_{mn} = (\phi_m \mid H_\theta \phi_n)_{\mathrm{c}}, \qquad N_{mn} = (\phi_m \mid \phi_n)_{\mathrm{c}}. \tag{6.103}$$

For an orthonormal basis, N is the identity. Gaussian bases are convenient because kinetic and many potential matrix elements are analytic. Even and odd sectors on the full line can be represented by

$$\phi^{(+)}_n(x) = \mathrm{e}^{-\alpha_n x^2}, \qquad \phi^{(-)}_n(x) = x\mathrm{e}^{-\alpha_n x^2}, \tag{6.104}$$

where every width satisfies $\operatorname{Re}\alpha_n > 0$. Complex-range Gaussians replace α_n by conjugate pairs $\alpha_n \pm \mathrm{i}\beta_n$ and resolve oscillatory tails more efficiently [8, 18, 101].

The generalized eigenproblem is ill conditioned when basis functions become nearly linearly dependent. A robust implementation first diagonalizes or factorizes the overlap matrix, removes directions below a documented tolerance, and only then solves the reduced problem. Since the matrix is non-normal, residuals must be checked for both right and left eigenvectors:

$$\begin{aligned} \epsilon^{\mathrm{R}}_n &= \frac{\|H^{\theta}\boldsymbol{c}_n - E_n N \boldsymbol{c}_n\|_2}{\|H^{\theta}\|_2\|\boldsymbol{c}_n\|_2 + |E_n|\|N\|_2\|\boldsymbol{c}_n\|_2}, \\ \epsilon^{\mathrm{L}}_n &= \frac{\|(\boldsymbol{d}_n)^{\dagger}H^{\theta} - E_n(\boldsymbol{d}_n)^{\dagger}N\|_2}{\|H^{\theta}\|_2\|\boldsymbol{d}_n\|_2 + |E_n|\|N\|_2\|\boldsymbol{d}_n\|_2}. \end{aligned} \tag{6.105}$$

Here $\boldsymbol{c}_n$ and $\boldsymbol{d}_n$ are coefficient vectors, and $\|\cdot\|_2$ is the Euclidean or induced matrix norm.

6.6.3 Pole-identification protocol

A reproducible complex-scaling calculation should separate theorem-level invariance from finite-basis evidence. We recommend the following tests.

First, track eigenvalue trajectories under a range of scaling angles. A continuum pseudostate follows the ray $\arg(E - E_a) \simeq -2\theta$, whereas a resonance develops a stationary segment after exposure. Second, repeat the tracking while increasing N and changing the distribution of basis widths. Third, compare at least two basis families when possible. Fourth, monitor the condition number of N, left–right overlap, and residuals. Fifth, inspect the smallest singular value of $zN - H^\theta$ around a candidate pole. A large pseudospectral cloud warns that small discretization errors can move the eigenvalue substantially even when its trajectory looks stationary.

For black-hole problems, a sixth test is available: compare low-lying frequencies against a method with different analytic systematics, such as Leaver's continued fraction [18, 102]. Agreement of a few digits is not the end of validation; the scaling-angle plateau and basis stability identify why the number belongs to the intended pole rather than to a coincidentally accurate pseudostate.

6.6.4 Complex absorbing potentials and stabilization

An alternative is to add a complex absorbing potential,

$$H(\eta) = H - \mathrm{i}\eta W, \qquad \eta > 0, \qquad W \succeq 0, \tag{6.106}$$

with W supported outside the interaction region. Resonances are inferred from stationary eigenvalue trajectories as η varies. The logic is close to complex scaling, but a finite absorber changes the operator rather than implementing an exact analytic deformation. Results should be extrapolated or optimized in η and absorber shape. Stabilization methods similarly identify resonances by weak dependence on box size or nonlinear basis scales. These methods are valuable cross-checks but do not replace a definition of the continued pole.

6.7 Pole calculus for widths, line shapes, and measured response

Calculation route

Prerequisites. The pole definition of Section 4.4, the derivative normalization of Section 3.2, and the continuum response of Section 6.6.

Calculation goal. Derive Breit–Wigner and Fano forms as controlled approximations to a pole plus background, including energy-dependent self-energies, partial widths, thresholds, and source dependence.

Completion criterion. Given a continued connection matrix, calculate a channel residue and know which real-axis peak parameters are, and are not, equal to the pole data.

A resonance formula is useful only after its numerator, denominator, sheet, and range of approximation have been specified. The pole position is an analytic invariant. A peak position, a full width at half maximum, a time delay, and a fitted Breit–Wigner mass are real-axis summaries that coincide with the pole parameters only under additional assumptions. This section derives those assumptions instead of adopting a resonance formula as a definition. The presentation follows the practical pole calculus emphasized in Ref. [35], but the denominator is kept in the exact-WKB form used throughout this book.

6.7.1 Every measurement contains a source, propagation, and a detector

Let $|F_a\rangle$ be the state produced by an entrance channel or external operator and let $\langle D_b|$ represent the detected channel. The energy- dependent amplitude has the form

$$\mathcal{A}_{ba}(E) = \langle D_b|\mathcal{R}(E+\mathrm{i}0)|F_a\rangle \tag{6.107}$$

up to kinematic and direct terms. If the continued resolvent has a simple pole z_{R}, then locally

$$\mathcal{A}_{ba}(E) = \mathcal{A}^{\mathrm{bg}}_{ba}(E) + \frac{g^{\mathrm{R}}_b \widetilde{g}^{\mathrm{R}}_a}{E - z_{\mathrm{R}}}, \tag{6.108}$$

where

$$g_b^{\mathrm{R}} = \langle D_b, \Psi_{\mathrm{R}} \rangle, \qquad \tilde{g}_a^{\mathrm{R}} = \langle \widetilde{\Psi}_{\mathrm{R}}, F_a \rangle. \tag{6.109}$$

The residue factorizes, but its two factors depend on preparation and detection. A pole can be prominent in one reaction and almost invisible in another. Conversely, a kinematic cusp or a zero of the background amplitude can create a peak or dip without a nearby pole.

For an inclusive response generated by an operator O from a normalized state $|0\rangle$, take $|F\rangle = O|0\rangle$ and

$$S_O(E) = -\frac{1}{\pi} \operatorname{Im} \langle F | \mathcal{R}(E + \mathrm{i}0) | F \rangle. \tag{6.110}$$

Positivity of the physical spectral measure makes the total $S_O(E)$ nonnegative. A separated pole term after contour deformation need not be positive by itself, because the continued left and right residues are not complex conjugates and the rotated continuum completes the physical boundary value.

6.7.2 Feshbach elimination and the exact scalar denominator

Let $P = |d\rangle\langle d|$ select one intrinsic doorway and $Q = \mathbf{1} - P$. Eliminating Q gives

$$G_{dd}(z) := \langle d | \mathcal{R}(z) | d \rangle = \frac{1}{D(z)}, \qquad D(z) = z - E_d - \Sigma(z), \tag{6.111}$$

with the self-energy

$$\Sigma(z) = \langle d | HQ(z - QHQ)^{-1} QH | d \rangle. \tag{6.112}$$

The resonance pole solves

$$D(z_{\mathrm{R}}) = 0 \tag{6.113}$$

on the continued sheet. For a simple pole,

$$G_{dd}(z) = \frac{Z_{\mathrm{R}}}{z - z_{\mathrm{R}}} + O(1), \qquad Z_{\mathrm{R}} = \frac{1}{1 - \Sigma'(z_{\mathrm{R}})}. \tag{6.114}$$

The quantity Z_{R} is generally complex. It is a residue renormalization, not a probability that must lie between zero and one.

On the upper rim of the physical cut write

$$\Sigma(E + \mathrm{i}0) = \Delta(E) - \frac{\mathrm{i}}{2}\Gamma(E), \tag{6.115}$$

where Δ is the dispersive shift. If channel c has continuum states $|E, c\rangle$ in a fixed flux normalization, then

$$\Gamma_c(E) = 2\pi \left|\langle E, c|H|d\rangle\right|^2, \qquad \Gamma(E) = \sum_{c \text{ open}} \Gamma_c(E) \tag{6.116}$$

in that normalization. Equation (6.116) is an on-shell identity for the imaginary part of the physical self-energy. At a broad complex pole, analytic continuation and the factor Z_{R} must be retained; simply substituting a real-energy golden- rule width into $z_{\mathrm{R}} = E_d + \Delta - \mathrm{i}\Gamma/2$ is an approximation.

6.7.3 The multichannel effective Hamiltonian and unitary S matrix

Let $W_{nc}(E)$ couple intrinsic states $|n\rangle$ to open channels c. With continuum states normalized per unit energy, define

$$H_{\mathrm{eff}}(E + \mathrm{i}0) = H_{PP} + \Delta(E) - \mathrm{i}\pi W(E)W(E)^{\dagger}, \tag{6.117}$$

$$S(E) = \mathbf{1} - 2\pi\mathrm{i}\, W(E)^{\dagger}[E - H_{\mathrm{eff}}(E + \mathrm{i}0)]^{-1}W(E). \tag{6.118}$$

The Hermitian principal-value term Δ and the anti-Hermitian term are the real and imaginary parts of one self-energy. Keeping both and using the same W makes Eq. (6.118) unitary on the retained open channels. Replacing the anti-Hermitian part by an unrelated fitted width can destroy that identity.

Suppose one isolated right–left eigenpair of the continued effective Hamiltonian dominates. Its contribution to Eq. (6.118) is

$$S_{ba}(E) = S_{ba}^{\mathrm{bg}}(E) - \frac{\mathrm{i}\,\gamma_b^{\mathrm{R}}\widetilde{\gamma}_a^{\mathrm{R}}}{E - z_{\mathrm{R}}} + \cdots, \tag{6.119}$$

where the channel residues contain W, the left and right intrinsic vectors, and the derivative of the energy-dependent effective operator. Only in the narrow, slowly varying, time-reversal-invariant limit can phases be chosen so that

$$|\gamma_c^{\mathrm{R}}|^2 \simeq \Gamma_c, \qquad \sum_c \Gamma_c \simeq \Gamma. \tag{6.120}$$

For overlapping resonances, the residues are coherent matrices and a sum of positive independent Breit–Wigner cross sections is not unitary.

6.7.4 Derivation of the one-channel Breit–Wigner factor

For one elastic channel, real analyticity and unitarity imply that an isolated simple pole $z_{\mathrm{R}} = E_* - \mathrm{i}\Gamma/2$ is accompanied by a zero at z_{R}^*. Factor the scattering matrix as

$$S(E) = \mathrm{e}^{2\mathrm{i}\delta_{\mathrm{bg}}(E)} \frac{E - z_{\mathrm{R}}^*}{E - z_{\mathrm{R}}} S_{\mathrm{far}}(E). \tag{6.121}$$

If δ_{bg} and S_{far} vary negligibly over an interval of several widths, absorb them into a constant phase. The resonant partial-wave amplitude then has denominator

$$E - E_* + \frac{\mathrm{i}}{2}\Gamma, \tag{6.122}$$

and its modulus squared contains

$$\frac{1}{(E - E_*)^2 + \Gamma^2/4}. \tag{6.123}$$

The pole definition came first; the Lorentzian followed after freezing the background, residue, phase space, and self-energy.

For the resonant phase shift one may take

$$\frac{E - z_{\mathrm{R}}^*}{E - z_{\mathrm{R}}} = \mathrm{e}^{2\mathrm{i}\delta_{\mathrm{R}}(E)}, \qquad \frac{\mathrm{d}\delta_{\mathrm{R}}}{\mathrm{d}E} = \frac{\Gamma/2}{(E - E_*)^2 + \Gamma^2/4}. \tag{6.124}$$

Thus the Wigner delay contributed by the isolated factor is

$$\tau_{\mathrm{R}}(E) = \frac{\hbar\Gamma}{(E - E_*)^2 + \Gamma^2/4}, \qquad \tau_{\mathrm{R}}(E_*) = \frac{4\hbar}{\Gamma}. \tag{6.125}$$

The peak delay differs by a numerical factor from the exponential lifetime $\hbar/\Gamma$ because it measures the energy derivative of a round-trip scattering phase, not the survival time of a normalized unstable packet.

6.7.5 Background interference and the Fano profile

Keep the coherent background in Eq. (6.108). Over a narrow interval approximate $\mathcal{A}^{\mathrm{bg}} = A_0$ and the residue by r_0. With

$$\epsilon = \frac{2(E - E_*)}{\Gamma}, \tag{6.126}$$

the amplitude can be written, after extracting a constant phase and scale, as

$$\mathcal{A}(E) = A_0 \frac{\epsilon + q}{\epsilon + \mathrm{i}}. \tag{6.127}$$

When time-reversal and channel conventions make q real, the intensity is

$$|\mathcal{A}(E)|^2 = |A_0|^2 \frac{(\epsilon + q)^2}{1 + \epsilon^2}. \tag{6.128}$$

A finite q shifts the maximum away from E_* and creates a zero at $\epsilon = -q$. With absorption or several coherent backgrounds, q is complex and the exact zero is filled. The asymmetric line shape is still a pole–background interference effect; its maximum is not a new definition of the resonance energy.

6.7.6 Threshold laws and why broad resonances are not Lorentzians

Near a neutral two-body threshold, phase space and the centrifugal barrier give the Wigner law

$$\Gamma_l(E) \propto k^{2l+1}, \qquad k = \sqrt{2\mu(E - E_{\mathrm{th}})}/\hbar. \tag{6.129}$$

The square root is the same branch that generates the energy sheets. A more faithful one-level denominator is therefore

$$D(E) = E - E_d - \Delta(E) + \frac{\mathrm{i}}{2}\Gamma(E), \tag{6.130}$$

not a constant-width expression. The dispersive part $\Delta(E)$ has the corresponding nonanalyticity. If the pole is close to threshold or Γ is comparable with its distance from other singularities, the maximum of $|D(E)|^{-2}$ need not occur at $\mathrm{Re}\, z_{\mathrm{R}}$, and its half-maximum width need not equal $-2\,\mathrm{Im}\, z_{\mathrm{R}}$.

For a charged channel the penetrability contains Coulomb functions and

an essential threshold factor related to $e^{-2\pi\eta}$. The ordinary power law must be replaced by the Coulomb-modified one. For a genuine three-body breakup the threshold density and final-state interactions are multidimensional; reducing them to a constant "three-body width" can erase the very correlations measured in an invariant-mass spectrum.

6.7.7 Connection-matrix residue: the exact-WKB resonance formula

In one channel the exact-WKB scattering amplitude can be arranged as

$$S(E) = \frac{\mathcal{N}(E)}{\mathcal{C}_{\mathrm{in}}(E)}. \tag{6.131}$$

If $\mathcal{C}_{\mathrm{in}}(z_{\mathrm{R}}) = 0$ is simple, then

$$\operatorname*{Res}_{E=z_{\mathrm{R}}} S(E) = \frac{\mathcal{N}(z_{\mathrm{R}})}{\partial_E \mathcal{C}_{\mathrm{in}}(z_{\mathrm{R}})}. \tag{6.132}$$

The numerator is fixed by the remaining connection data and flux convention. The denominator is a global derivative: both the perturbative WKB periods and the exponentially small Stokes multipliers must be differentiated.

For N channels, let $\mathcal{C}_{\mathrm{in}}(E)$ map the independent interior or left data to prohibited incoming amplitudes. At a simple resonance choose

$$\mathcal{C}_{\mathrm{in}}(z_{\mathrm{R}})u = 0, \qquad v^{\dagger}\mathcal{C}_{\mathrm{in}}(z_{\mathrm{R}}) = 0. \tag{6.133}$$

Then

$$\mathcal{C}_{\mathrm{in}}(E)^{-1} = \frac{uv^{\dagger}}{(E - z_{\mathrm{R}})v^{\dagger}\mathcal{C}'_{\mathrm{in}}(z_{\mathrm{R}})u} + O(1). \tag{6.134}$$

Multiplying Eq. (6.134) by the matrices that couple the source to u and v to the detector gives every channel residue. This is the same finite-dimensional obstruction obtained from analytic Fredholm theory, now calculated by exact-WKB transport.

At an exceptional point the scalar denominator in Eq. (6.134) vanishes together with the first derivative or the null space becomes defective. The Laurent expansion then contains a higher-order pole and associated vectors. Applying a simple Breit–Wigner formula at that point discards the defining Jordan data; Stage VII derives the correct replacement.

6.7.8 Complex scaling separates a pole term without discarding the cut

Using the extended complex-scaled resolution, the tested response becomes

$$S_O(E) \approx -\frac{1}{\pi}\,\mathrm{Im}\sum_{\nu}\frac{\langle F|U^{-1}(\theta)|\Phi_\nu^\theta\rangle\langle\widetilde{\Phi}_\nu^\theta|U(\theta)|F\rangle}{E-E_\nu^\theta}. \tag{6.135}$$

Stable isolated eigenvalues represent exposed poles; the eigenvalues aligned with rotated rays discretize the deformed cuts. Selecting one stable term is a useful diagnostic of its source-dependent residue. The remaining terms are not numerical contamination: they reconstruct nonresonant background, threshold cusps, and the interference needed for the physical line shape.

This point is essential for the broad 2_2^+ state of ^{6}He in Laboratory VI-A. The pole may be isolated in the complex-scaled spectrum while the observed energy distribution still depends strongly on nonresonant continuum terms. "The resonance contribution" must therefore name the Riesz pole term and the chosen source, not an arbitrary window of pseudostate energies.

6.7.9 A line-shape calculation that can be reproduced

For any proposed resonance formula, record the following in this order:

1. the continued variable and sheet on which z_{R} is found;
2. the analytic denominator and the test for a simple or multiple zero;
3. the left–right derivative normalization and channel residue;
4. the source and detector operators used to construct the numerator;
5. every open-channel threshold and the energy dependence of its penetrability;
6. the background amplitude retained coherently with the pole;
7. the energy interval over which that background and the residue were approximated as constant;
8. a comparison of the pole parameters with the peak, half-maximum, and time-delay parameters rather than an identification by notation.

Checkpoint

The reader should now be able to start from $D(z) = z - E_d - \Sigma(z)$, derive $Z_{\mathrm{R}} = [1 - \Sigma'(z_{\mathrm{R}})]^{-1}$, obtain the Breit–Wigner and Fano profiles only after declaring their approximations, and calculate a multichannel residue from $v^{\dagger}\mathcal{C}'_{\mathrm{in}}(z_{\mathrm{R}})u$.

6.8 Derive the continuum level-density relation

For a trace-class resolvent difference, define the perturbation determinant

$$\mathcal{D}(z) = \det\left[(z - H)(z - H_0)^{-1}\right]. \tag{6.136}$$

Its logarithmic derivative is

$$\frac{\mathrm{d}}{\mathrm{d}z}\log\mathcal{D}(z) = \mathrm{Tr}\left[(z - H)^{-1} - (z - H_0)^{-1}\right]. \tag{6.137}$$

Taking the imaginary part of the upper boundary value gives Eq. (6.97). The ratio of boundary values of $\mathcal{D}$ is related to $\det S$; with $\det S = \mathrm{e}^{2\mathrm{i}\delta_{\mathrm{tot}}}$, differentiation gives Eq. (6.101).

Complex deformation does not change $\mathcal{D}(z)$ in the analytic region between the original and rotated contours. This gives Eq. (6.98). In a finite basis, the determinant is a ratio of characteristic polynomials, whose logarithmic derivative gives the sum in Eq. (6.99).

Bound states contribute jumps to the integrated spectral shift. Care is therefore needed when comparing phases at threshold; Levinson-type constants depend on half-bound states, dimensions, and long-range tails.

6.9 Calculation laboratory IV-B: Transmission, the ABC mechanism, and the continuum

Calculation route

Prerequisites. The exact-WKB transfer matrix, resolvent boundary values, the ABC rotation of the continuum, and direct-integral spectral language.

Calculation goal. Exact-WKB transmission coefficients, the

ABC/Feshbach equivalence, and the organization of bound, continuum, and resonant sectors.

Completion criterion. Compute transmission and continuum/resonance contributions and identify the analytic statement behind the rotated ABC spectrum.

This Laboratory reconstructs the calculation underlying Ref. [17]. Its paper-level introduction and exact-WKB recapitulation are omitted: transmission starts from the canonical transfer matrix of Stage III, and the ABC comparison uses the theorem proved earlier in Stage IV.

6.9.1 Transmission via exact WKB analysis

For (pseudo-)bound states, exact WKB quantization of this kind has been well established. By contrast, in this paper we develop a general exact-WKB framework that extends to scattering states, i.e. the continuous spectrum. In earlier works [15, 16], the Voros symbols for the inverted Rosen–Morse potential were computed within the exact WKB framework, and were found to agree perfectly with the closed-form solution.[4] Here we present a methodology to analyze scattering problems for general scattering potentials by exploiting the geometric properties of the associated Stokes graphs.

Strategy to general scattering potentials

In scattering theory of a 1-dimensional system, we first assume that an incoming wave, $\mathrm{e}^{\mathrm{i}kx}$, is made incident from $x \to -\infty$. Then, the asymptotic form of the corresponding wave function ψ becomes $\psi(x \to -\infty) = \mathrm{e}^{\mathrm{i}kx} + R\mathrm{e}^{-\mathrm{i}kx}$ and $\psi(x \to \infty) = T\mathrm{e}^{\mathrm{i}kx}$, where R and T are the reflection and transmission coefficients. In general, for a 1-dimensional problem, the transmission coefficient T corresponds to the S-matrix and cross-section. In the exact WKB analysis, we also impose boundary conditions where the incident wave does not vanish to give continuum spectrum, while bound/resonant states are normalizable on an appropriate choice of analytically continuing path. Figure 6.6 shows that (i) for bound energies, say $E < 0$, there exist the Stokes curves, where $\psi^- \propto \mathrm{e}^{-\int S_{\mathrm{odd}}\mathrm{d}x}$ is dominant, at $x \to \pm\infty$; one may observe a nontrivial

[4] The techniques developed in Refs. [15, 16] can be extended in a straightforward manner, and they allow one to carry out Airy-type exact WKB computations also for general resonance potentials relevant to resonance physics.

Stokes structure, branch cut, and monodromy in the middle region, which gives rise to quantized energy spectrum based on the normalizability of wave functions. (ii) Above an energy threshold ($\mathrm{Re}\, E > 0$), the flat potential $V(x) \sim 0$ at $x \to \pm\infty$ indicates that there is no Stokes curves with index $\pm$ at $|\mathrm{Re}\, x| \to \infty$, but we see Stokes curves extending to $|\mathrm{Im}\, x| \to \infty$ and a nontrivial structure in between; Refs. [15, 16] addressed the quantized complex energies of resonance from the normalizability along these Stokes curves. (iii) Now, we expect that wave functions with monodromy applied to $\mathrm{e}^{\mathrm{i}kx}$ will become the scattered wave. The strategy to compute this scattering problem is as follows:

1. Specifically, impose $\psi(x \to \infty) = 1 \times \mathrm{e}^{\mathrm{i}kx}$.

2. This can be implemented as the boundary condition which is ψ^--dominant as $\mathrm{Im}\, x \to -\infty$ in $\mathrm{Re}\, x > 0$ (see Fig. 6.6 and discuss it as the Siegert boundary condition later).

3. By working on exact WKB framework, we obtain $\psi^{\pm}(x \to -\infty)$.

4. The coefficient for the incident wave $\mathrm{e}^{\mathrm{i}kx}$ is $1/T$, and one of the reflected wave $\mathrm{e}^{-\mathrm{i}kx}$ is R/T.

From this, we can observe the S-matrix, phase shift, and the Breit–Wigner formula straightforwardly.

Transmission coefficient in Rosen–Morse potential

For instance, let us focus on the Rosen–Morse potential, $\frac{U_0}{\cosh^2 \beta x}$ with $U_0 > 0$. The general solution of its Schrödinger equation is described by using the two linearly independent solutions as

$$\begin{aligned}
&\psi(x) \\
&= (1-\xi^2)^{-\frac{\mathrm{i}k}{2\beta}} \\
&\quad \times \left[C_1 F\left(-\frac{\mathrm{i}k}{\beta} - s, -\frac{\mathrm{i}k}{\beta} + s + 1, -\frac{\mathrm{i}k}{\beta} + 1, \frac{1-\xi}{2} \right) \right. \\
&\qquad \left. + C_2 \left(\frac{1-\xi}{2} \right)^{\frac{\mathrm{i}k}{\beta}} F\left(s+1, -s, \frac{\mathrm{i}k}{\beta} + 1, \frac{1-\xi}{2} \right) \right],
\end{aligned} \tag{6.138}$$

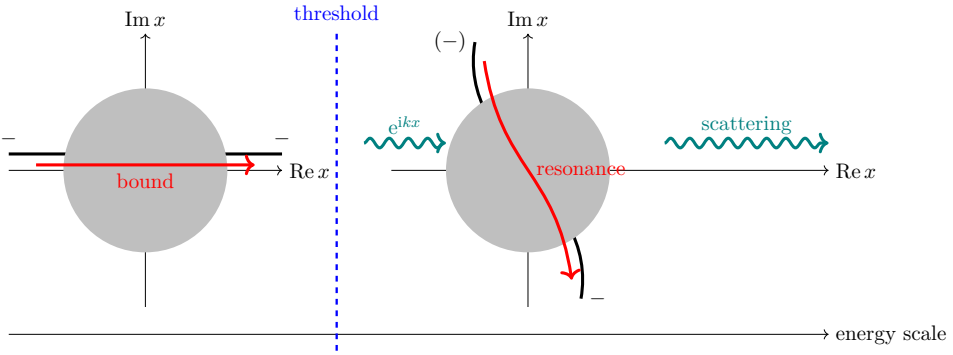

Figure 6.6: Schematic diagram of the energy scale for Stokes graphs. For energies below the threshold ($E \leq 0$), bound states are present, with the Stokes curve with index $-$ extending towards $\pm\infty$ along the red path, ensuring the normalizability of the discrete spectrum. In the gray region, the appropriate connection formula applies, and branch cuts may be needed. Beyond the threshold, where the potential becomes flat at large $\mathrm{Re}\, x$, the Stokes curve extends in the $\mathrm{Im}\, x$ direction. With the correct sheet choice and the Stokes curve with index $-$, normalizability along the red path is guaranteed, revealing resonances with a discrete but complex spectrum. The choice of path corresponds to the Siegert boundary condition, where incoming waves are prohibited. Assuming an incoming wave $\mathrm{e}^{\mathrm{i}kx}$ from $\mathrm{Re}\, x \to -\infty$, scattering states (transmitted and reflected waves) appear, corresponding to the continuum spectrum.

where F is the Gaussian hypergeometric function, $\xi = \tanh \beta x$, $k = \frac{\sqrt{2mE}}{\hbar}$, and $s = \frac{1}{2}\left(-1 + \sqrt{1 - \frac{8mU_0}{\beta^2\hbar^2}}\right)$. The first and second terms correspond to the outgoing and incoming wave, respectively, in the asymptotic region $x \to \infty$.

Airy-type local model (simple turning point). Let $Q(x;E) = V(x) - E$ and suppose x_t is a *simple* turning point, i.e.

$$Q(x_t;E) = 0, \qquad Q'(x_t;E) \neq 0. \tag{6.139}$$

Expanding Q near x_t gives

$$Q(x;E) = Q'(x_t;E)(x - x_t) + O\Big((x - x_t)^2\Big). \tag{6.140}$$

Keeping only the linear term and rescaling the coordinate reduces the Schrödinger equation locally to an Airy equation. This is the origin of the standard Airy-type connection formulas. Consequently, the Airy reduc-

tion is reliable only when the region relevant for matching is contained in a domain where the higher-order terms in Q are negligible. Now, following the above strategy, we take $C_1 = 4^{\frac{\mathrm{i}k}{2\beta}}$ and $C_2 = 0$ to impose the normalized transmitted wave; we see $\psi(x) \to \mathrm{e}^{\mathrm{i}kx}$ as $x \to \infty$. As a consequence of the Airy-type exact WKB analysis, we obtain

$$\frac{1}{T_{\mathrm{Airy}}} = \frac{1}{\sqrt{A}} - \sqrt{A}, \tag{6.141}$$

$$A = \left[\frac{F\left(-\frac{\mathrm{i}k}{\beta} - s, -\frac{\mathrm{i}k}{\beta} + s + 1, -\frac{\mathrm{i}k}{\beta} + 1, \frac{1-\tilde{\xi}}{2}\right)}{F\left(-\frac{\mathrm{i}k}{\beta} - s, -\frac{\mathrm{i}k}{\beta} + s + 1, -\frac{\mathrm{i}k}{\beta} + 1, \frac{1+\tilde{\xi}}{2}\right)} \right]^2. \tag{6.142}$$

Here $\tilde{\xi} = \tanh(\cosh^{-1}\sqrt{U_0/E})$, and the corresponding Voros symbol $\mathcal{V}_\gamma$ (called A-cycle), where a non-perturbative cycle γ encircles two turning points a_1 and a_2 and is defined as $A = \mathrm{e}^{\oint_\gamma \mathrm{d}x\, S_{\mathrm{odd}}}$, is computed in Refs. [15, 16]. The A-cycle has originally been used in the quantization condition for resonant states. Here we use it to express the Airy-type approximation to the transmission coefficient T_{Airy} and to specify the corresponding normalized scattering solution (with $C_1 = 4^{\mathrm{i}k/(2\beta)}$ and $C_2 = 0$). Note that T is divergent if E comes across resonances; so a naive analytical continuation of the wave function is ill-defined in some sense, such as completeness. A Hilbert space can be constructed by energy eigenstates with $\mathrm{Im}\, E = 0$, where the $*$-operation is well-defined and the Hamiltonian is self-adjoint; now, resonance is not a "state" but just a physical pole singularity. To include resonant states in our Hilbert space, we need to introduce CSM and show the ABC theorem.

Comparison with exact solution From the asymptotic expansion of the exact solution (6.138) near $x \to \pm\infty$, on the other hand, it is well-known [82] that the transmission coefficient is rigorously given by

$$T_{\mathrm{exact}} = \frac{\Gamma\left(-\frac{\mathrm{i}k}{\beta} - s\right)\Gamma\left(-\frac{\mathrm{i}k}{\beta} + s + 1\right)}{\Gamma\left(1 - \frac{\mathrm{i}k}{\beta}\right)\Gamma\left(-\frac{\mathrm{i}k}{\beta}\right)}. \tag{6.143}$$

The approximation by the Airy function is hindered by non-linearity around stationary points, and so works well at enough large $E > 0$ but at enough small $E < U_0$.[5] See Fig. 6.7. One may use the degenerate Weber to tackle

[5] In fact, a preliminary numerical simulation observes a slight discrepancy in the frequency of the quasi-normal mode in a black hole, while the resonant peak is completely

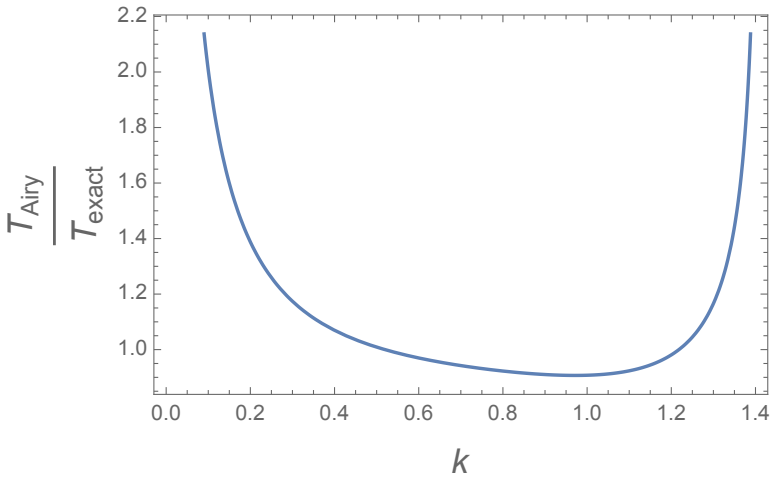

Figure 6.7: Ratio of the transmission coefficients, $|T_{\text{Airy}}|/|T_{\text{exact}}|$. Every parameter excluding E is set to unity. k and $\tilde{\xi}$ are written by E, and the k-dependence of the ratio is shown. $k = 0$ and $\sqrt{2}$ correspond to $E = 0$ and $E = U_0 = 1$, respectively.

$E \sim 0$ or U_0. In any case, it is remarkable that bound/resonant energy eigenvalues are sufficiently far from the stationary, and given by the exact WKB analysis rigorously. If the linear approximation of $Q(x; E)$ is poor (for instance, due to sizable curvature or because the effective barrier top is sampled), it is natural to replace the Airy normal form by a quadratic (parabolic) normal form. A prototypical choice is a Weber-type (parabolic-cylinder) equation, which captures the local behavior of

$$Q(x; E) \simeq a(x - x_0)^2 + b \tag{6.144}$$

and yields uniform connection data for "parabolic" turning-point configurations. In such a formulation, the local model remains accurate even when the linearized (Airy) neighborhood is too small, and one expects improved agreement with the exact solution in parameter regimes where Fig. 6.7 shows strong deviations.

Remark on cycles and matching data. Since different local normal forms (Airy, Weber, etc.) correspond to different choices of local coordinates and branch structures, the associated natural cycles (e.g. an "A-cycle" used to

reproduced [103].

define phase/connection data) need not coincide and may differ substantially except for poles. Therefore, the discrepancy in Fig. 6.7 should be interpreted as indicating that the Airy-type local model is not optimal for the chosen parameters, and that a Weber-type (or other higher-order) local treatment may be required. This improvement is conceptually independent of whether one employs a Zinn-Justin-type semiclassical expansion or a Borel-resummed (exact WKB) framework; it concerns the choice of an appropriate local normal form for $Q(x;E)$. This remains an important open problem.

6.9.2 The ABC invariants seen in exact WKB

Rotation of the Stokes data

The operator theorem and its dilation-analytic hypotheses were proved in Sec. 6.3. The present calculation does not replace that proof. It identifies its angle-independent data directly in the Stokes geometry. The resonant wave function is square-integrable on the deformed contour $\widetilde{\mathbb{R}}$ shown in Fig. 6.6; analytic pullback represents the same state in $L^2(\mathbb{R})$ after complex scaling [15, 16]. Second, from the discussion in Ref. [16], it is straightforward to show the θ-independence of bound/resonant energy spectrum because Stokes curves, any (non-)perturbative cycle and turning points are rotated simultaneously by the complex scaling, and hence the normalizability condition on Stokes curves is invariant and provides the same exact-WKB quantization. For instance, the non-perturbative cycle A is now given by

$$\begin{aligned} A &= \mathrm{e}^{\oint_{\gamma \mathrm{e}^{-\mathrm{i}\theta}} S^{\theta}_{\mathrm{odd}}} = \left[\frac{\psi_{\mathrm{CSM}}(a\mathrm{e}^{-\mathrm{i}\theta})}{\psi_{\mathrm{CSM}}(-a\mathrm{e}^{-\mathrm{i}\theta})}\right]^2 \\ &= \left[\frac{\psi(a)}{\psi(-a)}\right]^2 = \mathrm{e}^{\oint_{\gamma} S_{\mathrm{odd}}}, \end{aligned} \tag{6.145}$$

where $\psi_{\mathrm{CSM}}(x'\mathrm{e}^{-\mathrm{i}\theta}) = \psi(x')$, $\gamma\mathrm{e}^{-\mathrm{i}\theta}$ denotes the cycle between two turning points after complex rotation, and the original turning point is given with $\theta = 0$. This fact is nothing but the invariance of the energies of the bound and resonant states. Third, the above exact WKB strategy for scattering problem is also valid in CSM. Namely, when $x \to x\mathrm{e}^{\mathrm{i}\theta}$, we should take $k \to k\mathrm{e}^{-\mathrm{i}\theta}$ to maintain the transmission wave $\mathrm{e}^{\mathrm{i}kx}$ as the boundary condition. As mentioned in the case of resonance, the dominance of ψ^- at $|\operatorname{Im} x| \to \infty$ indicates a physical situation such that any incoming wave vanishes. Hence, this boundary condition requires that ψ^- is dominant as $\operatorname{Im} x \to -\infty$ in

$\mathrm{Re}\, x > 0$, while eliminating ψ^+; this can be interpreted as the physical meaning of the Siegert boundary condition.[6] Now, since $k = \frac{\sqrt{2mE}}{\hbar}$, the continuum spectrum E_{cont} is changed as $E_{\mathrm{cont}} \to E_{\mathrm{cont}} \mathrm{e}^{-2\mathrm{i}\theta}$.

Connection-geometric comparison with Feshbach elimination

We here make a remark on an equivalence with the Feshbach picture. The gray circle in Fig. 6.6 should be understood as a projection of the full scattering problem into an "interior" (gray-filled) sector and an "exterior" sector. More concretely, let P denote the degrees of freedom supported in the interior region that contains the nontrivial (resonant) Stokes graph. On the other hand, the dynamics in the exterior region, $Q = 1 - P$, is asymptotically free, and so the analytic structure is essentially trivial. In the Feshbach projection formalism, eliminating the Q-sector yields an energy-dependent effective Hamiltonian operator acting on the interior sector,

$$H_{\mathrm{eff}}(E) = PHP + PHQ \frac{1}{E - QHQ} QHP. \tag{6.146}$$

It has been known [4, 5, 9] that non-Hermiticity encodes the open boundary coupling to the environment, and complex poles of the effective resolvent of H_{eff} reproduce resonances. In the present exact WKB, the Q-elimination affects an effective boundary condition imposed at the edge of P. Choosing an outgoing (Siegert-type) condition excludes incoming components from the exterior. It thus implements precisely the same "radiation condition" that is built into $H_{\mathrm{eff}}(E)$ through the resolvent $(E - QHQ)^{-1}$ [84]. From the exact-WKB quantization condition (the normalizability at $|\mathrm{Im}\, x| \to \infty$), now the connection data across the interior Stokes graph matches the outgoing boundary condition at the edge, that is, a vanishing Jost function or a pole of the scattering amplitude. Accordingly, the exact-WKB resonant state can be viewed as a bound state along $\mathrm{Im}\, x$, and as the counterpart of the Feshbach-pole condition (openness along $\mathrm{Re}\, x$ and a pole of $(E - H_{\mathrm{eff}}(E))^{-1}$). We would like to clarify what we mean by the P/Q "cut" and its relation to the Feshbach picture. To avoid possible confusion, we spell out the viewpoint and the logical order of definitions.

- **Guiding idea (assumption).** We adopt the standard standpoint

[6] Here we are concerned solely with the physical interpretation of the Siegert boundary condition. Normally, this condition corresponds to eliminating ψ^+ for $\mathrm{Re}\, x < 0$. However, this is equivalent to requiring that ψ^- be dominant, as in the case of $\mathrm{Re}\, x > 0$.

that the *full* system $(P + Q)$ is governed by a Hermitian operator, while a *subsystem* becomes effectively non-Hermitian once the environmental/continuum sector is eliminated, i.e. openness is encoded in an energy-dependent effective description.

- ***A posteriori* Hilbert space in exact WKB.** In the exact WKB approach, the primary data are analytic solutions on the complexified coordinate plane and their Stokes geometry. A Hilbert-space structure (and hence "normalizability") is typically not assumed from the outset, but rather introduced *a posteriori* through a complex deformation (via the ABC/complex-scaling viewpoint) and the resulting decay/normalizability requirement.

- **Definition of the Q sector.** We define Q as the exterior region which is expected, from the Stokes-graph viewpoint, to carry no additional nontrivial connection data (in this sense its analytic structure is essentially trivial), and set $P = 1 - Q$. Equivalently, P is the region containing the nontrivial (resonant) Stokes graph. This P/Q decomposition should be regarded as a *partition of the complex x-plane* rather than an *a priori* Hilbert-space decomposition.

- **Remark (not yet exact WKB).** In the usual Feshbach projection formalism, after eliminating Q resonances correspond to complex poles of the effective resolvent $(E - H_{\text{eff}}(E))^{-1}$.

- **Proposition.** Imposing an outgoing (Siegert-type) condition at the P/Q boundary is equivalent to describing an open system with *no influx from Q into P* and *only outflux from P into Q*.

- **Remark.** It is known that the resonance spectrum selected by the Siegert boundary condition coincides with that obtained from the radiative/open effective Hamiltonian $H_{\text{eff}}(E)$.

- **Statement (exact WKB language).** The "matching" of exact WKB solutions in P and in Q across the boundary means the following: an exact-WKB solution in P that is normalizable as $|\operatorname{Im} x| \to \infty$ can be smoothly connected at the P/Q boundary to the (almost analytically trivial) outgoing solution in Q along the physical direction $\operatorname{Re} x$. Geometrically, this is precisely the condition that the interior Stokes connection data be compatible with the exterior outgoing condition, i.e., the exact-WKB characterization of resonances.

In particular, the exact WKB approach allows us to characterize all these states in terms of global analytic structures of the wave function, such as Stokes graphs and connection formulas. From this viewpoint, the Siegert boundary condition can be reinterpreted as the Stokes curve emanating from $|\operatorname{Im} x| \to \infty$. In the Feshbach formalism it can be understood as a consequence of analytic continuation in the complex plane (no Stokes curve along $\operatorname{Re} x$ axis), rather than as an external imposition. The conflict between the directions of Stokes curves connected with infinity and the real axis implies that the notion of an "outgoing wave" along the real coordinate becomes nontrivial and must be defined via analytic continuation along appropriate Stokes sectors. This is closely related to the emergence of resonant (Siegert) states and their interpretation within the Feshbach formalism, where one effectively projects onto subspaces associated with different asymptotic behaviors. In this sense, Fig. 6.6 provides a geometric realization of the resonance mechanism in the Feshbach formalism: interior (quasi-)bound structures defined by the resonant Stokes graph acquire decay widths through their coupling to the exterior continuum.

6.9.3 Continuum and resonant spectra in Hilbert space

In the previous section, our aim is to *physically interpret* the Aguilar–Balslev–Combes (ABC) theorem using the exact WKB framework, then establishing a completeness statement plays a central role for three reasons.

- **Correct extraction of resonance.** Exact WKB naturally produces local solutions and their connection data (via Stokes graphs). However, the ABC picture is a *global spectral statement*. A completeness relation makes this precise by stating that the identity (or the resolvent matrix elements) can be represented by (rotated continuum) + (sum over resonant poles) + (bound states). The "extraction" of resonance contributions is an actual reorganization of the spectral representation.

- **Consistent Hilbert-space setting.** Resonant states are not L^2 on the real axis, so they do not enter the standard Hilbert-space completeness for the self-adjoint H. In contrast, after complex scaling they may become L^2 eigenstates of the non-self-adjoint H_θ. A completeness statement clarifies *in which sense* resonant states are part of the spectral decomposition: typically via a biorthogonal resolution of the identity for H_θ or, equivalently, via contour deformation and residues for resolvent

matrix elements. Without this, the claim "resonances appear in the spectrum" risks being interpreted incorrectly as a literal Hilbert-space basis statement for the original H.

- **Physical observables.** Exact WKB yields scattering data and resonance conditions through Stokes phenomena (connection matrices, Voros symbols). To relate these quantities to physical observables (e.g. cross sections, spectral functions, time evolution), one needs a representation of the Green function or evolution kernel in which the contributions of continuum and resonance sectors are clearly separated and controlled. Completeness provides exactly that bridge: The residues and pole locations are the resonance data that exact WKB computes. This makes precise why the Stokes-graph geometry (WKB side) reproduces the ABC spectral separation (CSM side).

In an exact-WKB-based interpretation of ABC, "showing completeness" is meaningful because it is the statement that the WKB-derived resonance poles and connection coefficients are not just diagnostic features, but *enter the actual spectral representation* (resolvent or identity) together with the rotated continuum. It is the step that upgrades a physical picture ("continuum vs. resonances") into a mathematically and physically controlled decomposition.

It should be emphasized that, according to the picture we have presented, all wave functions—bound, scattering, and resonant—can be derived within the framework of the exact WKB method. Therefore, the notion of completeness referred to here is not that of the conventional scattering theory of the Schrödinger equation; rather, completeness must be formulated entirely in terms of wave functions derived via the exact WKB method. Establishing such a completeness is essential for completing the overall structure of exact WKB scattering theory. We introduce the standard Green function satisfying

$$HG(k;x,x') = -\delta(x-x'), \tag{6.147}$$

with a Hamiltonian operator H. One may write it as the resolvent,

$$G(k;x,x') = \int \mathrm{d}\rho(E') \frac{\psi(x)\psi(x')^*}{E-E'}, \tag{6.148}$$

where $\psi(x)$ is a generic wave function, which collectively denotes the bound and scattering states, before normalization and we should be careful of the branch cut to obtain the outgoing/incoming Green function, and have

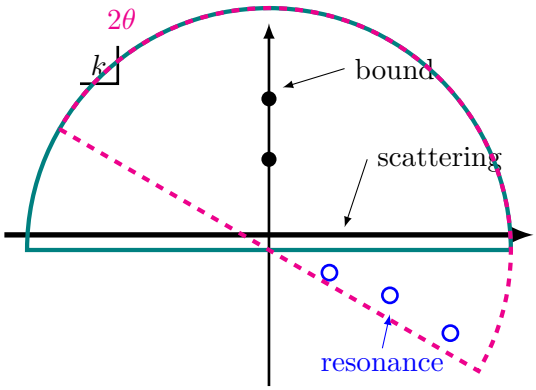

Figure 6.8: Integration contour in the complex k-plane of the Green function. The green contour indicates the original integration to prove the completeness (6.150). We find that in $\mathrm{Im}\, k < 0$ there exist resonant poles additionally. An integration along the magenta contour rotated by 2θ via CSM concludes these residues as a physical state depending on θ.

introduced the spectral function

$$\frac{\mathrm{d}\rho(E)}{\mathrm{d}E} \propto \begin{cases} \sum_n \frac{1}{(\mathcal{N}_n^B)^2}\delta(E - E_n^B) & E \leq 0, \\ \frac{1}{|\mathcal{F}_k|^2} \times (\text{const.}) & E > 0, \end{cases} \tag{6.149}$$

the bound energies E_n^B ($n \in \mathbb{Z}_+$), the normalization factor of the bound states $\mathcal{N}^B = (\int |\psi(x)|^2 \mathrm{d}x)^{1/2}$ for bound states $\psi(x)$, and the coefficient of waves in the continuum spectrum $\mathcal{F}_k$, that is, the Jost functions. From the self-consistency condition of an integral of the Green function given in Ref. [42], where we take into account the integration on the upper half k-plane surrounded by the solid line in Fig. 6.8, the completeness of the wave functions is proved as

$$\sum_n \psi_n^B(x)\psi_n^B(x')^* + \int \mathrm{d}k\, \psi(k,x)\psi(k,x')^* = \delta(x - x'). \tag{6.150}$$

Here, $\psi^B(x)$ implies a normalized bound state, and $\psi(k,x)$ is a normalized scattering one. If there exist resonances, the resolvent has pole singularities after an analytic continuation of k to $\mathrm{Im}\, k < 0$. In what follows, we consider the complete set of eigenstates in CSM QM. First of all, we notice that the Green function (6.148) is quite subtle at a resonant pole since its residue,

i.e., the spectral function, diverges due to $\mathcal{F}_k = 0$. In a mathematical context, the spectral function for the continuum spectrum is defined in a band around $\operatorname{Im} E = 0$ such that $\mathcal{F}_k \neq 0$. Nevertheless, under CSM, resonant states are also elements of the corresponding spectral representation. (Also, there are subtleties for the definition of the $*$-operation in Eq. (6.148).[7]) Note that $\psi(x)^\theta = U_\theta \psi(x)$ for a general wave function before normalization. Let $\psi^B(x)^\theta$ denote a normalized complex-scaled bound state, $\psi(k,x)^\theta$ is a normalized complex-scaled scattering one, and $\psi^R(x)^\theta$ imply a normalized resonant state. We shall define the CSM Green function

$$G_\theta(k;x,x') = \int d\rho_\theta(E') \frac{\psi(x)^\theta \psi(x')^\theta}{E - E'}, \tag{6.151}$$

and the CSM spectral function

$$\frac{\mathrm{d}\rho_\theta(E)}{\mathrm{d}E} \propto \begin{cases} \sum_n \frac{1}{(\mathcal{N}_n^B)^2} \delta(E - E_n^B) & E \leq 0 \quad \text{(bound)}, \\ \frac{1}{|\mathcal{F}_k|^2} f_\theta(E) & \arg E = -2\theta \quad \text{(rotated continuum)}, \\ \sum_m \frac{1}{(\mathcal{N}_m^R)^2} \delta(E - E_m^R)[1 - f_\theta(E)] & \operatorname{Im} E < 0 \quad \text{(resonant)}, \end{cases} \tag{6.152}$$

where $\mathcal{N}^R$ is the normalization factor of resonant states in exact WKB analysis, and E_m^R denotes the resonance energies. For each resonance energy E_m^R, we define the critical scaling angle by

$$\theta_R^m = \frac{1}{2} \arctan\left(-\frac{\operatorname{Im} E_m^R}{\operatorname{Re} E_m^R} \right). \tag{6.153}$$

Here θ_R^m is the value of θ at which the rotated continuum line $\arg E = -2\theta$ passes through the resonance energy E_m^R. For a fixed scaling angle θ, the

[7] The original (unscaled) Hamiltonian is self-adjoint on an appropriate domain, ensuring a real spectrum and a well-defined Banach-space-valued resolvent. CSM and the ABC theorem guarantee that, after analytic dilation, the rotated Hamiltonian remains a closed, sectorial operator with resonances and a well-behaved resolvent [92]. Although self-adjointness is lost after complex scaling, the operator remains diagonalizable and retains a modified form of elliptic regularity [32]. In genuinely non-Hermitian systems where such analytic control is absent, one must explicitly assume or prove diagonalizability and the existence of Riesz projectors [91, 93], since no elliptic regularity is automatically guaranteed.

resonant contribution is summed over all m such that

$$\theta_R^m < \theta. \tag{6.154}$$

Equivalently, if the critical angles are ordered as

$$\theta_1^R < \theta_2^R < \cdots, \tag{6.155}$$

then the resonant states included in the spectral decomposition are precisely those with $m = 1, \ldots, M(\theta)$, where $M(\theta)$ is determined by

$$\theta_{M(\theta)}^R < \theta < \theta_{M(\theta)+1}^R. \tag{6.156}$$

The borderline case $\theta = \theta_m^R$ requires separate care, since the resonance energy lies on the rotated continuum line. $f_\theta(E)$ denotes a θ-dependent support function on the spectrum. It equals 1 on the rotated continuum part that remains in the continuum representation, and vanishes at those resonance energies E_m^R for which $\theta_R^m < \theta$, i.e. for resonances that have already been isolated from the continuum and are counted separately in the discrete resonant sum. The integration is carried out along the dashed line in Fig. 6.8. In this case, the ill-definedness (divergences due to $\mathcal{F}_k = 0$) of the spectral function is remedied because of the support function $f_\theta(E)$[8], and near $\theta \gtrsim \theta_R$ the scattering $\psi(k,x)^\theta$ is reorganized by the corresponding resonant state $\psi^R(x)^\theta$ in the sense of spectral decomposition, both of which have an identical energy eigenvalue. Again, one may say that the divergence of the scattering state originates from the divergent coefficient of the incoming wave, and its appropriately normalized state is resonant with the Siegert boundary condition. When θ crosses θ_R^m, the rotated continuum itself does not disappear; rather, only the corresponding resonance energy E_m^R is extracted from the continuum contribution and is thereafter counted in the discrete resonant part. Thus, for $\theta > \theta_R^m$, the corresponding resonance is incorporated into the discrete resonant part of the spectral decomposition, while the rotated continuum contribution is modified accordingly. Finally, after defining our CSM spectral function, the completely identical approach to the self-consistency condition of integration of the Green function in Ref. [42] is valid;

[8]We assume that $f_\theta(E)$ is a smooth cutoff function. If no support function, the case that $\theta = \theta_R$ becomes an exceptional point; not only the energy eigenvalues but also the energy eigenvectors are degenerate (or defective/Jordan-blocking). Hence, the calculation requires the utmost caution. In the more recent work [20], we have developed non-Hermitian physics of exceptional point for resonant and continuum spectra under CSM.

similar calculations leads to our central result

$$\sum_n \psi_n^B(x)^\theta \psi_n^B(x')^\theta + \int_{\arg E=-2\theta} \mathrm{d}k\, \psi(k,x)^\theta \psi(k,x')^\theta + \sum_{m\,:\,\theta_R^m<\theta} \psi_m^R(x)^\theta \psi_m^R(x')^\theta = \delta(x-x'). \tag{6.157}$$

Here, all bound, scattering, and resonant wave functions are exact WKB-derived. The sum over m is taken over all resonances satisfying $\theta_R^m < \theta$, namely $m = 1, \ldots, M(\theta)$ in the above ordering. Note that the summation over m depends on θ, that is, whether the integral contour rotated by 2θ includes the poles or not (see Fig. 6.8).

Laboratory checkpoint

Before moving to the next stage, perform the following checks without copying the displayed final answer.

1. Extract the transmission denominator from the exact-WKB transfer matrix and locate its pole on the declared sheet.

2. Track a sample continuum eigenvalue and a resonance while changing the complex-scaling angle; only the former should follow the ray.

3. Reconstruct the continuum level density from the resolvent trace and separate one pole contribution from the nonresonant background.

6.10 Problems for Stage IV

IV.1 For a rank-one P space, evaluate the Feshbach self-energy for a flat continuum with a finite threshold. Separate its principal-value shift and imaginary width.

IV.2 Derive the action of a real dilation on x, p, and the kinetic energy. Analytically continue the parameter and obtain Eq. (6.14).

IV.3 For an outgoing wave $\mathrm{e}^{\mathrm{i}kr}$ with $\operatorname{Im} k < 0$, derive the range of scaling angles for which it becomes square integrable. Translate the result to the location of the rotated energy cut.

IV.4 Prove the free essential-spectrum rotation directly in momentum space. Then use relative compactness to explain the corresponding step in the ABC theorem.

IV.5 Carry out Berggren's Gaussian regularization for $u(r) \sim \mathrm{e}^{\mathrm{i}kr}$. Evaluate the integral first where it converges and then analytically continue to the resonance quadrant.

IV.6 Choose a Schwartz test space and show how a Gamow functional acts on it after contour deformation. Identify which continuity estimate would fail on the full Hilbert norm topology.

IV.7 Derive the continuum level density from the trace of a resolvent difference. Show how its integral is related to a scattering phase under trace-class hypotheses.

IV.8 Diagonalize a complex-scaled finite basis at three values of θ. Give an algorithm that classifies bound states, stable resonances, and rotated-continuum pseudostates without using their colors in a plot.

IV.9 For a complex-symmetric matrix, derive the c product and compare it with ordinary biorthogonality. Give an example in which using Hermitian conjugation produces the wrong pole residue.

IV.10 Explain, with a contour diagram, why Zel'dovich damping, complex rotation, and a rigged-space pairing can agree on a resonance norm even though none is an ordinary $L^2(\mathbb{R})$ norm.

IV.11 For $D(z) = z - E_d - \Sigma(z)$, expand about a simple complex zero and derive $Z_{\mathrm{R}} = [1 - \Sigma'(z_{\mathrm{R}})]^{-1}$. Give an example showing that Z_{R} need not be real or lie in $[0, 1]$.

IV.12 Starting from the unitary pole factor Eq. (6.121), derive the Lorentzian phase derivative and the peak time delay in Eq. (6.125).

IV.13 Add a constant coherent background to a simple pole and derive the Fano form. Determine the energy of the maximum and zero for real q, and show how an imaginary part of q fills the zero.

IV.14 Let a channel width obey $\Gamma_l(E) = \gamma k^{2l+1}$. Compare the complex pole, the maximum of $|D(E)|^{-2}$, and the half-maximum width as the pole approaches threshold.

Part III

Radial motion and weakly bound nuclei

Chapter 7

Stage V: Add a singular endpoint and renormalize monodromy

Reader contract

The origin of a radial equation carries Frobenius data and cannot be treated as an ordinary turning point. This stage derives the Langer correction and open-path quantization, then turns regulator independence of the global monodromy into a practical renormalization condition.

7.1 Radial exact WKB: add the origin as monodromy data

Calculation route

Prerequisites. The global connection algorithm of Stage I and the local Frobenius theory of a regular singular point.

Calculation goal. Include the origin index and Langer contribution in open-path and closed-cycle exact quantization conditions.

Completion criterion. Recover oscillator and Coulomb spectra before introducing a monodromy-preserving deformation or optimization.

7.1.1 Radial equation and the origin

For a central potential $V(r)$ in three dimensions, write the wave function as $u_l(r)Y_{lm}(\Omega)/r$. The reduced radial function obeys

$$\left[-\frac{\hbar^2}{2m}\frac{\mathrm{d}^2}{\mathrm{d}r^2}+V(r)+\frac{\hbar^2 l(l+1)}{2mr^2}\right]u_l(r)=Eu_l(r), \qquad r>0. \tag{7.1}$$

Here $l \in \mathbb{N} \cup \{0\}$ is the orbital angular momentum. The origin is a regular singular point. Its Frobenius solutions behave as

$$u_l^{\mathrm{reg}}(r) \sim r^{l+1}, \qquad u_l^{\mathrm{sing}}(r) \sim r^{-l}. \tag{7.2}$$

Physical regularity selects the first solution.

The centrifugal term is proportional to $\hbar^2$, but it cannot be treated as an innocuous high-order perturbation near $r = 0$. It determines the local indices and hence the monodromy. The Langer organization replaces

$$l(l+1) \longrightarrow \left(l + \frac{1}{2}\right)^2 \tag{7.3}$$

inside the leading WKB momentum [104]. The additional $1/4$ is the contribution of the WKB half-density near the regular singularity.

7.1.2 Open-path and closed-cycle quantization

There are two natural formulations. In the open-path formulation, transport a decaying solution from infinity to the origin and require the coefficient of u_l^{sing} to vanish. In the closed-cycle formulation, continue the same solution around a contour that encloses the origin and relevant turning points, then demand a compatible monodromy. The two conditions are equivalent when all connection matrices and the local origin monodromy are included [25, 105–107].

The equivalence can be stated schematically as

$$C_{\mathrm{sing}}(E, \hbar) = 0 \quad \Longleftrightarrow \quad \det\left[M_\Gamma(E, \hbar) - \mathbf{1}\right] = 0, \tag{7.4}$$

where C_{sing} is the open-path coefficient of the singular Frobenius solution and M_Γ is the ordered monodromy matrix around a closed contour Γ. The determinant notation is schematic because a specific quantization condition may select one eigenvalue or one matrix element rather than the full determinant. What is invariant is the vanishing of the undesired component.

The change of variables

$$r = \mathrm{e}^x, \qquad x \in (-\infty, \infty), \tag{7.5}$$

makes the equivalence intuitive. The punctured origin becomes the boundary $x \to -\infty$. A small-circle monodromy in the r plane becomes a boundary

condition at the left end of the x line, while $r \to \infty$ becomes $x \to +\infty$. The radial spectral problem is thereby converted into a two-ended connection problem.

7.1.3 Harmonic-oscillator benchmark

For

$$V(r) = \frac{1}{2} m\Omega^2 r^2, \qquad \Omega > 0, \tag{7.6}$$

the exact spectrum is

$$E_{n_r l} = \hbar\Omega \left(2n_r + l + \frac{3}{2}\right), \qquad n_r = 0, 1, 2, \ldots. \tag{7.7}$$

A connection using only the two ordinary turning points misses the l dependence. Adding the origin monodromy, or equivalently using the Langer momentum from the start, restores the exact result. This is a clean example of an order-$\hbar^2$ term carrying order-one topological data.

7.1.4 Coulomb benchmark

For an attractive Coulomb potential

$$V(r) = -\frac{g}{r}, \qquad g > 0, \tag{7.8}$$

the bound-state spectrum is

$$E_{n_r l} = -\frac{mg^2}{2\hbar^2 (n_r + l + 1)^2}. \tag{7.9}$$

Again the origin contribution supplies the $l + 1/2$ phase, while the ordinary turning point supplies the remaining Maslov half-unit. The total principal quantum number is $n = n_r + l + 1$. Exact evaluation of the closed Voros period shows that the open and closed quantization paths agree once the regular singularity is treated consistently [25].

7.1.5 Monodromy renormalization

Local WKB integrals around a singular point can contain regulator-dependent pieces. Introduce a small radius $\mu > 0$ and a circle $C_0(\mu)$ around the origin.

A useful coupling that keeps the origin index at leading order is

$$\lambda = \hbar\left(l + \frac{1}{2}\right). \tag{7.10}$$

After the WKB half-density is included, fix the physical small-circle phase to

$$\mathcal{M}_0^{\mathrm{phys}} = \mathrm{e}^{\mathrm{i}\pi(2l+1)}. \tag{7.11}$$

Define a counter-Voros factor $Z_{\mathrm{mon}}(\mu)$ by

$$\mathcal{M}_0^{\mathrm{phys}} = \frac{\mathcal{M}_0^{\mathrm{bare}}(\mu)}{Z_{\mathrm{mon}}(\mu)}. \tag{7.12}$$

Cutoff independence is summarized by an RG-type equation

$$\mu\frac{\mathrm{d}}{\mathrm{d}\mu}\log Z_{\mathrm{mon}}(\mu) = \gamma_{\mathrm{mon}}(E, \hbar, \lambda). \tag{7.13}$$

The function γ_{mon} is a monodromy anomalous dimension. A closed period may then be split into large and small circles with local counterterms chosen so that the sum is finite and independent of μ.

Equations (7.12) and (7.13) should be read with care. They organize regulator independence of connection data; they are not automatically a Wilsonian coarse graining of spatial degrees of freedom. For the harmonic oscillator and Coulomb benchmarks, the proposed scheme has $\gamma_{\mathrm{mon}} = 0$, corresponding to fixed monodromy data and the termination of higher closed-period corrections in the chosen organization [25]. For a generic potential, establishing the existence, scheme dependence, and physical content of a nonzero γ_{mon} remains an open mathematical problem.

7.1.6 Optimized perturbation around monodromy-preserving seeds

For a non-solvable radial potential, choose a solvable seed $Q^{(0)}$ that has the same local monodromy and introduce an interpolation parameter δ:

$$Q_\delta(r, E) = Q^{(0)}(r, E; \boldsymbol{a}) + \delta\left[Q(r, E) - Q^{(0)}(r, E; \boldsymbol{a})\right]. \tag{7.14}$$

The vector $\boldsymbol{a}$ contains variational scales. Expand the Borel-resummed Voros data in δ, set $\delta = 1$, and choose $\boldsymbol{a}$ by minimal sensitivity or fastest apparent convergence. Because the seed already contains the correct origin index, the

expansion does not repeatedly rebuild the most singular local information. This is an exact-WKB version of optimized or variational perturbation theory [108–112].

The method is promising for Cornell, screened Coulomb, and other radial potentials, but three checks are indispensable: independence of the auxiliary parameter at increasing order, compatibility with lateral Borel summation, and preservation of the physical origin boundary condition. Variational stationarity alone does not prove that a selected branch is the physical resurgent continuation.

7.2 Derive the exponential map and the Langer term

Set $r = \mathrm{e}^x$ and write

$$u_l(r) = \mathrm{e}^{x/2}\phi_l(x). \tag{7.15}$$

Using

$$\frac{\mathrm{d}^2 u_l}{\mathrm{d}r^2} = \mathrm{e}^{-3x/2}\left(\frac{\mathrm{d}^2\phi_l}{\mathrm{d}x^2} - \frac{1}{4}\phi_l\right), \tag{7.16}$$

the radial equation becomes

$$\left[-\frac{\hbar^2}{2m}\frac{\mathrm{d}^2}{\mathrm{d}x^2} + \mathrm{e}^{2x}\left(V(\mathrm{e}^x) - E\right) + \frac{\hbar^2}{2m}\left(l + \frac{1}{2}\right)^2\right]\phi_l(x) = 0. \tag{7.17}$$

The $1/4$ shift is exact; it comes from removing the first derivative generated by the coordinate change. The origin condition has become a convergence condition at $x \to -\infty$. Equation (7.17) therefore gives both an algebraic derivation of the Langer term and a geometric derivation of the open-path/closed-cycle equivalence.

7.3 Calculation laboratory V: Radial monodromy from oscillator to Coulomb

Calculation route

Prerequisites. Exact WKB on a regular contour, Frobenius indices at the origin, closed-cycle periods, and the Langer transformation.

Calculation goal. The radial Riccati problem, oscillator and Coulomb benchmarks, the exponential map, optimized perturbation theory, anharmonic and Cornell/Yukawa examples, and the open-path/closed-cycle theorem.

Completion criterion. Derive radial quantization from both open paths and closed cycles, then reproduce the oscillator, Coulomb, Cornell, and Yukawa checks.

This Laboratory reconstructs the calculation underlying Ref. [25]. The regular-contour exact-WKB recursion is not repeated. The starting point is the new datum introduced by a radial problem: the singular endpoint and its monodromy.

7.3.1 Benchmark I: the three-dimensional oscillator

All local Stokes matrices below are those of Sec. 5.1; only the origin monodromy and the radial path are new. Here we notice the following Theorem:

Theorem 7.1. *If we go across the Stokes curve starting from a turning point, M is represented as*

$$M_+^\bullet = \begin{pmatrix} 1 & i \\ 0 & 1 \end{pmatrix}, \qquad M_-^\bullet = \begin{pmatrix} 1 & 0 \\ i & 1 \end{pmatrix}. \tag{7.18}$$

On the other hand, if we go across one from a simple pole, M is written as

$$M_+^\circ = \begin{pmatrix} 1 & 2i\cos(\pi\sqrt{1+4Q_2}) \\ 0 & 1 \end{pmatrix} = \begin{pmatrix} 1 & 2i\cos(\pi\sqrt{1+4l(l+1)}) \\ 0 & 1 \end{pmatrix}, \tag{7.19}$$

$$M_-^\circ = \begin{pmatrix} 1 & 0 \\ 2i\cos(\pi\sqrt{1+4Q_2}) & 1 \end{pmatrix} = \begin{pmatrix} 1 & 0 \\ 2i\cos(\pi\sqrt{1+4l(l+1)}) & 1 \end{pmatrix}. \tag{7.20}$$

Here, $\sqrt{1+4Q_2}$ is the characteristic exponent of $Q(r)$.

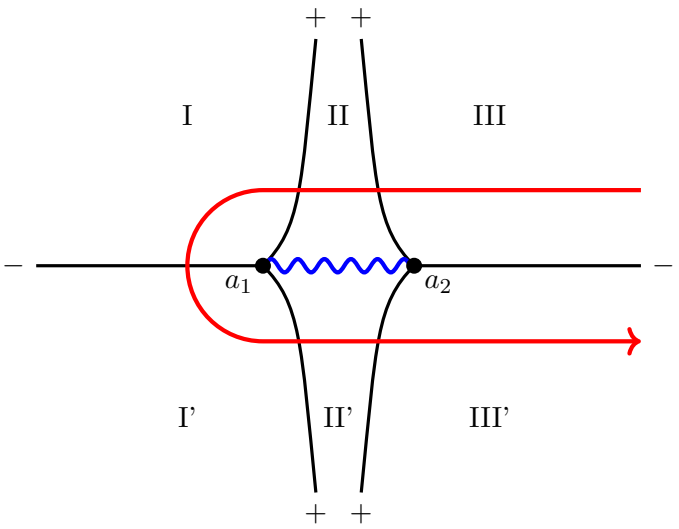

Figure 7.1: Stokes graph for the 3D harmonic oscillator. $\mathrm{Re}\, E > 0$. The black solid curves are the Stokes curves, and the black points are the turning points connecting three Stokes curves. The blue wavy line is a branch cut. The red arrowed curve is a possible physical path on which the wave function is defined. That is, this path means the normalizable wave function, which should be supposed to be subdominant along $r \to \infty \pm \mathrm{i}\epsilon$ with small $\epsilon > 0$.

7.3.2 Harmonic oscillator

Stokes graph for the harmonic oscillator and the choice of path

We begin with the 3D harmonic oscillator,

$$V(r) = \frac{1}{2} r^2. \tag{7.21}$$

Figure 7.1 shows the corresponding Stokes graph with $\mathrm{Re}\, E > 0$. The solid curves are the Stokes curves starting from the turning points depicted as the black points (bullets),

$$a_1 = -\sqrt{2E}, \qquad a_2 = \sqrt{2E}. \tag{7.22}$$

The sign $\pm$ indicates the index of the superscript of the dominant wave function $\varphi_l^{\pm}$. Each region is marked by I, II, or III (with prime). We should first notice that a nontrivial bound-state problem arises from the integration between the two turning points, while the closed loop including the turning

point is the perturbative cycle to trap physical states at the bottom of the potential barrier. Hence, at least, any physical path must encircle these turning points, and so the energy quantization occurs as the physical intuition. Now, one plausible choice of the path is given by the red curve in Fig. 7.1. This path starts from $r \to +\infty + \mathrm{i}\epsilon$, bulges into the $\mathrm{Re}\, r < a_1$ side in the complex plane, encircles a_1 and a_2, and goes to $r \to +\infty - \mathrm{i}\epsilon$ ($\epsilon > 0$). This is a kind of closed path. Around the two asymptotic regions $r \to +\infty \pm \mathrm{i}\epsilon$ (region III and region III'), we are supposed to impose the consistency of the (sub)dominance in the wave function; we can exhibit the closed-cycle quantization condition itself.

Derivation of the quantization condition for the harmonic oscillator

Naively speaking, beginning from the region III, that is, $(\varphi_l^+, \varphi_l^-)_{\mathrm{III}}$, one may find

$$\begin{pmatrix} \varphi_l^+ \\ \varphi_l^- \end{pmatrix}_{\mathrm{II}} = M_+^\bullet \begin{pmatrix} \varphi_l^+ \\ \varphi_l^- \end{pmatrix}_{\mathrm{III}} \tag{7.23}$$

$$\begin{pmatrix} \varphi_l^+ \\ \varphi_l^- \end{pmatrix}_{\mathrm{I}} \sim M_+^\bullet N_{a_1 a_2} M_+^\bullet \begin{pmatrix} \varphi_l^+ \\ \varphi_l^- \end{pmatrix}_{\mathrm{III}} \tag{7.24}$$

$$\begin{pmatrix} \varphi_l^+ \\ \varphi_l^- \end{pmatrix}_{\mathrm{I'}} \sim M_-^\bullet M_+^\bullet N_{a_1 a_2} M_+^\bullet \begin{pmatrix} \varphi_l^+ \\ \varphi_l^- \end{pmatrix}_{\mathrm{III}} \tag{7.25}$$

$$\begin{pmatrix} \varphi_l^+ \\ \varphi_l^- \end{pmatrix}_{\mathrm{II'}} \sim M_+^\bullet M_-^\bullet M_+^\bullet N_{a_1 a_2} M_+^\bullet \begin{pmatrix} \varphi_l^+ \\ \varphi_l^- \end{pmatrix}_{\mathrm{III}} \tag{7.26}$$

$$\begin{pmatrix} \varphi_l^+ \\ \varphi_l^- \end{pmatrix}_{\mathrm{III'}} \sim M_+^\bullet N_{a_2 a_1} M_+^\bullet M_-^\bullet M_+^\bullet N_{a_1 a_2} M_+^\bullet \begin{pmatrix} \varphi_l^+ \\ \varphi_l^- \end{pmatrix}_{\mathrm{III}} . \tag{7.27}$$

This is, however, not correct because of the regular singularity from the double pole of exact WKB. The eigenenergies obtained from the monodromy matrix in Eq. (7.27) do not have an angular-momentum dependence. We must need to estimate the closed-loop integral around $r = 0$ in an appropriate way! We shall focus on region II as in Fig. 7.2. The connection between the turning points depends on the closed-loop integration around the origin; this provides a nontrivial phase, that is, the angular-momentum phase or monodromy phase from the regular singularity. The actual path is now taken as the red curve encircling the origin as shown in Fig. 7.2. Therefore, after explicit calculations of the contour integral, the naive connection, $N_{a_1 a_2}$,

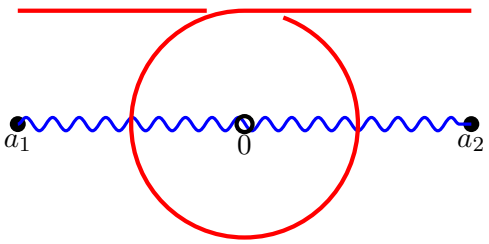

Figure 7.2: The Stokes graph with the regular singularity near the origin. The white circle is the origin and the regular singularity. The naive connection, $N_{a_1a_2}$, misses this nontrivial monodromy phase. We should improve it by adding the closed-loop integral around $r = 0$.

would be replaced by

$$\tilde{N}_{a_1a_2} = N_{a_10} M_+^{\circ} N_{0a_2}. \tag{7.28}$$

We obtain

$$\begin{pmatrix} \varphi_l^+ \\ \varphi_l^- \end{pmatrix}_{\mathrm{III}'} = M_+^{\bullet} \tilde{N}_{a_2a_1} M_+^{\bullet} M_-^{\bullet} M_+^{\bullet} \tilde{N}_{a_1a_2} M_+^{\bullet} \begin{pmatrix} \varphi_l^+ \\ \varphi_l^- \end{pmatrix}_{\mathrm{III}}, \tag{7.29}$$

and then, the coefficient of $(\varphi_l^-)_{\mathrm{III}}$ in $(\varphi_l^+)_{\mathrm{III}'}$ is given by

$$-2\mathrm{i}\cos(\pi\sqrt{1+4Q_2}) \left[\frac{1}{A} + A + 2\cos(\pi\sqrt{1+4Q_2})\right], \tag{7.30}$$

where

$$A = \mathrm{e}^{\oint_0^{a_2} \mathrm{d}r\, S_{\mathrm{odd}}}. \tag{7.31}$$

To be consistent, the above coefficient should vanish, and so the quantization condition is written as

$$\cosh\left(\oint_0^{a_2} \mathrm{d}r\, S_{\mathrm{odd}}\right) + \cos(\pi\sqrt{1+4Q_2}) = 0. \tag{7.32}$$

Note that $\sqrt{1+4Q_2} = \sqrt{1+4l(l+1)} = 2l+1$, as usual the higher order corrections do not affect the residue, and we should be careful of the singular

region $|r| < \epsilon$ with $0 < \epsilon = O(\hbar)$.[1] To make the origin behavior compatible with the global exact-WKB construction, we start from the Frobenius solution $u(r) \sim r^{l+1}$ and define the WKB transport from $r = \epsilon > 0$ along a lateral Borel direction that avoids Stokes curves. The global propagation is then obtained by multiplying the connection matrices at each Stokes crossing, and finally taking the limit $\epsilon \to 0$. Since the radial equation has a regular singular point at $r = 0$ due to the centrifugal term, the contour integral $\hbar^{-1} \oint \mathrm{d}r\, S_{-1}(r)$ must be defined with care: the term $\hbar^2 l(l+1)/r^2$ becomes $O(1)$ precisely in the singular region $|r| \lesssim \hbar$. Following Proposition A.1 of Ref. [113], we therefore excise a small disk $|r| < \epsilon$ with $0 < \epsilon = O(\hbar)$ and evaluate the integral on the punctured domain. More concretely, the original leading WKB solution is given by

$$S_{-1}(r) = \sqrt{r^2 - 2E}, \tag{7.34}$$

but we deform the contour to the boundaries of the punctured domain, namely a large circle at infinity and a small circle $|r| = \epsilon$, and then the centrifugal term can contribute even in the leading as follows:

$$S_{-1}(r) \Rightarrow \sqrt{r^2 - 2E + \underbrace{\hbar^2 \frac{l(l+1)}{r^2}}_{O(1) \text{ if } |r| \to \epsilon}}\,. \tag{7.35}$$

This yields

$$\hbar^{-1} \oint_0^{\sqrt{2E}} \mathrm{d}r\, S_{-1} \Rightarrow \frac{1}{2\hbar} \oint_{\{r|\,|r|\to\infty\}\setminus\{r|\,|r|=\epsilon\}} \mathrm{d}r \sqrt{r^2 - 2E + \underbrace{\hbar^2 \frac{l(l+1)}{r^2}}_{O(1) \text{ if } |r| \to \epsilon}} \tag{7.36}$$

$$= \frac{\mathrm{i}\pi}{\hbar} \mathrm{Res}_{|r|\to\infty} \sqrt{r^2 - 2E} - \frac{\mathrm{i}\pi}{\hbar} \mathrm{Res}_{|r|\to\epsilon} \frac{\hbar\sqrt{l(l+1)}}{r} \tag{7.37}$$

$$= -\hbar^{-1}\mathrm{i}\pi E - \mathrm{i}\pi\sqrt{l(l+1)}. \tag{7.38}$$

[1] For a given function $f(V)$, the symbols $O(f(V))$ and $o(f(V))$ are defined by the following relations:

$$\lim_{V\to\infty} \left| \frac{O(f(V))}{f(V)} \right| < \infty, \qquad \lim_{V\to\infty} \left| \frac{o(f(V))}{f(V)} \right| = 0. \tag{7.33}$$

The first term is the usual bulk WKB contribution determined by the residue at infinity, while the second term is the finite phase correction induced by the regular singularity at the origin. Importantly, this local contribution depends only on the coefficient of the $1/r^2$ term and hence is not modified by higher-order WKB corrections; equivalently, the residue is fixed by the Frobenius indices at $r = 0$. Combining this origin contribution with the Airy-type connection data at simple turning points, the consistency of the global connection formula requires the relevant coefficient to vanish. Section 7.3.5 will justify this fact in terms of some kind of renormalization-group theory. For simplicity, we can rewrite the quantization condition as

$$\mathrm{e}^{-\hbar^{-1}\mathrm{i}\pi E - \mathrm{i}\pi\sqrt{l(l+1)}} = -\mathrm{e}^{-\mathrm{i}\pi(2l+1)} \in \mathrm{e}^{-\mathrm{i}\pi[2\mathbb{Z}+1+(2l+1)]}. \tag{7.39}$$

Introducing a (radial) quantum number n_r, we have

$$E = \hbar\left[2n_r + 1 + (2l+1) - \sqrt{l(l+1)}\right], \qquad n_r \in \mathbb{Z}. \tag{7.40}$$

If we use the Langer correction [104] as $l(l+1) \simeq (l+1/2)^2$, which is also justified by renormalization technique in Section 7.3.5, we finally find the exact energy eigenvalues

$$E = \hbar\left(2n_r + l + \frac{3}{2}\right). \tag{7.41}$$

Moreover, Sec. 7.3.6 is devoted to computation of energies in the anharmonic oscillator case by using a technique we will introduce below.

7.3.3 Coulomb potential

Stokes geometry and the quantization condition for the Coulomb potential

Let us consider the Coulomb potential,

$$V(r) = -\frac{e^2}{r}. \tag{7.42}$$

Supposing that $\mathrm{Re}\, E < 0$, the turning point is at

$$a = -\frac{e^2}{E} > 0. \tag{7.43}$$

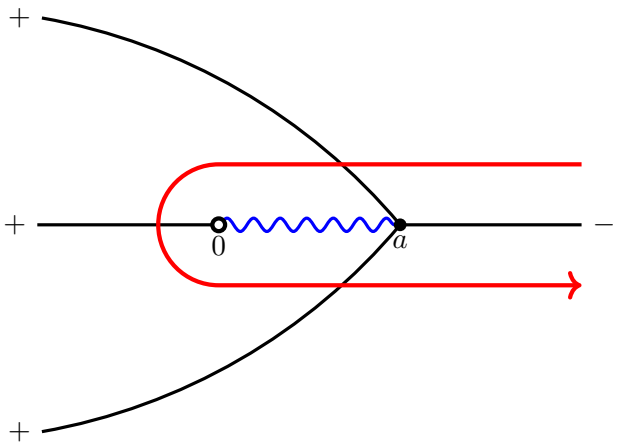

Figure 7.3: Stokes graph for the Coulomb potential. $\mathrm{Re}\, E < 0$. The solid curves correspond to the Stokes curves. The bullet denotes the turning point, a, and the open circle is the origin, $r = 0$. The blue wavy line between 0 and a is the branch cut. The red path means the normalizable wave function, which should be supposed to be subdominant along $r \to \infty \pm \mathrm{i}\epsilon$ with small $\epsilon > 0$.

The corresponding Stokes graph is shown in Fig. 7.3. Figure 7.3 shows the coherent normalizability condition of the wave function, depicted as the red path. We suppose that the wave function should dump sufficiently fast near $r \to \infty$ for its norm defined on $(\infty - \mathrm{i}\epsilon, 0 - \mathrm{i}\epsilon] \otimes [0 + \mathrm{i}\epsilon, \infty + \mathrm{i}\epsilon)$ with small $\epsilon > 0$ to have fast convergence. Thus, we obtain the connection formula on this path as

$$M_+^\bullet N_{a0} M_+^\circ N_{0a} M_+^\bullet = \begin{pmatrix} 1 & \mathrm{i}\left(\frac{1}{A} + A + 2\cos(\pi\sqrt{1+4Q_2})\right) \\ 0 & 1 \end{pmatrix}, \tag{7.44}$$

where the nontrivial cycle A is given by

$$A = \mathrm{e}^{\oint_0^a \mathrm{d}r\, S_{\mathrm{odd}}}. \tag{7.45}$$

Noting that $\sqrt{1+4Q_2} = \sqrt{1+4l(l+1)} = 2l+1$, the quantization condition is, from the boundary condition, given by

$$\cosh\left(\oint_0^a \mathrm{d}r\, S_{\mathrm{odd}}\right) + \cos(\pi(2l+1)) = 0, \tag{7.46}$$

and hence, we find

$$\frac{1}{2\pi}\oint_0^a \mathrm{d}r\, S_{\mathrm{odd}} = \mathrm{i}\left[n_r + \frac{1}{2} + \left(l + \frac{1}{2}\right)\right], \qquad n_r \in \mathbb{Z}. \tag{7.47}$$

Remarkably, the right-hand side in Eq. (7.47) is important as a homotopy invariant, the Maslov index. The Maslov index is the integer that counts the caustic/turning-point crossings along a classical path, where an appropriate phase should be added for each crossing. Then it supplies the semiclassical phase correction in Bohr–Sommerfeld quantization. The factor $1/2$ corresponds to the Maslov index at the turning point, while the factor $l + 1/2$ is that at the origin due to the angular momentum phase (monodromy phase). Note that since the Coulomb potential possesses shape invariance and so is exactly solvable, the contour integral of higher-order WKB perturbations S_i vanishes. In fact, S_i for $i \geq 0$ has no significant pole singularity that provides a nontrivial residue at $r = 0$ or $r \to \infty$. Now, the leading order solution gives rise to

$$\frac{1}{2\pi}\hbar^{-1}\oint_0^a \mathrm{d}r\, S_{-1} = \mathrm{i}\frac{e^2}{\hbar}\frac{1}{\sqrt{-2E}}. \tag{7.48}$$

Then we have

$$E = -\frac{e^4}{2\hbar^2 n^2}, \qquad \text{with } n = n_r + l + 1. \tag{7.49}$$

We can also take into account some variations of the Coulomb problem, such as the Cornell/Yukawa potential; see Sec. 7.3.7.

Open-path quantization and the regularity near the origin

We consider the path on $[0 - \mathrm{i}\epsilon, \infty - \mathrm{i}\epsilon)$ with an appropriate local basis, say, $u \sim r^{l+1}$ near $r = 0$. We introduce a pair of local WKB solutions $(u^+, u^-)^{\mathsf{T}}$ normalized so that the physically admissible combination near the origin is represented by the above regular branch. Starting instead from a convenient normalization at infinity, we take a reference pair of formal WKB solutions $(\varphi_l^+, \varphi_l^-)^{\mathsf{T}}$ defined in the sector $r \to \infty + \mathrm{i}\epsilon$. These functions are used only as *reference* (or *auxiliary*) solutions to specify the Stokes/connection data; in particular, no physical boundary condition is imposed at infinity at this stage. With this convention, the solutions transported to the ray $[0 - \mathrm{i}\epsilon, \infty - \mathrm{i}\epsilon)$ are

constructed as

$$\begin{pmatrix} u^+ \\ u^- \end{pmatrix} \equiv N_{0a} M_+^\bullet N_{a\infty} \begin{pmatrix} \varphi_l^+ \\ \varphi_l^- \end{pmatrix} \Bigg|_{r\to\infty+\mathrm{i}\epsilon} . \tag{7.50}$$

(Here, $N_{a\infty}$ is an abuse of notation.) Then, after the monodromy phase, $\cos(\pi(2l+1))$, is taken into account, the connection formula is reduced to $M_+^\bullet N_{a0}$. The quantization condition from this is identical to that in Eq. (7.47). Is the function u regular at the origin and so the local basis? It is well-known that, at infinity, the convergent wave function is given by

$$\varphi_{nl}(r) \propto r^{l+1} L_{n-l-1}^{(2l+1)}(2\alpha r)\mathrm{e}^{-\alpha r}, \tag{7.51}$$

where α is a parameter determined by the Bohr radius, e, and the quantum numbers. Straightforwardly, we can take the limit of $r \to \epsilon$,

$$u(r) = \varphi_{nl}(r) \sim r^{l+1}. \tag{7.52}$$

Also the divergent (dominant) wave function at infinity possesses the non-regularity at the origin. After all, the regularity at the origin is identical to the convergence of the wave function $\varphi_l^\pm$ at infinity. A more general statement of the equivalence between the open-path local basis and closed-loop quantization is discussed in Sec. 7.3.8.

7.3.4 Exponential mapping and boundary transfer

Let us introduce the transformation such as $r = k^{-1}e^x$ and $\varphi_l(r) = \mathrm{e}^{x/2}\tilde{\varphi}_l(x)$, where $x \in (-\infty, \infty)$ and $k = \frac{\sqrt{2E}}{\hbar}$. With this change of the variables, derivatives transform as

$$\frac{\mathrm{d}}{\mathrm{d}r} = k\mathrm{e}^{-x}\frac{\mathrm{d}}{\mathrm{d}x}, \qquad \frac{\mathrm{d}^2}{\mathrm{d}r^2} = k^2\mathrm{e}^{-2x}\left(\frac{\mathrm{d}^2}{\mathrm{d}x^2} - \frac{\mathrm{d}}{\mathrm{d}x}\right). \tag{7.53}$$

Then, the kinetic term becomes

$$\frac{\mathrm{d}^2}{\mathrm{d}r^2}\varphi_l(r) = k^2\mathrm{e}^{-2x}\left(\frac{\mathrm{d}^2}{\mathrm{d}x^2} - \frac{\mathrm{d}}{\mathrm{d}x}\right)\mathrm{e}^{x/2}\tilde{\varphi}_l(x) \tag{7.54}$$

$$= k^2\mathrm{e}^{-2x}\mathrm{e}^{x/2}\left(\frac{\mathrm{d}^2}{\mathrm{d}x^2} - \frac{1}{4}\right)\tilde{\varphi}_l(x) \tag{7.55}$$

The radial Schrödinger equation is rewritten as

$$\left[-\frac{k^2\hbar^2}{2}\mathrm{e}^{-2x}\left(\frac{\mathrm{d}^2}{\mathrm{d}x^2}-\frac{1}{4}\right)+V(k^{-1}e^x)+\frac{k^2\hbar^2}{2}\frac{l(l+1)}{\mathrm{e}^{2x}}-\frac{k^2\hbar^2}{2}\right]\tilde{\varphi}_l(x)=0, \tag{7.56}$$

and then,

$$\frac{\mathrm{d}^2}{\mathrm{d}x^2}\tilde{\varphi}_l(x)+\left\{\mathrm{e}^{2x}\left[1-\frac{V(k^{-1}e^x)}{E}\right]-\left(l+\frac{1}{2}\right)^2\right\}\tilde{\varphi}_l(x)=0. \tag{7.57}$$

That is, we define

$$\left[-\frac{\mathrm{d}^2}{\mathrm{d}x^2}+\hbar^{-2}\widetilde{Q}(x)\right]\tilde{\varphi}_l(x)=0, \tag{7.58}$$

$$\widetilde{Q}(x)\equiv\hbar^2\left[\left(l+\frac{1}{2}\right)^2-\mathrm{e}^{2x}\left(1-\frac{V(k^{-1}e^x)}{E}\right)\right]. \tag{7.59}$$

Crucially, the regular singular point at $r=0$ is sent to the boundary $x\to-\infty$. The physical Frobenius behavior $u(r)\sim r^{l+1}$ translates to

$$u(x)\sim\mathrm{e}^{(l+1)x}\qquad(x\to-\infty), \tag{7.60}$$

so "regularity at the origin" becomes a *subdominant boundary condition* at the left end of the real axis. Quantization may thus be formulated purely as an open connection problem between the subdominant sectors at $x\to\pm\infty$; the action is unchanged and the small-circle monodromy at $r=0$ should be encoded by the boundary choice at $x=-\infty$. For "large enough" x, the turning points are given by

$$1-\frac{V(k^{-1}e^x)}{E}\approx 0\qquad\text{at } x=b_i, \tag{7.61}$$

which is the same condition for the original turning points $a_i=k^{-1}\mathrm{e}^{b_i}$ with respect to $\mathrm{Re}\, r>0$. For this condition to hold, we need to impose $(l+\frac{1}{2})\ll e^x$ and $k^{-1}e^x=\frac{\hbar}{\sqrt{2E}}e^x=O(1)$. Thus it is reasonable that $\hbar(l+\frac{1}{2})=o(1)$, the monodromy phase, is the essential contribution and a relevant coupling in terms of renormalization group as we will show in Section 7.3.5. Therefore, when $e^x=o(\hbar^{-1})$, for instance $e^x=O(\hbar^{-2})$, there exist an additional turning point, $x=c(l)$, depending on $l+\frac{1}{2}$. Now, the singular region $x\in(-\infty,c]$

contributes in the same way as the subtracted region $|r| < \epsilon = O(\hbar)$ above. Noting that

$$Q(r) = k^2 \mathrm{e}^{-2x} \widetilde{Q}(x), \tag{7.62}$$

we find the identical structure of the formal WKB ansatz because of

$$\mathrm{d}r \sqrt{Q} = d(k^{-1} e^x) \sqrt{k^2 \mathrm{e}^{-2x} \widetilde{Q}} = \mathrm{d}x \sqrt{\widetilde{Q}}. \tag{7.63}$$

Then, the closed Voros period at infinity, $\oint_{-\infty}^{c} \mathrm{d}x \sqrt{\widetilde{Q}}$, provides the monodromy at $r = 0$ given in above Theorem. Closed Voros periods between the turning points, b_i and $c(l)$, are invariant

$$\oint \mathrm{d}r \sqrt{Q} = \oint \mathrm{d}x \sqrt{\widetilde{Q}}. \tag{7.64}$$

This viewpoint mirrors the boundary-to-boundary formulation familiar in black-hole QNM problems (ingoing at the horizon, outgoing at infinity), cf. Andersson [43] and Miyachi–Namba–Omiya–Oshita [113].

7.3.5 Monodromy renormalization

Minimal scheme of monodromy renormalization

Although the centrifugal term is formally $O(\hbar^2)$, it carries the *relevant* local index (small-circle monodromy) at $r = 0$. We therefore reorganize the bookkeeping in terms of the RG–invariant coupling

$$\lambda \equiv \hbar \left(l + \frac{1}{2} \right) \tag{7.65}$$

and define a minimal "monodromy renormalization" (MR) by fixing the physical small-circle monodromy $\mathcal{M}_0^{\mathrm{phys}} = \mathrm{e}^{\mathrm{i}\pi(2l+1)}$ while absorbing local WKB divergences into a counter–Voros constant $Z_{\mathrm{mon}}(\mu)$ at a microscopic radius μ:

$$\mathcal{M}_0^{\mathrm{phys}} = \frac{\mathcal{M}_0^{\mathrm{bare}}}{Z_{\mathrm{mon}}(\mu)}, \qquad \mu \frac{\mathrm{d}}{\mathrm{d}\mu} \ln Z_{\mathrm{mon}}(\mu) =: \gamma_{\mathrm{mon}}(\hbar, \lambda). \tag{7.66}$$

Here γ_{mon} is a "monodromy anomalous dimension." Let $C_{r'}(\mu)$ be a small circle of radius μ around $r = r'$. Closed Voros periods are then evaluated as

(infinity–circle) minus (origin–circle),

$$\oint \mathrm{d}r\, S_{\mathrm{odd}} = \left(\oint_{C_\infty} - \sum_p \oint_{C_p} \right) \mathrm{d}r\, S_{\mathrm{odd}} + \sum_p \left[\oint_{C_p} \mathrm{d}r\, S_{\mathrm{odd}} - \delta V_p(\mu) \right], \quad (7.67)$$

which is minimally subtracted by Z_{mon}. C_∞ is a large circle at infinity, p runs over poles/regular singularities, and $\delta V_p(\mu)$ are minimal counter–Voros constants chosen so that the total is μ-independent and finite, with the origin constrained by $\mathcal{M}_0^{\mathrm{phys}}$. In the 3D oscillator and Coulomb benchmarks, we find $\gamma_{\mathrm{mon}} = 0$ (fixed points), explaining the empirical cancellation of higher closed-period corrections; away from these integrable points, $\gamma_{\mathrm{mon}} \neq 0$ organizes genuine resurgent corrections as a trans-series controlled by Stokes automorphisms. Now, one can reconsider the formal power series in Q with λ as

$$Q_0(r) \equiv 2r \left[V(r) + \frac{\lambda^2}{2r^2} - E \right], \qquad Q_2(r) \equiv Q_2 = -\frac{1}{4}. \quad (7.68)$$

This is a renormalization improvement for γ_{mon} to vanish. This expression gives rise to Proposition A.1 in Ref. [113] if $\gamma_{\mathrm{mon}} = 0$ and $\oint \mathrm{d}r\, S_{\mathrm{odd}} = \hbar^{-1} \oint \mathrm{d}r \sqrt{Q_0/r}$, such as in 3D harmonic oscillator or Coulomb.[2] In this sense of the renormalization improvement, the Langer correction is readily adopted.

An optimized-perturbation-theory realization

We now realize the above MR in an *optimized/variational perturbation theory* (OPT) framework [108–111], directly at the level of the exact-WKB action. For other summation methods for perturbative quantum theory, see the review given in Ref. [112]. Let $Q(r;\lambda)$ be the radial WKB potential (with or without the Langer correction). Let us also introduce

$$Q^\delta(r;\lambda) = Q^0(r;\lambda) + \delta \left[Q(r;\lambda) - Q^0(r;\lambda) \right], \qquad \delta \in [0,1], \quad (7.69)$$

where the seed Q^0 is solvable and matches the small-circle monodromy:

$$\text{If } r \to 0\text{:} \quad Q^0(r;\lambda) \sim \frac{\lambda^2}{r^2} \qquad \oint_{C_0} \sqrt{Q^0}\mathrm{d}r = 2\mathrm{i}\pi\lambda. \quad (7.70)$$

[2] We would like to thank T. Miyachi and R. Namba, the authors of Ref. [113], for helpful discussion. We should make it public that they and we have also derived the identical quantization condition from their open-path technique.

The 3D oscillator and Coulomb are typical choices for Q^0. Expand the action as a δ-series at fixed parameters (omitting $\mathrm{d}r$ in what follows):

$$\oint S_{\mathrm{odd}}[Q^\delta] = \oint \mathcal{S}^0 + \oint \delta\mathcal{S}^1 + \int \delta^2\mathcal{S}^2 + \dots, \tag{7.71}$$

where

$$\mathcal{S}^0 = S_{\mathrm{odd}}[Q^0] = \sqrt{Q^0}, \qquad \mathcal{S}^1 = \frac{1}{2}\frac{Q-Q^0}{\sqrt{Q^0}}, \dots \qquad \mathcal{S}^i = \frac{1}{i!}\frac{\mathrm{d}^i}{\mathrm{d}\delta^i}\sqrt{Q^\delta}, \dots . \tag{7.72}$$

Closed Voros periods are computed as (infinity–circle) minus (origin–circle), with any local divergence on C_0 minimally subtracted by $Z_{\mathrm{mon}}(\mu)$ so that the physical small-circle monodromy $\mathrm{e}^{\mathrm{i}\pi(2l+1)}$ is maintained at every order. Thus the centrifugal contribution of order "$O(\hbar^2)$" in appearance is treated as a relevant coupling λ (never naively expanded). In practice, we consider a truncation order I, set $\delta = 1$ and impose

$$\frac{1}{2\mathrm{i}\pi\hbar}\oint \sum_{i=0}^{I} \mathcal{S}^i = n_r + \frac{1}{2}. \tag{7.73}$$

Close with the fastest apparent convergence condition, e.g.,

$$\partial_\alpha \left[\oint S_{\mathrm{odd}}\right]_I = 0, \tag{7.74}$$

on the variational couplings $\{\alpha\}$. Solving this yields $E^{(I)}$ and the optimal $\{\alpha^{(I)}\}$. In the case of the harmonic oscillator, we define $Q = r^2 + \frac{\lambda^2}{r^2} - 2E$ and $Q^0 = \alpha^2 r^2 + \frac{\lambda^2}{r^2} - 2E$,

$$\mathcal{S}^1 = \frac{1}{2}\frac{(1-\alpha^2)r^2}{\sqrt{Q^0}}. \tag{7.75}$$

Evaluating as (infinity–circle) minus (origin–circle) with MR subtraction,

$$\mathrm{Res}_{r\to\infty}\,\mathcal{S}^0 - \mathrm{Res}_{r=0}\,\mathcal{S}^0 = \left(\frac{E}{\alpha} - \lambda\right), \tag{7.76}$$

$$\mathrm{Res}_{r\to\infty}\,\mathcal{S}^1 - \mathrm{Res}_{r=0}\,\mathcal{S}^1 = -\frac{1}{2}E\frac{1-\alpha^2}{\alpha^3}. \tag{7.77}$$

Then, the fastest apparent convergence gives

$$\partial_\alpha \left[\left(\frac{E}{\alpha} - \lambda \right) - \frac{1}{2} E \frac{1-\alpha^2}{\alpha^3} \right] = \frac{3E(1-\alpha^2)}{2\alpha^4} = 0, \tag{7.78}$$

and hence $\alpha^{(1)} = 1$. Higher orders preserve $\alpha^{(I)} \to 1$ and closed-period corrections cancel[3], yielding from the leading action plus discrete phases

$$\frac{E}{\hbar} = 2n_r + l + \frac{3}{2}. \tag{7.79}$$

Here, note that $\oint_0^a = \frac{1}{2} \oint$ and $\lambda/\hbar = l + 1/2$. For the anharmonic oscillator case, the naive perturbation theory suffers from non-physical behavior of ground state energy, which should be larger than that of the harmonic oscillator, while the variational perturbation theory provides a coherent picture such that the energy is an increasing function of the corresponding deformed parameter as shown in Sec. 7.3.6.

Some remarks

The seed Q^0 (i) locks the origin monodromy via λ and MR, and (ii) approximates the infinity behavior up to variational scales; the δ-series expands only $Q - Q^0$. The fastest appearance convergence aligns variational couplings with the true problem so that, in integrable benchmarks, closed Voros corrections beyond leading order vanish (RG fixed-point behavior). For nonintegrable cases, the residual corrections assemble into a controlled trans-series governed by Stokes automorphisms; the MR supplies a consistent local regularization at the origin. The open-connection formulation in $x = \ln r$ parallels boundary-to-boundary treatments of black-hole QNMs along the real axis, e.g., Andersson [43]. Our bound-state analysis replaces the horizon ingoing condition with origin regularity, but the monodromy/connection algebra and the role of lateral Borel summation are closely analogous.

[3] In this case, we show that if one applies the variational method to an integrable model, the variational parameter always becomes trivial. In contrast, in the later nonintegrable examples we consider, where the variational parameter does not reduce to a trivial value.

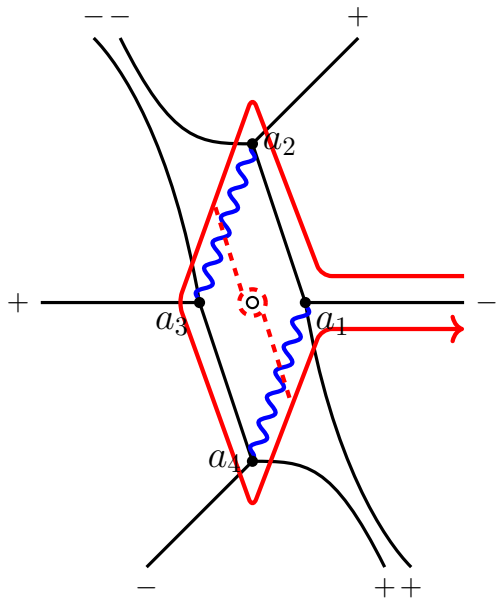

Figure 7.4: Stokes graph for the 3D anharmonic oscillator. $\mathrm{Re}\, E > 0$.

7.3.6 Anharmonic oscillator

The anharmonic oscillator with quartic term is given by

$$V(r) = \frac{1}{2}r^2 + \frac{g}{4}r^4. \tag{7.80}$$

This potential provides the Stokes geometry as in Fig. 7.4. We find the turning points, a_i, as

$$a_1 = \sqrt{\frac{-1+\sqrt{1+4gE}}{g}}, \qquad a_2 = \mathrm{i}\sqrt{\frac{1+\sqrt{1+4gE}}{g}}, \tag{7.81}$$

$$a_3 = -\sqrt{\frac{-1+\sqrt{1+4gE}}{g}}, \qquad a_4 = -\mathrm{i}\sqrt{\frac{1+\sqrt{1+4gE}}{g}}. \tag{7.82}$$

The dashed red curve is on another Riemann sheet through the branch cut. The corresponding connection in the current path becomes

$$\begin{pmatrix}\varphi_l^+\\ \varphi_l^-\end{pmatrix}_{\infty-\mathrm{i}\epsilon} = M_+^\bullet \tilde{N}_{a_4a_1} M_+^\bullet M_-^\bullet N_{a_3a_4}$$

$$\times M_+^\bullet M_-^\bullet \tilde{N}_{a_2a_3} M_-^\bullet M_+^\bullet N_{a_1a_2} \begin{pmatrix} \varphi_l^+ \\ \varphi_l^- \end{pmatrix}_{\infty+\mathrm{i}\epsilon} \qquad \text{for } \epsilon > 0. \quad (7.83)$$

Then, we have the quantization condition to vanish the coefficient of $\varphi_l^-|_{\infty+\mathrm{i}\epsilon}$ in $\varphi_l^+|_{\infty-\mathrm{i}\epsilon}$

$$\cosh\left(\oint_{a_4}^{a_1} \mathrm{d}r\, S_{\mathrm{odd}}\right) + \cos(\pi\sqrt{1+4Q_2}) = 0. \quad (7.84)$$

Note that this form of quantization is identical to the other models which we saw above; it is reasonable that the crucial cycle is in $\mathrm{Re}\, r > 0$. At first, the naive estimate of the next-to-leading order looks like

$$\oint_{a_4}^{a_1} S_{-1}\mathrm{d}r = -\mathrm{i}\pi E - \mathrm{i}\pi\left(l+\frac{1}{2}\right) - \frac{3}{16}\mathrm{i}\pi E^2 g + O(g^2). \quad (7.85)$$

Then, we have

$$\therefore E = \frac{4\left(\sqrt{3g(2n_r+l+\frac{3}{2})+4}-2\right)}{3g}, \quad (7.86)$$

but this energy is a monotonically decreasing function of g (see Fig. 7.5). For larger g, the ground state energy should increase as the physical sense. Now, we define $Q = r^2 + \frac{g}{2}r^4 + \frac{\lambda^2}{r^2} - 2E$ and $Q^0 = \alpha^2 r^2 + \frac{\lambda^2}{r^2} - 2E$, and so obtain

$$\mathcal{S}^0 = \sqrt{r^2 + \frac{\lambda^2}{r^2} - 2E}, \quad (7.87)$$

$$\mathcal{S}^1 = \frac{1}{2}\frac{\frac{g}{2}r^4}{\sqrt{r^2+\frac{\lambda^2}{r^2}-2E}}, \qquad \ldots, \quad (7.88)$$

and

$$\oint \mathrm{d}r\, \mathcal{S}^0 = 2\mathrm{i}\pi\left(\frac{E}{\alpha} - \lambda\right), \quad (7.89)$$

$$\oint \mathrm{d}r\, \mathcal{S}^1 = \pm\mathrm{i}\pi\frac{\alpha^2 - Eg(1-2\alpha^2)}{4g\alpha^3} + O(g). \quad (7.90)$$

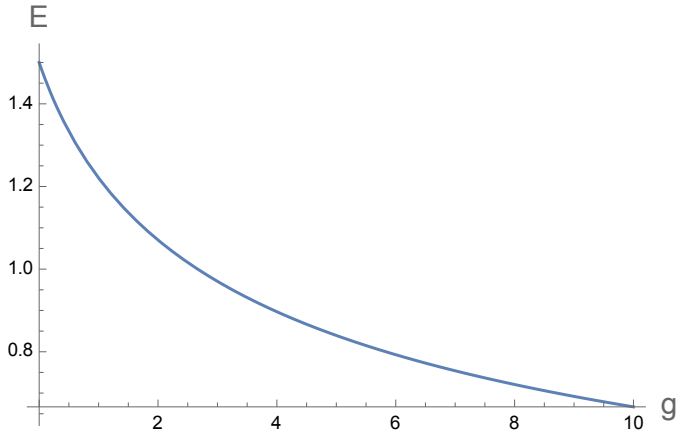

Figure 7.5: The ground state energy of the anharmonic oscillator as a function of g. This is based on the next-to-leading estimate in the perturbation theory in terms of g. The quantum numbers, n_r and l, are set to vanish, so $\lambda = 1/2$ under the Langer correction. Typically, the energy is damping monotonically with respect to the perturbation parameter g.

Note that $\mathcal{S}^1$ is expanded in terms of g before integrating. The fastest apparent convergence up to $O(g)$ gives

$$\partial_\alpha \left[\frac{E}{\alpha} - \lambda \pm \frac{1}{2} \frac{\alpha^2 - Eg(1-2\alpha^2)}{4g\alpha^3} \right] = 0, \tag{7.91}$$

and we obtain

$$\alpha^{(1)} = \pm\sqrt{\frac{3gE}{1+10gE}}, \qquad \pm\sqrt{\frac{3gE}{1-6gE}}, \tag{7.92}$$

where the first and second solutions are for $+$ and for $-$, respectively, in Eq. (7.91). Hence, for instance $\alpha^{(1)} = \sqrt{\frac{3gE}{1+10gE}}$, we see

$$\frac{\sqrt{1+10gE}}{12\sqrt{3E}g^{3/2}} + \frac{5\sqrt{E}\sqrt{1+10gE}}{6\sqrt{3g}} - \lambda = 2n_r + 1 \tag{7.93}$$

$$\frac{(1+10gE)^{3/2}}{\sqrt{E}} = 12\sqrt{3}g^{3/2}(2n_r + 1 + \lambda), \tag{7.94}$$

and depicted the ground state energy E with $n_r = 0$, $\lambda = 1/2$ in Fig. 7.6, which grows along large g typically. There are some roots of the algebraic equations with regard to E. Almost those are non-physical due to, e.g.,

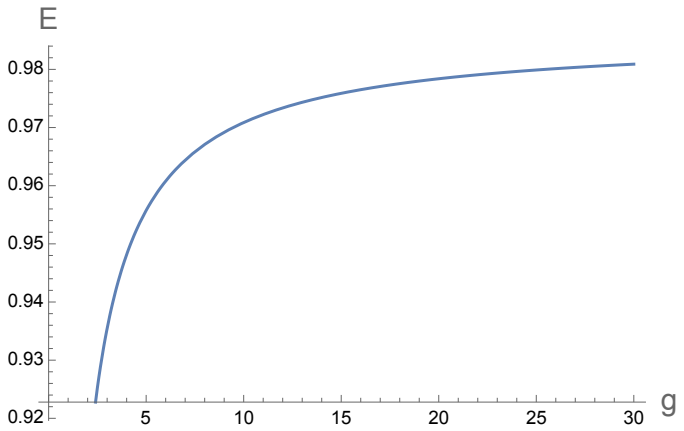

Figure 7.6: The ground state energy of the anharmonic oscillator as a function of g. The derivation is given by the variational method with the fastest apparent condition up to subleading of g, and the explicit function is given by Eq. (7.94). The quantum numbers, n_r and l, are set to vanish, so $\lambda = 1/2$ under the Langer correction. Typically, the energy is growing up monotonically with respect to g.

negative energy. We here illustrate a more plausible result for $g > \frac{1}{6}\sqrt{\frac{5}{2}}$. Of course, these are not results with such a high level of precision; even within the variational perturbation theory (with parameter δ), the function of g is expanded in powers of g, and we do not address the systematic issues of truncated fastest apparent convergence in any serious manner.

7.3.7 Variations of Coulomb

In this calculation module, we consider the Cornell/Yukawa potential,

$$V_C(r) = -\frac{\tilde{\alpha}}{r} + \sigma r, \qquad V_Y(r) = -\frac{\mathrm{e}^{-\mu r}}{r}, \tag{7.95}$$

where the turning points are given by

$$a_C^{\pm} = \frac{E}{2\sigma} \pm \sqrt{\frac{E^2}{4\sigma^2} + \frac{\tilde{\alpha}}{\sigma}}, \qquad a_Y^{+} = \frac{1}{\mu} W(-\mu/E), \tag{7.96}$$

respectively. Here $W(z)$ is the Lambert W-function. The Stokes structure of the Cornell potential is shown in Fig. 7.7. For the Yukawa potential, the Stokes structure is the same as for Coulomb potential in Fig. 7.3. Again, we

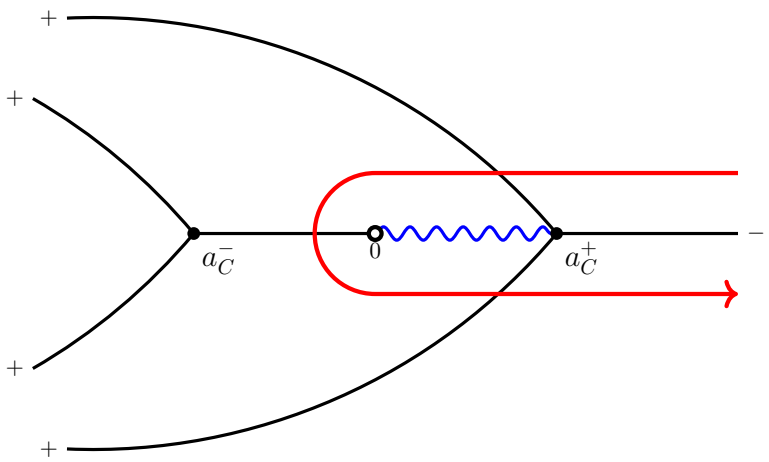

Figure 7.7: Schematic Stokes graph for the Cornell potential.

can find the same quantization condition

$$\cosh\left(\oint_0^{a^+} \mathrm{d}r\, S_{\mathrm{odd}}\right) + \cos(\pi(2l+1)) = 0. \tag{7.97}$$

The next-to-leading order contributes as

$$\frac{1}{2\pi}\oint_0^{a_C^+} \mathrm{d}r\, S_{-1} = \mathrm{i}\frac{\tilde{\alpha}}{\sqrt{-2E}} - \frac{3\mathrm{i}\tilde{\alpha}^2\sigma}{8\sqrt{2}(-E)^{5/2}} + O(\sigma^2), \tag{7.98}$$

$$\frac{1}{2\pi}\oint_0^{a_Y^+} \mathrm{d}r\, S_{-1} = \mathrm{i}\frac{1}{\sqrt{-2E}} - \frac{\mathrm{i}\mu}{2\sqrt{2}(-E)^{3/2}} + O(\mu^2). \tag{7.99}$$

Figure 7.8 shows the ground state energies of the two potentials as functions of the corresponding parameters introduced to deform the Coulomb potential. The behavior in terms of σ or μ is reasonable.

7.3.8 Open-path and closed-cycle equivalence: a general statement

Consider the radial Schrödinger equation

$$\left[-\frac{\hbar^2}{2}\frac{\mathrm{d}^2}{\mathrm{d}r^2} + V(r) + \frac{\hbar^2(\ell+\frac{1}{2})^2}{2r^2}\right] u(r) = E\,u(r), \tag{7.100}$$

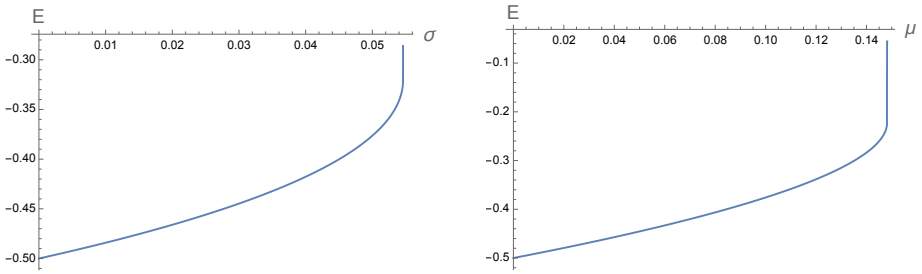

Figure 7.8: The ground state energy of the variations of the Coulomb potential: **(Left)** Cornell potential with $\tilde{\alpha} = 1$ as a function of σ, and **(Right)** Yukawa potential as a function of μ. The quantum numbers, n_r and l, are set to be zero. Typically, the energy is growing up monotonically with respect to the perturbation parameters, σ and μ.

where we have incorporated the Langer improvement $\ell(\ell+1) \to (\ell+\frac{1}{2})^2$. Suppose that V is meromorphic. We assume:

(A1) V extends analytically to a simply connected domain $\mathcal{D} \subset \mathbb{C}$ containing $[0, +\infty)$ and the Stokes graph relevant to the energy E.

(A2) $r = 0$ is a *regular* singular point of Eq. (7.100).

(A3) E belongs to the discrete spectrum, so that a subdominant solution exists as $r \to +\infty$ in some Stokes sector.

(A4) The Borel sums of the exact-WKB objects used below exist in a fixed lateral direction θ not crossing a Stokes curve.

Let Γ be a closed contour that goes from $+\infty$ to the vicinity of $r = 0$ within a Stokes sector, encircles $r = 0$ once counterclockwise on the same sheet, and returns to $+\infty$.

Proposition 7.2 (Open-path ⇔ Closed-cycle under A1–A4). *For a given E, the following are equivalent:*

(i) ***Open-path quantization:*** *There exists a nontrivial solution of Eq. (7.100) which is subdominant as $r \to +\infty$ and regular at $r = 0$ (i.e. no logarithmic growth in the Frobenius expansion).*

(ii) ***Closed-cycle exact-WKB quantization:*** *The monodromy gathered along Γ has a zero point, i.e.*

$$\cosh\left(\oint_\Gamma \mathrm{d}r\, S_{\mathrm{odd}}\right) + \cos(\pi\sqrt{1+4Q_2}) = 0. \tag{7.101}$$

In other words, the monodromy phase in terms of γ_{mon} has a unit with the ordered product of Stokes multipliers encountered along Γ.

Sketch of proof Fix a decaying solution ψ_∞ at $+\infty$ (lateral Borel sum at angle θ), and a local Frobenius basis $(\psi_0^{\mathrm{reg}}, \psi_0^{\mathrm{sing}})$ at $r = 0$, where ψ_0^{reg} and ψ_0^{sing} are the regular and singular solutions at the origin, respectively. Transport ψ_∞ to the origin across Stokes curves, multiplying by the corresponding monodromy matrices (AKT connection). One obtains

$$\psi_\infty = C_{\mathrm{reg}}(E,\hbar)\,\psi_0^{\mathrm{reg}} + C_{\mathrm{sing}}(E,\hbar)\,\psi_0^{\mathrm{sing}}, \tag{7.102}$$

with connection coefficients expressed through Voros and Stokes multipliers. Condition (i) in Proposition holds iff $C_{\mathrm{sing}}(E,\hbar) = 0$. Now close the path by a small counterclockwise loop around $r = 0$ and return to $+\infty$; the net transport along this closed contour amounts to multiplication by Stokes multipliers and $\mathrm{e}^{2\pi\mathrm{i}\gamma_{\mathrm{mon}}}$ in a suitable basis. Triangularity of the local monodromy at a regular singularity and Wronskian conservation (i.e., the condition so that the coefficient of dominant solution on the right hand side should vanish as usual) imply that $C_{\mathrm{sing}} = 0$ iff the closed monodromy has a zero point (monodromy unit), which is precisely Eq. (7.101). Independence of Eq. (7.101) from local normalizations follows from the standard arbitrariness of choosing Stokes data. □ For the 3D harmonic oscillator and for the Coulomb problem, one can choose Γ such that $\gamma_{\mathrm{mon}} = 0$; then the second term on the left-hand side in Eq. (7.101) is moved to the right-hand side (with the Langer improvement). The statement presumes regularity at the origin and excludes irregular singular points and energies for which Stokes curve accumulate around $r = 0$. If V has additional singularities or branch points in $\mathcal{D}$, the contour Γ must be chosen to avoid them (see Sec. 7.3.6); otherwise extra factors contribute. The Bohr–Sommerfeld quantization is now given in the form as

$$\frac{1}{2\pi\hbar}\oint_\Gamma p_{\mathrm{eff}}(r;E)\,\mathrm{d}r \;+\; \Phi_\Gamma(E,\hbar) \;+\; \gamma_{\mathrm{mon}}(E,\hbar) \;\in\; \mathbb{Z}, \tag{7.103}$$

where $p_{\mathrm{eff}}(r;E) := \sqrt{2m\,(E - V_{\mathrm{eff}}(r))}$ with $V_{\mathrm{eff}}(r) := V(r) + \hbar^2(\ell+\frac{1}{2})^2/(2r^2)$, and Φ_Γ collects all higher-order WKB/Voros corrections and Stokes contributions along Γ.

Laboratory checkpoint

Before moving to the next stage, perform the following checks without copying the displayed final answer.

1. Derive the Langer term directly from the exponential coordinate map rather than inserting it as a remembered replacement rule.

2. Recover the oscillator and Coulomb quantization conditions from both open-path matching and closed-cycle monodromy.

3. Vary the auxiliary deformation or optimization parameter and impose monodromy independence before treating the Cornell or Yukawa case.

7.4 Problems for Stage V

V.1 Remove the first derivative from the d-dimensional radial Schrödinger equation and derive the effective inverse-square coefficient.

V.2 Compute the two Frobenius indices at the origin for g/r^2. Classify the square-integrable solutions and discuss when a boundary condition beyond regularity is needed.

V.3 Perform the Langer map $r = \mathrm{e}^x$ including the wave-function rescaling. Show where $(l+1/2)^2$ enters and why it is not an arbitrary replacement rule.

V.4 Derive the three-dimensional harmonic-oscillator spectrum from a closed exact-WKB cycle. Repeat with an open path and the origin monodromy.

V.5 Derive the Coulomb bound spectrum from the radial action integral. Keep the angular-momentum and turning-point phases separate until the last line.

V.6 Introduce a small circle $r = \epsilon \mathrm{e}^{\mathrm{i}\phi}$ around the origin. Calculate the local monodromy and derive a condition that makes the global quantization independent of ϵ.

V.7 Treat a weak quartic perturbation of the radial oscillator with both ordinary perturbation theory and the optimized monodromy scheme. Compare the regimes in which each truncation is useful.

V.8 Construct the turning-point equation for the Cornell potential and locate its roots numerically on the relevant sheet. Test homotopy invariance of the quantization contour as parameters vary.

V.9 Repeat the previous problem for a Yukawa-screened Coulomb potential. Identify the threshold at which a bound-state pole approaches the cut.

V.10 Give an example in which a coordinate transformation creates an apparent singularity. Distinguish its Jacobian monodromy from a physical self-adjoint-extension parameter.

Chapter 8

Stage VI: Resolve a few-body continuum with CDCC and complex scaling

Reader contract

This stage derives Jacobi-coordinate few-body Hamiltonians and the continuum-discretized coupled-channels equations from the same projection logic used for a resonance. Pseudostates, channel truncation, smoothing, and complex-scaled level densities are then applied first to broad and fragmented ^{6}He resonances, and subsequently to lithium and beryllium-core reactions. The reader finishes with a reproducible pole-to-observable convergence protocol, not merely a catalogue of applications.

8.1 Nuclear reaction theory reconstructed from scattering principles

The usual vocabulary of nuclear reactions—optical potential, channel, form factor, distorted wave, compound state, breakup—can appear to be a collection of phenomenological devices. It is more coherent when read as a sequence of projections and boundary conditions. This section derives that sequence before any continuum discretization. The resulting formulas are standard; their placement in the book is not. Each will be tied to one of the analytic or operator-theoretic structures already constructed.

8.1.1 Translational invariance and Jacobi kinetic energy

For particles with masses m_i, positions $\boldsymbol{r}_i$, and momenta $\boldsymbol{p}_i$, the laboratory kinetic energy is

$$T = \sum_{i=1}^{A} \frac{\boldsymbol{p}_i^2}{2m_i}. \tag{8.1}$$

Introduce the total mass, center of mass, and total momentum,

$$M = \sum_i m_i, \qquad \boldsymbol{R}_{\rm cm} = \frac{1}{M}\sum_i m_i \boldsymbol{r}_i, \qquad \boldsymbol{P} = \sum_i \boldsymbol{p}_i. \tag{8.2}$$

A linear canonical transformation to mass-scaled Jacobi coordinates gives

$$T = \frac{\boldsymbol{P}^2}{2M} + \sum_{a=1}^{A-1} \frac{\boldsymbol{\pi}_a^2}{2\mu_a}. \tag{8.3}$$

Removing $\boldsymbol{R}_{\rm cm}$ is not optional in a basis calculation. If a single-particle basis mixes intrinsic and center-of-mass excitations, spurious levels may be misidentified as low-energy channels.

For three particles, one Jacobi set is

$$\boldsymbol{x} = \boldsymbol{r}_2 - \boldsymbol{r}_1, \qquad \boldsymbol{y} = \boldsymbol{r}_3 - \frac{m_1\boldsymbol{r}_1 + m_2\boldsymbol{r}_2}{m_1+m_2}, \tag{8.4}$$

with

$$\mu_x = \frac{m_1 m_2}{m_1+m_2}, \qquad \mu_y = \frac{m_3(m_1+m_2)}{M}. \tag{8.5}$$

The other two sets are obtained by cyclic permutation. No set is physically preferred, but a particular cluster asymptotic region is simple in one of them. A many-set expansion is therefore a coordinate atlas for correlations, not an introduction of new particles.

8.1.2 Cluster channels and antisymmetry

Suppose the asymptotic partition is $a + A$. A channel state has internal states $\phi_a^{I_a}$, $\phi_A^{I_A}$ and relative orbital momentum L, coupled to total JM:

$$\mathcal{Y}_c^{JM} = \mathcal{A}\left[[\phi_a^{I_a} \otimes \phi_A^{I_A}]_I \otimes Y_L(\hat{R})\right]_{JM}, \qquad c = (a, A, I_a, I_A, I, L, \ldots). \tag{8.6}$$

The intercluster antisymmetrizer $\mathcal{A}$ makes channel states nonorthogonal at small R. In a microscopic resonating-group formulation, projection therefore gives a norm kernel as well as a Hamiltonian kernel. In a cluster model one often replaces this exact exchange by a Pauli projector

$$V_{\rm Pauli} = \lambda_P \sum_f |u_f\rangle\langle u_f|, \qquad \lambda_P \to +\infty, \tag{8.7}$$

which removes forbidden relative orbits u_f. The limit changes the operator domain on the allowed subspace. It must be held fixed while continuum model spaces are compared.

A spectroscopic factor is a norm of a particular projected overlap and hence depends on the resolution, interaction, and channel convention. An asymptotic normalization coefficient is more directly tied to the tail fixed by a separation energy and Coulomb equation. Reaction observables probe these quantities through kernels; neither is an eigenvalue observable of the full many-body Hamiltonian.

8.1.3 The optical model as a Feshbach boundary value

Let P retain elastic relative motion with the target in its ground state and let Q contain every explicit excitation, transfer, breakup, and compound configuration not retained. Stage I gave the exact operator

$$H_{\mathrm{opt}}(E) = PHP + PHQ\frac{1}{E - QHQ + \mathrm{i}0}QHP. \tag{8.8}$$

In coordinate representation its second term is generally nonlocal, energy dependent, angular-momentum dependent, and complex above open thresholds. A local Woods–Saxon or folded g-matrix potential is an approximation to this object, not a fundamental interaction.

Writing $U = V + \mathrm{i}W$ and using the stationary Schrödinger equation gives the continuity relation

$$\nabla \cdot \boldsymbol{j} = \frac{2}{\hbar}W(\boldsymbol{R})|\psi(\boldsymbol{R})|^2. \tag{8.9}$$

An absorptive convention has $W \leq 0$. The lost elastic flux is the flux into the eliminated Q space only if the optical model consistently represents that space. When breakup channels are later included explicitly, leaving the same phenomenological absorption untouched may count part of them twice.

For spinless elastic scattering,

$$S_L = \eta_L \mathrm{e}^{2\mathrm{i}\delta_L}, \qquad 0 \leq \eta_L \leq 1, \tag{8.10}$$

and

$$\sigma_{\mathrm{el}} = \frac{\pi}{k^2}\sum_L (2L+1)|1 - S_L|^2, \tag{8.11}$$

$$\sigma_R = \frac{\pi}{k^2}\sum_L (2L+1)(1-|S_L|^2). \tag{8.12}$$

The first measures coherent deflection; the second measures missing open-channel flux. A resonance can be present in either through the analytic continuation of $S_L(E)$, but a peak in σ_R is not by itself a pole definition.

8.1.4 Coupled channels from an internal basis

Let $h_A\phi_n = \epsilon_n\phi_n$ describe discrete target states. With

$$H = K_R + h_A + U(\boldsymbol{R},\xi), \tag{8.13}$$

expand

$$\Psi^{JM} = \frac{1}{R}\sum_{nIL}\chi^J_{nIL}(R)[\phi_{nI}(\xi)\otimes Y_L(\hat{R})]_{JM}. \tag{8.14}$$

Projection produces

$$\left[-\frac{\hbar^2}{2\mu}\left(\frac{\mathrm{d}^2}{\mathrm{d}R^2} - \frac{L_c(L_c+1)}{R^2}\right) + \epsilon_c - E\right]\chi^J_c(R) + \sum_{c'} U^J_{cc'}(R)\chi^J_{c'}(R) = 0. \tag{8.15}$$

Thus the CDCC equation is not a special new dynamical law. It is the ordinary coupled-channel equation after continuum wave packets have been admitted as internal states.

Multipole expansion gives

$$U(\boldsymbol{R},\xi) = \sum_{\lambda\mu} F_{\lambda\mu}(R,\xi)Y_{\lambda\mu}(\hat{R}), \tag{8.16}$$

and reduced matrix elements of F_λ become radial coupling form factors. Angular momentum selection rules can make the coupling matrix sparse even when the number of channels is large. A good implementation tests Hermitian symmetry of $U_{cc'}$ before optical absorption is introduced.

8.1.5 Distorted waves and first-order transition theory

Choose an entrance channel Hamiltonian $H_i = K + U_i + h_i$ and write $H = H_i + V_i$. The exact transition amplitude to an outgoing solution of H_f

is

$$T_{fi}^{\text{prior}} = \langle \Psi_f^{(-)} | V_i | \Phi_i \chi_i^{(+)} \rangle. \tag{8.17}$$

Alternatively,

$$T_{fi}^{\text{post}} = \langle \Phi_f \chi_f^{(-)} | V_f | \Psi_i^{(+)} \rangle. \tag{8.18}$$

The two forms agree for exact wave functions with consistent interactions. Distorted-wave Born approximation (DWBA) replaces the complete scattering state on the right by the channel product:

$$T_{fi}^{\text{DWBA}} = \langle \Phi_f \chi_f^{(-)} | V_{\text{tr}} | \Phi_i \chi_i^{(+)} \rangle. \tag{8.19}$$

Post–prior disagreement then becomes a diagnostic of inconsistent optical potentials, remnant terms, nonorthogonality, or truncation.

The distorted waves resum elastic interaction with the target. The Born order refers only to the transition operator V_{tr}, not to replacing all waves by planes. In a knockout reaction, an impulse approximation further replaces the short collision by an embedded two-nucleon t matrix. This separation is valid when the elementary collision is short compared with the scale over which the nuclear overlap and distortions vary; it is a scale statement to be checked, not a definition.

8.1.6 The R-matrix split: an interior connection problem

Choose a channel radius a outside the dominant short-range interaction. Inside, expand the wave function in square-integrable functions X_λ. Outside, use known Coulomb or free channel functions. A Bloch operator

$$\mathcal{L}_B = \frac{\hbar^2}{2\mu} \delta(r-a) \left(\frac{\mathrm{d}}{\mathrm{d}r} - \frac{B}{a} \right) \tag{8.20}$$

makes the interior problem Hermitian with the chosen boundary parameter B. The channel R matrix has the pole expansion

$$R_{cc'}(E) = \sum_\lambda \frac{\gamma_{\lambda c} \gamma_{\lambda c'}}{E_\lambda - E}, \tag{8.21}$$

where $\gamma_{\lambda c}$ is a boundary amplitude at a [114].

The E_λ depend on a and B; observed scattering poles do not. The external logarithmic derivative converts the interior R matrix into the physical collision matrix. This is another global connection problem: interior basis coefficients

are representation data, while the matched incoming coefficient is invariant. Exact WKB replaces the arbitrary interior basis by resummed local analytic solutions; the algebra of matching is the common element.

For one isolated level and one channel, the denominator becomes

$$D(E) = E_\lambda - E - \gamma_\lambda^2[S(E) - B] - \mathrm{i}\gamma_\lambda^2 P(E), \tag{8.22}$$

where S and P are shift and penetration functions. The physical pole solves $D(E_\mathrm{R}) = 0$, not simply $E = E_\lambda$. Differentiating D gives the same energy-dependent normalization encountered for Feshbach operators.

8.1.7 Three-body equations before discretization

For three particles with pair interactions v_1, v_2, v_3, write

$$H = H_0 + v_1 + v_2 + v_3. \tag{8.23}$$

The direct Lippmann–Schwinger kernel contains disconnected iterations and is not compact in the useful sense. Decompose

$$|\Psi\rangle = |\psi_1\rangle + |\psi_2\rangle + |\psi_3\rangle, \qquad |\psi_\alpha\rangle = G_0 v_\alpha |\Psi\rangle, \tag{8.24}$$

with $G_0 = (E - H_0 + \mathrm{i}0)^{-1}$. Using the pair t matrix

$$t_\alpha = v_\alpha + v_\alpha G_0 t_\alpha \tag{8.25}$$

gives the Faddeev equations

$$|\psi_\alpha\rangle = G_0 t_\alpha \sum_{\beta \neq \alpha} |\psi_\beta\rangle. \tag{8.26}$$

Each component carries the asymptotic behavior of one pair partition, and the sum reconstructs the common solution [54, 115].

The operator form for transition amplitudes is the Alt–Grassberger–Sandhas system

$$U_{\beta\alpha} = (1 - \delta_{\beta\alpha}) G_0^{-1} + \sum_{\gamma \neq \beta} t_\gamma G_0 U_{\gamma\alpha}. \tag{8.27}$$

Its on-shell matrix elements generate elastic, rearrangement, and breakup amplitudes [116]. CDCC does not replace the exact three-body theory as an

identity. It approximates selected projectile continuum and reaction couplings in a basis optimized for high-energy or weakly bound projectile scattering. Comparisons with Faddeev/AGS calculations are valuable where both are feasible.

8.1.8 Why three-body Coulomb is structurally harder

For short-range pair forces, the channel resolvents separate cleanly at large Jacobi coordinates. Coulomb interactions act in every asymptotic region and leave a long-range tail in the Faddeev kernels. Merkuriev splitting writes each Coulomb interaction as a short-range piece adapted to the three-body region plus a long-range piece included in the channel Hamiltonian. The splitting function is auxiliary; physical amplitudes must be independent of it in a converged calculation [54].

This is a precise nuclear version of the infrared lesson from Stage II. A $p + p + {}^{7}\mathrm{Be}$ continuum cannot be assigned one plane-wave asymptotic form. Different Jacobi sectors carry different Coulomb distortions, and their overlap requires matching. CDCC with Coulomb functions in the projectile–target coordinate controls one part of the asymptotics; CSLS or a three-body Coulomb construction is needed to resolve fragment correlations in the final state.

8.1.9 Adiabatic and eikonal limits

Two scale separations lead to useful approximations. If projectile internal excitation energies are small compared with the collision energy over the interaction time, replace

$$h_P - \epsilon_0 \longrightarrow 0 \tag{8.28}$$

inside the reaction equation while retaining the projectile coordinates in the interaction. This adiabatic or sudden approximation resums breakup configurations at degenerate internal energy. Its failure is largest when energy conservation among continuum channels or a narrow resonance is important.

At high incident momentum K, write

$$\Psi(\boldsymbol{R}, \xi) = \mathrm{e}^{\mathrm{i}KZ}\widehat{\Psi}(\boldsymbol{b}, Z, \xi) \tag{8.29}$$

and neglect $\partial_Z^2 \widehat{\Psi}$ relative to $K\partial_Z \widehat{\Psi}$. The equation becomes first order,

$$\mathrm{i}\hbar v \frac{\partial}{\partial Z}\widehat{\Psi} = [h_P - \epsilon_0 + U(\boldsymbol{b}, Z, \xi)]\widehat{\Psi}. \tag{8.30}$$

Freezing h_P further gives a path-ordered eikonal phase. Equation (8.30) is a coupled-channel evolution along the beam coordinate; it retains excitation energy and is often called dynamical eikonal.

The approximation is checked by increasing energy, restricting scattering angle, and comparing with partial-wave CDCC. Coulomb deflection and the logarithmic phase must be corrected explicitly; the straight-line plane-wave eikonal is not uniformly valid at arbitrarily large impact parameter.

8.1.10 Threshold scales in lithium and beryllium systems

Weak binding creates large spatial scales

$$\ell_B \sim \frac{\hbar}{\sqrt{2\mu S}}, \tag{8.31}$$

where S is a separation energy. Small S means that low multipoles of the target field couple efficiently to continuum states near threshold. It also means that a cluster treated as inert may have its own comparable breakup scale. The sequence

$$^{9}\mathrm{C} \longleftrightarrow p + {}^{8}\mathrm{B} \longleftrightarrow p + p + {}^{7}\mathrm{Be} \tag{8.32}$$

is the central example in Laboratory VI-B. A two-body model may reproduce one tail but miss polarization of the intermediate ^{8}B subsystem.

For ^{6}Li, both $\alpha + d$ and $\alpha + p + n$ descriptions can be useful. The former is smaller and resolves deuteron-like breakup; the latter permits explicit proton–neutron rearrangement, closed pseudostates, knockout overlaps, and transition densities. Model selection should be made by the observable and energy scales, then verified by enlarging the space. “More bodies” is not automatically more accurate if their effective interactions and Pauli constraints are less controlled.

8.1.11 One dictionary for reaction approximations

method	retained object	eliminated object	invariance or check
optical model	elastic channel	excitation and reaction space	elastic S matrix and flux deficit
DWBA	entrance and exit distorted waves	repeated transition coupling	post–prior and potential dependence
R matrix	finite interior basis	exact interior continuum	channel-radius and boundary-parameter independence
Faddeev/ AGS	all pair partitions	disconnected overcounting	permutation, unitarity, and rearrangement consistency
adiabatic and eikonal	slow internal or transverse coordinates	selected time or longitudinal derivatives	energy and angle systematics
CDCC	finite continuum wave packets	Q_N continuum	model-space and smoothing convergence
complex scaling	exposed pole plus rotated cut	undeformed outgoing growth	angle and contour independence
exact WKB	resummed connection datum	divergent local formal series	Stokes, Wronskian, and homotopy consistency

The table prevents a common misuse of comparisons. Two methods can disagree because they approximate different eliminated spaces, not because one is simply of higher “order.” To compare them, match the retained Hamiltonian, asymptotic channels, and observable first. Only then vary the approximation specific regulator or truncation.

Checkpoint

The reader should now be able to derive optical absorption from a Feshbach boundary value, obtain ordinary coupled-channel equations, state the post–prior test of DWBA, interpret R-matrix levels as interior representation data, and explain why Faddeev components are adapted to different asymptotic partitions. CDCC will next be obtained by replacing the discrete internal basis of Eq. (8.14) with normalized continuum bins or pseudostates.

8.2 Few-body continua and CDCC

Calculation route

Prerequisites. Tensor-product channels, Jacobi coordinates, partial waves, projection operators, Coulomb asymptotics, and finite-basis diagonalization.

Calculation goal. Derive three- and four-body CDCC, construct bin and pseudostate model spaces, calculate coupling potentials and breakup amplitudes, and smooth discrete spectra with complex scaling.

Completion criterion. Write the coupled radial equations from a declared few-body Hamiltonian, impose open and closed channel conditions, demonstrate model-space convergence, and reconstruct an energy-differential observable.

A weakly bound projectile turns a two-body collision into a spectral problem with many nearby thresholds. The continuum is not a small correction: tidal and Coulomb fields can polarize or break the projectile while it traverses the target field. Continuum-discretized coupled channels (CDCC) is a controlled way to keep a finite part of that continuum in the reaction space [117–119]. The method is often introduced as a numerical prescription. Here we derive it as a projection of the direct-integral channel decomposition from Stage I.

This perspective also connects CDCC to the resonance program. A Feshbach operator eliminates the continuum and retains its effect in an energy-dependent self-energy. CDCC instead retains a finite-rank approximation to the important continuum fibers. Complex scaling supplies both resonance

pseudostates and a smoothing representation of the discarded continuum. Exact WKB identifies the invariant analytic boundary data that any such finite representation must approximate.

8.2.1 Two-cluster projectile: coordinates and Hamiltonian

Let a projectile $P = c + v$ consist of a core c and a valence particle v, and let it scatter from a target T. After removing the total center of mass, choose

$$\boldsymbol{r} = \boldsymbol{r}_v - \boldsymbol{r}_c, \tag{8.33}$$

$$\boldsymbol{R} = \frac{m_c \boldsymbol{r}_c + m_v \boldsymbol{r}_v}{m_P} - \boldsymbol{r}_T, \qquad m_P = m_c + m_v. \tag{8.34}$$

The fragment–target coordinates are

$$\boldsymbol{R}_c = \boldsymbol{R} - \frac{m_v}{m_P}\boldsymbol{r}, \qquad \boldsymbol{R}_v = \boldsymbol{R} + \frac{m_c}{m_P}\boldsymbol{r}. \tag{8.35}$$

With intrinsic core and target excitations temporarily frozen, the Hamiltonian is

$$H = K_R + h_P + U_{cT}(\boldsymbol{R}_c) + U_{vT}(\boldsymbol{R}_v), \tag{8.36}$$

where

$$h_P = K_r + V_{cv}(\boldsymbol{r}), \qquad K_R = -\frac{\hbar^2}{2\mu_R}\nabla_R^2, \qquad K_r = -\frac{\hbar^2}{2\mu_r}\nabla_r^2. \tag{8.37}$$

The optical interactions U_{xT} may be complex because target excitations not included explicitly have already been eliminated. This is an effective non-self-adjointness distinct from analytic dilation. The full microscopic Hamiltonian before elimination may still be self-adjoint.

The projectile has a bound ground state Φ_0 and continuum states $\Phi_{\epsilon\alpha}$,

$$h_P \Phi_0 = \epsilon_0 \Phi_0, \qquad \epsilon_0 < 0, \tag{8.38}$$

$$h_P \Phi_{\epsilon\alpha} = \epsilon \Phi_{\epsilon\alpha}, \qquad \epsilon \geq 0, \tag{8.39}$$

where α collects orbital angular momentum, spin coupling, and any rearrangement label. The exact projectile resolution is

$$\mathbf{1}_P = |\Phi_0\rangle\langle\Phi_0| + \sum_\alpha \int_0^\infty |\Phi_{\epsilon\alpha}\rangle\langle\Phi_{\epsilon\alpha}|\, \mathrm{d}\epsilon + \sum_{b \neq 0} |\Phi_b\rangle\langle\Phi_b|, \tag{8.40}$$

with the normalization and density convention absorbed into $\Phi_{\epsilon\alpha}$. CDCC replaces a physically selected part of the integral by a finite orthonormal set.

8.2.2 Model-space projection and the CDCC equation

Choose square-integrable projectile states $\{\Phi_i\}_{i=0}^{N}$ and define

$$P_N = \sum_{i=0}^{N} |\Phi_i\rangle\langle\Phi_i|, \qquad Q_N = \mathbf{1} - P_N. \tag{8.41}$$

The CDCC approximation is not simply $\Psi \approx P_N\Psi$. It is the projected boundary-value problem

$$P_N(H - E_{\rm tot})P_N\Psi_N = 0 \tag{8.42}$$

with scattering conditions imposed in every retained open channel. Expand for total angular momentum JM,

$$\Psi_N^{JM}(\boldsymbol{R},\xi) = \frac{1}{R}\sum_c \chi_c^J(R)\mathcal{Y}_c^{JM}(\hat{\boldsymbol{R}},\xi), \tag{8.43}$$

where ξ denotes all projectile internal coordinates and

$$\mathcal{Y}_c^{JM} = \left[\Phi_{iI}(\xi)\otimes Y_L(\hat{\boldsymbol{R}})\right]_{JM}, \qquad c = (i, I, L, \ldots). \tag{8.44}$$

Projecting onto $\mathcal{Y}_c^{JM}$ gives

$$\left[-\frac{\hbar^2}{2\mu_R}\left(\frac{\mathrm{d}^2}{\mathrm{d}R^2} - \frac{L_c(L_c+1)}{R^2}\right) + \epsilon_c - E_{\rm tot}\right]\chi_c^J(R) + \sum_{c'} U_{cc'}^J(R)\chi_{c'}^J(R) = 0, \tag{8.45}$$

with

$$U_{cc'}^J(R) = \left\langle \mathcal{Y}_c^{JM}\middle| U_{cT} + U_{vT}\middle|\mathcal{Y}_{c'}^{JM}\right\rangle_{\xi,\hat{R}}. \tag{8.46}$$

Equation (8.45) is the central computational object. The off-diagonal matrix elements contain excitation, breakup, de-excitation, and continuum–continuum coupling on equal footing.

The discarded space generates the exact correction

$$\Sigma_N(E) = P_N H Q_N \frac{1}{E - Q_N H Q_N + \mathrm{i}0} Q_N H P_N. \tag{8.47}$$

CDCC neglects Σ_N only after moving the dominant configurations into P_N. Convergence is therefore a statement that matrix elements of Σ_N relevant to the desired observables have become small, not that the continuum has ceased to exist.

8.2.3 Bin discretization

For a two-body projectile, a momentum-bin state in partial wave α is

$$\Phi_{n\alpha}^{\mathrm{bin}} = \frac{1}{\sqrt{N_{n\alpha}}} \int_{k_{n-1}}^{k_n} f_{n\alpha}(k)\Phi_{k\alpha}\,\mathrm{d}k, \tag{8.48}$$

with

$$N_{n\alpha} = \int_{k_{n-1}}^{k_n} |f_{n\alpha}(k)|^2\,\mathrm{d}k. \tag{8.49}$$

Nonoverlapping bins are orthonormal if the continuum states are delta normalized. A constant f represents a simple average; a phase such as $\mathrm{e}^{-\mathrm{i}\delta_\alpha(k)}$ can reduce rapid scattering-phase variation within the bin. Resonant bins may be narrowed around a phase-shift rise, but the bin width must remain finite until all continuum-normalized quantities have been combined.

The finite resolution has a direct-integral meaning. The characteristic functions of the bins generate a finite-dimensional subspace of $L^2([0, k_{\max}], \mathrm{d}k)$. Refining the partition produces strong convergence to the identity on square-integrable wave packets. It does not produce norm convergence on the whole continuum Hilbert space. This is the same distinction that makes an individual $|k\rangle$ distributional.

8.2.4 Pseudostate discretization and the Gaussian expansion method

For a many-body projectile, exact continuum wave functions are expensive and carry several momenta. The pseudostate method diagonalizes h_P in a finite L^2 basis,

$$\sum_{j=1}^{N_b} \langle\varphi_i|h_P|\varphi_j\rangle c_j^{(n)} = \epsilon_n \sum_{j=1}^{N_b} \langle\varphi_i|\varphi_j\rangle c_j^{(n)}. \tag{8.50}$$

Negative eigenvalues approximate bound states; positive eigenvalues provide quadrature-like samples of the continuum as seen by the chosen basis and operators. They are not physical bound levels. Their density changes with the basis and is itself useful information only after smoothing.

The Gaussian expansion method (GEM) uses ranges in geometric progression [101],

$$\varphi_{nlm}(\boldsymbol{r}) = N_{nl} r^l \mathrm{e}^{-(r/r_n)^2} Y_{lm}(\hat{\boldsymbol{r}}), \quad r_n = r_1 a^{n-1}. \tag{8.51}$$

Short and long ranges are then covered with relatively few functions. For a three-cluster projectile, products of Gaussians in several Jacobi coordinate sets efficiently represent both compact correlations and rearrangement tails. Complex-range Gaussians can improve oscillatory continuum resolution, but their overlap matrices require careful conditioning.

8.2.5 Open, closed, and Coulomb-distorted channels

For a channel with projectile energy ϵ_c, define

$$E_c = E_{\mathrm{tot}} - \epsilon_c, \qquad K_c = \sqrt{2\mu_R E_c}/\hbar. \tag{8.52}$$

If $E_c > 0$, the channel is open. With Coulomb interactions, the asymptotic condition for incidence in c_0 is

$$\chi_c^J(R) \longrightarrow \frac{\mathrm{i}}{2}\left[H_{L_c}^{(-)}(\eta_c, K_c R)\delta_{cc_0} - \sqrt{\frac{K_{c_0}}{K_c}} S_{cc_0}^J H_{L_c}^{(+)}(\eta_c, K_c R)\right]. \tag{8.53}$$

The normalization factor ensures flux normalization. For a neutral channel, $H_L^{(\pm)}$ reduce to spherical Hankel combinations. This is a concrete instance of the Stage II lesson: a charged channel is compared with a Coulomb wave, not a plane wave.

If $E_c < 0$, write $K_c = \mathrm{i}\kappa_c$ with $\kappa_c > 0$ and impose the decaying Whittaker solution,

$$\chi_c^J(R) \longrightarrow C_c W_{-\eta_c, L_c+1/2}(2\kappa_c R). \tag{8.54}$$

Closed channels carry no asymptotic outgoing flux, but they alter open-channel scattering through virtual transitions. Omitting them simply because they are not directly detected can be a large error at low collision energy.

Flux conservation supplies a stringent check when all interactions are real:

$$\sum_{c\,\mathrm{open}} |S_{cc_0}^J|^2 = 1. \tag{8.55}$$

For optical interactions the deficit equals absorption into eliminated channels. Numerically, one must distinguish that physical deficit from loss caused by

insufficient matching radius or an ill-conditioned basis.

8.2.6 Multipole expansion of the coupling

The fragment–target potentials depend on both R and internal coordinates. For a central fragment potential,

$$U_{xT}(|\boldsymbol{R} + \alpha_x \boldsymbol{r}|) = \sum_{\lambda\mu} \mathcal{U}_{x\lambda}(R, r) Y_{\lambda\mu}(\hat{R}) Y^*_{\lambda\mu}(\hat{r}), \tag{8.56}$$

where $\alpha_v = m_c/m_P$ and $\alpha_c = -m_v/m_P$. Angular momentum algebra reduces Eq. (8.46) to radial transition densities and Clebsch–Gordan, $6j$, and $9j$ coefficients. The long-range Coulomb multipoles behave as

$$\mathcal{U}^C_\lambda(R, r) \sim \frac{r^\lambda}{R^{\lambda+1}}, \qquad r < R, \tag{8.57}$$

so electric dipole or quadrupole breakup can couple to very large R. Convergence in matching radius and projectile excitation energy must therefore be tested together.

The diagonal monopole contains the projectile–target Coulomb comparison potential. Subtracting it before numerical propagation and restoring its known Coulomb functions in Eq. (8.53) prevents the long-range phase from being mistaken for a short-range coupling.

8.2.7 Three-cluster projectiles and four-body CDCC

Now let $P = a + b + c$. The projectile plus target is a four-body reaction system. A Jacobi set, for example,

$$\boldsymbol{x} = \boldsymbol{r}_b - \boldsymbol{r}_a, \qquad \boldsymbol{y} = \boldsymbol{r}_c - \frac{m_a \boldsymbol{r}_a + m_b \boldsymbol{r}_b}{m_a + m_b}, \tag{8.58}$$

gives

$$h_P = K_x + K_y + V_{ab} + V_{bc} + V_{ca} + V_{3b}. \tag{8.59}$$

The optional effective three-body interaction V_{3b} represents correlations not reproduced by pairwise cluster interactions and is calibrated only within a declared structure model.

There are three Jacobi rearrangement sets. A basis restricted to one set may resolve one clusterization well and another poorly. GEM therefore uses

the union

$$\Phi_{nI} = \sum_{c=1}^{3} \sum_{\alpha_c} C^{(c)}_{n\alpha_c} \left[\varphi^{(c)}_{n_x l_x}(\boldsymbol{x}_c) \otimes \varphi^{(c)}_{n_y l_y}(\boldsymbol{y}_c) \right]_I , \tag{8.60}$$

followed by antisymmetrization or Pauli projection as required. Diagonalizing h_P generates a ground state, physical resonances represented by stabilized pseudostates, and nonresonant continuum pseudostates. Inserting these states into Eq. (8.43) gives four-body CDCC [120, 121].

The name counts particles in the reaction Hamiltonian, not the number of coupled radial equations. A three-body projectile may yield thousands of channels after angular momentum coupling. Sparsity, selection rules, and model-space diagnostics are therefore part of the physics calculation.

8.2.8 Folding interactions and transition densities

For nucleon scattering from a composite projectile, a semi-microscopic coupling can be built by folding an effective nucleon–nucleon interaction with projectile transition densities. Schematically,

$$U^J_{cc'}(R) = \sum_{\tau=p,n} \int \mathrm{d}^3 s \, \rho^{cc'}_\tau(\boldsymbol{s}) g_{N\tau}(\boldsymbol{R} - \boldsymbol{s}; \rho, E), \tag{8.61}$$

where

$$\rho^{cc'}_\tau(\boldsymbol{s}) = \langle \Phi_c | \sum_{i \in \tau} \delta(\boldsymbol{s} - \boldsymbol{s}_i) | \Phi_{c'} \rangle. \tag{8.62}$$

The g matrix summarizes in-medium multiple scattering. A phenomenological renormalization

$$g \mapsto N_V \,\mathrm{Re}\, g + \mathrm{i} N_W \,\mathrm{Im}\, g \tag{8.63}$$

must be interpreted as model calibration, not as the monodromy renormalization of Stage V. The identical word “renormalization” refers to different operations; naming the varied scale and the invariant observable removes the ambiguity. The JLM interaction is a standard example [122].

8.2.9 From discrete breakup strengths to a continuous spectrum

The CDCC equations return transition amplitudes T_n to normalized pseudostates. An experiment resolves continuum energy and fragment angles, so the discrete amplitudes must be embedded back into the continuum. If $\Phi^{(-)}_{\epsilon\alpha}$

is the exact projectile scattering state, then

$$T_\alpha(\epsilon) \approx \sum_{n=1}^{N} \langle \Phi_{\epsilon\alpha}^{(-)} | \Phi_n \rangle T_n. \tag{8.64}$$

For a two-cluster projectile these overlaps can be calculated directly. For a three-cluster continuum, that approach is as hard as the original few-body scattering problem.

Complex scaling replaces the oscillatory continuum Green function by an L^2 spectral expansion. Start from the Lippmann–Schwinger state

$$|\Phi_\epsilon^{(-)}\rangle = |\phi_0\rangle + \frac{1}{\epsilon - h_P - \mathrm{i}0} V |\phi_0\rangle. \tag{8.65}$$

For dilation-analytic interactions,

$$\frac{1}{\epsilon - h_P - \mathrm{i}0} = U^{-1}(\theta) \frac{1}{\epsilon - h_P^\theta} U(\theta), \tag{8.66}$$

when the rotation exposes the required boundary value. Expanding the scaled resolvent in biorthogonal eigenvectors,

$$\frac{1}{\epsilon - h_P^\theta} \approx \sum_\nu \frac{|\Phi_\nu^\theta\rangle \langle \widetilde{\Phi}_\nu^\theta|}{\epsilon - \epsilon_\nu^\theta}, \tag{8.67}$$

turns the smoothing overlap into finite L^2 matrix elements. This is the complex-scaled Lippmann–Schwinger (CSLS) construction [123, 124].

For an inclusive energy distribution one may avoid constructing amplitudes channel by channel. If $|F\rangle = \sum_n T_n |\Phi_n\rangle$ is the projectile source produced by the reaction, the response is

$$\begin{aligned} \frac{\mathrm{d}\sigma}{\mathrm{d}\epsilon} &\propto -\frac{1}{\pi} \operatorname{Im} \langle F | (\epsilon - h_P + \mathrm{i}0)^{-1} | F \rangle \\ &\approx -\frac{1}{\pi} \operatorname{Im} \sum_\nu \frac{\langle F | U^{-1}(\theta) | \Phi_\nu^\theta \rangle \langle \widetilde{\Phi}_\nu^\theta | U(\theta) | F \rangle}{\epsilon - \epsilon_\nu^\theta}. \end{aligned} \tag{8.68}$$

This is the same resolvent identity used for continuum level density. The reaction determines the source F; the intrinsic complex-scaled spectrum determines how that source is distributed among poles and continuum.

8.2.10 Selecting a rearrangement channel

For three fragments, "the breakup cross section" is not a single asymptotic channel. One may observe sequential breakup through a two-body resonance, direct three-body breakup, or a different cluster partition. Let $h_P = h_\alpha + K_\alpha + V_\alpha^{\mathrm{rem}}$ be adapted to a chosen partition. The CSLS state constructed with the corresponding channel Hamiltonian $h_\alpha + K_\alpha$ projects the common CDCC source onto that asymptotic arrangement. Symbolically,

$$T_\alpha(\epsilon, \Omega) = \sum_n \langle \Phi^{(-)}_{\epsilon\Omega,\alpha} | \Phi_n \rangle T_n. \tag{8.69}$$

Summing mutually orthogonal arrangements is safe only when their asymptotic spaces and overlap regions have been defined so that double counting is controlled.

This point is where nuclear few-body scattering meets the long-range problem of Stage II. With three charged fragments, different cluster regions have different logarithmic Coulomb phases. A finite internal pseudostate basis can calculate observables over a controlled interaction region, but it does not constitute a proof of one uniform three-body Coulomb asymptotic formula. The comparison dynamics and channel atlas must be declared separately.

8.2.11 Observables from the channel S matrix

For spinless notation, the scattering amplitude from c_0 to an open channel c has the partial-wave form

$$f_{cc_0}(\Omega) = f_C(\Omega)\delta_{cc_0} + \frac{2\pi}{\mathrm{i}\sqrt{K_c K_{c_0}}} \sum_{JMLM_L} \mathcal{A}_c^{JM}(\Omega)[S^J_{cc_0} - \delta_{cc_0}], \tag{8.70}$$

where $\mathcal{A}$ contains the angular momentum coefficients and Coulomb phases. The differential cross section contains the flux ratio,

$$\frac{\mathrm{d}\sigma_{c\leftarrow c_0}}{\mathrm{d}\Omega} = \frac{K_c}{K_{c_0}} |f_{cc_0}(\Omega)|^2. \tag{8.71}$$

For pseudostates, summing Eq. (8.71) over a finite energy interval is meaningful after convergence. A density per unit energy requires Eq. (8.64) or Eq. (8.68); dividing a discrete value by an arbitrary pseudostate spacing is not a basis-independent observable.

The total reaction cross section for entrance wave number K_0 is

$$\sigma_R = \frac{\pi}{K_0^2} \sum_J (2J+1) \left[1 - \sum_{c\,\text{open}} |S^J_{cc_0}|^2 \right] \tag{8.72}$$

in a simple spin convention. With real couplings the bracket vanishes after all retained open channels are included. With absorptive optical potentials it measures loss into channels outside the explicit CDCC space.

8.2.12 CDCC as a spectral quadrature

The direct-integral view gives a compact mathematical statement of the method. Let $P(\Delta)$ be the projectile spectral measure. For functions of h_P tested between localized form factors,

$$\langle f|g(h_P)P([0,E_{\max}])|g\rangle = \int_0^{E_{\max}} g(\epsilon)\,\mathrm{d}\mu_{fg}(\epsilon). \tag{8.73}$$

A pseudostate model replaces this by a quadrature

$$\int_0^{E_{\max}} g(\epsilon)\,\mathrm{d}\mu_{fg}(\epsilon) \approx \sum_{n=1}^{N} g(\epsilon_n)\langle f|\Phi_n\rangle\langle\Phi_n|g\rangle. \tag{8.74}$$

Accuracy is therefore operator and source dependent. A model space that converges an elastic amplitude need not resolve a sharply differential three-fragment observable. Conversely, pseudostate eigenvalues need not approximate every point of the continuum uniformly for the tested integral to converge rapidly.

Complex scaling deforms the quadrature contour. Stable discrete poles remain fixed while the nonresonant quadrature points follow the rotated cut. This is precisely the pole-versus-representation separation established in Stage IV.

8.2.13 Connection data and coupled-channel exact WKB

For N retained channels, Eq. (8.45) is a matrix Schrödinger equation. Fundamental solution matrices replace scalar WKB branches, and the asymptotic coefficients form vectors. A global transfer matrix has blocks

$$\begin{pmatrix} \boldsymbol{a}^R_{\text{out}} \\ \boldsymbol{a}^R_{\text{in}} \end{pmatrix} = \mathcal{M}(E) \begin{pmatrix} \boldsymbol{a}^L_{\text{out}} \\ \boldsymbol{a}^L_{\text{in}} \end{pmatrix}. \tag{8.75}$$

A resonance satisfies the determinant condition

$$\det \mathcal{C}_{\mathrm{in}}(E) = 0, \tag{8.76}$$

where $\mathcal{C}_{\mathrm{in}}$ is the block multiplying prohibited incoming components. CDCC approximates this matrix connection problem on the real axis and can be analytically continued or complex scaled. Exact WKB supplies a nonperturbative construction when the matrix spectral curve and its Stokes data can be controlled. The scalar theory of Stage III is therefore the first member of a coupled-channel hierarchy rather than a separate subject.

The eigenvalues of the local potential matrix are sometimes called adiabatic surfaces. Their complex degeneracies generate nonadiabatic connection matrices. At a coalescence of resonant solutions, Eq. (8.76) has a multiple zero and the exceptional-point analysis of Stage VII applies. Few-body reaction theory, exact WKB, and non-Hermitian holonomy meet at the same determinant.

8.2.14 A reproducible convergence protocol

A CDCC result is accepted only after varying independent truncations. The minimum useful record is:

1. projectile Hamiltonian, Pauli prescription, and all fitted structure parameters;

2. Jacobi sets, internal partial waves, Gaussian ranges, and positive- energy cutoff;

3. projectile spins I, projectile–target orbital momenta L, total J, and coupling multipoles retained;

4. matching radius and radial mesh or propagator tolerance;

5. open and closed channel boundary conditions, including Coulomb functions and branch conventions;

6. optical or folding interactions and the density and energy at which they are evaluated;

7. convergence tables in $E_{\max}$, internal angular momentum, basis density, $L_{\max}$, $J_{\max}$, and matching radius;

8. flux or reaction-cross-section balance;

9. smoothing angle, scaled-basis size, and independence of the final continuous response from these auxiliary choices.

Vary one family of cutoffs at a time and then repeat selected variations jointly, because Coulomb multipoles can correlate the required excitation cutoff with the matching radius. A stable pole, a converged integrated strength, and a converged differential line shape are three different claims and require three different tests.

Checkpoint

Given a cluster Hamiltonian and fragment–target interactions, the reader should now be able to construct P_N, derive Eq. (8.45), distinguish open from closed channels, calculate the coupling form factors, and explain why pseudostate strengths must be smoothed before comparison with an energy-differential measurement. The next Laboratory performs these steps for ^{6}Li and for a $p+p+{}^7$Be description of ^{9}C.

8.3 Calculation laboratory VI-A: A broad ^{6}He resonance from pole to observable

Calculation route

Prerequisites. The three-body CDCC projection, complex-scaled resolution of the identity, Fredholm/Riesz pole projectors, and source-dependent response derived in Stages I–IV.

Calculation goal. Construct an $\alpha+n+n$ model of ^{6}He, isolate its 2^+ poles without deleting the nonresonant continuum, and propagate the same pole projector into proton inelastic scattering and a two-neutron invariant-mass distribution.

Completion criterion. Distinguish a stable complex pole, fragmented CDCC pseudostates, a coherent resonance doorway, and a measured line shape.

This Laboratory uses one chain of calculations to connect the mathematical structure of resonance to a nuclear observable. The published steps are the analysis of the broad 2^+_2 contribution in $^6\mathrm{He}(p,p')$, a model-space-

independent treatment of a fragmented 2_1^+ doorway, and a resonance-only decay distribution used to diagnose a dineutron correlation [125–128]. Here they are reorganized as one calculation rather than three applications.

The exact-WKB viewpoint supplies the organizing invariant. In a coupled radial representation the resonance is a zero of an incoming connection determinant. Complex scaling realizes that zero as a finite-rank Riesz eigenspace. CDCC represents the physical continuum by a quadrature. The reaction supplies a source and the detector selects a functional of the resulting state. Each layer has auxiliary choices, but the pole, its total root space, and its tested residue must agree in the converged limit.

8.3.1 Station A: choose Jacobi coordinates before choosing a basis

Treat ^{6}He as an inert α core and two valence neutrons. Let $\boldsymbol{r}_\alpha, \boldsymbol{r}_1, \boldsymbol{r}_2$ be their laboratory coordinates. In the Jacobi set adapted to the neutron pair define

$$\boldsymbol{x}_1 = \boldsymbol{r}_2 - \boldsymbol{r}_1, \tag{8.77}$$

$$\boldsymbol{y}_1 = \boldsymbol{r}_\alpha - \frac{m_n \boldsymbol{r}_1 + m_n \boldsymbol{r}_2}{2m_n}. \tag{8.78}$$

The two rearranged sets isolate an $\alpha + n$ pair, for example

$$\boldsymbol{x}_2 = \boldsymbol{r}_1 - \boldsymbol{r}_\alpha, \tag{8.79}$$

$$\boldsymbol{y}_2 = \boldsymbol{r}_2 - \frac{m_\alpha \boldsymbol{r}_\alpha + m_n \boldsymbol{r}_1}{m_\alpha + m_n}, \tag{8.80}$$

and set 3 is obtained by $1 \leftrightarrow 2$. Removing the center of mass gives

$$h_6 = K_{x_c} + K_{y_c} + V_{\alpha n}^{(1)} + V_{\alpha n}^{(2)} + V_{nn} + V_3 + V_{\mathrm{Pauli}}. \tag{8.81}$$

The equality is coordinate independent; the index c only chooses a useful representation of the kinetic energy and correlations.

The α core already occupies the $0s$ neutron orbit. A common orthogonality-condition realization is

$$V_{\mathrm{Pauli}} = \lambda_{\mathrm{P}} \sum_{i=1}^{2} |0s; \alpha n_i\rangle\langle 0s; \alpha n_i|, \qquad \lambda_{\mathrm{P}} \gg |E|. \tag{8.82}$$

The large finite value must be varied until physical eigenvalues and transition

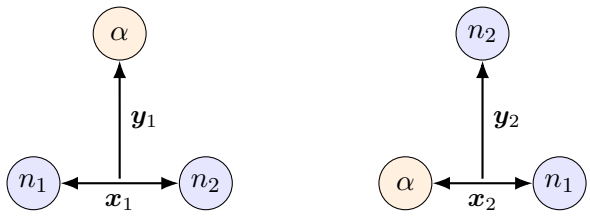

dineutron set $\qquad\qquad$ αn set

Figure 8.1: Two of the three Jacobi sets for $\alpha + n + n$. The dineutron invariant mass is simplest in set 1, whereas sequential decay through an αn correlation is simplest in sets 2 and 3. A converged wave function uses all rearrangements.

densities are insensitive to it. Merely deleting a basis vector in one Jacobi set does not guarantee that both equivalent αn Pauli components have been removed.

Expand a state of total spin I as

$$\Phi_{nIm_I}(\xi) = \sum_{c=1}^{3} \sum_{\alpha_c} C^{(c)}_{n\alpha_c} \mathcal{A}_{12} \mathcal{Y}^{(c)}_{\alpha_c I m_I}(\xi), \tag{8.83}$$

$$\mathcal{Y}^{(c)}_{\alpha_c I m_I} = \Big[[\varphi^{(c)}_{n_x l_x}(x_c) \otimes \varphi^{(c)}_{n_y l_y}(y_c)]_\Lambda \otimes \chi_S \Big]_{I m_I}. \tag{8.84}$$

Here $\chi_S = [\chi_{1/2}(1) \otimes \chi_{1/2}(2)]_S$ and $\mathcal{A}_{12}$ antisymmetrizes the neutrons. Gaussian ranges in each coordinate are placed on geometric meshes,

$$r_n = r_1 a^{n-1}, \qquad n = 1, \ldots, N, \tag{8.85}$$

and complex-range pairs may be added when oscillatory continuum structure requires them. Diagonalization of h_6 in this L^2 space gives the ground state and positive-energy pseudostates.

8.3.2 Station B: expose poles with a common complex dilation

Apply the same dilation to both internal Jacobi coordinates,

$$\boldsymbol{x}_c \mapsto \boldsymbol{x}_c e^{i\theta}, \qquad \boldsymbol{y}_c \mapsto \boldsymbol{y}_c e^{i\theta}, \qquad h_6^\theta = U(\theta) h_6 U(\theta)^{-1}. \tag{8.86}$$

Diagonalize the complex-symmetric matrix with the same antisymmetrization and Pauli prescription as on the real axis,

$$h_6^\theta|\Phi_\nu^\theta\rangle = E_\nu^\theta|\Phi_\nu^\theta\rangle, \qquad \langle\widetilde{\Phi}_\nu^\theta|h_6^\theta = E_\nu^\theta\langle\widetilde{\Phi}_\nu^\theta|. \tag{8.87}$$

The biorthogonal normalization is

$$\langle\widetilde{\Phi}_\nu^\theta|\Phi_{\nu'}^\theta\rangle = \delta_{\nu\nu'}. \tag{8.88}$$

For a complex-symmetric representation, the left vector is associated with the transpose bilinear form, not with an ordinary Hermitian probability norm.

In a finite basis the extended resolution is approximated by

$$\mathbf{1}_N \approx \sum_{\nu=1}^{N} |\Phi_\nu^\theta\rangle\langle\widetilde{\Phi}_\nu^\theta|. \tag{8.89}$$

Bound states remain on the real axis, exposed resonance poles remain stable as θ and the basis are varied, and nonresonant eigenvalues follow the rotated two- and three-body cuts. The classification is made by tracking clusters under changes of representation, not by drawing a fixed wedge after one diagonalization.

The 2_2^+ pole reported in the $\alpha+n+n$ model used for the proton inelastic-scattering analysis was

$$z_{2_2^+} = E_{\mathrm{R}} - \frac{\mathrm{i}}{2}\Gamma, \qquad E_{\mathrm{R}} = 2.25\ \mathrm{MeV}, \qquad \Gamma = 3.75\ \mathrm{MeV} \tag{8.90}$$

relative to the adopted three-body threshold [125]. Since Γ is comparable with E_{R}, this is a broad pole. A narrow Lorentzian approximation is not justified merely because the pole is isolated after complex scaling.

8.3.3 Station C: derive proton–^{6}He CDCC from the same internal model

Let $\boldsymbol{R}$ be the proton–projectile separation. With fragment–proton interactions $U_{p\alpha}, U_{pn_1}, U_{pn_2}$, the reaction Hamiltonian is

$$H = K_R + h_6 + U_{p\alpha} + U_{pn_1} + U_{pn_2}. \tag{8.91}$$

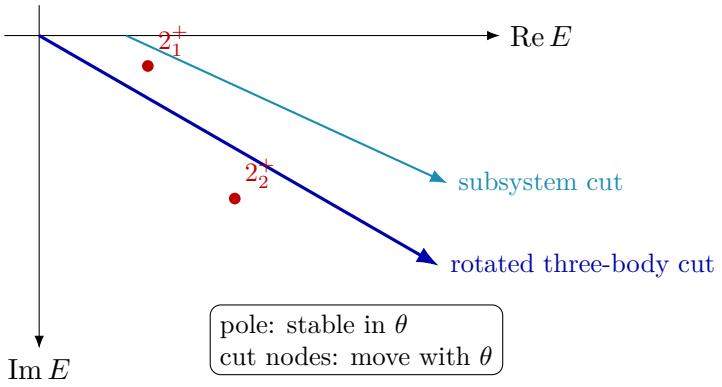

Figure 8.2: Schematic complex-energy classification for 2^+ states. The plotted pole labels are conceptual; a calculation must determine each threshold ray and scaling-angle window from its Hamiltonian.

Use the real-axis pseudostates of h_6 to define the CDCC projector

$$P_N = \sum_{nIm_I \in \mathcal{M}} |\Phi_{nIm_I}\rangle\langle\Phi_{nIm_I}|, \tag{8.92}$$

where $\mathcal{M}$ declares excitation, spin, and basis cutoffs. Expand

$$\Psi^{JM}(\boldsymbol{R}, \xi) = \frac{1}{R} \sum_{nIL} \chi^J_{nIL}(R)[\Phi_{nI}(\xi) \otimes Y_L(\widehat{\boldsymbol{R}})]_{JM}. \tag{8.93}$$

Projection of $(H - E_{\rm tot})\Psi = 0$ gives

$$\left[-\frac{\hbar^2}{2\mu_R}\left(\frac{\mathrm{d}^2}{\mathrm{d}R^2} - \frac{L(L+1)}{R^2}\right) + \epsilon_{nI} - E_{\rm tot}\right] \chi^J_{nIL}(R) = -\sum_{n'I'L'} U^J_{nIL,n'I'L'}(R)\chi^J_{n'I'L'}(R), \tag{8.94}$$

with

$$U^J_{cc'}(R) = \langle[\Phi_{nI} \otimes Y_L]_J|\, U_{p\alpha} + U_{pn_1} + U_{pn_2}\,|[\Phi_{n'I'} \otimes Y_{L'}]_J\rangle_{\xi,\widehat{R}}\,. \tag{8.95}$$

Use outgoing Coulomb or free channel functions only for open channels and decaying functions for closed channels. The positive internal energy of a pseudostate does not by itself make the relative channel open; the relevant quantity is $E_{\rm tot} - \epsilon_{nI}$.

Solving Eq. (8.94) produces discrete transition amplitudes T_n to pseu-

dostates. They are coefficients of the finite model-space source

$$|F\rangle = \sum_{n\in\mathcal{M}} T_n|\Phi_n\rangle, \tag{8.96}$$

not a continuous spectrum. A differential energy distribution requires the CSLS overlap or the resolvent response of Eq. (8.68).

8.3.4 Station D: calculate the continuous response before naming a peak

For a selected spin parity, complex scaling gives

$$\begin{aligned}\frac{\mathrm{d}\sigma}{\mathrm{d}\epsilon} &\propto -\frac{1}{\pi}\,\mathrm{Im}\langle F|(\epsilon - h_6 + \mathrm{i}0)^{-1}|F\rangle \\ &\approx -\frac{1}{\pi}\,\mathrm{Im}\sum_{\nu}\frac{M^{\theta}_{\nu}\widetilde{M}^{\theta}_{\nu}}{\epsilon - E^{\theta}_{\nu}},\end{aligned} \tag{8.97}$$

$$M^{\theta}_{\nu} = \langle F|U(\theta)^{-1}|\Phi^{\theta}_{\nu}\rangle, \qquad \widetilde{M}^{\theta}_{\nu} = \langle\widetilde{\Phi}^{\theta}_{\nu}|U(\theta)|F\rangle. \tag{8.98}$$

The full sum is independent of θ and of the L^2 representation in the converged limit. A selected isolated term defines the response of one Riesz pole to this source,

$$S^{(F)}_{\mathrm{R}}(\epsilon) = -\frac{1}{\pi}\,\mathrm{Im}\,\frac{M^{\theta}_{\mathrm{R}}\widetilde{M}^{\theta}_{\mathrm{R}}}{\epsilon - z_{\mathrm{R}}}. \tag{8.99}$$

The remainder is the nonresonant continuum and all other poles in the chosen contour representation.

For the broad 2^+_2 state, the calculation of Ref. [125] shows why both terms are needed. The pole contributes materially to the 2^+ energy spectrum, but the nonresonant continuum changes the line shape from which that contribution is inferred. Equation (8.99) is source dependent and need not be a positive Lorentzian by itself. The observable is the coherent, converged total in Eq. (8.97).

The following checks are distinct and all must be performed:

(a) z_{R} is stable under θ and scaled-basis changes;

(b) the product $M^{\theta}_{\mathrm{R}}\widetilde{M}^{\theta}_{\mathrm{R}}$ is stable in the same window;

(c) the full real-axis response is stable when rotated-cut states are added;

(d) the angular and energy integrations match the declared experimental acceptance.

A stable complex energy alone establishes only (a).

8.3.5 Station E: replace a fragmented energy window by a rank-one pole projector

In a real L^2 diagonalization, a resonance strength is generally spread over several pseudostates. Let $\mathcal{I}_R$ denote indices in a chosen energy window. The naive one-step quantity

$$\sigma^{(1)}_{R,\mathrm{naive}} \propto \sum_{i\in\mathcal{I}_R} |T^{(1)}_i|^2 \tag{8.100}$$

depends on the basis density and on the window boundary. When the basis is enlarged, one physical doorway can fragment into more vectors, so the phrase "turn off multistep coupling to every resonant state" becomes representation dependent.

Complex scaling supplies the missing invariant. For an isolated pole define the Riesz projector

$$P^\theta_R = |\Phi^\theta_R\rangle\langle\widetilde{\Phi}^\theta_R|, \qquad \mathcal{P}_R = U(\theta)^{-1} P^\theta_R U(\theta). \tag{8.101}$$

The pullback is understood between analytic test spaces; it is not an orthogonal Hilbert-space probability projector. Its representation in the real pseudostate space is the coherent rank-one matrix

$$(\mathcal{P}^{(N)}_R)_{ij} = \langle\Phi_i|U^{-1}(\theta)|\Phi^\theta_R\rangle\langle\widetilde{\Phi}^\theta_R|U(\theta)|\Phi_j\rangle. \tag{8.102}$$

All fragmented components and their phases are retained. The resonance doorway generated from the entrance channel is

$$|F_R\rangle = \mathcal{P}^{(N)}_R|F\rangle. \tag{8.103}$$

One-step and multistep comparisons should be made with this doorway held fixed while the pseudostate quadrature is refined. This is the projection logic behind the model-space-independent construction used in Ref. [126].

The full CDCC amplitude includes paths such as

$$|0\rangle \to |F_R\rangle, \qquad |0\rangle \to Q_R|F\rangle \to |F_R\rangle, \qquad |0\rangle \to |F_R\rangle \to Q_R|F\rangle, \tag{8.104}$$

where $Q_R = P_N - \mathcal{P}^{(N)}_R$ in the tested model space. Turning the second and third paths on and off diagnoses multistep coupling between the ground state,

the 2_1^+ doorway, and the nonresonant continuum. Changing the number of basis vectors inside an arbitrary energy window does not.

Domain or asymptotic warning

The operator $\mathcal{P}_R^{(N)}$ is generally non-Hermitian and may not be idempotent to machine precision in an incomplete basis. Check $\|(\mathcal{P}_R^{(N)})^2 - \mathcal{P}_R^{(N)}\|$ together with the stability of its tested matrix elements. Replacing it by an incoherent diagonal sum over $i \in \mathcal{I}_R$ destroys the pole phases and returns to Eq. (8.100).

8.3.6 Station F: construct a resonance-only double-differential breakup distribution

To study the decay of the 2_1^+ state, use Jacobi momenta conjugate to Fig. 8.1. In the dineutron set let

$$\varepsilon_{nn} = \frac{\hbar^2 k_x^2}{2\mu_x}, \qquad \varepsilon_{\alpha,nn} = \frac{\hbar^2 k_y^2}{2\mu_y}, \tag{8.105}$$

$$\varepsilon = \varepsilon_{nn} + \varepsilon_{\alpha,nn}. \tag{8.106}$$

The smoothed breakup amplitude is

$$T(\boldsymbol{k}_x, \boldsymbol{k}_y) = \sum_n \langle \Psi^{(-)}_{\boldsymbol{k}_x \boldsymbol{k}_y} | \Phi_n \rangle T_n. \tag{8.107}$$

The double-differential breakup cross section has the schematic form

$$\frac{\mathrm{d}^2\sigma}{\mathrm{d}\varepsilon_{nn}\mathrm{d}\varepsilon_{\alpha,nn}} = \int \mathrm{d}\Omega_x \mathrm{d}\Omega_y \, \mathcal{J}(k_x, k_y) |T(\boldsymbol{k}_x, \boldsymbol{k}_y)|^2, \tag{8.108}$$

where $\mathcal{J}$ contains the declared phase-space and incident-flux normalization. A resonance-only amplitude is constructed coherently by inserting $\mathcal{P}_R^{(N)}$ between the CDCC source and the CSLS detector,

$$T_R(\boldsymbol{k}_x, \boldsymbol{k}_y) = \langle \Psi^{(-)}_{\boldsymbol{k}_x \boldsymbol{k}_y} | \mathcal{P}_R^{(N)} | F \rangle. \tag{8.109}$$

Use T_R, not a difference of two separately normalized cross sections, in Eq. (8.108) to define the resonance-only DDBUX.

Project the two-neutron spin before squaring,

$$T_R = T_R^{S=0} + T_R^{S=1}. \tag{8.110}$$

Antisymmetry connects spin and spatial parity, so the two amplitudes must be constructed with consistent partial waves. The $S = 0$ part of the calculated 2_1^+ resonance distribution develops strength near the shoulder in the ε_{nn} spectrum identified in Ref. [127]. The inference of a dineutron correlation is therefore a statement about a resonance-projected, spin-resolved decay functional, not about the expectation value of r_{nn} in an unregularized Gamow wave function.

Final-state interaction is essential. Replacing $\langle \Psi^{(-)}|$ by a plane wave tests how much of the shoulder is generated by the decay interaction rather than by the pole residue. The following four curves form a useful diagnostic set:

(i) full $|T|^2$ with final-state interaction;

(ii) pole-projected $|T_R|^2$ with final-state interaction;

(iii) the $S = 0$ component of (ii);

(iv) the plane-wave or interaction-switched counterpart of (ii).

Only differences calculated with identical phase space, acceptance, and normalization isolate the intended physics.

8.3.7 Station G: identify the exact-WKB invariant inside the many-channel calculation

After hyperspherical or channel expansion, the internal three-body equation is a coupled radial system. Let $\mathcal{C}_{\rm in}(E)$ be its incoming connection block. A simple pole satisfies

$$\mathcal{C}_{\rm in}(z_R)u_R = 0, \qquad v_R^\dagger \mathcal{C}_{\rm in}(z_R) = 0, \tag{8.111}$$

and has invariant derivative denominator

$$\mathcal{N}_R = v_R^\dagger \mathcal{C}'_{\rm in}(z_R)u_R. \tag{8.112}$$

The published ^{6}He calculations obtained the pole projector by complex scaling rather than by an explicit exact-WKB construction of this large matrix connection problem. Equation (8.112) nevertheless states what must

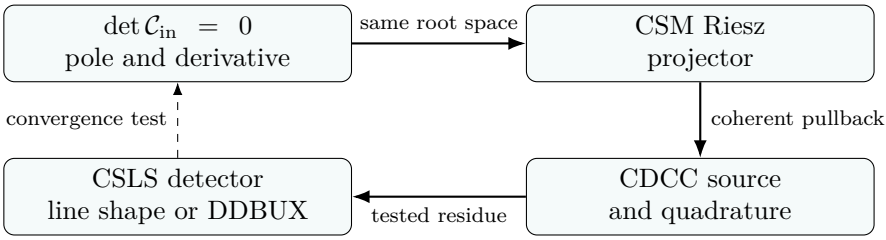

Figure 8.3: The ^{6}He calculation as one connection problem realized in several spaces. The arrows do not identify individual pseudostate eigenvalues with poles; they transport a finite-rank root space and its source–detector residue.

be representation independent. The CSM Riesz projector, the coherent pseudostate projector in Eq. (8.102), and the pole term in Eq. (8.97) are numerical realizations of the same null space and derivative residue.

This viewpoint suggests a concrete development program rather than a formal identification:

1. diagonalize the local coupled-channel potential to define adiabatic sheets and locate their complex degeneracies;

2. construct matrix exact-WKB transport on a controlled truncation;

3. compare its determinant zero and derivative with the CSM pole and Riesz projector;

4. increase the hyperspherical/channel space while testing the physical source–detector residue;

5. retain the nonresonant contour contribution when forming the real-axis ^{6}He response.

The exact-WKB core of the book is therefore not an assertion that a scalar formula has already solved every few-body reaction. It is a criterion for which objects a many-body approximation must preserve.

8.3.8 Station H: convergence ledger

Record four groups of variations separately.

Structure space. Vary all Jacobi sets, l_x, l_y, Λ, S, I, Gaussian endpoints and densities, the three-body interaction, and $\lambda_{\rm P}$. Check the ground-state

energy and radius, low-energy transition strengths, and phase-relevant subsystem information before starting the reaction calculation.

Complex scaling. Vary θ, complex-range basis parameters, and the maximum radial range. Track each pole as a cluster, measure the residual $\|h_6^\theta \Phi_R^\theta - z_R \Phi_R^\theta\|$, and test both z_R and source–detector residues. Approaching a rotated cut can make a well-converged pole numerically ill conditioned even before it ceases to be exposed.

Reaction space. Vary the projectile excitation cutoff, projectile spins, coupling multipoles, proton–projectile orbital angular momentum, total J, matching radius, and radial mesh. Compare ground-state-only, open-channel, and open-plus-closed calculations with identical interactions.

Smoothing and decay. Vary the CSLS scaled basis independently of the CDCC basis, the binning used only for plotting, Jacobi rearrangements, final-state interactions, and the experimental angular acceptance. Verify that integrating the smoothed distribution reproduces the corresponding converged discrete or inclusive strength.

The minimum table for a claimed resonance observable is

object	auxiliary variation	invariant monitored	acceptance criterion
2^+ pole	θ, scaled basis, Jacobi space	z_R and Riesz rank	common stability window
pole strength	left/right normalization and source basis	$M_R \widetilde{M}_R$ or tested residue	stable complex value
CDCC amplitude	$E_{\max}$, I, L, J, R_{match}	open-channel S matrix and flux	tolerance declared per observable
energy spectrum	smoothing basis and plotting bins	continuous response and its integral	bin independence

object	auxiliary variation	invariant monitored	acceptance criterion
dineutron signal	Jacobi set, spin projection, final-state interaction	resonance-only DDBUX shoulder	stable under controlled alternatives

Laboratory checkpoint

Before continuing to lithium and beryllium-core reactions, the reader should be able to:

1. write all three α+n+n Jacobi sets and implement neutron antisymmetry and the αn Pauli projector;
2. distinguish a real-axis pseudostate resolution from the complex-scaled resolution in Eq. (8.89);
3. derive the CDCC equations (8.94) from Eq. (8.91);
4. construct the pole term and nonresonant remainder of Eq. (8.97);
5. explain why the coherent projector Eq. (8.102) is more stable than an energy-window sum;
6. form the resonance-only DDBUX with final-state interaction and a spin projection; and
7. state which quantity in the calculation corresponds to $v_R^\dagger \mathcal{C}'_{\rm in}(z_R) u_R$.

8.4 Calculation laboratory VI-B: Lithium projectiles and beryllium-core breakup

Calculation route

Prerequisites. The CDCC projection, three-cluster Jacobi coordinates, Gaussian pseudostates, Coulomb boundary conditions, folding interactions, CSLS smoothing, and overlap functions.

Calculation goal. Build the $\alpha + p + n$ model of ^{6}Li, the $p + p + {}^{7}$Be model of ^{9}C, and the $p + {}^{5}$He overlap used in proton knockout.

Completion criterion. Account separately for elastic, closed-channel, rearrangement-resolved, and overlap-sensitive observables and reproduce the published stability logic without treating pseudostates as physical levels.

This Laboratory turns the formal CDCC construction into three related nuclear calculations. The first asks how breakup channels of ^{6}Li alter nucleon elastic scattering. The second asks how a fragile ^{8}B subsystem changes the extraction of the astrophysical factor S_{18} from ^{9}C breakup. The third asks how a small s-wave component of the unbound ^{5}He subsystem can have a large effect in a kinematically selective knockout observable. The three problems use the same $\alpha + p + n$ or proton-rich three-cluster logic but probe different functionals of the wave function.

8.4.1 Station A: construct the $\alpha + p + n$ Hamiltonian of ^{6}Li

Choose three Jacobi rearrangement sets. In the set adapted to a deuteron-like $p + n$ pair,

$$\boldsymbol{x}_1 = \boldsymbol{r}_p - \boldsymbol{r}_n, \qquad \boldsymbol{y}_1 = \boldsymbol{r}_\alpha - \frac{m_p \boldsymbol{r}_p + m_n \boldsymbol{r}_n}{m_p + m_n}. \tag{8.113}$$

The other two sets isolate $\alpha + p$ and $\alpha + n$ correlations. After removing the center of mass, take

$$h_6 = K_{x_c} + K_{y_c} + V_{\alpha p} + V_{\alpha n} + V_{pn} + V_3, \tag{8.114}$$

where the equality holds in every Jacobi set after the corresponding kinetic coordinates are used. The cluster potentials must reproduce the two-body phase information in the partial waves relevant to the chosen energy window. A Pauli-forbidden α–nucleon orbit is removed by an orthogonality- condition projector or by a phase-equivalent interaction.

Expand a state of spin I as

$$\Phi_{nIm_I}(\xi) = \sum_{c=1}^{3} \sum_{\alpha_c} C^{(c)}_{n\alpha_c} \mathcal{A} \left[[\varphi^{(c)}_{n_x l_x}(x_c) \otimes \varphi^{(c)}_{n_y l_y}(y_c)]_\Lambda \otimes [\chi_p \otimes \chi_n]_S \right]_{Im_I}, \tag{8.115}$$

where $\mathcal{A}$ implements the required nucleon antisymmetry. Gaussian ranges are chosen geometrically and enlarged until the ground-state radius, binding energy, low-lying resonance stabilization pattern, and transition densities are

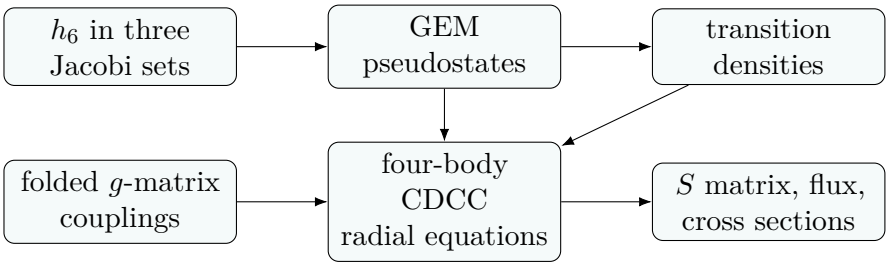

Figure 8.4: Dependency order for nucleon–^{6}Li four-body CDCC. A later change of the structure space must propagate through the transition densities and couplings before reaction observables are compared.

stable. Diagonalization gives

$$h_6 \Phi_{nIm_I} = \epsilon_{nI} \Phi_{nIm_I}. \tag{8.116}$$

Positive ϵ_{nI} label continuum pseudostates. In the calculation of Ref. [129], states up to a declared excitation cutoff are retained and convergence is checked rather than assigning a physical width to each positive eigenvalue.

8.4.2 Station B: derive nucleon–^{6}Li four-body CDCC

Let $\boldsymbol{R}$ point from ^{6}Li to the incident nucleon N. The reaction Hamiltonian is

$$H = K_R + h_6 + \sum_{i=1}^{6} g_{Ni}, \tag{8.117}$$

where the effective g_{Ni} is folded with the projectile transition density. Expand

$$\Psi^{JM}(\boldsymbol{R}, \xi) = \frac{1}{R} \sum_{nIL} \chi^J_{nIL}(R) \left[Phi_{nI}(\xi) \otimes Y_L(\hat{R}) \right]_{JM}. \tag{8.118}$$

With $c = (n, I, L)$, projection yields

$$\left[-\frac{\hbar^2}{2\mu} \left(\frac{\mathrm{d}^2}{\mathrm{d}R^2} - \frac{L(L+1)}{R^2} \right) + \epsilon_{nI} - E_{\mathrm{tot}} \right] \chi^J_c(R) = -\sum_{c'} U^J_{cc'}(R) \chi^J_{c'}(R). \tag{8.119}$$

The single-folding coupling is built from proton and neutron transition densities,

$$U^{J}_{cc'}(R) = \sum_{\tau=p,n} \int \mathrm{d}^3 s \, \rho^{cc'}_{\tau}(\boldsymbol{s}) g_{N\tau}(\boldsymbol{R} - \boldsymbol{s}; \rho, E). \tag{8.120}$$

The dependence of g on local density and incident energy must be evaluated with one stated prescription throughout the scan.

For the JLM form, write

$$g^{\mathrm{eff}}_{N\tau} = N_V \, \mathrm{Re}\, g^{\mathrm{JLM}}_{N\tau} + \mathrm{i} N_W \, \mathrm{Im}\, g^{\mathrm{JLM}}_{N\tau}. \tag{8.121}$$

The parameter study reported for nucleon–^{6}Li found a constant $N_V = 1.1$ and a smooth energy dependence of N_W; in the quoted energy convention the fitted form was

$$N_W(E) = 0.213 \ln E - 0.247. \tag{8.122}$$

This calibration gave a common description of proton and neutron elastic and integral observables over approximately 7–50 MeV [129]. Equation (8.122) is not a universal interaction: its energy units, density prescription, model space, and fitted dataset are part of its definition.

Open and closed channel test

Compute

$$E_{nI} = E_{\mathrm{tot}} - \epsilon_{nI}. \tag{8.123}$$

Use Coulomb incoming/outgoing functions for $E_{nI} > 0$ and a decaying Whittaker function for $E_{nI} \leq 0$. Then perform three calculations with identical potentials and numerical meshes:

(a) ground state only;

(b) all retained open projectile channels;

(c) open plus retained closed channels.

The difference between (a) and (c) is the net dynamical breakup coupling. The difference between (b) and (c) is a virtual closed-channel effect. Because a closed channel returns flux to the open sector, it should not be simulated by increasing an absorptive strength. At low incident energy this distinction is especially important; at higher energy the closed-channel correction becomes smaller in the reported model.

Convergence table to produce before plotting data

For each incident energy, record the elastic amplitude or selected cross sections while varying

$$(\epsilon_{\max}, I_{\max}, l_{x,\max}, l_{y,\max}, L_{\max}, J_{\max}, R_{\mathrm{match}}). \tag{8.124}$$

At least one observable sensitive to the nuclear interior and one sensitive to the forward Coulomb region should be tested. Re-fitting N_V, N_W after every model-space change would conceal structural nonconvergence; first hold them fixed, establish convergence, and only then reassess calibration.

8.4.3 Station C: ^{9}C as $p + p + {}^7$Be

The two-body approximation $^9\mathrm{C} = p + {}^8\mathrm{B}$ treats ^{8}B as an inert core. Its proton separation energy is only about 137 keV, so the core itself is fragile. A minimal enlargement uses

$$^9\mathrm{C} = p_1 + p_2 + {}^7\mathrm{Be} \tag{8.125}$$

and the internal Hamiltonian

$$h_9 = K_x + K_y + V_{pp} + V_{p_1{}^7\mathrm{Be}} + V_{p_2{}^7\mathrm{Be}} + V_3. \tag{8.126}$$

The two protons are antisymmetrized, and Pauli-forbidden proton–core states are projected out. The three Jacobi sets resolve the two equivalent $p + {}^8$B partitions and the $pp + {}^7$Be partition. GEM diagonalization produces ^{9}C pseudostates for a four-body CDCC calculation with the target.

For a heavy ^{208}Pb target at intermediate energy, the reaction Hamiltonian contains

$$H = K_R + h_9 + U_{p_1T} + U_{p_2T} + U_{^7\mathrm{Be}T}, \tag{8.127}$$

including both nuclear and Coulomb interactions. The CDCC expansion has the same form as Eq. (8.118), but each internal state is a three-body state. This is four-body CDCC.

8.4.4 Station D: separate sequential and direct breakup with CSLS

The experiment used to infer S_{18} is sensitive to the $p + {}^8$B arrangement, while the model also contains direct $p + p + {}^7$Be breakup. A sum over all ^{9}C

pseudostates does not by itself separate them. Build the CDCC source

$$|F\rangle = \sum_n T_n |\Phi_n\rangle, \tag{8.128}$$

and use a CSLS scattering state adapted to the chosen arrangement. The amplitude for a final $p + {}^8\mathrm{B}$ relative momentum $\boldsymbol{k}$ and an internal ${}^8\mathrm{B}$ configuration ν is

$$T_{p+{}^8\mathrm{B}}(\boldsymbol{k}, \nu) = \sum_n \langle \Phi^{(-)}_{\boldsymbol{k}\nu} | \Phi_n \rangle T_n. \tag{8.129}$$

The overlap is calculated with the complex-scaled resolvent as in Eq. (8.67). A complementary set of Jacobi momenta describes direct three-body breakup. Integrating both contributions and their controlled interference recovers the inclusive CDCC strength.

Domain or asymptotic warning

The two protons create equivalent $p + {}^8\mathrm{B}$ partitions. Symmetrization must be implemented before adding amplitudes. Adding two separately calculated cross sections would double count their overlap and erase interference.

The four-body analysis of Ref. [130] found that the $p + {}^8\mathrm{B}$-resolved low-energy line shape describes the breakup data used for the ANC extraction, while explicit fragility of ${}^8\mathrm{B}$ changes the inferred normalization. The resulting quoted value was

$$S_{18} = 38.4 \pm 1.1 \text{ eV b}, \tag{8.130}$$

about 45% below the earlier three-body-CDCC extraction in which ${}^8\mathrm{B}$ was inert. The point of the Laboratory is not the numerical shift alone. It is the diagnosis: an omitted low separation scale changes the asymptotic configuration whose coefficient is being inferred.

8.4.5 Station E: from a breakup ANC to S_{18}

Let $I_{p^8\mathrm{B}}(r)$ be the radial overlap between the ${}^9\mathrm{C}$ ground state and the $p + {}^8\mathrm{B}$ channel. At large r,

$$I_{lj}(r) \longrightarrow C_{lj} \frac{W_{-\eta_B, l+1/2}(2\kappa r)}{r}, \qquad \kappa = \sqrt{2\mu S_p}/\hbar. \tag{8.131}$$

The coefficient C_{lj} is the ANC. In a peripheral breakup, the calculated cross section in the fitted low-energy region scales approximately as

$$\frac{\mathrm{d}\sigma_{\mathrm{bu}}}{\mathrm{d}E} \simeq {C^2}_{\mathrm{R}} bu(E), \tag{8.132}$$

where $\mathcal{R}_{\mathrm{bu}}$ is computed once with the declared reaction and single-particle conventions. Fit C^2 rather than an arbitrary overall amplitude if peripherality has been verified by radial and optical-potential variations.

The radiative-capture cross section is conventionally written

$$\sigma_{p\gamma}(E) = \frac{S_{18}(E)}{E} \mathrm{e}^{-2\pi\eta(E)}. \tag{8.133}$$

At sufficiently low energy, external capture gives

$$S_{18}(0) = C^2 \mathcal{R}_{\gamma}(0), \tag{8.134}$$

with $\mathcal{R}_{\gamma}$ obtained from the Coulomb capture integral and the same channel normalization as Eq. (8.131). The ratio $\mathcal{R}_{\gamma}/\mathcal{R}_{\mathrm{bu}}$ converts the measured breakup normalization to S_{18} while canceling the arbitrary normalization used for the trial overlap. It does not cancel model dependence from nonperipheral contributions, target optical potentials, higher multipoles, or omitted three-body configurations; those are separate variations.

8.4.6 Station F: ^{6}Li$(p, 2p)^5$He as an overlap measurement

The $\alpha + p + n$ wave function can also be regrouped as $p + {}^5$He. The ^{5}He subsystem is unbound, so the overlap is energy dependent. Let $\Phi^{(-)}_{^5\mathrm{He};\epsilon lj}$ be an $\alpha + n$ scattering state. Projecting the ^{6}Li ground state gives

$$I_{lj}(\epsilon, \boldsymbol{r}_p) = \langle \Phi^{(-)}_{^5\mathrm{He};\epsilon lj} | \Phi_{^6\mathrm{Li}} \rangle_{\alpha n}, \tag{8.135}$$

where $\boldsymbol{r}_p$ is the proton coordinate relative to the ^{5}He center of mass. The p-wave ^{5}He resonance may dominate the integrated norm, while an s-wave continuum component remains smaller.

In distorted-wave impulse approximation, the knockout transition has the schematic factorized form

$$T^{lj}_{p,2p} = \left\langle \chi^{(-)}_1 \chi^{(-)}_2 \Phi^{(-)}_{^5\mathrm{He};\epsilon lj} \right| t_{pp} \left| \chi^{(+)}_0 \Phi_{^6\mathrm{Li}} \right\rangle, \tag{8.136}$$

where t_{pp} is the elementary proton–proton transition operator and the χ are distorted waves. Under a local semiclassical or factorization approximation, the structure dependence is concentrated in the Fourier transform

$$\widetilde{I}_{lj}(\epsilon, \boldsymbol{q}) = \int \mathrm{d}^3 r \, \mathrm{e}^{-\mathrm{i}\boldsymbol{q}\cdot\boldsymbol{r}} I_{lj}(\epsilon, \boldsymbol{r}), \tag{8.137}$$

sampled at a recoil momentum fixed by the detected protons.

At near-zero recoil, an s wave has no centrifugal zero and can contribute strongly to $\widetilde{I}(\boldsymbol{q} \simeq 0)$ even when its integrated probability is minor. A p wave carries a factor proportional to q near the origin in a simple smooth model. Thus "small component of the norm" does not imply "small contribution to every observable." The three-body plus DWIA analysis of Ref. [131] found both p- and s-wave ^{5}He components necessary, with the s wave important near zero recoil.

This is the same functional lesson encountered for a resonance residue. An observable probes the wave function through a source and detector kernel; it does not measure the coefficient norm in isolation. Direct-integral fibers make the statement precise: p and s waves are different continuum channels, and the reaction kernel weights them differently as a function of energy and recoil.

8.4.7 What the three stations teach about resonance representations

The calculations can be summarized without collapsing their distinctions:

problem	retained continuum	measured functional	decisive check
N+^{6}Li elastic	$\alpha + p + n$ pseudostates, including closed channels	elastic S matrix and integral loss	cutoff, matching-radius, and open/closed comparison
^{9}C breakup	$p + p + {}^7$Be pseudostates plus CSLS arrangements	low-energy p+^{8}B line shape and ANC	inclusive sum and rearrangement consistency

problem	retained continuum	measured functional	decisive check
$^6\mathrm{Li}(p, 2p)$	$\alpha + n$ continuum overlap	recoil-momentum-weighted p and s amplitudes	distorted-wave and partial-wave stability

In every row the finite L^2 basis is a representation. The invariant object is respectively an on-shell channel amplitude, an arrangement-resolved continuum amplitude, or a tested overlap functional. Stable pseudostate eigenvalues may diagnose an intrinsic resonance, but most pseudostates are quadrature nodes and should rotate or move when the representation changes.

Laboratory checkpoint

Before leaving this Laboratory, the reader should be able to:

1. draw all three Jacobi sets for $\alpha + p + n$ and $p + p + {}^7\mathrm{Be}$ and identify the Pauli projections;
2. derive Eq. (8.119) from Eq. (8.117);
3. explain why closed $^6\mathrm{Li}$ pseudostates modify elastic scattering without carrying asymptotic flux;
4. construct the CSLS overlap in Eq. (8.129) and state the no-double-counting condition for the equivalent protons;
5. trace the normalization from the breakup line shape through the ANC to Eq. (8.134); and
6. show from the small-q behavior of spherical Bessel transforms why a small s-wave component can dominate a selected recoil bin.

8.5 Problems for Stage VI

VI.1 Derive Eqs. (8.35) and the two reduced masses for a two-cluster projectile. Check the kinetic-energy separation.

VI.2 Starting from Eq. (8.36), project onto Eq. (8.44) and derive every term of Eq. (8.45).

VI.3 Normalize a momentum-bin state. Show strong convergence of a refined step-function projection on a fixed L^2 wave packet and explain why the projections do not converge in operator norm.

VI.4 Diagonalize a short geometric Gaussian basis for a one-dimensional short-range potential. Track a bound state, a stabilized resonance-like pseudostate, and nonresonant pseudostates as the largest range changes.

VI.5 Derive the Coulomb open-channel boundary condition and the Whittaker closed-channel condition. Verify the flux factor in Eq. (8.53).

VI.6 For a two-channel toy model with one closed channel, eliminate the closed component and compute the induced real polarization potential below threshold. Continue above threshold and identify its imaginary part.

VI.7 Derive the complex-scaled smoothing formula Eq. (8.68). Show explicitly which θ dependences cancel in a complete basis.

VI.8 Draw the three Jacobi sets for $\alpha+p+n$. Construct the exchange symmetry under $p \leftrightarrow n$ in the isospin limit and identify which electromagnetic terms break it.

VI.9 In the $p + p + {}^{7}\mathrm{Be}$ model, construct symmetrized amplitudes for the two $p + {}^{8}\mathrm{B}$ arrangements. Give a numerical test for double counting in the inclusive sum.

VI.10 Expand the spherical Bessel transforms at small recoil momentum and show why an s wave can dominate a selected zero-recoil bin over a larger integrated p-wave component.

VI.11 Write the three $\alpha + n + n$ Jacobi transformations, including their reduced masses. Construct basis combinations with the correct neutron exchange sign for $S = 0$ and $S = 1$.

VI.12 Starting from the extended complex-scaled resolution, derive Eq. (8.97). Explain why the selected pole term can have either sign while the complete physical response is nonnegative.

VI.13 Represent the Riesz projector Eq. (8.101) in a real pseudostate basis and prove Eq. (8.102). Give numerical tests for convergence of its rank and idempotency.

VI.14 Derive the phase-space Jacobian in Eq. (8.108) for one declared Jacobi momentum normalization. Show that integration over both subsystem energies recovers the corresponding three-body breakup strength.

VI.15 For a two-channel incoming block, choose explicit left and right null vectors and verify Eq. (6.134). Identify the combinations of CDCC source and CSLS detector overlaps that multiply its residue.

Part IV

Coalescing poles and horizon resonances

Chapter 9

Stage VII: Continue the quantization condition through an exceptional point

Reader contract

An exceptional point is treated as a multiple zero of the already constructed analytic determinant. Jordan chains, self-orthogonality, branch exchange, and geometric phase follow by differentiation and continuation; momentum bins separate physical holonomy from continuum normalization.

9.1 Exceptional points as multiple zeros of the pole condition

Calculation route

Prerequisites. A parameter-dependent incoming coefficient and left–right resonance normalization.

Calculation goal. Expand the analytic pole condition at a multiple zero and translate the result into a Jordan chain and self-orthogonality.

Completion criterion. Distinguish an exceptional resonance from an accidental crossing or a discretized-continuum artifact.

9.1.1 Degeneracy, defectiveness, and Jordan chains

Let $H(\lambda)$ be an analytic family of closed operators or of finite-basis approximations, with complex control parameter λ. A spectral degeneracy at $\lambda = \lambda_{\mathrm{EP}}$ is an exceptional point if the algebraic multiplicity exceeds the geometric multiplicity. For a second-order exceptional point, there is one

eigenvector $|\chi_0\rangle$ and one associated vector $|\chi_1\rangle$ satisfying

$$\begin{aligned}(H_{\mathrm{EP}} - E_{\mathrm{EP}})\,|\chi_0\rangle &= 0,\\ (H_{\mathrm{EP}} - E_{\mathrm{EP}})\,|\chi_1\rangle &= |\chi_0\rangle,\end{aligned} \tag{9.1}$$

where $H_{\mathrm{EP}} = H(\lambda_{\mathrm{EP}})$. The restriction of H_{EP} to the root subspace is a 2×2 Jordan block. A diabolic degeneracy of a self-adjoint family, by contrast, has two independent eigenvectors and no Jordan chain.

Near a generic second-order exceptional point, the characteristic equation has the local form

$$(E - E_{\mathrm{EP}})^2 - c(\lambda - \lambda_{\mathrm{EP}}) + \text{higher-order terms} = 0, \tag{9.2}$$

where $c \neq 0$ is a complex coefficient. The eigenvalues have Puiseux expansions

$$E_{\pm}(\lambda) = E_{\mathrm{EP}} \pm \alpha(\lambda - \lambda_{\mathrm{EP}})^{1/2} + O(\lambda - \lambda_{\mathrm{EP}}), \tag{9.3}$$

with $\alpha^2 = c$. Encircling the branch point once exchanges E_+ and E_-; two encirclements return the eigenvalue to its original sheet.

The square root is generic but not universal. A pth-order Jordan block gives fractional powers $(\lambda - \lambda_{\mathrm{EP}})^{1/p}$, while a continuum threshold can modify the exponent through the energy dependence of the self-energy in Eq. (6.7). The local singularity must be derived from the continued resolvent rather than inferred only from a finite matrix fit [10, 21].

9.1.2 Self-orthogonality and eigenvalue condition numbers

For a simple eigenvalue, choose right and left eigenvectors $|\Psi^{\mathrm{R}}\rangle$ and $\langle\Psi^{\mathrm{L}}|$. First-order perturbation theory contains the denominator

$$\langle\Psi^{\mathrm{L}}|\Psi^{\mathrm{R}}\rangle. \tag{9.4}$$

At an exceptional point, the left eigenvector is orthogonal to the coalesced right eigenvector in the biorthogonal pairing:

$$\langle\chi_0^{\mathrm{L}}|\chi_0^{\mathrm{R}}\rangle = 0. \tag{9.5}$$

If one enforces unit overlap away from the EP, the individual vector norms diverge as the EP is approached. A useful sensitivity measure is

$$\mathcal{K}_n = \frac{\|\Psi_n^{\mathrm{R}}\|\|\Psi_n^{\mathrm{L}}\|}{|\langle\Psi_n^{\mathrm{L}}|\Psi_n^{\mathrm{R}}\rangle|}. \tag{9.6}$$

The condition number $\mathcal{K}_n$ diverges at self-orthogonality. Large $\mathcal{K}_n$ also means that a small operator perturbation can move the eigenvalue substantially. This links EP physics to pseudospectral sensitivity.

For a complex-symmetric representation, the overlap in Eq. (9.5) becomes the c product. A vanishing c norm is therefore not evidence that the wave function itself vanishes; it is the diagnostic that right and left eigendirections have coalesced.

9.1.3 Exceptional points in an open scattering problem

There are three distinct situations that are sometimes grouped together. First, two isolated resonance poles may coalesce on a nonphysical sheet. Second, a resonance pole may meet a threshold branch point. Third, a pole may meet the complex-scaled continuum in a particular L^2 representation. Only when the analytic family develops a defective root subspace is the event an exceptional point in the operator-theoretic sense. A visual crossing of a finite-basis continuum ray is not sufficient.

The complex-scaling method provides a controlled setting for the third situation. An exposed resonance is a discrete eigenvalue of H_θ. As a physical parameter λ changes, its pole trajectory can reach the rotated continuum. In a momentum-bin discretization, one can identify a particular continuum pseudostate that coalesces with the resonance, verify the vanishing discriminant, and follow the resulting branch exchange. The continuum limit must then be taken through smeared states or a specified test space [20].

Changing the scaling angle θ at fixed physical Hamiltonian is different. The pole does not move in the exact problem; only the boundary of its L^2 representation moves. Loss of exposure at a critical angle need not be a physical EP. It becomes an EP problem only if the chosen analytic family and root subspace satisfy the defectiveness conditions. This distinction avoids assigning topological charge to a numerical continuum crossing created solely by truncation.

9.1.4 Feshbach description of pole coalescence

In a two-dimensional P space, the effective Hamiltonian can be written

$$H_{\text{eff}}(z,\lambda) = H_{PP}(\lambda) + \Sigma(z,\lambda). \tag{9.7}$$

The pole equation is

$$D(z,\lambda) = \det\left[z - H_{\text{eff}}(z,\lambda)\right] = 0. \tag{9.8}$$

A second-order pole coalescence satisfies

$$D(z_{\text{EP}},\lambda_{\text{EP}}) = 0, \qquad \left.\frac{\partial D}{\partial z}\right|_{\text{EP}} = 0. \tag{9.9}$$

Generically, a second control condition is needed if all parameters are restricted to be real. Complex continuation reduces the local geometry to the square-root form in Eq. (9.3). If $\partial_z\Sigma$ diverges at a threshold, the balance in Eq. (9.9) changes and noninteger orders other than $1/2$ can appear.

This formulation makes clear that an EP is a statement about both eigenvalues and residues. At a double pole, the resolvent contains

$$\mathcal{R}(z) = \frac{A_{-2}}{(z - z_{\text{EP}})^2} + \frac{A_{-1}}{z - z_{\text{EP}}} + \mathcal{R}_{\text{reg}}(z), \tag{9.10}$$

where A_{-2} and A_{-1} act on the Jordan root subspace. A fit of pole locations without residues cannot distinguish all possible near-degenerate line shapes.

9.1.5 Dynamics around an exceptional point

The spectral monodromy of Eq. (9.3) is independent of how a parameter loop is traversed. Actual time-dependent encircling is more subtle. The adiabatic theorem for a non-normal decaying system can fail because decay rates select the least lossy branch and exponentially amplify small nonadiabatic components. A geometric phase extracted from analytic continuation should therefore be distinguished from a state-transfer protocol in real time. Experiments on dissipative qubits and monitored systems probe both aspects but require an explicit unraveling or measurement model [132–135].

9.2 Derive the resolvent of a second-order Jordan block

On the two-dimensional root subspace, write

$$J = E_{\mathrm{EP}}\mathbf{1} + N, \qquad N^2 = 0, \qquad N \neq 0. \tag{9.11}$$

Then

$$(z - J)^{-1} = \frac{\mathbf{1}}{z - E_{\mathrm{EP}}} + \frac{N}{(z - E_{\mathrm{EP}})^2}. \tag{9.12}$$

The double-pole coefficient is nilpotent. Under a generic perturbation, N and the perturbation matrix combine to split the double pole into the two square-root branches in Eq. (9.3). Individual rank-one projectors diverge as the EP is approached, but their sum tends to the finite Riesz projector onto the root subspace. Numerically, it is therefore more stable to track the two-dimensional contour-integral projector than two separately normalized eigenvectors.

9.3 Transport a resonance around the multiple zero

9.3.1 Biorthogonal Berry connection

Away from degeneracies, choose a right–left pair normalized by

$$\langle \Psi_n^{\mathrm{L}}(\boldsymbol{\lambda}) | \Psi_n^{\mathrm{R}}(\boldsymbol{\lambda}) \rangle = 1, \tag{9.13}$$

where $\boldsymbol{\lambda}$ denotes control parameters. The biorthogonal Berry connection is

$$\mathcal{A}_n(\boldsymbol{\lambda}) = \mathrm{i}\langle \Psi_n^{\mathrm{L}}(\boldsymbol{\lambda}) | \boldsymbol{\nabla}_\lambda | \Psi_n^{\mathrm{R}}(\boldsymbol{\lambda}) \rangle. \tag{9.14}$$

For a closed loop C that returns the eigenspace to itself, the geometric holonomy is

$$\gamma_n(C) = \oint_C \mathcal{A}_n \cdot \mathrm{d}\boldsymbol{\lambda}. \tag{9.15}$$

In a non-self-adjoint problem γ_n may be complex; its real part is a phase and its imaginary part changes the transported amplitude. Under a biorthogonal gauge transformation

$$|\Psi_n^{\mathrm{R}}\rangle \longmapsto \mathrm{e}^{f_n} |\Psi_n^{\mathrm{R}}\rangle,$$

$$\langle \Psi_n^{\mathrm{L}}| \longmapsto \langle \Psi_n^{\mathrm{L}}|\mathrm{e}^{-f_n}, \tag{9.16}$$

the connection changes by $\mathrm{i}\boldsymbol{\nabla}_\lambda f_n$, while a properly closed holonomy is gauge invariant modulo the allowed branch and normalization conventions.

At a second-order EP, one circuit exchanges the two eigenlines. A scalar Berry phase for a single eigenline is therefore defined only after enough circuits to close the line, or by using a non-Abelian connection on the two-dimensional root bundle. In the standard finite-dimensional case, two circuits return the eigenvector with a minus sign under common conventions.

9.3.2 Momentum-bin regularization of the continuum

Let continuum states satisfy

$$\langle k|k'\rangle = \delta(k-k'). \tag{9.17}$$

Partition a complex-scaled momentum contour into bins $[k_n, k_{n+1}]$ with width $\Delta k_n = k_{n+1} - k_n$. Define

$$|n\rangle = \frac{1}{\sqrt{\Delta k_n}} \int_{k_n}^{k_{n+1}} \mathrm{d}k\, |k\rangle. \tag{9.18}$$

For nonoverlapping bins and a compatible contour pairing, $\langle m|n\rangle = \delta_{mn}$. The factor $1/\sqrt{\Delta k_n}$ converts Dirac-delta normalization into Kronecker-delta normalization. It is also the source of an additional branch when the bin width itself depends on the EP parameter.

Near a resonance–continuum coalescence, suppose the continued momentum has the local form

$$k_n(\lambda) = k_{\mathrm{EP}} + a_n(\lambda - \lambda_{\mathrm{EP}})^{1/2} + \cdots . \tag{9.19}$$

Then

$$\Delta k_n = (a_{n+1} - a_n)(\lambda - \lambda_{\mathrm{EP}})^{1/2} + \cdots . \tag{9.20}$$

The integral in Eq. (9.18) contributes one power of Δk_n, while the normalization contributes its inverse square root. Consequently the leading binned wave function scales as

$$|n(\lambda)\rangle \propto (\lambda - \lambda_{\mathrm{EP}})^{1/4}. \tag{9.21}$$

A 2π circuit in $\arg(\lambda - \lambda_{\mathrm{EP}})$ multiplies this factor by $\mathrm{e}^{\mathrm{i}\pi/2}$; two circuits give

a minus sign, and four circuits restore the original branch. The quarter root combines the square-root energy sheet with the square root required by continuum normalization [20].

The bin result is not an extra physical state. It is a regulated representation of a distributional continuum vector. A wave-packet regularization gives the same logic with a smooth width ϵ in place of Δk_n. Any claim of universality should be phrased in terms of the closed physical holonomy after the regulator is removed, not in terms of an individual normalization factor.

9.3.3 Chern data and branch exchange

On a parameter surface that avoids the EP, define the curvature

$$\mathcal{F}_n = \mathrm{d}\mathcal{A}_n. \tag{9.22}$$

If a closed two-cycle is well defined and the eigenline returns to itself, the first Chern number is

$$c_1 = \frac{1}{2\pi}\int \mathcal{F}_n. \tag{9.23}$$

Near an EP, a single eigenline is branched and may not define a line bundle on the punctured base without passing to a covering space. One may instead work on that cover or use the rank-two bundle of the exchanging pair. This avoids assigning an integer Chern number to a path that does not close in the original bundle. Non-Hermitian topological classifications use related biorthogonal constructions, with additional boundary sensitivity in spatially extended systems [136–138].

9.3.4 Renormalizing a distributional holonomy

The continuum limit of Eq. (9.14) can contain objects such as $\delta(0)$ or derivatives of a delta function if unsmeared continuum eigenvectors are inserted directly. These symbols are not numbers. They stand for normalization-volume or wave-packet-width dependence. Let $R > 0$ denote a small radius excised around the EP in parameter space, and let $\epsilon > 0$ denote a continuum smearing scale. Write a bare holonomy as

$$\gamma^{\mathrm{bare}}(R, \epsilon) = Z_\gamma(R, \epsilon)\gamma^{\mathrm{phys}}. \tag{9.24}$$

The physical holonomy is defined by a renormalization condition, for example by matching the finite-bin branch exchange. Regulator independence requires

$$\left(R\frac{\partial}{\partial R}+\epsilon\frac{\partial}{\partial \epsilon}\right)\gamma^{\mathrm{phys}}=0. \tag{9.25}$$

Equivalently, the running of Z_γ cancels the regulator dependence of the bare connection. This is the EP analogue of fixing the origin monodromy in Eq. (7.12).

The construction is best called *monodromy renormalization* or an *RG-type regulator-independence condition*. It does not by itself establish a Wilsonian renormalization group, a universal beta function, or a new thermodynamic scaling law. Its testable claim is narrower: different continuum regulators that preserve the analytic pole and the same matching condition should give the same closed holonomy. Demonstrating this regulator equivalence beyond solvable one-dimensional models is an important open problem.

9.3.5 What survives the continuum limit

Four pieces of data have different degrees of robustness. The location of the continued branch point is invariant under admissible spectral representations. The Puiseux order is invariant unless a threshold changes the analytic class. The exchange permutation of spectral sheets is topological. The phase assigned to an individual eigenvector depends on normalization and gauge, but a closed, matched holonomy is physical. This hierarchy prevents regulator-specific factors from being mistaken for new topological invariants.

In applications, one should report the analytic family being varied, the definition of the continuum regulator, the number of circuits required to close the state, and the left–right normalization. Without these data, two correct calculations can appear to disagree merely because they compare different covers or gauges.

9.4 Calculation laboratory VII: Encircling an exceptional resonance

Calculation route

Prerequisites. Complex-scaled left and right eigenvectors, a second-order exceptional point, Jordan chains, and Berry holonomy.

Calculation goal. The complex-scaled Rosen–Morse eigenfunctions, self-orthogonality, branch exchange, geometric phase, Chern data, monodromy renormalization, and momentum-bin continuum states.

Completion criterion. Track the branch exchange, self-orthogonality, and geometric phase through an EP while separating bin normalization from the holonomy.

This Laboratory reconstructs the calculation underlying Ref. [20]. Resonance boundary conditions and the ABC theorem are referenced from Stages II and IV. We retain the solvable Rosen–Morse eigenfunction because it is the input from which the EP derivatives and holonomy are calculated.

9.4.1 The solvable resonance family used at the exceptional point

Solving method within complex-scaling method

Our considerations in this paper will be applicable quite generically to scattering theory in one dimension. To illustrate it, we show explicit computations in an exactly solvable model: the inverted Rosen–Morse potential or Pöschl–Teller potential. It is well known that this system supports barrier resonance. For the inverted Rosen–Morse potential, the Schrödinger equation under the CSM is given by

$$\left[-\frac{\hbar^2}{2m}\frac{\mathrm{d}^2}{\mathrm{d}x'^2}+\frac{\lambda}{\cosh^2\beta x'}\right]\psi(x')=E\psi(x'), \tag{9.26}$$

where we have replaced $x\in\mathbb{R}$ by $x'=xe^{\mathrm{i}\theta}\in\mathbb{C}$ with the scaling angle θ and assume $\lambda>0$. m is the mass parameter, λ and β determine the height and the width of the potential, respectively. For simplicity—namely, to identify the differential equation with a hypergeometric-type equation—we introduce several somewhat technical but convenient variables. Letting $\xi=\tanh\beta x'$,

the equation is represented as

$$\left[\frac{\mathrm{d}}{\mathrm{d}\xi}(1-\xi^2)\frac{\mathrm{d}}{\mathrm{d}\xi}+s(s+1)-\frac{\kappa^2}{1-\xi^2}\right]\psi(x')=0, \tag{9.27}$$

$$\kappa=\frac{\sqrt{-2mE}}{\beta\hbar}, \qquad s=\frac{1}{2}\left(-1+\sqrt{1-\frac{8m\lambda}{\beta^2\hbar^2}}\right). \tag{9.28}$$

Substituting $\psi(x')=(1-\xi^2)^{\frac{\kappa}{2}}\omega(\xi)$ into Eq. (9.28), we obtain the hypergeometric differential equation explicitly in terms of β, κ, s, and u

$$u(1-u)\omega''+(\kappa+1)(1-2u)\omega'-(\kappa-s)(\kappa+s+1)\omega=0, \tag{9.29}$$

$$u=\frac{1-\xi}{2}. \tag{9.30}$$

Here primes denote derivatives with respect to u. The solution of this equation, which is regular at $x=0$, is given by

$$\psi_{\mathrm{CSM}}(x)=(1-\xi^2)^{\frac{\kappa}{2}}F\left(\kappa-s,\kappa+s+1,\kappa+1,\frac{1-\xi}{2}\right). \tag{9.31}$$

Here, F is the Gauss hypergeometric function. In general, as $x\to-\infty$ ($\xi\to-1$), the Gauss hypergeometric function diverges. This naive wave function is missing in Hilbert space but is called the Gamow state in a physical sense. However, physical wave functions of resonant states under CSM are normalizable because of the ABC theorem. To ensure the normalizability of the wave function, it is well-known that the hypergeometric function should be expressed as a finite-order polynomial. This requirement leads to the condition, $\kappa-s=-n$ ($n\in\mathbb{Z}_{\geq 0}$), which gives the exact energy spectrum of resonance,

$$E_n^{\mathrm{R}}=\frac{\hbar^2\beta^2}{8m}\left[\sqrt{\frac{8m\lambda}{\beta^2\hbar^2}-1}-\mathrm{i}(2n+1)\right]^2. \tag{9.32}$$

We have introduced some somewhat technical but convenient variables. In what follows, the resonance solutions obtained via the CSM, ψ_{CSM}, (given by hypergeometric functions times an overall factor) and the discrete resonance energy spectrum, E_n^{R}, (lying in the fourth quadrant) will be of primary importance.

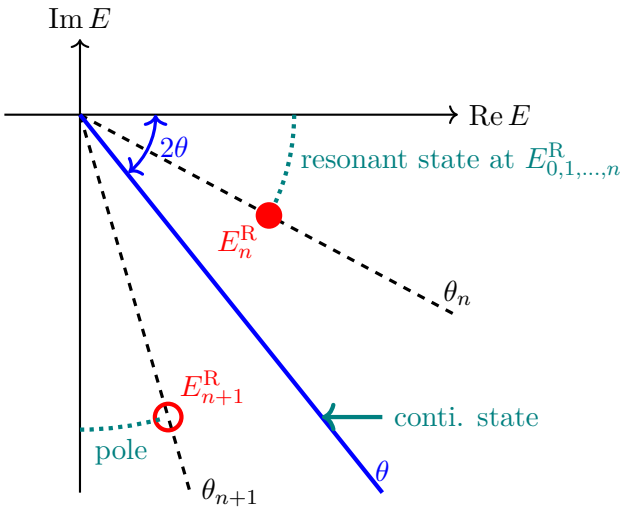

Figure 9.1: Schematic energy-plane picture of complex scaling. The complex-scaled continuum spectrum is rotated by -2θ (blue) from the positive real axis. We set $\theta_n < \theta < \theta_{n+1}$. Resonance poles at $E^{\mathrm{R}}_{n+1,n+2\ldots}$ appear below the rotated cut, and Gamow states at $E^{\mathrm{R}}_{0,1,\ldots,n}$ become regularized as discrete states.

Analyticity of the control parameter near the resonance pole

The ABC theorem states that, as mentioned above, the continuum spectrum is rotated by -2θ, $E_{\mathrm{CSM}}(\theta) = E\mathrm{e}^{-2\mathrm{i}\theta}$ with the positive and continuum energy E of an incoming wave as the parameter in scattering problem. Let θ_n be an angle for which the resonance pole with E^{R}_n contacts with the complex-scaled continuum spectrum, i.e., there exists E such that $E^{\mathrm{R}}_n = E_{\mathrm{CSM}}(\theta_n)$. The explicit form of θ_n would be given by

$$\theta_n = \frac{1}{2}\arctan\left(-\frac{\mathrm{Im}\, E^{\mathrm{R}}_n}{\mathrm{Re}\, E^{\mathrm{R}}_n}\right). \tag{9.33}$$

The number of basis vectors (wave functions) spanning the rigged Hilbert space is the total number of the bound states and continuum states when $0 \leq \theta < \theta_0$, while if we assume that $\theta_n < \theta < \theta_{n+1}$ then the number of bases is the original number of the bound and continuum states plus the number of the resonant states regularized by CSM, $n+1$, see Fig. 9.1. In other words, $\theta = \theta_n$ is an exceptional point (EP) where the number of (normalizable) wave functions changes (we will define more precisely). In what follows, we focus

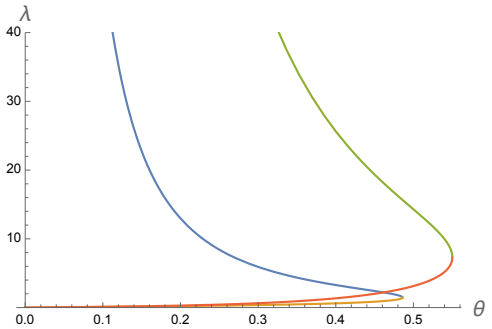

Figure 9.2: $\lambda_{0,1}^{\pm}$ as functions of θ. $\frac{\beta^2\hbar^2}{4m} = 1$. λ should be above the blue curve which denotes λ_0^+ (λ should be larger than it), or be below the orange curve which is λ_0^- (λ should be smaller than it). The green and red curves correspond to λ_1^+ and λ_1^-, respectively, and hence λ should be inside the region between these curves. Eventually, we find that λ is larger than λ_0^+ and smaller than λ_1^+ as long as θ is not too large.

on the first resonance pole, $n = 0$, and suppose that $\theta_0 < \theta < \theta_1$ to regularize the $n = 0$ resonant wave function. Note that the condition that $\theta_0 < \theta < \theta_1$ provides an inequality depending on λ, and so

$$-\frac{\operatorname{Im} E_0^{\mathrm{R}}}{\operatorname{Re} E_0^{\mathrm{R}}} < \tan 2\theta < -\frac{\operatorname{Im} E_1^{\mathrm{R}}}{\operatorname{Re} E_1^{\mathrm{R}}}. \tag{9.34}$$

One can find that

$$(\lambda < \lambda_0^- \ \vee \ \lambda_0^+ < \lambda) \quad \wedge \quad \lambda_1^- < \lambda < \lambda_1^+, \tag{9.35}$$

where, with $t = \tan^2(2\theta)$,

$$A_0 = \frac{1+t}{t}, \qquad A_1 = \frac{9+5t}{t}, \qquad B_1 = \frac{9+25t}{t}, \tag{9.36}$$

$$\begin{aligned}\lambda_0^{\pm} &= \frac{\beta^2\hbar^2}{4m}\left[A_0 \pm \sqrt{A_0^2 - A_0}\right] \\ &= \frac{\beta^2\hbar^2}{4m}\frac{1 \pm \cos 2\theta}{\sin^2 2\theta},\end{aligned} \tag{9.37}$$

$$\lambda_1^{\pm} = \frac{\beta^2\hbar^2}{4m}\left[A_1 \pm \sqrt{A_1^2 - B_1}\right]. \tag{9.38}$$

Figure 9.2 shows the functions $\lambda_{0,1}^{\pm}$ with respect to θ and indicates that $\lambda_0^+ < \lambda < \lambda_1^+$ for small enough θ.

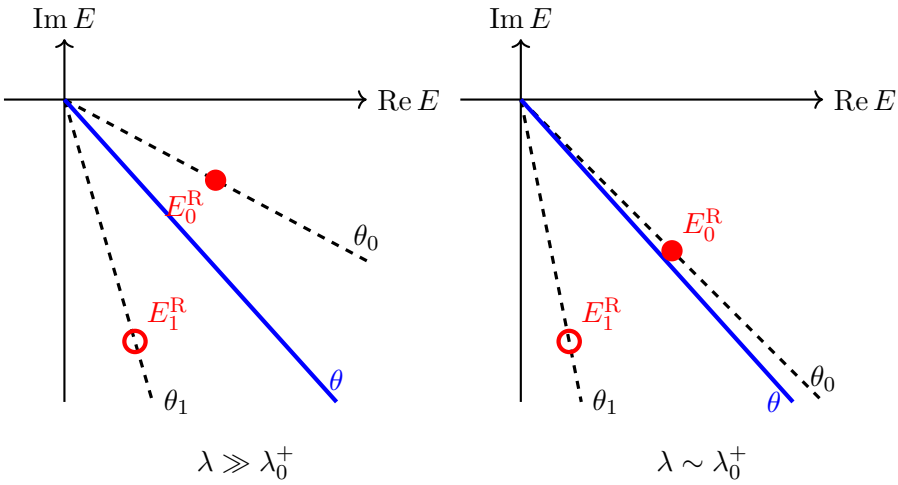

Figure 9.3: Changing λ and deformation of energy Riemann sheet. **Left:** For a moderate value of λ, the resonant spectrum is completely isolated. **Right:** Near λ_0^+, the resonance pole is embedded into the continuum spectrum.

9.4.2 Classification of wave functions and self-orthogonality

Let us change the parameter λ instead of θ to follow the well-discussed approach to usual EPs in finite-dimensional non-Hermitian systems [139]. It is straightforward that changing λ effectively deforms θ_n and so the wave function becomes ill defined outside $\lambda_0^+ < \lambda < \lambda_1^+$ (see Fig. 9.3). Then, the parameter λ can contact with its EP, say λ_{bp}, such that $\lim_{\lambda\to\lambda_{\mathrm{bp}}} E_0^{\mathrm{R}} = \lim_{\lambda\to\lambda_{\mathrm{bp}}} E_{\mathrm{CSM}}(\theta) \equiv E_{\mathrm{bp}}$ for a value of E. That is, precisely speaking, λ_{bp} is a root of the equation

$$\tan 2\theta = -\frac{\operatorname{Im} E_{\mathrm{bp}}}{\operatorname{Re} E_{\mathrm{bp}}} \tag{9.39}$$

with the critical energy

$$E_{\mathrm{bp}} = \frac{\hbar^2\beta^2}{8m}\left[\sqrt{\frac{8m\lambda_{\mathrm{bp}}}{\beta^2\hbar^2} - 1} - \mathrm{i}\right]^2. \tag{9.40}$$

We have

$$\lambda_{\mathrm{bp}} = \lambda_0^+ = \frac{\beta^2\hbar^2}{4m}\frac{1+\cos 2\theta}{\sin^2 2\theta} = \frac{\beta^2\hbar^2}{4m}\frac{1}{1-\cos 2\theta}. \tag{9.41}$$

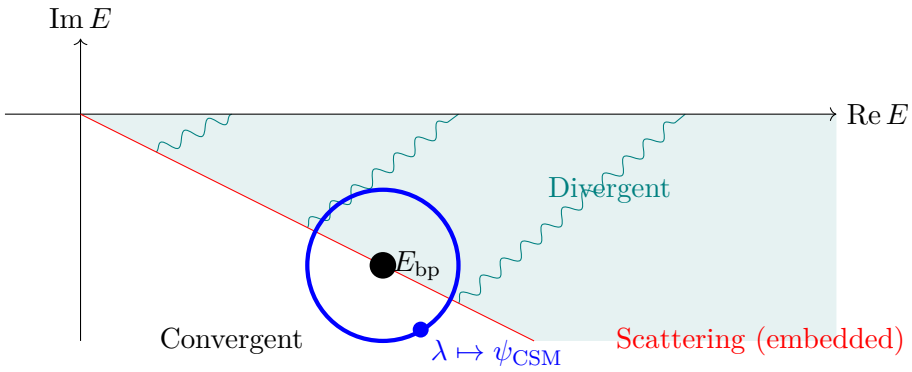

Figure 9.4: The resonance wave function as a function of λ around λ_{bp}. Given λ, we can see the behavior of $\psi_{\mathrm{CSM}}(\lambda)$ with $E_0^{\mathrm{R}}(\lambda)$. We consider the λ contour around λ_{bp} as depicted by the blue circle. Below the red line, ψ_{CSM} is convergent and a pseudobound state. Above it, the wave function is not regularized by CSM, so ψ_{CSM} diverges; this region is a kind of branch plane. At intersections between the red line and blue curve, the resonance is embedded into the continuum spectrum, and its wave function is identical to the scattering solution.

It is important to see the behavior of the wave function around λ_{bp}. Given λ, we have the Gamow state as $\psi_{\mathrm{CSM}}(\lambda)$. If $\theta > \theta_0(\lambda)$ then ψ_{CSM} is one wave function associated with the resonance with E_0^{R}. Thus, the resonance is just a pseudobound state in the regularized sense by CSM. Here, going across λ_{bp}, one may take a drastic value of λ such that $\theta < \theta_0(\lambda)$. It is trivial that ψ_{CSM} is divergent and there exists only a resonance pole at $n = 0$. When $\theta = \theta_0(\lambda = \lambda_{\mathrm{bp}})$, any damping factor in ψ_{CSM} disappears but the plane-wave behavior at the asymptotic region is left. Actually, this is identical to the scattering solution. Figure 9.4 illustrates a contour of $\lambda \in \mathbb{C}$ around λ_{bp} and shows that ψ_{CSM} is convergent, divergent, or scattering. The green region with the wavy lines implies the branch cut where the Gamow state should diverge; at the boundary (red line) a damping factor in the resonant wave function by CSM disappears. To follow explicitly how a resonance pole approaches and coalesces with the complex-scaled continuum, we use a momentum-bin discretization of the continuum spectrum. The method and the associated notation are summarized in Sec. 9.4.5, so that the present section can focus directly on the resulting branch-point structure and its physical consequences. The resonant wave function $\psi_{\mathrm{CSM}}^{\mathrm{R}}(\lambda)$ with $\lambda \neq \lambda_{\mathrm{bp}}$ is an independent solution of the non-Hermitian linear differential equation.

We also have the momentum-binned states $\psi^{\mathrm{bin}}_{\mathrm{CSM}}(n,\lambda)$ as the independent scattering solutions $\psi^{\mathrm{conti}}_{\mathrm{CSM}}$ in a bin. Originally, the linear eigenvalue problem possesses

$$\int \psi^{\mathrm{R}}_{\mathrm{CSM}}(\lambda)\psi^{\mathrm{R}}_{\mathrm{CSM}}(\lambda)\mathrm{d}x = 1, \tag{9.42}$$

$$\int \psi^{\mathrm{bin}}_{\mathrm{CSM}}(n',\lambda)\psi^{\mathrm{bin}}_{\mathrm{CSM}}(n,\lambda)\mathrm{d}x = \delta_{n'n}, \tag{9.43}$$

$$\int \psi^{\mathrm{R}}_{\mathrm{CSM}}(\lambda)\psi^{\mathrm{bin}}_{\mathrm{CSM}}(n,\lambda)\mathrm{d}x = 0. \tag{9.44}$$

Note that the binned states are normalized with a Kronecker delta, which makes the relevant formulas technically simpler and the branch structure easier to track explicitly. By contrast, the original continuum states are normalized with a Dirac delta, and this distribution normalization tends to obscure the algebraic steps and their physical interpretation in the present context. Let us consider the limit as $\lambda \to \lambda_{\mathrm{bp}}$. From the exact solution, we can find that

$$\lim_{\lambda\to\lambda_{\mathrm{bp}}} E^{\mathrm{R}}_0(\lambda) = E_{\mathrm{bp}}, \tag{9.45}$$

$$\lim_{\lambda\to\lambda_{\mathrm{bp}}} \psi^{\mathrm{R}}_{\mathrm{CSM}}(\lambda) = \psi^{\mathrm{conti}}_{\mathrm{CSM}}(k_{\mathrm{bp}},\lambda_{\mathrm{bp}}). \tag{9.46}$$

Thus, there exists only one general scattering solution with the identical eigenenergy. Now, exchanging the limit and the inner product (integral over x) is contradictory. This is because

$$\int \lim_{\lambda\to\lambda_{\mathrm{bp}}} \psi^{\mathrm{R}}_{\mathrm{CSM}}(\lambda)\psi^{\mathrm{bin}}_{\mathrm{CSM}}(n,\lambda)\mathrm{d}x = \int \psi^{\mathrm{conti}}_{\mathrm{CSM}}(k_{\mathrm{bp}},\lambda)\psi^{\mathrm{bin}}_{\mathrm{CSM}}(n,\lambda)\mathrm{d}x \neq 0 \quad \exists n, \tag{9.47}$$

$$\lim_{\lambda\to\lambda_{\mathrm{bp}}} \int \psi^{\mathrm{R}}_{\mathrm{CSM}}(\lambda)\psi^{\mathrm{bin}}_{\mathrm{CSM}}(n,\lambda)\mathrm{d}x = \lim_{\lambda\to\lambda_{\mathrm{bp}}} 0 = 0 \qquad \forall n. \tag{9.48}$$

Therefore, the biorthogonality cannot be ensured. To remedy this, it is natural in non-Hermitian quantum systems to introduce *left* eigenvectors in addition to the *right* (usual) eigenvectors. Without exchanging the limit and integral, all right continuum states $\psi^{\mathrm{bin}}_{\mathrm{CSM}}$ are orthogonal to a left scattering solution associated with the resonance, $\lim_{\lambda\to\lambda_{\mathrm{bp}}} \psi^{\mathrm{R}}_{\mathrm{CSM}} \sim \psi^{\mathrm{bin}}_{\mathrm{CSM}}(n_{\mathrm{bp}})$ with

$\exists n_{\rm bp}$.[1] This is called the self-orthogonality (no biorthogonal basis). This is a special phenomenon in non-Hermitian linear algebra so that not only the eigenvalues but also the eigenvectors are degenerate. The Hamiltonian is nondiagonalizable but has a Jordan block.

9.4.3 Geometric phase near resonance pole

Here the geometric phase is defined for adiabatic transport along a closed loop in parameter space. At the exceptional point itself the eigenvectors coalesce and the Berry connection is not well defined; our results therefore pertain to loops that encircle the EP (the associated branch point), capturing the monodromy or holonomy. Moiseyev's ansatz of non-Hermitian energy near EP [139] is given by

$$E^{\theta}_{\rm CSM}(\lambda) = E_{\rm bp} + \alpha\sqrt{\lambda - \lambda_{\rm bp}} + O(\lambda), \tag{9.49}$$

and we define λ as

$$\lambda = \lambda_{\rm bp} + R\mathrm{e}^{\mathrm{i}\phi} \quad (R \ll 1). \tag{9.50}$$

The parameter α in Moiseyev's ansatz is introduced to label the branch (Riemann sheet) of the analytically continued resonance energy. It is fixed once the continuation path and the continuity condition of the resonance pole are specified, and it is not a tunable parameter. The final holonomy or Berry phase is insensitive to α beyond this discrete sheet identification. Note that the square root of λ around $\lambda_{\rm bp}$ comes from its branch order 2, that is, if p wave functions coalesce into an EP then $(\lambda - \lambda_{\rm bp})^{1/p}$.[2] α is a complex parameter. Let us consider the geometric phase of the wave function in the CSM based on Moiseyev's ansatz. We rewrite the solution of Eq. (9.26) as

$$\psi_{\rm CSM}(k, \lambda, x') = (1-\xi^2)^{-\frac{\mathrm{i}k}{2\beta}} F\left(-\frac{\mathrm{i}k}{\beta} - s, -\frac{\mathrm{i}k}{\beta} + s + 1, -\frac{\mathrm{i}k}{\beta} + 1, \frac{1-\xi}{2}\right), \tag{9.51}$$

[1] For simplicity, one may rewrite it as $(\psi_{\rm Left}(n_{\rm bp}), \psi_{\rm Right}(n_{\rm bp})) = 0$ for the degenerate solution $\psi(n_{\rm bp})$ if no confusion arises.

[2] It looks hard to count the number of continuum states. Nevertheless, since there is one corresponding resonant pole/state, the rank of the projection operator to the resonance is definitely equal to one. This is the same situation as the spectrum intensity in Breit–Wigner peak of the Feshbach resonance. Thus, the associated continuum spectrum is unidentified, but one continuum state can be responsible for the EP phenomenon; it provides $p = 2$.

where $k = -\mathrm{i}\beta\kappa = \sqrt{2mE^{\theta}_{\mathrm{csm}}(\lambda)}/\hbar$ and the k and λ dependencies are written explicitly on the right-hand side. For simplicity, we discuss the geometric phase by using the asymptotic forms of the solution represented as (for instance, see Ref. [140])

$$\psi_{\mathrm{CSM}}(k,\lambda,x') \xrightarrow{x\to\infty} 4^{-\frac{\mathrm{i}k}{2\beta}}\mathrm{e}^{\mathrm{i}kx'}, \tag{9.52}$$

$$\psi_{\mathrm{CSM}}(k,\lambda,x') \xrightarrow{x\to-\infty} 4^{-\frac{\mathrm{i}k}{2\beta}}\left[\mathrm{e}^{-\mathrm{i}kx'}\mathcal{A}_{-}(k) + \mathrm{e}^{\mathrm{i}kx'}\mathcal{A}_{+}(k)\right]. \tag{9.53}$$

Here the two connection coefficients are

$$\mathcal{A}_{-}(k) = \frac{\Gamma(1-\frac{\mathrm{i}k}{\beta})\Gamma(\frac{\mathrm{i}k}{\beta})}{\Gamma(1+s)\Gamma(-s)}, \tag{9.54}$$

$$\mathcal{A}_{+}(k) = \frac{\Gamma(1-\frac{\mathrm{i}k}{\beta})\Gamma(-\frac{\mathrm{i}k}{\beta})}{\Gamma(-\frac{\mathrm{i}k}{\beta}-s)\Gamma(-\frac{\mathrm{i}k}{\beta}+s+1)}. \tag{9.55}$$

The above solution corresponds to a continuum state. To avoid some mathematical difficulties, we discretize the continuum state by using the momentum-bin method. We assume that Moiseyev's ansatz applies to a wavenumber as well if $|\lambda - \lambda_{\mathrm{bp}}| \ll 1$, and we define the discretized wavenumber k_n by

$$k_n = k_{\mathrm{bp}} + \alpha'_n\sqrt{\lambda-\lambda_{\mathrm{bp}}} \tag{9.56}$$

$$= k_{\mathrm{bp}} + \alpha'_n R^{\frac{1}{2}}\mathrm{e}^{\frac{\mathrm{i}\phi}{2}}, \tag{9.57}$$

where $k_{\mathrm{bp}} = \sqrt{2mE_{\mathrm{bp}}}/\hbar$. Using k_n, we see the geometric phase as follows.

Case I: $x \to \infty$ The momentum-binned state at $x \to \infty$ is given by

$$\begin{aligned}\psi^{\mathrm{bin}}_{\mathrm{CSM}}(n,\lambda,x') &\to \frac{1}{\sqrt{\Delta k}}\int_{k_n}^{k_{n+1}} 4^{-\frac{\mathrm{i}k}{2\beta}}\mathrm{e}^{\mathrm{i}kx'}\mathrm{d}k \\ &= \frac{1}{\sqrt{\Delta k}}\frac{\mathrm{e}^{\left(-\frac{\mathrm{i}\ln 4}{2\beta}+\mathrm{i}x'\right)k_{n+1}} - \mathrm{e}^{\left(-\frac{\mathrm{i}\ln 4}{2\beta}+\mathrm{i}x'\right)k_n}}{-\frac{\mathrm{i}\ln 4}{2\beta}+\mathrm{i}x'}.\end{aligned} \tag{9.58}$$

Substituting Eq. (9.56) into the above equation, we obtain a compact expression by defining $\zeta = -\mathrm{i}\ln 4/(2\beta) + \mathrm{i}x'$:

$$\psi^{\mathrm{bin}}_{\mathrm{CSM}}(n,\lambda,x') \to \frac{\mathrm{e}^{\zeta k_{\mathrm{bp}}}}{\sqrt{\Delta k}\,\zeta}\left\{\mathrm{e}^{\zeta\alpha'_{n+1}\sqrt{\lambda-\lambda_{\mathrm{bp}}}} - \mathrm{e}^{\zeta\alpha'_n\sqrt{\lambda-\lambda_{\mathrm{bp}}}}\right\}. \tag{9.59}$$

Provided that the exponents of the terms in the brace brackets on the right-hand side are sufficiently small, the Taylor expansion of the asymptotic wave function is given as

$$\begin{aligned}\psi^{\text{bin}}_{\text{CSM}}(n,\lambda,x') &\approx \frac{1}{\sqrt{\Delta k}}\frac{\mathrm{e}^{\zeta k_{\text{bp}}}}{\zeta}\,\zeta(\alpha'_{n+1}-\alpha'_n)\sqrt{\lambda-\lambda_{\text{bp}}}\\ &= \frac{1}{\sqrt{\Delta k}}\mathrm{e}^{\zeta k_{\text{bp}}}(\alpha'_{n+1}-\alpha'_n)\sqrt{\lambda-\lambda_{\text{bp}}}.\end{aligned} \tag{9.60}$$

Here noting that $\Delta k = (\alpha'_{n+1}-\alpha'_n)\sqrt{\lambda-\lambda_{\text{bp}}}$ and substituting Eq. (9.57),

$$\psi^{\text{bin}}_{\text{CSM}}(n,\lambda,x') \approx \mathrm{e}^{\zeta k_{\text{bp}}}\sqrt{\alpha'_{n+1}-\alpha'_n}R^{\frac{1}{4}}\mathrm{e}^{\mathrm{i}\frac{\phi}{4}}. \tag{9.61}$$

The factor $\mathrm{e}^{\mathrm{i}\frac{\phi}{4}}$ indicates that $\psi^{\text{bin}}_{\text{CSM}}(n,\lambda(\phi=0),x')|_{x\to\infty} = \psi^{\text{bin}}_{\text{CSM}}(n,\lambda(\phi=8\pi),x')|_{x\to\infty}$.

Case II: $x\to-\infty$ Now, $E^{\theta}_{\text{CSM}}(\lambda)$ is very close to E_{bp}, i.e., the resonant energy. Thus, by the Siegert boundary condition [1], the coefficient of the second term in Eq. (9.53) is negligible, and that term can be omitted. That is, the condition

$$\frac{\Gamma(1-\frac{\mathrm{i}k}{\beta})\Gamma(-\frac{\mathrm{i}k}{\beta})}{\Gamma(-\frac{\mathrm{i}k}{\beta}-s)\Gamma(-\frac{\mathrm{i}k}{\beta}+s+1)} \approx 0 \tag{9.62}$$

implies $\frac{\mathrm{i}k}{\beta}\approx s+1$.[3] Consequently, the asymptotic form reduces to

$$\psi_{\text{CSM}}(k,\lambda,x') \xrightarrow{x\to-\infty} 4^{-\frac{\mathrm{i}k}{2\beta}}\mathrm{e}^{-\mathrm{i}kx'}, \tag{9.63}$$

and its discrete form is

$$\begin{aligned}\psi^{\text{bin}}_{\text{CSM}}(n,\lambda,x') &\xrightarrow{x\to-\infty} \frac{1}{\sqrt{\Delta k}}\int_{k_n}^{k_{n+1}} 4^{-\frac{\mathrm{i}k}{2\beta}}\mathrm{e}^{-\mathrm{i}kx'}\,\mathrm{d}k\\ &= \frac{1}{\sqrt{\Delta k}}\frac{\mathrm{e}^{\left(-\frac{\mathrm{i}\ln 4}{2\beta}-\mathrm{i}x'\right)k_{n+1}}-\mathrm{e}^{\left(-\frac{\mathrm{i}\ln 4}{2\beta}-\mathrm{i}x'\right)k_n}}{-\frac{\mathrm{i}\ln 4}{2\beta}-\mathrm{i}x'}.\end{aligned} \tag{9.64}$$

[3] Note that the complex energy of the resonance at the fourth quadrant can be given by the condition $\frac{\mathrm{i}k}{\beta}=s+1$, while the complex energy of the anti-resonance at the first quadrant comes from $\frac{\mathrm{i}k}{\beta}=-s$.

This is essentially the same as **Case I**, and a similar calculation yields the factor $\mathrm{e}^{\mathrm{i}\frac{\phi}{4}}$.[4] Thus, the same periodicity condition, $\psi^{\mathrm{bin}}_{\mathrm{CSM}}(n, \lambda(\phi = 0), x')|_{x\to-\infty} = \psi^{\mathrm{bin}}_{\mathrm{CSM}}(n, \lambda(\phi = 8\pi), x')|_{x\to-\infty}$, is satisfied. Incorporating **Case I** and **Case II**, when we consider the contour depicted in Fig. 9.4, that is, encircling the critical energy E_{bp} by changing λ (or ϕ), the wave function should have the 8π periodicity (branch order is 4). This periodicity or branch structure is quite universal in non-Hermitian quantum mechanics with a 2×2 Jordan block. It is, however, much more nontrivial and remarkable that the additional branch structure arises due to the discretized momentum-bin size Δk, and so it essentially depends on the continuous (unbounded) parameter k after removing the cutoff scale. Here the additional branch structure is traced to the square-root normalization factor $1/\sqrt{\Delta k}$ in Eq. (9.59) that arises from momentum-bin discretization. While this introduces an apparent dependence on the bookkeeping parameter α_n [cf. Eq. (9.61)], the associated branch choice does not affect the final result: it is precisely this square-root branch that guarantees that the discretized formulation reproduces the Berry phase. To gain more physical insight, let us see what has happened by the ϕ rotation. Figure 9.5 shows how to encircle E_{bp} by the current rotation. The region A denotes the area where $\psi^{\mathrm{R}}_{\mathrm{CSM}}(\lambda(\phi))$ is normalizable, while the region B implies that any resonance is not regularized by CSM. At the boundary between A and B, the resonant state becomes the continuum one as Eq. (9.46). Also we set $\arg\alpha$ as the below panel in Fig. 9.5 so that Moiseyev's

[4] Alternatively, if the coefficient of the first term in Eq. (9.53) is retained exactly, Euler's reflection formula leads to the asymptotic form

$$4^{-\frac{\mathrm{i}k}{2\beta}}\,\mathrm{e}^{-\mathrm{i}kx'}\,\frac{\mathrm{i}\sin(\pi s)}{\sinh(\frac{\pi k}{\beta})}. \tag{9.65}$$

Using the formula

$$\frac{1}{\sinh(\frac{\pi k}{\beta})} = 2\sum_{n=0}^{\infty}\mathrm{e}^{-(2n+1)\frac{\pi k}{\beta}} \qquad \left(\mathrm{Re}\,\frac{\pi k}{\beta} > 0\right), \tag{9.66}$$

the momentum-binned state is modified as

$$\begin{aligned}\psi^{\mathrm{bin}}_{\mathrm{CSM}}(n, \lambda, x') &\xrightarrow{x\to-\infty} 2\frac{\sin(\pi s)}{\sqrt{\Delta k}}\sum_{n=0}^{\infty}\int_{k_n}^{k_{n+1}}\mathrm{e}^{\left(-\frac{\mathrm{i}\ln 4}{2\beta}-\mathrm{i}x'-\frac{(2n+1)\pi}{\beta}\right)k}\mathrm{d}k \\ &= 2\frac{\sin(\pi s)}{\sqrt{\Delta k}}\sum_{n=0}^{\infty}\frac{\mathrm{e}^{\left(-\frac{\mathrm{i}\ln 4}{2\beta}-\mathrm{i}x'-\frac{(2n+1)\pi}{\beta}\right)k_{n+1}}-\mathrm{e}^{\left(-\frac{\mathrm{i}\ln 4}{2\beta}-\mathrm{i}x'-\frac{(2n+1)\pi}{\beta}\right)k_n}}{-\frac{\mathrm{i}\ln 4}{2\beta}-\mathrm{i}x'-\frac{(2n+1)\pi}{\beta}}.\end{aligned} \tag{9.67}$$

Thus, the same calculation as in **Case I** gives $\mathrm{e}^{\mathrm{i}\frac{\phi}{4}}$ as an overall factor.

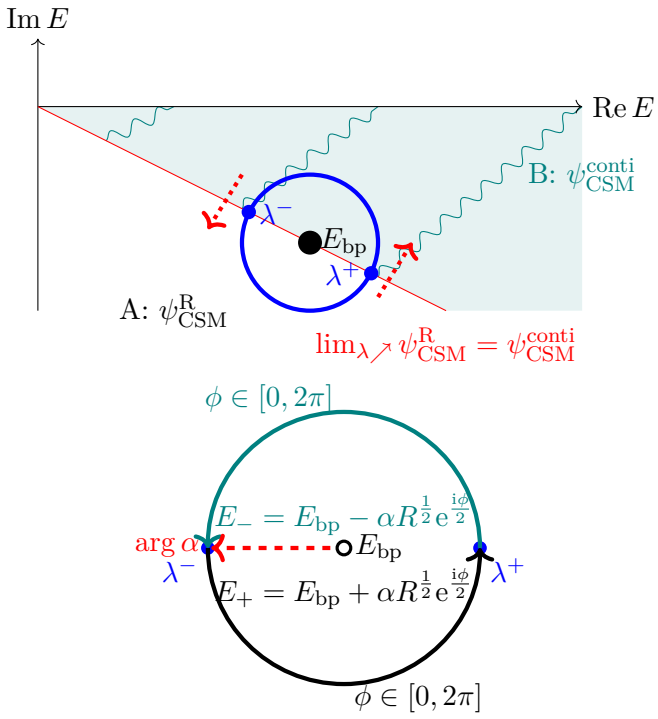

Figure 9.5: The resonance and continuum wave functions in the complex energy plane. The contour around $E_{\rm bp}$ is depicted by the blue circle. Below the red line, i.e., in the region A, $\psi^{\rm R}_{\rm CSM}$ is well defined. Otherwise, in the region B, we focus on $\psi^{\rm conti}_{\rm CSM}$. At intersections between the red line and blue curve, say λ^+ and λ^-, the resonance is identical to the continuum state $\psi^{\rm conti}_{\rm CSM}$ along the limit of λ as the left and/or right eigenfunction. We set the argument of α as the below panel so that Moiseyev's ansatz (9.49) becomes $E(\lambda^-)$ when $\phi=0$.

ansatz (9.49) becomes $E(\lambda^-)$ when $\phi=0$. In effect, now, we can decompose the complex-energy regions as

$$E_\pm = E_{\rm bp} \pm \alpha R^{\frac{1}{2}} e^{\frac{i\phi}{2}} \qquad \phi\in[0,2\pi]. \tag{9.68}$$

Here, the resonant state possesses its complex eigenenergy by E_+ in this convention. Suppose that $\psi^{\rm R}_{\rm CSM}(\lambda(0|_A))$ and $\psi^{\rm conti}_{\rm CSM}(\lambda(0|_B))$ are taken as the exact solution (9.51) (i.e., *their overall phase conform to that of the explicit expression*). First, we start from an intersection point in the region A defined by $\phi=0$, so $\psi^{\rm R}_{\rm CSM}(\lambda(0|_A))=\psi^{\rm R}_{\rm CSM}(\lambda^-)$. Second, we deform λ near the vicinity of another intersection, that is, $\lambda(2\pi|_A)=\lambda^+$. Note that the

overall factor $\mathrm{e}^{\frac{\mathrm{i}\phi}{4}}$ exists in each wave function, by which the dilated resonant wave function differs from the continuum state. We thus use the continuity condition as

$$\psi^{\mathrm{R}}_{\mathrm{CSM}}(\lambda(2\pi|_A)) = \mathrm{e}^{\frac{\mathrm{i}\pi}{2}}\psi^{\mathrm{conti}}_{\mathrm{CSM}}(\lambda(0|_B)) = \mathrm{i}\psi^{\mathrm{conti}}_{\mathrm{CSM}}(\lambda(0|_B)). \tag{9.69}$$

Next, by deformation in the region B, we have

$$\psi^{\mathrm{conti}}_{\mathrm{CSM}}(\lambda(2\pi|_B)) = \mathrm{e}^{\frac{\mathrm{i}\pi}{2}}\psi^{\mathrm{R}}_{\mathrm{CSM}}(\lambda(0|_A)) = \mathrm{i}\psi^{\mathrm{R}}_{\mathrm{CSM}}(\lambda(0|_A)). \tag{9.70}$$

If the complex energy rotates once, the wave function acquires a minus sign:

$$\psi^{\mathrm{R}}_{\mathrm{CSM}}(\lambda(4\pi|_A)) = -\psi^{\mathrm{R}}_{\mathrm{CSM}}(\lambda(0|_A)). \tag{9.71}$$

This is the reason why ϕ has the $4 \times 2\pi$ periodicity. We have observed the nontrivial Berry phase induced by the resonance pole as an EP.

9.4.4 Chern characteristic and monodromy renormalization

Finally, we consider a simple extension: the Chern-type characteristic of the quantum resonance pole as an EP in the parameter space. We show that it is associated with a resonance branch point in the λ-parameter space, and a renormalization viewpoint on the monodromy (holonomy) when continuum normalization becomes distributional.

Biorthogonal connection and bin-regularized holonomy

We first define an Abelian connection for a (generically) non-Hermitian eigenproblem. It is natural to define the Chern connection by

$$\mathcal{A}^{\theta}(\lambda) \equiv \mathrm{i}\int \psi^{\mathrm{bi(Left)}}_{\mathrm{CSM}}\frac{\partial}{\partial\lambda}\psi^{\mathrm{(Right)}}_{\mathrm{CSM}}\mathrm{d}x = \mathrm{i}(\psi(\lambda), \partial_\lambda\psi(\lambda)). \tag{9.72}$$

Here, $\psi^{\mathrm{(Left)}}$ denotes a left eigenvector, and $\psi^{\mathrm{(Right)}}$ is an associated right eigenvector (biorthogonal partner); those are corresponding to $\psi^{\mathrm{R}}_{\mathrm{CSM}}$ or $\psi^{\mathrm{conti,bin}}_{\mathrm{CSM}}$ in an appropriate way. We then define the holonomy around the branch point λ_{bp} as

$$\gamma \equiv \oint_{\mathrm{bp}} \mathcal{A}^{\theta}(\lambda)\mathrm{d}\lambda, \qquad\qquad c_1 \equiv \frac{1}{2\pi}\gamma, \tag{9.73}$$

where c_1 is a Chern-type characteristic (first Chern number when the underlying line bundle is globally well defined). We next evaluate γ within the momentum-bin regularization and focus on the most singular contribution in $\lambda - \lambda_{\rm bp}$. For simplicity, suppose that from the asymptotic relation in Eq. (9.61)

$$\frac{\partial}{\partial\lambda}\psi^{\rm bin}_{\rm CSM}(n,\lambda,x') \approx \frac{1}{4}\frac{1}{\lambda-\lambda_{\rm bp}}\psi^{\rm bin}_{\rm CSM}(n,\lambda,x'). \tag{9.74}$$

In this bin-level estimate, the left or right distinction affects only nonsingular gauge choices and does not modify the holonomy; hence we suppress it for notational simplicity.[5] Then, a nontrivial Abelian phase of holonomy around the resonance pole is obtained if $n = n_{\rm bp}$ by

$$\begin{aligned}\gamma(n_{\rm bp}) &\equiv \oint_{\rm bp}\mathcal{A}^{\theta}(n_{\rm bp},\lambda)\mathrm{d}\lambda &(9.75)\\ &= \mathrm{i}\oint_{\rm bp}\int \psi^{\rm bin(Left)}_{\rm CSM}(n_{\rm bp},\lambda,x')\frac{\partial}{\partial\lambda}\psi^{\rm bin(Right)}_{\rm CSM}(n_{\rm bp},\lambda,x')\mathrm{d}x\mathrm{d}\lambda\\ &= \mathrm{i}\oint_{\rm bp}\frac{1}{4}\frac{1}{\lambda-\lambda_{\rm bp}}\mathrm{d}\lambda = \frac{\pi}{2}. &(9.76)\end{aligned}$$

The four-rotations invariance is reflected in $\mathrm{e}^{\mathrm{i}\gamma} \in \mathbb{Z}_4$. The Chern characteristic suffers from the fractionality of its naive Chern number; the corresponding characteristic $c_1 = \gamma/2\pi = 1/4$ is fractional in this bin-regularized sense. That is, it indicates that the resonance eigenstate under CSM does not define a globally rigid (single-valued) line bundle over the punctured λ-plane without passing to a branched cover.

Continuum limit: Two sources of ill definedness

So far, the momentum-bin method and the exact solution of the inverted Rosen–Morse potential have enabled us to provide the explicit estimates in all of our observations. Averaging continuum states within a momentum bin is a technique in finite volume regularization. The continuum eigenvectors are, however, defined intrinsically by a distribution-valued construction (rigged Hilbert space, von Neumann ring with affiliated operators, semi-infinite measure, and so on). Even in the formal continuum spectrum, the physical picture remains intact and is not particularly sensitive to the choice of

[5] More precisely, the holonomy γ is invariant under $\psi \to \mathrm{e}^{\mathrm{i}\chi(\lambda)}\psi$ and the corresponding transformation of $\psi^{\rm bi}$, so the leading singular piece is sufficient for γ.

geometric path, so we do not confine the discussion to geometric paths alone. On the other hand, the definition of $\mathcal{A}(\lambda)$ becomes quite subtle due to the plausible normalization factor as $\delta(0)$ for the continuum states. Hence, in this section, the vector-bundle structure induced by λ is not straightforwardly applied to the continuum case. Here is a short summary: The problem is divided into (A) inner products of the continuum states and (B) the number of those. (A) Continuum eigenvectors are δ-function normalized, and inner products produce regulator-dependent singular factors such as $\delta(0)$ (or its derivatives). This affects the very meaning of $\mathcal{A}^\theta(\lambda)$ unless a specific regularization (finite volume box, wave-packet, test-function, etc.) is fixed. (B) Even after choosing a regulator, the set of continuum states is uncountable and the associated bundlelike structure over parameter space is not automatically inherited straightforwardly. To make the appearance of (A) explicit, in general, we have an asymptotic form of the scattering/resonant solution near the resonance pole

$$\psi^{\mathrm{as}}_{\mathrm{CSM}}(k,\lambda,x') = \begin{cases} \frac{1}{\sqrt{2\pi}}\mathrm{e}^{\mathrm{i}kx'} & \mathrm{Re}\, x' \gg 0, \\ \frac{1}{\sqrt{2\pi}}\mathrm{e}^{-\mathrm{i}kx'} & \mathrm{Re}\, x' \ll 0, \end{cases} \tag{9.77}$$

where $k = k_{\mathrm{bp}} + \alpha'\sqrt{\lambda - \lambda_{\mathrm{bp}}}$ and this is δ-function normalized. With attention to the self-orthogonality, we obtain

$$\mathcal{A}^\theta(\lambda) = \mathrm{i} \lim_{k'\to k,\lambda'\to\lambda} \int \psi^{\mathrm{as(Left)}}_{\mathrm{CSM}}(k',\lambda',x') \frac{\partial}{\partial\lambda} \psi^{\mathrm{as(Right)}}_{\mathrm{CSM}}(k,\lambda,x')\mathrm{d}x \tag{9.78}$$

$$= \mathrm{i} \lim_{k'\to k,\lambda'\to\lambda} \frac{\partial k}{\partial\lambda}\frac{\partial}{\partial k} \int \psi^{\mathrm{as(Left)}}_{\mathrm{CSM}}(k',\lambda',x') \psi^{\mathrm{as(Right)}}_{\mathrm{CSM}}(k,\lambda,x')\mathrm{d}x \tag{9.79}$$

$$= \mathrm{i}\left(\frac{\alpha'}{2\sqrt{\lambda - \lambda_{\mathrm{bp}}}} + \frac{\partial\alpha'}{\partial\lambda}\sqrt{\lambda - \lambda_{\mathrm{bp}}} \right) \delta'(0), \tag{9.80}$$

where we have assumed that $\alpha' = \alpha'(\lambda)$ to be λ dependent. Here $\delta'(0)$ is a shorthand for the regulator-dependent singular factor arising from differentiating the continuum overlap; its precise meaning depends on the chosen regularization scheme (e.g., box normalization or wave-packet regularization). The naive connection requires renormalization/regularization data in the continuum.

Monodromy renormalization: Fixing the physical holonomy

γ takes measurements of the monodromy around the EP. Now, we implement the monodromy renormalization method in Ref. [25] as a way to separate physical content from regulator dependence. Let us remove the microscopic circle around $\lambda_{\rm bp}$ with the radius R. Then, the physical holonomy being kept $\pi/2$, i.e., $\gamma^{\rm phys} = \pi/2$, the *bare* holonomy depends on R as

$$\gamma^{\rm phys} = \frac{\gamma^{\rm bare}(R)}{Z_\gamma(R)}. \tag{9.81}$$

$Z_\gamma(R)$ plays the role of a renormalization factor that absorbs regulator dependence [including distributional normalization factors such as $\delta(0)$ or $\delta'(0)$]. Still, $\gamma^{\rm bare}$ can be divergent by $\delta(0)$, but only the renormalized monodromy is observable. Notice that it appears that α (α') is a measure of the number of continuum states along the E (k) contour. In fact, the structure of $k = k_{\rm bp} + \alpha' R^{\frac{1}{2}} \mathrm{e}^{\frac{\mathrm{i}\phi}{2}}$ suggests that the coefficient α' controls how many continuum states effectively contribute along the k contour (equivalently, along the energy contour). Motivated by this, we introduce a redefinition (running) of $\alpha'(\lambda)$ such that the singular factor $\delta'(0)$ is absorbed into α'. We impose the renormalization-group-type condition

$$\alpha' + 2\frac{\partial \alpha'}{\partial \lambda}(\lambda - \lambda_{\rm bp}) = \frac{\alpha_0}{2\sqrt{\lambda - \lambda_{\rm bp}}\delta'(0)} \tag{9.82}$$

for finite α_0, and the solution is given by

$$\alpha'(\lambda) = \frac{\alpha_0}{4\delta'(0)} \frac{\ln(\lambda - \lambda_{\rm bp})}{\sqrt{\lambda - \lambda_{\rm bp}}} + \frac{(\text{const.})}{\sqrt{\lambda - \lambda_{\rm bp}}}. \tag{9.83}$$

Under this redefinition, the δ function from the connection can be absorbed by the *renormalization* of α'.[6] Then, the resulting holonomy becomes finite and proportional to α_0:

$$\gamma^{\rm bare}(R) = \frac{\pi}{2}\alpha_0. \tag{9.84}$$

[6] $\delta'(0)$ should not be interpreted as a literal number: the connection is meaningful only after specifying a regularization and/or considering smeared states (test functions), and in the present discussion its dependence is absorbed into renormalized quantities. For instance, in a box of length L one has $\delta(0) \sim L/2\pi$ (and derivatives thereof depend on boundary conditions), while in a wave-packet regularization δ is replaced by a narrow function of width ϵ. The renormalization group equation should therefore be read as a compact way to track this regulator dependence.

The physical monodromy is kept fixed while the regulator dependence is absorbed into $Z_\gamma(R) = \alpha_0$ and the running parameter $\alpha'(\lambda)$. Eventually, while $\gamma^{\mathrm{phys}} = \pi/2$ in this way, the bin-level result and the continuum viewpoint can be unified within a renormalization framework, providing a consistent physical picture of monodromy around a resonance branch point in the presence of continuum normalization singularities.

9.4.5 Complex-scaled continuum states in momentum-bin method

Since treating the continuum spectrum entails substantial technical difficulties, we introduce a discretization scheme; in particular, applying it also to the CSM makes subsequent computations considerably more tractable. In this calculation module, we briefly review the momentum-bin method and fix our notation, mainly to make the paper self-contained.

Hermitian quantum mechanics

It is complicated to treat continuum states because they are intrinsically δ-function normalized. Let $\phi(k, x)$ denote a continuum state with a momentum k, whose orthogonality is determined by

$$\int \phi^*(k', x)\phi(k, x)\mathrm{d}x = \delta(k' - k). \tag{9.85}$$

We therefore discretize the continuum states using the momentum-bin method, in which the resulting bin states provide an accurate representation of the continuum states in realistic nuclear reaction calculations [119]. In this method, a continuum state is averaged over the width of the momentum bin Δk. It is then natural to define a discretized state by

$$\hat{\phi}_n(x) = \frac{1}{\sqrt{\Delta k}} \int_{k_n}^{k_{n+1}} \phi(k, x)\mathrm{d}k, \qquad k_{n+1} - k_n = \Delta k,\ n \in \mathbb{Z}. \tag{9.86}$$

The orthogonality of the discretized states is shown as

$$\begin{aligned} \int \hat{\phi}^*_{n'}(x)\hat{\phi}_n(x)\mathrm{d}x &= \frac{1}{\Delta k} \int_{k'_{n'}}^{k'_{n'+1}} \int_{k_n}^{k_{n+1}} \delta(k' - k)\mathrm{d}k'\mathrm{d}k \\ &= \delta_{n'n}. \end{aligned} \tag{9.87}$$

One may use the bracket notation as

$$\langle \hat{\phi}_{n'}, \hat{\phi}_n \rangle = \delta_{n'n}. \tag{9.88}$$

Moreover, a Hamiltonian h is diagonalized with regard to $\hat{\phi}_n(x)$ as follow: in scattering problem, from the Schrödinger equation

$$h\phi(k,x) = \frac{\hbar^2 k^2}{2m}\phi(k,x), \tag{9.89}$$

we find that

$$\begin{aligned}\int \hat{\phi}^*_{n'}(x) h \hat{\phi}_n(x) \mathrm{d}x &= \frac{1}{\Delta k}\int_{k'_{n'}}^{k'_{n'+1}} \int_{k_n}^{k_{n+1}} \frac{\hbar^2 k^2}{2m}\delta(k'-k)\mathrm{d}k'\mathrm{d}k \\ &= \hat{\epsilon}_n \delta_{n'n},\end{aligned} \tag{9.90}$$

where

$$\hat{\epsilon}_n \equiv \frac{1}{\Delta k}\int_{k_n}^{k_{n+1}} \frac{\hbar^2 k^2}{2m}\mathrm{d}k. \tag{9.91}$$

The relation between $\hat{\phi}_n(x)$ and $\phi(k,x)$ is now represented as

$$\int \phi^*(k,x)\hat{\phi}_n(x)\mathrm{d}x = \begin{cases} \frac{1}{\sqrt{\Delta k}} & k_n \le k \le k_{n+1}, \\ 0 & \text{otherwise.} \end{cases} \tag{9.92}$$

As a simple example, the momentum-bin discretization of a plane wave

$$\frac{1}{\sqrt{\Delta k}}\int_{k_n}^{k_{n+1}} \mathrm{e}^{\mathrm{i}kx}\mathrm{d}k = \frac{1}{\sqrt{\Delta k}}\frac{\mathrm{e}^{\mathrm{i}k_n x} - \mathrm{e}^{\mathrm{i}k_{n+1}x}}{\mathrm{i}x} \tag{9.93}$$

falls off as $1/x$ for large x.

Complex-scaled Hamiltonian

The momentum-bin method is well-established in Hermitian quantum mechanics. In this section, we extend it to non-Hermitian quantum mechanics. Let us consider the complex-scaled continuum state $\phi^\theta(k,x)$, which is a solution of the complex-scaled Hamiltonian h^θ. It is natural to consider that

the discretization of the state is given by

$$\hat{\phi}_n^{\theta}(x) = \frac{1}{\sqrt{\Delta k}} \int_{k_n}^{k_{n+1}} \phi^{\theta}(k, x) \mathrm{d}k. \tag{9.94}$$

The biorthogonal state of $\phi^{\theta}(k, x)$ is $\phi^{*\theta}(k, x)$ (see Chap. 6.1 in Ref. [139]). Thus, the biorthogonal state of $\hat{\phi}_n^{\theta}(x)$ is represented as

$$\hat{\phi}_n^{\mathrm{bi},\theta}(x) \equiv \frac{1}{\sqrt{\Delta k}} \int_{k_n}^{k_{n+1}} \phi^{*\theta}(k, x) \mathrm{d}k. \tag{9.95}$$

Then, the orthogonality of the scaled and discretized state is shown as

$$\begin{aligned} \int \hat{\phi}_{n'}^{\mathrm{bi},\theta}(x) \hat{\phi}_n^{\theta}(x) \mathrm{d}x &= \frac{1}{\Delta k} \int_{k'_{n'}}^{k'_{n'+1}} \int_{k_n}^{k_{n+1}} \left\{ \int \phi^{*\theta}(k', x) \phi^{\theta}(k, x) \mathrm{d}x \right\} \mathrm{d}k' \mathrm{d}k \\ &= \frac{1}{\Delta k} \int_{k'_{n'}}^{k'_{n'+1}} \int_{k_n}^{k_{n+1}} \delta(k' - k) \mathrm{d}k' \mathrm{d}k \\ &= \delta_{n'n}. \end{aligned} \tag{9.96}$$

The corresponding bracket notation is given as

$$(\hat{\phi}_{n'}, \hat{\phi}_n) = \delta_{n'n}, \tag{9.97}$$

which is the bilinear inner product.

Laboratory checkpoint

Before moving to the next stage, perform the following checks without copying the displayed final answer.

1. Expand the resonance condition to second order at the EP and derive the square-root branches and the associated Jordan vector.

2. Verify self-orthogonality with the complex-symmetric bilinear product and relate it to the derivative of the pole condition.

3. Repeat the encircling calculation at two momentum-bin widths and separate the bin-dependent norm from the limiting holonomy.

9.5 Problems for Stage VII

VII.1 Diagonalize a generic 2×2 complex-symmetric matrix and derive the discriminant condition for a second-order exceptional point.

VII.2 Construct a Jordan chain and derive the double-pole and simple-pole terms of its resolvent. Compare with a double zero of $\mathcal{C}_{\text{in}}(E)$.

VII.3 Prove self-orthogonality of the coalesced right vector with its left partner by differentiating the eigenvalue equation.

VII.4 Encircle the square-root branch point once and twice. Track eigenvalues, eigenvectors, and all gauge choices needed to compare the final vector with the initial one.

VII.5 Calculate the biorthogonal Berry connection for the 2×2 model. Determine which part changes under rescaling of left and right vectors.

VII.6 Replace a delta-normalized continuum state by a momentum bin of width Δk. Find the divergent normalization as $\Delta k \to 0$ and isolate a finite holonomy.

VII.7 Derive an RG-type equation that enforces bin-width independence of a renormalized geometric phase. Identify its integration constant as a physical convention or datum.

VII.8 Investigate an EP approaching a continuum threshold. Explain how the square-root branch from the EP competes with the threshold branch of the resolvent.

VII.9 Compute eigenvalue condition numbers around a loop enclosing an EP. Relate their peaks to pseudospectral sensitivity.

VII.10 Formulate a multiple-zero search using $\mathcal{C} = \partial_E \mathcal{C} = 0$. Propose a numerical continuation test that distinguishes an EP from an accidental near crossing.

Chapter 10

Stage VIII: Turn horizons into a resonance connection problem

Reader contract

The Regge–Wheeler and related master equations are derived before a spectral method is chosen. Horizon conditions are translated into incoming and outgoing connection data, after which exact WKB and complex scaling are compared for Schwarzschild, charged, and de Sitter geometries, including continuum response and coupled channels.

10.1 Derive black-hole master equations and their connection data

Calculation route

Prerequisites. Linearized field equations, spherical harmonics, and the resonance boundary condition of Stage I.

Calculation goal. Derive the Regge–Wheeler/Zerilli-type radial equation and identify its horizon and asymptotic WKB branches.

Completion criterion. Write the QNM condition as the vanishing of a prohibited horizon or infinity coefficient before choosing a numerical representation.

10.1.1 Master equation and boundary conditions

Consider a static, spherically symmetric metric

$$\mathrm{d}s^2 = -f(r)\mathrm{d}t^2 + \frac{\mathrm{d}r^2}{f(r)} + r^2\mathrm{d}\Omega_2^2, \tag{10.1}$$

where $\mathrm{d}\Omega_2^2$ is the line element on the unit two-sphere. Introduce the tortoise coordinate r_* by

$$\frac{\mathrm{d}r_*}{\mathrm{d}r} = \frac{1}{f(r)}. \tag{10.2}$$

After separation into angular harmonics and time dependence $\mathrm{e}^{-\mathrm{i}\omega t}$, many perturbation sectors reduce to

$$\left[-\frac{\mathrm{d}^2}{\mathrm{d}r_*^2} + V_{sl}(r)\right]\psi_{sl}(r_*) = \omega^2\psi_{sl}(r_*). \tag{10.3}$$

Here s labels the field or perturbation sector, l is the angular harmonic number, and V_{sl} is an effective potential. Equation (10.3) is a one-dimensional scattering problem with spectral energy

$$E = \omega^2. \tag{10.4}$$

For an asymptotically flat black hole, the event horizon is at $r_* \to -\infty$ and spatial infinity is at $r_* \to +\infty$. A quasinormal mode satisfies

$$\begin{aligned} &\psi_{sl}(r_*) \sim \mathrm{e}^{-\mathrm{i}\omega r_*}, && r_* \to -\infty, \\ &\psi_{sl}(r_*) \sim \mathrm{e}^{+\mathrm{i}\omega r_*}, && r_* \to +\infty. \end{aligned} \tag{10.5}$$

The first wave is ingoing through the future event horizon; the second is outgoing toward infinity. Relative to the potential barrier, both carry flux away from the interaction region. With the chosen time convention, a stable mode has $\operatorname{Im}\omega < 0$. Consequently the radial function grows at both ends of the real r_* line, exactly like a Gamow–Siegert state.

This identifies a black-hole quasinormal mode with a resonance pole of the continued retarded Green function. The definition does not depend on a particular numerical method [11, 141, 142].

10.1.2 Derivation of the Regge–Wheeler equation

We now derive the axial gravitational master equation rather than simply quoting its potential. The derivation also explains why a four-dimensional gauge theory of metric perturbations reduces to a one-dimensional Schrodinger problem. We use the gauge-invariant $2 + 2$ formulation of Refs. [143–146].

Write the Schwarzschild geometry as a warped product

$$\mathrm{d}s^2 = g_{ab}(x)\mathrm{d}x^a\mathrm{d}x^b + r^2(x)\Omega_{AB}\mathrm{d}\theta^A\mathrm{d}\theta^B, \tag{10.6}$$

where $x^a = (t, r)$,

$$g_{ab}\mathrm{d}x^a\mathrm{d}x^b = -f(r)\mathrm{d}t^2 + f(r)^{-1}\mathrm{d}r^2, \qquad f(r) = 1 - \frac{2M}{r}, \tag{10.7}$$

and Ω_{AB} is the metric of the unit two-sphere. Lower-case Latin indices refer to the Lorentzian orbit space $\mathcal{M}^2$, upper-case Latin indices to S^2, and Greek indices to the full spacetime. Let ∇_a and D_A be the corresponding covariant derivatives, and let ε_{AB} be the volume form on S^2.

Scalar harmonics obey

$$D^A D_A Y_{lm} = -l(l+1)Y_{lm}. \tag{10.8}$$

From them construct the odd-parity vector and tensor harmonics

$$X^{lm}_A = -\varepsilon_A{}^B D_B Y_{lm}, \tag{10.9}$$

$$X^{lm}_{AB} = -\frac{1}{2}\left(\varepsilon_A{}^C D_B + \varepsilon_B{}^C D_A\right) D_C Y_{lm}. \tag{10.10}$$

Writing $L = l(l+1)$ and $\lambda = L - 2 = (l-1)(l+2)$, the identities needed in the projection are

$$D^A X^{lm}_A = 0, \qquad D^B D_B X^{lm}_A = (1-L)X^{lm}_A, \tag{10.11}$$

$$X^{lm}_{AB} = D_{(A}X^{lm}_{B)}, \qquad D^B X^{lm}_{AB} = -\frac{\lambda}{2}X^{lm}_A. \tag{10.12}$$

With unit-normalized scalar harmonics their norms are

$$\int_{S^2} \overline{X^{lm}_A} X^{A,l'm'}\,\mathrm{d}\Omega = L\,\delta_{ll'}\delta_{mm'}, \tag{10.13}$$

$$\int_{S^2} \overline{X^{lm}_{AB}} X^{AB,l'm'}\,\mathrm{d}\Omega = \frac{L\lambda}{2}\,\delta_{ll'}\delta_{mm'}. \tag{10.14}$$

The factor λ explains both why the tensor harmonic vanishes for $l = 1$ and why the radiative master variable is defined only for $l \geq 2$. Under the parity map $(\vartheta, \varphi) \mapsto (\pi - \vartheta, \varphi + \pi)$, these harmonics transform with parity $(-1)^{l+1}$. Orthogonality of spherical harmonics ensures that different (l, m) sectors decouple at linear order.

For a fixed l, m, the most general odd-parity metric perturbation is

$$\begin{aligned}\delta g_{ab}^{\rm odd} &= 0,\\ \delta g_{aB}^{\rm odd} &= h_a(t,r) X_B^{lm},\\ \delta g_{AB}^{\rm odd} &= h_2(t,r) X_{AB}^{lm}.\end{aligned} \tag{10.15}$$

In Schwarzschild coordinates $h_t = h_0$ and $h_r = h_1$ in the original Regge–Wheeler notation. There is no odd $l = 0$ harmonic. The $l = 1$ vacuum sector changes the angular momentum of the background and is not radiative; the wave equation below concerns $l \geq 2$.

An infinitesimal odd gauge transformation is generated by $\xi_A = \xi(t,r) X_A^{lm}$ and gives

$$h_a \longmapsto h_a - \nabla_a \xi + \frac{2}{r} r_a \xi, \tag{10.16}$$

$$h_2 \longmapsto h_2 - 2\xi, \tag{10.17}$$

where $r_a := \nabla_a r$. The combination

$$\widetilde{h}_a = h_a - \frac{1}{2}\nabla_a h_2 + \frac{1}{r} r_a h_2 \tag{10.18}$$

is gauge invariant. Choosing $\xi = h_2/2$ sets $h_2 = 0$; this is the Regge–Wheeler gauge, in which $\widetilde{h}_a = h_a$. The gauge choice is a convenience, while Eq. (10.18) shows that the final master field is not a gauge artifact.

The linearized vacuum equation is $\delta G_{\mu\nu} = 0$. Since the Schwarzschild background is Ricci flat, one may begin from

$$\delta R_{\mu\nu} = \frac{1}{2}\left(\nabla^\rho \nabla_\mu h_{\nu\rho} + \nabla^\rho \nabla_\nu h_{\mu\rho} - \nabla^\rho \nabla_\rho h_{\mu\nu} - \nabla_\mu \nabla_\nu h\right), \tag{10.19}$$

where $h = g^{\mu\nu} h_{\mu\nu}$. Substitute Eq. (10.15), use Eq. (10.8), and project onto X_A^{lm} and X_{AB}^{lm}. The independent gauge-invariant equations can be written

$$\begin{aligned} 0 = P_a = &-\Box_2 \widetilde{h}_a + \nabla_a \nabla_b \widetilde{h}^b + \frac{2}{r}\left(r_b \nabla_a \widetilde{h}^b - r_a \nabla_b \widetilde{h}^b\right)\\ &- \frac{2}{r^2} r_a r_b \widetilde{h}^b + \frac{l(l+1)}{r^2}\widetilde{h}_a, \end{aligned} \tag{10.20}$$

$$0 = P = \nabla_a \widetilde{h}^a, \tag{10.21}$$

where $\Box_2 = g^{ab}\nabla_a \nabla_b$. The remaining projected equation follows from these

through the linearized Bianchi identity. Equations (10.20) and (10.21) display the two operations hidden when the Regge–Wheeler potential is merely quoted: angular derivatives produce $l(l+1)/r^2$, while the warped-sphere curvature and radial derivatives produce the M/r^3 term.

The component equations and their elimination

The covariant equations can be checked without suppressing the intermediate calculation. In Regge–Wheeler gauge write

$$\widetilde{h}_a \mathrm{d}x^a = h_0(t,r)\mathrm{d}t + h_1(t,r)\mathrm{d}r. \tag{10.22}$$

Because the determinant of the orbit-space metric is -1, Eq. (10.21) becomes

$$-\frac{1}{f}\partial_t h_0 + \partial_r(f h_1) = 0. \tag{10.23}$$

Direct evaluation of $P_t = 0$ and $P_r = 0$ gives

$$0 = f\left(-\partial_r^2 h_0 + \partial_t\partial_r h_1 + \frac{2}{r}\partial_t h_1\right) + \left(\frac{L}{r^2} - \frac{4M}{r^3}\right) h_0, \tag{10.24}$$

$$0 = \frac{1}{f}\left(\partial_t^2 h_1 - \partial_t\partial_r h_0 + \frac{2}{r}\partial_t h_0\right) + \frac{\lambda}{r^2} h_1. \tag{10.25}$$

Only two of Eqs. (10.23)– (10.25) are independent. Substitution into the linearized Bianchi identity

$$\nabla_a P^a + \frac{2}{r} r_a P^a - \frac{\lambda}{r^2} P = 0 \tag{10.26}$$

shows which equation is propagated by the other two.

Now define the original Regge–Wheeler variable

$$Q(t,r) = \frac{f(r)}{r} h_1(t,r). \tag{10.27}$$

The constraint reconstructs the nondynamical component:

$$\partial_t h_0 = f\partial_r(rQ). \tag{10.28}$$

Insert $h_1 = rQ/f$ and Eq. (10.28) into Eq. (10.25). Before simplification one

obtains

$$\frac{r}{f}\partial_t^2 Q - \partial_r[f(Q + r\partial_r Q)] + \frac{2f}{r}(Q + r\partial_r Q) + \frac{\lambda}{r}Q = 0. \tag{10.29}$$

Using $f' = 2M/r^2$ and $\partial_{r_*} = f\partial_r$, this is exactly

$$\left[-\partial_t^2 + \partial_{r_*}^2 - f\left(\frac{L}{r^2} - \frac{6M}{r^3}\right)\right] Q = 0. \tag{10.30}$$

For a nonzero Fourier frequency, Eq. (10.28) also gives the explicit recovery formula

$$h_0(r) = \frac{\mathrm{i}f(r)}{\omega}\frac{\mathrm{d}}{\mathrm{d}r}[rQ(r)] \qquad \text{for time dependence } \mathrm{e}^{-\mathrm{i}\omega t}. \tag{10.31}$$

The static sector must be treated before division by ω; for $l = 1$ it contains the infinitesimal Kerr perturbation rather than radiation.

The Cunningham–Price–Moncrief master scalar is

$$\Psi_{\mathrm{odd}} = \frac{2r}{\lambda}\varepsilon^{ab}\left(\nabla_a \widetilde{h}_b - \frac{2}{r} r_a \widetilde{h}_b\right), \tag{10.32}$$

where ε^{ab} is the volume form on $\mathcal{M}^2$. The coordinate-free version of the component elimination applies $\varepsilon^{ab}\nabla_a$ to Eq. (10.20), uses Eq. (10.21), and uses the Schwarzschild background identities

$$\nabla_a \nabla_b r = \frac{M}{r^2} g_{ab}, \qquad r_a r^a = f(r). \tag{10.33}$$

Collecting the terms gives the explicit identity

$$\varepsilon^{ab}\nabla_a P_b = -\frac{\lambda}{2r}\left[\Box_2 - \frac{L}{r^2} + \frac{6M}{r^3}\right]\Psi_{\mathrm{odd}}. \tag{10.34}$$

Thus $P_a = 0$ gives the covariant Regge–Wheeler equation

$$\left[\Box_2 - \frac{l(l+1)}{r^2} + \frac{6M}{r^3}\right]\Psi_{\mathrm{odd}} = 0. \tag{10.35}$$

For a scalar on the orbit space,

$$\Box_2 \Psi = -\frac{1}{f}\partial_t^2 \Psi + \partial_r\left(f\partial_r \Psi\right). \tag{10.36}$$

Multiplying Eq. (10.35) by f and using $\partial_{r_*} = f\partial_r$ gives

$$\left[-\partial_t^2 + \partial_{r_*}^2 - V_l^{\mathrm{RW}}(r)\right]\Psi_{\mathrm{odd}} = 0, \tag{10.37}$$

with

$$V_l^{\mathrm{RW}}(r) = f(r)\left[\frac{l(l+1)}{r^2} - \frac{6M}{r^3}\right]. \tag{10.38}$$

Finally, $\Psi_{\mathrm{odd}}(t,r) = \mathrm{e}^{-\mathrm{i}\omega t}\psi_l(r)$ turns Eq. (10.37) into

$$\left[-\frac{\mathrm{d}^2}{\mathrm{d}r_*^2} + V_l^{\mathrm{RW}}(r)\right]\psi_l = \omega^2\psi_l. \tag{10.39}$$

The familiar one-dimensional resonance equation is therefore the gauge-invariant curl of the projected linearized Einstein equations. The original Regge–Wheeler master function

$$\Psi_{\mathrm{RW}} = \frac{1}{r}r^a\widetilde{h}_a = \frac{f(r)}{r}h_1 \tag{10.40}$$

in Regge–Wheeler gauge satisfies the same vacuum equation and is related to a time derivative of Ψ_{odd}. Different normalizations of the master variable therefore produce the same potential and QNM spectrum.

10.1.3 Schwarzschild potentials

For a Schwarzschild black hole of mass $M > 0$,

$$f(r) = 1 - \frac{2M}{r}, \qquad r_* = r + 2M\log\left(\frac{r}{2M} - 1\right). \tag{10.41}$$

For a scalar field ($s = 0$), electromagnetic axial perturbation ($s = 1$), and gravitational axial perturbation ($s = 2$), a compact Regge–Wheeler-type potential is

$$V_{sl}^{\mathrm{RW}}(r) = f(r)\left[\frac{l(l+1)}{r^2} + \frac{2M(1-s^2)}{r^3}\right]. \tag{10.42}$$

For $s = 2$, this is the Regge–Wheeler potential [143]. Even-parity gravitational perturbations obey the Zerilli equation. With

$$\Lambda_l = \frac{(l-1)(l+2)}{2}, \tag{10.43}$$

the Zerilli potential is

$$V_l^{\mathrm{Z}}(r) = f(r)\frac{2\Lambda_l^2(\Lambda_l+1)r^3 + 6\Lambda_l^2 M r^2 + 18\Lambda_l M^2 r + 18M^3}{r^3(\Lambda_l r + 3M)^2}. \tag{10.44}$$

The axial and polar gravitational spectra are isospectral under the standard boundary conditions, although their wave functions and source couplings differ [147, 148].

The potentials vanish exponentially at the horizon but only as inverse powers at spatial infinity. The long-range tail produces a branch cut in the frequency-domain Green function and a late-time power-law tail. A pure sum of QNMs is therefore not a globally complete time-domain expansion for asymptotically flat geometry [149–151].

10.1.4 Reissner–Nordström backgrounds

For electric charge Q_{e},

$$f(r) = 1 - \frac{2M}{r} + \frac{Q_{\mathrm{e}}^2}{r^2}, \qquad r_\pm = M \pm \sqrt{M^2 - Q_{\mathrm{e}}^2}. \tag{10.45}$$

The radii r_+ and r_- are the outer and inner horizons when $|Q_{\mathrm{e}}| < M$. Electromagnetic and gravitational perturbations couple, but gauge-invariant combinations reduce the problem to two decoupled master equations of the form (10.3). Their effective potentials can be written schematically as the eigenvalues of a 2×2 potential matrix

$$\boldsymbol{V}_l(r) = \begin{pmatrix} V_l^{\mathrm{em}}(r) & V_l^{\mathrm{mix}}(r) \\ V_l^{\mathrm{mix}}(r) & V_l^{\mathrm{grav}}(r) \end{pmatrix}. \tag{10.46}$$

The diagonalizing combinations and parity relations are described by Moncrief and Chandrasekhar [148, 152, 153].

At extremality, $|Q_{\mathrm{e}}| = M$ and

$$f(r) = \left(1 - \frac{M}{r}\right)^2. \tag{10.47}$$

The horizon is a double zero of f, so the tortoise coordinate has a pole as well as a logarithm. Near-horizon asymptotics and analytic continuation are qualitatively different from the nonextremal case. This makes extremal Reissner–Nordström a stringent test of both complex scaling and exact WKB

[18, 154, 155].

10.1.5 Green functions, poles, cuts, and excitation

Let $\psi_{\rm in}(\omega, r_*)$ satisfy the horizon condition and $\psi_{\rm up}(\omega, r_*)$ satisfy the infinity condition. The radial retarded Green function is

$$G_{\rm ret}(\omega; r_*, r'_*) = \frac{\psi_{\rm in}(\omega, r_<)\psi_{\rm up}(\omega, r_>)}{W(\omega)}, \tag{10.48}$$

where $r_< = \min(r_*, r'_*)$, $r_> = \max(r_*, r'_*)$, and $W(\omega)$ is the Wronskian. A QNM is a zero of $W(\omega)$, hence a pole of $G_{\rm ret}$. The pole residue depends on the derivative $W'(\omega_n)$ and on the source and observation points.

After inverse Fourier transformation, the response separates schematically into a prompt part, a sum over QNM poles, and branch-cut integrals. The onset time and practical number of modes depend on the source, observer, and analytic contour. This is why identifying accurate frequencies is necessary but not sufficient for ringdown reconstruction [156–159].

10.2 Read black-hole spectra from quantum periods and horizon monodromy

10.2.1 Spectral curve and complex horizons

Equation (10.3) has the exact-WKB form with

$$Q(r_*, \omega) = V(r(r_*)) - \omega^2. \tag{10.49}$$

Turning points solve $V(r) = \omega^2$. In the complex r plane, horizons are singular points of the transformation to r_*. Logarithms generate branch cuts and Stokes curves that can spiral around a horizon. An analytic continuation from the event horizon to infinity must account for these spirals and for the residues of $S_{\rm odd}$ at regular singular points [113].

The QNM condition is again a vanishing incoming coefficient. Starting with an ingoing solution at the event horizon, transport it across the complex Stokes graph and require the incoming component at the outer boundary to vanish. This is an open-path connection problem. Highly damped monodromy methods instead use closed contours around horizons and singularities. The two approaches share connection data but organize approximations differently

[160].

10.2.2 Quantum periods and Borel–Padé resummation

Let γ_i be cycles of the black-hole spectral curve. The quantum periods are Borel-resummed Voros integrals

$$\Pi_i(\omega,\hbar) = \mathcal{S}_\varphi \oint_{\gamma_i} S_{\rm odd}(r,\omega,\hbar)\mathrm{d}r. \tag{10.50}$$

In black-hole perturbation theory $\hbar$ is often a bookkeeping parameter and is set to one after the WKB coefficients are generated. A quantization condition has the form

$$\mathcal{Q}\left(\mathrm{e}^{\Pi_1},\ldots,\mathrm{e}^{\Pi_g};\omega\right) = 0, \tag{10.51}$$

where g is the number of independent periods relevant to the connection problem. High-order coefficients can be Borel transformed and approximated by Padé rational functions before Laplace integration. The procedure has successfully reproduced black-hole QNMs and has been extended to extremal Reissner–Nordström and Kerr quantum periods [155, 161, 162].

10.2.3 Relation to complex scaling

Complex scaling and exact WKB answer different numerical questions about the same analytic object. Complex scaling converts the boundary problem into a matrix eigenproblem and displays the rotated continuum explicitly. Exact WKB reduces the pole condition to a small number of resummed periods and connection multipliers. The former is well suited to coupled channels and continuum response; the latter can achieve high precision when the spectral curve and its cycles are tractable.

Their agreement can be checked at three levels. Pole locations should match. The scaling angle should select the same subdominant sectors as the WKB contour. Finally, residues computed from left–right eigenvectors should match derivatives of the exact connection coefficient. The third comparison is largely unexplored and would connect ringdown excitation factors directly to resurgent data.

10.2.4 Kerr as the next major test

Kerr perturbations are governed by the Teukolsky equation [163]. Separation introduces the azimuthal number m, the spin-weighted spheroidal eigenvalue,

and a radial equation whose coefficients depend on ω. Superradiance changes flux signs for $\omega - m\Omega_H$, where Ω_H is the horizon angular velocity. A direct CSM implementation must therefore handle a nonlinear, coupled angular–radial eigenvalue problem and choose analytic branches consistently.

Exact WKB can work with the associated quantum curve, but turning points and periods move with both ω and the angular eigenvalue. A promising hybrid strategy is to solve the angular problem spectrally, construct its analytic derivative with respect to ω, and insert it into either a nonlinear complex-scaled solver or a resummed radial quantization condition. Cross-validation against Leaver's method remains essential.

10.2.5 Late-time tails and branch cuts

In asymptotically flat spacetime, inverse-power tails of $V(r_*)$ produce a branch point at $\omega = 0$. The late-time signal is governed by the discontinuity across this cut rather than by the least damped QNM at arbitrarily late times. In exact WKB, the threshold appears through coalescing turning points and a change of Stokes topology. In complex scaling, it is the endpoint of the rotated continuum. A uniform treatment should combine pole residues, threshold scaling, and the continuum spectral density rather than attempting to approximate the cut by an ever larger set of overtones.

10.3 Represent black-hole QNMs by complex scaling

10.3.1 Complex deformation of the tortoise coordinate

Set

$$r_* = \mathrm{e}^{\mathrm{i}\theta} x, \qquad x \in \mathbb{R}, \qquad \theta > 0. \tag{10.52}$$

The complex-scaled master operator is

$$H_\theta = -\mathrm{e}^{-2\mathrm{i}\theta} \frac{\mathrm{d}^2}{\mathrm{d}x^2} + V_{sl}\Big(r(\mathrm{e}^{\mathrm{i}\theta} x)\Big) . \tag{10.53}$$

The QNM equation becomes

$$H_\theta \psi_{sl}^\theta = \omega^2 \psi_{sl}^\theta . \tag{10.54}$$

For a mode with $\omega = |\omega|e^{-i\varphi}$, both asymptotic waves in Eq. (10.5) decay on the deformed line when

$$\theta > \varphi. \tag{10.55}$$

Equivalently, $E = \omega^2$ lies above the continuum ray rotated by -2θ.

The formula is simple, but its analytic implementation is not automatic. The inverse map $r(r_*)$ is multivalued because the tortoise coordinate contains logarithms. A deformation must specify branches and avoid metric singularities. One may work directly with an analytically continued $V(r_*)$, use exterior scaling where the asymptotic form is controlled, or formulate the contour in the complex r plane. A numerical result without a documented branch choice is not reproducible.

10.3.2 Why the spectral parameter is ω^2

Complex scaling rotates the continuum of the Schrödinger operator in the E plane. Because $E = \omega^2$, the map to the frequency plane is two-to-one. A ray with $\arg E = -2\theta$ corresponds to frequency rays with $\arg\omega = -\theta$ and $\arg\omega = \pi - \theta$. The retarded QNM branch is selected by the time convention and the horizon/infinity boundary conditions. Plotting eigenvalues directly in the ω plane without tracking the square-root branch can misidentify time-reversed or negative-frequency partners.

If the potential depends on ω, as happens after some transformations of the Kerr or coupled-channel equations, the problem is a nonlinear eigenvalue problem rather than Eq. (10.54). Linearizing it by enlarging the state space is possible only for particular rational or polynomial dependence. This is one reason the extension from static spherical backgrounds to Kerr is nontrivial.

10.3.3 Basis construction and parity

The effective barrier is centered in a finite range of r_*. One may use even and odd Gaussian functions as in Eq. (6.104), even though the black-hole potential itself need not have exact reflection symmetry. Both parity families together span general functions. Polynomial times Gaussian bases,

$$\phi_{np}(x) = x^p e^{-\alpha_n x^2}, \qquad p = 0,\, 1,\, \ldots,\, p_{\max}, \tag{10.56}$$

and complex-range Gaussians improve oscillatory resolution. Nonorthogonal blocks can grow or decay exponentially under scaling, so block balancing and overlap truncation are essential for coupled channels [18, 19].

The output should be analyzed in $E = \omega^2$ first. A candidate QNM is an isolated eigenvalue stable under θ, N, basis widths, integration range, and branch conventions. Only then should a square root be taken to quote ω. Low-lying, weakly damped modes are usually much more stable than high overtones because they lie farther from the rotated continuum and are represented by less oscillatory scaled wave functions.

10.3.4 Schwarzschild and extremal RN benchmarks

Leaver's continued-fraction method provides accurate benchmark frequencies for Schwarzschild and Reissner–Nordström backgrounds [102, 149, 164]. Complex-scaling calculations reproduce low-lying Schwarzschild Regge–Wheeler modes and extend to scalar, electromagnetic, and gravitational sectors of extremal Reissner–Nordström [18]. The most robust agreement occurs for the fundamental modes. First overtones require broader basis scans, while still higher modes can be difficult to distinguish from continuum pseudostates in an unoptimized Gaussian basis.

This pattern has a spectral explanation. For fixed θ, the distance between a pole and the rotated continuum controls isolation in the non-normal eigenproblem. Higher overtones have larger negative imaginary parts and lie closer to, or below, the accessible ray. Increasing θ exposes them but also probes a wider complex-coordinate sector where the potential and basis may be less well conditioned. There is therefore no monotonic rule that a larger scaling angle is numerically better.

10.3.5 Spectral instability and pseudospectra

Black-hole QNM operators can be highly non-normal. Define the ϵ-pseudospectrum of the matrix pencil (H^θ, N) by

$$\sigma_\epsilon(H^\theta, N) = \left\{ z \in \mathbb{C} : s_{\min}(H^\theta - zN) < \epsilon \right\}, \tag{10.57}$$

where $s_{\min}$ is the smallest singular value after a documented basis normalization. Large pseudospectral contours indicate that a small potential or discretization perturbation can move eigenvalues far from their unperturbed positions [165, 166].

Spectral instability does not imply identical instability of all time-domain observables. The resolvent norm, residues, source projection, and duration of the observation determine whether a shifted pole has appreciable effect.

Greybody factors and suitably integrated response functions can be more stable than individual high overtones [167]. Complex scaling is useful here because it gives access to both poles and the deformed continuum resolvent.

10.4 Calculation laboratory VIII-A: Schwarzschild and extremal Reissner–Nordstrom QNMs

Calculation route

Prerequisites. The Regge–Wheeler/Zerilli reduction, QNM boundary conditions, analytic dilation of the tortoise coordinate, and basis stability.

Calculation goal. The Regge–Wheeler/Zerilli–Moncrief reduction, complex-scaled basis construction, matrix elements, stability tests, numerical spectra, Leaver benchmarks, continuum density, and complex-range Gaussians.

Completion criterion. Construct the complex-scaled black-hole matrix problem, identify stable QNMs, and reproduce the Schwarzschild and extremal-RN benchmarks.

This Laboratory reconstructs the calculation underlying Ref. [18]. The Regge–Wheeler and Zerilli–Moncrief derivations are given once in Sec. 10.1, including the charged background; general complex scaling is fixed in Stage IV. We therefore begin with the basis and matrix construction specific to the QNM calculation.

10.4.1 Finite-basis realization of the black-hole resonance problem

Numerical implementation and some schemes of choosing bases

Variational procedure to eigenvalue problem We now turn to the practical implementation of the complex-scaled eigenvalue problem. The purpose of this section is not to introduce a new mathematical structure, but rather to explain how the complex-scaled radial equation is converted into a finite-dimensional matrix problem suitable for numerical computation. As discussed in the previous subsection, the essential effect of complex scaling is to transform the outgoing-wave resonance problem into a non-Hermitian

eigenvalue problem. For the Schwarzschild case, this begins with the Regge–Wheeler equation, which has the Schrödinger-type form

$$\left[-\frac{\mathrm{d}^2}{\mathrm{d}r_*^2} + V_l(r)\right]\psi_l(r_*) = \omega^2\psi_l(r_*). \tag{10.58}$$

After complex scaling, the kinetic term acquires the factor $\mathrm{e}^{-2\mathrm{i}\theta}$, while the potential is evaluated along the deformed contour. The resulting equation can then be treated as an eigenvalue problem for the complex-scaled operator. To solve this problem numerically, we expand the complex-scaled wave function in a finite set of square-integrable basis functions and apply the Rayleigh–Ritz variational procedure. In the present work, we adopt several types of Gaussian basis functions of both even and odd parity. This choice is convenient because such a basis is analytically simple, provides stable matrix elements for the kinetic term, and allows a flexible coverage of the tortoise-coordinate domain through a geometric progression of Gaussian ranges. The complex-scaled differential equation is thereby reduced to a generalized matrix eigenvalue problem for the expansion coefficients. This basis-expansion strategy is particularly suitable for the present purpose. First, it is fully compatible with the CSM framework, in which resonance wave functions become effectively L^2-integrable after complex scaling. Second, it does not rely on a Frobenius expansion tied to a specific horizon structure, unlike continued-fraction approaches of Leaver type. This point is important for our broader goal of treating not only the Schwarzschild problem but also the Reissner–Nordström family within a common framework. In what follows, we first construct the matrix representation of the complex-scaled Regge–Wheeler operator in a simple Gaussian basis. We then explain how the generalized complex eigenvalue problem is solved in practice and how physically relevant QNM frequencies are identified among the resulting eigenvalues.

Demonstration in a simpler case: $\mathrm{e}^{-\alpha r_*^2}$ and $r_*\mathrm{e}^{-\alpha r_*^2}$ As a first implementation of the complex scaling method, we discretize the complex-scaled Regge–Wheeler equation in a Gaussian basis. The purpose of this subsection is mainly illustrative: it provides a direct realization of the CSM eigenvalue problem in terms of explicit basis functions and matrix elements, and it serves as a useful reference point before introducing more efficient basis choices in the next subsubsection. We begin with the Regge–Wheeler equation derived in Sec. 10.1, with the potential in Eq. (10.38). Under complex scaling, the

equation is transformed into

$$\left[-\mathrm{e}^{-2\mathrm{i}\theta}\frac{\mathrm{d}^2}{\mathrm{d}r_*^2}+V_l^\theta(r_*)\right]\psi_l^\theta(r_*\mathrm{e}^{\mathrm{i}\theta})=(\omega^\theta)^2\psi_l^\theta(r_*\mathrm{e}^{\mathrm{i}\theta}), \tag{10.59}$$

where V_l^θ denotes the potential evaluated along the complex-rotated contour. To solve Eq. (10.59), we use the Gaussian expansion method [101] and expand the complex-scaled wave function in square-integrable Gaussian basis functions. Since, in practice, an expansion restricted to even functions alone is not sufficient to reproduce the quasinormal frequencies accurately, we include both even- and odd-parity Gaussian functions:

$$\psi_l^\theta(r_*\mathrm{e}^{\mathrm{i}\theta})=\sum_{i=1}^{i_{\max}}C_{li}^{\theta,(\mathrm{even})}\phi_i^{(\mathrm{even})}(r_*)+\sum_{i=1}^{i_{\max}}C_{li}^{\theta,(\mathrm{odd})}\phi_i^{(\mathrm{odd})}(r_*). \tag{10.60}$$

$i_{\max}$ is the truncation order of a basis. We choose

$$\phi_i^{(\mathrm{even})}(r_*)=N_i^{(\mathrm{even})}\mathrm{e}^{-\left(\frac{r_*}{r_i}\right)^2}=N_i^{(\mathrm{even})}\mathrm{e}^{-\alpha_i r_*^2}, \tag{10.61}$$

$$\phi_i^{(\mathrm{odd})}(r_*)=N_i^{(\mathrm{odd})}\left(\frac{r_*}{r_i}\right)\mathrm{e}^{-\left(\frac{r_*}{r_i}\right)^2}=N_i^{(\mathrm{odd})}(\sqrt{\alpha_i}\,r_*)\mathrm{e}^{-\alpha_i r_*^2}, \tag{10.62}$$

with

$$\alpha_i=\frac{1}{r_i^2}. \tag{10.63}$$

The normalization constants are chosen as

$$N_i^{(\mathrm{even})}=\left(\frac{2\alpha_i}{\pi}\right)^{1/4},\qquad N_i^{(\mathrm{odd})}=\left(\frac{2^5\alpha_i}{\pi}\right)^{1/4}. \tag{10.64}$$

The Gaussian ranges are taken in geometric progression,

$$r_i=r_{*0}\,a^{\,i-1},\qquad a=\left(\frac{r_{*\max}}{r_{*0}}\right)^{1/(i_{\max}-1)}, \tag{10.65}$$

so that the basis efficiently covers both short- and long-distance regions in the tortoise coordinate. Applying the Rayleigh–Ritz variational procedure to

the expansion (10.60), we obtain a generalized complex eigenvalue problem,

$$\sum_j \left[H_{ij}^{\theta} - (\omega^{\theta})^2 N_{ij} \right] C_j^{\theta} = 0, \tag{10.66}$$

where the Hamiltonian matrix has the block form

$$H_{ij}^{\theta} = \begin{pmatrix} T_{ij}^{\theta,(\text{even})} + V_{l,ij}^{\theta,(\text{even})} & V_{l,ij}^{\theta,(\text{even-odd})} \\ V_{l,ij}^{\theta,(\text{odd-even})} & T_{ij}^{\theta,(\text{odd})} + V_{l,ij}^{\theta,(\text{odd})} \end{pmatrix}, \tag{10.67}$$

and the overlap matrix is

$$N = \begin{pmatrix} N_{ij}^{(\text{even})} & 0 \\ 0 & N_{ij}^{(\text{odd})} \end{pmatrix}. \tag{10.68}$$

The overlap matrix elements are given analytically by

$$N_{ij}^{(\text{even})} = \int_{-\infty}^{\infty} \mathrm{d}r_* \, \phi_i^{(\text{even})}(r_*) \phi_j^{(\text{even})}(r_*) = N_i^{(\text{even})} N_j^{(\text{even})} \frac{\sqrt{\pi}}{(\alpha_i + \alpha_j)^{1/2}}, \tag{10.69}$$

$$N_{ij}^{(\text{odd})} = \int_{-\infty}^{\infty} \mathrm{d}r_* \, \phi_i^{(\text{odd})}(r_*) \phi_j^{(\text{odd})}(r_*) = N_i^{(\text{odd})} N_j^{(\text{odd})} \sqrt{\alpha_i \alpha_j} \frac{\sqrt{\pi}}{2(\alpha_i + \alpha_j)^{3/2}}. \tag{10.70}$$

Similarly, the kinetic-energy matrix elements can also be evaluated in closed form:

$$T_{ij}^{\theta,(\text{even})} = \mathrm{e}^{-2\mathrm{i}\theta} N_i^{(\text{even})} N_j^{(\text{even})} \frac{2\sqrt{\pi}\, \alpha_i \alpha_j}{(\alpha_i + \alpha_j)^{3/2}}, \tag{10.71}$$

$$T_{ij}^{\theta,(\text{odd})} = \mathrm{e}^{-2\mathrm{i}\theta} N_i^{(\text{odd})} N_j^{(\text{odd})} \frac{3\sqrt{\pi}\, (\alpha_i \alpha_j)^{3/2}}{(\alpha_i + \alpha_j)^{5/2}}. \tag{10.72}$$

The potential matrix elements are expressed as[1]

$$V_{l,ij}^{\theta,(\text{even})} = \mathrm{e}^{-\mathrm{i}\theta} N_i^{(\text{even})} N_j^{(\text{even})} \int_{-\infty}^{\infty} \mathrm{d}r_*\, V_l(r)\, \mathrm{e}^{-(\alpha_i+\alpha_j)\mathrm{e}^{-2\mathrm{i}\theta} r_*^2}, \tag{10.73}$$

$$V_{l,ij}^{\theta,(\text{odd})} = \mathrm{e}^{-3\mathrm{i}\theta} N_i^{(\text{odd})} N_j^{(\text{odd})} \sqrt{\alpha_i \alpha_j} \int_{-\infty}^{\infty} \mathrm{d}r_*\, V_l(r)\, r_*^2 \mathrm{e}^{-(\alpha_i+\alpha_j)\mathrm{e}^{-2\mathrm{i}\theta} r_*^2}, \tag{10.74}$$

$$V_{l,ij}^{\theta,(\text{even-odd})} = \mathrm{e}^{-2\mathrm{i}\theta} N_i^{(\text{even})} N_j^{(\text{odd})} \sqrt{\alpha_j} \int_{-\infty}^{\infty} \mathrm{d}r_*\, V_l(r)\, r_* \mathrm{e}^{-(\alpha_i+\alpha_j)\mathrm{e}^{-2\mathrm{i}\theta} r_*^2}, \tag{10.75}$$

$$V_{l,ij}^{\theta,(\text{odd-even})} = V_{l,ji}^{\theta,(\text{even-odd})}. \tag{10.76}$$

Here $r = r(r_*)$ is understood through the inverse tortoise-coordinate relation. For Schwarzschild spacetime, this relation may be written explicitly in terms of the Lambert W function, which is convenient for the numerical evaluation of the potential matrix elements. The resulting matrix is complex symmetric, and the quasinormal frequencies are obtained by solving the generalized complex eigenvalue problem (10.66). Although this Gaussian discretization is not yet the most efficient basis for the present problem, it is conceptually transparent and provides a direct illustration of how the CSM formulation can be implemented in practice. This representation therefore serves as a useful starting point before turning to improved basis choices in the next subsubsection.

Variations of Gaussian basis functions and diagonalization In addition to the Gaussian basis introduced in the previous subsubsection, it is useful to consider several alternative basis sets. The purpose of this subsubsection is to summarize the candidate basis functions used in our exploration of the CSM eigenvalue problem. While the real range Gaussian basis already provides a direct implementation of the CSM eigenvalue problem, other basis choices can offer improved flexibility for oscillatory or resonance-like wave functions.

[1] In the present implementation, the practical upper bound on the scaling angle is not set by the resonance physics itself, but by the convergence of the basis representation. The Gaussian basis, $\mathrm{e}^{-(\alpha_i+\alpha_j)\mathrm{e}^{-2\mathrm{i}\theta} r_*^2}$, converges only if $\cos 2\theta > 0$, i.e., $\theta < \pi/4$. More generally, in black-hole problems the inverse relation $r = r(r_*)$ may develop nontrivial branch structures after analytic continuation, so that the allowed range of the scaling angle can be restricted not only by the basis representation but also by the branch structure of $r(r_*)$ itself.

- **Real range Gaussian** The wave function is expanded as

$$\psi^{\theta}(r_* \mathrm{e}^{\mathrm{i}\theta}) = \sum_{i=1}^{i_{\max}} C_i^{\mathrm{even}} N_i^{\mathrm{even}} \mathrm{e}^{-\alpha_i r_*^2} + \sum_{i=1}^{i_{\max}} C_i^{\mathrm{odd}} N_i^{\mathrm{odd}} (\sqrt{\alpha_i}\, r_*) \mathrm{e}^{-\alpha_i r_*^2}. \tag{10.77}$$

- **Polynomial × real range Gaussian** The wave function is expanded as

$$\psi^{\theta}(r_* \mathrm{e}^{\mathrm{i}\theta}) = \sum_{p=0}^{p_{\max}} \sum_{i=1}^{i_{\max}} C_i^p N_i^p \, (\sqrt{\alpha_i}\, r_*)^p \, \mathrm{e}^{-\alpha_i r_*^2}. \tag{10.78}$$

  $p_{\max}$ is the highest degree of the polynomial of r_*; for each i, the basis is spanned by 1, r_*, r_*^2, …, $r_*^{p_{\max}}$ with the Gaussian factor.

- **sin/cos × real range Gaussian** The wave function is expanded as

$$\begin{aligned} \psi^{\theta}(r_* \mathrm{e}^{\mathrm{i}\theta}) = & \sum_{i=1}^{i_{\max}} C_i^{\sin} N_i^{\sin} \sin(\sqrt{\alpha_i}\, r_*) \, \mathrm{e}^{-\alpha_i r_*^2} \\ & + \sum_{i=1}^{i_{\max}} C_i^{\cos} N_i^{\cos} \cos(\sqrt{\alpha_i}\, r_*) \, \mathrm{e}^{-\alpha_i r_*^2}. \end{aligned} \tag{10.79}$$

The Real range Gaussian basis corresponds to the Polynomial × real range Gaussian one with $p_{\max} = 1$. Among these candidates, the Polynomial or sin/cos × real range Gaussian basis is expected to be particularly effective for representing oscillatory behavior while maintaining the analytic convenience of Gaussian matrix elements. After choosing a basis set, we represent the complex-scaled wavefunction as

$$\psi^{\theta}(r_* \mathrm{e}^{\mathrm{i}\theta}) = \sum_i c_i^{\theta} \phi_i(r_*), \tag{10.80}$$

where $\{\phi_i\}$ denotes one of the basis sets introduced above. Substituting this expansion into the complex-scaled wave equation and applying the Rayleigh–Ritz procedure, we obtain the generalized eigenvalue problem

$$H_\theta c = \lambda N c, \qquad \lambda = \omega^2, \tag{10.81}$$

where H_θ is the complex-scaled Hamiltonian matrix, N is the overlap matrix of the non-orthogonal basis, and c is the coefficient vector. For basis sets with

sufficiently mild overlap, one may solve Eq. (10.81) directly as a generalized complex eigenvalue problem. In practice, however, the basis functions used here are often strongly non-orthogonal, and the overlap matrix may contain nearly linearly dependent directions. To improve numerical stability, we therefore orthogonalize the basis before the final diagonalization whenever necessary. More precisely, we first diagonalize the overlap matrix,

$$N = UKU^{\dagger}, \tag{10.82}$$

where

$$K = \mathrm{diag}(\kappa_1, \kappa_2, \dots) \tag{10.83}$$

contains the eigenvalues of N, and U is the corresponding eigenvector matrix. Small eigenvalues of N indicate nearly redundant directions in the truncated basis. We therefore discard basis components whose overlap eigenvalues satisfy

$$|\kappa_i| \leq \epsilon_N, \tag{10.84}$$

with ϵ_N a numerical cutoff. We set $\epsilon_N = 10^{-5}$, a value often adopted empirically. After this truncation, the Hamiltonian is transformed to the orthonormalized basis according to

$$\tilde{H}_\theta = K^{-1/2} U^{\dagger} H_\theta U K^{-1/2}, \tag{10.85}$$

where only the retained subspace is understood. The generalized eigenvalue problem (10.81) is thereby reduced to the ordinary eigenvalue problem

$$\tilde{H}_\theta \tilde{c} = \lambda \tilde{c}. \tag{10.86}$$

We then diagonalize the complex matrix $\tilde{H}_\theta$ and obtain a set of complex eigenvalues λ_k. The corresponding quasinormal-frequency candidates are defined by

$$\omega_k = \sqrt{\lambda_k}, \tag{10.87}$$

where the physically relevant branch is selected by the usual QNM convention, namely

$$\operatorname{Im}\omega_k < 0. \tag{10.88}$$

In the present implementation, this orthogonalization step is particularly important for the polynomial and trigonometric Gaussian bases, for which the overlap matrix can become ill-conditioned as the basis size increases. The orthogonalized formulation substantially improves the numerical stability of the diagonalization and suppresses spurious directions associated with near-linear dependence in the original non-orthogonal basis. It should be emphasized that the output of a single diagonalization is not yet sufficient to identify the physical QNMs. The resulting spectrum generally contains not only resonance candidates but also discretized continuum states. For this reason, the physical QNM frequencies are identified only after the stability analysis described below, in particular through their dependence on the scaling angle, basis size, and basis parameters.

Stability analysis and identification of QNM frequencies

The eigenvalues obtained from a single diagonalization generally contain not only resonance candidates but also discretized continuum states and basis-dependent artifacts. Physical QNM frequencies are therefore identified through their stability under variations of the complex-scaling angle θ. In particular, resonance eigenvalues are expected to remain nearly invariant as θ is varied, whereas continuum-related eigenvalues typically move along the rotated continuum. A second diagnostic is the dependence on the basis size. Genuine QNM frequencies should approach stable values as the basis is enlarged. One should also examine the dependence on the basis parameters, such as the range parameters of the Gaussian basis. Physical resonances are expected to be much less sensitive to such changes than spurious states. Only eigenvalues that are simultaneously stable against variations of θ, basis size, and basis parameters are identified as physical QNM frequencies. When reference results are available, such as those obtained by Leaver's method, the identified QNM frequencies should also be compared with them in order to assess the numerical accuracy of the method.

10.4.2 Numerical simulation of QNM via CSM

Benchmark strategy

The complex-scaling eigenvalues shown in this section are compared with the standard Schwarzschild QNM data obtained by Leaver's continued-fraction method and others summarized in Sec. 10.4.3. In the present paper, the main role of this benchmark is not to rederive the continued-fraction formalism itself, but to use its established numerical values as a reference for identifying stable resonance eigenvalues under variations of the scaling angle, basis choice, and radial cutoff. When an isolated eigenvalue remains approximately invariant under these variations and agrees with the tabulated Leaver frequencies, we regard it as strong evidence that the mode is a genuine QNM rather than a discretized continuum artifact.

Trial run of the methodology and comparison of basis dependence

As a first trial run of the present methodology, we compare the complex-scaled spectra obtained with several basis sets. The purpose of this comparison is twofold. First, it provides a basic numerical check that the physically relevant QNM frequencies are reproduced in a reasonably stable manner across different basis choices. Second, it illustrates that, although the detailed distribution of the nonphysical eigenvalues depends on the basis, the low-lying resonance candidates are much more robust. We focus on the $l = 2$ gravitational mode ($s = 2$) for the Regge–Wheeler equation with $M = 0.5$ and consider three representative basis sets: the Real range Gaussian basis (equivalently, the Polynomial $\times$ real range Gaussian basis with $p_{\max} = 1$), the Polynomial $\times$ real range Gaussian basis with $p_{\max} = 3$, and the sin/cos $\times$ real range Gaussian basis. In each case, we diagonalize the complex-scaled Hamiltonian for nearby values of the scaling angle θ and compare the resulting eigenvalue distributions in the complex ω plane. The stability of the lowest resonance candidates under such changes provides a basic diagnostic for identifying the physical QNMs. Figure 10.1 shows the result obtained with the real range Gaussian basis. The scaling angle is taken to be $\theta = 25°$, $30°$ in the upper panel, and $\theta = 40°$, $42°$ in the lower panel. As seen in the figure, a sequence of discrete eigenvalues appears roughly along a rotated branch in the complex ω plane. This sequence represents the discretized continuum spectrum in the present finite-basis calculation. By contrast, the isolated points on the real-axis side of this branch are

interpreted as resonance eigenvalues, namely the QNM frequencies. This is the standard spectral pattern expected in the CSM: continuum-related states move with the scaling angle and align along the rotated branch, whereas genuine resonance states remain relatively isolated from it and show much weaker θ dependence. For this reason, the identification of QNM frequencies is based not on a single diagonalization result alone, but on whether an eigenvalue remains isolated from the rotated continuum and stable under changes of θ. The lowest mode in Fig. 10.1 is already rather stable under the changes $\theta = 25^\circ \to 30^\circ$ and $\theta = 40^\circ \to 42^\circ$, while the second mode exhibits a visibly larger displacement for $\theta \gtrsim 40^\circ$. This behavior is consistent with the general expectation that the fundamental QNM is more robust than higher-lying states against basis and scaling-angle variations. Figure 10.2 shows the corresponding result for the Polynomial $\times$ real range Gaussian basis with $p_{\max} = 3$. Compared with the previous case, the fundamental mode is again highly stable, whereas the second mode still shows a more noticeable θ dependence. At the same time, the polynomial basis yields a visibly better reproduction of the low-lying frequencies than the simple real range Gaussian basis, in particular for the first overtone. This indicates that the present CSM formulation robustly captures the lowest QNM, while higher modes remain more sensitive to the details of the truncated basis representation. Finally, Fig. 10.3 displays the result for the sin/cos $\times$ real range Gaussian basis. This basis is designed to incorporate more explicit oscillatory structure into the trial space and is therefore expected to be advantageous for resonance wave functions. However, in practice its performance is more delicate. Although the detailed eigenvalue distribution is broadly similar to the other cases, the low-lying resonance candidates are reproduced less accurately than with the polynomial basis. Moreover, obtaining results of comparable quality appears to require a more careful tuning of the numerical setup, including the number of basis functions, the Gaussian ranges, and the integration interval used for the interaction matrix. At the present stage, this makes the trigonometric basis less suitable for a systematic survey. Taken together, these figures show that the fundamental QNM is reproduced rather stably across different basis choices, while higher-lying states are more sensitive to the basis and to the scaling angle. This is precisely the behavior expected in a CSM calculation: physical resonance eigenvalues should remain comparatively stable, whereas continuum-related or spurious states tend to move more substantially under changes of the numerical representation. For convenience, the lowest and next resonance candidates obtained with the different basis sets are summarized in

Table 10.1. For the $l = 2$ Regge–Wheeler mode, the fundamental frequency is reproduced very stably and is already close to Leaver's value across the basis sets considered here. By contrast, the second-mode candidate shows a visibly stronger dependence on the basis choice and on the scaling angle. Among the basis sets examined here, the polynomial basis with $p_{\max} = 3$ gives the best overall agreement for both the fundamental mode and the first overtone, while the sin/cos basis reproduces even the fundamental mode less accurately in the present implementation. It is therefore natural to regard the Polynomial × real range Gaussian basis as the most practical choice for the subsequent calculations. The trial run in this subsection thus serves not only as a demonstration of basis dependence, but also as a concrete basis-selection step for the main numerical analysis below.

Table 10.1: Comparison of the lowest and next resonance candidates for the $l = 2$ Regge–Wheeler mode obtained with different basis sets. In this analysis, we set $s = 2$ and $M = 0.5$. For reference, the corresponding Schwarzschild QNM frequencies from Leaver's method are also shown.

Basis	Angle	Lowest mode ω_1	Next mode ω_2
Reference (Leaver)			
Leaver	—	$0.747343 - \mathrm{i}0.177925$	$0.693422 - \mathrm{i}0.547830$
Real range Gaussian basis			
Real range Gaussian	$\theta = 40°$	$0.747343 - \mathrm{i}0.177958$	$0.750229 - \mathrm{i}0.481678$
Real range Gaussian	$\theta = 42°$	$0.747349 - \mathrm{i}0.177940$	$0.738955 - \mathrm{i}0.497959$
Polynomial × real range Gaussian basis ($p_{\max} = 3$)			
Polynomial × Gaussian	$\theta = 40°$	$0.747348 - \mathrm{i}0.177926$	$0.712209 - \mathrm{i}0.485971$
Polynomial × Gaussian	$\theta = 42°$	$0.747345 - \mathrm{i}0.177925$	$0.704895 - \mathrm{i}0.502870$
sin/cos × real range Gaussian basis			
sin / cos × Gaussian	$\theta = 40°$	$0.743544 - \mathrm{i}0.168990$	$0.672161 - \mathrm{i}0.389585$
sin / cos × Gaussian	$\theta = 42°$	$0.746374 - \mathrm{i}0.169193$	$0.673930 - \mathrm{i}0.403464$

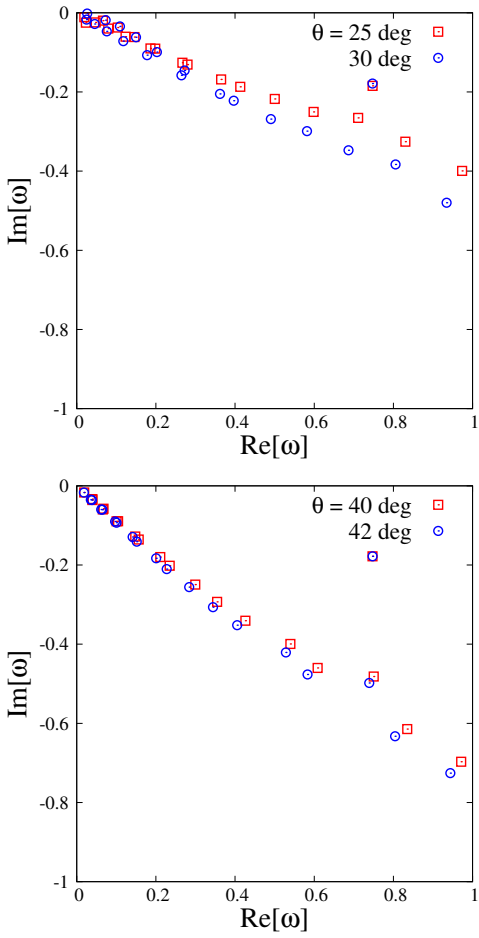

Figure 10.1: $l = 2$, Real range Gaussian basis. The scaling angle is taken to be $\theta = 25°$, $30°$ on the upper panel, and $\theta = 40°$, $42°$ on the lower panel. We take $i_{\max} = 30$, $r_{*0} = 0.1$, and $r_{*\,\max} = 60$. The sequence of points aligned approximately along the θ-rotated direction represents the discretized continuum spectrum, while the isolated points on the real-axis side are interpreted as resonance eigenvalues, namely the QNM frequencies. The lowest resonance candidate is $\omega_1 = 0.747343 - \mathrm{i}0.177958$ ($\theta = 40°$) and $\omega_1 = 0.747349 - \mathrm{i}0.177940$ ($\theta = 42°$). The next candidate is $\omega_2 = 0.750229 - \mathrm{i}0.481678$ ($\theta = 40°$) and $\omega_2 = 0.738955 - \mathrm{i}0.497959$ ($\theta = 42°$).

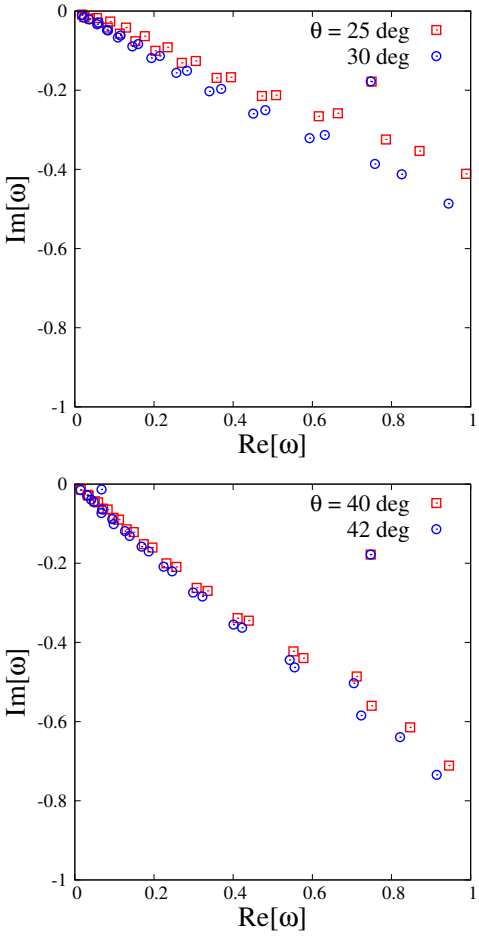

Figure 10.2: $l = 2$, Polynomial $\times$ real range Gaussian basis with $p_{\max} = 3$. We take $i_{\max} = 30$, $r_{*0} = 0.1$, and $r_{*\,\max} = 60$. The lowest resonance candidate is $\omega_1 = 0.747348 - \mathrm{i}0.177926$ ($\theta = 40°$) and $\omega_1 = 0.747345 - \mathrm{i}0.177925$ ($\theta = 42°$). The next candidate is $\omega_2 = 0.712209 - \mathrm{i}0.485971$ ($\theta = 40°$), $\omega_2 = 0.704895 - \mathrm{i}0.502870$ ($\theta = 42°$).

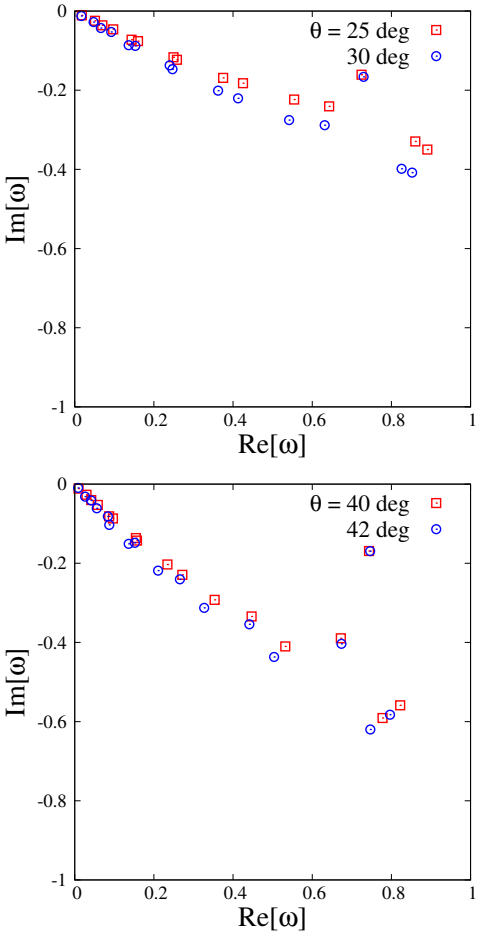

Figure 10.3: $l = 2$, sin/cos $\times$ real range Gaussian basis. We take $i_{\max} = 30$, $r_{*0} = 0.1$, and $r_{*\max} = 80$. The lowest resonance candidate is $\omega_1 = 0.743544 - \mathrm{i}0.168990$ ($\theta = 40°$) and $\omega_1 = 0.746374 - \mathrm{i}0.169193$ ($\theta = 42°$). The second-mode candidate is $\omega_2 = 0.672161 - \mathrm{i}0.389585$ ($\theta = 40°$) and $\omega_2 = 0.673930 - \mathrm{i}0.403464$ ($\theta = 42°$).

Basis selection from trial run of more general cases

Before presenting the main numerical results, we briefly summarize the outcome of a broader trial run aimed at selecting a practical working basis for the subsequent calculations. The purpose of this subsection is not yet to establish the final numerical accuracy of the method, but rather to identify which class of basis functions captures the low-lying QNM spectrum in a stable and manageable way in the Schwarzschild and extremal Reissner–Nordström problems. As candidate trial spaces, we considered several basis families built from real-range Gaussians. Among them, a particularly natural choice is the Polynomial × real range Gaussian basis,

$$\phi_{i,n}(r_*) \propto r_*^n \mathrm{e}^{-\alpha_i r_*^2}, \qquad n = 0,\, 1,\, 2,\, \ldots, \tag{10.89}$$

which extends the simplest Gaussian basis by increasing the polynomial degree. We also tested more explicitly oscillatory trial spaces, such as the sin/cos × real range Gaussian basis. The motivation for the latter is clear: since QNM wave functions are oscillatory, one may expect a trigonometric basis to be advantageous. In practice, however, the situation turned out to be more delicate. Our exploratory calculations indicate that the polynomial basis is the most practical choice among those examined here. For the low-lying modes, it reproduces the known QNM frequencies rather well over a moderate range of basis parameters. By contrast, the sin/cos basis appears to require a more careful tuning of the numerical setup, including the number of basis functions, the Gaussian ranges, and the integration interval used for the interaction matrix. At the present stage, this makes the trigonometric basis less convenient for a systematic study. This tendency is already visible in the Schwarzschild benchmark. The fundamental mode is reproduced stably across different basis parameter sets, whereas the first overtone shows a noticeably larger spread, and still higher modes become increasingly difficult to identify. This is consistent with the general expectation that relatively narrow resonances are easier to isolate in a finite-basis CSM calculation, while broad and strongly damped modes are more sensitive to basis truncation and to the vicinity of the rotated continuum. A similar tendency persists in the extremal Reissner–Nordström case. The lowest modes can still be identified in reasonable agreement with existing reference values, while higher and broader modes become more ambiguous. From the present exploratory viewpoint, the important practical conclusion is therefore the following: although several basis choices are in principle possible, the Polynomial × real range Gaussian

basis provides the best balance between numerical stability, flexibility, and ease of implementation at the current stage of the calculation. For this reason, in the following subsection we adopt the polynomial basis as our main working basis and present the numerical results obtained within that setup. The trial run described above should thus be understood as a preparatory step, which clarifies both the range of validity and the practical limitations of the present implementation.

Numerical results

Having selected the Polynomial × real range Gaussian basis as the main working basis, we now present the numerical results obtained with the present CSM formulation. Our emphasis is on the low-lying QNM frequencies, for which the stability of the calculation is best under control.

Schwarzschild case We begin with the Schwarzschild case, which serves as the primary benchmark. To examine the sensitivity of ω to Gaussian parameters, we performed calculations for several values of θ between 42° and 44° using the four parameter sets listed in Table 10.2. The results are shown

Table 10.2: Parameter sets used to examine the sensitivity of ω to the Gaussian basis parameters.

Set	$i_{\max}$	r_{*0}	$r_{*\max}$
1	30	0.1	60
2	30	0.1	80
3	40	0.1	60
4	40	0.1	80

in Fig. 10.4. The upper panels show the states obtained by diagonalizing H_θ for $l = 2$ and $l = 3$. In the lower panels, the values of ω identified as QNMs are compared with those obtained by Leaver's method for each case. For the Regge–Wheeler equation, the fundamental mode is reproduced with high accuracy, and the agreement with Leaver's continued-fraction values is very good. The first overtone can also be identified, although its numerical spread is already noticeably larger than that of the fundamental mode. For still higher overtones, the identification becomes substantially more difficult within the present implementation, and the extracted values are more sensitive to the basis parameters and the scaling angle. This behavior is natural in

CSM, since highly damped modes lie closer to the rotated continuum and are therefore more vulnerable to finite-basis effects.

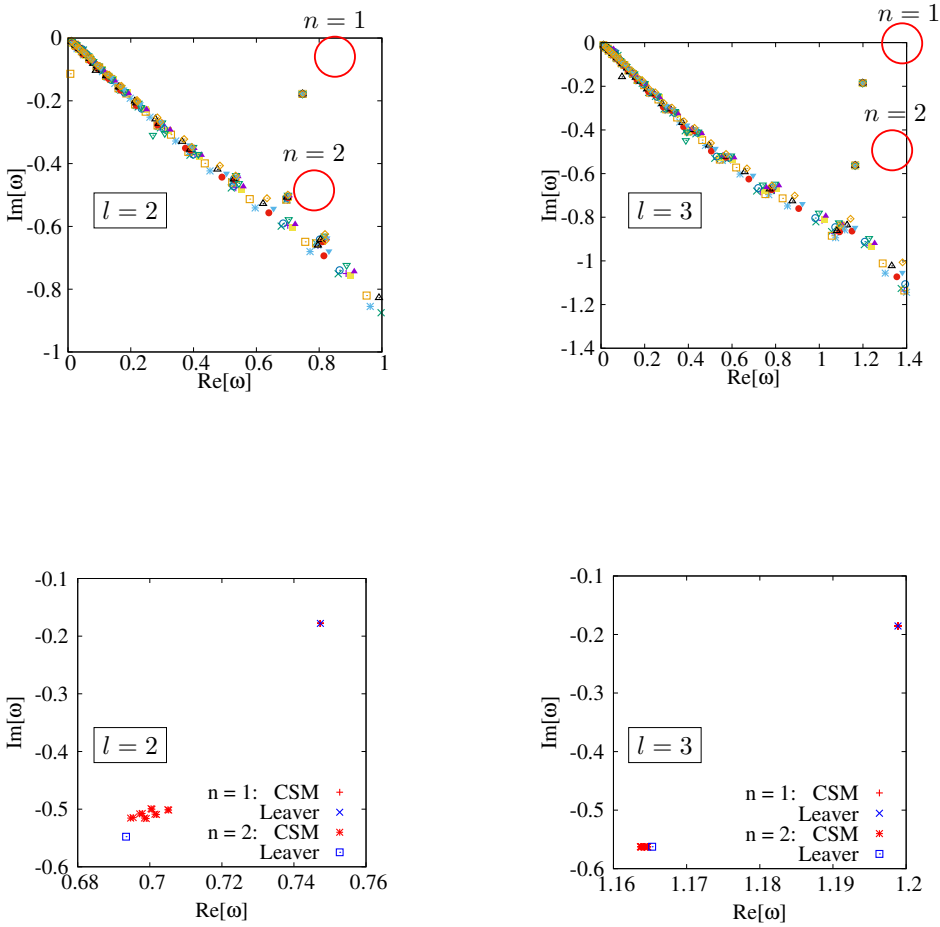

Figure 10.4: The Schwarzschild case. $M = 0.5$. **Upper panels:** eigenvalues of the complex-scaled Hamiltonian H_θ for $l = 2$ and $l = 3$. $\theta = 42°$–$44°$. **Lower panels**: comparison of the QNM candidates with Leaver's values.

Extremal Reissner–Nordström case We next turn to the extremal Reissner–Nordström problem. Here the present framework is particularly useful, since the standard continued-fraction treatment becomes more delicate in the extremal limit. As in the Schwarzschild case, we examine the sensitivity of the extracted frequencies to the Gaussian basis parameters. For $(s, l) = (0, 0)$, we use the same Gaussian parameter sets as listed in Table 10.2.

For the other cases, we adopt the parameter sets listed in Table 10.3. We again performed calculations for several values of θ from 42° to 44° The

Table 10.3: Parameter sets used to examine the sensitivity of ω to the Gaussian basis parameters.

Set	$i_{\max}$	r_{*0}	$r_{*\max}$
I	40	0.1	60
II	40	0.1	80
III	50	0.1	60
IV	50	0.1	80

numerical results are shown in Figs. 10.5, 10.6, and 10.7 for scalar ($s = 0$), odd-parity electromagnetic ($s = 1$), and odd-parity gravitational ($s = 2$) perturbations, respectively. As in the Schwarzschild case, the upper panels show the eigenvalues obtained by diagonalizing the complex-scaled Hamiltonian H_θ for several values of l, while the lower panels compare the frequencies identified as QNMs with existing reference values. In the extremal Reissner–Nordström case, the lower panels include the results of Onozawa *et al.* [154] for comparison. For the perturbations considered here, the low-lying QNM frequencies are again reproduced in reasonable agreement with the existing calculations. The agreement is especially good for the lowest and relatively narrow modes, whereas broader and more strongly damped modes exhibit a larger spread under changes of the basis parameters and the scaling angle. This is qualitatively the same tendency as in the Schwarzschild benchmark and is consistent with the general expectation that highly damped modes, being closer to the rotated continuum, are more sensitive to finite-basis effects in the CSM. It is also worth noting that, whenever both Onozawa *et al.* and WKB values are available, the present CSM results tend in general to lie closer to the former than to the latter. From the viewpoint of resonance identification, this is an encouraging sign that the present implementation is correctly capturing the low-lying QNM spectrum in the extremal Reissner–Nordström background. Another useful consistency check is provided by the known isospectrality between the odd-parity electromagnetic and odd-parity gravitational sectors in extremal Reissner–Nordström spacetime. Within the numerical precision of the present calculation, we confirm that the same QNM frequencies are obtained in these two sectors. This agreement provides an additional indication that the present CSM implementation is correctly

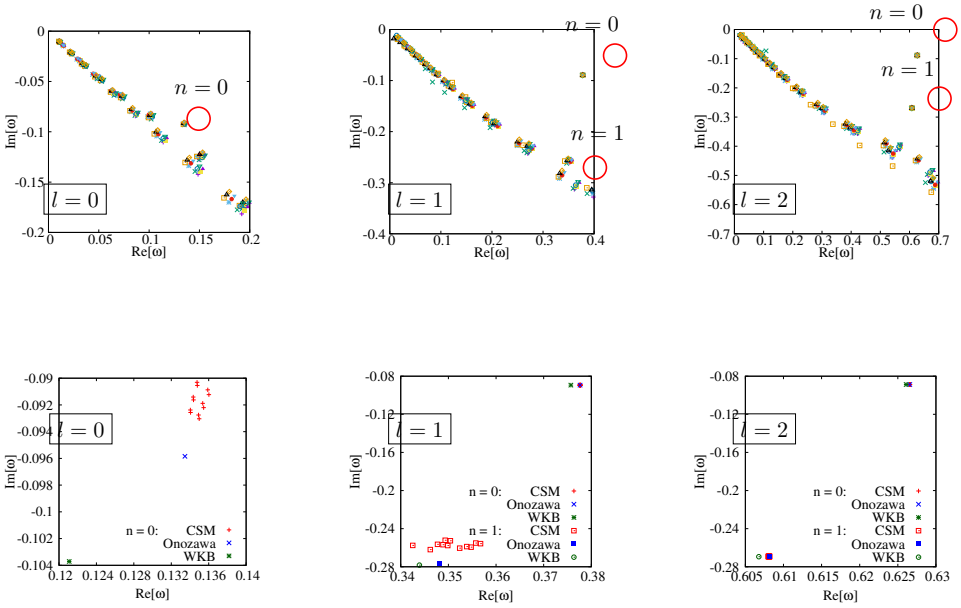

Figure 10.5: The extremal Reissner–Nordström scalar case. $M = 1$. Identification and comparison for $l = 0$, 1 and 2 with Onozawa *et al.*

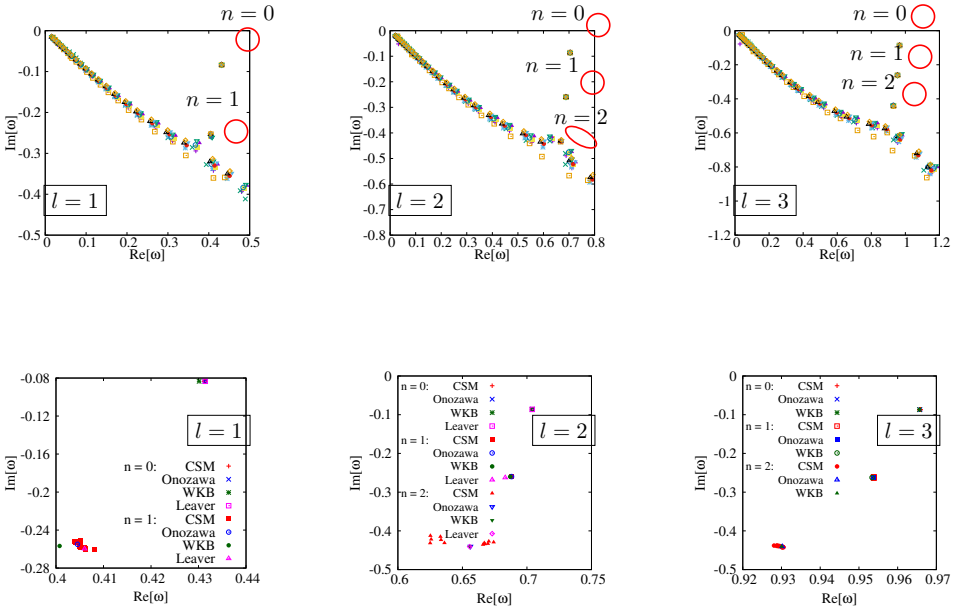

Figure 10.6: The extremal Reissner–Nordström odd-parity electromagnetic case. $M = 1$.

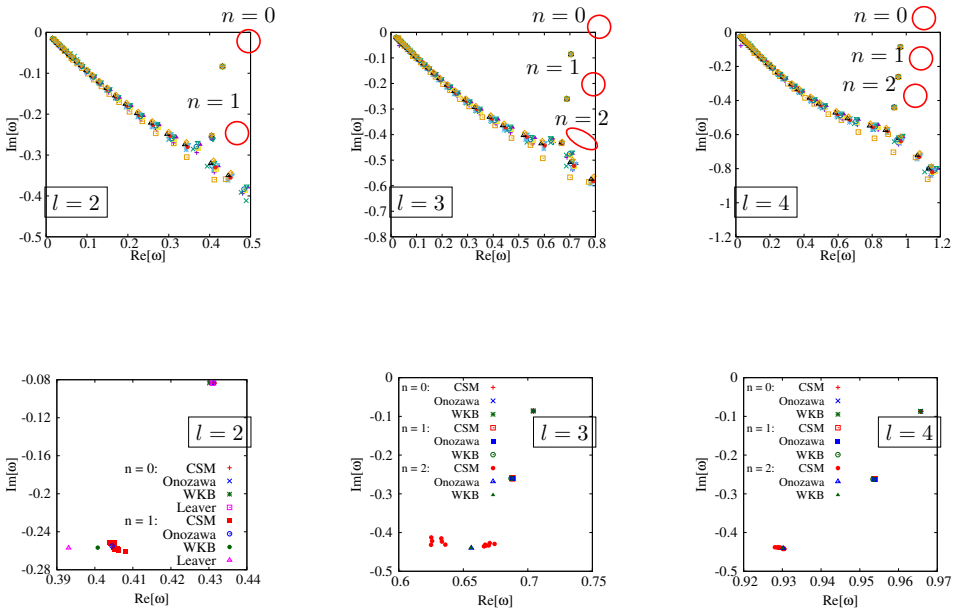

Figure 10.7: The extremal Reissner–Nordström odd-parity gravitational case. $M = 1$.

capturing the low-lying resonance spectrum.

Summary of low-lying QNM frequencies Overall, the numerical results support the following picture. For relatively narrow, isolated modes, the present CSM formulation performs well and yields QNM frequencies in good agreement with established methods. For broader, more strongly damped modes, however, numerical stability is reduced, and a more careful analysis of convergence with respect to basis size, basis parameters, integration range, and scaling angle will be required. Accordingly, the present results should be regarded as a first systematic demonstration of the method rather than as its final optimized form. In the remainder of this section, we summarize the low-lying frequencies obtained for the Schwarzschild and extremal Reissner–Nordström cases, and compare them with the available reference values reviewed in Sec. 10.4.3. Table 10.4 presents the numerical results obtained by the CSM for the Schwarzschild case. To estimate the numerical uncertainty of the extracted QNM frequencies, we use the spread of the results obtained from different numerical parameter sets. Let ω_i denote the frequency obtained in the ith run, and let N_{samp} be the total number of runs. We then define

the average frequency by

$$\bar{\omega} = \frac{1}{N_{\mathrm{samp}}} \sum_{i=1}^{N_{\mathrm{samp}}} \omega_i, \tag{10.90}$$

and the numerical uncertainty by

$$\Delta\omega = \max_i \left| \omega_i - \bar{\omega} \right|. \tag{10.91}$$

Accordingly, we quote the final result as

$$\omega = \bar{\omega} \pm \Delta\omega. \tag{10.92}$$

Here, $\Delta\omega$ should be understood as a practical measure of numerical stability rather than as a statistical error bar. Tables 10.5–10.6, 10.7–10.8, and 10.9–

Table 10.4: Numerical results of QNM frequencies of Schwarzschild. The numbers in parentheses indicate the estimated numerical uncertainty in the last quoted digits.

n	Method	$l = 2$		$l = 3$	
1	CSM	0.7473434(10)	−i0.17792461(83)	1.19888660(11)	−i0.18540611(13)
	Leaver	0.747343	−i0.177925	1.198887	−i0.185406
2	CSM	0.6998(55)	−i0.5081(90)	1.16423(53)	−i0.56265(27)
	Leaver	0.693422	−i0.547830	1.165288	−i0.562596
3	CSM		—	not identified	
	Leaver	0.602107	−i0.956554	1.103370	−i0.958186

10.10 show the corresponding results for the extremal Reissner–Nordström case with scalar ($s = 0$), odd-parity electromagnetic ($s = 1$), and odd-parity gravitational ($s = 2$) perturbations, respectively. Particular attention will be paid to the degree of stability under changes of the basis parameters, as well as to the distinction between robust resonance eigenvalues and basis-dependent artifacts. A few general trends may be read off from Tables 10.4–10.10. In both the Schwarzschild and extremal Reissner–Nordström cases, the agreement with the reference values is best for the lowest and relatively narrow modes. The fundamental mode is reproduced very accurately, whereas the numerical spread becomes larger for higher overtones. This is consistent with the general expectation in the CSM that strongly damped modes lie closer to the rotated continuum and are therefore more sensitive to finite-basis

Table 10.5: QNMs of extremal Reissner–Nordström scalar ($s = 0$) for $l = 0$ and $l = 1$

Method	$l = 0$		$l = 1$	
		$n = 0$		
CSM	0.1349(11)	−i0.0917(14)	0.3776424(14)	−i0.08938386(76)
Onozawa	0.13346	−i0.095844	0.37764	−i0.089384
WKB	0.12109	−i0.10371	0.37570	−i0.08936
		$n = 1$		
CSM		—	0.3507(82)	−i0.2571(49)
Onozawa	0.092965	−i0.33065	0.34818	−i0.27614
WKB	0.09157	−i0.33742	0.34392	−i0.27828
		$n = 2$		
CSM		—		—
Onozawa	0.075081	−i0.58833	0.29846	−i0.48643
WKB	0.05056	−i0.57164	0.29661	−i0.48145

Table 10.6: QNMs of extremal Reissner–Nordström scalar ($s = 0$) for $l = 2$

Method	$l = 2$	
	$n = 0$	
CSM	0.62657272(19)	−i0.088748359(98)
Onozawa	0.62657	−i0.088748
WKB	0.62609	−i0.08873
	$n = 1$	
CSM	0.60810(10)	−i0.26920(11)
Onozawa	0.60817	−i0.26909
WKB	0.60677	−i0.26944
	$n = 2$	
CSM	not identified	
Onozawa	0.57287	−i0.45820
WKB	0.57254	−i0.45750

Table 10.7: QNMs of extremal Reissner–Nordström odd-parity electromagnetic ($s = 1$) for $l = 1$ and $l = 2$

Method	$l = 1$		$l = 2$	
		$n = 0$		
CSM	0.431340738(82)	−i0.08346031(23)	0.704304022(14)	−i0.085973391(76)
Onozawa	0.43134	−i0.083460	0.70430	−i0.085973
Leaver	0.431415	−i0.08343	0.704075	−i0.086205
WKB	0.43013	−i0.08349	0.70398	−i0.08596
		$n = 1$		
CSM	0.4054(27)	−i0.2556(53)	0.688059(56)	−i0.259911(49)
Onozawa	0.40452	−i0.25498	0.68804	−i0.25992
Leaver	0.40602	−i0.259705	0.68315	−i0.26256
WKB	0.40076	−i0.25675	0.68701	−i0.26014
		$n = 2$		
CSM		—	0.649(25)	−i0.427(15)
Onozawa	0.35340	−i0.44137	0.65624	−i0.44007
Leaver	0.35347	−i0.44260	0.655675	−i0.4408
WKB	0.35136	−i0.44210	0.65575	−i0.43986

Table 10.8: QNMs of extremal Reissner–Nordström odd-parity electromagnetic ($s = 1$) for $l = 3$

Method	$l = 3$	
	$n = 0$	
CSM	0.965762603(31)	−i0.087001340(45)
Onozawa	0.96576	−i0.087001
Leaver		—
WKB	0.96563	−i0.08700
	$n = 1$	
CSM	0.953816(10)	−i0.2621206(52)
Onozawa	0.95381	−i0.26212
Leaver		—
WKB	0.95339	−i0.26218
	$n = 2$	
CSM	0.9296(16)	−i0.4403(26)
Onozawa	0.93020	−i0.44064
Leaver		—
WKB	0.93004	−i0.44056

Table 10.9: QNMs of extremal Reissner–Nordström odd-parity gravitational ($s = 2$) for $l = 2$ and $l = 3$

Method	$l = 2$		$l = 3$	
		$n = 0$		
CSM	0.431340738(82)	−i0.08346031(23)	0.704304022(14)	−i0.085973391(76)
Onozawa	0.43134	−i0.083460	0.70430	−i0.085973
Leaver	0.431415	−i0.08343	0.704075	−i0.086205
WKB	0.43013	−i0.08349	0.70398	−i0.08596
		$n = 1$		
CSM	0.4054(27)	−i0.2556(53)	0.688059(56)	−i0.259911(49)
Onozawa	0.40452	−i0.25498	0.68804	−i0.25992
Leaver	0.40602	−i0.259705	0.68315	−i0.26256
WKB	0.40076	−i0.25675	0.68701	−i0.26014
		$n = 2$		
CSM		—	0.649(25)	−i0.427(15)
Onozawa	0.35340	−i0.44137	0.65624	−i0.44007
Leaver	0.35347	−i0.44260	0.655675	−i0.4408
WKB	0.35136	−i0.44210	0.65575	−i0.43986

Table 10.10: QNMs of extremal Reissner–Nordström odd-parity gravitational ($s = 2$) for $l = 4$

Method	$l = 4$	
	$n = 0$	
CSM	0.965762603(31)	−i0.087001340(45)
Onozawa	0.96576	−i0.087001
Leaver		—
WKB	0.96563	−i0.08700
	$n = 1$	
CSM	0.953816(10)	−i0.2621206(52)
Onozawa	0.95381	−i0.26212
Leaver		—
WKB	0.95339	−i0.26218
	$n = 2$	
CSM	0.9296(16)	−i0.4403(26)
Onozawa	0.93020	−i0.44064
Leaver		—
WKB	0.93004	−i0.44056

effects. In the extremal Reissner–Nordström case, the present CSM values tend in general to be closer to the results of Onozawa *et al.* than to the corresponding WKB values. Moreover, the odd-parity electromagnetic and odd-parity gravitational sectors yield the same low-lying frequencies within the present numerical precision, in agreement with the known isospectrality of these sectors in the extremal Reissner–Nordström background. Taken together, these results indicate that the present implementation already captures the robust low-lying resonance spectrum reliably, while broader and more highly damped modes still require a more systematic study of convergence and numerical stability.

10.4.3 Leaver's method and benchmark tables

For later comparison, we briefly summarize Leaver's method for computing quasinormal mode frequencies given in Refs. [102, 149]. Let $\psi_l(r)$ denote the radial wave function. For the Regge–Wheeler equation, the effective potential vanishes both at the horizon and at spatial infinity. Hence the quasinormal-mode boundary conditions are

$$\psi_l(r)\big|_{\text{in}} \sim \mathrm{e}^{-\mathrm{i}\omega r_*} \sim (r-2M)^{-2\mathrm{i}M\omega} \qquad r \to 2M, \tag{10.93}$$

and

$$\psi_l(r)\big|_{\text{out}} \sim \mathrm{e}^{+\mathrm{i}\omega r_*} \sim \mathrm{e}^{\mathrm{i}\omega r}\, r^{2\mathrm{i}M\omega} \qquad r \to \infty, \tag{10.94}$$

where M is the black-hole mass, ω is the complex quasinormal frequency, and r_* is the tortoise coordinate. A convenient starting point is the generalized radial equation

$$\left[\Delta^{-s}\frac{\mathrm{d}}{\mathrm{d}r}\left(\Delta^{s+1}\frac{\mathrm{d}}{\mathrm{d}r}\right) - V(r)\right]\psi_l(r) = 0, \tag{10.95}$$

where s is the spin weight, $V(r)$ is the radial potential, and

$$\Delta = r^2 - 2Mr + a^2. \tag{10.96}$$

Here a is the Kerr rotation parameter. The Schwarzschild case is recovered by setting $a = 0$. To implement the boundary conditions, one introduces the

series ansatz

$$\psi_l(r) = \mathrm{e}^{\mathrm{i}\omega r}(r-r_-)^{-1-s+2\mathrm{i}M\omega+2\mathrm{i}M\sigma}(r-r_+)^{-s-2\mathrm{i}M\sigma}\sum_{n=0}^{\infty} a_n\left(\frac{r-r_+}{r-r_-}\right)^n, \tag{10.97}$$

with

$$r_\pm = M \pm \sqrt{M^2-a^2}, \qquad \sigma = \frac{1}{r_+-r_-}\left(r_+\omega - \frac{ma}{2M}\right). \tag{10.98}$$

Here m is the azimuthal quantum number. Substituting Eq. (10.97) into Eq. (10.95) yields a three-term recurrence relation for the expansion coefficients a_n:

$$\alpha_0 a_1 + \beta_0 a_0 = 0, \tag{10.99}$$

$$\alpha_n a_{n+1} + \beta_n a_n + \gamma_n a_{n-1} = 0, \qquad n \geq 1. \tag{10.100}$$

The coefficients α_n, β_n, and γ_n depend on the mode parameters, in particular on a, m, and ω. It is useful to define the ratio

$$A_n \equiv -\frac{a_n}{a_{n-1}}. \tag{10.101}$$

Then the recurrence relation implies

$$A_n = \frac{\gamma_n}{\beta_n - \alpha_n A_{n+1}}. \tag{10.102}$$

Iterating this relation gives the continued-fraction equation

$$\beta_0 = \alpha_0 A_1 = \frac{\alpha_0\gamma_1}{\beta_1 - \dfrac{\alpha_1\gamma_2}{\beta_2 - \dfrac{\alpha_2\gamma_3}{\beta_3 - \cdots}}}. \tag{10.103}$$

The quasinormal frequencies are obtained by solving Eq. (10.103). In practice, one truncates the continued fraction at sufficiently large order. Leaver solved, for example, the cases $l = 2, 3$ up to $N = 60$ as in Table 10.11. Nollert later improved the large-N convergence [164]. Table 10.12 summarizes QNM frequencies for extremal Reissner–Nordström black hole given by Onozawa *et al.* in Ref. [154].

Table 10.11: $l = 2$ and $l = 3$ Schwarzschild gravitational QNMs by Leaver's method [102, 149]. $(\mathrm{Re}\,\omega, \mathrm{Im}\,\omega)$ is shown. Here $s = 2$ and $M = 0.5$.

n	$l = 2:\ \omega_n$	$l = 3:\ \omega_n$
1	(0.747343, −0.177925)	(1.198887, −0.185406)
2	(0.693422, −0.547830)	(1.165288, −0.562596)
3	(0.602107, −0.956554)	(1.103370, −0.958186)
4	(0.503010, −1.410296)	(1.023924, −1.380674)
5	(0.415029, −1.893690)	(0.940348, −1.831299)
6	(0.338599, −2.391216)	(0.862773, −2.304303)
7	(0.266505, −2.895822)	(0.795319, −2.791824)
8	(0.185617, −3.407676)	(0.737985, −3.287689)
9	(0.000000, −3.998000)	(0.689237, −3.788066)
10	(0.126527, −4.605289)	(0.647366, −4.290798)
11	(0.153107, −5.121653)	(0.610922, −4.794709)
12	(0.165196, −5.630885)	(0.578768, −5.299159)
20	(0.175608, −9.660879)	(0.404157, −9.333121)
30	(0.165814, −14.677118)	(0.257431, −14.363580)
40	(0.156368, −19.684873)	(0.075298, −19.415545)
41	(0.154912, −20.188298)	(−0.000259, −20.015653)
42	(0.156392, −20.685530)	(0.017662, −20.566075)
50	(0.151216, −24.693716)	(0.134153, −24.119329)
60	(0.148484, −29.696417)	(0.163614, −29.135345)

Table 10.12: Quasinormal frequencies for the extremal Reissner–Nordström black hole with $M = 1$. The values $(\mathrm{Im}\,\omega, \mathrm{Re}\,\omega)$ are shown for each s and l. This table is taken from Ref. [154] (Onozawa *et al.*).

n	Method	$(s,l) = (2,2)$	$(2,3)$	$(2,4)$
0	Onozawa	(−0.083460, 0.43134)	(−0.085973, 0.70430)	(−0.087001, 0.96576)
	Leaver	(−0.083645, 0.43098)	—	—
	WKB	(−0.08349, 0.43013)	(−0.08596, 0.70398)	(−0.08700, 0.96563)
1	Onozawa	(−0.25498, 0.40452)	(−0.25992, 0.68804)	(−0.26212, 0.95381)
	Leaver	(−0.257055, 0.39309)	—	—
	WKB	(−0.25675, 0.40076)	(−0.26014, 0.68701)	(−0.26218, 0.95339)
2	Onozawa	(−0.44137, 0.35340)	(−0.44007, 0.65624)	(−0.44064, 0.93020)
	Leaver	(−0.442035, 0.353515)	—	—
	WKB	(−0.44210, 0.35136)	(−0.43986, 0.65575)	(−0.44056, 0.93004)
n	Method	$(s,l) = (1,1)$	$(1,2)$	$(1,3)$
0	Onozawa	(−0.083460, 0.43134)	(−0.085973, 0.70430)	(−0.087001, 0.96576)
	Leaver	(−0.08343, 0.431415)	(−0.086205, 0.704075)	—
	WKB	(−0.08349, 0.43013)	(−0.08596, 0.70398)	(−0.08700, 0.96563)
1	Onozawa	(−0.25498, 0.40452)	(−0.25992, 0.68804)	(−0.26212, 0.95381)
	Leaver	(−0.259705, 0.40602)	(−0.26256, 0.68315)	—
	WKB	(−0.25675, 0.40076)	(−0.26014, 0.68701)	(−0.26218, 0.95339)
2	Onozawa	(−0.44137, 0.35340)	(−0.44007, 0.65624)	(−0.44064, 0.93020)
	Leaver	(−0.44260, 0.35347)	(−0.4408, 0.655675)	—
	WKB	(−0.44210, 0.35136)	(−0.43986, 0.65575)	(−0.44056, 0.93004)
n	Method	$(s,l) = (0,0)$	$(0,1)$	$(0,2)$
0	Onozawa	(−0.095844, 0.13346)	(−0.089384, 0.37764)	(−0.088748, 0.62657)
	WKB	(−0.10371, 0.12109)	(−0.08936, 0.37570)	(−0.08873, 0.62609)
1	Onozawa	(−0.33065, 0.092965)	(−0.27614, 0.34818)	(−0.26909, 0.60817)
	WKB	(−0.33742, 0.09157)	(−0.27828, 0.34392)	(−0.26944, 0.60677)
2	Onozawa	(−0.58833, 0.075081)	(−0.48643, 0.29846)	(−0.45820, 0.57287)
	WKB	(−0.57164, 0.05056)	(−0.48145, 0.29661)	(−0.45750, 0.57254)

10.4.4 A note on continuum level density in the complex-scaling framework

In the main text, we have focused on the extraction of quasinormal-mode (QNM) frequencies as isolated resonance eigenvalues of the complex-scaled operator. For the present paper, this is the primary use of the complex scaling method (CSM). However, the CSM is not limited to discrete resonance poles. It also provides a natural framework for treating the continuum sector, which is physically important in black-hole perturbation theory. From the black-hole point of view, this issue is closely related to the late-time tail. While the intermediate-time ringdown is governed by QNM poles, the late-time signal is associated with continuum contributions, often described in terms of a branch cut of the Green function and the resulting power-law decay. For this reason, a quantity that probes the continuum sector is of direct physical interest. In the CSM framework, such a quantity is the continuum level density (CLD) [168]. Let H be the full operator and H_0 a suitable reference operator. The CLD is formally defined by

$$\Delta\rho(E) = -\frac{1}{\pi}\,\mathrm{Im}\,\mathrm{Tr}\left[\frac{1}{E-H+\mathrm{i}0} - \frac{1}{E-H_0+\mathrm{i}0}\right], \tag{10.104}$$

where E is the spectral parameter [169]. After complex scaling, this becomes

$$\Delta\rho^{\theta}(E) = -\frac{1}{\pi}\,\mathrm{Im}\,\mathrm{Tr}\left[\frac{1}{E-H^{\theta}} - \frac{1}{E-H_0^{\theta}}\right] \tag{10.105}$$

$$= -\frac{1}{\pi}\,\mathrm{Im}\left[\sum_{\nu}\frac{1}{E-E_{\nu}^{\theta}} - \sum_{\nu'}\frac{1}{E-E_{0,\nu'}^{\theta}}\right], \tag{10.106}$$

where E_{ν}^{θ} and $E_{0,\nu'}^{\theta}$ are complex energies of complex-scaled Hamiltonians H^{θ} and H_0^{θ}, respectively. The point is that, in the CSM, both isolated resonances and the rotated continuum are represented within the same non-Hermitian spectral problem. Therefore, the same framework that extracts QNM frequencies can, in principle, also be used to analyze continuum observables relevant to late-time tails. Another important point should be emphasized. As seen from Eq. (10.106), the CLD is expressed as an incoherent sum of terms of the form $1/(E-E_{\nu}^{\theta})$. This means that, because each resonance is completely isolated as a single eigenstate in the CSM, its contribution to the CLD can be extracted separately. It is helpful to explain the meaning of this expression in simple terms. If one considers only discrete bound states, then the spectrum

consists of isolated energy levels. By contrast, in a scattering problem the spectrum also contains a continuum. The CLD describes how this continuum is modified by the interaction. In other words, it is not merely a count of isolated states, but a spectral measure of how the interacting system differs from the free or reference one throughout the continuum region. In standard scattering theory, the CLD is closely related to phase-shift information. For a single channel, one may schematically write

$$\Delta\rho(E) \propto \frac{\mathrm{d}\delta(E)}{\mathrm{d}E}, \tag{10.107}$$

where $\delta(E)$ is the scattering phase shift. This relation is well known in other areas of physics and is one of the reasons why the CLD is a useful bridge between spectral theory and scattering observables. We do not make direct use of this relation in the present paper, but it is worth keeping in mind because it clarifies that the CLD is fundamentally a continuum quantity. In the present work, we do not attempt a systematic CLD analysis for all backgrounds. A full study would require a careful choice of the reference operator H_0, together with a dedicated investigation of the dependence on the scaling angle, basis truncation, and numerical integration range. Nevertheless, it is useful to record that the present CSM formulation is in principle capable of treating not only resonance poles but also the continuum sector. As a simple illustration, one may consider the extremal Reissner–Nordström case in a channel where the QNM calculation is numerically most stable, for example the odd-parity electromagnetic mode with $(s, l) = (1, 3)$ or equivalently the odd-parity gravitational mode with $(s, l) = (2, 4)$. In such a case, the low-lying resonance poles are already well separated and accurately reproduced in the main analysis, so the same setup is a natural starting point for a CLD plot. In the present formulation, the spectral variable of the Schrödinger-type equation is $E = \omega^2$. Therefore, when we express the CLD in terms of ω rather than E, the Jacobian of the transformation should be taken into account as

$$\Delta^\theta(\omega) = \frac{\mathrm{d}E}{\mathrm{d}\omega}\Delta^\theta(E) = 2\omega\Delta^\theta(E). \tag{10.108}$$

A representative result is shown in Fig. 10.8 as a function of ω (or equivalently of E) with $\theta = 40°$. The full CLD (the solid line) exhibits the characteristic resonance profile familiar in the CSM: it is negative on the low-energy side, develops a pronounced peak near the resonance region, and then gradually

approaches zero at higher energies. Since the CSM allows one to separate the contributions from individual resonance states, we also show the decomposition into the contributions of the lowest mode ω_0 and of the higher modes ω_1 and ω_2, which are represented by the dotted, dot-dashed, and dashed curves, respectively. The dominant peak structure is produced mainly by the lowest resonance ω_0, whose contribution already shows essentially the same qualitative behavior as the full CLD, namely a negative low-energy part, a resonance peak, and an asymptotic approach to zero. By contrast, the contributions from ω_1 and ω_2 do not display comparably visible isolated peaks in the present range, but rather yield a smoother component that changes from a negative value toward zero. Again, the purpose of this figure is only

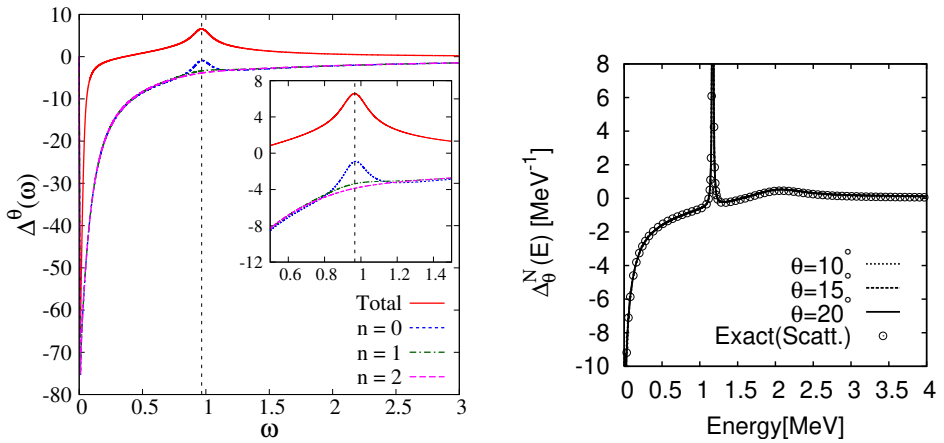

Figure 10.8: **Left panel:** Illustrative CLD in the CSM for the extremal Reissner–Nordström case in the odd-parity electromagnetic channel $(s, l) = (1, 3)$, together with its decomposition into contributions from the low-lying modes $\omega_{n=0,1,2}$. We set $H_0 = -\mathrm{d}^2/\mathrm{d}r_*^2$ and $\theta = 40°$. The vertical dashed line represents the value of $\mathrm{Re}\,\omega_1$. The CLD shows a characteristic structure: it is negative on the low-energy side, develops a pronounced peak near the resonance energy, and then gradually approaches zero at higher energies. This is qualitatively the same pattern as in standard CSM applications to resonance problems, indicating that the present black-hole calculation captures a resonance embedded in the continuum in essentially the same spectral manner. In black-hole language, this is the sector that is expected to be related to branch-cut contributions and late-time power-law tails. **Right panel:** A typical CLD in a nuclear system taken from Ref. [168], where one finds the same qualitative behavior: a negative contribution on the low-energy side, a resonance peak, and an asymptotic approach to zero.

illustrative. It is included here simply to show that the CSM framework used in the main text for QNM frequencies can also be extended to continuum observables. Our emphasis in this paper remains on the simpler and more immediate problem of extracting QNM frequencies from the complex-scaled eigenvalue spectrum. Once the numerical implementation is sufficiently mature, it should be possible to extend the analysis to continuum observables of CLD type. This would be especially interesting in black-hole problems where the balance between resonance poles and continuum contributions is physically important. Thus, the main message of this calculation module is simple: the CSM is useful not only because it turns QNM boundary conditions into a tractable eigenvalue problem, but also because it provides, in principle, a way to study the continuum sector relevant to the late-time tail. In this sense, the CLD should be viewed as a natural next step beyond the frequency calculations presented in the main text.

Laboratory checkpoint

Before moving to the next stage, perform the following checks without copying the displayed final answer.

1. Derive the Regge–Wheeler potential from the odd-parity perturbation equations, including the tortoise-coordinate boundary conditions.

2. Assemble one finite complex-scaled basis matrix and scan scaling angle, basis size, and radial range to identify a stable QNM.

3. Compare the extracted frequency with a Leaver benchmark and inspect the corresponding continuum-level-density contribution.

10.5 Two horizons: de Sitter QNMs and continuum response

10.5.1 Two-horizon scattering problem

For a four-dimensional Schwarzschild–de Sitter black hole,

$$f(r) = 1 - \frac{2M}{r} - \frac{\Lambda r^2}{3}, \qquad \Lambda > 0. \tag{10.109}$$

In the static region, $f(r)$ has a black-hole horizon r_h and a cosmological horizon $r_c > r_h$. The tortoise coordinate maps

$$r \to r_h^+ \Longrightarrow r_* \to -\infty, \qquad r \to r_c^- \Longrightarrow r_* \to +\infty. \tag{10.110}$$

The QNM boundary conditions are

$$\begin{aligned} \psi(r_*) &\sim \mathrm{e}^{-\mathrm{i}\omega r_*}, & r_* &\to -\infty, \\ \psi(r_*) &\sim \mathrm{e}^{+\mathrm{i}\omega r_*}, & r_* &\to +\infty. \end{aligned} \tag{10.111}$$

They have the same two-ended outgoing form as Eq. (10.5), with the right end now representing the cosmological horizon.

For scalar, electromagnetic, and axial gravitational sectors, one may again use

$$V_{sl}(r) = f(r)\left[\frac{l(l+1)}{r^2} + \frac{f'(r)}{r}\,\delta_{s0} - \frac{6M}{r^3}\,\delta_{s2}\right], \tag{10.112}$$

with the sector labels interpreted appropriately. The potential decays exponentially at both horizons for a nonextremal static patch. This short-range behavior makes global complex scaling in r_* particularly natural, subject to the analytic branches of $r(r_*)$.

10.5.2 Pole motion with the cosmological constant

Changing Λ changes the horizon separation, surface gravities, barrier height, and barrier width. Quasinormal poles therefore move in the complex ω plane. A complex-scaling calculation follows these pole trajectories without changing the outgoing boundary implementation. The same diagonalized spectrum also contains the rotated continuum, allowing pole motion to be distinguished from redistribution of background response [19].

Near the Nariai limit, the two horizons approach one another and an

appropriate rescaled potential approaches a solvable barrier. This gives an analytic benchmark related to the Pöschl–Teller family. Away from that limit, a numerical comparison should keep fixed a dimensionless convention, such as $M\omega$ or a frequency scaled by a surface gravity; otherwise apparent motion partly reflects a changing unit.

10.5.3 Continuum level density for black-hole response

Choose a reference operator H_0 that has the same horizon asymptotics as the black-hole master operator but no scattering barrier. The CLD is

$$\Delta\rho(E) = -\frac{1}{\pi}\,\mathrm{Im}\,\mathrm{Tr}\left[(E - H_\theta)^{-1} - (E - H_{0,\theta})^{-1}\right], \qquad E = \omega^2. \tag{10.113}$$

A stable peak can be decomposed locally into a pole contribution and a smooth background, but the total CLD is the more invariant finite quantity. Its integral measures the total scattering phase relative to the reference. It therefore probes changes in continuum response even when no isolated pole crosses the observation window.

For a two-ended one-dimensional potential, the scattering matrix contains reflection and transmission amplitudes. The determinant phase fixes the CLD through Eq. (6.101), while the greybody factor is the transmission probability

$$\mathcal{G}_l(\omega) = |T_l(\omega)|^2. \tag{10.114}$$

Knowing $\det S$ does not in general determine $|T|^2$. Additional symmetry or channel-resolved information is required. The CLD and greybody factor are therefore complementary rather than interchangeable observables [19, 170].

10.5.4 Coupled channels and string-inspired backgrounds

For N_c coupled perturbation channels, write

$$\left[-\mathbf{1}_{N_c}\frac{\mathrm{d}^2}{\mathrm{d}r_*^2} + \boldsymbol{V}(r)\right]\boldsymbol{\psi}(r_*) = \omega^2\boldsymbol{\psi}(r_*). \tag{10.115}$$

Complex scaling acts on the common coordinate, while $\boldsymbol{V}$ mixes channels. The asymptotic channel basis must be chosen so that incoming and outgoing directions are defined at each horizon. If different channels have different thresholds or asymptotic wave numbers, the rotated spectrum contains several rays and the Riemann sheet must be labeled channel by channel.

String-inspired metric–dilaton systems provide a natural application [171]. Numerically, the main new issue is matrix-block imbalance: one channel or basis sector can acquire exponentially larger matrix elements under deformation. Similarity balancing can improve conditioning without changing eigenvalues, but left–right residues must be transformed consistently.

10.5.5 Higher dimensions

Tensor, vector, and scalar gravitational perturbations of higher-dimensional static black holes also reduce to Schrödinger-type master equations in many sectors [172–174]. When the potential is frequency independent and has two asymptotically free ends, the same complex-scaling construction applies. The angular spectrum and near-horizon indices change, but the pole/continuum geometry does not. Scalar-type coupled systems and rotating backgrounds require additional work.

10.6 Calculation laboratory VIII-B: Two-horizon spectra and continuum response

Calculation route

Prerequisites. Two-horizon boundary conditions, black-hole complex scaling, continuum level density, and coupled-channel diagonalization.

Calculation goal. Two-horizon complex scaling, QNM and continuum-level-density data, greybody response, coupled string-inspired channels, higher dimensions, and block-balancing diagnostics.

Completion criterion. Compute two-horizon QNMs and continuum response, then diagnose coupled-channel and block-balancing effects.

This Laboratory reconstructs the calculation underlying Ref. [19]. Two-horizon boundary conditions, the Gaussian basis, and continuum level density have already been derived. The worked calculation therefore opens with the parameter scan and retains the numerical response, coupled-channel, higher-dimensional, and conditioning analyses.

10.6.1 QNM and CLD for dS black holes

Numerical results of QNMs

We first present the QNM frequencies obtained by applying the present CSM framework to four-dimensional Schwarzschild–dS black holes. The purpose of this subsection is twofold. First, we check that the complex-scaled formulation can identify isolated resonance eigenvalues also in the presence of a nonzero cosmological constant. Second, we examine how the low-lying QNM spectrum changes as the cosmological constant Λ is varied. We consider scalar, electromagnetic, and gravitational perturbations, corresponding to $s = 0$, $s = 1$, and $s = 2$, respectively. For each spin sector, we compute two representative angular momenta, which we denote by $l = 2$ and $l = 3$. The notation l is used throughout this paper for the angular momentum quantum number. For each value of Λ, the corresponding Schwarzschild–dS Regge–Wheeler-type potential is inserted into the complex-scaled Schrödinger equation, and the QNM candidates are extracted as isolated eigenvalues separated from the rotated continuum. The identification of QNM candidates is performed by looking for isolated eigenvalues that remain stable under changes of the numerical parameters. In the numerical analysis below, we focus on the low-lying modes. As in the Schwarzschild and Reissner–Nordström analysis of our previous work, these modes are expected to be the most stable against changes of the basis size, basis parameters, integration range, and scaling angle. By contrast, higher overtones are typically broader and lie closer to the rotated continuum, making their identification more sensitive to numerical details. For this reason, the present calculation should be understood as a first systematic test of the CSM framework for Schwarzschild–dS backgrounds, rather than as a final optimized computation of all overtones. For each channel, we perform calculations for several values of the cosmological constant. Positive values,

$$\Lambda > 0, \tag{10.116}$$

correspond to Schwarzschild–dS backgrounds. The limit $\Lambda \to 0$ connects the present setup to the asymptotically flat Schwarzschild problem and therefore serves as an important reference point. Particular attention will be paid to how the real and imaginary parts of the QNM frequencies move as Λ is varied. The numerical results are summarized in Figs. 10.9–10.11 for Schwarzschild–dS. Here Fig. 10.9 shows the scalar results, Fig. 10.10 shows

the electromagnetic results, and Fig. 10.11 shows the gravitational results. In these figures, we fix the magnitude of the cosmological constant to $\Lambda = 0.08$. For each channel, we combine the results obtained for several values of the scaling angle,

$$\theta = 42^\circ\text{–}44^\circ, \tag{10.117}$$

and for the Gaussian parameter sets

$$i_{\max} = 30,\ 40, \qquad r_{*0} = 0.1, \qquad r_{*\max} = 60,\ 80. \tag{10.118}$$

The complex eigenvalues of the complex-scaled Hamiltonian are displayed in the complex ω plane. The QNM candidates are identified as isolated eigenvalues that remain stable under these moderate changes of the scaling angle and basis parameters. The QNM candidates are identified as the

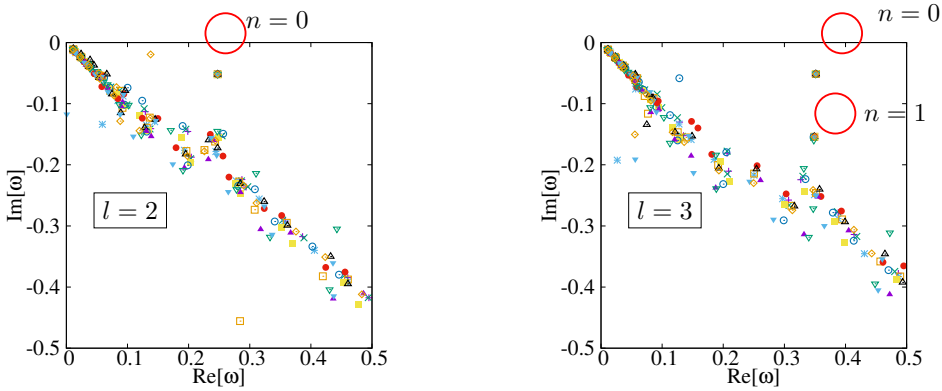

Figure 10.9: The Schwarzschild–dS case with $s = 0$. $M = 1.0$. The discretized continuum spectrum is represented by the sequence of points aligned approximately along the θ-rotated direction. The isolated points on the real-axis side are the QNM frequencies. Eigenvalues of the complex-scaled Hamiltonian H^θ for $l = 2$ and $l = 3$ are shown. The scaling angle is taken to be $\theta = 42^\circ\text{–}44^\circ$. In these figures, we fix the cosmological-constant parameter to $\Lambda = 0.08$. The eigenvalues enclosed by red circles are identified as QNM candidates, since they appear as isolated points separated from the rotated continuum and remain stable under moderate changes of the scaling angle and basis parameters.

eigenvalues enclosed by the red circles in Figs. 10.9–10.11. These eigenvalues appear as isolated points separated from the rotated continuum and remain

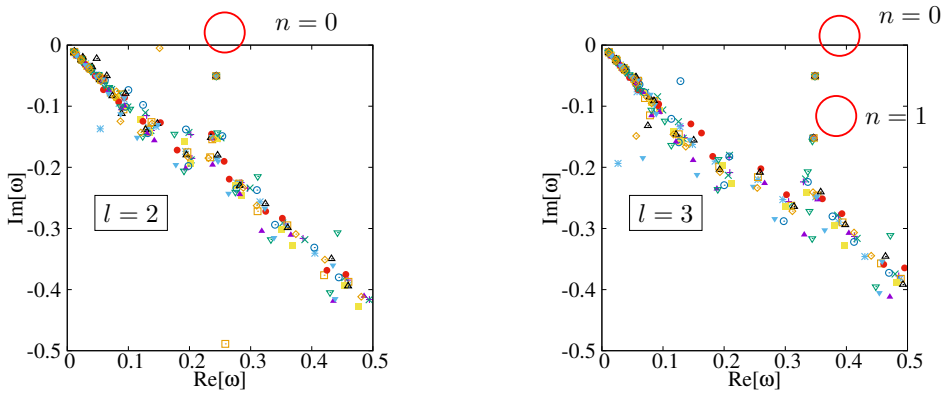

Figure 10.10: The Schwarzschild–dS case with $s = 1$. $M = 1.0$.

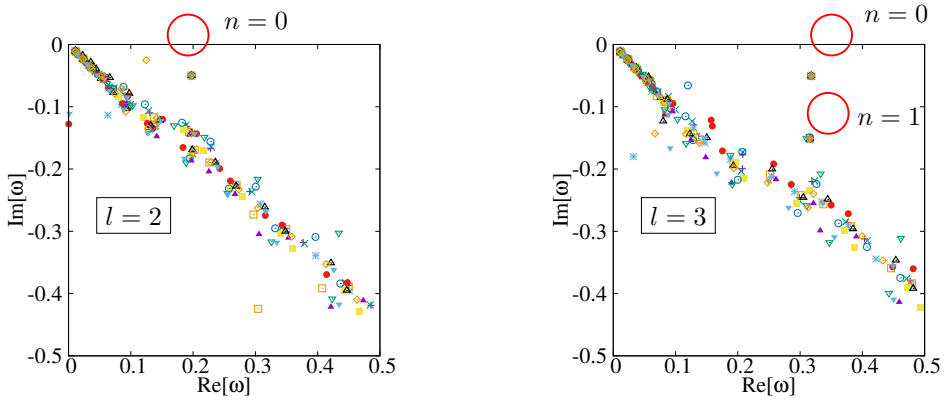

Figure 10.11: The Schwarzschild–dS case with $s = 2$. $M = 1.0$.

stable under moderate changes of the scaling angle and basis parameters. We find that the resulting frequencies agree with the previous results of Ref. [175] with high accuracy, which provides a nontrivial validation of the present CSM identification procedure. Table 10.13 presents the numerical results obtained by the CSM for the Schwarzschild–dS case. In this table, we list the lowest QNM frequencies, $n = 0$, for scalar ($s = 0$), electromagnetic ($s = 1$), and gravitational ($s = 2$) perturbations. For each spin sector, the results for $l = 2$ and $l = 3$ are shown for several values of the cosmological constant Λ. The numbers in parentheses indicate the numerical uncertainty estimated from the spread of the results obtained with different values of the scaling angle and basis parameters. For the Schwarzschild–dS case shown in Table 10.13, both $\mathrm{Re}\,\omega$ and $|\mathrm{Im}\,\omega|$ decrease as the positive cosmological constant Λ is increased. This tendency is observed in all spin sectors considered here and for both angular momenta $l = 2$ and $l = 3$. It is consistent with the approach to the near-Nariai regime, in which the black-hole and cosmological horizons become closer and the characteristic oscillation and damping scales are reduced. We also list the Schwarzschild results obtained from a separate calculation for comparison. For small Λ, the low-lying Schwarzschild–dS QNM frequencies vary smoothly from the Schwarzschild values. The QNM candidates selected from the complex-scaled spectra agree with the previous results of Ref. [175] with high accuracy. This agreement provides a nontrivial validation of the present CSM identification procedure: the stable isolated eigenvalues separated from the rotated continuum are correctly identified with the physical QNM poles. The quoted uncertainties are estimated from the spread of the results under moderate changes of the scaling angle and basis parameters. They should therefore be understood as practical measures of numerical stability, rather than as statistical error bars. The small uncertainties of the low-lying modes indicate that these resonance eigenvalues are robustly extracted within the present finite-basis CSM calculation. These QNM results serve as a benchmark for the subsequent CLD analysis. While the QNM frequencies characterize the isolated pole sector, the CLD probes how the continuum part of the spectral response is modified by the black-hole potential. In the following subsection, we therefore use the same complex-scaled framework to analyze the continuum level density for the Schwarzschild–dS background.

Table 10.13: Numerical results of lowest QNM frequencies ($n = 0$) of Schwarzschild–dS black hole for $l = 2$ and $l = 3$. The entries are given as $\omega = \mathrm{Re}\,\omega - \mathrm{i}|\,\mathrm{Im}\,\omega|$. For comparison, the table also includes the Schwarzschild results obtained from a separate calculation ($\Lambda = 0$). The numbers in parentheses indicate the numerical uncertainty estimated from the spread under changes of the scaling angle and basis parameters.

Λ	$l = 2$	$l = 3$
	$s = 0$	
0	0.483646(91)−i0.09676(15)	0.67539(23) −i0.09654(11)
0.02	0.43462(38) −i0.08859(15)	0.60907(12) −i0.08789(25)
0.04	0.38078(15) −i0.07875(10)	0.53583(12) −i0.07789(16)
0.06	0.320020(55)−i0.066838(67)	0.45235(10) −i0.06608(33)
0.08	0.247470(18)−i0.051904(44)	0.351393(55)−i0.051402(57)
0.10	0.146608(13)−i0.030685(18)	0.209096(16)−i0.030556(24)
	$s = 1$	
0	0.457595(89)−i0.09500(11)	0.65692(27) −i0.095648(80)
0.02	0.41503(28) −i0.08614(14)	0.59527(13) −i0.08665(23)
0.04	0.36723(12) −i0.076233(92)	0.52630(12) −i0.07662(15)
0.06	0.311815(48)−i0.064772(63)	0.44657(17) −i0.06505(30)
0.08	0.243642(13)−i0.050673(45)	0.348668(52)−i0.050791(56)
0.10	0.145816(11)−i0.030372(18)	0.208523(17)−i0.030400(23)
	$s = 2$	
0	0.37366(24) −i0.08896(15)	0.59947(23) −i0.09270(28)
0.02	0.338393(88)−i0.081754(78)	0.54308(14) −i0.08451(19)
0.04	0.298896(51)−i0.073288(68)	0.480033(87)−i0.07517(26)
0.06	0.253287(44)−i0.063047(71)	0.40718(19) −i0.064137(89)
0.08	0.197474(19)−i0.049874(42)	0.317804(32)−i0.050378(49)
0.10	0.117916(21)−i0.030209(21)	0.189991(12)−i0.030313(21)

Numerical results of CLD

We next analyze the continuum level density for the Schwarzschild–dS backgrounds using the same complex-scaled spectra as those used for the QNM analysis. The CLD introduced in Eq. (6.98) is defined as a density with respect to the spectral variable $E = \omega^2$. In the following plots, however, we display the corresponding density with respect to the frequency variable ω. We therefore define

$$\begin{aligned}\Delta^\theta(\omega) &= \frac{\mathrm{d}E}{\mathrm{d}\omega}\Delta\rho^\theta(E)\Big|_{E=\omega^2} \\ &= 2\omega\,\Delta\rho^\theta(\omega^2).\end{aligned} \tag{10.119}$$

This Jacobian factor should be kept in mind when comparing the CLD plotted as a function of ω with the original definition in terms of E. Figures 10.12–10.17 show $\Delta^\theta(\omega)$ for scalar, electromagnetic, and gravitational perturbations with $l = 2$ and $l = 3$. In each figure, the six panels from left to right correspond to

$$\Lambda = 0,\ 0.02,\ 0.04,\ 0.06,\ 0.08,\ 0.10. \tag{10.120}$$

The red solid curve denotes the total CLD obtained from the full complex-scaled spectrum. The blue dashed curve shows a partial reconstruction in which only the lowest QNM pole, namely the $n = 0$ mode, is retained in the full-Hamiltonian contribution. The same reference contribution is subtracted in both cases. This partial curve is therefore used as a diagnostic of the role of the lowest QNM pole in the full continuum response. Let E^θ_ν be the complex-scaled eigenvalues of the full Hamiltonian and let $E^\theta_{0,\nu'}$ be those of the reference Hamiltonian. The total quantity plotted in the figures is

$$\Delta^\theta_{\mathrm{tot}}(\omega) = -\frac{2\omega}{\pi}\,\mathrm{Im}\left[\sum_\nu \frac{1}{\omega^2 - E^\theta_\nu} - \sum_{\nu'} \frac{1}{\omega^2 - E^\theta_{0,\nu'}}\right]. \tag{10.121}$$

The $n = 0$ partial reconstruction is obtained by replacing the first sum by the single contribution of the lowest QNM pole,

$$\Delta^\theta_{n=0}(\omega) = -\frac{2\omega}{\pi}\,\mathrm{Im}\left[\frac{1}{\omega^2 - E^\theta_{n=0}} - \sum_{\nu'} \frac{1}{\omega^2 - E^\theta_{0,\nu'}}\right]. \tag{10.122}$$

This comparison allows us to see how much of the nontrivial structure of the CLD is already controlled by the lowest QNM pole. For $l = 3$, the $n = 1$ mode is also identifiable for the scaling angle $\theta = 43°$. In this case, we additionally show the $n = 1$ partial reconstruction, defined analogously to the $n = 0$ partial reconstruction. For the representative scalar case

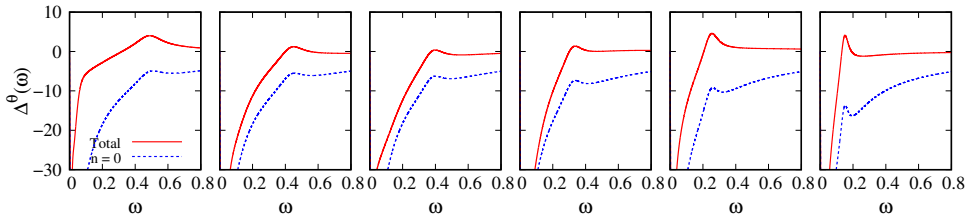

Figure 10.12: CLD. $s = 0$, $l = 2$, $\theta = 43°$. The six panels correspond, from left to right, to $\Lambda = 0$, 0.02, 0.04, 0.06, 0.08, 0.10. The red solid curve denotes the total CLD obtained from the full complex-scaled spectrum. The blue dashed curve is the $n = 0$ partial reconstruction, in which only the lowest QNM pole is retained in the full-Hamiltonian contribution while the same reference contribution is subtracted.

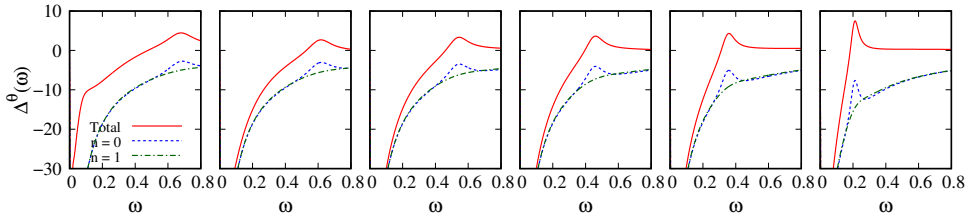

Figure 10.13: CLD. Same as Fig. 10.12, but for $s = 0$, $l = 3$. The green dashed-dotted curve is the $n = 1$ partial reconstruction.

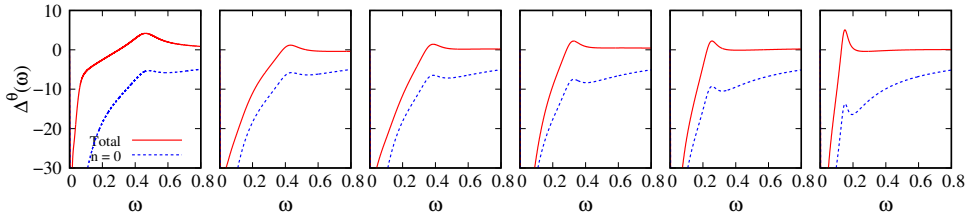

Figure 10.14: CLD. Same as Fig. 10.12, but for $s = 1$, $l = 2$.

with $s = 0$ and $l = 2$, the total CLD shows a broad structure for small Λ. As Λ is increased, the dominant structure moves toward lower frequency

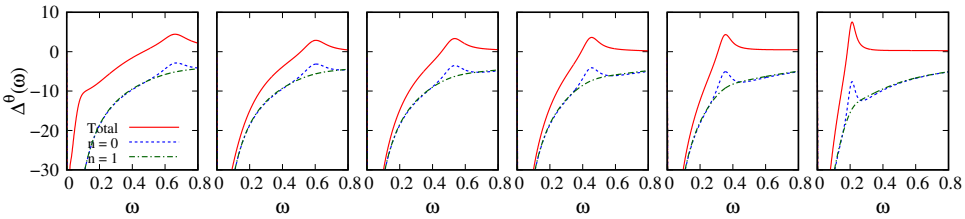

Figure 10.15: CLD. Same as Fig. 10.13, but for $s = 1$, $l = 3$.

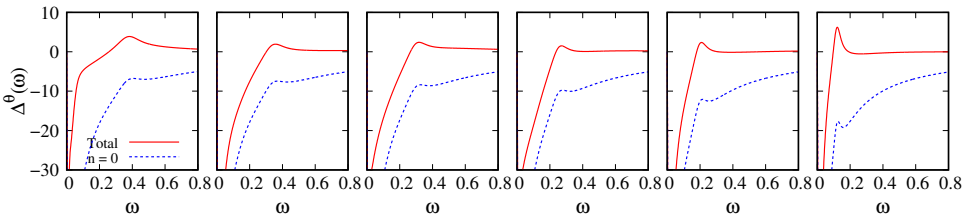

Figure 10.16: CLD. Same as Fig. 10.12, but for $s = 2$, $l = 2$.

and becomes sharper. This behavior is consistent with the movement of the lowest QNM frequency shown in Table 10.13: both $\mathrm{Re}\,\omega$ and $|\mathrm{Im}\,\omega|$ decrease as the system approaches the near-Nariai regime. A smaller value of $|\mathrm{Im}\,\omega|$ corresponds to a narrower resonance contribution, while the decrease of $\mathrm{Re}\,\omega$ shifts the dominant CLD structure toward smaller ω. The same qualitative behavior is observed for the other spin and angular momentum sectors. The detailed peak positions and widths depend on the effective potential, and hence on s and l, but the dominant CLD structure is largely governed by the lowest QNM pole. This is seen by comparing the red solid and blue dashed curves: the partial $n = 0$ reconstruction captures the main peak or shoulder structure of the total CLD, while the remaining poles and nonresonant continuum mainly modify the smooth background. The generic near-threshold decrease and the approach to zero at large ω are common features of the reference-subtracted continuum response and should not be attributed to a single resonance alone. For the $l = 3$ cases, the additional $n = 1$ partial reconstruction provides a useful comparison with the first overtone contribution. Although it gives a visible correction in some frequency regions, the main peak structure of the total CLD is still primarily governed by the lowest QNM pole. This observation is consistent with the behavior found in Appendix B of our previous CSM analysis of Schwarzschild and Reissner–Nordström black holes [18]. There, the lowest QNM contribution was also found to control the dominant structure of the

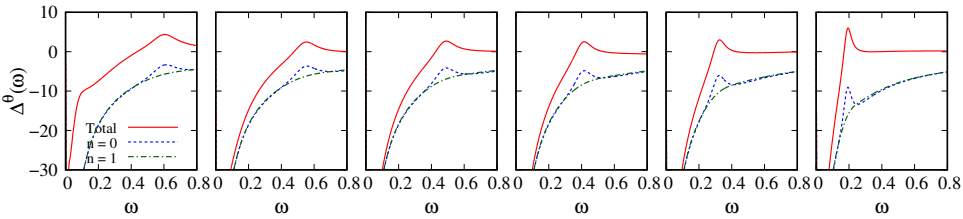

Figure 10.17: CLD. Same as Fig. 10.13, but for $s = 2$, $l = 3$.

CLD, while higher modes and the rotated continuum provided subleading corrections to the overall background. The present Schwarzschild–dS results show that the same pole-dominance pattern persists in the presence of a positive cosmological constant.

10.6.2 Discussion

On spectral response

The CLD results clarify how the spectral response of a Schwarzschild–dS black hole is organized in the CSM representation. The QNM frequencies listed in Table 10.13 characterize the isolated pole sector, whereas the CLD probes the reference-subtracted continuum response. The advantage of the CSM is that these two pieces of information are obtained from the same non-Hermitian spectral problem: isolated QNM poles and the rotated continuum appear simultaneously in the complex-scaled spectrum. The comparison between the total CLD and the $n = 0$ partial reconstruction shows that the lowest QNM pole plays a dominant role in shaping the observable peak structure of the CLD. This does not mean that the continuum background is negligible. Rather, the total CLD is produced by the interplay between the pole contribution and the reference-subtracted continuum. The lowest QNM pole determines the location and width of the most prominent structure, while the nonresonant continuum and higher poles contribute to the smooth background and to the common threshold behavior. This point is particularly visible in the dependence on the cosmological constant. As Λ increases, the low-lying QNM frequencies move toward smaller $\mathrm{Re}\,\omega$ and smaller $|\mathrm{Im}\,\omega|$. The corresponding CLD peak therefore shifts toward lower frequency and becomes narrower. In this sense, the CLD provides a frequency-space representation of the same spectral reorganization that is seen in the QNM table. However, unlike the QNM table, the CLD also

retains information about the nonresonant sector. It is therefore sensitive not only to the position of isolated poles but also to how the continuum spectrum is redistributed by the black-hole potential. The behavior near $\omega = 0$ should be interpreted with some care. Both the total CLD and the partial reconstructions exhibit a common near-threshold decrease and approach zero at sufficiently large ω. These features are not specific signatures of a single QNM pole. They arise from the reference-subtracted continuum representation and from the conversion from the E-density to the ω-density in Eq. (10.119). For this reason, the most useful information in the present plots is not the overall sign of the CLD near threshold, but the position, width, and evolution of the dominant structures as Λ, s, and l are varied. From this viewpoint, the present results support the following picture. The ringdown sector is encoded in isolated QNM poles, but the full linear response is better described as a combined pole-continuum response. For the low-lying modes considered here, the lowest QNM pole already captures the leading structure of the CLD. The remaining continuum contribution provides a nonresonant background that is invisible in a list of QNM frequencies alone. Thus, the CLD complements the usual QNM analysis by giving a direct diagnostic of how the continuum sector participates in the black-hole spectral response.

CLD, transmission phase, and greybody factors

It is useful to clarify the relation between the present CLD analysis and greybody factors. Greybody factors are transmission probabilities associated with black-hole scattering problems. They describe how the effective potential outside the black hole modifies the spectrum of radiation from a perfect blackbody spectrum and are therefore more directly connected to observable fluxes. They have been studied in a variety of black-hole backgrounds, including higher-dimensional, charged, dS, and AdS cases [170]. More recently, greybody factors have also been discussed in connection with black-hole ringdown amplitudes and as quantities complementary to the usual QNM description [176, 177]. The CLD is not itself a transmission coefficient. Rather, it measures the change of the continuum density of states relative to a reference problem. In the CSM, the CLD (6.98) is evaluated as

$$\Delta\rho^{\theta}(E) = -\frac{1}{\pi}\,\mathrm{Im}\,\mathrm{Tr}\left[\frac{1}{E - H^{\theta}} - \frac{1}{E - H_0^{\theta}}\right]$$

$$= -\frac{1}{\pi}\,\mathrm{Im}\left[\sum_{\nu}\frac{1}{E-E_{\nu}^{\theta}} - \sum_{\nu'}\frac{1}{E-E_{0,\nu'}^{\theta}}\right], \tag{10.123}$$

where H^{θ} and H_0^{θ} are the complex-scaled full and reference Hamiltonians, respectively, and E_{ν}^{θ} and $E_{0,\nu'}^{\theta}$ denote their complex eigenvalues. Equation (10.123) naturally decomposes the CLD into individual spectral contributions,

$$\Delta\rho^{\theta}(E) = \sum_{\nu}\rho_{\nu}^{\theta}(E) - \sum_{\nu'}\rho_{0,\nu'}^{\theta}(E). \tag{10.124}$$

This decomposition is one of the practical advantages of the CSM: resonance poles and the rotated continuum can be analyzed within the same non-Hermitian spectral representation. In ordinary one-dimensional scattering theory, the change in the density of states is related to the energy derivative of the phase of the transmission amplitude [178]. Writing

$$t(E) = |t(E)|\mathrm{e}^{\mathrm{i}\delta(E)}, \tag{10.125}$$

one obtains, up to the conventional normalization of the phase,

$$\Delta\rho(E) = \frac{1}{\pi}\frac{\mathrm{d}\delta(E)}{\mathrm{d}E}. \tag{10.126}$$

Equivalently,

$$\delta(E) = \pi\int^{E}\mathrm{d}E'\,\Delta\rho(E') + \delta_0, \tag{10.127}$$

where δ_0 is an energy-independent constant fixed by the choice of reference phase. Using the CSM decomposition of Eq. (10.123), this phase may be written as

$$\delta(E) = \sum_{\nu}\delta_{\nu}(E) - \sum_{\nu'}\delta_{0,\nu'}(E) + \delta_0, \tag{10.128}$$

with

$$\delta_{\nu}(E) = \pi\int^{E}\mathrm{d}E'\,\rho_{\nu}^{\theta}(E'). \tag{10.129}$$

Thus, the CSM gives a way of separating the transmission phase into contributions from resonance and continuum eigenstates. This observation suggests

a possible bridge to greybody factors. For a black-hole scattering problem, the greybody factor is essentially a transmission probability,

$$\Gamma(E) = |t(E)|^2, \tag{10.130}$$

up to possible channel-dependent normalization factors. The CLD does not by itself determine $\Gamma(E)$, because Eq. (10.126) gives the phase of the transmission amplitude rather than its modulus. Nevertheless, the two quantities probe different aspects of the same underlying scattering problem: the greybody factor probes the probability for transmission through the black-hole effective potential, whereas the CLD probes the rearrangement of the continuum spectrum. From the present CSM viewpoint, the most promising role of the CLD is not to replace a direct real-frequency scattering calculation of the greybody factor. Rather, the CSM can decompose the spectral phase response into resonant and nonresonant parts. If the transmission amplitude is written as

$$t(E) = |t(E)|\mathrm{e}^{\mathrm{i}\delta(E)}, \tag{10.131}$$

then the CSM decomposition gives, at least formally,

$$t(E) = |t(E)| \prod_{\nu} \mathrm{e}^{\mathrm{i}\delta_\nu(E)} \prod_{\nu'} \mathrm{e}^{-\mathrm{i}\delta_{0,\nu'}(E)} \times \mathrm{e}^{\mathrm{i}\delta_0}. \tag{10.132}$$

This expression should be understood as a decomposition of the phase part of the transmission amplitude, not of the transmission probability itself. A direct computation of greybody factors requires the modulus $|t(E)|$, which is most directly obtained from a real-frequency scattering calculation with appropriate boundary conditions. However, Eq. (10.132) indicates what the CSM can add: it can identify how much of the scattering phase, and hence of the continuum spectral response, is controlled by QNM poles and how much is carried by the nonresonant background. In this sense, the CLD provides a bridge between the pole-based QNM description and more directly observable scattering quantities such as greybody factors. A full CSM-based reconstruction of greybody factors, including both phase and modulus information, is left for future work.

10.6.3 Further applications

Coupled-channel systems: toward stringy black holes

Recent work on the two-dimensional Mandal–Sengupta–Wadia (MSW) black hole shows that intrinsic metric–dilaton perturbations can be reduced not to a single Schrödinger equation but to a coupled matrix Schrödinger problem,

$$-\frac{\mathrm{d}^2}{\mathrm{d}r_*^2}\Phi(r_*) + V_{\mathrm{eff}}(r_*)\Phi(r_*) = \omega^2\Phi(r_*), \tag{10.133}$$

with a 2×2 effective potential matrix. Here, Φ is a two-component field describing the coupled metric–dilaton perturbation sector. In the field basis used in Ref. [171],[2] the elements of the effective potential are given by

$$V_{\mathrm{eff}}^{11,22} = \frac{8\Lambda^2 \mathrm{e}^{2\Lambda r_*}}{M\Lambda + \mathrm{e}^{2\Lambda r_*}}, \tag{10.134}$$

$$V_{\mathrm{eff}}^{12} = \frac{4V_{\mathrm{eff}}^{11}}{8 - V_{\mathrm{eff}}^{11}/\Lambda^2}, \tag{10.135}$$

$$V_{\mathrm{eff}}^{21} = \frac{1}{128} V_{\mathrm{eff}}^{11} \left(8 - \frac{V_{\mathrm{eff}}^{11}}{\Lambda^2}\right)\left(32 - \frac{V_{\mathrm{eff}}^{11}}{\Lambda^2}\right). \tag{10.136}$$

Usually, the kinetic term and the overlap matrix can be evaluated analytically for the basis functions used in the numerical variational method, whereas the potential matrix elements require numerical integration. Here, let us adopt the Polynomial $\times$ real range Gaussian basis. Using Kummer's transformation for the confluent hypergeometric function, we obtain

$$\int_{-\infty}^{\infty} \mathrm{d}r_*\, r_*^n \mathrm{e}^{-\alpha r_*^2} V_{\mathrm{eff}}^{12} = \begin{cases} \frac{4\sqrt{\pi}\,k!\,\Lambda}{M} \alpha^{-k-\frac{1}{2}} \mathrm{e}^{\frac{\Lambda^2}{\alpha}} L_k^{-\frac{1}{2}}\left(-\frac{\Lambda^2}{\alpha}\right) & \text{for } n = 2k, \\ \frac{4\sqrt{\pi}\,k!\,\Lambda^2}{M} \alpha^{-k-\frac{3}{2}} \mathrm{e}^{\frac{\Lambda^2}{\alpha}} L_k^{\frac{1}{2}}\left(-\frac{\Lambda^2}{\alpha}\right) & \text{for } n = 2k+1. \end{cases} \tag{10.137}$$

Here, $L_k^a(z)$ denotes the generalized Laguerre polynomial. Thus, the potential matrix element associated with V_{eff}^{12} can be evaluated analytically, without performing the numerical integration.[3] We next apply the CSM to the

[2] This basis is obtained by redefining the original metric and dilaton perturbations so that Eq. (10.133) has a Schrödinger-type form without first-derivative terms.

[3] In the coupled-channel problem, some off-diagonal components of the effective potential can become exponentially large in the original field basis, while the eigenvalues of the potential matrix remain finite. This indicates that the difficulty is not a physical divergence of the potential, but a numerical conditioning problem associated with the choice of

coupled-channel system (10.133). A characteristic feature of this problem is that the asymptotic effective potential has two eigenvalue thresholds. Consequently, the complex-scaled spectrum contains two rotated continuum branches, each starting from a different threshold. This is in contrast to the single-channel Schwarzschild–dS examples discussed above, where the continuum branch starts from a single threshold. The result is shown in Fig. 10.18. The two lines show the corresponding complex-scaled continua rotated by the angle 2θ. To examine whether an isolated QNM eigenvalue

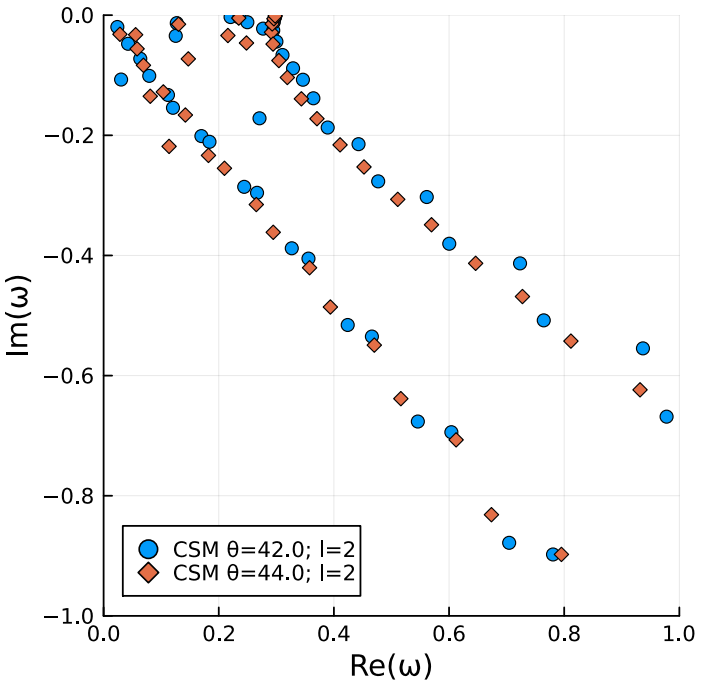

Figure 10.18: Complex-scaled spectrum for the coupled-channel MSW black-hole perturbation problem with $\Lambda = 0.08$. $l = 2$. The scaling angle is $\theta = 42°$ and $44°$. We set $i_{\max} = 50$, $r_0 = 0.1$, and $r_{*\max} = 80$. Because the asymptotic effective potential has two eigenvalue thresholds, two continuum branches are observed. Within the parameter sets examined in this work, no stable isolated resonance eigenvalue was identified for $\theta < 45°$.

can be exposed between the real axis and the rotated continua, we performed a parameter scan over the basis size, Gaussian range, integration range, and

channel basis. A suitable channel rescaling or matrix balancing is therefore required before performing the complex-scaled diagonalization. See Sec. 10.6.4.

scaling angle. The representative parameter sets used in this search are summarized in Table 10.14. In all cases, we restricted the scaling angle to

$$\theta < \frac{\pi}{4}, \tag{10.138}$$

which is the practical range of the present real-range Gaussian basis. Within

Table 10.14: Representative parameter sets used in the CSM search for isolated resonance eigenvalues in the coupled-channel MSW black-hole perturbation problem.

Set	$i_{\max}$	$p_{\max}$	r_{*0}	$r_{*\,\max}$	θ	Λ
1	40	3	0.1	60	30°–44°	0.01–0.1
2	40	3	0.1	80	30°–44°	0.01–0.1
3	50	3	0.1	60	30°–44°	0.01–0.1
4	50	3	0.1	80	30°–44°	0.01–0.1

this survey, we did not find a stable isolated eigenvalue that can be identified as a QNM for $\theta < 45°$. This should not be interpreted as evidence for the absence of QNMs in the underlying stringy black-hole perturbation problem. Rather, it indicates a limitation of the present real-range Gaussian CSM implementation. Indeed, the QNMs reported in Ref. [171] are strongly damped in the parameter region studied there. For such modes, the corresponding position in the complex $E = \omega^2$ plane can lie in a region that requires a larger rotation angle to expose the pole from the continuum background. However, the present basis representation becomes ill-conditioned as θ approaches $\pi/4$, and therefore does not allow us to reliably search for such poles beyond this angle. The present result is nevertheless informative. It shows that the coupled-channel CSM calculation correctly resolves the multi-threshold continuum structure, while also revealing that the extraction of highly damped QNM poles requires further stabilization. Possible improvements include complex-range Gaussian bases, exterior complex scaling, and channel-basis or matrix balancing of the type discussed in Sec. 10.6.4. We therefore regard the stringy coupled-channel example as a useful diagnostic problem for future extensions of the CSM framework, rather than as a completed QNM computation in the present implementation.

Higher-dimensional dS black holes

As another natural direction, one may consider higher-dimensional Schwarzschild–dS spacetimes. In d dimensions, the metric may be written as [172–174][4]

$$\mathrm{d}s^2 = -f_d(r)\mathrm{d}t^2 + f_d^{-1}(r)\mathrm{d}r^2 + r^2\mathrm{d}\Omega_{d-2}, \tag{10.140}$$

$$f_d(r) = K - \lambda r^2 - \frac{2M}{r^{d-3}}, \tag{10.141}$$

$$\lambda \equiv \frac{2\Lambda}{(d-1)(d-2)}. \tag{10.142}$$

K denotes the sectional curvature of the $(d-2)$-dimensional base space. In the present discussion, we mainly restrict ourselves to the case $K = 1$. For tensor-type perturbations on the $(d-2)$-dimensional angular sector with $d \geq 5$, the effective potential is given by

$$V_T(r) = \frac{f_d(r)}{r^2}\left[l(l+d-3) + \frac{(d-2)rf_d'(r)}{2} + \frac{(d-2)(d-4)f_d(r)}{4}\right]. \tag{10.143}$$

For vector-type perturbations, one has

$$V_V(r) = \frac{f_d(r)}{r^2}\left[l(l+d-3) + (d-4) + \frac{d(d-2)f_d(r)}{4} - \frac{(d-2)rf_d'(r)}{2}\right]. \tag{10.144}$$

The scalar-type potential is considerably more complicated. These expressions suggest that higher-dimensional dS black holes provide a natural class of backgrounds in which the present CSM framework may be extended. At least for the tensor- and vector-type sectors, the perturbation equations remain of Schrödinger type, so that the basic spectral strategy should carry over in a relatively direct manner. As a simple illustration of the higher-dimensional extension, we also perform a trial calculation for five-dimensional Schwarzschild–dS (Schwarzschild–dS$_5$) black holes. Here we do not attempt a systematic survey of the higher-dimensional parameter space. Rather, our

[4]The black-hole mass parameter M is related to a horizon radius r_0 as

$$M = \frac{(d-2)A_{d-2}r_0^{d-3}}{16\pi G_d}, \qquad A_{d-2} = \frac{2\pi^{(d-1)/2}}{\Gamma((d-1)/2)}, \tag{10.139}$$

where A_{d-2} denotes the area of the unit $(d-2)$-sphere.

purpose is to check whether the same CSM prescription used in the four-dimensional analysis can be applied directly to the tensor- and vector-type master equations. Figure 10.19 shows the result for the Schwarzschild–dS_5 case in the tensor-type sector. The complex-scaled spectra are shown for two angular momenta, $l = 2$ and $l = 3$, and for two scaling angles, $\theta = 40°$ and $42°$. As in the four-dimensional case, the complex-scaled continuum is rotated in the complex energy plane, and resonance candidates are identified as isolated eigenvalues that are separated from the rotated continuum and remain stable under a moderate change of the scaling angle. Figure 10.20

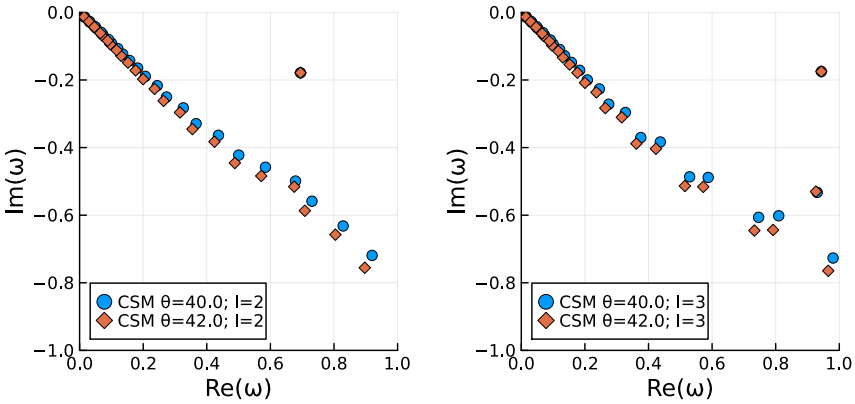

Figure 10.19: The Schwarzschild–dS_5 case for the tensor-type sector. $\Lambda = 0.4$. The scaling angle is taken to be $\theta = 40°$, $42°$. We take $i_{\max} = 30$, $r_{*0} = 0.1$, and $r_{*\max} = 60$. $l = 2$ on the left panel and $l = 3$ on the right panel.

shows the corresponding example for the Schwarzschild–dS_5 case in the vector-type sector. Again, the same qualitative spectral structure is observed. The appearance of stable isolated eigenvalues in these trial calculations suggests that the CSM strategy can be extended to higher-dimensional Schwarzschild–dS backgrounds at least for the tensor- and vector-type sectors. The present numerical results are in good agreement with those reported by Konoplya [179].[5] A detailed convergence analysis and a systematic comparison among different dimensions, angular momenta, and perturbation sectors are left for future work.

[5]When comparing the numerical values, we take into account the difference in the normalization of the cosmological-constant parameter. The cosmological constant in the present convention is related to that used in Ref. [179] by $\Lambda = 2\Lambda_{\text{Konoplya}}$.

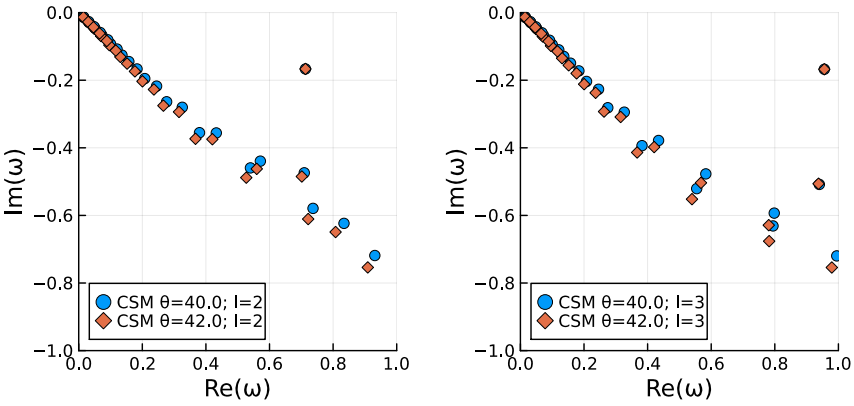

Figure 10.20: The Schwarzschild–dS$_5$ case for the vector-type sector. $\Lambda = 0.4$. The scaling angle is taken to be $\theta = 40°, 42°$. We take $i_{\max} = 30$, $r_{*0} = 0.1$, and $r_{*\max} = 60$. $l = 2$ on the left panel and $l = 3$ on the right panel.

10.6.4 Exponentially growing matrix blocks in diagonalization

Let us consider the generalized complex eigenvalue problem

$$Hc = ENc, \tag{10.145}$$

or, equivalently,

$$\sum_j \left[H_{ij} - EN_{ij}\right] c_j = 0. \tag{10.146}$$

For a two-channel problem, the Hamiltonian matrix has the block structure

$$H = \begin{pmatrix} T_{11} + V_{11} & V_{12} \\ V_{21} & T_{22} + V_{22} \end{pmatrix}. \tag{10.147}$$

In coupled-channel problems such as string-inspired black-hole perturbations, some off-diagonal blocks can become exponentially large in the original field basis. For example, as seen in Eq. (10.137), the matrix element associated with V_{12} contains the factor

$$\mathrm{e}^{\frac{\Lambda^2}{\alpha}}, \tag{10.148}$$

which can become very large for small Gaussian range parameters α. This does not necessarily indicate a physical divergence of the effective potential.

Rather, it can reflect a poor conditioning of the chosen channel basis. In such a situation, the direct diagonalization of Eq. (10.145) becomes numerically unstable.

Block balancing

A simple stabilization strategy is to apply a similarity transformation at the matrix level. We introduce the block scaling matrix

$$S = \begin{pmatrix} I & 0 \\ 0 & sI \end{pmatrix}, \qquad s > 0, \tag{10.149}$$

and write

$$c = S\tilde{c}. \tag{10.150}$$

Then Eq. (10.145) becomes

$$\left(S^{-1}HS - ES^{-1}NS\right)\tilde{c} = 0. \tag{10.151}$$

The scaled Hamiltonian is

$$S^{-1}HS = \begin{pmatrix} T_{11} + V_{11} & sV_{12} \\ s^{-1}V_{21} & T_{22} + V_{22} \end{pmatrix}. \tag{10.152}$$

The eigenvalues are unchanged by this similarity transformation, while the conditioning of the matrix problem can be improved. A natural choice is to balance the norms of the two off-diagonal blocks:

$$s = \sqrt{\frac{\|V_{21}\|}{\|V_{12}\|}}. \tag{10.153}$$

Alternatively, if the exponential growth is dominated by the factor $\mathrm{e}^{\Lambda^2/\alpha}$, one may use a scale estimate such as

$$s \sim \mathrm{e}^{-\frac{\Lambda^2}{\alpha_{\mathrm{eff}}}}, \tag{10.154}$$

where α_{eff} is a representative Gaussian range parameter. The norm-balancing prescription is usually more robust, because it uses the actual matrix elements after discretization.

Channel-basis balancing

A more structural approach is to change the channel basis before discretization. Consider the coupled Schrödinger-type equation

$$-\frac{\mathrm{d}^2}{\mathrm{d}r_*^2}\Phi(r_*) + V(r_*)\Phi(r_*) = E\Phi(r_*). \tag{10.155}$$

We introduce a local channel rescaling

$$\Phi(r_*) = D(r_*)\Xi(r_*), \qquad D(r_*) = \begin{pmatrix} \mathrm{e}^{\Lambda r_*} & 0 \\ 0 & \mathrm{e}^{-\Lambda r_*} \end{pmatrix}. \tag{10.156}$$

Substituting this into the original equation and multiplying by D^{-1} from the left, we obtain

$$-\frac{\mathrm{d}^2}{\mathrm{d}r_*^2}\Xi - 2D^{-1}D'\frac{\mathrm{d}}{\mathrm{d}r_*}\Xi + \left(D^{-1}VD - D^{-1}D''\right)\Xi = E\Xi. \tag{10.157}$$

Thus, the exponentially unbalanced off-diagonal potential is replaced by

$$V_{12} \mapsto \mathrm{e}^{-2\Lambda r_*}V_{12}, \qquad V_{21} \mapsto \mathrm{e}^{2\Lambda r_*}V_{21}. \tag{10.158}$$

This can reduce the exponential hierarchy between the two off-diagonal blocks. The price of this transformation is the appearance of a first-derivative coupling term,

$$-2D^{-1}D'\frac{\mathrm{d}}{\mathrm{d}r_*}\Xi. \tag{10.159}$$

Therefore, the resulting problem is no longer in the standard Schrödinger form without first derivatives. Nevertheless, this formulation may be numerically preferable if the original off-diagonal blocks are so unbalanced that the direct diagonalization becomes ill-conditioned. In practice, the matrix-level block balancing is the simplest first test, because it does not modify the differential equation. If the instability persists, the channel-basis balancing of Eq. (10.157) provides a more systematic way to remove the exponential hierarchy at the level of the continuum problem.

Laboratory checkpoint

Before moving to the next stage, perform the following checks without copying the displayed final answer.

1. Derive the local ingoing/outgoing exponents at both horizons and translate them into admissible complex-deformation wedges.

2. Reproduce one de Sitter QNM spectrum together with its continuum level density while varying the cosmological parameter.

3. For a coupled example, monitor the norms of every matrix block and demonstrate the effect of block balancing on the stable poles.

10.7 Problems for Stage VIII

VIII.1 Starting from the Schwarzschild metric, derive the tortoise coordinate and its asymptotic forms at the horizon and infinity.

VIII.2 Verify the parity of scalar, vector, and tensor spherical harmonics. Count the independent odd-parity metric amplitudes before and after gauge fixing.

VIII.3 Fill in the projection steps from the linearized Ricci tensor to the covariant Regge–Wheeler equation. Check every use of a warped-product identity.

VIII.4 Derive the Regge–Wheeler potential and verify its limiting behavior. Show that $l = 0$ and the vacuum odd $l = 1$ sector require separate treatment.

VIII.5 Translate ingoing horizon and outgoing infinity conditions into a vanishing connection coefficient. Check the sign using $\mathrm{e}^{-\mathrm{i}\omega t}$.

VIII.6 Perform a leading barrier-top WKB estimate of the fundamental Schwarzschild QNM and compare its scaling with M to the exact numerical result.

VIII.7 Derive the analytic complex-scaling exposure condition in the tortoise coordinate. Explain why the inverse map $r(r_*)$ and its branch cuts restrict a naive global rotation.

VIII.8 Build Gaussian-basis kinetic and overlap matrices for the Regge–Wheeler equation. Diagnose loss of precision as the range ratio and polynomial order increase.

VIII.9 For Schwarzschild–de Sitter, locate both horizons and map them to $r_* \to \pm\infty$. Determine the near-Nariai scaling of the barrier width.

VIII.10 Derive the QNM contribution to a continuum level density and compare it with the reference-subtracted cut contribution. Explain why the peak of the full response need not coincide with $\mathrm{Re}\,\omega_{\mathrm{QNM}}$.

Part V

Synthesis and frontiers

Chapter 11

What is invariant and what is chosen

11.1 Invariant resonance data versus representations

11.1.1 The invariant core

Across the constructions in the preceding Stages, the invariant core consists of four items: an analytically continued singularity, its spectral sheet, its residue or root subspace, and the continuum contour relative to which it is exposed. The wave function, norm, and operator domain depend on the representation. A claim of equivalence should therefore compare resolvent matrix elements or connection coefficients, not the pointwise form of two regularized wave functions.

For a simple resonance, the comparison is most usefully read from the connection problem outward:

$$\begin{aligned} \mathcal{C}_{\mathrm{in}}(E_{\mathrm{R}},\hbar)=0 &\Longleftrightarrow F(k_{\mathrm{R}})=0 \\ &\Longleftrightarrow S(k) \text{ has a pole at } k_{\mathrm{R}} \\ &\Longleftrightarrow W(k_{\mathrm{R}})=0 \\ &\Longleftrightarrow H_\theta\Psi_\theta=E_{\mathrm{R}}\Psi_\theta. \end{aligned} \tag{11.1}$$

Here F is a Jost function, W is an incoming/outgoing Wronskian, and $\mathcal{C}_{\mathrm{in}}$ is an exact-WKB connection coefficient. The complex-scaled eigenvalue relation holds for an angle that exposes the pole. The rigged Hilbert space supplies the pole functional associated with the common residue.

11.1.2 A compact dictionary

Language	Resonance object	Reliability test
Exact WKB	Zero of a Borel-resummed incoming connection coefficient	Stokes graph, lateral sum, sheets, and monodromy are documented
Scattering theory	Pole of S, T, or a continued resolvent	Sheet, outgoing boundary value, residue, and threshold structure are specified
Complex scaling	Isolated eigenvalue of H_θ	Stability under θ and basis changes; separation from the rotated continuum
Feshbach projection	Nonlinear root of $\det[z - H_{\mathrm{eff}}(z)]$	Retarded branch of the self-energy and its energy dependence are retained
Rigged Hilbert space	Pole functional in $\Phi^\times$	Test space and dual topology admit the required analytic continuation
Zel'dovich method	Gaussian-regularized bilinear residue	The regulator is removed by analytic continuation, not by an ordinary real-axis limit
Black-hole perturbation	Pole of the retarded radial Green function	Horizon and outer boundary conditions match the time convention; cuts and residues are included

The table is deliberately phrased in terms of tests rather than slogans. For example, "complex eigenvalue" is absent from the first column because it is not by itself a definition. Likewise, "normalizable state" means different things before and after deformation.

11.1.3 What non-self-adjointness does and does not mean

A non-self-adjoint operator may arise in at least four ways. It may be a fundamental effective generator after environmental degrees of freedom are discarded. It may be an energy-dependent Feshbach operator. It may be an analytic representation, such as H_θ, of a self-adjoint scattering problem. Or it may be a finite numerical approximation whose non-self-adjointness includes discretization artifacts. Physical conclusions depend on which situation applies.

Complex scaling belongs primarily to the third category. It does not claim that microscopic quantum mechanics violates unitarity. Instead, it moves a pole from a nonphysical sheet into the point spectrum of a deformed operator. The rotated continuum completes the representation and restores the analytic information needed to reconstruct real-energy unitary scattering.

An open-system Lindblad generator belongs to the first category after a Markovian approximation. Its eigenvalues describe decay of density-matrix modes, not automatically poles of a one-particle S matrix. Quantum-jump unravelings can relate the two in particular models, but complex scaling should not be identified with a no-jump Hamiltonian without an explicit derivation [134, 135, 180].

11.1.4 Observables beyond pole positions

A mature resonance calculation should aim at more than a table of complex energies. The next layer consists of residues, channel projectors, phase shifts, time delays, and continuum level densities. For black holes, this means excitation factors, source-dependent Green functions, greybody factors, and branch-cut discontinuities. For exceptional points, it means the full Jordan resolvent and a normalized holonomy, not only the eigenvalue square root.

Exact WKB and complex scaling are complementary at this layer. A derivative of the exact connection coefficient gives a pole residue, whereas a left–right complex-scaled eigenvector gives the same residue in an L^2 representation. Establishing this equality numerically in nontrivial models would be a stringent test of the unified framework.

11.2 What exact WKB changed in the present research program

The novelty of the program is not exhausted by obtaining several new pole tables. Exact WKB changed which pieces of the problem are regarded as primary. Before choosing a Hilbert-space realization one can construct an analytic incoming coefficient, follow it across Stokes sectors, and ask which features survive every admissible representation. This produces the following shifts of emphasis:

conventional starting point	connection-first understanding
complex eigenvalue	zero of a globally transported incoming coefficient; the eigenvalue is one realization of the zero
divergent Gamow norm	derivative or residue of the analytic connection datum; regularizations must reproduce it
isolated resonance level	pole and continuum as parts of one continued spectral resolution
Langer correction as a prescription	local singular monodromy required by global consistency
EP square root of a matrix	multiple zero of a scattering determinant with continuum normalization kept explicit
black-hole damping boundary condition	horizon-to-horizon connection problem on a complex spectral curve

These shifts have several consequences for how the theory is used.

First, a resonance can be constructed before choosing a non-self-adjoint operator. Exact WKB transports local solutions, produces $\mathcal{C}_{\mathrm{in}}(E)$, and defines a simple pole by $\mathcal{C}_{\mathrm{in}}(E_{\mathrm{R}}) = 0$ together with $\mathcal{C}'_{\mathrm{in}}(E_{\mathrm{R}}) \neq 0$. A complex-scaled eigenvalue is then a calculational realization of this datum. This order prevents an arbitrary complex eigenvalue of a truncation from being mistaken for a resonance.

Second, equivalence of regularizations becomes a checkable residue identity. The Zel'dovich pairing, the rigged-space functional, and the left–right complex-scaled dyad must reproduce the derivative of the same connection coefficient.

Agreement of pole positions without agreement of the residue is only a partial test.

Third, the continuum is not a background that may be deleted after a pole is found. Rotating the continuum, deforming a Berggren contour, or extracting a resonance term reorganizes one spectral response. Threshold cuts, continuum level density, and source-dependent excitation survive that reorganization and control where a pole approximation is accurate.

Fourth, new applications are classified by the connection data they add. A radial origin adds Frobenius indices and singular monodromy; an exceptional point changes a simple zero into a multiple zero and requires a Jordan chain; a black-hole horizon replaces spatial infinity by a second radiation sector. The local differential equation may still look Schrödinger-like, but the global connection problem has changed and must be rebuilt accordingly.

Finally, the same organization separates theorem, representation, and numerics. Analytic dilation supplies the theorem-controlled wedge. A basis and scaling angle supply a representation. Stability under the parameters that should be inessential supplies a numerical falsification test. The three layers cooperate, but none can be substituted silently for another.

The research articles in which these calculations were first developed are Refs. [15–20, 25]. Their chronology is bibliographic provenance; the logical order used here is the dependency order of the connection problem.

11.3 Where the connection-first framework is incomplete

11.3.1 Operator theory for black-hole complex scaling

The numerical success of complex scaling for black-hole master equations does not yet amount to a general ABC theorem for black-hole geometry. A rigorous result should specify weighted spaces, analytic branches of $r(r_*)$, domains at horizons, long-range asymptotics at flat infinity, and the relation between the deformed operator and the retarded resolvent. de Sitter static patches, with exponential decay at both ends, are likely a cleaner starting point than asymptotically flat spacetime.

Exterior deformation may be essential for asymptotically flat tails. One would like a theorem that isolates a finite set of QNM poles while keeping the zero-frequency branch point and its cut under control. The output should

be a resonance expansion with a quantified remainder, not merely a rotated spectrum.

11.3.2 Uniform analysis at thresholds

Standard WKB fails when turning points coalesce, while standard pole perturbation fails when a pole reaches a branch point. Uniform local models, such as Airy, parabolic-cylinder, or higher catastrophe equations, should be matched to the exact-WKB and complex-scaled resolvents. This would give a common treatment of virtual states, anomalous EP orders, zero-damped black-hole modes, and long-time tails.

The relevant universal data include the threshold exponent of the density of states, the Puiseux order of the pole trajectory, and the scaling of the residue. A finite matrix can reproduce these only if its energy-dependent self-energy or continuum limit is retained.

11.3.3 Residues and excitation factors from exact WKB

Most exact-WKB spectral calculations focus on zeros of a quantization condition. For response theory, one needs derivatives of that condition and normalization of left and right solutions. In the notation of Eq. (5.32), a program for residues requires a Borel-resummed evaluation of $\mathcal{C}'_{\mathrm{in}}(E_{\mathrm{R}})$ and of the source overlap. Comparing the result with complex-scaled biorthogonal projectors would connect resurgence directly to measurable line strengths and black-hole ringdown amplitudes.

11.3.4 A regulator-independent EP continuum limit

Momentum bins make the resonance–continuum EP calculable, but they select a particular discretization. The next step is to repeat the construction with Gaussian wave packets, a finite box, Berggren contours, and exterior complex scaling. After matching the same physical holonomy, all regulators should agree. If they do not, the discrepancy will identify which part of the claimed topology belongs to the test-function choice rather than to the pole.

It is also important to formulate the EP in terms of the continued resolvent and its Riesz projection before taking a continuum limit. This would separate a genuine higher-order pole from an avoided crossing with a discretization pseudostate.

11.3.5 Status of monodromy renormalization

Monodromy renormalization is presently a useful organization principle, not a complete universal theory. To develop it further one should define the class of allowed local counter-Voros terms, prove scheme-independent statements, and relate the anomalous dimension to Stokes automorphisms. In radial problems, one should test nonintegrable potentials for which higher quantum periods do not cancel. At EPs, one should derive the running from smeared resolvent pairings rather than formal symbols such as $\delta(0)$.

A successful theory would explain when the Langer reorganization is a fixed point, how monodromy data mix under confluence of singularities, and which trans-series parameters act as relevant couplings. Until then, the phrase "renormalization group" should always be accompanied by the regulator and the invariant quantity being held fixed.

11.3.6 Kerr, superradiance, and nonlinear spectral problems

Kerr is the most important gravitational extension. The angular eigenvalue and radial operator depend on ω, and the superradiant threshold $\omega = m\Omega_H$ changes the flux interpretation. A stable numerical scheme must solve a nonlinear eigenvalue problem with correct left–right derivatives. Exact WKB additionally faces a moving spectral curve. A hybrid solver combining angular spectral methods, analytic differentiation, complex scaling, and quantum periods is a concrete route forward.

Near-extremal Kerr brings coalescing horizons, zero-damped modes, and near-horizon conformal structure. It is a natural laboratory for the joint threshold/EP/monodromy analysis outlined above.

11.3.7 Coupled channels and many-body resonances

Nuclear complex scaling already treats many-body continua and cluster thresholds [8, 181]. Exact WKB is most developed for ordinary differential equations. Extending the unified picture to matrix differential equations requires non-Abelian Stokes matrices and a careful treatment of channel thresholds. The resulting framework would connect continuum- discretized coupled channels, Berggren bases, and resurgent monodromy [119].

Unscreened Coulomb forces make the problem qualitatively harder. The three-body breakup region and each two-cluster region require different asymptotic coordinates and logarithmic phases. Existing 3C, Redmond,

and sectorial expansions determine important leading terms, while Faddeev–Merkuriev splitting yields well-posed channel equations [49, 51, 52, 54]. What is still missing for the present resonance program is a uniform analytic atlas with controlled overlap errors, a corresponding global outgoing resolvent, and a continuation prescription that follows poles through rearrangement thresholds. This is a more precise target than seeking one formal *three-body Coulomb wave*.

The direct-integral viewpoint suggests how to state the channel problem. At each real energy the fiber should contain all open cluster channels, while the asymptotic comparison dynamics must be modified by the appropriate pairwise Coulomb phases. The difficult step is to continue this measurable fiber description analytically across thresholds without losing the cluster-dependent boundary conditions. A multivariable exact-WKB or microlocal construction would have to reproduce the same atlas.

11.3.8 Quantum field theory

In quantum field theory, unstable particles are poles of analytically continued correlation functions, while semiclassical saddles and renormalons control resurgent large-order behavior. The one-particle exact-WKB dictionary suggests a field-theoretic question: can the pole mass, width, spectral density, and Borel singularity data be organized in a common rigged space of correlation-function boundary values? A direct lift is obstructed by multiparticle cuts, gauge constraints, and ultraviolet renormalization, so the monodromy renormalization introduced here should not be conflated with ordinary QFT renormalization.

For a massive theory with isolated one-particle mass shells, Haag–Ruelle or LSZ scattering supplies the field-theoretic counterpart of ordinary wave operators. QED violates the decisive premise: Gauss' law and massless photons turn a charged particle into an infraparticle, and the coherent soft dressing is not a vector in the vacuum Fock representation [58–60]. A resonance theory for charged fields must therefore continue correlation functions between the correct infrared representations, not add a width to a nonexistent sharp Fock particle.

Gauge-invariant charged interpolating operators are nonlocal composites carrying an electric dressing to infinity. Their infrared sensitivity, Wilson-line endpoint and cusp renormalization, and multiparticle cross correlations must be separated carefully. A concrete operator-algebraic program is to construct

an asymptotic observable algebra, classify the relevant soft-charge or flux representations, express physically mixed preparations as direct integrals over an explicitly chosen measure space, and define the scattering map between incoming and outgoing fibers. Only then should one ask which continued resolvent or correlation functional carries an unstable pole and how its residue is normalized.

Solvable large-N models, massive theories coupled to a controllable massless field, nonrelativistic QED, false-vacuum decay, and semiclassical backgrounds with a one-dimensional fluctuation equation provide intermediate tests. The goal is not to replace unitarity or the Källén–Lehmann representation, but to relate their sector-dependent spectral densities to resurgent connection data. A mathematically complete four-dimensional QED scattering theory with charged infraparticles and asymptotic completeness remains beyond the present framework; this limitation should be stated rather than hidden by an infrared regulator.

11.3.9 Numerical certification

Non-normal eigenvalues require stronger certification than a standard Hermitian spectrum. Promising tools include interval arithmetic for matrix elements, validated singular-value bounds, contour-integral eigenprojectors, and independent residual estimates in weighted function spaces. For exact WKB, rigorous Borel summability bounds and controlled Padé errors would play the analogous role. Benchmark models should report not only digits but also which analytic sheet and deformation domain those digits certify.

11.4 Reproducibility checklist for every representation

For a complex-scaling calculation, the following information is sufficient to reconstruct most systematic choices:

1. the coordinate contour, scaling angle, and analytic branches of every multivalued function;

2. the basis functions, nonlinear scales, truncation size, quadrature, and overlap-matrix cutoff;

3. right and left residuals, matrix condition estimates, and the normalization convention;

4. eigenvalue trajectories under changes of θ, basis family, nonlinear scales, and precision;

5. the reference Hamiltonian and matched discretization used for a CLD;

6. an independent benchmark for representative poles and, when possible, residues;

7. the square-root branch used to convert E to ω in a black-hole problem.

For an exact-WKB calculation, report the spectral curve, branch cuts, Stokes graph, Borel direction, lateral prescription, integration cycles, truncation order, Borel–Padé order, and stability under changes of resummation parameters. If a monodromy counterterm is used, report the regulator, matching condition, and scheme-dependent finite parts.

11.5 Conclusions: resonance theory as a connection problem

Quantum resonance is a meeting point of scattering theory, non-self-adjoint spectral analysis, asymptotics, and time-dependent response. The calculation is least ambiguous when it starts from Borel-resummed local branches and their global connection matrix. The no-incoming condition selects a zero of an analytic coefficient; the continued resolvent and S matrix have a pole at that zero. Feshbach projection packages the same continuum dependence into an energy-dependent operator, complex scaling exposes the pole as an L^2 eigenvalue, Zel'dovich regularization defines its bilinear normalization, and a rigged Hilbert space places its residue vector in a continuous dual. These are not competing definitions but calculational realizations reached after the invariant connection datum has been fixed.

Functional analysis makes this dictionary more physical, not less. The operator domain specifies the observable, topology specifies the admissible limit, the spectral measure specifies the continuum, and a locally convex test space specifies which generalized eigenvectors are continuous. In the direct-integral spectral representation, energy is the base measure and open channels form the fibers; the scattering operator is literally the direct integral of the on-shell matrices. von Neumann algebras extend this organization to factor and superselection decompositions. Resonances sit at the controlled interface between that measurable self-adjoint structure and analytic continuation.

The framework remains useful when the problem is enlarged. A radial singular point contributes monodromy that cannot be discarded as a formally higher-order term. An exceptional point turns pole continuation into a branched Jordan problem and forces continuum normalization to be regulated. A black-hole quasinormal mode is an outgoing resonance on the tortoise line, and complex scaling treats its pole and continuum response within one spectral representation.

Long-range forces also show where the elementary picture must change. A two-body Coulomb state is asymptotic to a logarithmically distorted Coulomb wave, not to a free plane wave. Three charged particles require an atlas of breakup and cluster asymptotics rather than a universal product state. In QED, Gauss' law and the soft cloud can move charged asymptotic states out of the vacuum Fock representation altogether. The growing complexity with particle number is therefore not merely combinatorial: long-range correlations change the representation and the composite operator that creates the channel.

The unification does not erase the assumptions of the individual methods. Dilation analyticity, test-function topology, threshold sheets, Borel directions, and numerical non-normality all matter. Stating those assumptions is what converts a suggestive analogy into a transferable method. The most promising next steps are to compare residues and continuum response—not only pole positions—across complex scaling and exact WKB, to construct uniform long-range channel asymptotics for charged few-body systems, and to formulate the corresponding resonance problem between infrared representations in field theory.

Part VI

Computational appendices

Appendix A

Resummation, variational reorganization, and instantons

Reader contract

This appendix is a calculation chapter, not a catalogue of summation methods. One benchmark is carried through ordinary truncation, Borel summation, Padé and Borel–Padé approximation, optimized and variational perturbation theory, and order-dependent mapping. The same calculation then identifies the saddle action which controls large order. The final section translates every object into the exact-WKB language used in Stage III.

Calculation route

Prerequisites. Gaussian integration, analytic continuation, and the Borel transform in Sec. 5.1.2.

Calculation goal. Recover a function from its divergent weak-coupling coefficients, diagnose the failure of that recovery, and read the missing exponential scale from large order.

Completion criterion. The reader can reproduce Figs. or tables of convergence from the supplied Wolfram Language file, locate the leading Borel singularity, and explain why lateral sums and exact-WKB Stokes data are the same kind of information.

The perturbative series and the exact-WKB series are not rival approximations. They are two coordinate descriptions of an analytic problem. Ordinary perturbation theory expands a quantity in a coupling; exact WKB expands a local solution in a semiclassical parameter. In both cases the coefficients generally grow factorially, the formal series alone does not determine a function, and global analytic continuation supplies the missing information. The point of the present calculation is to make that statement operational.

A.1 A benchmark with an exact answer

For $\operatorname{Re} g > 0$, define

$$I(g) = \frac{1}{\sqrt{2\pi}} \int_{-\infty}^{\infty} \mathrm{e}^{-x^2/2 - g x^4/4} \, \mathrm{d}x. \tag{A.1}$$

This zero-dimensional integral is deliberately elementary. It has a Gaussian perturbative vacuum, a nontrivial saddle after analytic continuation, factorial large order, a Borel singularity, and an exact answer. It therefore separates the logic of resummation from the numerical and domain questions of a differential operator. The repository accompanying the calculations in this appendix uses the same benchmark [182].

The substitution $y = x^2$ and a standard integral representation of the modified Bessel function give

$$I(g) = \frac{\mathrm{e}^{1/(8g)}}{2\sqrt{\pi g}} K_{1/4}\!\left(\frac{1}{8g}\right). \tag{A.2}$$

Equation (A.2) is a benchmark, not an input to the resummation algorithms. In a realistic quantum problem the exact answer is unknown; one instead compares independent continuations, stability under the order, and known asymptotic constraints.

A.1.1 Derive the weak-coupling coefficients

Expand only the quartic exponential:

$$I(g) \sim \sum_{n=0}^{\infty} a_n g^n, \tag{A.3}$$

$$a_n = \frac{(-1)^n}{4^n n! \sqrt{2\pi}} \int_{-\infty}^{\infty} x^{4n} \mathrm{e}^{-x^2/2} \, \mathrm{d}x \tag{A.4}$$

$$= (-1)^n \frac{\Gamma(2n + 1/2)}{\sqrt{\pi}\, n!}. \tag{A.5}$$

The second line is a Gaussian moment. No diagrammatic combinatorics has been hidden: its rapid growth is the number of Wick contractions in its simplest form.

Using Stirling's formula in the ratio a_{n+1}/a_n gives

$$\frac{a_{n+1}}{a_n} = -\frac{(2n+1/2)(2n+3/2)}{n+1} = -4n\left[1+O(n^{-1})\right]. \tag{A.6}$$

Thus the coefficients have the schematic behavior

$$a_n \sim (-4)^n \Gamma(n) \times \text{a power of } n. \tag{A.7}$$

The radius of convergence is zero. This does not mean that the first few terms are useless. It means that truncation is an asymptotic operation whose order is part of the approximation.

A.1.2 Optimal truncation is the first nonperturbative estimate

Let $T_n = a_n g^n$. From Eq. (A.6), successive terms have comparable magnitude near

$$4|g|n \simeq 1, \qquad n_\star \simeq \frac{1}{4|g|}. \tag{A.8}$$

Truncating substantially beyond $n_\star$ makes the approximation worse. The size of the least term is exponentially small,

$$|T_{n_\star}| \sim \mathrm{e}^{-1/(4|g|)} \times \text{a power of } g. \tag{A.9}$$

Already at this stage perturbation theory predicts the scale of the effect which it cannot resolve. Section A.6 will derive the same number $1/4$ from a nontrivial saddle.

Checkpoint

A divergent series should never be judged from one fixed truncation order. Plot the partial sums against the order. The useful region is the plateau near the least term; the later divergence is part of the prediction, not a software failure.

A.2 Borel and lateral summation

For a formal series $F(g) \sim \sum_{n\geq 0} a_n g^n$, define the Borel transform and a directional Laplace transform by

$$\widehat{F}(t) = \sum_{n=0}^{\infty} \frac{a_n}{n!} t^n, \tag{A.10}$$

$$\mathcal{S}_\theta F(g) = \frac{1}{g} \int_0^{\mathrm{e}^{\mathrm{i}\theta}\infty} \mathrm{e}^{-t/g} \widehat{F}(t)\, \mathrm{d}t. \tag{A.11}$$

Termwise integration recovers the original formal series because

$$\frac{1}{g} \int_0^{\infty} \mathrm{e}^{-t/g} t^n \, \mathrm{d}t = n! g^n. \tag{A.12}$$

The factorial division in Eq. (A.10) repairs the leading divergence, while the Laplace integral restores the coefficients.

For the quartic integral, Eq. (A.7) implies that the nearest singularity of $\widehat{I}(t)$ lies at

$$t = -\frac{1}{4}. \tag{A.13}$$

For positive real g, this singularity is away from the positive Laplace ray, and the perturbative series is Borel summable. For negative real g, the relevant ray meets the continued singularity. One must specify whether the contour passes above or below it:

$$\mathcal{S}_{0\pm} F(g) = \lim_{\epsilon \downarrow 0} \frac{1}{g} \int_0^{\mathrm{e}^{\pm \mathrm{i}\epsilon}\infty} \mathrm{e}^{-t/g} \widehat{F}(t)\, \mathrm{d}t. \tag{A.14}$$

Their difference is exponentially small in g. The two values are not a defect of the formalism: they are the analytic record of choosing a side of a Stokes ray. A complete physical problem supplies compensating saddle or boundary-condition data so that the final observable has the required reality or outgoing property; this is the elementary form of a transseries completion [13, 183].

A.2.1 What the Borel plane tells us before integration

The Borel plane is a map of competing saddles. If, locally,

$$\widehat{F}(t) \sim \frac{C}{(1 - t/A)^{\beta}}, \tag{A.15}$$

then singularity analysis gives

$$a_n \sim \frac{C}{\Gamma(\beta)} A^{-n} \Gamma(n+\beta). \tag{A.16}$$

The position A determines the exponential $\mathrm{e}^{-A/g}$; the exponent β determines the power-law prefactor; the discontinuity coefficient determines the Stokes multiplier. Numerical large-order data can therefore be used in the reverse direction: coefficient ratios estimate A, and subleading Richardson-type fits estimate β and corrections.

Domain or asymptotic warning

A numerical Laplace integral through a Padé pole is not a definition of a Borel sum. First inspect the poles, then choose a direction or a specified principal-value prescription. An integration routine which silently steps around a pole has made a physical choice on the user's behalf.

A.3 Padé and Borel–Padé approximation

Given $N+1$ coefficients, the $[L/M]$ Padé approximant is the rational function

$$[L/M]_F(g) = \frac{P_L(g)}{Q_M(g)}, \qquad L+M=N, \qquad Q_M(0)=1, \tag{A.17}$$

whose Taylor expansion agrees with F through order N. Padé approximation can represent poles and mimic a branch cut by a sequence of zeros and poles. It does not, by itself, remove factorial divergence.

The robust combination is therefore:

1. divide a_n by $n!$ to form a truncated Borel transform;
2. replace that polynomial by a near-diagonal Padé approximant;
3. inspect its pole pattern in the Borel plane;
4. Laplace integrate along a prescribed contour.

Explicitly,

$$\widehat{F}_N(t) = \sum_{n=0}^{N} \frac{a_n}{n!} t^n, \tag{A.18}$$

$$\widehat{F}_N^{[L/M]}(t) = [L/M]_{\widehat{F}_N}(t), \tag{A.19}$$

$$F_N^{\mathrm{BP}}(g) = \frac{1}{g} \int_0^\infty \mathrm{e}^{-t/g} \widehat{F}_N^{[L/M]}(t)\, \mathrm{d}t. \tag{A.20}$$

For Eq. (A.1), stable near-diagonal sequences recover Eq. (A.2) for positive g. Alternating poles and zeros accumulate along the negative Borel axis, resolving the branch cut which starts at Eq. (A.13).

A.3.1 A convergence protocol rather than one decimal number

For each g, calculate a family of $[L/M]$ approximants with $|L - M| \leq 1$. Record the result together with the closest pole to the integration ray. A trustworthy digit is one which survives:

- increasing N;
- exchanging $[L/M]$ and $[M/L]$;
- a small contour rotation which crosses no singularity;
- increased working precision;
- comparison with an independent method such as ODM.

Near-cancelling pole–zero pairs are often finite-order artifacts. They may be diagnosed, but should not be deleted without reporting the criterion.

A.4 Optimized and variational perturbation theory

Resummation can also be organized by changing the unperturbed problem. Add and subtract a solvable term containing a trial parameter Ω, insert a bookkeeping parameter δ, expand at fixed Ω, set $\delta = 1$, and only then choose Ω. For the quartic integral, write

$$\frac{x^2}{2} + \frac{g x^4}{4} = \frac{\Omega x^2}{2} + \delta \left[\frac{(1-\Omega)x^2}{2} + \frac{g x^4}{4} \right]. \tag{A.21}$$

At order N, expand the second exponential through δ^N and evaluate all moments with the Gaussian of width $\Omega^{-1/2}$. Denote the result after setting $\delta = 1$ by $I_N(g, \Omega)$.

The exact integral is independent of Ω, but the truncated result is not. The principle of minimal sensitivity chooses a locally stationary approximant,

$$\frac{\partial I_N(g,\Omega)}{\partial \Omega} = 0, \tag{A.22}$$

while fastest apparent convergence sets a selected highest-order correction to zero. Multiple stationary points are common. One follows a continuous root sequence with N and reports the selection rule; choosing the most favorable root after seeing the exact answer is not an algorithm.

Optimized perturbation theory emphasizes the invariance of a complete answer under the artificial parameter and uses stationarity as the finite-order criterion [108]. The linear delta expansion makes the bookkeeping construction explicit, with convergence results available in important model problems [109, 110]. Variational perturbation theory further builds known strong-coupling scaling into the reorganization [111]. The names overlap in the literature; the defining data are therefore the splitting, the truncation rule, and the optimization condition, not the label.

A.4.1 Why optimization can recover strong coupling

Rescale $x = g^{-1/4}y$ in Eq. (A.1). Then

$$I(g) = g^{-1/4}\frac{1}{\sqrt{2\pi}}\int_{-\infty}^{\infty} \mathrm{e}^{-y^4/4 - y^2/(2\sqrt{g})}\,\mathrm{d}y, \tag{A.23}$$

so the leading strong-coupling power is $g^{-1/4}$ and corrections occur in powers of $g^{-1/2}$. A variational mapping which respects these exponents has information unavailable to a raw weak-coupling polynomial. In operator problems the analogous information comes from dimensional analysis, semiclassical scaling, or a solvable strong-coupling limit.

Checkpoint

Optimization does not make an approximation variational in the sense of an upper bound. Unless a Rayleigh–Ritz theorem applies to the precise functional being optimized, stationarity supplies stability, not

an inequality.

A.5 Order-dependent mapping

Order-dependent mapping combines analytic continuation with an optimized parameter. Introduce

$$g = \rho \frac{\lambda}{(1-\lambda)^{\alpha}}. \tag{A.24}$$

The exponent α is chosen from the analytic or strong-coupling behavior. For the present quartic integral a useful map is

$$g = \rho \frac{\lambda}{(1-\lambda)^{2}}. \tag{A.25}$$

Substitute Eq. (A.25) into the weak-coupling series, reexpand in λ through order N, and write

$$I_N(g;\rho) = \sum_{n=0}^{N} c_n(\rho)\lambda(g,\rho)^n. \tag{A.26}$$

The parameter is allowed to depend on the order. A common condition is

$$c_N(\rho_N) = 0, \tag{A.27}$$

or, alternatively, stationarity with respect to ρ. As N grows, ρ_N moves so that the finite analytic domain in λ resolves a larger part of the cut g plane. The general construction and its convergence mechanisms are reviewed in Ref. [112]; the specific implementation used here follows Ref. [182].

A.5.1 How ODM differs from a fixed conformal Borel map

A conformal Borel method maps a known cut Borel domain to a disk using a fixed singularity location. ODM maps the coupling itself and changes the scale ρ_N with the order. The former is strongest when the Borel singularity geometry is known; the latter can infer an efficient scale from the coefficient sequence and strong-coupling exponent. They may be combined, but then each source of input must be stated to avoid counting the same analytic information twice.

A.6 Instantons and the origin of large order

Continue the quartic coupling to $g = -|g|$. The exponent can be written as

$$S(x) = \frac{x^2}{2} - \frac{|g|x^4}{4}. \tag{A.28}$$

Besides $x = 0$, the stationary points satisfy

$$S'(x) = x - |g|x^3 = 0, \qquad x_\star = \pm\frac{1}{\sqrt{|g|}}. \tag{A.29}$$

Their action relative to the perturbative saddle is

$$S(x_\star) - S(0) = \frac{1}{4|g|}. \tag{A.30}$$

This is precisely the exponential scale inferred from the least term in Eq. (A.9), and its reduced action $A = 1/4$ is precisely the Borel singularity in Eq. (A.13). Three calculations have found the same invariant:

$$\text{large-order ratio} \quad \longleftrightarrow \quad \text{Borel singularity} \quad \longleftrightarrow \quad \text{saddle action.} \tag{A.31}$$

In quantum mechanics the nontrivial saddle is a finite-action trajectory in Euclidean time rather than a point. Expanding about it gives a fluctuation determinant and zero-mode measure. Multi-instanton sectors generate powers of $\mathrm{e}^{-A/g}$, possible logarithms, and interactions between saddles [77, 184]. The perturbative coefficients around one saddle encode fluctuations around the others. This is the practical content of resurgence, not merely the statement that a divergent series can sometimes be summed.

A.6.1 Dispersion relation for the coefficients

Suppose $F(g)$ is analytic in a cut plane and has a discontinuity on the negative axis. Cauchy's formula gives, under the appropriate subtractions,

$$a_n = \frac{(-1)^{n+1}}{\pi}\int_0^\infty \frac{\operatorname{Im} F(-s + \mathrm{i}0)}{s^{n+1}}\,\mathrm{d}s. \tag{A.32}$$

If the discontinuity has the semiclassical form

$$\operatorname{Im} F(-s + \mathrm{i}0) \sim C s^{-b}\mathrm{e}^{-A/s}\left[1 + O(s)\right], \tag{A.33}$$

then $u = A/s$ in Eq. (A.32) yields

$$a_n \sim \frac{(-1)^{n+1}C}{\pi} A^{-n-b}\Gamma(n+b)\left[1+O(n^{-1})\right]. \tag{A.34}$$

Thus the imaginary part of an unstable continuation controls the late terms of the stable perturbative problem. For a resonance, the same imaginary part becomes a decay width after the outgoing boundary value has been fixed.

A.7 The exact-WKB translation

The exact-WKB construction in Sec. 5.1 begins from a local Riccati series, Borel resums it in a direction, and transports the resulting basis through Stokes sectors. The global connection coefficient $\mathcal{C}_{\rm in}(E)$ is then an analytic function assembled from local data. The dictionary is exact at the structural level:

Coupling expansion	Exact-WKB connection problem
formal perturbative coefficients	formal Riccati coefficients
Borel singularity at action A	finite action path or WKB cycle
lateral Borel sum	directional exact-WKB sum $\mathcal{S}_{\theta\pm}$
Stokes discontinuity	change of the resummed WKB basis
instanton sector	exponential of a Voros period $\mathcal{V}_\gamma$
physical transseries parameter	boundary or connection data
zero of a continued denominator	zero of $\mathcal{C}_{\rm in}(E)$

The last two rows are the reason this appendix belongs in the present book. For a generic perturbative observable, a transseries parameter can look like an extra constant. In a scattering problem it is fixed by preparation and asymptotic boundary conditions. The outgoing condition selects a lateral continuation and imposes

$$\mathcal{C}_{\rm in}(E_{\rm R}) = 0. \tag{A.35}$$

The resonance is therefore not obtained by adding a complex energy by hand. It is the zero of the globally continued coefficient. Its residue depends on $\partial_E \mathcal{C}_{\rm in}$, so the fluctuation and normalization information which accompanies the exponential sector remains observable.

A.7.1 What ordinary resummation cannot decide

A coefficient list does not specify:

- the physical sheet of the energy or momentum plane;
- which asymptotic channel is incoming or outgoing;
- the test space on which a continued eigenfunctional acts;
- whether a Borel ambiguity is cancelled, retained as a width, or moved by a change of observable;
- which continuum background accompanies a pole.

These are connection, domain, and representation data. Exact WKB is useful because it keeps them in the calculation from the beginning.

A.8 A reproducible Wolfram Language laboratory

The file `notebooks/resummation_workflow.wl` supplied with the source archive implements the coefficient generation, direct truncation, Borel–Padé summation, Borel-plane pole inspection, and the ODM map. It is a compact, text-readable companion to the larger public notebook collection [182]. A separate Wolfram Community article demonstrates how symbolic and numerical code can accompany the exact-WKB resonance analysis itself [185].

The core commands are included here so that the printed book remains self-contained:

Listing A.1: Minimal Wolfram Language workflow for the quartic integral.

```
(* Quantum Resonance as a Global Connection Problem
   Compact resummation workflow for Appendix A.
   Wolfram Language source; no notebook front end is required. *)

ClearAll[quarticExact, quarticCoefficient, quarticTruncated,
  borelPolynomial, borelPade, borelPadeSum, borelPoles,
  odmMap, odmSeries, odmRoots, odmValue];

quarticExact[g_?NumericQ, precision_: 50] :=
  N[Exp[1/(8 g)] BesselK[1/4, 1/(8 g)]/(2 Sqrt[Pi g]),
    precision];

quarticCoefficient[n_Integer?NonNegative] :=
  (-1)^n Gamma[2 n + 1/2]/(Sqrt[Pi] n!);
```

```
quarticTruncated[g_, order_Integer?NonNegative] :=
  Sum[quarticCoefficient[n] g^n, {n, 0, order}];

borelPolynomial[t_, order_Integer?NonNegative] :=
  Sum[quarticCoefficient[n] t^n/n!, {n, 0, order}];

borelPade[t_, order_Integer?Positive] := Module[{left, right},
  left = Floor[order/2];
  right = order - left;
  PadeApproximant[borelPolynomial[t, order], {t, 0, {left, right}}]
];

borelPoles[order_Integer?Positive, precision_: 50] := Module[{t},
  t /. N[Solve[Denominator[Together[borelPade[t, order]]] == 0, t],
    precision]
];

borelPadeSum[g_?NumericQ, order_Integer?Positive,
    precision_: 50] := Module[{t, rational},
  rational = borelPade[t, order];
  NIntegrate[Exp[-t/g] rational/g, {t, 0, Infinity},
    WorkingPrecision -> precision,
    AccuracyGoal -> Floor[precision/2],
    PrecisionGoal -> Floor[precision/2]]
];

odmMap[lambda_, rho_] := rho lambda/(1 - lambda)^2;

odmSeries[lambda_, rho_, order_Integer?Positive] :=
  Normal@Series[
    Sum[quarticCoefficient[n] odmMap[lambda, rho]^n,
      {n, 0, order}], {lambda, 0, order}];

odmRoots[order_Integer?Positive, precision_: 50] := Module[
  {lambda, rho, highest},
  highest = Coefficient[odmSeries[lambda, rho, order], lambda, order];
  Select[rho /. NSolve[highest == 0, rho, WorkingPrecision -> precision],
    Im[#] == 0 && Re[#] > 0 &]
];

odmValue[g_?NumericQ, order_Integer?Positive, rho_?NumericQ,
    precision_: 50] := Module[{lambda, physicalRoot},
  physicalRoot = lambda /. FindRoot[
    g == odmMap[lambda, rho], {lambda, Min[0.8, g/(g + rho)]},
    WorkingPrecision -> precision];
```

```
  N[odmSeries[lambda, rho, order] /. lambda -> physicalRoot, precision]
];

(* Reproducible benchmark. Inspect borelPoles before integrating. *)
Do[
  Print["g = ", g, ", exact = ", quarticExact[g, 40]];
  Print["Borel-Pade, N = 20: ", borelPadeSum[g, 20, 40]],
  {g, {1/5, 2/5}}
];
```

A.8.1 Protocol for comparing methods

Use exactly the same coefficient list and working precision for every method. For $g = 0.2$ and $g = 0.4$, carry out the following steps.

1. Evaluate Eq. (A.2) at high precision only to create withheld validation data.
2. Plot partial sums for all $0 \le N \le N_{\max}$ and mark the least term predicted by Eq. (A.8).
3. Compute near-diagonal Borel–Padé sequences and reject no pole without recording its pole–zero distance.
4. Follow one continuous PMS or FAC root for OPT/VPT as N changes.
5. Follow one continuous positive ODM root ρ_N and record both ρ_N and the mapped variable $\lambda(g, \rho_N)$.
6. Compare errors against the exact answer only after all selection rules have been fixed.

Representative exact values are

$$I(0.2) = 0.9079847774\ldots, \tag{A.36}$$

$$I(0.4) = 0.8576085854\ldots. \tag{A.37}$$

The purpose is not to declare a universal winner. Borel–Padé is strongest when the Borel geometry is well resolved; VPT is strongest when reliable strong-coupling exponents are available; ODM is attractive when a useful map and a stable order-dependent root can be identified. Exact WKB adds the global channel geometry needed for spectral and scattering questions.

Exercises

R.1 Derive Eq. (A.2) from Eq. (A.1) and verify its $g \downarrow 0$ asymptotic expansion.

R.2 Use Eq. (A.5) to estimate the Borel singularity from three successive coefficient ratios. Determine the leading $1/n$ correction.

R.3 Compare direct Padé and Borel–Padé at $g = 0.4$. Plot all Borel poles and explain which sequences can be integrated on the positive axis without a prescription.

R.4 Derive $I_N(g, \Omega)$ through $N = 3$ from Eq. (A.21). Find all real positive PMS roots and track them from $g = 0.05$ to $g = 1$.

R.5 Implement Eqs. (A.25)–(A.27) without using the supplied function. Explain why selecting a different root independently at each order destroys the meaning of convergence.

R.6 Starting from Eq. (A.32), derive Eq. (A.34), including the overall power of A.

R.7 For the inverted Rosen–Morse problem in Sec. 5.3.2, identify the WKB action which replaces $A = 1/4$ and explain how its Stokes multiplier enters $\mathcal{C}_{\text{in}}(E)$.

A.9 What to retain for the rest of the book

The reusable lesson is a five-step discipline.

1. Determine the domain, coupling variable, and asymptotic boundary condition before manipulating coefficients.
2. Diagnose late terms and locate candidate action scales.
3. Choose a summation or reorganization whose analytic assumptions are explicit.
4. Test order, precision, contour, root, and representation stability.
5. Translate the recovered analytic function back into invariant pole, residue, and continuum data.

This discipline is the perturbative analogue of the calculation spine in Sec. 1.3: local data are useful only after a global connection prescription has been fixed.

Hints and selected solutions

The problems are intended to be worked with the conventions and canonical definitions of the corresponding Stage. The following hints give the key step or a check; they do not replace the intermediate algebra. A companion volume, built from `solutions_ja.tex`, gives complete Japanese solutions to all ninety-nine Stage problems and all seven problems in the resummation appendix. The present chapter remains intentionally compact so that it can be used while reading the English text without duplicating that companion volume.

Stage I

For I.2, the boundary form is $-\mathrm{i}\hbar[\phi^*(L)\psi(L) - \phi^*(0)\psi(0)]$; the same phase condition on ϕ and ψ makes it vanish and exhausts the adjoint domain. For I.4, $p^2\mathrm{d}p = \mu p\mathrm{d}E$, so multiplication by $(\mu p)^{1/2}$ preserves the norm. For I.8, solve the Q equation with the chosen outgoing boundary value before substitution; differentiation acts both on the eigenvector and on the resolvent inside H_{eff}. For I.11, approximate the image of the unit ball under the compact operator by a finite ε-net and use strong convergence on that finite set. For I.12, square integrability of the kernel is precisely the Hilbert–Schmidt criterion; inspect the diagonal singularity locally before estimating the tails. For I.13, move $V^{1/2}$ through the eigenvalue equation and keep the sign convention in the Birman–Schwinger operator. For I.14, insert a Laurent ansatz in $A(z)^{-1}A(z) = \mathbf{1}$ and pair its leading equation with the left and right null vectors. For I.15, choose normalized functions with mutually disjoint supports: a nonzero multiplier cannot turn that sequence into a norm-convergent one.

Stage II

For II.3, Fourier transform $(E - p^2/2\mu + \mathrm{i}0)^{-1}$ and close the radial momentum contour on the outgoing pole. For II.6, the radial Green kernel is a product of the solution regular at the origin and the outgoing solution, divided by their Wronskian. For II.7–II.8, the divergent phase is the time integral of $1/|\boldsymbol{v}t|$ and is logarithmic; the comparison dynamics must carry exactly that term.

For II.11, integrate the differential expression against a test function twice and retain the endpoint Wronskian. For II.12, the two Frobenius powers are $r^{1/2\pm\sqrt{g+1/4}}$; testing both in $L^2(0,1)$ locates the limit-point threshold at $g = 3/4$. For II.13, continuity fixes one Green kernel coefficient and the derivative jump fixes the other. For II.14, match the sine solution in the well to the two exterior exponentials and read the Jost function from the incoming coefficient. For II.15, differentiate the differential equation with respect to momentum, subtract the original equation times the differentiated solution, and integrate the resulting Wronskian derivative.

Stage III

For III.1, equate powers after inserting $S = \sum_{n=-1}^{\infty} \hbar^n S_n$ into $S^2 + S' = Q/\hbar^2$. For III.2, the Borel transform has a pole at unit Borel time; the two Laplace contours differ by $2\pi\mathrm{i}$ times its residue. For III.7, a double zero gives a $(E - E_*)^{-2}$ term unless the numerator vanishes simultaneously.

Stage IV

For IV.1, use $(x \pm \mathrm{i}0)^{-1} = \mathrm{PV}(1/x) \mp \mathrm{i}\pi\delta(x)$. For IV.3, write $k = |k|\mathrm{e}^{-\mathrm{i}\varphi}$; the scaled wave decays when $\theta > \varphi$. For IV.7, differentiate the Birman–Krein determinant or take the imaginary part of the reference-subtracted resolvent trace. For IV.11, expand $D(E) = E - E_0 - \Sigma(E)$ at its simple zero; the residue is $1/D'(E_\mathrm{R}) = 1/[1 - \Sigma'(E_\mathrm{R})]$. For IV.12, differentiate the argument of the partial-wave S matrix before setting $E = E_\mathrm{R}$. For IV.13, combine the background and pole terms over the common denominator $\epsilon + \mathrm{i}$ and complete the modulus square. For IV.14, put the same square-root branch into the self-energy, phase space, and analytic continuation; changing only one of the three changes the sheet.

Stage V

For V.3, $u(r) = \mathrm{e}^{x/2}\chi(x)$ removes the first derivative created by $r = \mathrm{e}^x$. The $1/4$ from this rescaling completes $l(l+1)$ to $(l+1/2)^2$. For V.5, evaluate the radial momentum contour by residues at zero and infinity rather than integrating between turning points directly.

Stage VI

For VI.3, step functions approximate every fixed L^2 function, but a unit vector supported inside a newly resolved sub-bin keeps the operator-norm difference equal to one. For VI.6, the closed-channel resolvent is real below threshold and acquires a discontinuity above it. For VI.10, use $j_l(qr) \sim (qr)^l/(2l+1)!!$. For VI.11, write both Jacobi sets explicitly and transform the exchange operator before imposing the Pauli projector. For VI.12, the full extended completeness relation restores the positive response even though individual rotated-continuum terms need not be positive. For VI.13, take the outer product of the right and left pole vectors and divide by their biorthogonal overlap; a fragmented cluster is treated by a contour integral instead. For VI.14, begin from the invariant three-body phase-space measure and only then change variables to the measured energy pair. For VI.15, if $\mathcal{C}_{\mathrm{in}}(E_{\mathrm{R}}) = 0$ is simple, solve the connection problem for right and left null vectors and divide their outer product by $v_L^{\top}\mathcal{C}'_{\mathrm{in}}(E_{\mathrm{R}})v_R$.

Stage VII

For VII.1, the discriminant is $(\operatorname{tr} H)^2 - 4 \det H$; an EP also requires defectiveness, not only equal numerical eigenvalues. For VII.4, one circuit exchanges sheets and two circuits return the eigenvalue labels while leaving a possible geometric factor. For VII.10, solve the determinant and its energy derivative simultaneously and verify a rank-one null space.

Stage VIII

For VIII.1, integrate $\mathrm{d}r_*/\mathrm{d}r = (1-2M/r)^{-1}$ and choose the additive constant only after specifying a dimensionless logarithm. For VIII.5, $\mathrm{e}^{-\mathrm{i}\omega(t+r_*)}$ is ingoing at the future horizon and $\mathrm{e}^{-\mathrm{i}\omega(t-r_*)}$ outgoing at infinity. For VIII.10, retain the reference-subtracted rotated continuum when reconstructing the response; a single Lorentzian pole is not the full level density.

Worked solutions as calculation templates

The solutions below are deliberately more explicit than the preceding hints. Each one isolates a calculation that recurs in later Stages. The point is not

to memorize the final formula, but to make the domain, boundary value, sheet, or projection choice visible at the line where it enters.

I.2: self-adjoint momentum on an interval

Begin with the differential expression $-\mathrm{i}\hbar\mathrm{d}/\mathrm{d}x$ on $L^2(0,L)$ and the domain

$$\mathcal{D}(p_\alpha) = \{\psi \in H^1(0,L) : \psi(L) = \mathrm{e}^{\mathrm{i}\alpha}\psi(0)\}. \tag{A.38}$$

For $\phi, \psi \in H^1(0,L)$, integration by parts gives the boundary form

$$\langle \phi, p\psi\rangle - \langle p\phi, \psi\rangle = -\mathrm{i}\hbar\left[\phi^*(L)\psi(L) - \phi^*(0)\psi(0)\right]. \tag{A.39}$$

It vanishes on $\mathcal{D}(p_\alpha)$. Conversely, if ϕ belongs to the adjoint domain, the boundary form must vanish for every admissible ψ. Using $\psi(L) = \mathrm{e}^{\mathrm{i}\alpha}\psi(0)$ and varying $\psi(0)$ freely yields $\phi(L) = \mathrm{e}^{\mathrm{i}\alpha}\phi(0)$. Thus the adjoint has the same domain and p_α is self-adjoint.

The eigenvalue equation gives $\psi_k(x) = C\mathrm{e}^{\mathrm{i}kx}$. Its boundary condition is $\mathrm{e}^{\mathrm{i}kL} = \mathrm{e}^{\mathrm{i}\alpha}$, hence

$$k_n = \frac{2\pi n + \alpha}{L}, \qquad p_n = \hbar k_n, \qquad n \in \mathbb{Z}. \tag{A.40}$$

The calculation is a compact model of a rule used throughout the book: a differential expression has no spectrum until its domain has been fixed.

I.8: Feshbach reduction and the derivative metric

Let $P + Q = \mathbf{1}$, $PQ = 0$, and write $(E - H)\Psi = 0$ in blocks:

$$(E - H_{PP})P\Psi - H_{PQ}Q\Psi = 0, \tag{A.41}$$

$$-H_{QP}P\Psi + (E - H_{QQ})Q\Psi = 0. \tag{A.42}$$

With the specified outgoing boundary value of the Q resolvent,

$$Q\Psi = (E - H_{QQ})^{-1}H_{QP}P\Psi. \tag{A.43}$$

Substitution gives

$$[E - H_{\mathrm{eff}}(E)]P\Psi = 0, \qquad H_{\mathrm{eff}}(E) = H_{PP} + H_{PQ}(E - H_{QQ})^{-1}H_{QP}. \tag{A.44}$$

For a rank-one P space write the secular function as $F(E) = E - E_0 - \Sigma(E)$. At a simple pole E_{R},

$$\frac{1}{F(E)} = \frac{Z_R}{E - E_{\mathrm{R}}} + O(1), \qquad Z_R = \frac{1}{1 - \Sigma'(E_{\mathrm{R}})}. \tag{A.45}$$

The same factor follows before taking rank one. Differentiate $[E - H_{\mathrm{eff}}(E)]\psi_E = 0$, pair with the left pole vector, and evaluate at E_{R}. The coefficient of the pole is controlled by $\langle\widetilde{\psi}_R|[\mathbf{1} - \partial_E H_{\mathrm{eff}}(E_{\mathrm{R}})]|\psi_R\rangle$. Dropping the derivative would normalize the projected vector as if the eliminated continuum carried no probability.

II.3: outgoing free Green function and the Born amplitude

For $E = \hbar^2 k^2/(2\mu)$, the outgoing free kernel is

$$G_0^{(+)}(\boldsymbol{r}; E) = \int \frac{\mathrm{d}^3 p}{(2\pi\hbar)^3} \frac{\mathrm{e}^{\mathrm{i}\boldsymbol{p}\cdot\boldsymbol{r}/\hbar}}{E - p^2/(2\mu) + \mathrm{i}0}. \tag{A.46}$$

After the angular integral, extend the radial momentum integral to the whole line. For $r > 0$ close the contour in the upper half-plane for the factor $\mathrm{e}^{\mathrm{i}pr/\hbar}$. The $+\mathrm{i}0$ prescription selects the outgoing pole, and the residue gives

$$G_0^{(+)}(\boldsymbol{r}; E) = -\frac{\mu}{2\pi\hbar^2} \frac{\mathrm{e}^{\mathrm{i}kr}}{r}. \tag{A.47}$$

Insert this kernel in $\psi^{(+)} = \mathrm{e}^{\mathrm{i}\boldsymbol{k}\cdot\boldsymbol{r}} + G_0^{(+)} V \psi^{(+)}$. For $r \gg r'$ use $|\boldsymbol{r} - \boldsymbol{r}'| = r - \widehat{\boldsymbol{r}} \cdot \boldsymbol{r}' + O(r^{-1})$. The coefficient of $\mathrm{e}^{\mathrm{i}kr}/r$ is

$$f(\boldsymbol{k}', \boldsymbol{k}) = -\frac{\mu}{2\pi\hbar^2} \int \mathrm{d}^3 r' \, \mathrm{e}^{-\mathrm{i}\boldsymbol{k}'\cdot\boldsymbol{r}'} V(\boldsymbol{r}') \psi^{(+)}(\boldsymbol{r}'). \tag{A.48}$$

Replacing $\psi^{(+)}$ by the incident plane wave gives the first Born amplitude. The sign is therefore fixed by the time convention and the boundary value of the resolvent, not by a remembered scattering formula.

II.6: Jost Green kernel and pole residue

For a fixed partial wave let $\varphi_l(k, r)$ be regular at the origin and $f_l^{(+)}(k, r)$ outgoing at infinity. Their Wronskian is independent of r. Solving the jump

condition of the radial Green equation gives

$$G_l^{(+)}(r,r';k) = -\frac{2\mu}{\hbar^2}\frac{\varphi_l(k,r_<)f_l^{(+)}(k,r_>)}{W[\varphi_l, f_l^{(+)}](k)}. \tag{A.49}$$

Up to the convention-dependent nonzero factor, the denominator is the Jost function $F_l(k)$. If $F_l(k_R) = 0$ and $F_l'(k_R) \neq 0$, regular and outgoing solutions become proportional, say $\varphi_l(k_R, r) = A_R u_R(r)$ and $f_l^{(+)}(k_R, r) = B_R u_R(r)$. Therefore

$$\operatorname*{Res}_{k=k_R} G_l^{(+)}(r,r';k) = -\frac{2\mu}{\hbar^2}\frac{A_R B_R}{F_l'(k_R)}u_R(r)u_R(r'). \tag{A.50}$$

This is the coordinate-space version of "pole position plus residue." The state u_R alone is normalization dependent; the full residue is not.

III.1: the exact-WKB Riccati recursion

Write the Schr"odinger equation as $[-\hbar^2\partial_x^2 + Q(x)]\psi = 0$ and set $\psi = \mathrm{e}^{\int^x S(x',\hbar)\mathrm{d}x'}$. Then

$$S^2 + \partial_x S = \frac{Q}{\hbar^2}. \tag{A.51}$$

With $S = \sum_{n=-1}^{\infty}\hbar^n S_n$, the first equations are

$$S_{-1}^2 = Q, \qquad 2S_{-1}S_0 + S_{-1}' = 0, \tag{A.52}$$

$$2S_{-1}S_1 + S_0^2 + S_0' = 0, \qquad 2S_{-1}S_2 + 2S_0S_1 + S_1' = 0. \tag{A.53}$$

Choosing $S_{-1}^{(\pm)} = \pm\sqrt{Q}$ gives

$$S_0 = -\frac{Q'}{4Q}, \tag{A.54}$$

$$S_1^{(\pm)} = \pm\left(\frac{Q''}{8Q^{3/2}} - \frac{5(Q')^2}{32Q^{5/2}}\right), \tag{A.55}$$

$$S_2 = -\frac{Q'''}{16Q^2} + \frac{9Q'Q''}{32Q^3} - \frac{15(Q')^3}{64Q^4}. \tag{A.56}$$

The coefficients that change sign with the square-root sheet form S_{odd}; the sheet-even coefficients form S_{even}, with $S_{\mathrm{even}} = -(1/2)\partial_x \log S_{\mathrm{odd}}$. This identity fixes the all-order prefactor and provides a useful algebraic check on any recursion code.

III.7: simple and double zeros of a connection coefficient

Let $S(E) = N(E)/\mathcal{C}_{\mathrm{in}}(E)$ and put $z = E - E_*$. At a simple zero,

$$\mathcal{C}_{\mathrm{in}}(E) = c_1 z + \tfrac{1}{2} c_2 z^2 + O(z^3), \qquad N(E) = n_0 + n_1 z + O(z^2). \tag{A.57}$$

Long division gives

$$S(E) = \frac{n_0/c_1}{z} + \left(\frac{n_1}{c_1} - \frac{n_0 c_2}{2 c_1^2} \right) + O(z). \tag{A.58}$$

At a double zero, $c_1 = 0$ and $c_2 \neq 0$. Including the cubic coefficient,

$$S(E) = \frac{2 n_0/c_2}{z^2} + \frac{2}{c_2} \left(n_1 - \frac{n_0 c_3}{3 c_2} \right) \frac{1}{z} + O(1). \tag{A.59}$$

The second-order pole is the scalar shadow of a length-two Jordan chain. Notice the necessary caveat: if N vanishes at the same point, cancellation can lower the pole order. A multiple zero of a numerical determinant must therefore be checked against the relevant numerator and nullity.

IV.1: a flat-continuum self-energy

Take one bare state of energy E_0, continuum energies $\epsilon \in [E_{\mathrm{th}}, E_c]$, constant density ρ, and constant coupling g. The outgoing self-energy is

$$\Sigma(E + \mathrm{i}0) = \rho |g|^2 \int_{E_{\mathrm{th}}}^{E_c} \frac{\mathrm{d}\epsilon}{E - \epsilon + \mathrm{i}0}. \tag{A.60}$$

Using the distribution identity before performing the integral,

$$\Sigma(E + \mathrm{i}0) = \rho |g|^2 \log \left| \frac{E - E_{\mathrm{th}}}{E - E_c} \right| - \mathrm{i}\pi \rho |g|^2 \Theta(E - E_{\mathrm{th}}) \Theta(E_c - E). \tag{A.61}$$

Thus the real part shifts the level and depends on the ultraviolet model, whereas inside the band $\Gamma(E) = -2 \operatorname{Im} \Sigma(E + \mathrm{i}0) = 2\pi\rho|g|^2$. The pole solves $E_{\mathrm{R}} - E_0 - \Sigma^{\mathrm{II}}(E_{\mathrm{R}}) = 0$ on the continued sheet. Keeping the logarithm rather than replacing it immediately by a constant width also retains the threshold branch point and the nonexponential tail.

IV.5: Berggren–Zel'dovich Gaussian continuation

The asymptotic contribution to the Gamow pairing contains

$$I_\epsilon(q) = \int_0^\infty \mathrm{e}^{-\epsilon r^2 + \mathrm{i}qr}\,\mathrm{d}r, \qquad \operatorname{Re}\epsilon > 0. \tag{A.62}$$

Complete the square and use the complementary error function:

$$I_\epsilon(q) = \frac{\sqrt{\pi}}{2\sqrt{\epsilon}}\mathrm{e}^{-\frac{q^2}{4\epsilon}}\operatorname{erfc}\left(-\frac{\mathrm{i}q}{2\sqrt{\epsilon}}\right). \tag{A.63}$$

In a sector where $\operatorname{Im} q > 0$, the undamped integral already converges and $I_\epsilon(q) \to -1/(\mathrm{i}q)$ as $\epsilon \downarrow 0$. The right-hand side is analytic in q away from the Stokes boundary, so this value defines its continuation to the resonance quadrant even though the original undamped real-axis integral diverges there. For a full wave function one performs this continuation term by term only after controlling the subleading asymptotics. Berggren's proof is precisely what prevents "insert a Gaussian and discard it" from becoming a regulator-dependent prescription.

V.3: deriving, not guessing, the Langer term

For the reduced three-dimensional radial function,

$$-\hbar^2 u''(r) + \left[2\mu V(r) + \frac{\hbar^2 l(l+1)}{r^2}\right] u(r) = 2\mu E u(r). \tag{A.64}$$

Set $r = \mathrm{e}^x$ and $u(r) = \mathrm{e}^{x/2}\chi(x)$. Since $\partial_r = \mathrm{e}^{-x}\partial_x$,

$$u''(r) = \mathrm{e}^{-3x/2}\left(\chi'' - \frac{1}{4}\chi\right). \tag{A.65}$$

Multiplying the equation by $\mathrm{e}^{3x/2}$ produces

$$-\hbar^2\chi''(x) + \left\{2\mu\mathrm{e}^{2x}[V(\mathrm{e}^x) - E] + \hbar^2\left(l + \frac{1}{2}\right)^2\right\}\chi(x) = 0. \tag{A.66}$$

The extra $1/4$ is the Jacobian contribution required to remove the first derivative. The replacement $l(l+1) \mapsto (l+1/2)^2$ is therefore a coordinate-and-half-density statement; using it without transforming the wave function mixes two different differential equations.

V.5: the radial Coulomb action

For $V(r) = -\kappa/r$ and $E < 0$, put $K = \sqrt{-2\mu E}$ and $L = \hbar(l + 1/2)$. The Langer radial momentum is

$$p_r(r) = \sqrt{-K^2 + \frac{2\mu\kappa}{r} - \frac{L^2}{r^2}}. \tag{A.67}$$

The closed contour around the two positive turning points can be deformed to small and large circles on the two-sheeted curve. Expanding at zero and infinity, or evaluating the corresponding residues, yields

$$\frac{1}{2\pi}\oint p_r \mathrm{d}r = \frac{\mu\kappa}{K} - L. \tag{A.68}$$

Bohr–Sommerfeld quantization of the radial oscillation is $(2\pi)^{-1}\oint p_r \mathrm{d}r = \hbar(n_r + 1/2)$. Hence

$$\frac{\mu\kappa}{K} = \hbar(n_r + l + 1), \qquad E = -\frac{\mu\kappa^2}{2\hbar^2(n_r + l + 1)^2}. \tag{A.69}$$

Keeping the origin residue $-L$ and the turning-point half phase separate shows how the Frobenius monodromy and ordinary turning points cooperate.

VI.2: projection to the CDCC equations

Let $\boldsymbol{r}$ be the projectile internal coordinate and $\boldsymbol{R}$ its target separation. Expand the total wave function in retained projectile states and channel angular functions,

$$\Psi^{JM}(\boldsymbol{R}, \boldsymbol{r}) = \sum_c \frac{\chi_c^J(R)}{R}\left[\phi_{nI}(\boldsymbol{r}) \otimes Y_L(\widehat{\boldsymbol{R}})\right]_{JM}, \qquad c = (n, I, L). \tag{A.70}$$

Insert this expansion in $[T_R + h(\boldsymbol{r}) + U_{aA} + U_{bA} - E]\Psi = 0$, multiply by the conjugate channel function, and integrate over $\boldsymbol{r}$ and $\widehat{\boldsymbol{R}}$. Orthogonality and $h\phi_{nI} = \epsilon_{nI}\phi_{nI}$ give

$$\left[-\frac{\hbar^2}{2\mu_R}\left(\frac{\mathrm{d}^2}{\mathrm{d}R^2} - \frac{L_c(L_c+1)}{R^2}\right) + \epsilon_c - E\right]\chi_c^J(R) + \sum_{c'} U_{cc'}^J(R)\chi_{c'}^J(R) = 0, \tag{A.71}$$

where

$$U^{J}_{cc'}(R) = \langle [\phi_{nI} \otimes Y_L]_{JM} | \, U_{aA}(\boldsymbol{R}_a) + U_{bA}(\boldsymbol{R}_b) \, | [\phi_{n'I'} \otimes Y_{L'}]_{JM} \rangle \, . \quad \text{(A.72)}$$

Nothing in this derivation makes a positive-energy pseudostate a bound state. It is a basis vector in the finite model-space projection; physical breakup information is recovered only after convergence and smoothing.

VI.6: eliminating a closed reaction channel

For two coupled radial channels write

$$(E - H_{11})\chi_1 = V_{12}\chi_2, \qquad (E - H_{22})\chi_2 = V_{21}\chi_1. \quad \text{(A.73)}$$

The boundary condition in channel 2 fixes its Green operator, so

$$[E - H_{11} - U_{\rm pol}(E)]\,\chi_1 = 0, \qquad U_{\rm pol}(E) = V_{12}(E - H_{22})^{-1}V_{21}. \quad \text{(A.74)}$$

Below the second threshold, a self-adjoint H_{22} has no on-shell spectral weight at E. Its resolvent boundary value is real, and $U_{\rm pol}$ shifts and distorts the elastic potential without absorbing flux. Above threshold, Stone's formula gives

$$\operatorname{Im} U_{\rm pol}(E + \mathrm{i}0) = -\pi V_{12}\delta(E - H_{22})V_{21}, \quad \text{(A.75)}$$

which is negative semidefinite and supplies the reaction loss. Omitting closed CDCC channels can nevertheless change an elastic observable below threshold because their real dispersive contribution remains.

VII.1: the algebraic test for a second-order EP

For

$$H = \begin{pmatrix} a & b \\ b & d \end{pmatrix}, \qquad a, b, d \in \mathbb{C}, \quad \text{(A.76)}$$

the eigenvalues are

$$\lambda_{\pm} = \frac{a + d}{2} \pm \frac{1}{2}\sqrt{(a - d)^2 + 4b^2}. \quad \text{(A.77)}$$

They coalesce when the discriminant $D = (a - d)^2 + 4b^2$ vanishes. This condition is necessary but must be joined to a rank test. If $H = \lambda_* \mathbf{1}$, the eigenspace is two-dimensional and the degeneracy is ordinary. Otherwise

$\operatorname{rank}(H - \lambda_* \mathbf{1}) = 1$, the nullity is one, and the algebraic multiplicity two exceeds the geometric multiplicity: the point is an EP. Near a generic control value g_*, $D(g) = D'(g_*)(g - g_*) + \cdots$, so

$$\lambda_+ - \lambda_- \sim \sqrt{D'(g_*)}\,(g - g_*)^{1/2}. \tag{A.78}$$

The square-root exchange is thus derived from the secular equation. A plot showing close eigenvalues is not an EP diagnostic until defectiveness and the local Puiseux law have also been checked.

VII.2: resolvent of a length-two Jordan chain

Choose right vectors satisfying

$$(H - E_*)\psi_0 = 0, \qquad (H - E_*)\psi_1 = \psi_0, \tag{A.79}$$

and a dual chain normalized so that the nilpotent part is represented by $N = |\psi_0\rangle\langle\widetilde{\psi}_1|$ with $N^2 = 0$ on the root subspace. There $H = E_*\mathbf{1} + N$. For $z \neq E_*$,

$$(z - H)^{-1} = [(z - E_*)\mathbf{1} - N]^{-1} \tag{A.80}$$

$$= \frac{\mathbf{1}}{z - E_*} + \frac{N}{(z - E_*)^2}, \tag{A.81}$$

because the geometric series terminates at $N^2 = 0$. Restoring the explicit root-space identity gives a simple-pole projector assembled from both chain vectors and a double-pole coefficient proportional to $|\psi_0\rangle\langle\widetilde{\psi}_1|$. This is why solving only for the coalesced eigenvector loses information: the associated vector controls the principal part of the response.

VIII.1: Schwarzschild tortoise coordinate

For $f(r) = 1 - 2M/r$, radial null curves suggest defining $\mathrm{d}r_*/\mathrm{d}r = f^{-1}$. Partial fractions give

$$r_* = r + 2M \log\left|\frac{r}{2M} - 1\right| + C. \tag{A.82}$$

Outside the horizon, $r > 2M$. As $r = 2M + \varepsilon$ with $\varepsilon \downarrow 0$,

$$r_* = 2M \log\frac{\varepsilon}{2M} + O(1) \longrightarrow -\infty. \tag{A.83}$$

At large radius, $r_* = r + 2M\log(r/2M) + O(1) \to +\infty$. The logarithm's argument has been made dimensionless; changing its reference scale merely changes C. Under complex continuation, however, the logarithm also records a branch choice. That branch structure is why an unrestricted rotation of the entire r_* plane cannot be assumed to induce a single-valued rotation of r.

VIII.5: horizon signs as connection data

With time dependence $\mathrm{e}^{-\mathrm{i}\omega t}$, introduce $v = t + r_*$ and $u = t - r_*$. Near the future event horizon a smooth ingoing wave depends on v:

$$\mathrm{e}^{-\mathrm{i}\omega v} = \mathrm{e}^{-\mathrm{i}\omega t}\mathrm{e}^{-\mathrm{i}\omega r_*}. \tag{A.84}$$

At spatial infinity an outgoing wave depends on u:

$$\mathrm{e}^{-\mathrm{i}\omega u} = \mathrm{e}^{-\mathrm{i}\omega t}\mathrm{e}^{+\mathrm{i}\omega r_*}. \tag{A.85}$$

Let $f_{\mathrm{H}}^{\mathrm{in}}$ be the horizon-normalized ingoing solution. At infinity it has the connection expansion

$$f_{\mathrm{H}}^{\mathrm{in}} = \mathcal{C}_{\mathrm{out}}(\omega) f_{\infty}^{\mathrm{out}} + \mathcal{C}_{\mathrm{in}}(\omega) f_{\infty}^{\mathrm{in}}. \tag{A.86}$$

A QNM satisfies both physical conditions exactly when $\mathcal{C}_{\mathrm{in}}(\omega) = 0$. For $\operatorname{Im}\omega < 0$ these exponentials diverge on parts of the real r_* axis; that divergence is not a sign error but the reason analytic continuation, complex scaling, or a rigged-space pairing is needed to represent the same connection zero.

Glossary of recurring structures

Aguilar–Balslev–Combes theorem (ABC theorem).
Under dilation-analytic and relative-compactness hypotheses, complex dilation leaves bound eigenvalues fixed, rotates the essential spectrum, and exposes resonance poles as discrete eigenvalues independent of the dilation angle inside their exposure wedge. The theorem concerns an analytic operator family and is stronger than the visual stabilization of a finite matrix spectrum.

Adjoint operator.
For a densely defined operator A, the domain of A^* consists of vectors for which $\psi \mapsto \langle \phi, A\psi \rangle$ is continuous in the Hilbert norm. The domain is part of the definition; formal integration by parts alone does not prove that $A = A^*$.

Analytic dilation.
Continuation of a real coordinate dilation to a complex parameter in a sector where the Hamiltonian is an analytic family. It is theorem-controlled and is not synonymous with adding an absorber.

Analytic family of operators.
A parameter-dependent family whose resolvent, quadratic form, or action on a common domain is analytic in the sense specified by Kato. Stating the type and domain prevents a moving numerical matrix from being mistaken for analytic deformation of an unbounded Hamiltonian.

Analytic Fredholm theorem.
For an analytic compact-operator family $K(z)$, either $\mathbf{1} - K(z)$ is nowhere invertible or its inverse is meromorphic, with finite-rank principal parts at isolated poles. This is the operator-level bridge from an integral equation to a resonance pole.

Antiresonance.
The pole or connection zero paired with a resonance by the relevant reality, time-reversal, or sheet symmetry. It is not a second decaying state on the same physical boundary-value problem.

Asymptotic completeness.

The assertion that the ranges of the incoming and outgoing wave operators, together with bound states, exhaust the physical Hilbert space. Existence of Møller operators is weaker than completeness.

Berggren completeness relation.

A contour-deformed resolution combining discrete bound and resonant poles with a nonresonant continuum integral. Moving the contour can change which poles appear explicitly while leaving a complete observable unchanged.

Biorthogonal system.

Right and left vectors ψ_n and $\widetilde{\psi}_n$ satisfying $\langle\widetilde{\psi}_m|\psi_n\rangle = \delta_{mn}$ where diagonalization is possible. Near an exceptional point the normalization becomes singular and must be replaced by Jordan-chain data.

Birman–Schwinger operator.

A compactly sandwiched resolvent, for example $K(z) = |V|^{1/2}(H_0 - z)^{-1}\,\mathrm{sgn}(V)|V|^{1/2}$. Under the stated domain and compactness hypotheses, z is an eigenvalue or continued pole exactly when the corresponding $K(z)$ has eigenvalue one.

Borel transform and lateral sum.

The Borel transform divides the coefficient of $\hbar^n$ by a factorial so that a divergent formal series may acquire a finite convergence radius. Laplace integration just above or below a singular Borel ray defines the two lateral sums; their difference is a Stokes discontinuity.

Breit–Wigner approximation.

The Lorentzian real-axis form obtained from an isolated simple pole only after the background, residue, phase space, and self-energy are treated as slowly varying. Pole energy and fitted peak parameters need not agree for a broad or threshold-adjacent resonance.

Branch cut and sheet.

A cut is a convention used to make a multivalued analytic function single-valued on one chart; a sheet is the corresponding branch of its Riemann surface. Resonance statements must specify continuation relative to thresholds, not merely say “the second sheet.”

Channel.

A chosen asymptotic internal state, relative orbital motion, and set of conserved quantum numbers. An open channel carries flux at the selected energy; a closed channel decays asymptotically but can still generate a real polarization potential.

Continuum-discretized coupled channels (CDCC).

A projection method that replaces selected projectile-continuum sectors by normalized bins or pseudostates and solves the resulting coupled radial equations. Convergence is a statement about observables under enlargement of the model-space projection, not about individual positive-energy eigenvalues.

Continuum level density (CLD).

The imaginary part of a reference-subtracted resolvent trace. Under trace-class hypotheses it is the derivative of a scattering spectral shift and includes both pole and nonresonant continuum information.

Complex-scaled Lippmann–Schwinger method (CSLS).

A representation of a scattering resolvent in a complex-scaled basis, commonly used to smooth CDCC pseudostate amplitudes and resolve breakup spectra. Angle independence is recovered only after a sufficiently complete basis and consistent inverse transformation.

Complex scaling.

Analytic continuation of a dilation, commonly $r \mapsto r\mathrm{e}^{\mathrm{i}\theta}$, which converts an exposed outgoing resonance into an L^2 eigenproblem and rotates continuum cuts. Exterior and smooth variants modify the map while preserving the same analytic aim.

Connection coefficient.

A scalar minor or matrix block relating local solution bases in distinct asymptotic sectors. Its prohibited- incoming component is denoted $\mathcal{C}_{\mathrm{in}}$.

Continuous spectrum.

The spectral part in which $H - E$ fails to have a bounded inverse although E is not a normalizable eigenvalue. Generalized energy eigenvectors are distributions or fiber labels, not additional vectors of $\mathcal{H}$.

Continuum pseudostate.

A positive-energy L^2 eigenvector of a finite-basis diagonalization used

as a quadrature state. Its individual energy is normally representation dependent.

c product.
The bilinear pairing natural for a complex-symmetric matrix or a suitably scaled differential operator. It transposes rather than Hermitian conjugates the coefficient vector and must not be used when the operator's left problem has a different structure.

Direct integral.
A measure-theoretic continuum of Hilbert-space fibers, used here to represent energy and channel multiplicity.

Dollard comparison dynamics.
A long-range modifier of free motion that includes the logarithmic Coulomb phase before taking the scattering limit. It repairs the failure of the ordinary free Møller operator for Coulomb interactions.

Dressing sector.
An infrared representation in which charged asymptotic states carry a correlated cloud of soft gauge quanta. The required profile generally has infinite norm in the naive Fock one-particle space, so changing charge or velocity can move between inequivalent infrared sectors.

Effect and POVM.
An effect is an operator $0 \leq F \leq \mathbf{1}$ representing one measurement outcome. A positive-operator-valued measure assigns effects to measurable outcome sets and includes finite-resolution measurements that are not projection-valued.

Essential spectrum.
The part of the spectrum stable under the appropriate compact perturbations. Complex scaling rotates its threshold rays; finite-basis points sampling those rays are pseudostates rather than isolated spectrum of the exact operator.

Exceptional point (EP).
A parameter value at which eigenvalues and eigenvectors coalesce so that algebraic multiplicity exceeds geometric multiplicity. In the connection formulation it is a multiple zero supplemented by a defectiveness test.

Feshbach operator.

The energy-dependent operator on a retained P space obtained by solving the Q equation with a specified resolvent boundary value. Its derivative enters pole normalization because the eliminated sector remains encoded in the self-energy.

Fano profile.

The asymmetric intensity $|A_0|^2(\epsilon + q)^2/(1 + \epsilon^2)$ produced by coherent interference between a pole amplitude and a smooth background. Its maximum and zero are reaction dependent.

Fiber Hilbert space.

The multiplicity space $\mathcal{H}_E$ attached to almost every energy in a direct integral. Channel labels live in the fiber; measurable wave packets are square-integrable sections $E \mapsto \psi(E)$.

Gamow–Siegert state.

A solution satisfying outgoing boundary conditions at complex energy. It is generally not in the original Hilbert space.

Gelfand–Naimark–Segal construction (GNS).

The construction of a Hilbert-space representation from a positive linear functional on a C^* algebra. It makes explicit that a state is primary and a chosen Hilbert-space representation can depend on its physical sector.

Infrared divergence.

Failure of an integral at vanishing momentum or energy. In long-range scattering it can signal that the assumed asymptotic state space is wrong, rather than merely that a finite parameter needs renormalization.

Hilbert–Schmidt operator.

A compact operator whose squared singular values are summable. An integral kernel $K(x, y)$ is Hilbert–Schmidt when $\int |K(x, y)|^2 \mathrm{d}x\mathrm{d}y < \infty$; then finite-rank kernel approximations converge in Hilbert–Schmidt, hence operator, norm.

Jost function.

A Wronskian coefficient between a solution regular at an interior endpoint and an asymptotic incoming/outgoing basis. Under suitable short-

range and analyticity assumptions, its zeros identify bound, virtual, resonant, or antiresonant poles according to their sheet and quadrant.

Jordan chain.
Vectors satisfying $(H - E_*)\psi_0 = 0$ and $(H - E_*)\psi_{j+1} = \psi_j$. A chain of length two produces both simple and double terms in the resolvent principal part.

Langer correction.
The $l(l+1) \mapsto (l+1/2)^2$ term obtained when the radial equation is transformed logarithmically and its wave function is treated as a half-density. It records origin monodromy rather than an empirical WKB patch.

Møller or wave operator.
The strong limit comparing full and reference time evolution at early or late times. Its definition includes the comparison Hamiltonian; for Coulomb or QED asymptotics, free Fock or free-particle comparison may be inadequate.

Monodromy.
The linear transformation of a local solution basis after analytic continuation around a closed path. Turning points, regular singular points, and coordinate Jacobians contribute distinguishable factors.

Nuclear optical potential.
A generally complex, energy-dependent effective interaction for an elastic or selected channel. Its absorptive part represents flux into eliminated channels and should not be confused with fundamental nonunitarity of the full many-body Hamiltonian.

Projection-valued measure (PVM).
The countably additive family of orthogonal projections supplied by the spectral theorem for a self-adjoint operator. Matrix elements of the PVM define scalar spectral measures and direct-integral decompositions.

Quasinormal mode (QNM).
A mode satisfying ingoing conditions at a future black-hole horizon and outgoing or appropriate cosmological/AdS conditions at the other endpoint. With $\mathrm{e}^{-\mathrm{i}\omega t}$, a decaying mode has $\operatorname{Im}\omega < 0$.

Resolvent.
$\mathcal{R}(z) = (z - H)^{-1}$ on the resolvent set. Its boundary values encode the spectral measure; matrix elements or weighted versions may admit analytic continuation through a continuous-spectrum cut even though the bounded Hilbert-space operator does not.

Resonance.
A pole of an analytically continued resolvent or scattering matrix, equivalently a zero of the appropriate Jost or incoming connection function under the stated hypotheses.

Residue.
The coefficient of $(z - z_R)^{-1}$ in a Laurent expansion. It contains the normalization-invariant product of left and right pole data and is required to predict response strength; a pole position alone is incomplete.

Representation datum.
A contour, scaling angle, test topology, basis, bin width, or infrared sector chosen to realize an invariant analytic quantity.

Riesz projection.
For an isolated spectral cluster inside a contour Γ, the operator $(2\pi\mathrm{i})^{-1} \oint_\Gamma (z - H)^{-1}\mathrm{d}z$. It is invariant under basis changes and treats a fragmented or nearly degenerate resonance as a subspace rather than as a preferred list of eigenvectors.

Rigged Hilbert space.
A continuous dense embedding $\Phi \subset \mathcal{H} \subset \Phi^\times$ in which generalized eigenvectors act as continuous functionals on a test space. The topology of Φ determines which Gamow and scattering functionals exist.

***R*-matrix.**
A boundary relation obtained by solving an interior problem at a chosen channel radius and matching it to known exterior functions. Physical observables should become insensitive to the channel radius and boundary parameter in a complete expansion.

Self-adjoint extension.
A choice of operator domain, often encoded by boundary data, that makes a symmetric differential operator equal to its adjoint. Different extensions can represent different physical contact or endpoint data.

Spectral measure.

For a vector ψ and PVM $P(\cdot)$, the positive measure $\mu_\psi(B) = \langle \psi, P(B)\psi \rangle$. Survival amplitudes are Fourier transforms of such measures; exponential decay is therefore an intermediate-time approximation when a threshold is present.

Spectral shift.

The reference-subtracted change in spectral counting associated with a pair (H, H_0). Its derivative is a continuum level density and its exponential is related to $\det S$ by the Birman–Krein formula under the appropriate hypotheses.

Sturm–Liouville operator.

The differential expression $w^{-1}[-(pu')' + qu]$ together with its weighted Hilbert space, maximal domain, and endpoint boundary conditions. The expression alone does not define a self-adjoint operator.

Stokes curve and Stokes matrix.

A Stokes curve is a locus where the phase relation between local WKB branches changes dominance. Crossing it changes the resummed basis by a triangular Stokes matrix; the path-ordered product with propagation factors is the global connection matrix.

Threshold.

The endpoint of an asymptotic channel continuum and hence a branch point of its resolvent. Threshold powers can dominate late-time decay and can compete with the square-root branching of a nearby exceptional point.

Topology.

A specification of which sets are open, equivalently which convergence and continuity statements are meaningful. Norm, strong, weak, weak-star, and test-function topologies answer different physical questions and must not be silently interchanged.

von Neumann algebra.

A unital $*$ algebra of bounded operators closed in the weak-operator topology, equivalently equal to its bicommutant. Abelian spectral algebras are multiplication algebras; their direct-integral fibers expose channel multiplicity and superselection structure.

Voros symbol.

The Borel-resummed exponential of an exact-WKB period integral on the spectral curve.

Wronskian.

The determinant of two local solutions and their derivatives. It is constant for a second-order equation without a first-derivative term, fixes the Green-kernel denominator, and provides a sensitive determinant check for transfer and Stokes matrices.

Weyl–Titchmarsh function.

The coefficient $m(z)$ selecting the solution square integrable at a limit-point endpoint. Its boundary value determines the spectral measure, while its analytically continued poles encode the same denominator as the Jost or Green-function construction.

Zel'dovich regularization.

Gaussian damping of a divergent outgoing pairing followed by analytic continuation in the regulator.

Bibliographical notes

These notes are a reading map, not an additional review chapter. The main text was written to be calculationally self-contained; references here record sources, alternative proofs, and routes to subjects which lie beyond the book's connection-first line. A work listed here is cited at the point where it becomes useful, rather than being placed in an undifferentiated list of "further references."

Mathematical and quantum-mechanical foundations

For Hilbert-space quantum mechanics, unbounded operators, and the spectral theorem, the volumes of Reed and Simon remain a standard bridge between physics and functional analysis [26]; Kato is the natural next reference for closed operators, analytic families, and perturbation theory [33]. Trace ideals and determinant technology are treated systematically by Simon [34]. Titchmarsh and Zettl give complementary classical and modern routes through Sturm–Liouville theory [40, 41]. The point of Stages I-A and I-B is not to replace these books, but to derive exactly the subset needed when a continuum spectral problem is analytically continued.

The direct-integral and operator-algebra discussion is indebted to the decomposition theory initiated by von Neumann and to modern accounts of von Neumann algebras [27, 28]. Bratteli and Robinson develop the C^*- and von Neumann-algebraic language in a form adapted to quantum statistical mechanics [31]; Haag is the standard physical entrance to local quantum physics [30]. These sources also make clear why an energy-fiber direct integral, a central factor decomposition, and a superselection decomposition answer different questions. The book keeps those three decompositions separate before using them in scattering or gauge theory.

For rigged Hilbert spaces, the foundational distribution-theoretic setting is due to Gelfand and collaborators [32]. Pedagogical treatments of continuous spectra and Gamow vectors may be found in Refs. [96, 98]. They are best read after the explicit Gaussian continuation in Stage IV, where the topology on the test space is seen to be part of the construction rather than decorative notation.

Scattering, Jost functions, and long-range sectors

Newton and Taylor are broad references for nonrelativistic scattering [37, 42]; Yafaev gives a mathematically systematic account of wave operators and spectral methods [29]. The Zel'dovich school emphasizes resonances and quasistationary states [38]. Rakityansky and Elander organize multichannel scattering around the Jost matrix [39], while the Japanese textbook tradition represented here by Sasakawa provides a compact route from elementary quantum mechanics to practical scattering calculations [36]. Kukulin and collaborators connect this material to resonant-state expansions and nuclear applications [35]; the Berggren ensemble and its modern many-body use are surveyed in Ref. [95].

Long-range scattering requires a different comparison dynamics, not a small correction to a plane wave. Dollard's construction is fundamental [46, 47]. For three charged particles, the Faddeev–Merkuriev framework and subsequent asymptotic analyses display why pairwise Coulomb phases do not by themselves give a single uniform global form [49–55]. This is the few-body counterpart of the infrared warning in field theory: the asymptotic state is part of the dynamics.

The soft-photon problem begins historically with inclusive cancellation [56, 61], but a state-level description requires dressing. Chung and Kulish–Faddeev are classic constructions [57, 58]; Buchholz explains the charge-sector obstruction in algebraic terms [59]. Modern dressed-state and asymptotic-symmetry formulations relevant to the discussion in Stage II include Refs. [60, 62–64]. Dirac's gauge-invariant charged field is an important precursor [65].

For gauge constraints, BRST cohomology in the form used by particle physicists is represented by Kugo and Ojima [66]. Gribov copies and Singer's obstruction explain why the global nonperturbative problem cannot be inferred from local gauge fixing alone [67, 68]. Algebraic sector theory starts from observables [69, 70]. Discussions of gauge-theory entanglement and edge structures make the loss of a naive tensor product operational [73–75]; the Hamiltonian lattice starting point goes back to Kogut and Susskind [71]. Quantum-simulation encodings give a current computational realization of the same constraint issue [72].

Exact WKB and resurgence

Voros's analysis of the quartic oscillator is a landmark in the passage from formal WKB to exact spectral information [12]. The Japanese school developed the microlocal and connection-formula foundations; useful entry points include Refs. [105–107, 186]. Problems with many phases and global Stokes geometry are treated in Refs. [187–189]. Hypergeometric benchmarks provide a useful laboratory for checking normalization and connection conventions [190].

Delabaere and Pham give a classical resurgent treatment of semiclassical asymptotics [13]; Dorigoni is a convenient field-theory introduction to transseries and alien calculus [183]. Nikolaev's work gives a modern geometric view of exact WKB and abelianization [191–193]. Wall-crossing formulations for quadratic differentials and related spectral networks connect this material to wider geometric structures [194, 195]. These developments are not required to execute the one-dimensional connection calculations in Stage III, but they clarify which parts of the construction survive for higher-order or coupled systems.

The calculation program underlying the present book began by formulating resonances nonperturbatively in exact WKB [17, 140], then unified Zel'dovich regularization, complex scaling, and rigged Hilbert spaces [25, 196]. Continuum spectra and radial equations were developed next [15, 20, 197]. The ordering of Stage III reflects the conceptual conclusion of that sequence: the connection coefficient is primary; its operator and functional realizations are representations of the same analytic datum.

Complex scaling, resonance functionals, and response

The Aguilar–Balslev–Combes theorem originates in Refs. [6, 7]; Simon's account isolates the operator-theoretic mechanism [89], and Herbst treats important dilation-analytic spectral questions [198]. Exterior complex scaling is developed in Ref. [86]. Moiseyev's book and reviews connect the theorem to practical non-Hermitian spectral calculations [88, 139, 199].

Zel'dovich introduced Gaussian regularization for decaying states [2]. Berggren supplied the decisive resonant-state normalization and completeness constructions [3, 94, 200, 201]. Stage IV repeats the regulated integrations

because the angular sector in which the Gaussian limit exists is exactly what later becomes a complex-scaling or exact-WKB Stokes-sector statement.

Feshbach's projection formalism is the source of the energy-dependent effective Hamiltonian used throughout the book [4, 5]. Modern discussions of the equivalence between effective Hamiltonians and resonant boundary conditions include Ref. [202]. Continuum level-density and complex-scaled response methods in nuclear physics are reviewed in Refs. [8, 181]. Pseudospectral cautions should be read alongside the elementary resolvent estimates; Trefethen's introduction is a compact entry point [93].

Radial motion, few-body nuclei, and CDCC

The Langer modification is traced to the original connection-formula paper [104]; the earlier geometric quantization context is represented by Maslov and Arnol'd [203, 204]. Recent studies of power-law radial spectra provide useful numerical and semiclassical comparisons [205, 206]. The monodromy-renormalization proposal in Stage V is more specific: it keeps the singular endpoint data invariant while changing the perturbative seed, and its present limitations are stated in Sec. 11.3.5.

CDCC grew from coupled-channel discretizations of breakup [117, 118] and now has a broad reaction-theory formulation [119]. Four-body CDCC and complex-scaled Lippmann–Schwinger smoothing are developed in Refs. [120, 123, 124]. Gaussian expansion methods are described in Ref. [101]; the microscopic effective interaction used in many folding calculations is represented by Ref. [122]. The relation to exact few-body equations is anchored by the Faddeev and Alt–Grassberger–Sandhas equations [115, 116]; the R-matrix interior–exterior split is traced to Lane and Thomas [114].

The lithium and beryllium laboratories are not generic examples appended to the formalism. They record the line of nuclear-structure and reaction work from which the model-space and channel questions arise [125–131]. Their role in the book is to test whether pole positions, residues, smoothing, and measured cross sections remain stable under one common truncation protocol.

Exceptional points

Non-Hermitian effective Hamiltonians in open systems and their resonance interpretation are reviewed by Rotter [9, 207]. Broader modern perspectives

are given in Ref. [10]. Experiments and models which expose encircling, state transfer, and topology include Refs. [133, 135, 136]. Thresholds can modify exceptional-point decay laws and apparent order [21, 24]; this is why Stage VII keeps the continuum regulator visible.

The complex-scaling calculation of resonance holonomy developed by the authors treats an exceptional point as a multiple zero of the same incoming connection coefficient used for an isolated resonance [16]. Black-hole applications make the relation between mode coalescence, excitation, and spectral instability especially current [208, 209]. These papers motivate the open problem of a regulator-independent continuum holonomy, but do not yet settle it.

Black-hole quasinormal modes

The Regge–Wheeler equation begins with Regge and Wheeler [143]; Zerilli supplied the even-parity formulation and charged generalizations [147, 210]. Moncrief's gauge-invariant Hamiltonian treatments [144, 152, 153] and the covariant derivation of Martel and Poisson [145] are the main checks on the derivation in Stage VIII. Chandrasekhar's monograph remains the standard source for transformations between master equations [148, 211].

General reviews of quasinormal modes include Refs. [11, 141, 212]. Leaver's continued fractions and Green-function analysis are central numerical and analytic benchmarks [102, 149]; Nollert developed the high-overtone implementation [164]. Late-time tails and branch-cut response are treated in Ref. [150]. Hyperboloidal formulations clarify the operator and continuum structure [213, 214], while pseudospectral instability is emphasized in Ref. [165].

Exact-WKB approaches to black-hole spectra include Refs. [142, 155, 161, 162]. The complex-scaling program developed in the final laboratories treats the horizon conditions as rotated asymptotic sectors and retains continuum response [18, 19]. The de Sitter extension makes the two-horizon connection problem explicit. For comparisons with current spectroscopy and excitation questions, see Refs. [215–218].

Resummation appendix

The instanton and large-order background for Chap. A is presented pedagogically by Mariño [184]. Optimized perturbation, linear delta expansion, variational perturbation, and ODM are represented by Refs. [108–112]. Multi-instanton structure in quantum mechanics is developed in Refs. [77, 219]. The public calculation repository and Wolfram Community article give the software provenance of the supplied compact code [182, 185]. The book's conclusion is intentionally narrower than any one of these sources: resummation becomes resonance theory only after its directional analytic continuation is tied to a physical connection condition.

Bibliography

[1] A. J. F. Siegert, "On the derivation of the dispersion formula for nuclear reactions," *Phys. Rev.* **56** (Oct, 1939) 750–752.

[2] Y. B. Zel'dovich, "On the theory of unstable states," *Zh. Éksp. Teor. Fiz.* **39** (1961) 776. [Sov. Phys. JETP 12, 542 (1961)].

[3] T. Berggren, "On the use of resonant states in eigenfunction expansions of scattering and reaction amplitudes," *Nucl. Phys. A* **109** (1968) 265–287.

[4] H. Feshbach, "Unified theory of nuclear reactions," *Annals of Physics* **5** no. 4, (Dec., 1958) 357–390. https://doi.org/10.1016/0003-4916(58)90007-1.

[5] H. Feshbach, "A unified theory of nuclear reactions. ii," *Annals of Physics* **19** no. 2, (Aug., 1962) 287–313. https://doi.org/10.1016/0003-4916(62)90221-X.

[6] J. Aguilar and J. M. Combes, "A class of analytic perturbations for one-body schroedinger hamiltonians," *Commun. Math. Phys.* **22** (1971) 269–279.

[7] E. Balslev and J. M. Combes, "Spectral properties of many-body schroedinger operators with dilatation-analytic interactions," *Commun. Math. Phys.* **22** (1971) 280–294.

[8] T. Myo, Y. Kikuchi, H. Masui, and K. Katō, "Recent development of complex scaling method for many-body resonances and continua in light nuclei," *Prog. Part. Nucl. Phys.* **79** (2014) 1–56, arXiv:1410.4356 [nucl-th].

[9] I. Rotter, "A non-Hermitian Hamilton operator and the physics of open quantum systems," *J. Phys. A* **42** no. 15, (2009) 153001, arXiv:0711.2926 [quant-ph].

[10] Y. Ashida, Z. Gong, and M. Ueda, "Non-Hermitian physics," *Adv. Phys.* **69** no. 3, (2020) 249–435, arXiv:2006.01837 [cond-mat.mes-hall].

[11] E. Berti, V. Cardoso, and A. O. Starinets, "Quasinormal modes of black holes and black branes," *Class. Quant. Grav.* **26** (2009) 163001, arXiv:0905.2975 [gr-qc].

[12] A. Voros, "The return of the quartic oscillator. the complex wkb method," *Ann. Inst. Henri Poincaré* **39** no. 3, (1983) 211–338.

[13] E. Delabaere and F. Pham, "Resurgent methods in semi-classical asymptotics," *Ann. Inst. Henri Poincaré* **71** (1999) 1–94.

[14] K. Iwaki and T. Nakanishi, "Exact WKB analysis and cluster algebras," *J. Phys. A* **47** no. 47, (2014) 474009, arXiv:1401.7094 [math.CA].

[15] O. Morikawa and S. Ogawa, "Nonperturbative Formulation of Resonances in Quantum Mechanics Based on Exact WKB Method," *PTEP* **2025** no. 10, (2025) 103B01, arXiv:2503.18741 [hep-th].

[16] O. Morikawa and S. Ogawa, "Unified exact WKB framework for resonance – Zel'dovich/complex-scaling regularization and rigged Hilbert space," *JHEP* **10** (2025) 049, arXiv:2505.02301 [hep-th].

[17] O. Morikawa and S. Ogawa, "On continuum and resonant spectra from exact WKB analysis," *J. Phys. A* **59** no. 22, (2026) 225306, arXiv:2508.09211 [quant-ph].

[18] S. Ogawa, T. Hirose, and O. Morikawa, "Complex scaling approach to quasinormal modes of Schwarzschild and Reissner–Nordström black holes," arXiv:2604.20442 [hep-th].

[19] S. Ogawa, O. Morikawa, and T. Hirose, "Quasinormal modes and continuum response of de Sitter black holes via complex scaling method," arXiv:2605.03277 [hep-th].

[20] O. Morikawa, S. Ogawa, and S. Onoda, "Geometric phase from encircling an exceptional point of a quantum resonance in the complex-scaling method," *Phys. Rev. A* **113** no. 5, (2026) 052225, arXiv:2512.24528 [quant-ph].

[21] S. Garmon, G. Ordonez, and N. Hatano, "Anomalous-order exceptional point and non-Markovian Purcell effect at threshold in one-dimensional continuum systems," *Phys. Rev. Research* **3** (2021) 033029, arXiv:2104.06929 [quant-ph].

[22] M. Peshkin, A. Volya, and V. Zelevinsky, "Non-exponential and oscillatory decays in quantum mechanics," *EPL* **107** no. 4, (2014) 40001, arXiv:1703.05238 [nucl-th].

[23] F. Giacosa, "Non-exponential decay in quantum field theory and in quantum mechanics: The case of two or more decay channels," *Found. Phys.* **42** (2012) 1262–1299.

[24] S. Garmon and G. Ordonez, "Non-exponential decay near the continuum threshold," *J. Math. Phys.* **58** (2017) 062101.

[25] O. Morikawa and S. Ogawa, "Exact WKB method for radial Schrödinger equation," *J. Phys. A* **59** no. 14, (2026) 145202, arXiv:2510.11766 [quant-ph].

[26] M. Reed and B. Simon, *Methods of Modern Mathematical Physics. Vol. I: Functional Analysis*. Academic Press, San Diego, revised and enlarged ed., 1980.

[27] M. Takesaki, *Theory of Operator Algebras I*, vol. 124 of *Encyclopaedia of Mathematical Sciences*. Springer, Berlin, 2002.

[28] J. von Neumann, "On Rings of Operators. Reduction Theory," *Annals Math.* **50** no. 2, (1949) 401–485.

[29] D. R. Yafaev, *Mathematical Scattering Theory: General Theory*, vol. 105 of *Translations of Mathematical Monographs*. American Mathematical Society, Providence, 1992.

[30] R. Haag, *Local Quantum Physics: Fields, Particles, Algebras*. Theoretical and Mathematical Physics. Springer, Berlin, 2 ed., 1996.

[31] O. Bratteli and D. W. Robinson, *Operator Algebras and Quantum Statistical Mechanics 1*. Springer, Berlin, 2 ed., 1987.

[32] I. Gel'fand and N. Vilenkin, eds., *Generalized Functions Vol. 4: Applications of Harmonic Analysis*. Academic Press, 1964. https://www.sciencedirect.com/science/article/pii/B9781483229744500019.

[33] T. Kato, *Perturbation Theory for Linear Operators*. Classics in Mathematics. Springer, Berlin, 2 ed., 1995.

[34] B. Simon, *Trace Ideals and Their Applications*, vol. 120 of *Mathematical Surveys and Monographs*. American Mathematical Society, Providence, Rhode Island, 2 ed., 2005.

[35] V. I. Kukulin, V. M. Krasnopol'sky, and J. Horáček, *Theory of Resonances: Principles and Applications*, vol. 3 of *Reidel Texts in the Mathematical Sciences*. Kluwer Academic Publishers, Dordrecht, 1989.

[36] T. Sasakawa, *Scattering Theory*, vol. 20 of *Butsurigaku Sensho*. Shokabo, Tokyo, 1991. In Japanese; print-on-demand edition, 2018, ISBN 978-4-7853-0638-0.

[37] J. R. Taylor, *Scattering Theory: The Quantum Theory of Nonrelativistic Collisions*. John Wiley & Sons, Inc., New York, 1972.

[38] A. M. Perelomov and Y. B. Zel'dovich, *Quantum Mechanics: Selected Topics*. World Scientific, Singapore, 1998.

[39] S. A. Rakityansky, *Jost Functions in Quantum Mechanics: A Unified Approach to Scattering, Bound, and Resonant State Problems*. Springer, Cham, 2022.

[40] E. C. Titchmarsh, *Eigenfunction Expansions Associated with Second-Order Differential Equations, Part I*. Clarendon Press, Oxford, 2 ed., 1962.

[41] A. Zettl, *Sturm–Liouville Theory*, vol. 121 of *Mathematical Surveys and Monographs*. American Mathematical Society, Providence, Rhode Island, 2005.

[42] R. G. Newton, "Analytic properties of radial wave functions," *Journal of Mathematical Physics* **1** no. 4, (07, 1960) 319–347. https://doi.org/10.1063/1.1703665.

[43] N. Andersson, "Excitation of Schwarzschild black-hole quasinormal modes," *Phys. Rev. D* **51** (1995) 353–363.

[44] N. Oshita and V. Cardoso, "Reconstruction of ringdown with excitation factors," *Phys. Rev. D* **111** no. 10, (2025) 104043, arXiv:2407.02563 [gr-qc].

[45] K.-i. Kubota and H. Motohashi, "Resonance in black-hole ringdown: Benchmarking quasinormal-mode excitation and extraction," *Phys. Rev. D* **113** no. 4, (2026) 043053, arXiv:2509.06411 [gr-qc].

[46] J. D. Dollard, "Asymptotic Convergence and the Coulomb Interaction," *J. Math. Phys.* **5** no. 6, (1964) 729–738.

[47] J. D. Dollard, "Quantum-Mechanical Scattering Theory for Short-Range and Coulomb Interactions," *Rocky Mountain J. Math.* **1** no. 1, (1971) 5–88.

[48] J. Dereziński and C. Gérard, *Scattering Theory of Classical and Quantum N-Particle Systems*. Theoretical and Mathematical Physics. Springer, Berlin, 1997.

[49] E. O. Alt and A. M. Mukhamedzhanov, "Asymptotic Solution of the Schrödinger Equation for Three Charged Particles," *Phys. Rev. A* **47** no. 3, (1993) 2004–2022.

[50] A. M. Mukhamedzhanov and M. Lieber, "Asymptotic Wave Function for Three Charged Particles in the Continuum," *Phys. Rev. A* **54** no. 4, (1996) 3078–3085.

[51] A. S. Kadyrov, A. T. Stelbovics, I. Bray, A. M. Mukhamedzhanov, and F. Pirlepesov, "Asymptotic Behavior of the Coulomb Three-Body Scattered Wave," *Phys. Rev. A* **68** no. 2, (2003) 022703.

[52] A. M. Mukhamedzhanov, A. S. Kadyrov, and F. Pirlepesov, "Leading Asymptotic Terms of the Three-Body Coulomb Scattering Wave Function," *Phys. Rev. A* **73** (2006) 012713, arXiv:nucl-th/0509012.

[53] S. L. Yakovlev, "Asymptotic Behavior of the Wavefunction for the Scattering of Three Particles with the Coulomb Interaction," *JETP Lett.* **116** (2022) 268–274, arXiv:2206.07374 [math-ph].

[54] L. D. Faddeev and S. P. Merkuriev, *Quantum Scattering Theory for Several Particle Systems*, vol. 11 of *Mathematical Physics and Applied Mathematics*. Springer, Dordrecht, 1993.

[55] S. Keller, A. Marotta, and Z. Papp, "Faddeev–Merkuriev Integral Equations for Atomic Three-Body Resonances," *J. Phys. B* **42** no. 4, (2009) 044003, arXiv:0810.3036 [physics.atom-ph].

[56] F. Bloch and A. Nordsieck, "Note on the Radiation Field of the Electron," *Phys. Rev.* **52** (1937) 54–59.

[57] V. Chung, "Infrared Divergence in Quantum Electrodynamics," *Phys. Rev.* **140** (1965) B1110–B1122.

[58] P. P. Kulish and L. D. Faddeev, "Asymptotic Conditions and Infrared Divergences in Quantum Electrodynamics," *Theor. Math. Phys.* **4** (1970) 745–757.

[59] D. Buchholz, "Gauss' Law and the Infraparticle Problem," *Phys. Lett. B* **174** no. 3, (1986) 331–334.

[60] T. Chen, J. Fröhlich, and A. Pizzo, "Infraparticle Scattering States in Non-Relativistic QED: I. The Bloch–Nordsieck Paradigm," *Commun. Math. Phys.* **294** (2010) 761–825, arXiv:0709.2493 [math-ph].

[61] D. R. Yennie, S. C. Frautschi, and H. Suura, "The Infrared Divergence Phenomena and High-Energy Processes," *Annals Phys.* **13** no. 3, (1961) 379–452.

[62] H. Hirai and S. Sugishita, "Dressed States from Gauge Invariance," *JHEP* **06** (2019) 023, arXiv:1901.09935 [hep-th].

[63] H. Hirai and S. Sugishita, "IR Finite S-Matrix by Gauge Invariant Dressed States," *JHEP* **02** (2021) 025, arXiv:2009.11716 [hep-th].

[64] H. Hirai and S. Sugishita, "Dress Code for Infrared Safe Scattering in QED," *PTEP* **2023** no. 5, (2023) 053B04, arXiv:2209.00608 [hep-th].

[65] P. A. M. Dirac, "Gauge-Invariant Formulation of Quantum Electrodynamics," *Can. J. Phys.* **33** no. 11, (1955) 650–660.

[66] T. Kugo and I. Ojima, "Local Covariant Operator Formalism of Non-Abelian Gauge Theories and Quark Confinement Problem," *Prog. Theor. Phys. Suppl.* **66** (1979) 1–130.

[67] V. N. Gribov, "Quantization of Non-Abelian Gauge Theories," *Nucl. Phys. B* **139** (1978) 1–19.

[68] I. M. Singer, "Some Remarks on the Gribov Ambiguity," *Commun. Math. Phys.* **60** (1978) 7–12.

[69] S. Doplicher, R. Haag, and J. E. Roberts, "Local Observables and Particle Statistics. I," *Commun. Math. Phys.* **23** (1971) 199–230.

[70] D. Buchholz and K. Fredenhagen, "Locality and the Structure of Particle States," *Commun. Math. Phys.* **84** (1982) 1–54.

[71] J. Kogut and L. Susskind, "Hamiltonian Formulation of Wilson's Lattice Gauge Theories," *Phys. Rev. D* **11** (1975) 395–408.

[72] G. Pardo, T. Greenberg, A. Fortinsky, N. Katz, and E. Zohar, "Resource-Efficient Quantum Simulation of Lattice Gauge Theories in Arbitrary Dimensions: Solving for Gauss' Law and Fermion Elimination," *Phys. Rev. Research* **5** (2023) 023077, arXiv:2206.00685 [quant-ph].

[73] H. Casini, M. Huerta, and J. A. Rosabal, "Remarks on Entanglement Entropy for Gauge Fields," *Phys. Rev. D* **89** (2014) 085012, arXiv:1312.1183 [hep-th].

[74] W. Donnelly and L. Freidel, "Local Subsystems in Gauge Theory and Gravity," *JHEP* **09** (2016) 102, arXiv:1601.04744 [hep-th].

[75] C. J. Fewster, "The Split Property for Locally Covariant Quantum Field Theories in Curved Spacetime," *Lett. Math. Phys.* **105** (2015) 1633–1661, arXiv:1501.02682 [math-ph].

[76] E. B. Bogomolny, "CALCULATION OF INSTANTON - ANTI-INSTANTON CONTRIBUTIONS IN QUANTUM MECHANICS," *Phys. Lett. B* **91** (1980) 431–435.

[77] J. Zinn-Justin, "Multi - Instanton Contributions in Quantum Mechanics," *Nucl. Phys. B* **192** (1981) 125–140.

[78] G. V. Dunne, "Perturbative - nonperturbative connection in quantum mechanics and field theory," in *Continuous Advances in QCD 2002 / ARKADYFEST (honoring the 60th birthday of Prof. Arkady Vainshtein)*, pp. 478–505. 7, 2002. arXiv:hep-th/0207046.

[79] G. V. Dunne and M. Ünsal, "What is QFT? Resurgent trans-series, Lefschetz thimbles, and new exact saddles," *PoS* **LATTICE2015** (2016) 010, arXiv:1511.05977 [hep-lat].

[80] N. Rosen and P. M. Morse, "On the vibrations of polyatomic molecules," *Phys. Rev.* **42** (Oct, 1932) 210–217. https://link.aps.org/doi/10.1103/PhysRev.42.210.

[81] M. Zhao, "Dynamical resonances and lifetimes in rigged hilbert spaces," *Phys. Lett. A* **204** (1995) 319–322.

[82] L. D. Landau and E. M. Lifshits, *Quantum Mechanics: Non-Relativistic Theory*, vol. v.3 of *Course of Theoretical Physics*. Butterworth-Heinemann, Oxford, 1991.

[83] V. Ryaboy and N. Moiseyev, "Cumulative reaction probability from siegert eigenvalues: Model studies," *The Journal of Chemical Physics* **98** no. 12, (06, 1993) 9618–9623.

[84] N. Hatano, "Equivalence of the effective Hamiltonian approach and the Siegert boundary condition for resonant states," *Fortsch. Phys.* **61** (2013) 238, arXiv:1405.7021 [quant-ph].

[85] N. Michel, W. Nazarewicz, M. Płoszajczak, and T. Vertse, "Shell model in the complex energy plane," *Journal of Physics G: Nuclear and Particle Physics* **36** no. 1, (Oct, 2008) 013101.

[86] B. Simon, "The definition of molecular resonance curves by the method of exterior complex scaling," *Phys. Lett. A* **71** (1979) 211–214.

[87] W. P. Reinhardt, "Complex coordinates in the theory of atomic and molecular structure and dynamics," *Annual Review of Physical Chemistry* **33** no. Volume 33,, (1982) 223–255. https://www.annualreviews.org/content/journals/10.1146/annurev.pc.33.100182.001255.

[88] N. Moiseyev, *Non-Hermitian Quantum Mechanics*. Cambridge University Press, Cambridge, 2011.

[89] B. Simon, "Quadratic form techniques and the Balslev-Combes theorem," *Commun. Math. Phys.* **27** no. 1, (1972) 1–9.

[90] B. Simon, "Resonances in n-body quantum systems with dilatation analytic potentials and the foundations of time-dependent perturbation theory," *Annals of Mathematics* **97** no. 2, (1973) 247–274. http://www.jstor.org/stable/1970847.

[91] E. B. Davies, "Non-self-adjoint differential operators," *Bulletin of the London Mathematical Society* **34** no. 5, (2002) 513–532.

[92] E. B. Davies, *Linear Operators and their Spectra*. Cambridge Studies in Advanced Mathematics. Cambridge University Press, 2007.

[93] L. N. Trefethen, *Spectra and Pseudospectra*, pp. 217–250. Springer Berlin Heidelberg, Berlin, Heidelberg, 1999. https://doi.org/10.1007/978-3-662-03972-4_6.

[94] T. Berggren, "Expectation value of an operator in a resonant state," *Physics Letters B* **373** no. 1, (1996) 1–4.

[95] N. Michel and M. Płoszajczak, *Gamow Shell Model: The Unified Theory of Nuclear Structure and Reactions*, vol. 983 of *Lecture Notes in Physics*. Springer, Cham, 2021.

[96] R. de la Madrid, A. Bohm, and M. Gadella, "Rigged Hilbert Space Treatment of Continuous Spectrum," *Fortsch. Phys.* **50** (2002) 185–216, arXiv:quant-ph/0109154.

[97] R. de la Madrid, "Rigged Hilbert Space Approach to the Schrodinger Equation," *J. Phys. A* **35** (2002) 319–342, arXiv:quant-ph/0110165.

[98] R. de la Madrid and M. Gadella, "A Pedestrian introduction to Gamow vectors," *Am. J. Phys.* **70** (2002) 626–638, arXiv:quant-ph/0201091.

[99] R. de la Madrid, "The rigged Hilbert space approach to the Gamow states," *J. Math. Phys.* **53** (2012) 102113.

[100] I. Antoniou, Y. Melnikov, and E. Yarevsky, "The connection between the rigged hilbert space and the complex scaling approaches for resonances. the friedrichs model," *Chaos, Solitons & Fractals* **12** (2001) 2683–2688.

[101] E. Hiyama, Y. Kino, and M. Kamimura, "Gaussian expansion method for few-body systems," *Prog. Part. Nucl. Phys.* **51** (2003) 223–307.

[102] E. W. Leaver, "An Analytic representation for the quasi normal modes of Kerr black holes," *Proc. Roy. Soc. Lond. A* **402** (1985) 285–298.

[103] T. Miyachi and R. Namba, "Private communication," 2025. Private communication.

[104] R. E. Langer, "On the connection formulas and the solutions of the wave equation," *Phys. Rev.* **51** (1937) 669–676.

[105] T. Aoki, T. Kawai, and Y. Takei, "New turning points in the exact WKB analysis for higher-order ordinary differential equations," 1991. RIMS Preprint.

[106] T. Kawai and Y. Takei, *Algebraic Analysis of Singular Perturbation Theory*. American Mathematical Society, Providence, Rhode Island, 2005.

[107] T. Aoki, K. Iwaki, and T. Takahashi, "Exact WKB analysis of Schrödinger equations with a Stokes curve of loop type," *Funkcial. Ekvac.* **62** no. 1, (2019) 1–34.

[108] P. M. Stevenson, "Optimized Perturbation Theory," *Phys. Rev. D* **23** (1981) 2916.

[109] A. Duncan and H. F. Jones, "Convergence proof for optimized delta expansion: The anharmonic oscillator," *Phys. Rev. D* **47** (1993) 2560–2572.

[110] I. R. C. Buckley, A. Duncan, and H. F. Jones, "Proof of the convergence of the linear delta expansion," *Phys. Rev. D* **47** (1993) 2554–2559.

[111] H. Kleinert and W. Janke, "Convergence behavior of variational perturbation expansion: A method for locating Bender–Wu singularities," *Phys. Lett. A* **206** (1995) 283, arXiv:quant-ph/9509005.

[112] J. Zinn-Justin, "Summation of divergent series: Order-dependent mapping," 2010. Contribution to Approximation and Extrapolation of Convergent and Divergent Sequences and Series.

[113] T. Miyachi, R. Namba, H. Omiya, and N. Oshita, "Path to an exact WKB analysis of black hole quasinormal modes," *Phys. Rev. D* **111** no. 12, (2025) 124045, arXiv:2503.17245 [hep-th].

[114] A. M. Lane and R. G. Thomas, "R-Matrix Theory of Nuclear Reactions," *Rev. Mod. Phys.* **30** (1958) 257–353.

[115] L. D. Faddeev, "Scattering theory for a three-particle system," *Sov. Phys. JETP* **12** (1961) 1014–1019.

[116] E. O. Alt, P. Grassberger, and W. Sandhas, "Reduction of the three-particle collision problem to multi-channel two-particle Lippmann–Schwinger equations," *Nucl. Phys. B* **2** (1967) 167–180.

[117] M. Kamimura, M. Yahiro, Y. Iseri, Y. Sakuragi, H. Kameyama, and M. Kawai, "Projectile breakup processes in nuclear reactions," *Prog. Theor. Phys. Suppl.* **89** (1986) 1–10.

[118] N. Austern, Y. Iseri, M. Kamimura, M. Kawai, G. Rawitscher, and M. Yahiro, "Continuum-discretized coupled-channels calculations for three-body models of deuteron-nucleus reactions," *Phys. Rept.* **154** (1987) 125–204.

[119] M. Yahiro, K. Ogata, T. Matsumoto, and K. Minomo, "The continuum discretized coupled-channels method and its applications," *PTEP* **2012** (2012) 01A206, arXiv:1203.5392 [nucl-th].

[120] T. Matsumoto, E. Hiyama, K. Ogata, Y. Iseri, M. Kamimura, S. Chiba, and M. Yahiro, "Continuum-discretized coupled-channels method for four-body nuclear breakup in ^{6}He+^{12}C scattering," *Phys. Rev. C* **70** (2004) 061601, arXiv:nucl-th/0409016.

[121] T. Matsumoto, K. Kato, and M. Yahiro, "New description of four-body breakup reaction," *Phys. Rev. C* **82** (2010) 051602, arXiv:1006.0668 [nucl-th].

[122] J.-P. Jeukenne, A. Lejeune, and C. Mahaux, "Optical-model potential in finite nuclei from Reid's hard core interaction," *Phys. Rev. C* **16** (1977) 80–96.

[123] Y. Kikuchi, T. Myo, M. Takashina, K. Kato, and K. Ikeda, "Coulomb breakup reactions in complex-scaled solutions of the Lippmann–Schwinger equation," *Prog. Theor. Phys.* **122** (2009) 499–510, arXiv:0905.1541 [nucl-th].

[124] Y. Kikuchi, K. Kato, T. Myo, M. Takashina, and K. Ikeda, "Two-neutron correlations in ^{6}He in a Coulomb breakup reaction," *Phys. Rev. C* **81** (2010) 044308.

[125] S. Ogawa and T. Matsumoto, "Investigation of contributions of the 2^{+}_{2} resonance in ^{6}He via analysis of the $^{6}\mathrm{He}(p,p')$ reaction," *Phys. Rev. C* **102** (2020) 021602, arXiv:2003.05123 [nucl-th].

[126] S. Ogawa, T. Matsumoto, Y. Kanada-En'yo, and K. Ogata, "Investigation of multistep effects for proton inelastic scattering to the 2^{+}_{1} state in ^{6}He," *Phys. Rev. C* **104** (2021) 044608, arXiv:2103.16865 [nucl-th].

[127] S. Ogawa and T. Matsumoto, "Dineutron in the 2^{+}_{1} state of ^{6}He," *Phys. Rev. C* **105** (2022) L041601, arXiv:2111.04285 [nucl-th].

[128] S. Ogawa, *Study on the Resonant Structure via the Analysis of Breakup Reaction*. Doctoral thesis, Kyushu University, 2022. https://hdl.handle.net/2324/4784400.

[129] K. Ogata and S. Ogawa, "Description of nucleon elastic scattering off ^{6}Li with the four-body continuum-discretized coupled-channels method," arXiv:2602.15492 [nucl-th].

[130] S. Ogawa, T. Fukui, J. Singh, and K. Ogata, "Determination of S_{18} from ^{9}C breakup reaction within a four-body reaction model," *PTEP* **2026** no. 7, (2026) 073D03, arXiv:2504.04026 [nucl-th].

[131] S. Ogawa, K. Yoshida, Y. Chazono, and K. Ogata, "Three-body analysis reveals a significant contribution of a minor ^{5}He s-wave component in the $^{6}\mathrm{Li}(p,2p)^{5}\mathrm{He}$ cross section," *Phys. Rev. C* **111** no. 3, (2025) 034622, arXiv:2404.17814 [nucl-th].

[132] N. Foroozani, M. Naghiloo, D. Tan, K. Mølmer, and K. W. Murch, "Correlations of the time-dependent signal and the state of a continuously monitored quantum system," *Phys. Rev. Lett.* **116** (2016) 110401, arXiv:1508.01185 [quant-ph].

[133] M. Naghiloo, M. Abbasi, Y. N. Joglekar, and K. W. Murch, "Quantum state tomography across the exceptional point in a single dissipative qubit," *Nature Phys.* **15** no. 12, (2019) 1232–1236, arXiv:1901.07968 [quant-ph].

[134] H.-P. Breuer, E.-M. Laine, J. Piilo, and B. Vacchini, "Colloquium: Non-Markovian dynamics in open quantum systems," *Rev. Mod. Phys.* **88** (2016) 021002, arXiv:1505.01385 [quant-ph].

[135] C. Gneiting, A. V. Rozhkov, and F. Nori, "Jumptime unraveling of Markovian open quantum systems," *Phys. Rev. A* **104** (2021) 062212, arXiv:2001.08929 [quant-ph].

[136] Z. Gong, Y. Ashida, K. Kawabata, K. Takasan, S. Higashikawa, and M. Ueda, "Topological phases of non-Hermitian systems," *Phys. Rev. X* **8** (2018) 031079.

[137] S. Yao and Z. Wang, "Edge states and topological invariants of non-Hermitian systems," *Phys. Rev. Lett.* **121** (2018) 086803.

[138] A. Alase, E. Cobanera, G. Ortiz, and L. Viola, "Exact Solution of Quadratic Fermionic Hamiltonians for Arbitrary Boundary Conditions," *Phys. Rev. Lett.* **117** (2016) 076804, arXiv:1601.05486 [cond-mat.supr-con].

[139] N. Moiseyev, *Non-Hermitian Quantum Mechanics*. Cambridge University Press, Cambridge, 2011.

[140] O. Morikawa and S. Ogawa, "Nonperturbative Formulation of Resonances in Quantum Mechanics Based on Exact WKB Method," *PTEP* **2025** no. 10, (2025) 103B01, arXiv:2503.18741 [hep-th].

[141] K. D. Kokkotas and B. G. Schmidt, "Quasinormal modes of stars and black holes," *Living Rev. Rel.* **2** (1999) 2, arXiv:gr-qc/9909058.

[142] Y. Hatsuda and M. Kimura, "Spectral Problems for Quasinormal Modes of Black Holes," *Universe* **7** no. 12, (2021) 476, arXiv:2111.15197 [gr-qc].

[143] T. Regge and J. A. Wheeler, "Stability of a Schwarzschild singularity," *Phys. Rev.* **108** (1957) 1063–1069.

[144] V. Moncrief, "Gravitational perturbations of spherically symmetric systems. I. The exterior problem," *Annals Phys.* **88** (1974) 323–342.

[145] K. Martel and E. Poisson, "Gravitational perturbations of the Schwarzschild spacetime: A practical covariant and gauge-invariant formalism," *Phys. Rev. D* **71** (2005) 104003, arXiv:gr-qc/0502028.

[146] A. Nagar and L. Rezzolla, "Gauge-invariant non-spherical metric perturbations of Schwarzschild black-hole spacetimes," *Class. Quant. Grav.* **22** (2005) R167–R192, arXiv:gr-qc/0502064.

[147] F. J. Zerilli, "Gravitational field of a particle falling in a schwarzschild geometry analyzed in tensor harmonics," *Phys. Rev. D* **2** (1970) 2141–2160.

[148] S. Chandrasekhar, *The Mathematical Theory of Black Holes*. Oxford University Press, 09, 1998. https://doi.org/10.1093/oso/9780198503705.001.0001.

[149] E. W. Leaver, "Spectral decomposition of the perturbation response of the Schwarzschild geometry," *Phys. Rev. D* **34** (1986) 384–408.

[150] E. S. C. Ching, P. T. Leung, W. M. Suen, and K. Young, "Late time tail of wave propagation on curved space-time," *Phys. Rev. Lett.* **74** (1995) 2414–2417, arXiv:gr-qc/9410044.

[151] M. Casals, S. Dolan, A. C. Ottewill, and B. Wardell, "Self-Force and Green Function in Schwarzschild spacetime via Quasinormal Modes and Branch Cut," *Phys. Rev. D* **88** (2013) 044022, arXiv:1306.0884 [gr-qc].

[152] V. Moncrief, "Odd-parity stability of a Reissner-Nordstrom black hole," *Phys. Rev. D* **9** (1974) 2707–2709.

[153] V. Moncrief, "Stability of Reissner-Nordstrom black holes," *Phys. Rev. D* **10** (1974) 1057–1059.

[154] H. Onozawa, T. Mishima, T. Okamura, and H. Ishihara, "Quasinormal modes of maximally charged black holes," *Phys. Rev. D* **53** (1996) 7033–7040, arXiv:gr-qc/9603021.

[155] Y. Hatsuda and T. Shiga, "Exact WKB and Quantum Periods for Extremal Black Hole Quasinormal Modes," arXiv:2605.01321 [gr-qc].

[156] V. Baibhav, M. H.-Y. Cheung, E. Berti, V. Cardoso, G. Carullo, R. Cotesta, W. Del Pozzo, and F. Duque, "Agnostic black-hole spectroscopy: Quasinormal-mode content of numerical-relativity waveforms and limits of validity of linear perturbation theory," *Phys. Rev. D* **108** no. 10, (2023) 104020, arXiv:2302.03050 [gr-qc].

[157] M. H.-Y. Cheung, E. Berti, V. Baibhav, and R. Cotesta, "Extracting linear and nonlinear quasinormal modes from black-hole merger simulations," *Phys. Rev. D* **109** no. 4, (2024) 044069, arXiv:2310.04489 [gr-qc]. [Errata: Phys. Rev. D 110, 049902 (2024); 112, 049901 (2025)].

[158] K. Mitman *et al.*, "Probing the ringdown perturbation in binary black-hole coalescences with an improved quasinormal-mode extraction algorithm," *Phys. Rev. D* **112** no. 6, (2025) 064016, arXiv:2503.09678 [gr-qc].

[159] N. Oshita, E. Berti, and V. Cardoso, "Unstable chords and destructive resonant excitation of black-hole quasinormal modes," *Phys. Rev. Lett.* **135** no. 3, (2025) 031401, arXiv:2503.21276 [gr-qc].

[160] L. Motl and A. Neitzke, "Asymptotic black hole quasinormal frequencies," *Adv. Theor. Math. Phys.* **7** no. 2, (2003) 307–330, arXiv:hep-th/0301173.

[161] Y. Hatsuda, "Quasinormal modes of black holes and Borel summation," *Phys. Rev. D* **101** no. 2, (2020) 024008, arXiv:1906.07232 [gr-qc].

[162] Y. Hatsuda and M. Kimura, "Perturbative quasinormal mode frequencies," *Phys. Rev. D* **109** no. 4, (2024) 044026, arXiv:2307.16626 [gr-qc].

[163] S. A. Teukolsky, "Rotating black holes - separable wave equations for gravitational and electromagnetic perturbations," *Phys. Rev. Lett.* **29** (1972) 1114–1118.

[164] H.-P. Nollert, "Quasinormal modes of Schwarzschild black holes: The determination of quasinormal frequencies with very large imaginary parts," *Phys. Rev. D* **47** (1993) 5253–5258.

[165] J. L. Jaramillo, R. Panosso Macedo, and L. Al Sheikh, "Pseudospectrum and Black Hole Quasinormal Mode Instability," *Phys. Rev. X* **11** no. 3, (2021) 031003, arXiv:2004.06434 [gr-qc].

[166] Y. Yang, Z.-F. Mai, R.-Q. Yang, L. Shao, and E. Berti, "Spectral instability of black holes: Relating the frequency domain to the time domain," *Phys. Rev. D* **110** no. 8, (2024) 084018, arXiv:2407.20131 [gr-qc].

[167] R. F. Rosato, K. Destounis, and P. Pani, "Ringdown stability: Greybody factors as stable gravitational-wave observables," *Phys. Rev. D* **110** no. 12, (2024) L121501, arXiv:2406.01692 [gr-qc].

[168] R. Suzuki, T. Myo, and K. Katō, "Level density in complex scaling method," *AIP Conf. Proc.* **768** no. 1, (2005) 455, arXiv:nucl-th/0502012.

[169] Y. Avishai and Y. B. Band, "One-dimensional density of states and the phase of the transmission amplitude," *Phys. Rev. B* **32** (Aug, 1985) 2674–2676. https://link.aps.org/doi/10.1103/PhysRevB.32.2674.

[170] T. Harmark, J. Natario, and R. Schiappa, "Greybody Factors for d-Dimensional Black Holes," *Adv. Theor. Math. Phys.* **14** no. 3, (2010) 727–794, arXiv:0708.0017 [hep-th].

[171] W.-H. Bian and Z.-F. Cui, "Quasinormal modes of coupled metric-dilaton perturbations in two-dimensional stringy black holes," arXiv:2604.05988 [gr-qc].

[172] H. Kodama and A. Ishibashi, "A Master equation for gravitational perturbations of maximally symmetric black holes in higher dimensions," *Prog. Theor. Phys.* **110** (2003) 701–722, arXiv:hep-th/0305147.

[173] A. Ishibashi and H. Kodama, "Stability of higher dimensional Schwarzschild black holes," *Prog. Theor. Phys.* **110** (2003) 901–919, arXiv:hep-th/0305185.

[174] A. Ishibashi and H. Kodama, "Perturbations and Stability of Static Black Holes in Higher Dimensions," *Prog. Theor. Phys. Suppl.* **189** (2011) 165–209, arXiv:1103.6148 [hep-th].

[175] A. Zhidenko, "Quasinormal modes of Schwarzschild de Sitter black holes," *Class. Quant. Grav.* **21** (2004) 273–280, arXiv:gr-qc/0307012.

[176] N. Oshita, "Greybody factors imprinted on black hole ringdowns: An alternative to superposed quasinormal modes," *Phys. Rev. D* **109** no. 10, (2024) 104028, arXiv:2309.05725 [gr-qc].

[177] R. A. Konoplya and A. Zhidenko, "Correspondence between grey-body factors and quasinormal modes," *JCAP* **09** (2024) 068, arXiv:2406.11694 [gr-qc].

[178] Y. Avishai and Y. B. Band, "One-dimensional density of states and the phase of the transmission amplitude," *Phys. Rev. B* **32** (1985) 2674(R)–2676(R).

[179] R. A. Konoplya, "Gravitational quasinormal radiation of higher dimensional black holes," *Phys. Rev. D* **68** (2003) 124017, arXiv:hep-th/0309030.

[180] J. Piilo, S. Maniscalco, K. Härkönen, and K.-A. Suominen, "Non-Markovian Quantum Jumps," *Phys. Rev. Lett.* **100** no. 18, (2008) 180402, arXiv:0706.4438 [quant-ph].

[181] T. Myo and K. Katō, "Possible interpretation of the complex expectation values associated with resonances," *Phys. Rev. C* **107** no. 1, (2023) 014301, arXiv:2301.05355 [nucl-th].

[182] O. Morikawa, "Resummation: Some Resummation Techniques Based on Perturbation Theory." Github repository, 2024. https://github.com/o-morikawa/Resummation. Version inspected at commit 11a9b71b8038c82080d31b803a40129921235934.

[183] D. Dorigoni, "An Introduction to Resurgence, Trans-Series and Alien Calculus," *Annals Phys.* **409** (2019) 167914, arXiv:1411.3585 [hep-th].

[184] M. Marino, *Instantons and Large N: An Introduction to Non-Perturbative Methods in Quantum Field Theory*. Cambridge University Press, 2015.

[185] O. Morikawa, "Nonperturbative Formulation of Resonances in Quantum Mechanics Based on Exact WKB Method." Wolfram community, publication materials, 2026. https://community.wolfram.com/groups/-/m/t/3635564.

[186] T. Aoki and J.-i. Yoshida, "Microlocal reduction of ordinary differential operators with a large parameter," *Publ. Res. Inst. Math. Sci.* **29** no. 6, (1993) 959–975.

[187] T. Aoki, T. Kawai, T. Koike, and Y. Takei, "On global aspects of exact WKB analysis of operators admitting infinitely many phases," 2003. RIMS Preprint.

[188] T. Aoki, T. Kawai, T. Koike, and Y. Takei, "On the exact WKB analysis of operators admitting infinitely many phases," *Adv. Math.* **181** no. 1, (2004) 165–189.

[189] T. Aoki, T. Kawai, T. Koike, and Y. Takei, "On the exact WKB analysis of microdifferential operators of WKB type," *Ann. Inst. Fourier* **54** no. 5, (2004) 1393–1421.

[190] T. AOKI, T. TAKAHASHI, and M. TANDA, "The hypergeometric function, the confluent hypergeometric function and WKB solutions," *J. Math. Soc. Jap.* **73** no. 4, (2021) 1019–1062.

[191] N. Nikolaev, "Abelianisation of logarithmic $\mathfrak{sl}_2$-connections," *Selecta Math.* **27** no. 5, (2021) 78, arXiv:1902.03384 [math.AG].

[192] N. Nikolaev, "Existence and Uniqueness of Exact WKB Solutions for Second-Order Singularly Perturbed Linear ODEs," *Commun. Math. Phys.* **400** no. 1, (2023) 463–517, arXiv:2106.10248 [math.AP].

[193] N. Nikolaev, "Geometry and Resurgence of WKB Solutions of Schrödinger Equations," 2410.17224 [math.DG].

[194] D. G. L. Allegretti, "On the Wall-Crossing Formula for Quadratic Differentials," *Int. Math. Res. Not.* **2023** no. 9, (2023) 8033–8077, arXiv:2006.08059 [math.GT].

[195] A. Grassi, Q. Hao, and A. Neitzke, "Exponential Networks, WKB and Topological String," *SIGMA* **19** (2023) 064, arXiv:2201.11594 [hep-th].

[196] O. Morikawa and S. Ogawa, "Unified exact WKB framework for resonance – Zel'dovich/complex-scaling regularization and rigged Hilbert space," *JHEP* **10** (2025) 049, arXiv:2505.02301 [hep-th].

[197] O. Morikawa and S. Ogawa, "On continuum and resonant spectra from exact WKB analysis," *J. Phys. A* **59** no. 22, (2026) 225306, arXiv:2508.09211 [quant-ph].

[198] I. W. Herbst and B. Simon, "DILATION ANALYTICITY IN CONSTANT ELECTRIC FIELD. II. N BODY PROBLEM, BOREL SUMMABILITY," *Commun. Math. Phys.* **80** (1981) 181–216.

[199] N. Moiseyev, "Quantum theory of resonances: calculating energies, widths and cross-sections by complex scaling," *Phys. Rept.* **302** no. 5-6, (1998) 212–293.

[200] T. Berggren, "On the treatment of resonant final states in direct reactions," *Nuclear Physics A* **169** no. 2, (1971) 353–362.

[201] T. Berggren, "On the interpretation of complex cross sections for production of resonant final states," *Physics Letters B* **73** no. 4, (1978) 389–392.

[202] N. Hatano, "Equivalence of the effective Hamiltonian approach and the Siegert boundary condition," arXiv:1405.7021 [quant-ph].

[203] V. P. Maslov, *Teoriya vozmushchenii i asimptoticheskie metody.* Moscow University Press, Moscow, 1965. In Russian.

[204] V. I. Arnol'd, "Characteristic class entering in quantization conditions," *Funct. Anal. Appl.* **1** no. 1, (1967) 1–13.

[205] J. C. del Valle and A. V. Turbiner, "Power-like potentials: From the Bohr—Sommerfeld energies to exact ones," *Int. J. Mod. Phys. A* **36** no. 29, (2021) 2150221, arXiv:2108.00327 [quant-ph].

[206] J. C. del Valle and A. V. Turbiner, "Radial power-like potentials: From the Bohr–Sommerfeld S-state energies to the exact ones," *Int. J. Mod. Phys. A* **38** no. 17, (2023) 2350092, arXiv:2305.11363 [quant-ph].

[207] I. Rotter, "Non-hermitian hamilton operator in open quantum systems," arXiv:0711.2926 [quant-ph].

[208] R. Panosso Macedo, T. Katagiri, K.-i. Kubota, and H. Motohashi, "Exceptional Points and Resonance in Black Hole Ringdown," arXiv:2512.02110 [gr-qc].

[209] T. Takahashi, H. Motohashi, and K. Takahashi, "Resonance of black hole quasinormal modes in coupled systems," *Phys. Rev. D* **112** no. 6, (2025) 064006, arXiv:2505.03883 [gr-qc].

[210] F. J. Zerilli, "Perturbation analysis for gravitational and electromagnetic radiation in a reissner-nordstroem geometry," *Phys. Rev. D* **9** (1974) 860–868.

[211] S. Chandrasekhar, "On the equations governing the perturbations of the Schwarzschild black hole," *Proc. Roy. Soc. Lond. A* **343** no. 1634, (1975) 289–298.

[212] R. A. Konoplya and A. Zhidenko, "Quasinormal modes of black holes: From astrophysics to string theory," *Rev. Mod. Phys.* **83** (2011) 793–836, arXiv:1102.4014 [gr-qc].

[213] M. Ansorg and R. Panosso Macedo, "Spectral decomposition of black-hole perturbations on hyperboloidal slices," *Phys. Rev. D* **93** no. 12, (2016) 124016, arXiv:1604.02261 [gr-qc].

[214] R. Panosso Macedo and A. Zenginoglu, "Hyperboloidal approach to quasinormal modes," *Front. in Phys.* **12** (2024) 1497601, arXiv:2409.11478 [gr-qc].

[215] H. Motohashi, "Resonant Excitation of Quasinormal Modes of Black Holes," *Phys. Rev. Lett.* **134** no. 14, (2025) 141401, arXiv:2407.15191 [gr-qc].

[216] M. De Amicis, E. Cannizzaro, G. Carullo, and L. Sberna, "Dynamical quasinormal-mode excitation," *Phys. Rev. D* **113** no. 2, (2026) 024048, arXiv:2506.21668 [gr-qc].

[217] J. Abedi *et al.*, "Black-hole spectroscopy: From theory to experiment," arXiv:2505.23895 [gr-qc].

[218] J. Su, N. Khera, M. Casals, S. Ma, A. Chowdhuri, and H. Yang, "Decomposition of Schwarzschild Green's Function," arXiv:2601.22015 [gr-qc].

[219] U. D. Jentschura and J. Zinn-Justin, "Multi-instantons and exact results. IV: Path integral formalism," *Annals Phys.* **326** (2011) 2186–2242.

Subject index